Anatomy, biomechanics, and evolution of the archosaur ribcage with implications for the evolution of ventilation

by

Yan-Yin Wang

A thesis submitted in partial fulfillment of the requirements for the degree of

Doctor of Philosophy

in

Systematics and Evolution

Department of Biological Sciences
University of Alberta

Abstract

Extant birds and crocodylians are modern representatives of Archosauria, a group of amniote vertebrates with a long evolutionary history that may be traced back to the Triassic Period. On the paths to extant bird and crocodylians, early archosaurs diversified and occupied many niches available for large-bodied amniotes throughout the Mesozoic Era. As with other amniotes, respiration is one of the fundamental biological processes needed to sustain the life of archosaurs, which consists of multiple steps that range from ventilating air into and out of the respiratory organs, to gas exchange at the blood-air barrier in the lung, to cellular respiration. This contribution pertains to the trunk anatomy and ventilatory biomechanics in archosaurs.

The cervicodorsal transition marks the start of the trunk, and is traditionally defined by the first connection between the vertebral column and the sternum via rib segments. However, most archosaurs had cartilaginous sterna and sternal ribs, which are not well documented in the fossil record, and no consensus exists on how to identify cervicodorsal transitions in archosaurs without preserved sterna. We survey 29 extant and 32 fossil archosaurs for anatomical features that appear to change across the cervicodorsal transition, and use this information to propose criteria that identify regions of the vertebral series where the first sternal connection is likely to be located. Supervised statistical models based on features of vertebrae are created using a combination of linear discriminant analysis, logistic regressions, NaïveBayes classifier, and RandomForest, but the models can only accurately identify the cervicodorsal transition in sampled extant archosaurs.

Vertebral ribs of the trunk in extant birds carry bony prongs called uncinate processes, which have been hypothesised to enhance a bird's ability to expand the trunk and draw

ventilatory airflow into the respiratory organs. Tab-like cartilaginous uncinate processes are present in crocodylians. In the fossil record, uncinate processes occur as ossified prongs only in maniraptoriform dinosaurs, but occur as mineralised cartilage in several ornithischian dinosaurs and one notosuchian crocodyliform. We establish an osteological correlate, termed the uncinate scar, by removing uncinate processes from vertebral ribs of extant archosaurs, and use the correlate to infer the presence of cartilaginous uncinate processes in 19 fossil archosaurs. Using the augmented distribution of uncinate processes by inferences from uncinate scars, we further infer that uncinate processes, with their capacity to enhance ventilation, are likely a homologous feature shared by most dinosaurs and may even be plesiomorphic for Archosauria. Histological sections through dorsal vertebral ribs carrying uncinate processes or uncinate scars are made for two extant archosaurs and four fossil dinosaurs, and we consistently find bundles of coarse collagen fibres at uncinate scars, bolstering the conclusion that uncinate scars are attachment sites for uncinate processes.

Trunk muscles of the common raven *Corvus corax*, the emu *Dromaius novaehollandiae*, and three crocodylians are dissected to document the attachment sites of trunk muscles, which are used as a basis to compare the trunk muscle configuration among archosaurs carrying and lacking uncinate processes. We find that m. appendicocsotalis, a muscle attached to uncinate processes in most birds, remains present in the emu *Dromaius novaehollandiae*, which lacks uncinate processes.

We construct three kinematic models, from ribcages of the ostrich *Struthio camelus* and the spectacled caiman *Caiman crocodilus*. Using tidal volume documented in the literature, we estimate the plausible motions of the ribcage, which are comparable to observations from *in vivo* studies. To infer the contributions made to ventilation by various trunk muscles, we construct

two three-dimensional kinetic models to estimate changes in their moment arms during ventilation. The results suggest that uncinate processes in palaeognath birds provide an enhanced ability to protract the vertebral ribs, while limiting their potential for abduction by altering the mechanical leverage and fibre orientation of m. appendicocostalis. By comparison, uncinate processes in crocodylians likely provide an enhanced ability to protract and abduct simultaneously. The contrasts in muscle function between palaeognath birds and crocodylians are likely related to the morphology and muscle configuration of the trunk.

Our anatomical and biomechanical studies, taken together, indicate that ventilation enhanced by the additional mechanical leverage provided by uncinate processes was likely widespread in, and may even have been plesiomorphic for, Archosauria.

Preface

This thesis contains my original work and the results of collaborative research with scholars in evolutionary biology and palaeontology.

Chapter 2 is an unpublished collaboration by Y. Y. Wang and C. Sullivan on the cervicodorsal transition in archosaurs. I was responsible for designing the study, collect raw data from museum collections, analysing the data, and drafting the manuscript. C. Sullivan contributed to designing the study, interpreting the data, and writing the manuscript.

Chapter 3 is an unpublished collaboration by Y. Y. Wang, Y. Ma, and C. Sullivan on the cervicodorsal transition in archosaurs. I was responsible for designing the study, collecting the raw data, running the statistical analyses, and drafting the manuscript. Y. Ma and C. Sullivan contributed to the raw data collection, and may also contribute to preparing the manuscript for publication.

A version of Chapter 4 has been published as Y. Y. Wang, L.P.A.M. Claessens, C. Sullivan, 2023. Deep reptilian evolutionary roots of a major avian respiratory adaptation. Commun Biol 6, 3. https://doi.org/10.1038/s42003-022-04301-z. I was responsible for designing the study, collecting and analysing the data, and drafting the manuscript. C. Sullivan contributed towards designing the study, interpreting the data, and writing the manuscript. L.P.A.M. Claessens contributed to interpreting the data and writing the manuscript.

Chapter 5 is an unpublished collaboration by Y. Y. Wang, A.R.H. LeBlanc, L.P.A.M. Claessens, and C. Sullivan on the histology of uncinate process attachment in archosaurs. I was responsible for designing the study, making the histological thin sections, analysing the data, and drafting the manuscript. A.R.H. LeBlanc contributed to designing the study, making the histological thin sections, interpreting the data, and writing the manuscript. L.P.A.M. Claessens and C. Sullivan contributed to interpreting the data and writing the manuscript.

Chapter 6 is an unpublished collaboration by Y. Y. Wang, M.M. Rhodes, and C. Sullivan on the myology of the trunk and pelvis in archosaurs. I was responsible for designing the study, carrying out the trunk dissections, and drafting the manuscript. M.M. Rhodes was responsible for the pelvic dissections, and performing the Phylogenetic Generalised Least Squares regressions,

and drafting the manuscript. C. Sullivan contributed to the trunk dissections and to writing the manuscript.

Chapter 7 is an unpublished collaboration by Y. Y. Wang and C. Sullivan on estimating ventilatory motions in archosaurs using kinematic models. I was responsible for designing the study, creating the kinematic models, analysing the data, and drafting the manuscript. C. Sullivan contributed to designing the study, interpreting the data, and writing the manuscript.

Chapter 8 is an unpublished collaboration by Y. Y. Wang and C. Sullivan on inferring the ventilatory functions of various trunk muscles in archosaurs using kinetic models. I was responsible for designing the study, creating the kinetic models, analysing the moment arm data, and drafting the manuscript. C. Sullivan contributed to designing the study, interpreting the data, and writing the manuscript.

To my family, for their unconditional love and support.

Acknowledgement

The necessity of respiration in vertebrate life has continuously been a subject of wonder, discussion, and dispute. Following the guiding steps of scholars who came before me, I have been fortunate to continue on their path in fathoming the nature of archosaur respiration and evolution.

My academic journey would not be possible without all the support and nourishments I have received, and I express my deepest gratitude to everyone who has supported and encouraged me throughout my journey.

First and foremost, I would like to express my sincere gratitude to my supervisor Corwin Sullivan, for the opportunity to pursue my academic interests. Corwin sparked my interest in functional morphology when I took his class on comparative osteology, and subsequently introduced me to classical studies by Steven Vogel, which most definitely fueled my decision to pursue a PhD. Over the past five years as a member of the Sullivan lab, I have systematically acquired knowledge of the deep evolutionary history of archosaurs, and at times, even had my moments of erudition. Corwin's wisdoms and scholarly insights have been sources of inspirations and guidance. I am honoured to have been part of the Sullivan lab.

I am extremely grateful to my other supervisory committee members, Leon P.A.M. Claessens and Alison Murray. Leon's expertise in archosaur respiration has guided me in navigating through the large body of literature on this subject, without which flipping through pages of Perry's work would have been challenging. Alison's guidance and knowledge always helped me stay on track and improve my scholarly capacity beyond the topic of respiration in archosaurs.

I would like to express my gratitude to my additional examining committee members, John Acorn and Darla Zelenitsky. Thank you for critically examining my thesis and providing constructive feedback. Special thank you to John Acorn and Philip Currie for serving on my candidacy committee.

Many scholars have shared insights, research equipment, and specimens that have facilitated my professional growth, and the development of this thesis over the past years. I would like to express my appreciation to John Acorn, Michael Caldwell, Philip Currie, Eva

Koppelhus, Aaron LeBlanc, and Heather Proctor for the opportunities and nurturing environment you have provided.

Studies of fossils would not be possible without their preparation and management by dedicated staff working at museum collections. I would like to thank Braden Barr, Eva Biedron, Daniel Brinkman, Di Binghe, Clive Coy, Margaret Currie, Howard Gibbons, Jordan Mallon, Carl Mehling, Kevin Seymour, Nicole Ridgwell, Robin Ssissons, and Brandon Strilisky for facilitating the collections of data presented in this thesis.

I have been extremely fortunate to work with and alongside brilliant scholars, including scholars in training like myself. I would like to thank Phil Bell, Emily Bamforth, Katherine Bramble, Amy Cameron, Nicolàs Campione, Margaret Cross, Colton Coppock, Julien Divay, Meghan Dueck, Aaron Dyer, Nathan J. Enriquez, Greg Funston, Christiana Garros, Samantha Hamilton, Michael Hudgins, Qigao Jiangzuo, Lindsay Kastroll, Jasdeep Kaur, Lu Li, Hao Liang, Jun Liu, Brayden Longley-Holland, Yubo Ma, Annie McIntosh, Tetsuto Miyashita, Sydney Mohr, Nathaniel Morley, Khoi Nguyen, Alessandro Palci, Ilaria Paparella, Scott Persons, Mark Powers, Tiago Simões, Hallie Street, Luthfur Rahman, Cameron Reed, Aaron van der Reest, Matthew Rhodes, Henry Sharpe, Sinjini Sinha, Jordon Stock, Brandon Theurer, Matthew Vavrek, Oksana V. Vernygora, Rebekah Vice, Wei Wang, Matt White, Taia Wyenberg-Henzler, Xiao-Chun Wu, and Cong-Yu Yu for insightful discussions and all the positive influence you have had on me.

Above all, I would not have embarked on this academic journey without unconditional love and support from my family. Despite being on the opposite side of the Earth, love, support, and faith from my family members have helped me navigate many challenges throughout this journey. I am eternally grateful to you.

Table of Contents

List of Tables

List of Figures

Institutional Abbreviations

AMNH: American Museum of Natural History; **CMN:** Canadian Museum of Nature; **IVPP:** Institute of Vertebrate Paleontology and Paleoanthropology; **MCZ:** Harvard Museum of Comparative Zoology; **ROM:** Royal Ontario Museum; **TMP:** Tyrrell Museum of Palaeontology; **UALVP:** University of Alberta Laboratory for Vertebrate Palaeontology; **YPM:** Yale Peabody Museum.

Anatomical Abbreviations

APC, m. appendicocostalis; CFP, mm. caudofemorales pars pelvica; COT, m. costosternalis; CP, m. costoplumonare; dIC, dorsal part of m. iliocostalis; IC, m. iliocostalis; IE, mm. intercostales externi; IFI, m. iliofemoralis internus; II, mm. intercostales interni; ISF, m. ischiofemoralis; ISTR, m. ischiotrochantericus; ITCR, m. iliotrochantericus cranialis; ITM, m. iliotrochantericus medius; LC, m. levator costarum; OE, m. obliquus externuss; OL, m. obturatorius lateralis; OM, m. obturatorius medialis; PIFI1, m. puboischiofemoralis internus 1; PIFI2, m. puboischiofemoralis internus 2; SC, m. subcostalis; SN, m. scalenus; vIC, ventral part of m. iliocostalis.

CHAPTER 1
Introduction

1.1 General introduction to archosaurs

Extant birds are “warm blooded” vertebrates capable of powered flight, with more than 10,000 species (Barrowclough et al. 2016), whereas extant crocodylians are semiaquatic, “cold blooded” vertebrates with fewer than 30 species (Grigg 2015). However, birds and crocodylians both belong to the clade Archosauria, which was classified as a subclass of “reptiles” by Romer (1966). Following the cladistic methods pioneered by Hennig (1966), Archosauria has been redefined as monophyletic group within diapsid amniotes (Gauthier 1984; Gauthier et al. 1985; Sereno 2005). As defined by Nesbitt (2011), the clade Archosauria includes the most recent common ancestor of the Nile crocodile *Crocodylus niloticus* and the house sparrow *Passer domesticus*, and all its descendants.

Accordingly, archosaurs include birds, crocodylians, fossil dinosaurs, and their close relatives that may be dated back as early as the Triassic Period (Wu 1981; Nesbitt 2011; Benton 2014; Kardong 2015; Nesbitt et al. 2017). The clade Archosauria is divided into Avemetatarsalia, the lineage including modern birds, and Pseudosuchia, the lineage including modern crocodylians (Gauthier et al. 1985; Sereno 1991; Benton 2014). Avemetatarsalia further diverged into the volant pterosaurs (Kellner 2003; Wang et al. 2005), and a number of different dinosaur groups notably including the horned ceratopsians, the duck-billed hadrosaurs, the armored ankylosaurs, the plate-bearing stegosaurs, and the bipedal theropods, the group that contains extant birds (Weishampel et al. 2007; Ryan et al. 2010; Eberth and Evans 2014). Likewise, Pseudosuchia diverged into the armored aetosaurs, the “sail-backed” poposaurids, the cursorial notosuchians, the fully aquatic dyrosaurids, and the semi-aquatic extant crocodylians (Ortega et al. 2000; Salisbury et al. 2006; Georgi and Krause 2010; Hastings et al. 2015; Hoffman et al. 2018; Stefanic and Nesbitt 2018).

Throughout the Mesozoic Era, the many members of archosaurs listed above explored and filled many ecological niches available to large-bodied terrestrial vertebrates, and at least two clades of archosaurs (i.e. pterosaurs and pennaraptoran dinosaurs) gained the capacity for powered flight (Claessens et al. 2009; Nesbitt 2011; Benton 2014). Based on the form and function relationship, the anatomical diversity seen among archosaurs represents evidence for a similarly wide spectrum of behaviours and lifestyles (Gatesy and Biewener 1991; Gatesy 1997; Holliday and Witmer 2007; Sullivan 2007; Wedel 2009; Abourachid et al. 2011; Schachner et al. 2011; Brink et al. 2015; Molnar et al. 2015; Brocklehurst et al. 2018; Stefanic and Nesbitt 2018; Iijima and Kubo 2019; Bishop et al. 2021). The great variety of lifestyles engaged in by archosaurs were all fueled by physiological processes using oxygen obtained through respiration.

1.2 Brief history of respiratory biology in archosaurs

Scholarly interest in respiration as a fundamental biological process can be traced back to ancient Greece and Rome and the pioneering work of Aristotle and Galen, though the significance of blood as a medium for circulating gas throughout the body, and pulmonary function, was not discerned until the seventeenth century (Perry et al. 2019). That the trunk had functional significance in generating ventilatory airflow was first proposed by Townson (1799), who rejected the previously established consensus view that the lungs could spontaneously generate airflow. Perry et al. (2019) revised the definition of respiration into a cascade of five generalised processes from mechanical transportation of fluids containing oxygen (e.g. air) in and out of the respiratory organs (ventilation) to gas exchange at the interface between air and blood, and ending with cellular respiration that generates ATP using oxygen. Although the five generalised processes may not always occur in vertebrates (e.g. ventilation may be limited and even absent in fishes), they can be assumed to be presence in archosaurs.

Interest in respiratory biology in archosaurs seemingly developed much later, potentially from general interest in comparative pulmonary anatomy among vertebrate animals and functional studies of avian flight (Lord et al. 1962; Berger et al. 1970b; Duncker 1972; Butler 1982; Perry 1988; Boggs et al. 1997; Boggs et al. 1997). A large volume of data accordingly has

been amassed on the amount of air that enters and leaves the body during a normal and regular ventilatory cycle, called the tidal volume, in various modern archosaurs (i.e. birds and crocodylians) and under various conditions (Lord et al. 1962; Kadono et al. 1963; Cohn and Shannon 1968; Schmidt-Nielsen et al. 1969; Berger et al. 1970b; Perry 1988; Funk et al. 1993; Boggs et al. 1997; Carrier and Farmer 2000b; Farmer and Carrier 2000; Claessens 2009a).

Also, in the domain of comparative pulmonary anatomy, studies of birds revealed the presence of a highly efficient respiratory apparatus consisting of a fixed volume lung and high compliance pneumatic sacs capable of generating unidirectional airflow for cross-current gas exchange (Scheid and Piiper 1969; Duncker 1972; Scheid 1979; Powell and Wagner 1982; Maina 2002; Powell 2015). More recent advances in pulmonary studies have suggested that unidirectional airflow is present in extant crocodylians, and may even be an ancestral condition shared by archosaurs if not their diapsid precursors (Farmer and Sanders 2010; Schachner et al. 2013; Farmer 2015; Lambertz 2016). Indirect evidence for the presence of pneumatic sacs has been found in the vertebrae of fossil saurischian dinosaurs (O'Connor 2006; O'Connor 2007; Wedel 2009; Schachner et al. 2011; Yates et al. 2012; Brocklehurst et al. 2018), suggesting that the anatomical capacity to separate airflow and gas exchange may have appeared in early archosaurs.

Beyond studies of pulmonary morphology, trunk muscle activity has been measured in both birds and crocodylians using electromyographic techniques to measure the changes in voltage of muscles, allowing muscle activation to be correlated with inspiration or expiration. (Fedde et al. 1964; dewet et al. 1967; Naifeh et al. 1970; Codd et al. 2005; Codd et al. 2019).

In crocodylians, comparative anatomy, cineradiographic observations, and electromyographic studies have provided evidence that ventilation is enhanced by a mechanism called the "hepatic piston", which refers to craniocaudal movements of the visceral organs in crocodylians driven by a muscle called m. diaphragmaticus (Carrier and Farmer 2000a; Claessens 2009a; Munns et al. 2012). Fossil evidence also suggest that some form of "hepatic piston" may have existed in fossil crocodyliforms and non-avian dinosaurs (Claessens 2004; Claessens and Vickaryous 2012). However, m. diagphramaticus and by extension, the "hepatic

piston" may not be a mechanism exclusively for ventilation, as the movement of visceral organs may alter buoyancy and improve a crocodylian's ability to maneuver underwater (Uriona and Farmer 2008).

With non-invasive methods such as cineradiography and X-ray Reconstruction of Moving Morphology (XROMM), *in vivo* movements of the skeleton during ventilation have been examined three-dimensionally in several birds and crocodylians (Claessens 2009a; Claessens 2009b; Brocklehurst et al. 2017; Brocklehurst et al. 2019). Studies of crocodylians using cineradiography and XROMM have found that the caudal portion of the thorax expands laterally to increase thoracic volume, and the capacity to laterally expand the thorax may be related to the anatomical positions of the parapophysis (Claessens 2009a; Brocklehurst et al. 2017).

Although the use of mechanical principles to analyse physical aspects of biology can be traced back to René Descartes (Perry et al. 2019), ventilation in birds has only been analysed from a mechanical perspective using two dimensional geometric models (Zimmer 1935; Tickle et al. 2007). Both Zimmer (1935) and Tickle et al. (2007) found that uncinate processes, bony prongs that extend caudally from dorsal vertebral ribs, provide enhanced mechanical leverage to muscles that protract the vertebral ribs cranially, enhancing the bird's ability to expand the thorax for inspiration. Uncinate processes in the form of bony prongs have been reported in fossil pennaraptorans, a group of theropod dinosaurs including birds, and in *Pelecanimimus polyodon*, a close pennaraptoran relative (Codd et al. 2008; Cuesta et al. 2022). Accordingly, avian-like enhancement of ventilatory capacity by uncinate processes may have occurred in fossil theropod dinosaurs. Uncinate processes in the forms of cartilaginous tabs are present in extant crocodylians, at least one fossil notosuchian crocodyliform, and several ornithischian dinosaurs (Zhou 1983; Cong et al. 1988; Frey 1988; Turner 2006; Boyd et al. 2011; Park et al. 2021), and m. iliocostalis, an epaxial trunk muscle that envelops the uncinate processes, was found to be active during expiration in an electromyographic study conducted on the American alligator *Alligator mississippiensis* (Codd et al. 2019). Accordingly, uncinate processes and their ventilatory function may have evolved independently in pennaraptorans, ornithischians,

notosuchians, and crocodylians, or alternatively the enhanced ventilatory capacity provided by uncinate processes may have been inherited from ancestral archosaurs.

1.3 Challenges in studies of archosaur ventilation

The ventilatory process of respiration in archosaurs remains somewhat perplexing. Firstly, physiological experiments have shown that tidal volume is highly variable across levels of physical activity (e.g. during locomotion, during recovery, at rest), and under different environmental conditions (e.g. at various altitudes and temperatures) (Schmidt-Nielsen et al. 1969; Berger et al. 1970a; Brackenbury et al. 1982; Kiley et al. 1982; Farmer and Carrier 2000; York et al. 2017). In addition, the physical property of compliance, which determines how easily the respiratory organs can be inflated, differs between the bronchoalveolar lung of crocodylians and the pneumatic sacs of birds (Scheid and Piiper 1969; Perry 1988; Maina 2007; Farmer 2017). Connective tissue proteins such as elastin, organised in a polygonal manner can increase structural strength of respiratory organs (Maina 2007). To expand the thorax and generate tidal volumes, various species of archosaurs may move their ribcages at a spectrum of magnitudes as quantitatively described by the amounts of rotations at joints in the ribcages. Accordingly, identifying the amount of ribcage movement that can characterise a given archosaur species or its capacity in certain physical activities would be difficult, if not impossible.

In addition, soft tissue structures such as pneumatic sacs, lungs, and unmineralised cartilages are not commonly preserved in the fossil record, although plausible lung tissues have been reported from an exceptionally preserved fossil bird (Wang et al. 2018). Traces on the skeleton of an extant bird can indicate where pneumatic sacs originally attached to bones, or penetrated into them, and similar traces documented in the fossil record can be used to infer the presence of pneumatic sacs in saurischian dinosaurs (O'Connor 2006; O'Connor 2007; Wedel 2009; Yates et al. 2012), following the logic of extant phylogenetic bracketing (Witmer 1995). However, even the certain existence of pneumatic sacs in a given fossil dinosaur would not guarantee their involvement in ventilation, just as the existence of pennaceous feathers in some

non-avian dinosaurs does not guarantee a capacity for powered flight comparable to that seen in extant birds (Currie et al. 2004; Foth and Rauhut 2020).

Lastly, the muscle-driven motions involved in expanding the thorax are three dimensionally complex, and can be described as rotations about three orthogonal joint axes following various conventions (Brainerd et al. 2015; Brocklehurst et al. 2017; Brocklehurst et al. 2019; Capano et al. 2019). Furthermore, the ribcage in extant birds and crocodylians is constituted of thoracic vertebrae each connected to the sternum via two or three rib segments, forming something like a closed kinematic chain (Levin 2013; Levin et al. 2017), and this was presumably true of extinct archosaurs as well. The segments of the ribcage would likely have rotated in tandem to expand the thorax, and the entire ribcage would accordingly need to be analysed as a single, integrated system.

1.4 Thesis objectives

This doctoral dissertation is focused on the form and function of the trunk in extant and fossil archosaurs. The goal of my thesis is to provide updated anatomical knowledge of the archosaur trunk, and to gain new insights on how musculoskeletal structures in the trunk contribute to ventilation in modern archosaurs, and would plausibly have contributed to ventilation in extinct ones. In this interdisciplinary study, I combined traditional comparative anatomy and histology techniques with statistical methods from the field of data science, and with 3D modelling techniques and principles from the field of biomechanics.

More specifically, my thesis has six main objectives: (1) to identify the cervicodorsal transition in various archosaurs using the morphology of the presacral vertebrae, so that the vertebral column can be regionalised accurately and consistently; (2) to evaluate whether uncinate processes are homologous structures shared by most archosaurs, or were gained independently to improve ventilatory performance in different archosaur groups; (3) to evaluate how uncinate processes are attached to the vertebral ribs in extant taxa and may have been attached in fossil ones, such that the mobility of uncinate processes relative to the vertebral ribs

can be inferred, providing insights into ventilatory mechanisms in archosaurs; (4) to provide updated information on the muscle architecture of the trunk in extant archosaurs, so that osteological correlates that will be useful in reconstructing trunk muscles in their fossil relatives can be established; (5) to develop a new workflow and set of kinematic models of extant archosaur thoracic skeletons for estimating ventilatory motions of the ribcage comparable to those observed in *in vivo* studies, so that ventilatory motions of the ribcage can be reconstructed in a reasonable manner for fossil archosaurs; and (6) to develop an updated workflow and a set of kinetic models for drawing inferences about the ventilatory function of the trunk musculature in archosaurs.

1.5 Literature Cited

Abourachid, A. et al. 2011. Bird terrestrial locomotion as revealed by 3D kinematics. *Zoology* 114(6), pp. 360–368. doi: 10.1016/j.zool.2011.07.002.

Barrowclough, G.F., Cracraft, J., Klicka, J. and Zink, R.M. 2016. How Many Kinds of Birds Are There and Why Does It Matter? *PLOS ONE* 11(11), p. e0166307. doi: 10.1371/journal.pone.0166307.

Benton, M.J. 2014. *Vertebrate Palaeontology*. John Wiley & Sons.

Berger, M., Hart, J.S. and Roy, O.Z. 1970a. Respiration, oxygen consumption and heart rate in some birds during rest and flight. *Zeitschrift für vergleichende Physiologie* 66(2), pp. 201–214. doi: 10.1007/BF00297779.

Berger, M., Roy, O.Z. and Hart, J.S. 1970b. The co-ordination between respiration and wing beats in birds. *Zeitschrift für vergleichende Physiologie* 66(2), pp. 190–200. doi: 10.1007/BF00297778.

Bishop, P.J., Falisse, A., De Groote, F. and Hutchinson, J.R. 2021. Predictive simulations of running gait reveal a critical dynamic role for the tail in bipedal dinosaur locomotion. *Science Advances* 7(39), p. eabi7348.

Boggs, D.F., Jenkins, F.A. and Dial, K.P. 1997. The effects of the wingbeat cycle on respiration in black-billed magpies (pica pica). *The Journal of Experimental Biology* 200, pp. 1403–1412.

Boyd, C.A., Cleland, T.P. and Novas, F. 2011. Osteogenesis, homology, and function of the intercostal plates in ornithischian dinosaurs (Tetrapoda, Sauropsida). *Zoomorphology* 130(4), pp. 305–313. doi: 10.1007/s00435-011-0136-x.

Brackenbury, J.H., Gleeson, M. and Avery, P. 1982. Respiration in exercising fowl. III. ventilation. *Journal of Experimental Biology* 96(1), pp. 315–324. doi: 10.1242/jeb.96.1.315.

Brainerd, E.L., Moritz, S. and Ritter, D.A. 2015. XROMM analysis of rib kinematics during lung ventilation in the green iguana, *Iguana iguana*. *Journal of Experimental Biology* 219, p. jeb.127928. doi: 10.1242/jeb.127928.

Brink, K.S. et al. 2015. Developmental and evolutionary novelty in the serrated teeth of theropod dinosaurs. *Scientific Reports* 5(1), p. 12338. doi: 10.1038/srep12338.

Brocklehurst, R.J., Moritz, S., Codd, J., Sellers, W.I. and Brainerd, E.L. 2017. Rib kinematics during lung ventilation in the American alligator (*Alligator mississippiensis*): an XROMM analysis. *Journal of Experimental Biology* 220(17), pp. 3181–3190. doi: 10.1242/jeb.156166.

Brocklehurst, R.J., Moritz, S., Codd, J., Sellers, W.I. and Brainerd, E.L. 2019. XROMM kinematics of ventilation in wild turkeys (*Meleagris gallopavo*). *Journal of Experimental Biology* 222(23), p. jeb209783. doi: 10.1242/jeb.209783.

Brocklehurst, R.J., Schachner, E.R. and Sellers, W.I. 2018. Vertebral morphometrics and lung structure in non-avian dinosaurs. *Royal Society Open Science* 5(10), p. 180983. doi: 10.1098/rsos.180983.

Butler, P.J. 1982. Respiration during Flight and Diving in Birds. In: *Invited Lectures*. Elsevier, pp. 103–114. Available at: https://linkinghub.elsevier.com/retrieve/pii/B9780080279862500153 [Accessed: 11 January 2023].

Capano, J.G., Moritz, S., Cieri, R.L., Reveret, L. and Brainerd, E.L. 2019. Rib motions don't completely hinge on joint design: costal joint anatomy and ventilatory kinematics in a teiid lizard, *Salvator merianae*. *Integrative Organismal Biology* 1(1), p. oby004. doi: 10.1093/iob/oby004.

Carrier, D.R. and Farmer, C.G. 2000a. The evolution of pelvic aspiration in archosaurs. *Paleobiology* 26(2), pp. 271–293. doi: 10.1666/0094-8373(2000)026<0271:TEOPAI>2.0.CO;2.

Carrier, D.R. and Farmer, C.G. 2000b. The integration of ventilation and locomotion in archosaurs. *American Zoologist* 40, pp. 87–100.

Claessens, L.P.A.M. 2004. Archosaurian respiration and the pelvic girdle aspiration breathing of crocodyliforms. *Proceedings of the Royal Society of London. Series B: Biological Sciences* 271(1547), pp. 1461–1465. doi: 10.1098/rspb.2004.2743.

Claessens, L.P.A.M. 2009a. A cineradiographic study of lung ventilation in *Alligator mississippiensis*. *Journal of Experimental Zoology Part A: Ecological Genetics and Physiology* 311A(8), pp. 563–585. doi: 10.1002/jez.530.

Claessens, L.P.A.M. 2009b. The skeletal kinematics of lung ventilation in three basal bird taxa (emu, tinamou, and guinea fowl). *Journal of Experimental Zoology Part A: Ecological Genetics and Physiology* 311A(8), pp. 586–599. doi: 10.1002/jez.501.

Claessens, L.P.A.M., O'Connor, P.M. and Unwin, D.M. 2009. Respiratory Evolution Facilitated the Origin of Pterosaur Flight and Aerial Gigantism. Sereno, P. ed. *PLoS ONE* 4(2), p. e4497. doi: 10.1371/journal.pone.0004497.

Claessens, L.P.A.M. and Vickaryous, M.K. 2012. The evolution, development and skeletal identity of the crocodylian pelvis: Revisiting a forgotten scientific debate. *Journal of Morphology* 273(10), pp. 1185–1198. doi: 10.1002/jmor.20059.

Codd, J.R., Boggs, D.F., Perry, S.F. and Carrier, D.R. 2005. Activity of three muscles associated with the uncinate processes of the giant Canada goose *Branta canadensis maximus*. *Journal of Experimental Biology* 208(5), pp. 849–857. doi: 10.1242/jeb.01489.

Codd, J.R., Manning, P.L., Norell, M.A. and Perry, S.F. 2008. Avian-like breathing mechanics in maniraptoran dinosaurs. *Proceedings of the Royal Society B: Biological Sciences* 275(1631), pp. 157–161. doi: 10.1098/rspb.2007.1233.

Codd, J.R., Rose, K.A.R., Tickle, P.G., Sellers, W.I., Brocklehurst, R.J., Elsey, R.M. and Crossley, D.A. 2019. A novel accessory respiratory muscle in the American alligator (*Alligator mississippiensis*). *Biology Letters* 15(7), p. 20190354. doi: 10.1098/rsbl.2019.0354.

Cohn, J.E. and Shannon, R. 1968. Respiration in unanathesitized geese. *Respiration Physiology* 5, pp. 259–268.

Cong, L.Y., Hou, L.H. and Wu, X.C. 1988. *The Gross anatomy of Alligator sinensis Fauvel: Integument, Osteology, and Myology (In Chinese with English summary)*. Beijing, China: China Science Publishing & Media Ltd.

Cuesta, E., Vidal, D., Ortega, F., Shibata, M. and Sanz, J.L. 2022. *Pelecanimimus* (Theropoda: Ornithomimosauria) postcranial anatomy and the evolution of the specialized manus in Ornithomimosaurs and sternum in maniraptoriforms. *Zoological Journal of the Linnean Society* 194(2), pp. 553–591. doi: 10.1093/zoolinnean/zlab013.

Currie, P.J., Koppelhus, E.B., Shugar, M.A. and Wright, J.L. 2004. *Feathered Dragons: Studies on the Transition from Dinosaurs to Birds*. Indiana University Press.

dewet, P.D., Fedde, M.R. and Kitchell, R.L. 1967. Innervation of the respiratory muscles of *Gallus domesticus*. *Journal of Morphology* 123(1), pp. 17–34. doi: 10.1002/jmor.1051230103.

Duncker, H.-R. 1972. Structure of avian lungs. *Respiration Physiology* 14(1), pp. 44–63. doi: 10.1016/0034-5687(72)90016-3.

Eberth, D.A. and Evans, D.C. 2014. *Hadrosaurs*. Indiana University Press.

Farmer, C.G. 2015. The evolution of unidirectional pulmonary airflow. *Physiology* 30(4), pp. 260–272.

Farmer, C.G. 2017. Pulmonary Transformations of Vertebrates. In: *The Biology of the Avian Respiratory System*. Cham: Springer International Publishing, pp. 99–112. doi: 10.1007/978-3-319-44153-5_3.

Farmer, C.G. and Carrier, D.R. 2000. Respiration and gas exchange during recovery from exercise in the American alligator. *Respiration Physiology* 120(1), pp. 81–87. doi: 10.1016/S0034-5687(00)00098-0.

Farmer, C.G. and Sanders, K. 2010. Unidirectional airflow in the lungs of alligators. *Science* 327(5963), pp. 338–340. doi: 10.1126/science.1180219.

Fedde, M.R., Burger, R.E. and Kitchell, R.L. 1964. Anatomic and electromyographic studies of the costo-pulmonary muscles in the cock. *Poultry Science* 43(5), pp. 1177–1184. doi: 10.3382/ps.0431177.

Foth, C. and Rauhut, O.W.M. eds. 2020. *The Evolution of Feathers: From Their Origin to the Present*. Cham: Springer International Publishing. Available at: http://link.springer.com/10.1007/978-3-030-27223-4 [Accessed: 12 January 2023].

Frey, T. von E. 1988. Anatomie des Körperstammes von *Alligator mississippiensis* Daudin. *Stuttgarter Beitraege zur Naturkunde, Serie A* 424, pp. 1–106.

Funk, G.D., Sholomenko, G.N., Valenzuela, I.J., Steeves, J.D. and Milsom, W.K. 1993. Coordination of wing beat and respiration in Canada geese during free flight. *Journal of Experimental Biology* 175, pp. 317–323.

Gatesy, S.M. 1997. An electromyographic analysis of hindlimb function in *Alligator* during terrestrial locomotion. *Journal of Morphology* 234(2), pp. 197–212. doi: 10.1002/(SICI)1097-4687(199711)234:2<197::AID-JMOR6>3.0.CO;2-9.

Gatesy, S.M. and Biewener, A.A. 1991. Bipedal locomotion: effects of speed, size and limb posture in birds and humans. *Journal of Zoology* 224(1), pp. 127–147. doi: 10.1111/j.1469-7998.1991.tb04794.x.

Gauthier, J., Padian, K., Hecht, M.K., Ostrom, J.H., Viohl, G. and Wellnhofer, P. 1985. Phylogenetic, functional, and aerodynamic analyses of the origin of birds and their flight. *The beginning of birds*, pp. 185–197.

Gauthier, J.A. 1984. *A cladistic analysis of the higher systematic categories of the Diapsida*. PhD Dissertation, University of California, Berkeley.

Georgi, J.A. and Krause, D.W. 2010. Postcranial axial skeleton of *Simosuchus clarki* (Crocodyliformes: Notosuchia) from the Late Cretaceous of Madagascar. *Journal of Vertebrate Paleontology* 30(sup1), pp. 99–121. doi: 10.1080/02724634.2010.519172.

Grigg, G. 2015. *Biology and Evolution of Crocodylians*. Csiro Publishing.

Hastings, A.K., Bloch, J.I. and Jaramillo, C.A. 2015. A new blunt-snouted dyrosaurid, *Anthracosuchus balrogus* gen. et **sp. nov.** (Crocodylomorpha, Mesoeucrocodylia), from the Palaeocene of Colombia. *Historical Biology* 27(8), pp. 998–1020. doi: 10.1080/08912963.2014.918968.

Hennig, W. 1966. *Phylogenetic systematics*. University of Illinois Press, Illinois.

Hoffman, D.K., Heckert, A.B. and Zanno, L.E. 2018. Under the armor: X-ray computed tomographic reconstruction of the internal skeleton of *Coahomasuchus chathamensis* (Archosauria: Aetosauria) from the Upper Triassic of North Carolina, USA, and a phylogenetic analysis of Aetosauria. *PeerJ* 6, p. e4368. doi: 10.7717/peerj.4368.

Holliday, C.M. and Witmer, L.M. 2007. Archosaur adductor chamber evolution: Integration of musculoskeletal and topological criteria in jaw muscle homology. *Journal of Morphology* 268(6), pp. 457–484. doi: 10.1002/jmor.10524.

Iijima, M. and Kubo, T. 2019. Comparative morphology of presacral vertebrae in extant crocodylians: taxonomic, functional and ecological implications. *Zoological Journal of the Linnean Society*. doi: 10.1093/zoolinnean/zly096.

Kadono, H., Okada, T. and Ono, K. 1963. Electromyographic studies on the respiratory muscles of the chicken. *Poultry Science* 42(1), pp. 121–128. doi: 10.3382/ps.0420121.

Kardong, K.V. 2015. *Vertebrates: comparative anatomy, function, evolution*. Seventh edition. New York, NY: McGraw-Hill Education.

Kellner, A.W.A. 2003. Pterosaur phylogeny and comments on the evolutionary history of the group. *Geological Society, London, Special Publications* 217(1), pp. 105–137. doi: 10.1144/GSL.SP.2003.217.01.10.

Kiley, J.P., Kuhlmann, W.D. and Fedde, M.R. 1982. Ventilatory and blood gas adjustments in exercising isothermic ducks. *Journal of comparative physiology* 147(1), pp. 107–112. doi: 10.1007/BF00689298.

Lambertz, M. 2016. Recent advances on the functional and evolutionary morphology of the amniote respiratory apparatus: Morphology of the amniote respiratory apparatus. *Annals of the New York Academy of Sciences* 1365(1), pp. 100–113. doi: 10.1111/nyas.13022.

Levin, S., de Solórzano, S.L. and Scarr, G. 2017. The significance of closed kinematic chains to biological movement and dynamic stability. *Journal of Bodywork and Movement Therapies* 21(3), pp. 664–672. doi: 10.1016/j.jbmt.2017.03.012.

Levin, S.M. 2013. Closed kinematic chain mechanisms comprise the fundamental mechanics of biologic movement and stability. doi:https://www.researchgate.net/publication/256196463_Closed_kinematic_chain_mechanisms_comprise_the_fundamental_mechanics_of_biologic_movement_and_stability.

Lord, R.D., Bellrose, F.C. and Cochran, W.W. 1962. Radiotelemetry of the Respiration of a Flying Duck. *Science* 137(3523), pp. 39–40. doi: 10.1126/science.137.3523.39.

Maina, J.N. 2002. *Functional Morphology of the Vertebrate Respiratory Systems*. Science Publishers.

Maina, J.N. 2007. Spectacularly robust! Tensegrity principle explains the mechanical strength of the avian lung. *Respiratory Physiology & Neurobiology* 155(1), pp. 1–10. doi: 10.1016/j.resp.2006.05.005.

Molnar, J.L., Pierce, S.E., Bhullar, B.-A.S., Turner, A.H. and Hutchinson, J.R. 2015. Morphological and functional changes in the vertebral column with increasing aquatic adaptation in crocodylomorphs. *Royal Society Open Science* 2(11), p. 150439. doi: 10.1098/rsos.150439.

Munns, S.L., Owerkowicz, T., Andrewartha, S.J. and Frappell, P.B. 2012. The accessory role of the diaphragmaticus muscle in lung ventilation in the estuarine crocodile *Crocodylus porosus*. *Journal of Experimental Biology* 215(5), pp. 845–852. doi: 10.1242/jeb.061952.

Naifeh, K.H., Huggins, S.E., Hoff, H.E., Hugg, T.W. and Norton, R.E. 1970. Respiratory patterns in crocodilian reptiles. *Respiration Physiology* 9(1), pp. 21–42. doi: 10.1016/0034-5687(70)90003-4.

Nesbitt, S.J. 2011. The early evolution of archosaurs: relationships and the origin of major clades. *Bulletin of the American Museum of Natural History* 352, pp. 1–292. doi: 10.1206/352.1.

Nesbitt, S.J. et al. 2017. The earliest bird-line archosaurs and the assembly of the dinosaur body plan. *Nature* 544(7651), pp. 484–487. doi: 10.1038/nature22037.

O'Connor, P.M. 2006. Postcranial pneumaticity: An evaluation of soft-tissue influences on the postcranial skeleton and the reconstruction of pulmonary anatomy in archosaurs. *Journal of Morphology* 267(10), pp. 1199–1226. doi: 10.1002/jmor.10470.

O'Connor, P.M. 2007. The postcranial axial skeleton of *Majungasaurus crenatissimus* (Theropoda: Abelisauridae) from the Late Cretaceous of Madagascar. *Journal of Vertebrate Paleontology* 27(sup2), pp. 127–163. doi: 10.1671/0272-4634(2007)27[127:TPASOM]2.0.CO;2.

Ortega, F., Gasparini, Z., Buscalioni, A.D. and Calvo, J.O. 2000. A new species of *Araripesuchus* (Crocodylomorpha, Mesoeucrocodylia) from the lower Cretaceous of Patagonia (Argentina). *Journal of Vertebrate Paleontology* 20(1), pp. 57–76. doi: 10.1671/0272-4634(2000)020[0057:ANSOAC]2.0.CO;2.

Park, J.-Y. et al. 2021. A new ankylosaurid skeleton from the Upper Cretaceous Baruungoyot Formation of Mongolia: its implications for ankylosaurid postcranial evolution. *Scientific Reports* 11(1), p. 4101. doi: 10.1038/s41598-021-83568-4.

Perry, S.F. 1988. Functional morphology of the lungs of the nile crocodile, *Crocodylus niloticus:* non-respiratory parameters. *Journal of Experimental Biology* 134(1), pp. 99–117. doi: 10.1242/jeb.134.1.99.

Perry, S.F., Lambertz, M. and Schmitz, A. 2019. *Respiratory Biology of Animals: evolutionary and functional morphology*. Oxford University Press.

Powell, F.L. 2015. Respiration. In: *Sturkie's Avian Physiology*. Elsevier, pp. 301–336. doi: 10.1016/B978-0-12-407160-5.00013-0.

Powell, F.L. and Wagner, P.D. 1982. Ventilation-perfusion inequality in avian lungs. *Respiration Physiology* 48(2), pp. 233–241. doi: 10.1016/0034-5687(82)90083-4.

Romer, A.S. 1966. *Vertebrate paleontology*. 3rd ed. Chicago: University of Chicago Press.

Ryan, M.J., Chinnery-Allgeier, B.J. and Eberth, D.A. 2010. *New Perspectives on Horned Dinosaurs: The Royal Tyrrell Museum Ceratopsian Symposium*. Indiana University Press.

Salisbury, S.W., Molnar, R.E., Frey, E. and Willis, P.M.A. 2006. The origin of modern crocodyliforms: new evidence from the Cretaceous of Australia. *Proceedings of the Royal Society B: Biological Sciences* 273(1600), pp. 2439–2448. doi: 10.1098/rspb.2006.3613.

Schachner, E.R., Farmer, C.G., McDonald, A.T. and Dodson, P. 2011. Evolution of the dinosauriform respiratory apparatus: New evidence from the postcranial axial skeleton. *The Anatomical Record: Advances in Integrative Anatomy and Evolutionary Biology* 294(9), pp. 1532–1547. doi: 10.1002/ar.21439.

Schachner, E.R., Hutchinson, J.R. and Farmer, C. 2013. Pulmonary anatomy in the Nile crocodile and the evolution of unidirectional airflow in Archosauria. *PeerJ* 1, p. e60. doi: 10.7717/peerj.60.

Scheid, P. 1979. Mechanisms of gas exchange in bird lungs. In: *Reviews of Physiology, Biochemistry and Pharmacology, Volume 86*. Reviews of Physiology, Biochemistry and Pharmacology. Berlin, Heidelberg: Springer Berlin Heidelberg, pp. 137–186. Available at: http://link.springer.com/10.1007/BFb0031533 [Accessed: 11 January 2023].

Scheid, P. and Piiper, J. 1969. Volume, ventilation and compliance of the respiratory system in the domestic fowl. *Respiration Physiology* 6(3), pp. 298–308. doi: 10.1016/0034-5687(69)90029-2.

Schmidt-Nielsen, K., Kanwisher, J., Lasiewski, R.C., Cohn, J.E. and Bretz, W.L. 1969. Temperature regulation and respiration in the ostrich. *The Condor* 71(4), pp. 341–352. doi: 10.2307/1365733.

Sereno, P.C. 1991. Basal Archosaurs: Phylogenetic Relationships and Functional Implications. *Journal of Vertebrate Paleontology* 11(sup004), pp. 1–53. doi: 10.1080/02724634.1991.10011426.

Sereno, P.C. 2005. The logical basis of phylogenetic taxonomy. *Systematic Biology* 54(4), pp. 595–619.

Stefanic, C.M. and Nesbitt, S.J. 2018. The axial skeleton of *Poposaurus langstoni* (Pseudosuchia: Poposauroidea) and its implications for accessory intervertebral articulation evolution in pseudosuchian archosaurs. *PeerJ* 6, p. e4235. doi: 10.7717/peerj.4235.

Sullivan, C. 2007. *Function and evolution of the hind limb in Triassic archosaurian reptiles*. PhD Dissertation, Harvard University.

Tickle, P.G., Ennos, A.R., Lennox, L.E., Perry, S.F. and Codd, J.R. 2007. Functional significance of the uncinate processes in birds. *Journal of Experimental Biology* 210(22), pp. 3955–3961. doi: 10.1242/jeb.008953.

Townson, R. 1799. *Tracts and observations in natural history and physiology*. London: Printed for the author by J. White.

Turner, A.H. 2006. Osteology and phylogeny of a new species of *Araripesuchus* (Crocodyliformes: Mesoeucrocodylia) from the Late Cretaceous of Madagascar. *Historical Biology* 18(3), pp. 255–369. doi: 10.1080/08912960500516112.

Uriona, T.J. and Farmer, C.G. 2008. Recruitment of the diaphragmaticus, ischiopubis and other respiratory muscles to control pitch and roll in the American alligator (*Alligator mississippiensis*). *Journal of Experimental Biology* 211(7), pp. 1141–1147. doi: 10.1242/jeb.015339.

Wang, X. et al. 2018. Archaeorhynchus preserving significant soft tissue including probable fossilized lungs. *Proceedings of the National Academy of Sciences* 115(45), pp. 11555–11560. doi: 10.1073/pnas.1805803115.

Wang, X., Kellner, A.W.A., Zhou, Z. and Campos, D. de A. 2005. Pterosaur diversity and faunal turnover in Cretaceous terrestrial ecosystems in China. *Nature* 437(7060), pp. 875–879. doi: 10.1038/nature03982.

Wedel, M.J. 2009. Evidence for bird-like air sacs in saurischian dinosaurs. *Journal of Experimental Zoology Part A: Ecological Genetics and Physiology* 311A(8), pp. 611–628. doi: 10.1002/jez.513.

Weishampel, D.B., Dodson, P. and Osmólska, H. 2007. *The Dinosauria*. Univ of California Press.

Witmer, L.M. 1995. The extant phylogenetic bracket and the importance of reconstructing soft tissues in fossils. *Functional morphology in vertebrate paleontology* 1, pp. 19–33.

Wu, X.C. 1981. The discovery of a new thecodont from north east Shanxi. *Vertebrata PalAsiatica* 19, pp. 122–132.

Yates, A.M., Wedel, M.J. and Bonnan, M.F. 2012. The Early Evolution of Postcranial Skeletal Pneumaticity in Sauropodomorph Dinosaurs. *Acta Palaeontologica Polonica* 57(1), pp. 85–100. doi: 10.4202/app.2010.0075.

York, J.M. et al. 2017. Respiratory mechanics of eleven avian species resident at high and low altitude. *Journal of Experimental Biology* 220(6), pp. 1079–1089. doi: 10.1242/jeb.151191.

Zhou, S.W. 1983. A nearly complete skeleton of a stegosaur from the Middle Jurassic of Dashanpu, Zigong, Sichuan. *Journal of Chengdu University of Geology* 1, pp. 15–26.

Zimmer, K. 1935. Beiträge zur Mechanik der Atmung bei den Vögeln in Stand-und Flug. *Zoologica* 33, pp. 1–69.

CHAPTER 2

A qualitative anatomical approach to the understudied problem of pinpointing the boundary between cervical and dorsal vertebrae in fossil archosaurian reptiles

2.1 Introduction

Archosaurs appeared in the Triassic Period, diversified rapidly, and accounted for major portion of amniote diversity throughout the rest of the Mesozoic Era (Nesbitt 2011; Nesbitt et al. 2013; Benton 2014). The vertebral column of an archosaur may be divided for descriptive or analytical purpose into cervical, thoracic, lumbar, sacral, and caudal regions, the vertebrae of the first three regions being conventionally referred to as presacral (Cong et al. 1988; Baumel et al. 1993; Kardong 2015). The vertebrae of thoracic and lumbar regions are generally not morphologically distinct in archosaurs, compared to those of mammals, and thoracic and lumbar vertebrae are often collectively called the dorsal vertebrae (Benton 2014; Kardong 2015). The thoracic region is traditionally defined by the presence of connections between the vertebral column and the sternum via rib segments, and the transition from cervical to dorsal vertebrae (cervicodorsal transition) is pinpointed by the first presacral connected to the sternum (Romer 1956).

A relatively large number of cervical vertebrae, ranging from 10 to 26 occurs in extant birds (Böhmer et al. 2019), whereas nine cervical vertebrae are found in extant crocodylians (Cong et al. 1988; Frey 1988). Based on the logic of extant phylogenetic bracketing (Witmer 1995) and the parsimony principle in phylogenetic inference (Sober 1988), the plesiomorphic condition in ancestral archosaurs could theoretically have been closer to either the avian condition or the crocodylian one.

In principle, the rich Triassic record of archosaurs (Brusatte et al. 2010) should shed considerable light on the question of the number of cervical vertebrae in plesiomorphic members of the group, but the number of cervical vertebrae present in a given fossil archosaur is difficult

to precisely determine even if a well-preserved skeleton is available. Although the first connection between a presacral vertebrae and the sternum via rib segments provides a clear criterion for identifying the cervicodorsal transition, the criterion is inapplicable in most fossil archosaurs due to preservational factor (Walker 1990) except in the case of exquisitely preserved specimens (Fisher et al. 2000; Turner 2006). Even the so call "complete skeletons" representing members of most archosaur clades do not include the sternum or sternal ribs, suggesting that these structures were generally cartilaginous as in most living reptiles (Maidment et al. 2015; Currie et al. 2016; Drysdale et al. 2018). With the criterion of sternal connectedness off the table, several alternate approaches have been used in the literature to address the difficulty of identifying the cervicodorsal transition in fossil archosaurs and, by extension, distinguishing between their cervical and dorsal vertebrae.

Identifying the cervicodorsal transition as accurately and consistently as possible is more than a trivial point of anatomical pedantry. In phylogenetic studies, anatomical comparisons and character scorings that involve the vertebral column are meaningful only when they pertain to regions that are homologous across all taxa being considered (e.g. the posterior cervical vertebrae) (Nesbitt, 2011, Cau et al., 2017). In the domain of functional morphology, the vertebral column displays a wide range of adaptations associated with enhancing rigidity (e.g. hyposphene-hypantrum) (Stefanic and Nesbitt, 2019), facilitating locomotion (Abourachid et al., 2011, Molnar et al., 2015), and respiration (Schachner et al., 2011, Brocklehurst et al., 2018). Identification of the cervicodorsal transition can facilitate sound interpretation of such adaptations, by ensuring that functionally relevant features can be correctly situated with respect to the first costal connection to the sternum and potentially other landmarks associated with the transition.

2.1.1 Five alternate methods to identify the cervicodorsal transition

Locating the transition using intuition. Some anatomical studies of archosaurs have drawn a distinction between cervical and dorsal vertebrae without clearly and explicitly describing how the cervicodorsal transition was identified (Luca, 1984, Altangarel et al., 1994, Chen et al., 1998, Wang et al., 2010, Xu et al., 2010, Carpenter et al., 2011, Makovicky et al., 2011, Nobre and Carvalho, 2013, McDonald et al., 2014, Prieto-Márquez, 2014, Lecuona et al.,

2016), suggesting the authors may have partitioned the presacral column into cervical and dorsal regions based on intuition. Scholarly expertise could conceivably provide a solid foundation for an "educated guess" regarding the location of the cervicodorsal transition. However, this intuitive approach is likely to introduce confusion, because it offers no explicit criteria that can be followed. Such disagreements are likely to be small, in the sense that all but the posteriormost cervical vertebrae in a fossil archosaur can generally be recognized as unambiguous cervicals and all but the anteriormost dorsal vertebrae can generally be recognized as unambiguous dorsals. However, inconsistencies across studies regarding whether even one or two vertebrae should be assigned to the cervical or to the dorsal region may introduce confusion, result in discrepant scoring of phylogenetic characters pertaining to posterior cervicals or anterior dorsals, and/or affect reconstructions of soft tissues associated with the transitional region.

Avoiding the cervical-dorsal distinction. The challenge of identifying the cervicodorsal transition may be circumvented by simply treating the presacral vertebrae as a single undifferentiated series, and referring to them based on their ordinal position within this "super-region" (presacral numbering). This approach highlights the fact that the total number of presacral vertebrae is relatively strongly conserved in extant and fossil archosaurs: for example, 24 presacrals are present in *Alligator sinensis*, 23 in *Rhea*, 23 in *Tyrannosaurus rex*, 23 in *Majungasaurus crenatissimus*, and 24 in *Changchunsaurus parvus*, although there are 30 presacrals in *Parasaurolophus walkeri* (Mivart, 1877, Parks, 1922, Cong et al., 1988, Brochu, 2003, O'Connor, 2007, Butler et al., 2011). Presacral numbering is feasible for descriptive purposes, but is not very satisfactory for anatomical comparisons across taxa because cervical and dorsal counts are variable among extant birds, and between birds and crocodylians (Mivart, 1877, Cong et al., 1988, Baumel, 1993). Therefore, presacral vertebrae in different taxa with similar presacral numbers are not guaranteed to be from homologous parts of the vertebral column, if the cervicodorsal transition is regarded as an important landmark for determining homology. Alternatively, some scholars have referred informally to a "pectoral" region or a "cervico-dorsal" region of the vertebral column encompassing the posterior cervical and anterior dorsal vertebrae (Mivart 1877; Wilson et al. 2011; Novas et al. 2015). Precisely defining the anterior and posterior limits of the pectoral region using criteria that can be applied across a wide

range of taxa, however, is hardly guaranteed to be easier than precisely identifying the cervicodorsal transition.

Locating the transition using living analogues. Cervical counts from extant birds and/or crocodylians are occasionally used as an extant point of reference for identifying the cervicodorsal transition in fossil archosaurs (Walker, 1990, Salisbury et al., 2006, Sereno and Larsson, 2009). Although all extant crocodylians have nine cervical vertebrae (Cong et al., 1988, Frey, 1988), the number of cervicals is variable in extant birds: for example, 16 cervical vertebrae are present in *Rhea americana* (UAMZ 1368, 5019), 19 in *Casuarius australis* (UAMZ 1369) and 22 in *Olor columbianus* (UAMZ 5229, 5230). Given the lack of consistency in extant birds, identifying the cervicodorsal transition by assuming that a fossil archosaur will have the same number of cervicals as a living analogue is not feasible except in crocodylians and their closest relatives. This assumption, however, becomes increasingly uncertain as we move phylogenetically away from Crocodylia. Walker (1990), for example, assumed by analogy with modern crocodylians that nine cervicals were present in the basal crocodylomorph *Sphenosuchus*, but explicitly acknowledged the difficulty of identifying the cervicodorsal transition in fossil archosaurs.

Locating the transition using cervical rib features. In extant birds and crocodylians, unambiguous cervical ribs are short and are oriented anteroposteriorly, whereas the last one or two cervical ribs and unambiguous dorsal ribs are long and are oriented mostly dorsoventrally (Mivart 1877; Cong et al. 1988; Frey 1988; Baumel et al. 1993). In well-preserved fossil archosaurs, the vertebral ribs from unambiguous cervicals to unambiguous dorsals change in length and orientation as in their extant counterparts (Ostrom 1978; Dalla Vecchia 2009; Dilkes and Sues 2009; Maidment et al. 2015). Accordingly, vertebral ribs that are elongated but not reaching the same length as the vertebral ribs of unambiguous dorsals could conceivably be used to recognise the last cervical ribs, and by extension, the cervicodorsal transition. Most of the cervical ribs are short in extant crocodylians, but the last cervical rib is strikingly different from the others, being so elongate as to resemble the anterior dorsal vertebral ribs (Cong et al., 1988, Frey, 1988). In extant birds, the last and penultimate cervical ribs can both be elongated (e.g. *Struthio camelus* (UAMZ 7159), *Falco sparverius* (UAMZ 4022) and *Tympanuchus*

phasianellus (UAMZ 4668)). In both birds and crocodylians, the last cervical ribs can extend ventrally to a position adjacent to the sternum. If the last cervical ribs in fossil archosaurs also closely approached the sternum, the last cervical ribs could readily be misidentified as the anteriormost dorsal ribs in the absence of fossilized sterna and sternal ribs. Therefore, the last cervical ribs cannot be used to reliably identify the first sternal connection except perhaps in crocodylians and their closest fossil relatives. Nonetheless, changes in length and orientation of the last cervical ribs compared to unambiguous cervical and dorsal ribs can help locating the approximate position of the first sternal connection in exquisitely preserved specimens (Currie et al., 2016).

Locating the transition using vertebral features. Morphological features known to differ between unambiguous cervical and unambiguous dorsal vertebrae are frequently used to identify the cervicodorsal transition in fossil archosaurs (Ewer, 1965, Cuthbertson and Holmes, 2010, Maidment et al., 2015, Norell et al., 2018). We refer to these morphological features as "transitional features" for the sake of clarity and brevity. Three transitional features are used most often in the literature.

(5.1) Parapophyseal displacement. Along the length of the presacral vertebral column, the parapophysis undergoes a gradual change in position, often being situated ventral to the neurocentral suture (NCS) on unambiguous cervicals but dorsal to the NCS more on unambiguous dorsals (Whetstone and Whybrow, 1983, Luca, 1984, Wu and Chatterjee, 1993, Maidment and Barrett, 2010, Pol et al., 2012, Wang et al., 2013, Campione, 2014, Lautenschlager and Rauhut, 2015, Drymala and Zanno, 2016). However, the parapophysis may be intersected the NCS in presacral vertebrae in the vicinity of the first sternal connection, so that portion of the parapophysis is positioned ventral to the NCS whereas the remaining portion is positioned dorsal to the NCS. This may result in ambiguous interpretation of the state of the feature. A clear standard for interpreting the parapophyseal position is needed for accurate and consistent practices.

(5.2) Loss of distinct hypapophysis. In many archosaurs hypapophyses, ventral midline keels situated on the centra, are present on at least the more posteriorly situated unambiguous

cervicals, and absent on unambiguous dorsals (Luca, 1984, Chatterjee, 1985, Sues et al., 2003, Jouve et al., 2006, Fiorelli and Calvo, 2008, Peyer et al., 2008, Butler et al., 2011). However, hypapophyses are entirely absent in many fossil archosaurs, limiting even the potential usefulness of this feature in identifying the cervicodorsal transition (Currie and Zhao, 1993, Brochu, 2003, Carballido and Sander, 2013, Campione, 2014, Lecuona et al., 2016, McPhee et al., 2016). Among archosaurs with hypapophyses, at least two patterns of occurrence exist for this transitional feature. In extant crocodylians, hypapophyses are present on all postaxial cervical vertebrae and several dorsal vertebrae (Iijima and Kubo, 2019), whereas in extant birds, hypapophyses are present only on the posterior cervical vertebrae and anterior dorsal vertebrae (Ghetie, 1976, Baumel, 1993). The posterior disappearance of the hypapophysis is therefore helpful in locating the cervicodorsal transition, at best, in phylogenetically restricted subgroups of Archosauria.

(5.3) Angle of zygapophyseal facets. The zygapophyseal facets are gradually reoriented across the cervicodorsal transition, often being steeply inclined in unambiguous postaxial cervicals but sub-horizontal in unambiguous dorsals (Schwarz et al., 2006, Peyer et al., 2008, Georgi and Krause, 2010, Pol et al., 2012, Nobre and Carvalho, 2013, Blanco et al., 2015, Leardi et al., 2015, Han et al., 2018). As with parapophyseal position, however, ambiguity arises with respect to "scoring" this transitional feature, in this case because no standard, explicit angular threshold has been established for determining whether a given zygapophyseal facet should be considered steeply inclined or sub-horizontal. In addition, the zygapophyseal facets are steeply inclined on all preserved presacral vertebrae in at least two basal crocodylomorphs, namely *Junggarsuchus sloani* and *Dibothrosuchus elaphros* (Wu and Chatterjee, 1993, Clark et al., 2004). For these reasons, zygapophyseal facet orientation may not provide a good criterion for identifying the cervicodorsal transition.

Among the five approaches to identifying the cervicodorsal transition in fossil archosaurs, reliance on transitional features appears to be the most promising because (1) these features can be described and potentially scored in explicit terms, (2) they can be directly observed in both articulated skeletons and disarticulated vertebrae, and (3) their distribution along the vertebral column can be examined with respect to the traditionally defined

cervicodorsal transition in extant archosaurs and fossil specimens that are either exceptionally well-preserved or have the sternal ribs and sternum mineralized. In this study, we survey transitional features in extant birds and crocodylians and propose three classes of criteria for narrowing down the location of the cervicodorsal transition in extant and fossil archosaurs.

2.2 Materials and Methods

For the sake of clarity, brevity and consistency, a simplified terminology is used throughout the rest of this study. The anteriormost presacral connected to the sternum via rib segments is referred to as the first true dorsal. Presacral vertebrae and dorsal vertebrae are referred to as presacrals and dorsals, respectively. Postaxial cervical vertebrae, or post-syncervical cervical vertebrae in taxa in which a syncervical is present, are referred to simply as cervicals, because the atlas, the axis, and the syncervical each have unique morphological features unrelated to the cervicodorsal transition. The term cervicodorsal region is used for a transitional region made up of posterior cervicals and anterior dorsals, corresponding essentially to the "pectoral" region of some authors. The number of vertebrae within the presacral, cervical, cervicodorsal, or dorsal region is referred to as the count of the respective region (e.g. presacral count). Individual presacrals are referenced according to their sequential numbers starting from atlas, from anterior to posterior, within their respective regions (i.e. P#, C#, CD#, and D#). For convenience and brevity, morphological changes along the presacral column are described as if the frame of observation is moving from anterior to posterior; thus, if a feature is said to "shift from" condition A to condition B, this means that condition B is characteristic of more posteriorly located presacrals. Unless specified otherwise, statements about the distribution of trasitional features are based on the extant and fossil archosaur taxa sampled in this study.

Data pertaining to transitional features in the presacral region were collected directly from 27 extant birds, two extant crocodylians, and 38 fossil archosaur specimens, six of which were taxonomically indeterminate. Specimens sampled directly in this study are housed in collections in Canada, China, and the United States. Data on an additional 15 fossil archosaur

species represented by articulated or associated skeletons were taken from the literature (Table 1 and Supplementary Table 1).

No feature, or combination of features, unambiguously diagnostic of the first sternal connection across a wide diversity of archosaurs could be identified in this study (see Result section for additional information). However, it was possible to identify criteria that were useful in defining a relatively short cervicodorsal region within which, or at least adjacent to could be presumed with a high degree of confidence to lie. Three classes of criteria were developed based on data from extant birds and crocodylians, using a two-step procedure. First, eight transitional features, including two commonly used in the literature, were scored as categorical characters for each presacral in each specimen considered in this study. The parts of the presacral region in which the eight transitional features changed from one state to the other were documented in extant archosaurs, relative to the first sternal connection. Second, the four transitional features that most consistently showed discernible changes in the vicinity of the first sternal connection were used to formulate the three classes of criteria for delineating the cervicodorsal region, the classes having different strengths and weaknesses. Each class included two of the four selected transitional features, one feature defining the anterior limit of the cervicodorsal region and the other the posterior limit. The cervicodorsal regions delineated by the three classes of criteria were assessed for reliability in birds and crocodylians based on whether they included the first sternal connection.

Using the three classes of criteria developed based on the data from extant birds and crocodylians, the presacrals of the fossil archosaurs in the study sample were regionalized into cervicals, cervicodorsals, and dorsals, a procedure that required the anteroposterior order of the presacrals to first be established. For articulated specimens, the order of the presacrals was known a priori. For disarticulated skeletons with anteroposterior order of the presacrals stated in the literature or labelled on/with the specimens, the stated order was accepted (see Supplementary Information for the presacral numbering in the original studies). For disarticulated presacrals without additional information, the order was established based on parapophyseal positioning, presacrals with more dorsally situated parapophyses being considered to lie farther posteriorly. This approach is predicated on the observation that the typical condition

in archosaurs, seen in almost all the well-preserved, articulated presacral series examined in this study, is for the parapophysis to gradually transition from a ventral position on the centrum in anterior cervicals to a relatively dorsal position on the neural arch pedicle in posterior dorsals. The sole exception is the presacral series of *Po. gracilis* YPM 51700, a specimen in which the presacrals were originally articulated and were labelled before being separated during preparation. *Po. gracilis* YPM 51700 might represent a unique case, as the position of the parapophysis follows the usual anteroposterior trend in another poposauroid, *Lotosaurus adentus* IVPP V 4910.

The patterns of regionalization dictated by applying the three classes of criteria to well-preserved fossil archosaurs were contrasted, to better assess the utility of each class. As all classes of criteria defined the anterior boundary of the cervicodorsal region in the same way, the number of cervicals (i.e. cervical count) was consistent across all classes of criteria. Therefore, the cervical counts were compared across Archosauria, to infer patterns of cervical count evolution in the avian and crocodylian lineages.

2.3 Results

2.3.1 Individual transitional features

Four of the eight transitional features sampled in this study show relatively consistent and discernible morphological shifts adjacent to the first sternal connection. Below, patterns of change are described first for these four relatively consistently varying characters, and subsequently for the other four, which are less regular in their anteroposterior variation.

Parapophyseal drift — The parapophysis gradually drifts dorsally across the neurocentral suture (NCS) in most archosaur taxa, a condition referred to in this study as complete parapophyseal drift. Observed exceptions include most neognaths and the poposauroid *Po. gracilis* (YPM 51700). In most neognaths, the parapophysis either drifts dorsally but remains ventral to the NCS, as in all galliforms and most anseriforms (e.g. *Meleagris gallopavo* (UAMZ 5351)), or the parapophysis becomes divided by the NCS but never drifts fully onto the neural

arch (e.g. *Gavia immer* (UAMZ 1793)). The former condition is referred to as absence of parapophyeal drift, and the latter as partial parapophyseal drift. *Accipiter gentilis* (UAMZ 5708), *Aquila chrysaetos* (UAMZ 5029), *Falco peregrinus* (UAMZ 6769), *Grus monacha* (UAMZ 6806), and *Haliaeetus leucocephalus* (UAMZ 5028) were the only five extant birds found to display complete parapophyseal drift. In *Po. gracilis* (YPM 51700), the parapophysis does not deviate far from the NCS, but instead fluctuates eight times between being divided by the NCS and being positioned dorsal to it. In another poposauroid, *Lotosaurus adentus* (IVPP V 4910), the parapophysis unidirectionally drifts from being positioned ventral to the NCS, to being divided by the NCS, and finally to being positioned dorsal to the NCS, as in most archosaurs.

In extant crocodylians (e.g. *Caiman crocodilus* ROM R7707 and ROM R275) and the five extant birds with complete parapophyseal drift, the number of presacrals divided by the NCS may be one (e.g. *Cai. crocodilus* (ROM R7707)), two (e.g. *Aq. chrysaetos*(UAMZ 5029)), three (e.g. *Gr. monacha* (UAMZ 6806)), or five (e.g. *Ac. gentilis* (UAMZ 5708)).

In extant crocodylians, the parapophysis becomes divided by the NCS either one presacral anterior to (e.g. *Alligator mississippiensis* (ROM R395)), on the same presacral as (e.g. *Cai. crocodilus* (ROM R275)), or two presacrals posterior to (e.g. *Cai. crocodilus* (ROM R7707)) the first sternal connection. In the five extant birds with complete parapophyseal drift, the parapophysis becomes divided by the NCS either two presacrals anterior to (e.g. *Gr. monacha* (UAMZ 6806)), or on the same presacral as, the first sternal connection (e.g. *Ac. gentilis* (UAMZ 5708)). After becoming divided by the NCS, the parapophysis drifts dorsal to the NCS one to five presacrals posterior to the first sternal connection in crocodylians, and in four of the five birds with complete parapophyseal drift. In *F. peregrinus* (UAMZ 6769), the parapophysis drifts dorsal to the NCS on one presacral anterior to the first sternal connection, but this condition is unique among birds examined in this study. In the 14 extant birds in the sample with partial parapophyseal drift, the parapophysis becomes divided by the NCS one presacral anterior to (e.g. *Bubo virginianus* (UAMZ 6846)), on the same presacral as (e.g. *Gavia immer* (UAMZ 1793)), or up to five presacrals posterior to, the first sternal connection (e.g. *Pica pica* (UAMZ 3725)). A noteworthy intrageneric variation is that the parapophysis becomes divided by the NCS one presacral anterior to the first sternal connection in *Larus californicus* (UAMZ

5066), but three presacrals posterior to the first sternal connection in *Larus delawarensis* (UAMZ 5103). Similar variations occur in some bird species (e.g. *Olor columbianus* (UAMZ 5229, 5230)). Overall, the parapophysis becomes divided by the NCS at a level posterior to the first sternal connection in most extant crocodylians, and in most extant birds with complete or partial parapophyseal drift.

Complete parapophyseal drift, as seen in extant crocodylians, was observed in most fossil archosaur taxa in our study sample. In five well-preserved cerapodans (e.g. *Edmontosaurus regalis* (CMN 2289), *Leptoceratops gracilis* (CMN 8889)), the parapophysis shiftts abruptly from being ventral to the NCS to being dorsal to it, a condition which was not observed in extant birds or crocodylians. Parapophyseal drift could also be observed even in fossil taxa with disarticulated presacrals whose anteroposterior order could only be established based on parapophyseal position. However, these disarticulated presacral series were all highly incomplete, as indicated by the small number of presacrals available in each case, so each of them provided only limited information about the pattern of parapophyseal drift in the taxon in question.

Diapophyseal orientation — The diapophysis gradually shifts its orientation from ventrolateral to lateral, and a second shift, to dorsolateral, may occur subsequently. At least the first shift occurs in almost all taxa sampled in this study. The only exceptions are *Po. gracilis* (YPM 51700) and seven less well-preserved fossil taxa with relatively few presacrals available for sampling in this study, in which the diapophysis has the same orientation on all preserved presacrals.

In almost all extant archosaurs in our sample, except three birds, diapophyseal orientation gradually shifts once, from ventrolateral to lateral. Diapophyseal orientation shifts twice in *M. gallopavo* (UAMZ 5351), and three times in *Cas. australis* (UAMZ 1369) and *R. americana* (UAMZ 1368). In all three of these species the second shift is from lateral to dorsolateral, as is typical. In the last one or two presacrals of *Cas. australis* (UAMZ 1369) and *R. americana* (UAMZ 1368), however, diapophyseal orientation reverts from dorsolateral to lateral.

The shift in diapophyseal orientation from ventrolateral to lateral consistently occurs from one to four presacrals anterior to the first sternal connection in extant birds and crocodylians. The shift from lateral to dorsolateral takes place one or two preacrals anterior to the first sternal connection in *Cas. australis* (UAMZ 1369) and *M. gallopavo* (UAMZ 5351), but on the same presacral as the first sternal connection in *R. americana* (UAMZ 1368). The final shift from dorsolateral back to lateral occurs three and four presacrals posterior to the first sternal connection in *Cas. australis* (UAMZ 1369) and *R. americana* (UAMZ 1368), respectively.

The number of observed shifts in diapophyseal orientation shows greater variation in fossil taxa than in extant birds and crocodylians. Among the fossil archosaurs examined in this study, diapophyseal orientation shifts only once in 25 taxa, twice in ten texa, three times in seven taxa, and four times in two taxa, namely *Camptosaurus dispar* (YPM 1877) and *Crocodylus grinnelli* (YPM 300). Some taxa are represented by well-preserved specimens in which the anteroposterior order of the presacrals is known (e.g. *Ty. rex* (FMNH PR2081) (Brochu, 2003)), but for others the only available specimens are relatively poorly preserved ones with disarticulated presacrals (e.g. *Hesperosuchus agilis* (AMNH 6758)) It is possible that the distribution of transition counts would be slightly different if every taxon were represented by complete and articulated material, but overall patterns are clear. Some fossil taxa (e.g. *Sinraptor dongi* (Currie and Zhao, 1993)) display gradual transitions in diapophyseal orientation as in extant birds and crocodylians, but some observed transitions are abrupt, resulting from a single presacral that differs in diapophyseal orientation from the anteriorly and posteriorly adjacent ones (e.g. the second and third shifts from between the seventh and the ninth preserved presacrals in *Cro. grinnelli* (YPM 300)).

Shifts in diapophyseal orientation typically demonstrate similar patterns across closely related fossil taxa, and may have both functional and phylogenetic implications. In most fossil pseudosuchian taxa, diapophyseal orientation shifts once from ventrolateral to lateral, as in extant crocodylians. Only *Cro. grinnelli* (YPM 300), *Simosuchus clarki* and two less well-preserved taxa show evidence of multiple shifts in diapophyseal orientation. By comparison, half of the fossil avemetatarsalians in the sample show evidence of multiple shifts. In *Le. gracilis* (CMN 8889) and four less well-preserved fossil taxa (e.g. *Majungasaurus crenatissimus*

(O'Connor, 2007)), diapophyseal orientation shifts directly from ventrolateral to dorsolateral, a phenomenon not observed in other taxa. However, this may be a result of incomplete preservation at least in the four less well-preserved taxa, because intervening presacrals with horizontally oriented diapophyses may originally have been present. In the ceratopsian *Le. gracilis* (CMN 8889), the anteriormost preserved presacral identified as P4 has laterally directed diapophyses, but diapophyseal orientation gradually transitions to dorsolateral. Ventrolaterally oriented diapophyses are not present on any presacral of *Le. gracilis* (CMN 8889) but occur in two well-preserved ceratopsians (i.e. *Montanoceratops cerorhynchus* (AMNH 5464) and *Chasmosaurus belli* (NHMUK R4948) (Maidment and Barrett 2011)), suggesting variation in patterns of diapophyseal orientation within Ceratopsia.

Foramen transversarium — The foramen transversarium gradually decreases in size, and is entirely absent from the posterior presacrals of most archosaurs in the study sample. The only exceptions are extant birds, *Si. dongi* (Currie and Zhao, 1993), and nine less well-preserved taxa, in which the foramen transversarium is present on all preserved presacrals.

In extant crocodylians, the foramen transversarium consistently disappears two or three presacrals posterior to the first sternal connection (e.g. *Al. mississippiensis* ROM R395), leaving 12 or 13 presacrals without foramina transversaria.

In most well-preserved fossil taxa outside Theropoda sampled in this study, 10 to 13 posterior presacrals were observed to lack foramina transversaria, approximately as in extant crocodylians. In *Lo. adentus* (IVPP V 4910), all sampled theropods (e.g. *Ty. rex* (Brochu, 2003)), and two ceratopsians (e.g. *Mo. cerorhynchus* AMNH 5464), however, fewer than 10 presacrals lack foramina transversaria. By contrast, 13 and 15 preserved presacrals lack foramina transversaria in the ornithopods *Tenontosaurus tilletti* (Forster, 1990) and *Ed. regalis* (CMN 2289), respectively. Despite these exceptions, a pattern of foramen transversarium loss similar to that seen in extant crocodylians is clearly common in fossil archosaurs. The condition seen in extant birds may have been acquired in theropods situated phylogenetically closer to birds than are tyrannosaurids.

Hypapophysis — Well-developed or not, hypapophysis as an anatomical structure is not prevalent in fossil archosaurs, but occurs in extant birds and crocodylians, *Hesperosuchus agilis* (AMNH 6758), *Junggarsuchus sloani* (IVPP V 14010), *Hesperornis regalis* (YPM 1207), *Deinonychus antirrhopus* (YPM 5204), and *Si. dongi* (Currie and Zhao, 1993). Unlike in most crocodyliforms, all available presacrals of *Baurusuchus albertoi* (Nascimento and Zaher, 2010) and *Simosuchus clarki* (Georgi and Krause, 2010) lack the hyapophysis, even though both species are represented by well-preserved specimens.

Two general patterns were observed in extant birds and crocodylians. In most extant birds, hypapophyses are typically absent on the anterior presacrals, though the first three presacrals may carry distinct hypapophyses. Throughout the presacral series, hypapophyses become present and well-developed on more than two presacrals in vicinity of the first sternal connection, and either remain present on all successive presacrals as in most neognaths (e.g. *Gallus gallus* (UAMZ 5919)) or eventually become absent again as in all palaeognaths (e.g. *Cas. australis* (UAMZ 1369)) and 11 neognaths examined in this study. In *Branta canadensis* (UAMZ 4685), however, the nature of the hypapophysis changes between present and absent six times throughout the presacral series. P6 in *Ardea herodias* (UAMZ 4048) and P14 in *L. delawarensis* (UAMZ 5103) carries hypapophysis, which are absent on the immediately adjacent presacrals. In *O. columbianus* (UAMZ 5229, 5230), the hypapophysis is absent on P20 but is present on the immediately adjacent presacrals. In extant crocodylians, unlike in extant birds, hypapophyses are present on from anterior cervicals to anterior dorsals, and only become absent posterior to the first sternal connection.

In extant palaeognaths, the hypapophysis disappears one or two presacrals posterior to the first sternal connection. In the 11 neognaths in which the hypapophysis disappears close to the first sternal connection, the hypapophysis can disappear one presacral before (e.g. *Gr. monacha* (UAMZ 6806)), on the same presacral as (e.g. *F. sparverius* (UAMZ 4022)), or two to five presacrals posterior to (e.g. *Ha. leucocephalus* (UAMZ 5028)) the first sternal connection. In extant crocodylians, the hypapophysis disappears three to five presacrals posterior to the first sternal connection. Extant palaeognaths and crocodylians thus resemble one another in that the

hypapophysis disappears at a point posterior to the first sternal connection, although the exact region in which disappearance occurs differs between the two groups.

De. antirrhopus (YPM 5204) and *Si. dongi* (Currie and Zhao, 1993) resemble extant birds in having distinct hypapophyses on two presacrals in vicinity of the first sternal connection, but not on more anterior and posterior presacrals. In fossil crocodyliforms and *J. sloani* (IVPP V 14010), distinct hypapophyses are present on anterior presacrals and absent on posterior ones, as in extant crocodylians. In *He. agilis* (AMNH 6758), hypapophyses are present on all preserved presacrals, except one in which the ventral part of the centrum is damaged. The distribution of hypapophyses in particular fossil taxa seemingly resembles that observed in their closest extant relatives. Hypapophysis is absent on all presacrals in other fossil archosaurs sampled in this study.

Uninformative transitional features — Parapophyseal morphology, presence of neural spines, neural spine orientation, and presence of epipophyses are transitional features that do not appear to have the potential to act as good indicators of the location of the first sternal connection in the archosaurs examined in this study. These four transitional features (1) do not display consistent patterns of change in extant archosaurs, and/or (2) are phylogenetically variable to the extent that they are only informative in relatively exclusive clades.

In all archosaur presacrals examined, the outline of the parapophysis in lateral view could be scored as subcircular, anteroposteriorly elongated, or dorsoventrally elongated. In extant birds, the parapophysis is anteroposteriorly elongated in the anterior presacrals, and becomes subcircular or dorsoventrally elongated in the posterior presacrals. However, four distinct patterns of change were observed. In the first pattern, seen in six birds (e.g. *Anas rubripes* (UAMZ 4683)), the parapophysis becomes and remains dorsoventrally elongated. In the second pattern, seen in 16 birds, the parapophysis initially becomes subcircular, and only subsequently becomes dorsoventrally elongated. The number of subcircular parapophyses in the intermediate zone varies, and in posterior presacrals the parapophysis may revert from dorsoventrally elongated to subcircular (e.g. *Ha. leucocephalus* (UAMZ 5028)). In the third pattern, seen in six birds, the parapophysis first becomes subcircular, then reverts to anteroposteriorly elongated, and

finally becomes either dorsoventrally elongated or subcircular in the posterior preasacrals. In *Dendragapus canadensis* (UAMZ 5702), the parapophysis first changes from anteroposteriorly elongated to dorsoventrally elongated, then reverts to anteroposteriorly elongated, and finally becomes dorsoventrally elongated again.

In extant crocodylians, the parapophysis changes from anteroposteriorly elongated to subcircular along the presacral series, and two patterns of change are observed. In the first pattern, the parapophysis initially becomes dorsoventrally elongated, and subsequently changes to subcircular (e.g. *Al. mississippiensis* (ROM R4406)). In the second pattern, the parapophysis initially becomes subcircular, then changes to dorsoventrally elongated, and finally reverts to subcircular (e.g. *Al. mississippiensis* (ROM R395)). Crocodylians thus resemble birds in that the parapophysis consistently changes from being anteroposteriorly elongated to having a different outline, but also in that anteroposterior elongation of the parapophysis cannot be used to unambiguously identify a given presacral as being from the anterior part of the series, because the anteroposteriorly elongated condition may eventually reappear in the posterior presacrals.

In fossil crocodylomorphs and ornithopods, as in extant archosaurs, the parapophysis is anteroposteriorly elongated in the anteriormost presacrals, but changes shape more posteriorly, with the specifics varying across taxa. The parapophysis may undergo several such changes along the presacral series (e.g. *Le. gracilis* (CMN 8889)), making patterns difficult to interpret. In 12 fossil theropods and ceratopsians (e.g. *Mo. cerorhynchus* (AMNH 5464)) of this study sample, the parapophysis is either subcircular or dorsoventrally elongated on the anteriormost presacrals, rather than anteroposteriorly elongated. Given the lack of consistent patterns of change in both extant and fossil archosaurs, parapophyseal morphology is unhelpful in identifying the cervicodorsal transition.

A distinct neural spine that is approximately as tall as the centrum is present on all presacrals in extant crocodylians, but is absent on the anterior presacrals of extant birds, which bear at most a small, subdued protuberance. The neural spine gradually becomes taller along the presacral series. Although a distinct neural spine is typically absent on anterior cervicals, it was found on P3 to P6 in 17 birds examined in this study (e.g. *Pica pica* (UAMZ 3725)). A variation

was observed in *Ga. immer* (UAMZ 1793), in which the neural spine becomes distinct on P6 but immediately reverts to being subdued on P7, only to again become distinct four presacrals later on P11. Among extant birds included in this study, the minimum number of presacrals without a distinct neural spine is five (e.g. *Ga. immer* (UAMZ 1793)), and the maximum number is 17 (e.g. *O. columbianus* (UAMZ 5229, 5230)). The neural spine consistently becomes distinct anterior to the first sternal connection. However, this change can take place one to six, presacrals anterior to the first sternal connection. The most extreme case was observed in *Cas. australis* (UAMZ 1369), in which the neural spine becomes distinct 12 presacrals anterior to the first sternal connection. Absence of a distinct neural spine may thus be unambiguously diagnostic of avian cervicals, but presence of a distinct spine is not diagnostic of unambiguous dorsals even in extant birds.

Only ten of the fossil archosaur taxa examined in this study lacked a distinct neural spine on one or more presacrals, including the fossil bird *Hp. regalis* (YPM 1207), two non-avian theropods (*Coelurus fragilis* (YPM 2010) and Coelophysidae indet. (NMMNH P 61887, 61888, 61897)), the sauropod *Camarasaurus grandis* (YPM 1905), five ornithopods (e.g. *Ed. regalis* (CMN 2289), and the stegosaur *Stegosaruus stenops* (Maidment et al., 2015). In contrast to the condition in extant birds, only two ornithopods and *St. stenops* (Maidment et al., 2015) have more than five presacrals lacking a prominent neural spine. Taken together, these observations suggest that absence of a distinct neural spine may be a useful character for identifying unambiguous cervicals in several specific extinct archosaur clades, but that presence of a distinct neural spine is unlikely to be a reliable indicator that a presacral belongs to the dorsal part of the column, even in these same groups.

Changes in neural spine orientation were observed in nine extant birds and all five crocodylians examined in this study. In most of the extant birds, however, the neural spine is oriented dorsally on all presacrals with distinct neural spines. Among the nine extant birds that show changes in neural spine orientation, there are five (e.g. *Pi. pica* (UAMZ 3725)) in which the change occurs prior to P6 and all distinct neural spines present beyond the point of transition are dorsally oriented. In *Bu. virginianus* (UAMZ 6846), the neural spine is posterodorsally oriented on P3 and P4, inconspicuous on P5 to P12, anterodorsally oriented on P13, and dorsally

oriented on all successive presacrals. *Aq. chrysaetos* (UAMZ 5029), *Br. canadensis* (UAMZ 4685), and *O. columbianus* (UAMZ 5229) display patterns of change similar to that seen in *Bu. virginianus* (UAMZ 6846). In *Aq. chrysaetos* (UAMZ 5029), *Bu. virginianus* (UAMZ 6846), *Br. canadensis* (UAMZ 4685), and *O. columbianus* (UAMZ 5229), the first change in neural spine orientation after the neural spine variously takes place one, two, three, or five presacrals anterior to the first sternal connection.

In the extant crocodylians examined, except *Cai. crocodilus* (ROM R7707), the neural spine is dorsally oriented on the anterior presacrals, but spine orientation first changes to posterodorsal and then reverts back to dorsal along the presacral series. A variation was observed in *Al. mississippiensis* (ROM R4406), in which neural spine orientation undergoes four gradual shifts between dorsal and posterodorsals. In *Cai. crocodilus* (ROM R7707), the neural spine is posterodorsally oriented on the anterior presacrals, but neural spine orientation gradually changes to dorsal. In these extant crocodylians, the first change in neural spine orientation may take place four to six presacrals anterior to (e.g. *Cai. crocodilus* (ROM R275)), on the same presacral as (e.g. *Cai. crocodilus* (UAMZ unnumbered)), or eight presacrals posterior to (e.g. *Cai. crocodilus* (ROM R7077)), the first sternal connection. Using the posteriormost change in neural spine orientation yields similar results in both extant birds and crocodylians.

Neural spine orientation shifts along the presacral series in highly variable ways in the 28 fossil taxa included in this study, as in extant birds and crocodylians. Among the taxa represented by well-preserved specimens, neural spine orientation changes from dorsal to posterodorsal only once along the presacral series in *Mo. cerorhynchus* (AMNH 5464), *Le. gracilis* (CMN 8889), *Ba. albertoi* (Nascimento and Zaher, 2010), and *Lo. adentus* (IVPP V 4910). However, the neural spine is anterodorsally oriented on the first three or four preserved presacrals in three notosuchians (e.g. *Sm. clarki* (Georgi and Krause, 2010)), and on the first ten preserved presacrals in *Lo. adentus* (IVPP V 4910). Patterns of change in neural spine orientation are highly variable in extant and fossil archosaurs, making this transitional feature unreliable for identifying the cervicodorsal transition.

The epipophysis, a distinct dorsal protuberance on the postzygapophysis, was observed in 30 extant birds, six fossil theropods (e.g. *Co. fragilis* (YPM 2010)), the sauropod *C. grandis* (YPM 1905), the ornithopod *Cp. dispar* (YPM 1877), and two ankylosaurs (e.g. *Ankylosaurus magniventris* (AMNH 5895)), but not in other archosaur taxa. In extant birds, multiple transitional patterns were observed. In the first pattern, seen in eight birds (e.g. *A. rubripes* (UAMZ 4683)), the epipophysis is present on the anterior presacrals, and disappears on subsequent presacrals. *Pi. pica* (UAMZ 3725) displays a variation on this pattern, in which the epipophysis is conversely absent on the anterior presacrals and present on subsequent presacrals. In the second pattern, seen in in *R. americana* (UAMZ 1368) and *O. columbianus* (UAMZ 5230), the epipophysis is absent on the anterior presacrals, becomes distinctly developed on subsequent presacrals, and then disappears again. In the third pattern, seen in 19 birds (e.g. *Bu. virginianus* (UAMZ 6846)), the epipophysis switches between being present and absent multiple times throughout the presacral series. As the epipophysis comes and goes more than once in most birds in the study sample, neither the presence nor the absence of this feature is unambiguously diagnostic of a particular region of the presacral column across avian taxa.

Non-avian dinosaurs that have the epipophysis differ from extant birds in that this structure is distinct on the anterior presacrals but absent on subsequent presacrals, and does not reappear towards the posterior end of the presacral series. The presence of the epipophysis may thus distinguish anterior from posterior presacrals, but only within non-avian dinosaur clades in which this feature occurs in the first place.

Summary of findings on transitional features — None of the transitional features examined in this study can pinpoint the exact presacral on which the first sternal connection is established, at least when considered individually. Nevertheless, parapophyseal position, diapophyseal orientation, occurrence of a foramen transversarium, and occurrence of a distinct hypapophysis change consistently enough along the presacral series to offer transition points that are likely to be within several presacrals of the first sternal connection.

2.3.2 Sequential orders of transitional features

Among the observed changes in the four consistent transitional features in both extant birds and crocodylians, only the first shift in diapophyseal orientation consistently takes place anterior to the first sternal connection. Movement of the parapophysis to a position dorsal to the NCS, disappearance of the foramen transversarium, and loss of a distinct hypapophysis predominantly take place following the first sternal connection. The first appearance of a parapophysis that is divided by the NCS lacks a consistent relationship with the first sternal connection, but is helpful for incorporating archosaur taxa with partial parapophyseal drift (e.g. *Cas. australis* (UAMZ 1369)) for comparisons across Archosauria.

The first shift in diapophyseal orientation is the earliest shift in any transitional feature to take place in most archosaur taxa examined in this study. The sole exception is *De. antirrhopus* (YPM 5204), in which the parapophysis becomes divided by the NCS one presacral anterior to the first shift in diapophyseal orientation. Next, the parapophysis typically becomes divided by the NCS. Drift of the parapophysis into a position dorsal to the NCS, loss of a distinct foramen transversarium, and disappearance of the hypapophysis occur subsequently, and these changes do not consistently occur in any particular sequence. Accordingly, no single sequential order that includes all four transitional features could be determined. However, it was nevertheless possible to establish four classes of plausible criteria for delineating a distinct cervicodorsal region of the vertebral column that is likely to contain, or at least be adjacent to, the first sternal connection. Each class of criteria uses the first shift in diapophyseal orientation to mark the beginning of the cervicodorsal region (i.e. the first vertebra with laterally rather than ventrolaterally diapophyses is the first cervicodorsal vertebra) and a change in one of the remaining three transitional features to mark the end of the cervicodorsal region (i.e. identify the first post-cervicodorsal vertebra).

The respective gaps between the first shift in diapophyseal orientation and changes of other transitional features can be measured in presacral vertebrae. The number of presacrals between the first presacral with horizontally orientated diapophysis and the first presacral with a parapophysis divided by the NCS range from zero to seven in extant birds with parapophyseal drift, one to eight in fossil ornithischians, zero to five in fossil pseudosuchians, two or three in extant crocodylians, and zero or one in most fossil theropods. A higher number of presacrals is

present between the first presacral with horizontally orientated diapophysis and the first presacral with a parapophysis dorsal to the NCS, the count being 13 in *Lo. adentus* (IVPP V 4910), zero to nine in fossil dinosaurs including the fossil bird *Hp. regalis* YPM 1207, one to six in extant birds, one to four in most non-crocodylian pseudosuchians, and four in extant crocodylians. The number of presacrals between the first shift in diapophyseal orientation and the disappearance of the foramen transversarium is ten in *Lo. adentus* (IVPP V 4910), zero to nine in fossil dinosaurs, zero to five presacrals in most pseudosuchians, and three to five in extant crocodylians. The number of presacrals between the first shift in diapophyseal orientation and the disappearance of the hypapophysis is one to six in extant birds, five or six in extant crocodylians and fossil pseudosuchians, and two in non-avian theropods.

2.3.3 Transitional criteria for identifying the cervicodorsal transition

The transitional features considered in this study cannot provide a basis for pinpointing the exact location of the first sternal connection, but morphological evidence suggests that the first shift in diapophyseal orientation seen in any extinct archosaur can be used to identify the first vertebra of a cervicodorsal region that the first sternal connection is almost certainly either located within or adjacent to. The last vertebra of the cervicodorsal region, in turn, is delimited by one of three other transitions in vertebral morphology that shows a relatively high level of positional consistency. The cervicodorsal region used by early anatomists (e.g. (Mivart, 1877)) is redefined using the combinations of the first shift in diapophyseal orientation and another transitional feature. Three classes of transitional criteria are proposed.

The first shift in diapophyseal orientation is from ventrolateral to lateral in all extant and most fossil archosaurs sampled in this study, the sole exception among well-preserved specimens being *Le. gracilis* (CMN 8889). In practice, any change in diapophyseal orientation from ventrolateral to lateral observed in an incomplete fossil archosaur vertebral column can be assumed with minimal uncertainty to represent the first such shift.

2.4 Discussion

2.4.1 Implications of using parapophyseal position as a basis for anteroposterior ordering of presacrals

In this study, dorsoventral parapophyseal location was used as a basis for establishing the anteroposterior order of disarticulated presacrals in fossil archosaurs, presacrals with more dorsally placed parapophyses being assigned more posterior positions. Once anteroposterior order had been determined, the distributions of several transitional features along the presacral series were documented. Use of parapophyseal location as the ordering criterion potentially introduced a subtle bias, as two of the transitional features (i.e. parapophyseal drift, and presence or absence of a foramen transversarium) are related to the position of the parapophysis on the presacrals. More dorsally positioned parapophyses were naturally more likely to lie dorsal to the NCS, or at least be divided by the NCS, than to lie ventral to the NSC, and presacrals with more dorsally positioned parapophyses were more likely to lack foramina transversaria because of close association of the parapophysis with the diapophysis. If parapophyseal location is unreliable as a basis for determining the anteroposterior sequence of a series of disarticulated presacrals, then some presacrals in such series are being incorrectly placed too far posteriorly in our analysis. Relative to their true anterior and posterior neighbors, the presacrals being placed too far posteriorly will have dorsally displaced parapophyses, and may therefore lack a foramen transversarium when this feature is present in their neighbors, have a parapophysis that lies dorsal to the NCS when their neighbors have one that lies on or ventral to the NCS, or have a parapophysis that lies on the NCS when their neighbors have one that lies ventral to the NCS. As a result, the number of observed shifts in parapophyseal position relative to the NCS and in presence of the foramen transversarium may be artificially reduced, and the locations of the shifts may be artificially displaced posteriorly along the presacral series.

However, this bias likely had at most a minor effect on the findings reported herein, for the following reasons. In most neognaths sampled in this study, the parapophysis remains ventral to the NCS throughout the presacral column, despite drifting closer to the NCS along the series. Accordingly, some taxa lack a scorable shift in parapophyseal position that could be affected by errors in establishing the anteroposterior order of the presacrals. Disappearance of the foramen transversarium is universal, but the correlation between presence of a foramen transversarium

and dorsoventral position of the parapophysis is imprecise, so a presacral with a slightly more dorsally placed parapophysis is not necessarily less likely to have an open foramen transversarium. Therefore, parapophyseal drift and occurrence of a foramen transversarium can be legitimately scored as transitional features on disarticulated preacrals whose anteroposterior order has been established based on the dorsoventral position of the parapophysis.

The relationship between parapophyseal position and presence of a foramen transversarium is complex. If the parapophysis lies ventral to the NCS, a foramen transversarium is invariably present, based on data collected in this study. In taxa in which the parapophysis shifts to a position dorsal to the NCS, however, this shift may take place anterior to, on the same presacral as, or posterior to disappearance of the foramen transversarium (e.g. extant crocodylians (ROM R395, 7707), *Ty. rex* (Brochu, 2003)). Parapophyseal drift relative to the NCS therefore cannot be used as an unambiguous proxy for presence/absence of a foramen transversarium. Alternatively, the two transitional features (i.e. parapophyseal drift and foramen transversarium) can be combined into one feature, in which the disappearance of the foramen transversarium becomes a state of parapophyseal drift and is identified by the parapophyseal position being immediately ventral to the diapophysis. Combining parapophyseal drift and presence of a foramen transversarium in this way would be feasible for extant birds and crocodylians, and for fully prepared fossil archosaur specimens. In some fossil archosaur specimens in which the presacral vertebrae remain in articulation with the corresponding ribs, however, the locations of the parapophyses may be difficult to observe (Drysdale et al., 2019). Treating the foramen transversarium as a separate transitional feature allows character states for this feature to be scored based on whether a visible, distinct gap exits between the vertebra and vertebral rib, and the topological relationship between the capitulum and tuberculum, potentially increasing the number of fossil archosaur taxa that can be sampled in future studies.

2.4.2 Comparisons among three classes of transitional criteria

Among the three classes of transitional criteria, the Type I Diapophysis-Parapophysis (DP) criteria can be applied to most of the archosaur taxa considered in this study, the exceptions being *De. antirrhopus* (YPM 5204), *Po. gracilis* (YPM 51700), five cerapodans, one indeterminate ceratopsid (AMNH 5422), and 12 taxa represented only by less well-preserved

specimens. In *De. antirrhopus* (YPM 5204), the parapophysis becomes divided by the NCS before diapophyseal orientation becomes lateral. In *Po. gracilis* (YPM 51700), the parapophysis lacks a clear transitional pattern, fluctuating along the column in its dorsoventral position with respect to the NCS. In the five cerapodans and AMNH 5422, the parapophysis goes directly from being ventral to the NCS to being dorsal to the NCS, without ever being divided by the NCS. The Type II DP criteria, by contrast, can be applied regardless of whether the parapophysis is ever divided by the NCS. However, the Type II DP criteria cannot be applied in most neognaths, in which the parapophysis never drifts dorsal to the NCS, or in *De. antirrhopus* (YPM 5204), *Po. gracilis* (YPM 51700), and two taxa represented only by less well-preserved specimens. The Diapophysis-Foramen-Transversarium (DFT) criteria are the most versatile, being applicable to the vast majority of the archosaurs in the sample. The only exceptions are the consistently problematic *Po. gracilis* (YPM 51700) and three taxa represented only by less well-preserved specimens. The Diapophysis-Hypapophysis (DH) criteria can be applied to most of the theropods and crocodylomorphs in the sample that possess distinct hypapophyses, the exceptions being *Br. canadensis* (UAMZ 4685), *Hp. regalis* (YPM 1207), and two pseudosuchian taxa represented by less well-preserved specimens. The advantages and disadvantages of each class of criteria are discussed here, with a focus on how each class of criteria performs when applied to the various archosaur taxa in the sample.

Type I DP criteria — The Type I DP criteria regionalise the presacrals into cervicals, cervicodorsals, and dorsals in the extant birds and crocodylians in the sample, and the first sternal connection is often located within or immediately posterior to the cervicodorsal region.

Across the five palaeognaths and 14 neognaths in the sample, the presacrals are regionalized into cervicals, cervicodorsals, and dorsals in five ways. (1) In four palaeognaths and six neognaths, the first sternal connection is located in the cervicodorsal region, which includes two to seven presacrals and is situated between P12 and P26 inclusively. CD1 is positioned one to three presacrals anterior to the first sternal connection, and D1 is positioned one to four presacrals posterior to the first sternal connection. (2) In five neognaths, the first sternal connection is located on D1, and CD1 is positioned one to three presacrals anterior to the first sternal connection. The cervicodorsal region includes one to three presacrals and is situated from

P13 to P17. (3) In *Cas. australis* (UAMZ 1369) and three neognaths, the first sternal connection is on a dorsal posterior to D1, and the cervicodorsal region includes only one or two cervicodorsals, situated either between P13 and P14 or between P17 and P19. CD1 is positioned two to four presacrals anterior to the first sternal connection, and D1 is positioned one or two presacrals anterior to the first sternal connection. (4) There is no cervicodorsal region in *F. peregrinus* (UAMZ 6769), as diapophyseal orientation shifts to lateral on the same presacral on which the parapophysis becomes divided by the NCS. D1 is positioned two presacrals anterior to the first sternal connection. (5) In all seven galliforms included in the study, and most anseriforms, the presacrals are regionalized into cervicals and cervicodorsals, as the parapophysis remains ventral to the NCS on all presacrals. The first sternal connection is located within the cervicodorsal region, which includes five to seven presacrals and is situated between P14 and P24. CD1 is positioned one to three presacrals anterior to the first sternal connection.

In all five extant crocodylians in the sample, the presacrals are regionalized into cervicals, cervicodorsals, and dorsals in one of three ways. (1) In *Cai. crocodilus* (ROM R7077) and *Al. mississippiensis* (ROM R4406), the first sternal connection is located within the cervicodorsal region, which comprises three presacrals (from P9 to P11). CD1 and D1 are positioned one presacral anterior and two presacrals posterior to the first sternal connection, respectively. (2) In *Cai. crocodilus* (ROM R275), the first sternal connection is located on D1, and only P8 and P9 are identified as cervicodorsals. In *Cai. crocodilus* (UAMZ unnumbered), the first sternal connection is located on D1, and CD1 is positioned two presacrals anterior to the first sternal connection. Therefore, Type I DP criteria can sometimes pinpoint the first dorsal in the same way as regionalisation based on the first sternal connection. (3) In *Al. mississippiensis* (ROM R395), the first sternal connection is located in the dorsal region, and only P7 and P8 are identified as cervicodorsals. CD1 and D1 are positioned three presacrals and one presacral anterior to the first sternal connection, respectively.

Under the Type I DP criteria, the first sternal connection is commonly located either in the cervicodorsal region or on D1 in extant birds and crocodylians, notwithstanding the variations described above. As the total presacral count is known in extant birds and crocodylians, the ratio of cervicals to cervicodorsals to dorsals can be determined for particular

sets of taxa in the study sample, based on the average count for each region. The average ratio is 12:7:0 in extant galliforms and those anseriforms lacking a dorsal region, 4:1:1 in other extant birds, and 5:2:17 in extant crocodylians.

The vertebral counts of the cervical, cervicodorsal and dorsal regions can be ranked with a high degree of certainty in relatively well-preserved specimens that have ten or more preserved presacrals. In most fossil taxa represented by such specimens, the dorsal count is higher than the cervical count, which is in turn higher than the cervicodorsal count, as in extant crocodylians. Unlike extant birds and crocodylians, the cervical count is only three and the cervicodorsal count is eight in *St. stenops* (Maidment et al., 2015). Unlike the other fossil taxa, *Si. dongi* (Currie and Zhao, 1993), *Sm. clarki* (Georgi and Krause, 2010), and *Edentosuchus tienshanensis* (IVPP V 3236) lack a cervicodorsal region, as in the neognath *F. peregrinus* (UAMZ 6769).

Type II DP criteria — In the extant birds and crocodylians in the sample, other than *F. peregrinus* (UAMZ 6769) and those neognaths to which the Type II DP criteria are inapplicable, the presacrals are regionalized by these criteria into cervicals, cervicodorsals, and dorsals, and the first sternal connection is consistently located in the cervicodorsal region.

The presacrals are regionalized in three ways in extant birds. (1) In most extant birds, complete parapophyseal drift is absent. All presacrals posterior to the first shift in diapophyseal orientation are accordingly identified as cervicodorsals, and the cervicodorsal count ranges from four to eight. CD1 is positioned one to three presacrals anterior to the first sternal connection. (2) In four of the five extant birds with complete parapophyseal drift, the cervicodorsal region includes three to six presacrals and is situated from P13 to P21. CD1 is positioned one, two, or four presacrals anterior to the first sternal connection, and D1 is positioned one, two, or five presacrals posterior to the first sternal connection. (3) In *F. peregrinus* (UAMZ 6769), the first sternal connection is located within the dorsal region. CD1 and D1 are positioned two and one presacrals anterior to the first sternal connection, respectively.

In extant crocodylians, the cervicodorsal region consistently includes four presacrals, situated from P7 to P12. CD1 and D1 are positioned one to three presacrals anterior and posterior to the first sternal connection, respectively.

In extant archosaurs, the first sternal connection is commonly located within the cervicodorsal region. Average C:CD:D ratios are broadly similar to those resulting from use of the Type I DP criteria, namely 2:1:0 for most birds, 11:4:4 for the five extant birds with complete parapophyseal drift, and 5:4:15 for extant crocodylians.

In fossil taxa with ten or more preserved presacrals, the greatest number of presacrals may be present in either the cervical region (*Si. dongi* (Currie and Zhao, 1993)), the cervicodorsal region (e.g. *Lo. adentus* (IVPP V 4910)), or the dorsal region (e.g. *Cro. grinnelli* (YPM 300)). The cervical region contains the greatest number of presacrals only in *Si. dongi* (Currie and Zhao, 1993), among taxa in the sample. Consistent ranking in the number of cervicals, cervicodorsals, and dorsals is only evident among species of cerapodans, and among species of *Stegosaurus*, respectively. Among the sampled species of both clades, the dorsal region contains the greatest number of presacrals, as in extant crocodylians.

DFT criteria — In the extant birds in the study sample, the presacrals are regionalized by the DFT criteria into cervicals and cervicodorsals only, whereas in the extant crocodylians the presacrals are regionalized into cervicals, cervicodorsals, and dorsals.

In extant birds, all presacrals posterior to the first shift in diapophyseal orientation are identified as cervicodorsals, and the cervicodorsal count ranges from four to nine. As a result, the DFT regionalization is identical to the Type II DP regionalization in most extant birds. The exceptions are the five birds with complete parapophyseal drift, in which the DFT criteria place CD1 one to four presacrals anterior to the first sternal connection.

The first sternal connection is consistently located within the cervicodorsal region in all five extant crocodylians, though the exact location varies. (1) In *Cai. crocodilus* (ROM R275, 7707, UAMZ unnumbered), four presacrals (either P8 to P11, or P9 to P12) are identified as cervicodorsals, as in the Type II DP regionalization. CD1 is therefore positioned one or two

presacrals anterior to the first sternal connection, and D1 is positioned two or three presacrals posterior to the first sternal connection. (2) In *Al. mississippiensis* (ROM R395, 4406), either three (P9 to P11) or five (P7 to P11) presacrals are identified as cervicodorsals. CD1 is positioned either one or three presacrals anterior to the first sternal connection, and D1 is positioned two presacrals posterior to the first sternal connection.

The average C:CD:D ratio is 2:1:0 for extant birds and 5:4:15 in extant crocodylians, values identical to those resulting from use of the Type II DP criteria.

In fossil taxa with ten or more preserved presacrals, no consistent ranking among the vertebral counts of the presacral regions is evident. However, the dorsal count is consistently the highest in ornithischians (e.g. *Mo. cerorhynchus* (AMNH 5464)) and the three well-preserved crocodyliforms in the study sample (e.g. *Cro. grinnelli* (YPM 300)), and is followed by either the cervical or the cervicodorsal count. The cervicodorsal count is the same as the dorsal count in *Iguanodon bernissartensis* (Norman, 1980) and *Necrosuchus ionensis* (AMNH 3219), but this finding may be biased by taphonomic factors if additional dorsals were originally present but have not been preserved or sampled. Unlike in ornithischians, the cervicodorsal count is the highest in non-avian theropods and *Lo. adentus* (IVPP V4910). The dorsal count is zero in *Si. dongi* (Currie and Zhao, 1993), as in extant birds, but *De. antirrhopus* (YPM 5204) has at least one dorsal despite having close avian affinities (Pittman et al., 2020).

DH criteria — Presacrals in extant birds are typically regionalised in one mode with a few examples deviated from it, whereas presacrals in crocodylians is consistently regionalised in the same way. The first sternal connection is often located either within or immediately posterior to the cervicodorsal region. *Br. canadensis* (UAMZ 4685) is the only extant bird in which the DH criteria could not be applied, because the hypapophysis undergoes multiple shifts between distinct and absent after the diapophyseal orientation shifts to lateral.

In extant birds, the presacrals may be regionalized into cervicals, cervicodorsals, and dorsals in any of three ways. (1) In 16 extant birds, the hypapophysis shifts from conspicuous to inconspicuous after the first shift in diapophyseal orientation, and the presacrals are therefore

regionalized into cervicals, cervicodorsals, and dorsals. The cervicodorsal region includes two to six presacrals, situated from P12 to P22. The first sternal connection is located within the cervicodorsal region in 13 of the 16 birds. CD1 is positioned one to three presacrals anterior to the first sternal connection, and D1 is positioned one to five presacrals posterior to the first sternal connection. (2) In *F. peregrinus* (UAMZ 6769) and *Pelecanus erythrorhynchos* (UAMZ 5181) of the remaining three birds deviated from the typical mode, CD1 is positioned two or three presacrals anterior to the first sternal connection, which is located on D1. In *Gr. monacha* (UAMZ 6806), CD1 and D1 are respectively positioned four and one presacrals anterior to the first sternal connection, which is located within the dorsal region. In 11 extant birds, the hypapophysis is distinct on all presacrals posterior to the first shift in diapophyseal orientation, so the presacrals are regionalized into cervicals and cervicodorsals. The cervicodorsal region includes five to eight presacrals, situated from P13 to P28. CD1 is positioned one to three presacrals anterior to the first sternal connection. (3) In *O. columbianus* (UAMZ 5229) and *L. delawarensis* (UAMZ 5103), the presacrals are regionalised into cervicals and dorsals, as the first presacral without a conspicuous hypapophysis is also the first with laterally oriented diapophyses. D1 is positioned two presacrals anterior to the first sternal connection. The DH criteria may not regionalize the presacrals consistently in birds that display multiple shifts between the presence and absence of conspicuous hypapophyses. For example, the DH criteria regionalize the presacrals into cervicals and dorsals in *O. columbianus* (UAMZ 5229), and into cervicals and cervicodorsals in *O. columbianus* (UAMZ 5230).

In all five extant crocodylians, the DH criteria regionalize the presacrals into cervicals, cervicodorsals, and dorsals. The first sternal connection is consistently located with the cervicodorsal region, and the cervicodorsal region includes five or six presacrals, situated from P7 to P14. CD1 is one to three presacrals anterior to the first sternal connection, and D1 is three to five presacrals posterior to the first sternal connection.

The average C:CD:D ratio is 12:4:3 in most extant birds, 11:7:0 in birds with only cervicals and cervicodorsals, 2:0:1 in birds with only cervicals and dorsals, and 5:6:13 in extant crocodylians.

Among fossil specimens in the study sample, the DH criteria can only be applied to two theropods and 12 crocodylomorphs. In *Si. dongi* (Currie and Zhao, 1993), the dorsal region includes the greatest number of presacrals, followed by the cervical region. In *De. antirrhopus* (YPM 5204), the cervical and dorsal counts are both three, which is one presacral more than the two cervicodorsals. This is likely a taphonomic artifact given that only eight presacrals are present in this specimen. Fossil crocodylomorphs with more than ten preserved presacrals uniformly resemble extant crocodylians in that the dorsal region contains the highest number of presacrals, followed by the cervicodorsal region, whereas counts of each region are too variable to be informative in less complete fossil crocodylimorphs. It is likely that the dorsal region consistently contains the most presacrals in fossil theropods and crocodylomorphs under the DH criteria, but additional sampling would be needed to confirm this.

Special cases — For almost all well-preserved archosaur specimens in the study sample, the presacrals are regionalized into cervicals, cervicodorsals, and dorsals by at least one class of transitional criteria. In all seven galliforms and two anseriforms in the sample, however, the presacrals are regionalized into only cervicals and cervicodorsals.

Le. gracilis (CMN 8889) is the only well-preserved specimen in which all the preserved presacrals are regionalized into only cervicodorsals and dorsals by Type II DP and DFT criteria, there being six of the former and 11 of the latter. The first preserved presacral sampled in this study in *Le. gracilis* (CMN 8889) is labelled as P4, and the first post-syncervical presacral in both *Ch. belli* (NHMUK R4948) (Maidment and Barrett 2011) and the first preserved presacral *Mo. cerorhynchus* has likewise been identified in the literature as P4 (Brown and Schlaikjer, 1942, Maidment and Barrett, 2010). CD1 is the second post-syncervical presacral in *Ch. belli* (Maidment and Barrett, 2010), and the fourth preserved presacral presacral in *Mo. cerorhynchus* (AMNH 5464). Occurrence of the first shift in diapophyseal orientation within the anteriormost part of the presacral series may be a general feature of euceratopsians, with *Le. gracilis* (CMN 8889) as an exception.

Selecting transitional criteria — None of the three classes of transitional criteria considered above is clearly superior to the others. In any study that adopts the general approach

introduced here, the choice of transitional criteria will need to be made carefully, taking into account the study's objectives and taxonomic scope. None of the three classes can be applied across the entire diversity of Archosauria, so investigators will wish to avoid choosing a class that is inapplicable to at least some of the taxa of interest. Moreover, the variations among species discussed above suggest that transitional features sampled in this study for criteria may have been altered by functional demands and phylogenetic inheritance in the long evolutionary history of archosaur. Therefore, the transitional criteria introduced above would inevitably contain some functional and phylogenetic signals, which could potentially impact the reliability of the transitional criteria for studies with a broad scope across the Archosauria. Three specific recommendations are proposed here. (1) The Type II DP criteria are likely to be appropriate for studies that include extant birds, extant crocodylians, and fossil archosaurs, whereas the Type II DP and the DH criteria are equally promising for studies that only include pseudosuchians. (2) The DFT and DH criteria can be used to avoid dependency on parapophyseal position, but care will need to be taken if extant birds are included in the study. (3) The Type I DP criteria may be useful for estimating minimum cervicodorsal counts, or for ranking the cervical, cervicodorsal and dorsal regions according to the number of presacrals they contain.

2.4.3 Implications for the evolution of cervical count in archosaurs

Under all three classes of transitional criteria, the first shift in diapophyseal orientation, from ventrolateral to lateral, is used to identify the transition from cervicals to dorsals. The (postaxial) cervical count is therefore consistent across classes of transitional criteria, and can be compared across studies in which different criteria have been used. Although the sample size of this study is limited, basic inferences can be drawn regarding evolutionary transitions in cervical count. Well-preserved fossil taxa in which the order of the presacrals is known are given particular weight in the following discussion, and the two types of DP criteria are used where discussion of cervicodorsal and dorsal counts is necessary.

Cervical counts of nine or greater are observed only in extant birds, whereas comparatively low counts of three to six are observed in extant crocodylians. Either extant birds or crocodylians may theoretically be closer to the plesiomorphic archosaurian condition. In most fossil pseudosuchians (e.g. *Sm. clarki*, *Sebecus icaeorhinus* (Georgi and Krause, 2010, Pol et al.,

2012)), three to six cervicals are identified, positioned from P3 to P8, and fewer than four presacrals are identified as cervicodorsals. The only clear exception is observed in *Lo. adentus* (IVPP V 4910) in which seven cervicals are identified, positioned from P3 to P9. *Lo. adentus* (IVPP V 4910) is further distinguished from other pseudosuchians in that five or 13 presacrals are identified as cervicodorsals using the Type I and Type II DP criteria, respectively. Taken together with the unusual, fluctuating pattern of parapophyseal placement described above for *Po. gracilis*, the condition seen in *Lo. adentus* suggests that the evolution of the presacral series may have been relatively unconstrained in poposauroids. Outside Poposauroidea, however, the regionalization of the presacrals likely remained largely uniform in fossil pseudosuchians. Although considerable differences in habitat and lifestyle existed across Pseudosuchia, with taxa varying from carnivorous to herbivorous and from terrestrial to marine (Georgi and Krause, 2010), this ecological diversity may not have resulted in a commensurate range of functional demands on the presacral series, or by extension a commensurate range of regionalization schemes.

Compared to pseudosuchians, non-avian dinosaurs appear to have been more diverse in their patterns of presacral regionalization, based on hints provided by the study sample. In the two theropods represented by well-preserved specimens, *Ty. rex* (Brochu, 2003) and *Si. dongi* (Currie and Zhao, 1993), the anteriormost six presacrals are identified as cervicals, and eight and five presacrals, respectively, as cervicodorsals, by the Type II DP criteria (cervicodorsal counts are one and zero, respectively, under the Type I DP criteria). The cervicodorsal counts in *Ty. rex* and *Si. dongi* resemble those of extant birds, but *Ty. rex* differs from extant birds in that the number of cervicodorsals exceeds the number of cervicals under the Type II DP criteria. Previous studies have identified eight post-axial cervicals in fossil theropods, including at least one fossil bird (e.g., *Coelophysis bauri*, *Linheraptor exquisitus*, *Sapeornis chaoyangensis*) (Zhou and Zhang, 2003, Rinehart et al., 2009, Xu et al., 2015).

A low cervical count is observed in most ornithischians in the study sample. The ceratopsians, except *Le. gracilis* (CMN 8889), have three or fewer cervicals, positioned from P4 to P6. The next two to four presacrals are identified as cervicodorsals. The low cervical count in ceratopsians reflects the fact that the first shift in diapophyseal orientation takes place among the

anteriormost presacrals. The presence of a syncervical in ceratopsian would also reduce the number of cervicals available for regionalisation. In most ornithopods and *St. stenops* (Maidment et al., 2015), there are two or three cervicals and five, six or nine cervicodorsals under the Type II DP criteria (compared to one to eight cervicodorsals under the Type I DP criteria). However, six cervicals and four cervicodorsals are present in *Te. tilletti* (Forster, 1990) under the Type II DP criteria (the Type I DP criteria are not applicable), counts that resemble those for *Ty. rex* (Brochu, 2003), *Si. dongi* (Currie and Zhao, 1993) and most pseudosuchians.

Overall, the low cervical count in extant crocodylians likely represents the plesiomorphic archosaur condition as the high cervical counts are restricted to birds in this study sample. This would unfortunately align with the infamous misconception that crocodylians are in some sense "living fossils". The low cervical count was retained in most pseudosuchians, and further reduced in many ornithischians. The high cervical count observed in extant birds might not have appeared until after the origin of Avialae.

2.4.3. Implications for pulmonary morphology in archosaurs

In extant birds, the immobile lung is fixed to the thoracic ceiling and functions solely as an apparatus for gas exchange, as air is ventilated into and out of the lung via changes in the pressure applied to pneumatic sacs attached to the ribcage (Scanes, 2015). Being positioned ventrolaterally on the vertebral centra, the parapophyses likely restricts the capitulum of the vertebral ribs to be positioned lateral to the vertebral centrum, which could contribute to immobilizing the avian lung (Maina, 2002, Brocklehurst et al., 2018). The fact that the parapophyses are relatively ventral in position over a large portion of the presacral series has been adduced as evidence for the presence of a heterogeneous, multi-chambered, avian-like lung in fossil theropods (e.g., *Ty. rex*, *Si. dongi*) (Schachner et al., 2009, Brocklehurst et al., 2018).

The parapophysis remains ventral to, or divided by, the NCS on the first 14 and 11 preserved presacrals in *Ty. rex* and *Si. dongi* respectively, which hints at the presence of an avian-like, rigid lung as inferred by Schachner et al. (2009). However, ventral positioning of the parapophysis throughout most of the presacral series is not unique to theropods. In the poposauroid *Lo. adentus* (IVPP V4910), but not in the other pseudosuchians in our study sample,

the parapophysis is ventral to or divided by the NCS from P3 to P22. However, a rigid lung was likely absent in *Lo. adentus* (IVPP V4910), given the lack of vertebral pneumaticity. Movements of the ribcage have been found to contribute to both respiration by rhythmical expansion of the ribcage to generate airflow and locomotion by undulating the trunk in squamates (Brainerd et al., 2016, Capano et al., 2019, Cieri et al., 2020). There is no direct evidence that the thorax has, or had, a locomotor role in archosaurs. Multiple congruent osteological correlates may be needed to justify inferring the presence of avian-like pulmonary structures in fossil taxa from anatomical evidence, which should be interpreted with caution.

In extant crocodylians, the "hepatic piston" mechanism is achieved by M. diaphragmaticus pulling the viscera posteriorly to generate inspiratory airflow, which can then passively rebound anteriorly (Carrier and Farmer 2000a; Farmer and Carrier 2000). In crocodyliforms leading to extant crocodylians, the pubis can be elevated and depressed by a small amount relative to the rest of the pelvis, which potentially would secondarily enhance the effects of the "hepatic piston". (Claessens, 2004, Claessens and Vickaryous, 2012). A form of visceral pump resembling the "hepatic piston" has been considered plesiomorphic for archosaurs (Carrier and Farmer, 2000). Anteroposterior movement of the viscera may require a smooth thoracic ceiling, which results in extant crocodylians from dorsal drift of the parapophysis onto the neural arch to unite with the diapophysis (transverse process) along the presacral series (Schachner et al., 2011). By contrast, two important studies (Schachner et al., 2011, Brocklehurst et al., 2018) examined the degree of separation between the parapophysis and diapophysis in a wide variety of dinosauriforms, for vertebrae that had been previously identified in the literature as dorsals, and concluded that the gap between the two processes was large enough to suggest absence of a crocodylian-like hepatic piston. A caveat, however, is that consistent criteria may not have been used to distinguish the 'dorsals' from the rest of the presacral series. Based on the well-preserved fossil archosaur taxa examined in the present study, a different inference may be drawn regarding the evolution of the hepatic piston mechanism, if the DFT criteria are applied. In the extant crocodylians in the sample, the foramen transversarium disappears on P13 or P14, as reported in the literature (Schachner et al., 2011). In fossil crocodylomorphs, the foramen transversarium is present on the first six to ten preserved presacrals, and absent on the following presacral. Assuming the presacral series to be largely complete in these well-preserved

specimens, the foramen transversarium in fossil crocodylomorphs seems to consistently disappear no further posteriorly than the true P12 (ten preserved presacrals + atlas + axis). By comparison, the foramen transversarium is present on the first five or six preserved presacrals in ceratopsians, on the first eight to ten preserved presacrals in ornithopods and *Ak. magniventris* (AMNH 5985), and on the first 12 presacrals in *St. stenops* (Maidment et al., 2015). Accounting for the atlas and axis, disappearance of the foramen transversarium, potentially interpretable as defining the anterior boundary of the dorsal region, appears to take place anterior to P14 in ornithopods, *Ak. magniventris* (AMNH 5895), and *St. stenops*, and anterior to P9 in ceratopsians. Therefore, a smooth thoracic ceiling and a form of visceral pump could have been present not only in crocodylomorphs, but also in ornithischians, as has been suggested for *Heterodontosaurus* (Radermacher et al., 2021). However, drift of the parapophysis onto the neural arch along the presacral series could be an adaptation to increase the range of vertebrocostal motion, as demonstrated by a cineradiographic study on the ventilation of *Al. mississippiensis* (Claessens, 2009), rather than an adaptation to uniquely facilitate "hepatic piston" style ventilation. As many archosaur taxa considered in this study have parapohpysis drifts dorsal to the NCS and onto the neural arch, they would presumably have a smooth thoracic ceiling. We postulate that an anatomical foundation for increasing the range of vertebrocostal motion and for the advent of "hepatic piston" might have been plesiomorphic for archosaurs, but its initial function remains uncertain.

2.5 Conclusions

(1) Sampled transitional features of the preascrals could not consistently identify the first sternal connection as D1.

(2) The Type II DP criteria among the three classes is most promising at locating the first sternal connection in the cervicodorsal region.

(3) Ancestral archosaurs likely have low cervical counts as in extant crocodylians, and the high cervical counts in extant birds may be obtained after the origin of Avialae.

Tables

Table 2. 1 List of archosaur taxa sampled for transitional features (see Supplementary Information for the full list of taxa and the sequential orders of presacrals where available)

Pseudosuchia		**Avemetatarsalia**	
Clade	Number of Taxa	Clade	Number of Taxa
Crocodylia	11	Aves	26
Pholidosauridae	1	Hesperornithidae	1
Dyrosauridae	2	Tyrannosauroidea	2
Thalattosuchia	1	Allosauroidea	4
Ziphosuchia	4	Ceratosauria	1
Protosuchidae	1	Coelophysidae	1
"Sphenosuchia"	3	Camarasauridae	1
Poposauroidea	2	Ceratopsia	4
Gracilisuchidae	1	Ornithopoda	7
Rauisuchidae	1	Stegosauridae	3
Phytosauria	2	Ankylosauria	3
		Dromaeosauridae	1
		Basal avemetatarsalians	2

Table 2. 2. Definition of the eight transitional features examined in this study (see Supplementary Information for detailed definition of the transitional features)

Transitional features	Definitions
Parapophyseal drift	The position of the parapophysis drifts from a position ventral to the neurocentral suture (NCS), to a position divided by the NCS, and to a position dorsal to the NCS. The parapophysis may drift dorsal to the NCS without being divided by it, and the parapophysis on posterior presacrals may merge with the diapophysis/transverse process.
Diapophyseal orientation	The diapophyseal orientation shifts from ventrolateral to lateral, or from lateral to dorsolateral. After the initial shift from ventrolateral to lateral, the laterally oriented diapophysis can shift secondarily from lateral to dorsolateral on successive presacrals.
Foramen transversarium	The foramen transversarium formed by presacrals and presacral ribs becomes smaller and disappears posteriorly. In the absence of presacrals ribs, the foramen transversarium is interpred as absent if the parapophysis drifts to a position immediately next to or merged with the diapophysis.
Hypapophysis	The hypapophysis changes from being a distinct, ventral blade to inconspicuous or absent
Parapophyseal morphology	The outline of the parapophysis in lateral view changes from anteroposteriorly elongated, to subcircular, and to dorsoventrally elongated.
Neural spine absence	The neural spine changes from being absent or small protuberance, to a distinct blade with the height that approximate the height of the centrum
Neural spine orientation	The neural spine orientation changes from anterodorsal to posterodorsal, and to dorsal. Alternatively, the neural spine orientation could change from posterodorsal to dorsal.
Epipophysis	Epipophysis changes from being a distinct protuberance to indistinguishable from the postzygapophysis

Table 2. 3 Definitions of three classes of transitional criteria

Criteria	Definitions of the cervicodorsal regions
Type I DP	AM: The first shift of the diapophyseal orientation, from ventrolateral to lateral. PM: Parapophysis drifts from being ventral to the NCS, to being divided by the NCS.
Type II DP	AM: The first shift of the diapophyseal orientation, from ventrolateral to lateral. PM: Parapophysis drifts from being ventral to or divided by the NCS, to being dorsal to the NCS.
DFT	AM: The first shift of the diapophyseal orientation, from ventrolateral to lateral. PM: Foramen transversarium disappears.
DH	AM: The first shift of the diapophyseal orientation, from ventrolateral to lateral. PM: Hypapophysis becomes and remains inconspicuous as or after the first shift in diapophyseal orientation.

Abbreviations: AM, anterior margin; DP criterion, Diapophysis-Parapophysis criterion; DFT criterion, Diapophysis-Foramen transversarium criterion; DH mode, diapophysis-hypapophysis criterion; NCS, neurocentral suture; PM, posterior margin.

Figures

Figure 2.1. Eight transitional features from unambiguous cervicals to unambiguous dorsals sampled in this study depicted on schematic diagrams of presacrals.

Parapophysis drifts dorsally across the NCS in anterior views (A); Diapophyseal orientation shifts from ventrolateral to lateral in anterior view (B); Foramen transversarium gradually disappears in anterior views (C); Hypapophysis gradually disappears in anterior views (D); Parapophyseal morphology changes from anteroposteriorly elongated to, subcircular, and to dorsoventrally elongated in lateral views (E); Neural spine gradually becomes distinct in lateral views (F); Neural spine orientation gradually shifts from anterodorsal, to posterodorsal, and to dorsal in lateral views (G); Epipophysis gradually disappears from the postzygapophysis in lateral views (H). The star shape indicates presacrals transitioning between two states of each transitional feature. Abbreviations: CV: cervical; DV, dorsals; NCS, neurocentral suture.

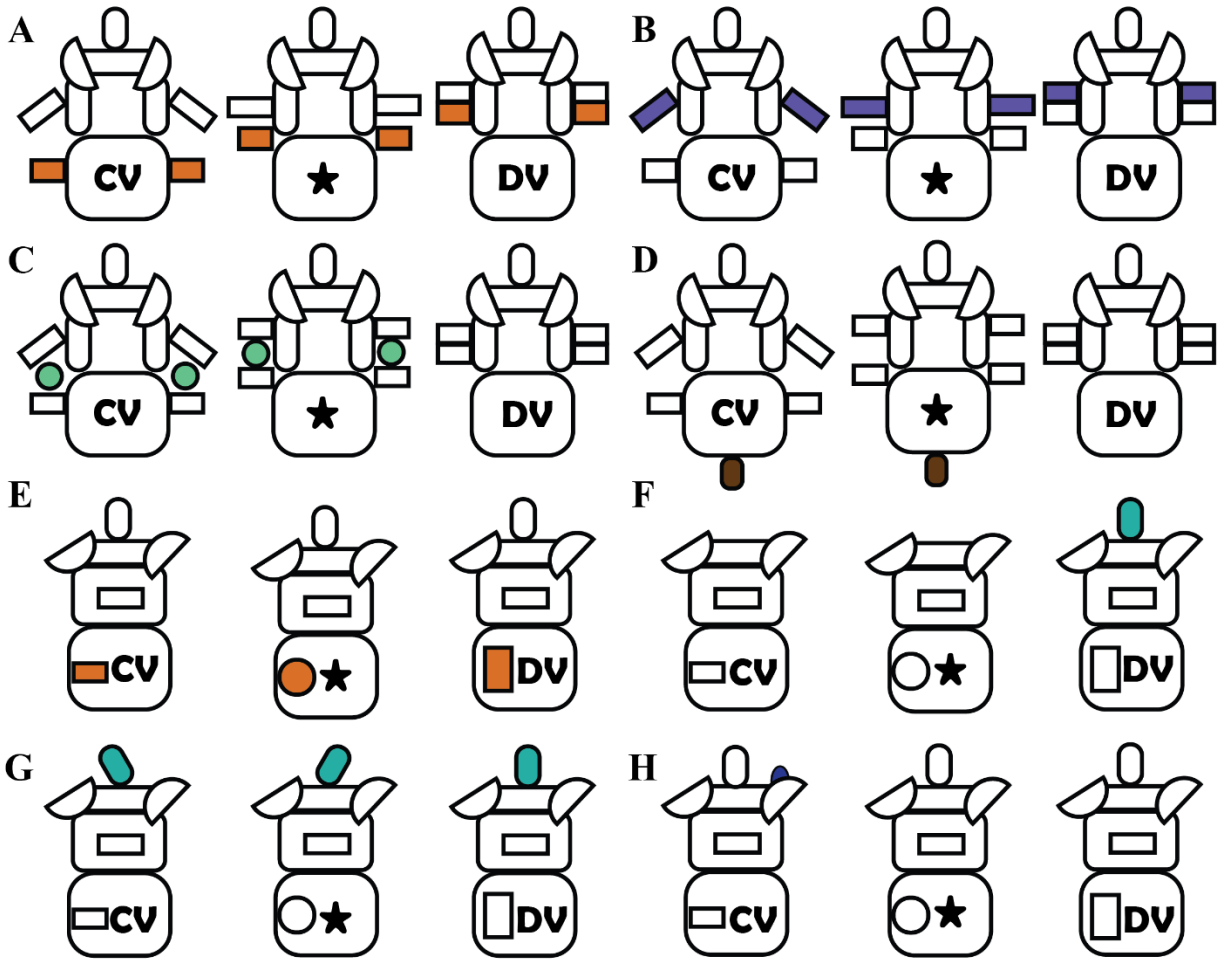
A
CV
DV
B
CV
DV
C
CV
DV
D
CV
DV
E
CV
DV
F
CV
DV
G
CV
DV
H
CV
DV

Figure 2.2. Four consistent transitional features in representative extant archosaurs.

Line drawings of presacrals in lateral views sampled from *Struthio camelus* (UAMZ 7159) (A), *Gavia immer* (UAMZ 1793) (B), *Haliaeetus leucocephalus* (UAMZ 5028) (C), and *Caiman crocodilus* (UAMZ unnumbered) (D). Vertical lines mark the first sternal connection. Abbreviations: CS0, character state 0; CS1, character state 1; CS2, character state 2; DO, diapophyseal orientation; FT, foramen transversarium; Hy, hypapophysis; PD, parapophyseal drift.

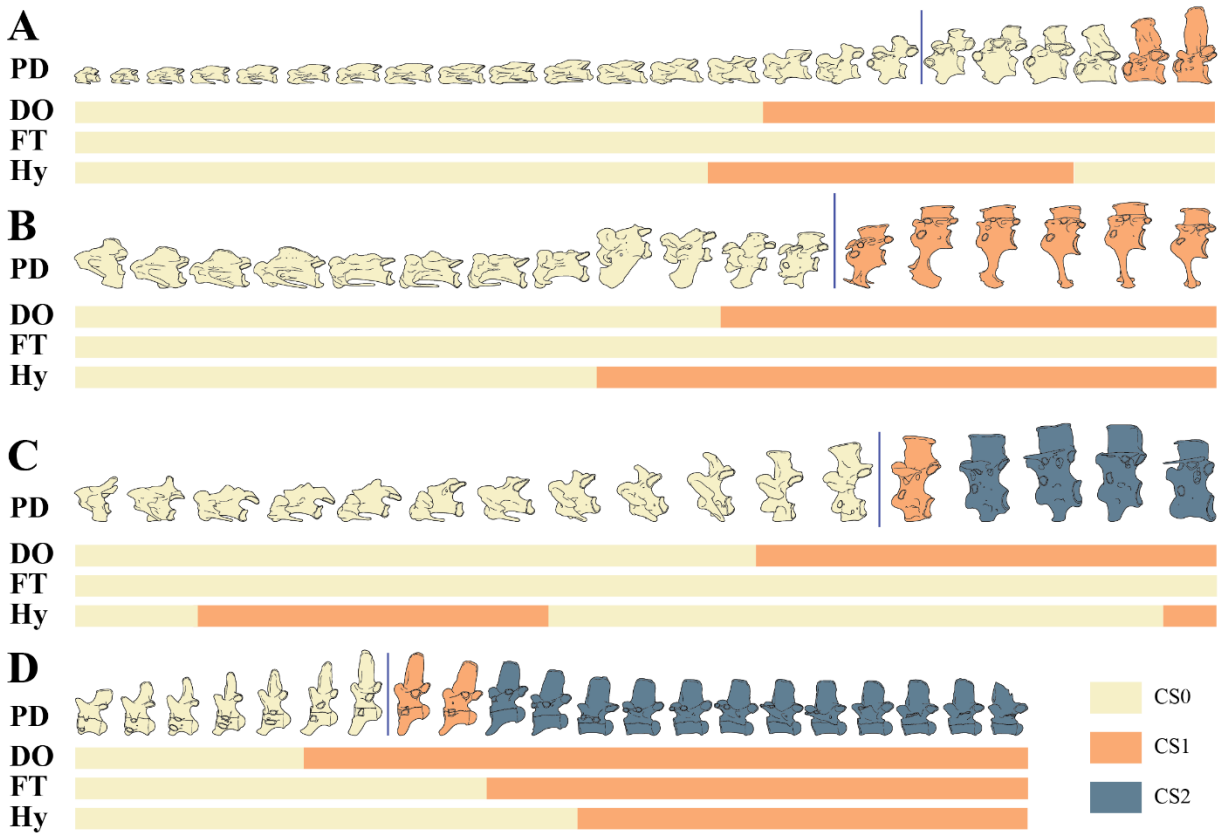
A
PD
DO
FT
Hy
B
PD
DO
FT
Hy
C
PD
DO
FT
Hy
D
PD
DO
FT
Hy
CS0
CS1
CS2

Figure 2.3. Four consistent transitional features in representative fossil dinosaurs.

Line drawings of presacrals in lateral views sampled from *Deinonychus antirrhopus* (YPM 5204) (A), *Sinraptor dongi* (drawn from (Currie and Zhao 1993)) (B), *Tyrannosaurus rex* (drawn from (Brochu 2003)) (C), *Camarasaurus grandis* (YPM 1905) (D), *Stegosaurus stenops* (drawn from (Maidment et al. 2015)) (E), *Iguanodon bernissati* (drawn from (Norman 1980)) (F), *Montanoceratops cerorhynchus* (AMNH 5464) (G), *Leptoceratops gracilis* (CMN 8889) (H), *Chasmosaurus belli* (drawn from (Maidment and Barrett 2011)) (I), *Ankylosaurus magniventris* (AMNH 5895) (J), and *Euoplocephalus tutus* (AMNH 5377) (K). Abbreviations: CS0, character state 0; CS1, character state 1; CS2, character state 2; DO, diapophyseal orientation; FT, foramen transversarium; Hy, hypapophysis; NA, missing data; PD, parapophyseal drift.

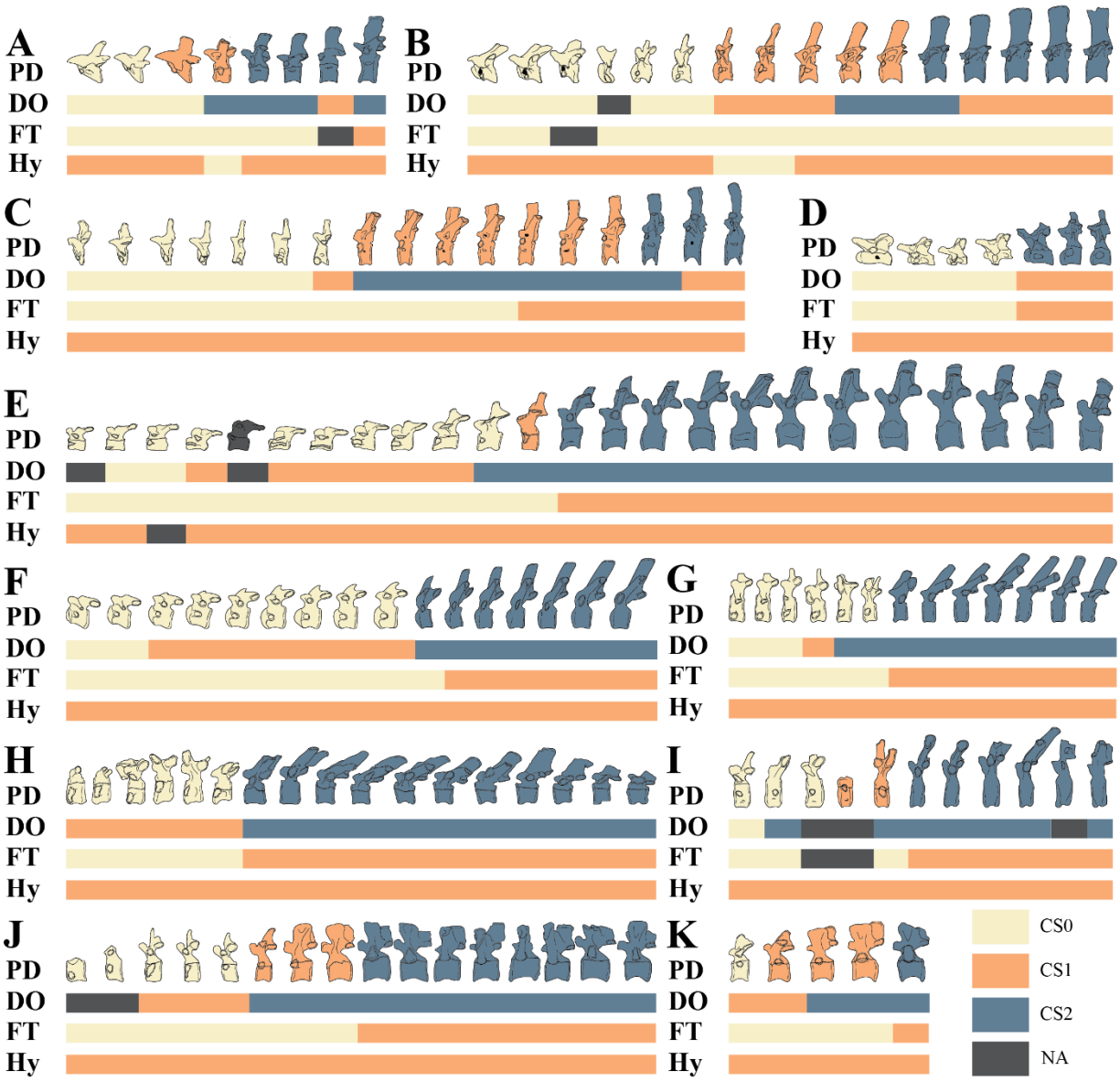
A
PD
DO
FT
Hy
B
PD
DO
FT
Hy
C
PD
DO
FT
Hy
D
PD
DO
FT
Hy
E
PD
DO
FT
Hy
F
PD
DO
FT
Hy
G
PD
DO
FT
Hy
H
PD
DO
FT
Hy
I
PD
DO
FT
Hy
J
PD
DO
FT
Hy
K
PD
DO
FT
Hy
CS0
CS1
CS2
NA

Figure 2.4. Four consistent transitional features in representative fossil pseudosuchians.

Line drawings of presacrals in lateral views sampled from *Crocodilus grinnelli* (YPM 300) (A), *Simosuchus clarki* (drawn from (Georgi and Krause 2010)) (B), *Baurusuchus albertoi* (drawn from (Nascimento and Zaher 2010)) (C), *Sebecus icaeornis* (drawn from (Pol et al. 2012)) (D), *Dibothrosuchus elaphros* (drawn from(Wu and Chatterjee 1993)) (E), and *Lotosaurus adentus* (IVPP V 4880) (F). Abbreviations: CS0, character state 0; CS1, character state 1; CS2, character state 2; DO, diapophyseal orientation; FT, foramen transversarium; Hy, hypapophysis; NA, missing data; PD, parapophyseal drift.

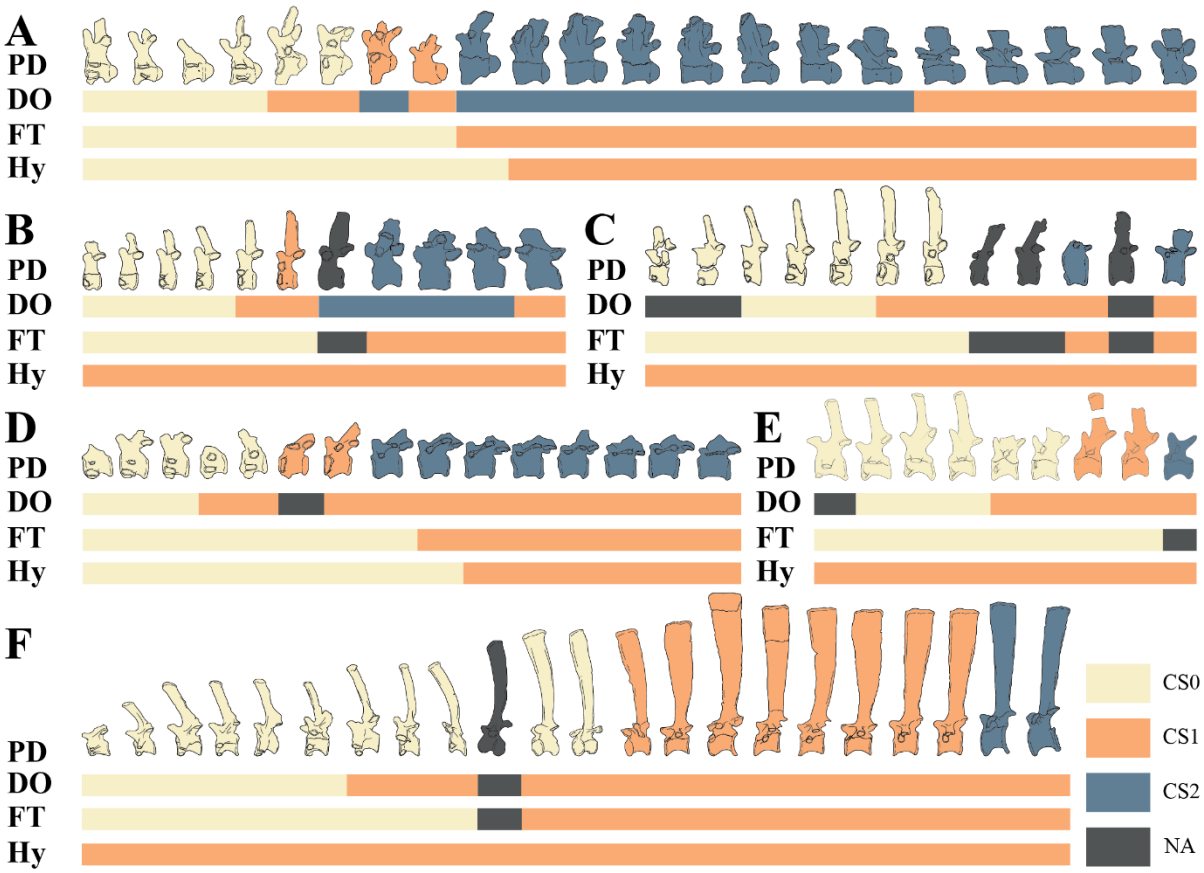
A
PD
DO
FT
Hy
B
PD
DO
FT
Hy
C
PD
DO
FT
Hy
D
PD
DO
FT
Hy
E
PD
DO
FT
Hy
F
PD
DO
FT
Hy
CS0
CS1
CS2
NA

Figure 2.5. Three classes of transitional criteria proposed in this study.

Transitional criteria defined by the combination of the shift in the diapophyseal orientation (A - D) and one of the three consistent transitional features (B – D). Regionalization of hypothetical presacrals is provided under each class of transitional criteria with colour labelled. The anterior and posterior margins of the cervicodorsal regions are emphasised by the red and blue vertical lines. Abbreviations: C, cervicals; CD, cervicodorsals; CS0, character state 0; CS1, character state 1; CS2, character state 2; D, dorsals; DFT, diapophysis-foramen transversarium; DH, diapophysis-hypapophysis; DO, diapophyseal orientation; Di, diapophysis; DP, diapophysis-parapophysis; FT, foramen transversarium; Hy, Hypapophysis; NCS, neurocentral suture; Pa, parapophysis; PD, parapophyseal drift.

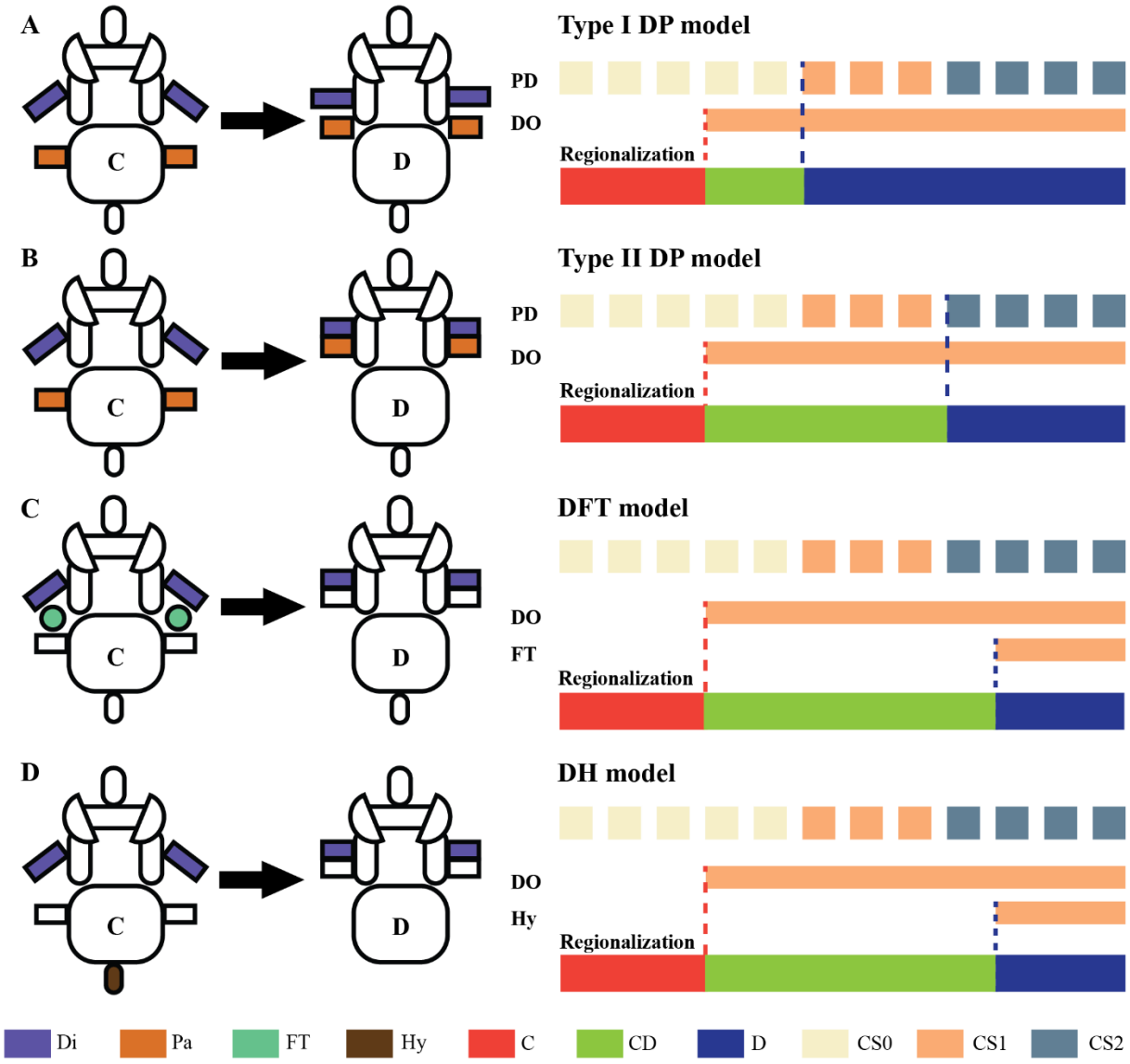
A
C
D
Type I DP model
PD
DO
Regionalization
B
C
D
Type II DP model
PD
DO
Regionalization
C
C
D
DFT model
DO
FT
Regionalization
D
C
D
DH model
DO
Hy
Regionalization
Di
Pa
FT
Hy
C
CD
D
CS0
CS1
CS2

Figure 2.6. Comparisons of the three classes of transitional criteria in representative archosaurs. Regionalization delineated by three classes of transitional criteria in *Haliaeetus leucocephalus* (UAMZ 5028) (A), Caiman crocodilus (UAMZ unnumbered), *Sinraptor dongi* (drawn from (Currie and Zhao 1993)) (C), *Tyrannosaurus rex* (drawin from (Brochu, 2003)) (D), *Chasmosaurus belli* (drawn from (Maidment and Barrett 2011)) (E), *Stegosaurus stenops* (drawn from (Maidment et al. 2015)) (F), *Iguanodon bernissati* (drawn from (Norman 1980)) (G), *Montanoceratops cerorhynchus* (AMNH 5464) (H), and *Lotosaurus adentus* (IVPP V 4880) (I). Vertical lines mark the first sternal connection. Abbreviations: C, cervicals; CD, cervicodorsals; D, dorsals; DFT, diapophysis-foramen transversarium criteria; DH, diapophysis-hypapophysis criteria; DP I, Type I DP criteria; DP II, Type II DP criteria.

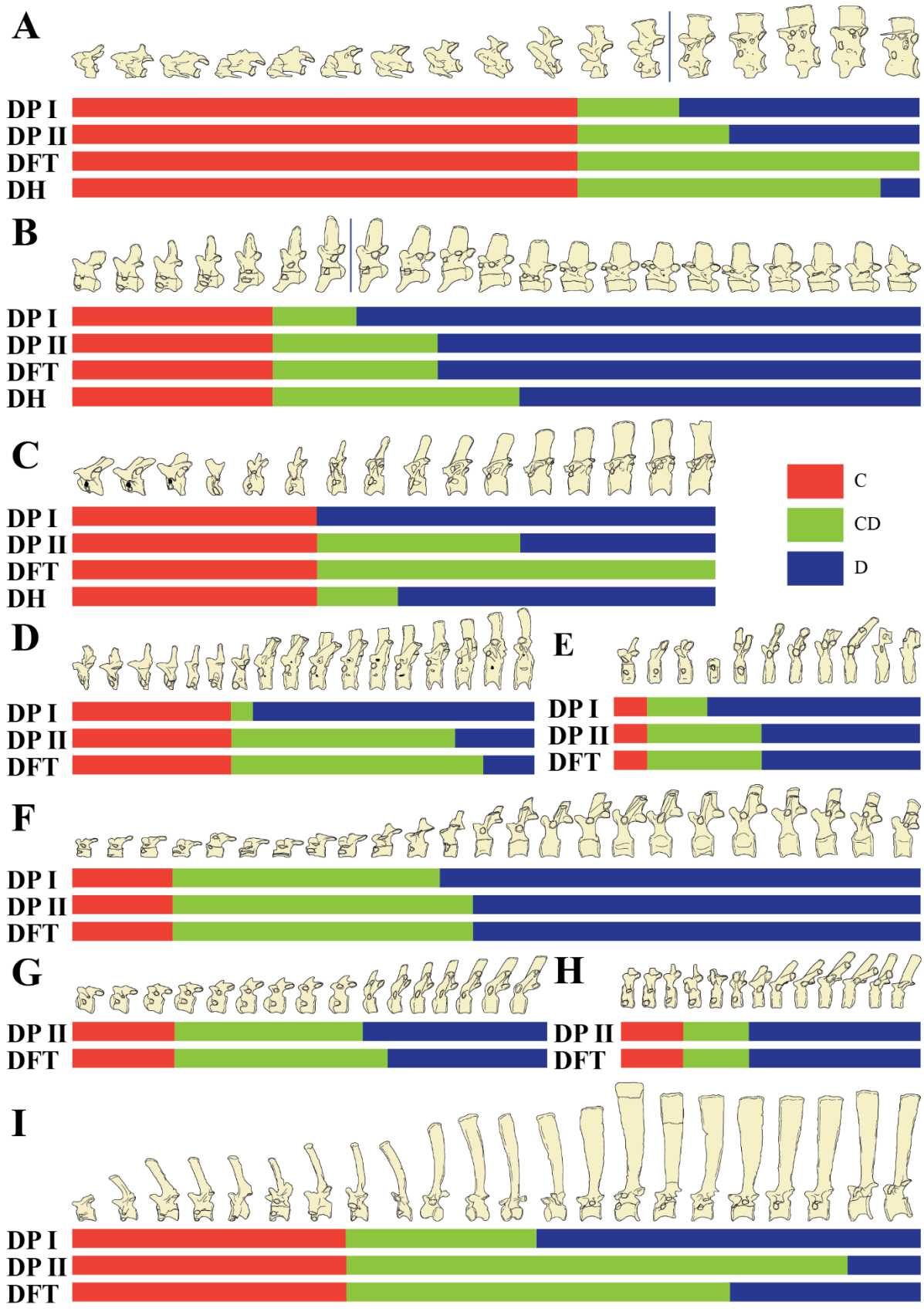
A
DP I
DP II
DFT
DH
B
DP I
DP II
DFT
DH
C
DP I
DP II
DFT
DH
C
CD
D
D
DP I
DP II
DFT
E
DP I
DP II
DFT
F
DP I
DP II
DFT
G
DP II
DFT
H
DP II
DFT
I
DP I
DP II
DFT

Figure 2.7. Regionalization of representative archosaurs mapped on an archosaur cladogram.

Presacrals regionalized using the Type II DP criteria of representative fossil archosaurs placed under a phylogenetic context. Cladogram modified from Fig 4.3 in Chapter 4, and clades with sky blue background are clades with well-preserved specimen(s).

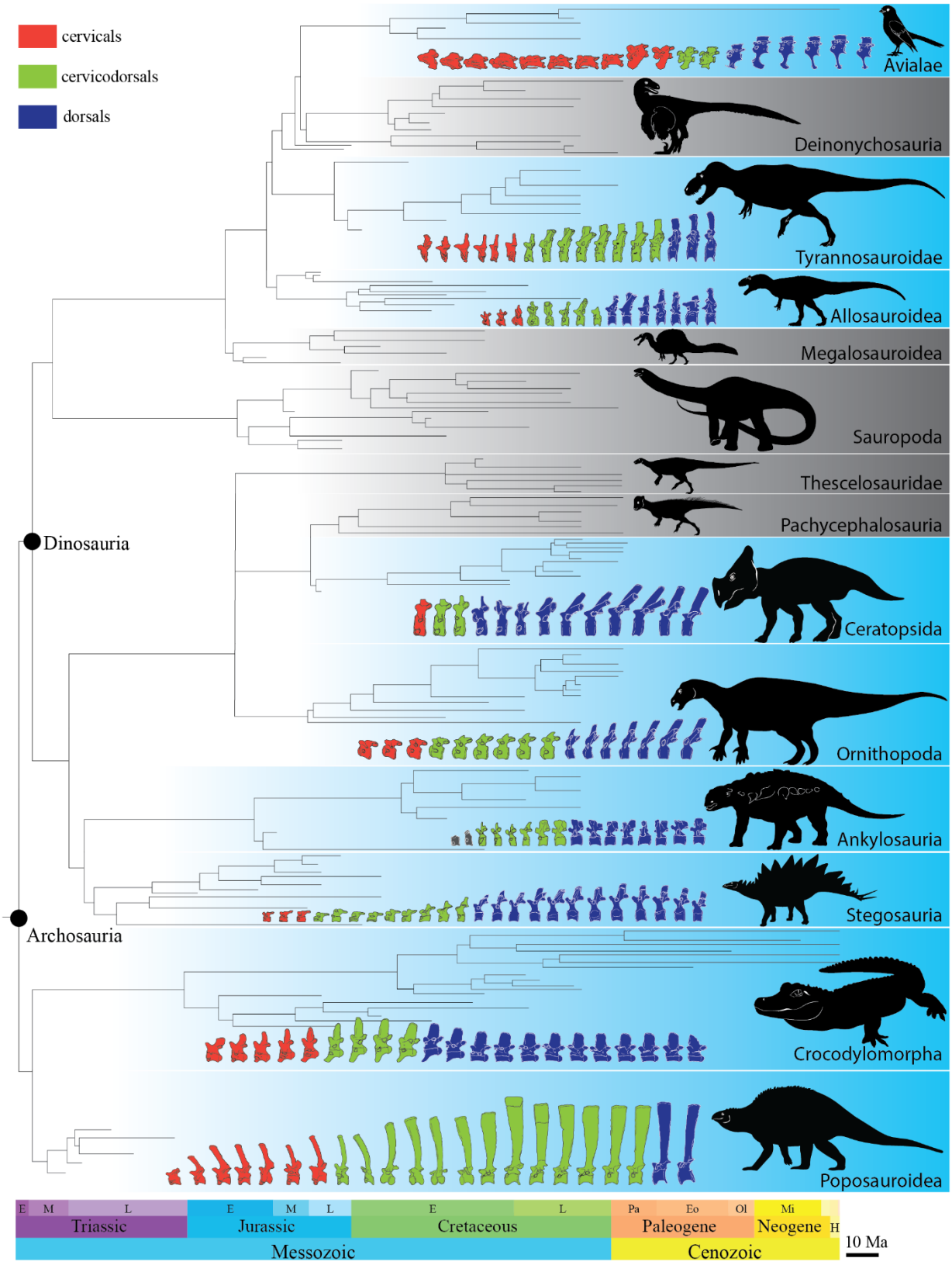
cervicals
cervicodorsals
dorsals
Avialae
Deinonychosauria
Tyrannosauroidae
Allosauroidea
Megalosauroidea
Sauropoda
Thescelosauridae
Pachycephalosauria
Dinosauria
Ceratopsida
Ornithopoda
Ankylosauria
Stegosauria
Archosauria
Crocodylomorpha
Poposauroidea
E M L
Triassic
E M L
Jurassic
E L
Cretaceous
Pa Eo Ol
Paleogene
Mi
Neogene
H
Messozoic
Cenozoic
10 Ma

2.6 Literature Cited

Baumel, J.J., King, A.S., Breazile, J.E., Evans, H.E. and Vanden Berge, J.C. 1993. *Handbook of avian anatomy: Nomina anatomica avium*. second edition. Cambridge: Nuttall Ornithological Club.

Benton, M.J. 2014. *Vertebrate Palaeontology*. John Wiley & Sons.

Böhmer, C., Plateau, O., Cornette, R. and Abourachid, A. 2019. Correlated evolution of neck length and leg length in birds. *Royal Society Open Science* 6(5), p. 181588. doi: 10.1098/rsos.181588.

Borinder, N. 2015. *Postcranial anatomy of* Tanius sinensis *Wiman, 1929 (Dinosauria; Hadrosauroidea)*. PhD Dissertation, Uppsala University.

Brainerd, E.L., Moritz, S. and Ritter, D.A. 2015. XROMM analysis of rib kinematics during lung ventilation in the green iguana, *Iguana iguana*. *Journal of Experimental Biology* 219, p. jeb.127928. doi: 10.1242/jeb.127928.

Brochu, C. 2011. Phylogenetic relationships of *Necrosuchus ionensis* Simpson, 1937 and the early history of caimanines. *Zoological Journal of the Linnean Society* 163(sup 1), pp. S228–S256. doi: 10.1111/j.1096-3642.2011.00716.x.

Brochu, C.A. 2003. Osteology of *Tyrannosaurus Rex*: Insights from a nearly complete skeleton and high-resolution computed tomographic analysis of the skull. *Journal of Vertebrate Paleontology* 22(sup 4), pp. 1–138. doi: 10.1080/02724634.2003.10010947.

Brocklehurst, R.J., Schachner, E.R. and Sellers, W.I. 2018. Vertebral morphometrics and lung structure in non-avian dinosaurs. *Royal Society Open Science* 5(10), p. 180983. doi: 10.1098/rsos.180983.

Brown, B. and Schlaikjer, E.M. 1942. The skeleton of *Leptoceratops* with the description of a new species. *American Museum Novitates* 1169, pp. 1–15.

Brusatte, S.L., Benton, M.J., Desojo, J.B. and Langer, M.C. 2010. The higher-level phylogeny of Archosauria (Tetrapoda: Diapsida). *Journal of Systematic Palaeontology* 8(1), pp. 3–47. doi: 10.1080/14772010903537732.

Campione, N.E. 2014. Postcranial anatomy of *Edmontosaurus regalis* (Hadrosauridae) from the Horseshoe Canyon Formation, Alberta, Canada. In: *Hadrosaurs*. Indiana University Press, pp. 208–244.

Capano, J.G., Moritz, S., Cieri, R.L., Reveret, L. and Brainerd, E.L. 2019. Rib motions don't completely hinge on joint design: costal joint anatomy and ventilatory kinematics in a teiid lizard, *Salvator merianae*. *Integrative Organismal Biology* 1(1), p. oby004. doi: 10.1093/iob/oby004.

Carpenter, K. 2004. Redescription of *Ankylosaurus magniventris* Brown 1908 (Ankylosauridae) from the Upper Cretaceous of the Western Interior of North America. *Canadian Journal of Earth Sciences* 41(8), pp. 961–986. doi: 10.1139/e04-043.

Carrier, D.R. and Farmer, C.G. 2000a. The evolution of pelvic aspiration in archosaurs. *Paleobiology* 26(2), pp. 271–293. doi: 10.1666/0094-8373(2000)026<0271:TEOPAI>2.0.CO;2.

Carrier, D.R. and Farmer, C.G. 2000b. The integration of ventilation and locomotion in archosaurs. *American Zoologist* 40, pp. 87–100.

Chatterjee, S. 1985. *Postosuchus*, a new thecodontian reptile from the Triassic of Texas and the origin of tyrannosaurs. *Philosophical Transactions of the Royal Society of London. B, Biological Sciences* 309, pp. 395–460.

Cieri, R.L., Hatch, S.T., Capano, J.G. and Brainerd, E.L. 2020. Locomotor rib kinematics in two species of lizards and a new hypothesis for the evolution of aspiration breathing in amniotes. *Scientific Reports* 10(1), p. 7739. doi: 10.1038/s41598-020-64140-y.

Claessens, L.P.A.M. 2004. Archosaurian respiration and the pelvic girdle aspiration breathing of crocodyliforms. *Proceedings of the Royal Society of London. Series B: Biological Sciences* 271(1547), pp. 1461–1465. doi: 10.1098/rspb.2004.2743.

Claessens, L.P.A.M. 2009. A cineradiographic study of lung ventilation in *Alligator mississippiensis*. *Journal of Experimental Zoology Part A: Ecological Genetics and Physiology* 311A(8), pp. 563–585. doi: 10.1002/jez.530.

Claessens, L.P.A.M. and Vickaryous, M.K. 2012. The evolution, development and skeletal identity of the crocodylian pelvis: Revisiting a forgotten scientific debate. *Journal of Morphology* 273(10), pp. 1185–1198. doi: 10.1002/jmor.20059.

Cong, L.Y., Hou, L.H. and Wu, X.C. 1988. *The Gross anatomy of Alligator sinensis Fauvel: Integument, Osteology, and Myology (In Chinese with English summary)*. Beijing, China: China Science Publishing & Media Ltd.

Currie, P.J., Holmes, R.B., Ryan, M.J. and Coy, C. 2016. A juvenile chasmosaurine ceratopsid (Dinosauria, Ornithischia) from the Dinosaur Park Formation, Alberta, Canada. *Journal of Vertebrate Paleontology* 36(2), p. e1048348. doi: 10.1080/02724634.2015.1048348.

Currie, P.J. and Zhao, X.-J. 1993. A new carnosaur (Dinosauria, Theropoda) from the Jurassic of Xinjiang, People's Republic of China. *Canadian Journal of Earth Sciences* 30(10), pp. 2037–2081. doi: 10.1139/e93-179.

Dalla Vecchia, F.M. 2009. *Tethyshadros insularis* , a new hadrosauroid dinosaur (Ornithischia) from the Upper Cretaceous of Italy. *Journal of Vertebrate Paleontology* 29(4), pp. 1100–1116. doi: 10.1671/039.029.0428.

Dilkes, D. and Sues, H.-D. 2009. Redescription and phylogenetic relationships of *Doswellia kaltenbachi* (Diapsida: Archosauriformes) from the Upper Triassic of Virginia. *Journal of Vertebrate Paleontology* 29, pp. 58–79.

Drysdale, E.T., Therrien, F., Zelenitsky, D.K., Weishampel, D.B. and Evans, D.C. 2018. Description of juvenile specimens of *Prosaurolophus maximus* (Hadrosauridae: Saurolophinae) from the Upper Cretaceous Bearpaw Formation of southern Alberta, Canada, reveals ontogenetic changes in crest morphology. *Journal of Vertebrate Paleontology* 38(6), p. e1547310. doi: 10.1080/02724634.2018.1547310.

Farmer, C.G. and Carrier, D.R. 2000. Pelvic aspiration in alligators. *The Journal of Experimental Biology* 203, pp. 1679–1687.

Fisher, P.E., Russell, D.A., Stoskopf, M.K., Barrick, R.E., Hammer, M. and Kuzmitz, A.A. 2000. Cardiovascular evidence for an intermediate or higher metabolic rate in an ornithischian dinosaur. *Science* 288(5465), pp. 503–505. doi: 10.1126/science.288.5465.503.

Forster, C. 1990. The postcranial skeleton of the ornithopod dinosaur *Tenontosaurus tilletti*. *Journal of Vertebrate Paleontology* 10(3), pp. 273–294. doi: 10.1080/02724634.1990.10011815.

Frey, T. von E. 1988. Anatomie des Körperstammes von *Alligator mississippiensis* Daudin. *Stuttgarter Beitraege zur Naturkunde, Serie A* 424, pp. 1–106.

Georgi, J.A. and Krause, D.W. 2010. Postcranial axial skeleton of *Simosuchus clarki* (Crocodyliformes: Notosuchia) from the Late Cretaceous of Madagascar. *Journal of Vertebrate Paleontology* 30(sup1), pp. 99–121. doi: 10.1080/02724634.2010.519172.

Gilmore, C.W. 1920. Osteology of the carnivorous Dinosauria in the United States National Museum: with special reference to the Genera *Antrodemus* (*Allosaurus*) and *Ceratosaurus*. *Bulletin of the United States National Museum* 110, pp. 1–154.

Kardong, K.V. 2015. *Vertebrates: comparative anatomy, function, evolution*. Seventh edition. New York, NY: McGraw-Hill Education.

Leardi, J.M., Pol, D., Novas, F.E. and Suárez Riglos, M. 2015. The postcranial anatomy of *Yacarerani boliviensis* and the phylogenetic significance of the notosuchian postcranial skeleton. *Journal of Vertebrate Paleontology* 35(6), p. e995187. doi: 10.1080/02724634.2014.995187.

Li, J. and Downs, T.B.W. 1985. A revision of *Edentosuchus tienshanensis* Young from the Tugulu Group of Xinjiang Autonomous Region. *Vertebrata PalAsiatica* 23, pp. 196–206.

Lio, G., Agnolin, F.L., Martinelli, A.G., Ezcurra, M.D. and Novas, F.E. 2018. New specimen of the enigmatic, Late Cretaceous crocodyliform *Neuquensuchus universitas* sheds light on the anatomy of the species. *Cretaceous Research* 83, pp. 62–74. doi: 10.1016/j.cretres.2017.09.014.

Maidment, S.C.R. and Barrett, P.M. 2011. A new specimen of *Chasmosaurus belli* (Ornithischia: Ceratopsidae), a revision of the genus, and the utility of postcrania in the taxonomy and systematics of ceratopsid dinosaurs. *Zootaxa* 2963(1), p. 1. doi: 10.11646/zootaxa.2963.1.1.

Maidment, S.C.R., Brassey, C. and Barrett, P.M. 2015. The postcranial skeleton of an exceptionally complete individual of the plated dinosaur *Stegosaurus stenops* (Dinosauria: Thyreophora) from the Upper Jurassic Morrison Formation of Wyoming, U.S.A. *PLOS ONE* 10(10), p. e0138352. doi: 10.1371/journal.pone.0138352.

Maina, J.N. 2002. *Functional Morphology of the Vertebrate Respiratory Systems*. Science Publishers.

McDonald, A.T., Maidment, S.C.R., Barrett, P.M., You, H. and Dodson, P. 2014. Osteology of the basal hadrosauroid *Equijubus normani* (Dinosauria, Ornithopoda) from the Early Cretaceous of China. In: *Hadrosaurs*. Bloomington and Indianapolis: Indiana University Press.

Mivart, St.G. 1877. On the axial skeleton of the Struthionidce. *The Transactions of the Zoological Society of London* 10(1), pp. 1–52. doi: 10.1111/j.1096-3642.1877.tb00282.x.

Nascimento, P.M. and Zaher, H. 2010. A new species of *Baurusuchus* (Crocodyliformes, Mesoeucrocodylia) from the Upper Cretaceous of Brazil, with the first complete postcranial

skeleton described for the Family Baurusuchidae. *Papéis Avulsos de Zoologia (São Paulo)*. doi: 10.1590/S0031-10492010002100001.

Nesbitt, S.J. 2011. The early evolution of archosaurs: relationships and the origin of major clades. *Bulletin of the American Museum of Natural History* 352, pp. 1–292. doi: 10.1206/352.1.

Nesbitt, S.J., Desojo, J.B. and Irmis, R.B. 2013. Anatomy, phylogeny and palaeobiology of early archosaurs and their kin. *Geological Society, London, Special Publications* 379(1), pp. 1–7. doi: 10.1144/SP379.21.

Norman, D.B. 1980. On the ornithischian dinosaur *Iguanodon bernissartensis* from the Lower Cretaceous of Bernissart (Belgium). *Institut royal des Sciences naturelles de Belgique*, pp. 1–106.

Novas, F.E. et al. 2015. An enigmatic plant-eating theropod from the Late Jurassic period of Chile. *Nature* 522(7556), pp. 331–334. doi: 10.1038/nature14307.

O'Connor, P.M. 2007. The postcranial axial skeleton of *Majungasaurus crenatissimus* (Theropoda: Abelisauridae) from the Late Cretaceous of Madagascar. *Journal of Vertebrate Paleontology* 27(sup2), pp. 127–163. doi: 10.1671/0272-4634(2007)27[127:TPASOM]2.0.CO;2.

Ostrom, J.H. 1969. Osteology of *Deinonychus antirrhopus*, an unusual theropod from the Lower Cretaceous of Montana. *Bulletin of the Peabody Museum of Natural History* 30, pp. 1–165.

Ostrom, J.H. 1978. The osteology of *Compsognathus longipes* WAGNER. *Zitteliana* 4, pp. 73–118.

Pol, D., Leardi, J.M., Lecuona, A. and Krause, M. 2012. Postcranial anatomy of *Sebecus icaeorhinus* (Crocodyliformes, Sebecidae) from the Eocene of Patagonia. *Journal of Vertebrate Paleontology* 32(2), pp. 328–354. doi: 10.1080/02724634.2012.646833.

Radermacher, V.J. et al. 2021. A new *Heterodontosaurus* specimen elucidates the unique ventilatory macroevolution of ornithischian dinosaurs. *eLife* 10, p. e66036. doi: 10.7554/eLife.66036.

Romer, A.S. 1956. The axial skeleton. In: *The osteology of reptiles*. Illinois: University of Chicago Press, pp. 275–279.

Scanes, C.G. and Dridi, S. 2021. *Sturkie's avian physiology*. Academic Press.

Schachner, E.R., Farmer, C.G., McDonald, A.T. and Dodson, P. 2011. Evolution of the dinosauriform respiratory apparatus: New evidence from the postcranial axial skeleton. *The Anatomical Record: Advances in Integrative Anatomy and Evolutionary Biology* 294(9), pp. 1532–1547. doi: 10.1002/ar.21439.

Schachner, E.R., Lyson, T.R. and Dodson, P. 2009. Evolution of the respiratory system in nonavian theropods: evidence from rib and vertebral morphology. *The Anatomical Record: Advances in Integrative Anatomy and Evolutionary Biology* 292(9), pp. 1501–1513. doi: 10.1002/ar.20989.

Sober, E. 1988. *Reconstructing the past: Parsimony, evolution, and inference*. Cambridge, Mass: MIT press.

Turner, A.H. 2006. Osteology and phylogeny of a new species of *Araripesuchus* (Crocodyliformes: Mesoeucrocodylia) from the Late Cretaceous of Madagascar. *Historical Biology* 18(3), pp. 255–369. doi: 10.1080/08912960500516112.

Walker, A.D. 1990. A revision of *Sphenosuchus acutus* Haughton, a crocodylomorph reptile from the Elliot Formation (Late Triassic or Early Jurassic) of South Africa. *Philosophical Transactions: Biological Sciences* 330(1256), pp. 1–120.

Wilson, J.A., D'Emic, M.D., Ikejiri, T., Moacdieh, E.M. and Whitlock, J.A. 2011. A Nomenclature for Vertebral Fossae in Sauropods and Other Saurischian Dinosaurs. Farke, A. ed. *PLoS ONE* 6(2), p. e17114. doi: 10.1371/journal.pone.0017114.

Witmer, L.M. 1995. The extant phylogenetic bracket and the importance of reconstructing soft tissues in fossils. *Functional morphology in vertebrate paleontology* 1, pp. 19–33.

Wu, X.-C. and Chatterjee, S. 1993. *Dibothrosuchus elaphros*, a crocodylomorph from the Lower Jurassic of China and the phylogeny of the Sphenosuchia. *Journal of Vertebrate Paleontology* 13(1), pp. 58–89. doi: 10.1080/02724634.1993.10011488.

2.7 Supplementary Information

2.7.1 Detailed description on the criteria used to score the eight transitional features

Parapophyseal drift — Throughout the presacral series, the parapophyseal position gradually drifts from being ventral to the neurocentral suture (NCS) to a position dorsal to it, which was characterized into three discrete states. In extant birds or skeletally matured archosaurs, NCS may be inconspicuous, and a straight line at the contact between the pedicle and the centrum was used to approximate the location of the NCS. Character state 0 was defined as the parapophysis positioned ventral to the NCS, which can leave a distinct gap between the parapophysis and the NCS, or the NCS tangentially contacts the dorsal aspect of the parapophysis. Character state 1 was defined as the parapophysis divided by the NCS, in which case the paraophysis has distinct portions both dorsal and ventral to the NCS. Character state 2 was defined as the parapophysis positioned dorsal to the NCS, which can leave a distinct gap between the parapophysis and the NCS, the NCS tangentially contacts the ventral margin of the parapophysis, or the parapophysis merges with the diapophysis.

Diapophyseal orientation — Throughout the presacral series, the diapophyseal orientation gradually shifts from ventrolateral to lateral, which may shift again to dorsolateral (see the result section for description on the variations of the transitional pattern). The changes of the diapophyseal orientation were characterized into two discrete states. Character state 0, 1, and 2 were defined as the diapophysis being oriented ventrolaterally, laterally, and dorsolaterally, respectively. The approximate angles between the long axis of the diapophysis and the sagittal/horizontal plane was used to estimate the diapophyseal orientation, and the arch or bend at the distal end of the diapophysis was not included in the estimation of the diapophyseal orientation. A diapophysis nearly perpendicular to the sagittal/horizontal plane was considered laterally oriented. Diapophyseal orientations clear deviated from the perpendicular position are interpreted as ventrolateral or dorsolateral. Quantitative measurements were not taken due to two limitations. Firstly, the exact angles between the long axis of the diapophysis and the sagittal/horizontal plane may not be measurable from articulated skeleton (e.g. *Ankylosaurus magniventris* (AMNH 5895)). In addition, taphonomic impacts could distort the diapophyseal orientation (e.g. *Allosaruus fragilis* (AMNH 666)), and precise, quantitative measurements may take the taphonomic signals as that of the changes in diapophyseal orientation.

Foramen transversarium — Throughout the presacral series, the foramen transversarium gradually becomes inconspicuous/absent, which was characterized into two discrete states. Character state 0 and 1 were defined as the presence and absence of a distinct foramen transversarium, respectively. In sampled archosaurs taxa in which the presacrals and the presacral ribs are not articulated or associated, the parapophyseal position was used to interpret the presence/absence of a foramen transversarium. A foramen transversarium was interpreted as absence if the parapophysis is immediately ventral to or merged with the diapophysis.

Hypapophysis — Throughout the presacral series in most sampled extant birds, the hypapophysis gradually becomes distinct, which gradually fade to absence in successive presacrals. By comparison, throughout the presacral series in extant crocodylians, the hypapophysis is gradually changes from distinct to absent. The changes in hypapophysis were characterized into two discrete states. Character state 0 was defined as the presence of a distinct, blade-like hypapophysis, whereas character state 1 was defined as the absence of a distinct hypapophysis. Presence of a ventral keel (e.g. *Neuquensuchus universitas* (Lio et al. 2018) and ventrolateral protrusions from the centrum are not interpreted as equivalent to a hypapophysis.

Parapophyseal morphology — Throughout the presacrals series in extant birds and crocodylians, the parapophyseal morphology changes from anteroposteriorly elongated, to subcircular, and to dorsoventrally elongated. The parapophysis could change from being anteroposteriorly elongated directly to dorsoventrally elongated (e.g. *Larus californicus* (AMNH 5066)). In extant crocodylians, the parapophysis is merged with the diapophysis on posterior presacrals, which render the interpretation on the parapophyseal morphology impossible. The changes in the parapophyseal morphology were characterized into three discrete states. Character state 0, 1, 2, and 3 as the parapophysis is anteroposteriorly elongated, subcircular, dorsoventrally elongated, and merged with the diapophysis, respectively. The parapophysis could be in articulated or fused with the capitulum of the presacral rib (e.g. extant birds), and the contact between the parapophysis and the capitulum was used to interpret the parapophyseal morphology.

Neural spine absence — Throughout the presacrals in extant birds, the neural spine is inconspicuous/absent on most if not all anterior presacrals, which gradually becomes a distinct, blade-like neural spine on successive presacrals. The changes in the neural spine absence were

characterized into two discrete states. Character state 0 and 1 were defined as the absence and presence of a distinct neural spine, respectively. A neural spine was interpreted as present only if its height at least approximates the height of the centrum.

Neural spine orientation — Throughout the presacrals in extant birds and crocodylians, the neural spine orientation typically changes from posterodorsal to dorsal. In some extant birds (e.g. *Grus monachal* (UAMZ 6806)) and *Lotosaurus adentus* (IVPP V 4910), the neural spine is oriented anterodorsally on one or multiple anterior presacrals. The changes in the neural spine orientation were characterized into three discrete states. Character state 0, 1, and 2 were defined as the neural spine oriented anterodorsally, posterodorsally, and dorsally, respectively. Orientations of the neural spine was qualitatively estimated based on the approximate angle between the long axis of the neural spine and the long axis of the centrum. The long axis of the neural spine was estimated using its the anterior and posterior margins. In extant crocodylians, the anterior margin of the posterior presacrals (e.g. P16 in *Caiman crocodilus* (UAMZ unnumbered)) is inclined posteriorly whereas the posterior margin is positioned vertically. In this cases, the inclination of the dorsal margin of the neural spine was used to assist in the interpretation of the neural spine orientation.

Epipophysis — Throughout the presacrals in extant birds, the epipophysis gradually becomes inconspicuous from the postzygapophysis, which was characterized into two discrete states. Character state 0 and 1 were defined as the presence and absence of a distinct epipophysis, respectively. The epipophysis was interpreted as present only if a distinct protuberance was observed on top of the postzygapophysis. The presence of a rugose surface on the postzygapophysis was not interpreted as equivalent to a distinct epipophysis.

Table S2. 1. List of archosaur taxa sampled in this study for transitional features, the regionalization identified in the original studies, and the regionalization identified using the three classes of transitional criteria proposed in this study.

Refer to raw_data.csv for the regionalization of individual presacral.

Taxa	Specimen Number	Presacral number	TYPE I DP	TYPE II DP	DFT	DH
***Casuarius australis* (*)**	UAMZ 1369	P3 to P24 (22 PV)	C: 14 CD: 2 D: 6	C: 14 CD: 8 D: 0	C: 14 CD: 8 D: 0	C: 14 CD: 4 D: 4
***Dromaius novehollandiae* (*)**	UAMZ unnumbered	P3 to P25 (23 PV)	C:15 CD: 5 D: 3	C: 15 CD: 8 D: 0	C: 15 CD: 8 D: 0	C: 15 CD: 5 D: 3
***Rhea americana* (*)**	UAMZ 5019	P5 to P22 (18 PV)	C: 11 CD: 5 D: 2	C: 11 CD: 7 D: 0	C: 11 CD: 7 D: 0	C: 11 CD: 3 D: 4
***Rhea americana* (*)**	UAMZ 1368	P5 to P21 (17 PV)	C: 10 CD: 4 D: 3	C: 10 CD: 7 D: 0	C: 10 CD: 7 D: 0	C: 10 CD: 4 D: 3
***Struthio camelus* (*)**	UAMZ 7159	P3 to P25 (23 PV)	C: 15 CD: 6 D: 2	C: 15 CD: 8 D: 0	C: 15 CD: 8 D: 0	C: 15 CD: 5 D: 3
***Gallus gallus* (*)**	UAMZ 5919	P3 to P20 (18 PV)	C: 11 CD: 7 D: 0	C: 11 CD: 7 D: 0	C: 11 CD: 7 D: 0	C: 11 CD: 7 D: 0
***Dendragopus canadensis* (*)**	UAMZ 5702	P3 to P20 (18 PV)	C: 12 CD: 6 D: 0	C: 12 CD: 6 D: 0	C: 12 CD: 6 D: 0	C: 12 CD: 6 D: 0
***Dendragopus canadensis* (*)**	UAMZ 5841	P3 to P20 (18 PV)	C: 13 CD: 5 D: 0	C: 13 CD: 5 D: 0	C: 13 CD: 5 D: 0	C: 13 CD: 5 D: 0
***Meleagris gallopavo* (*)**	UAMZ 5351	P5 to P21 (17 PV)	C: 11 CD: 6 D: 0	C: 11 CD: 6 D: 0	C: 11 CD: 6 D: 0	C: 11 CD: 6 D: 0
***Phasianus colchicus* (*)**	UAMZ 6890	P3 to P20 (18 PV)	C: 11 CD: 7 D: 0	C: 11 CD: 7 D: 0	C: 11 CD: 7 D: 0	C: 11 CD: 7 D: 0
***Canachites canadensis* (*)**	UAMZ 5097	P4 to P20 (17 PV)	C: 10 CD: 7 D: 0	C: 10 CD: 7 D: 0	C: 10 CD: 7 D: 0	C: 10 CD: 7 D: 0
***Tympanuchus phasianellus* (*)**	UAMZ 4668	P3 to P20 (18 PV)	C: 12 CD: 6 D: 0	C: 12 CD: 6 D: 0	C: 12 CD: 6 D: 0	C: 12 CD: 6 D: 0
***Anas rubripes* (*)**	UAMZ 4683	P3 to P21 (19 PV)	C: 12 CD: 7	C: 12 CD: 7	C: 12 CD: 7	C: 12 CD: 6

			D: 0	D: 0	D: 0	D: 1
***Branta canadensis* (*)**	UAMZ 4685	P3 to P24 (22 PV)	C: 15 CD: 7 D: 0	C: 15 CD: 7 D: 0	C: 15 CD: 7 D: 0	—
***Bucephala clangula* (*)**	UAMZ 4892	P3 to P20 (18 PV)	C: 11 CD: 7 D: 0	C: 11 CD: 7 D: 0	C: 11 CD: 7 D: 0	C: 11 CD: 7 D: 0
***Chauna chavaria* (*)**	UAMZ 1249	P3 to P24 (22 PV)	C: 16 CD: 3 D: 3	C: 16 CD: 6 D: 0	C: 16 CD: 6 D: 0	C: 16 CD: 3 D: 3
***Olor columbianus* (*)**	UAMZ 5229	P3 to P27 (25 PV)	C: 18 CD: 3 D: 4	C: 18 CD: 7 D: 0	C: 18 CD: 7 D: 0	C: 18 CD: 0 D: 7
***Olor columbianus* (*)**	UAMZ 5230	P3 to P28 (26 PV)	C: 19 CD: 5 D: 2	C: 19 CD: 7 D: 0	C: 19 CD: 7 D: 0	C: 19 CD: 7 D: 0
***Larus californicus* (*)**	UAMZ 5066	P3 to P20 (18 PV)	C: 11 CD: 1 D: 6	C: 11 CD: 7 D: 0	C: 11 CD: 7 D: 0	C: 11 CD: 4 D: 3
***Larus delawarensis* (*)**	UAMZ 5103	P3 to P20 (18 PV)	C: 11 CD: 4 D: 3	C: 11 CD: 7 D: 0	C: 11 CD: 7 D: 0	C: 11 CD: 0 D: 7
***Ardea herodias* (*)**	UAMZ 4048	P3 to P20 (17 PV)	C: 12 CD: 2 D: 3	C: 12 CD: 5 D: 0	C: 12 CD: 5 D: 0	C: 12 CD: 4 D: 1
***Grus monachal* (*)**	UAMZ 6806	P3 to P25 (23 PV)	C: 14 CD: 2 D: 7	C: 14 CD: 5 D: 4	C: 14 CD: 9 D: 0	C: 14 CD: 3 D: 6
***Gavia immer* (*)**	UAMZ 1793	P3 to P20 (18 PV)	C: 10 CD: 2 D: 6	C: 10 CD: 8 D: 0	C: 10 CD: 8 D: 0	C: 10 CD: 8 D: 0
***Bubo virginianus* (*)**	UAMZ 6846	P3 to P19 (17 PV)	C: 10 CD: 1 D: 6	C: 10 CD: 7 D: 0	C: 10 CD: 7 D: 0	C: 10 CD: 4 D: 3
***Falco peregrinus* (*)**	UAMZ 6769	P3 to P20 (18 PV)	C: 11 CD: 0 D: 7	C: 11 CD: 1 D: 6	C: 11 CD: 7 D: 0	C: 11 CD: 2 D: 5
***Accipiter gentilis* (*)**	UAMZ 5708	P4 to P20 (17 PV)	C: 9 CD: 1 D: 7	C: 9 CD: 6 D: 2	C: 9 CD: 8 D: 0	C: 9 CD: 6 D: 2
***Haliaeetus leucocephalus* (*)**	UAMZ 5028	P3 to P19 (17 PV)	C: 10 CD: 2 D: 5	C: 10 CD: 3 D: 4	C: 10 CD: 7 D: 0	C: 10 CD: 6 D: 1
***Aquila chrysaetos* (*)**	UAMZ 5029	P3 to P19 (17 PV)	C: 10 CD: 2 D: 5	C: 10 CD: 4 D: 3	C: 10 CD: 7 D: 0	C: 10 CD: 7 D: 0

***Pelecanus erythrorhynchos* (*)**	UAMZ 5181	P6 to P18 (13 PV)	C: 9 CD: 3 D: 1	C: 9 CD: 4 D: 0	C: 9 CD: 4 D: 0	C: 9 CD: 3 D: 1
***Pica pica* (*)**	UAMZ 3725	P3 to P19 (17 PV)	C: 9 CD: 7 D: 1	C: 9 CD: 8 D: 0	C: 9 CD: 8 D: 0	C: 9 CD: 4 D: 4
Hesperornis regalis	YPM 1270	(7 PV)	C: 0 CD: 1 D: 5 NA: 1	C: 0 CD: 6 D: 0 NA: 1	C: 0 CD: 6 D: 0 NA:1	C: 0 CD: 0 D: 0 NA: 7
***Deinonychus antirrhopus* (*) ((Ostrom 1969) + collection labels)**	YPM 5204	C4, C5, C7, D1, D6, D7, D9, D10 (8 PV)	—	—	C: 3 CD: 3 D: 1 NA: 1	C: 3 CD: 2 D: 3 NA: 0
***Tyrannosaurus rex* (*) (Brochu 2003)**	FMNH PR2081	P3 to P19 (17 PV)	C: 6 CD: 1 D: 10 NA: 0	C: 6 CD: 8 D: 3 NA: 0	C: 6 CD: 9 D: 2 NA: 0	—
***Coelurus agilis* (*) (Collection labels)**	YPM 2010	C5, C8, C9, C10, D1 (5 PV)	C: 3 CD: 2 D: 0 NA: 0	C: 3 CD: 2 D: 0 NA: 0	C: 3 CD: 1 D: 1 NA: 0	—
***Allosaurus fragilis* (*) ((Gilmore 1920) + collection labels)**	AMNH 666	P8 to P22 (15 PV)	C: 3 CD: 1 D: 11 NA: 0	C: 3 CD: 5 D: 7 NA: 0	C: 3 CD: 8 D: 4 NA: 0	—
***Allosaurus* sp.**	AMNH 680	(3 PV)	C: 0 CD: 0 D: 3 NA: 0	C: 0 CD: 0 D: 3 NA: 0	C: 0 CD: 0 D: 3 NA: 0	—
***Allosaurus* sp.**	AMNH 813	(4 PV)	C: 0 CD: 1 D: 3 NA: 0	C: 0 CD: 2 D: 2 NA: 0	C: 0 CD: 2 D: 2 NA: 0	—
***Sinraptor dongi* (*) (Currie and Zhao 1993)**	IVPP V 10600	C3 to C6, D3 to D14 (16 PV)	C: 6 CD: 0 D: 10 NA: 0	C: 6 CD: 5 D: 5 NA: 0	C: 6 CD: 10 D: 0 NA: 0	C: 6 CD: 2 D: 8 NA: 0
***Majungasaurus crenatissimus* (*) (O'Connor 2007)**	FMNH PR 2295	C3, C5, C10, D5, D9 (5 PV)	C: 3 CD: 0 D: 0 NA: 2	C: 3 CD: 0 D: 2 NA: 0	C: 3 CD: 1 D: 1 NA: 0	—
Coelophysidae sp.	NMMNH P61888	(5 PV)	C: 1 CD: 0	C: 1 CD: 0	C: 1 CD: 0	—

	NMMNH P61887 NMMNH P61897 NMMNH P61898 NMMNH P61899		D: 0 NA: 4	D: 4 NA: 0	D: 4 NA: 0	
Camarasaurus grandis	YPM 1905	(7 PV)	C: 4 CD: 0 D: 0 NA: 3	C: 4 CD: 0 D: 3 NA: 0	C: 4 CD: 0 D: 3 NA: 0	—
***Chasmosaurus belli* (*) (Maidment and Barrett 2011)**	NHMUK R4948	C4 to C8, D1 to D6 (11 PV)	C: 1 CD: 2 D: 8 NA: 0	C: 1 CD: 4 D: 6 NA: 0	C: 1 CD: 4 D: 6 NA: 0	—
***Montanoceratops cerhrhynchos* (*) ((Brown and Schlaikjer 1942) + collection labels)**	AMNH 5464	P4 to P16 (13 PV)	C: 3 CD: 3 D: 0 NA: 7	C: 3 CD: 3 D: 7 NA: 0	C: 3 CD: 3 D: 7 NA: 0	—
***Leptoceratops gracilis* (*) (Collection labels)**	CMN 8889	P4 to P22 (17 PV)	C: 0 CD: 6 D: 0 NA: 11	C: 0 CD: 6 D: 11 NA: 0	C: 0 CD: 6 D: 11 NA: 0	—
Ceratopsidae indet.	AMNH 5422	(8 PV)	—	C: 0 CD: 0 D: 7 NA: 1	C: 0 CD: 0 D: 7 NA: 1	—
***Edmontosaurus regalis* (*) (Campione 2014)**	CMN 2289	(18 PV)	C: 2 CD: 1 D: 0 NA: 15	C: 2 CD: 1 D: 15 NA: 0	C: 2 CD: 1 D: 15 NA: 0	—
***Equijubus normani* (*) (McDonald et al. 2014)**	IVPP V 12534	C3, C4, C7 to C10, D1, D2, D5 (9 PV)	C: 2 CD: 1 D: 6 NA: 0	C: 2 CD: 5 D: 2 NA: 0	C: 2 CD: 5 D: 1 NA: 1	—
***Tanius sinensis* (*) (Borinder 2015)**	PMUR248 PMUR249 PMUR244 PMUR250 PMUR251 PMUR247 PMUR260	P3 to P11 (9 PV)	C: 3 CD: 3 D: 0 NA: 3	C: 3 CD: 3 D: 1 NA: 2	C: 3 CD: 3 D: 1 NA: 2	—

	PMUR252 PMUR237					
Gilmoreosaurus mongoliensis	AMNH 30671 AMNH 30672 AMNH 30673 AMNH 30678 AMNH 30680 AMNH 30681	(6 PV)	C: 1 CD: 1 D: 4 NA: 0	C: 1 CD: 2 D: 3 NA: 0	C: 1 CD: 2 D: 3 NA: 0	—
***Camptosaurus dispar* (Collection labels)**	YPM 1877	P3 to P10 (8 PV)	C: 1 CD: 2 D: 4 NA: 1	C: 1 CD: 5 D: 1 NA: 1	C: 1 CD: 5 D: 1 NA: 1	—
***Iguanodon bernissartensis* (*) (Norman 1980)**	IRSNB 1536 IRSNB 1561	C3 to C11, D1 to D8 (17 PV)	C: 3 CD: 6 D: 0 NA: 8	C: 3 CD: 6 D: 8 NA: 0	C: 3 CD: 7 D: 7 NA: 0	—
***Tenontosaurus tilletti* (*) (Forster 1990)**	AMNH 3040	C3 to C12, D1 to D15 (25 PV)	C: 6 CD: 4 D: 0 NA: 15	C: 6 CD: 4 D: 15 NA: 0	C: 10 CD: 0 D: 15 NA: 0	—
***Ankylosaurus magniventris* (*) ((Carpenter 2004)+ collection labels)**	AMNH 5895	C3 to C7, D1 to D11 (16 PV)	C: 0 CD: 3 D: 11 NA: 2	C: 0 CD: 6 D: 8 NA: 2	C: 0 CD: 6 D: 8 NA: 2	—
Euoplocephalus tutus	AMNH 5377	(5 PV)	C: 0 CD: 1 D: 4 NA: 0	C: 0 CD: 4 D: 1 NA: 0	C: 0 CD: 4 D: 1 NA: 0	—
Sauropelta edwardsi	YPM 5167 YPM 5168 YPM 5166 YPM 5145 YPM 5148	(5 PV)	C: 0 CD: 3 D: 0 NA: 2	C: 0 CD: 3 D: 2 NA: 0	C: 0 CD: 3 D: 2 NA: 0	—
***Stegosaurus stenops* (*) (Maidment et al. 2015)**	NHMUK PV R36730	C3 to C13, D1 to D13 (24 PV)	C: 2 CD: 8 D: 13 NA: 1	C: 2 CD: 9 D: 12 NA: 1	C: 2 CD: 9 D: 12 NA: 1	—
***Stegosaurus* sp.**	AMNH 536	(11 PV)	C: 0 CD: 0	C: 0 CD: 0	C: 0 CD: 0	—

			D: 11 NA: 0	D: 11 NA: 0	D: 11 NA: 0	
Stegosaurus stenops	YPM 1856	(12 PV)	C: 0 CD: 4 D: 8 NA: 0	C: 0 CD: 5 D: 7 NA: 0	C: 0 CD: 5 D: 7 NA: 0	—
Scutellosaurus lawleri	MCZ 8800	(6 PV)	—	—	C: 1 CD: 0 D: 5 NA: 0	—
Lagosuchus chanensis	MCZ 4137	(10 PV)	C: 0 CD: 0 D: 9 NA: 1	C: 0 CD: 1 D: 8 NA: 1	C: 0 CD: 1 D: 8 NA: 1	—
***Caiman crocodilus* (*)**	ROM R 275	P4 to P18 (15 PV)	C: 4 CD: 2 D: 9	C: 4 CD: 4 D: 7	C: 4 CD: 4 D: 7	C: 4 CD: 6 D: 5
***Caiman crocodilus* (*)**	ROM R 7707	P4 to P18 (15 PV)	C: 5 CD: 3 D: 7	C: 5 CD: 4 D: 6	C: 5 CD: 4 D: 6	C: 5 CD: 6 D: 4
***Caiman crocodilus* (*)**	UAMZ unnumbered	P3 to P23 (21 PV)	C: 5 CD: 2 D: 14	C: 5 CD: 4 D: 12	C: 5 CD: 4 D: 12	C: 5 CD: 6 D: 10
***Alligator mississippiensis* (*)**	ROM R 395	P3 to P24 (22 PV)	C: 4 CD: 2 D: 16	C: 4 CD: 4 D: 14	C: 4 CD: 5 D: 13	C: 4 CD: 6 D: 12
***Alligator mississippiensis* (*)**	ROM R 4406	P3 to P20 (18 PV)	C: 6 CD: 3 D: 9	C: 6 CD: 4 D: 8	C: 6 CD: 3 D: 9	C: 6 CD: 5 D: 7
***Alligator mcgrewi* (*) (Articulated skeleton)**	AMNH 10316	P4 to P11 (8 PV)	C: 5 CD: 1 D: 2 NA: 0	C: 5 CD: 3 D: 0 NA: 0	C: 5 CD: 3 D: 0 NA: 0	C: 5 CD: 3 D: 0 NA: 0
Alligator olseni	MCZ 4753	(10 PV)	C: 2 CD: 3 D: 5 NA: 0	C: 2 CD: 4 D: 4 NA: 0	C: 2 CD: 4 D: 4 NA: 0	C: 2 CD: 6 D: 2 NA: 0
***Crocodylus grinnelli* (*) (Collection labels)**	YPM 300	C4 to C8, D1 to D16 (21 PV)	C: 4 CD: 2 D: 15 NA: 0	C: 4 CD: 4 D: 13 NA: 0	C: 4 CD: 4 D: 13 NA: 0	C: 4 CD: 5 D: 12 NA: 0
***Necrosuchus ionensis* (*) ((Brochu 2011) + collection labels)**	AMNH 3129	C5 to C9, D1 to D8 (11 PV)	C: 3 CD: 1 D: 7 NA: 0	C: 3 CD: 4 D: 4 NA: 0	C: 3 CD: 4 D: 4 NA: 0	C: 3 CD: 5 D: 3 NA: 0

***Pristichampsus vorax* (*) (Collection labels)**	AMNH 29993	C3 to C9 (7 PV)	C: 6 CD: 1 D: 0 NA: 0	C: 6 CD: 1 D: 0 NA: 0	C: 6 CD: 1 D: 0 NA: 0	C: 6 CD: 1 D: 0 NA: 0
Diplocynodon ratelii	AMNH 19135	(5 PV)	C: 2 CD: 1 D: 0 NA: 2	C: 2 CD: 1 D: 2 NA: 0	C: 2 CD: 1 D: 2 NA: 0	C: 2 CD: 1 D: 2 NA: 0
Terminonaris browni	AMNH 5844	(3 PV)	C: 2 CD: 1 D: 0 NA: 0	C: 2 CD: 1 D: 0 NA: 0	C: 2 CD: 1 D: 0 NA: 0	C: 2 CD: 1 D: 0 NA: 0
***Baurusuchus albertoi* (*) (Nascimento and Zaher 2010)**	MZSP-PV 140	C3 to C8, D1 to D7 (12 PV)	C: 5 CD: 2 D: 0 NA: 5	C: 5 CD: 2 D: 3 NA: 2	C: 5 CD: 2 D: 3 NA: 2	—
***Sebecus icaeorhinus* (*) (Pol et al. 2012)**	MPEF-PV 1776	C3 to C7, D1 to D12 (15 PV)	C: 3 CD: 2 D: 10 NA: 0	C: 3 CD: 4 D: 8 NA: 0	C: 3 CD: 5 D: 7 NA: 0	C: 3 CD: 5 D: 7 NA: 0
***Simosuchus clarki* (*) (Georgi and Krause 2010)**	UA 8679	C3 to C8, D1 to D9 (11 PV)	C: 5 CD: 0 D: 6 NA: 0	C: 5 CD: 1 D: 4 NA: 1	C: 5 CD: 1 D: 4 NA: 1	—
***Yacarerani boliviensis* (*) (Leardi et al. 2015)**	MNK-PAL5064-E	C3 to C7, D3 to D7 (10 PV)	C: 4 CD: 1 D: 5 NA: 0	C: 4 CD: 3 D: 3 NA: 0	C: 4 CD: 3 D: 3 NA: 0	C: 4 CD: 6 D: 0 NA: 0
***Hyposaurus natotor* (*) (Collection labels)**	YPM 985	P3, P6, P8, P9, P10, P15 (6 PV)	C: 2 CD: 0 D: 4 NA: 0	C: 2 CD: 3 D: 1 NA: 0	C: 2 CD: 3 D: 1 NA: 0	C: 2 CD: 3 D: 1 NA: 0
***Hyposaurus* sp.**	YPM 764	(2 PV)	—	—	—	—
***Metriorhynchus* sp.**	AMNH 997	(8 PV)	C: 4 CD: 1 D: 3 NA: 0	C: 4 CD: 1 D: 3 NA: 0	C: 4 CD: 1 D: 0 NA: 3	—
***Edentosuchus tienshanensis* (*) (Li and Downs 1985)**	IVPP V 3236	C3 to C9, D1 to D3 (10 PV)	C: 5 CD: 0 D: 5 NA: 0	C: 5 CD: 4 D: 1 NA: 0	C: 5 CD: 5 D: 0 NA: 0	—
Hesperosuchus agilis	AMNH 6758	(8 PV)	C: 4 CD: 3 D: 0 NA: 2	C: 4 CD: 3 D: 0 NA: 2	C: 4 CD: 1 D: 0 NA: 4	C: 4 CD: 4 D: 0 NA: 1

***Dibothrosuchus elaphros* (*) (Wu and Chatterjee 1993)**	IVPP V 7907	P3 to P12 (10 PV)	C: 3 CD: 2 D: 3 NA: 2	C: 3 CD: 4 D: 1 NA: 2	C: 3 CD: 4 D: 1 NA: 2	—
***Junggarsuchus sloani* (*) (Articulated skeleton)**	IVPP V 14010	(21 PV)	C: 3 CD: 2 D: 0 NA: 10	C: 3 CD: 2 D: 6 NA: 4	C: 3 CD: 1 D: 5 NA: 6	C: 3 CD: 0 D: 6 NA: 6
***Lotosaurus adentus* (*) (Collection labels)**	IVPP V 4910	P3 to P24 (22 PV)	C: 7 CD: 5 D: 10 NA: 0	C: 7 CD: 13 D: 2 NA: 0	C: 7 CD: 10 D: 5 NA: 0	—
***Poposaurus gracilis* (*) (Collection labels)**	YPM 51700	C8, D1 to D13 (14 PV)	—	—	—	—
***Gracilisuchus stipanicicorum* (*) (Articulated skeleton)**	MCZ 4118_1	(4 PV)	C: 4 CD: 0 D: 0 NA: 0	C: 4 CD: 0 D: 0 NA: 0	C: 4 CD: 0 D: 0 NA: 0	—
***Gracilisuchus stipanicicorum* (*) (Articulated skeleton)**	MCZ 4118_2	(3 PV)	C: 0 CD: 0 D: 3 NA: 0	C: 0 CD: 0 D: 3 NA: 0	C: 0 CD: 0 D: 3 NA: 0	—
***Pseudopalatus buceros* (*) (Articulated skeleton)**	NMMNH P4256	(10 PV)	—	—	—	—
Pseudopalatus pristinus	NMMNH P 4679	(8 PV)	C: 4 CD: 0 D: 0 NA: 4	C: 4 CD: 0 D: 4 NA: 0	C: 4 CD: 0 D: 4 NA: 0	—
***Postosuchus kirkpatricki* (*) (Chatterjee 1985)**	TTU P9000 TTU P9002	C3, C4, C8, D2, D4, D7, D16 (7 PV)	C: 2 CD: 0 D: 0 NA: 5	C: 2 CD: 0 D: 4 NA: 1	C: 2 CD: 1 D: 3 NA: 1	—

Taxa marked with * are taxa with known anteroposterior order, either from articulated/associated skeleton or from the original studies. Transitional criteria inapplicable to the taxa are labelled by "—". Presacrals are labelled as "NA" if regionalization could not be determined. Abbreviations: C, cervical; CD, cervicodorsal; D, dorsal; NA, not identifiable; P, presacral; PV, presacral vertebrae.

2.8 Digital Supplementary Data

Digital supplementary data is stored and managed by the author, the documents of which are listed as follow:

(1) criteria used to code states of transitional features sampled in this study.

(2) raw data and R script to visualised transitional features in all sampled taxa.

latest version of this script may be found at:

https://github.com/Wani2Y/Bioinformatics/blob/main/Qualitative%20feature%20to%20identify%20cervicodorsal%20transition/visualise%20transitional%20features

(3) raw results of transitional features mapped against presacrals in anteroposterior order in 90 sampled taxa

CHAPTER 3
Characterizing the cervicodorsal transition in archosaurs using supervised statistical models

3.1 Introduction

Birds and crocodylians are modern representatives of archosaurs, a group of amniotes first appeared in the Triassic Period and utilised the many ecological niches available for large-bodied vertebrate throughout the Mesozoic Era (Nesbitt 2011; Nesbitt et al. 2013; Benton 2014).

The axial skeleton of an archosaur is constituted of skull and four or five regions of the vertebral column. Vertebrae anterior to the sacral region at the pelvis are conventionally referred to as the presacral vertebrae, which can be further divided into the cervical, thoracic, and lumbar series, constituting the neck, chest, and back regions, respectively (Cong et al. 1988; Baumel et al. 1993; Kardong 2015). The thoracic region is traditionally defined by the presence of connections between the vertebral column and the sternum via rib segments, and the transition from cervical to thoracic vertebrae is pinpointed by the first presacral connected to the sternum (Romer 1956). Dorsal vertebra(e) is often used to collectively represent the combination of thoracic and lumbar vertebrae, and the transition from cervical to thoracic vertebrae is conventionally termed the cervicodorsal transition.

Using the traditional definition of cervicodorsal transition, extant birds have long necks typically constituted of 10 to 26 cervical counts (Böhmer et al. 2019), whereas nine cervical vertebrae consistently constitute the short necks in extant crocodylians (Cong et al. 1988; Frey 1988). Following the rationale of extant phylogenetic bracketing (Witmer 1995), if the short necks in extant crocodylians represent the ancestral condition of archosaurs, a long neck with high number of cervical counts may be acquired on the evolutionary path to birds. Alternatively, the high cervical counts seen in extant birds may be the ancestral condition, which is reduced on the evolutionary path to crocodylians.

The fossil record houses direct evidence for evolutionary inferences on the cervical count. However, the traditional definition is not applicable in most fossil archosaurs with cartilaginous sterna, because cartilages, if unmineralized, have low preservation potential in the

fossil record. Several alternate methods are used in the literature to identify the cervicodorsal transition and by extension, identify the cervical and dorsal vertebrae in fossil archosaurs (Wu and Chatterjee 1993; Brochu 2003; Sereno and Larsson 2009; McDonald et al. 2014; Han et al. 2018), and anatomical features of the cervical and dorsal vertebrae are used most often. As a consensus is absent on which alternate method should be used, the cervical counts, and by extension, the "long" and "short" necks identified in some fossil dinosaurs may not be accurate (Rauhut et al. 2005; Mateus et al. 2009; Müller et al. 2018).

Combinations of two anatomical features that transitions between character states from unambiguous cervical to univocal dorsal vertebrae can consistently regionalise presacral vertebrae into cervical, cervicodorsal, and dorsal vertebrae (see Chapter 2). Cervicodorsal vertebrae accordingly represent a transitional region that most likely includes the first connection between the presacral vertebrae and the sternum. However, the number of cervicodorsal vertebrae is variable, and may exceed six in some taxa (e.g. *Tyrannosaurus rex*, *Lotosaurus adentus*) (see Chapter 2).

Identifying the cervicodorsal transition as accurate and precise as possible is relevant to accurate inference in multiple fields of evolutionary study. In systematic studies, morphological characters used to generate phylogenies need to be made on homologous regions (e.g. cervical vertebrae vs cervical vertebrae) (Nesbitt 2011; Turner et al. 2012; Pittman et al. 2020). In functional studies, traces of a variety of adaptations can be found from the vertebral column, including aspects of weight bearing (Stefanic and Nesbitt 2018), locomotion (Abourachid et al. 2011; Cieri et al. 2020), and respiration (O'Connor 2007; Wedel 2009; Schachner et al. 2011). Accurate identifications of the cervicodorsal transition aid the students in locating positions of these functional adaptations on the axial skeletons.

In this Chapter, we establish supervised statistical models based on linear measurements taken from presacral vertebrae of extant birds and crocodylians, which are compared and selected based on the accuracy of their predictions. Using the newly established supervised models, presacral vertebrae of fossil archosaurs in the study sample are regionalised into only cervical and dorsal vertebrae without cervicodorsal vertebrae as a transitional reagion in between. Finally, regionalisations of fossil presacral vertebrae using supervised models are compared to those regionalised using the Type II DP criterion in Chapter 2 and in the literature.

3.2 Materials and Methods

Following the terminology used in Chapter 2, the first connection between the presacral vertebrae and the sternum is termed the first sternal connection. Presacral vertebrae, cervical vertebrae, cervicodorsal vertebrae, and dorsal vertebrae are termed presacrals, cervicals, cervicodorsals, and dorsals, respectively. Individual presacral is referred by the sequential number of the respective regions (i.e. P#, C#, CD#, and D#) where necessary.

Seven linear measurements on presacrals (Fig. 3.1) (Table 3.1) were taken as continuous variables from species of nine extant birds, five extant crocodylians, 26 fossil archosaurs, and five taxonomically indeterminate archosaurs (Table 3.2). Linear measurements were taken directly from specimens using digital calipers, except three measurements in the sampled fossil archosaurs (i.e. *appp*, *lpre*, *lpost*) which were measured using ImageJ (Schneider et al. 2012) from specimen photos. Specimens sampled in this study are housed in collections in Canada and the United States. To test whether supervised statistical models can be developed using measurements only from presacrals, femoral lengths (*f_length*) were taken from sampled extant archosaurs to standardise other sampled measurements as training data for the supervised models, the accuracy of which are compared with supervised models trained with data standardised by linear measurements taken from the presacrals. Data processing and supervised modelling were performed using R in RStudio 4.4.2 (RStudio Team 2020; R Core Team 2021).

An eight-step procedure was followed to develop supervised models using data from extant archosaurs (Fig. 3.2). (1) To standardise the sampled continuous variables and account for size discrepancies among the sampled taxa, the seven variables were examined individually. Distributions of centrum anterior width (*caw*) and zygapophyseal length (*appp*) were found overall to have the lowest statistical mode values and the distributions were least spread. To standardise the continuous variables in this study sample, all variables were divided by *f_length*, and all variables except *caw* were divided by *caw*, respectively. (2) data from extant archosaurs were organised into an avian dataset, a crocodylian dataset, and a total archosaurian dataset combining the other two. For each dataset, 70% of the data was used as training data, and the remaining 30% was used as validation data. (3) multicollinearity among the variables was examined using the *psych* package (Revelle 2022), and variables with Pearson correlation

coefficient less than 0.65 were considered independent enough to be used in the same model. Two sets of independent variables were recovered: centrum length (*cl_f*), centrum anterior width (*caw_f*), and prezygapophyseal width (*lpre_f*) standardised by *f_length*, and centrum anterior heigh (*cah_caw*), height of the pedicle (*hp_caw*), and prezygapophyseal width (*lpre_caw*) standardised by *caw*. (4) As the sample of linear measurements collected in this study is relatively small, the training data from the avian, crocodylian, and archosaurian datasets were upsampled with replacement, so that supervised statistical models were trained from 1,000 cervicals and 1,000 dorsals. (5) the *Boruta* package (Kursa and Rudnicki 2010) was used to examine the significance of all sampled variables in distinguishing cervicals from dorsals, and no variable was found to be uninformative. (6) four types of supervised models were created from the avian, crocodylian, and archosaurian training datasets both standardised by *f_length* and *caw*: linear discriminant analysis (LDA), logistic regression, NaïveBayse classifier, and randomForest (Liaw and Wiener 2002; Marschner 2011; Venables and Ripley 2013; Majka 2019). Independent variables were used collectively for creating multivariate models. As the sampled variables are not all independent, additional univariate models were created using all sampled variable. A total of 146 supervised models including multivariate and univariate models were trained from the training datasets of this study sample. (7) for each supervised model, presacrals from validation data were regionalised into cervicals and dorsals. Regionalisations predicted by the supervised statistical models were compared to the known true regionalisation based on the position of the first sternal connection. The accuracy of each supervised model was examined using the *caret* package (Kuhn 2008). (8) Final regionalisations based on the validation, termed majority rule models, were were made using a majority rule procedure from the regionalisations predicted by the supervised models that demonstrated at least 80% accuracy using validation data in the previous stage. This resulted in majority rule models based on archosaurian, avian, and crocodylain datasets, respectively. Accuracy of the final regionalisation was examined again using the *caret* package (Kuhn 2008). R script is provided in the supplementary information.

As *f_length* was not available in the sampled fossil archosaurs at the time of this study, all variables were standardised by *caw*. Presacrals of fossil archosaurs were regionalised into cervicals and dorsals using majority rule model on supervised models trained from archosaurian, avian, and crocodylain datasets standardised by *caw*. The results were then compared to

regionalisation using the type II DP criterion (see Chapter 2) and to the regionalisation in the literature where possible.

3.3 Results

3.3.1. Overall accuracies of sampled variables in supervised models

As represented by the medians of the supervised models presented in this study, models trained from data standardised by *f_length* typically have moderately higher accuracies than those trained from data standardised by *caw* (Fig. 3.3). Among the supervised models, multivariate model and majority rule model trained from data standardised by *f_length* have highest accuracies (> 80%) than multivariate models and majority rule models trained from data standardised by *caw*, and higher than the univariate models. The use of majority rule does not significantly impact model accuracy when the models are trained from data standardised by *f_length*. For models trained from data standardised by *caw*, however, using majority rule to summarise predictions increases accuracy from a median of 76.1% to 80.4% which is just above the threshold accepted by this study.

Among univariate models, models trained from data standardised by *f_length* have higher accuracies when they are trained from *cah* and *hp*, whereas models trained from data standardised by caw have higher accuracies when they are trained using the variable *appp*. Models trained from variables *cl*, *lpre*, and *lpost* have similar accuracies below 80% regardless how the data is standardised. Eight out of 76 supervised models trained from data standardised by *f_length* and six out of 70 supervised models trained on data standardised by *caw* have accuracies below 50% (Table S3.1). Of the models with accuracies lower than 50%, three have accuracies below 30% and they are all based on data standardised by *caw*, whereas only one model based on data standardised by *f_length* has accuracy below 40%. Accordingly, multivariate supervised models are preferred over univariate ones, and majority rule should be performed especially when the data is standardised by *caw*.

3.3.2 Accuracies of the four training methods

LDA models — Accuracies of the trained LDA models trained on archosaurian, avian, and crocodylian datasets are overall similar, with models trained the avian datasets being slightly more accurate (Fig. 3.4, A – C). Among models trained on archosaurian and avian datasets,

multivariate models and univariate models trained on *cah* and *hp* standardised by *f_length* have higher accuracies compared to their counterparts standardised by *caw*. Furthermore, models based on variables standardised by *caw* are decently accurate if the supervised models are trained on variables *appp* and *cl* using archosaurian dataset, and on variables *lpre* and *lpost* using avian dataset. By comparison, all models trained on crocodylian dataset have higher accuracies when the variables are standardised by *f_length*, except for *cl* and *hp* which have higher and similar accuracies when the variables are standardised by *caw*. The multivariate model trained on crocodylian dataset from variables standardised by *f_length* reaches 100% accuracy, which may be related to the small training sample available for this study. Accordingly, training multivariate LDA models with small data such as the one we presented using the crocodylian dataset may have overfitting issues, and could be abandoned if individual or subsets of variables have high enough predictive accuracies (Qiao et al. 2008; Mai 2013).

Logistic regression models — Accuracies of the trained logistic regression models trained from archosaurian and avian datasets are overall similar, whereas those trained from crocodylian dataset from variables standardised by *caw* have substantially lower accuracies (Fig. 3.4, D – F). Among models trained on archosaurian and avian datasets, standardising the variables by *f_length* and *caw* of our training data resulted in similar accuracies, except for *cl* from archosaurian dataset, and *appp*, *lpre*, and *lpost* from the avian dataset which standardising the variables by *caw* offers decently higher accuracies. Models trained from crocodylian dataset have substantially higher accuracies when variables are standardised by *f_length*, with the exception of *cah* that have similar accuracies between standardisation by *f_length* and *caw*.

NaïveBayse models — Accuracies of the trained NaïveBayse models trained on archosaurian, avian, and crocodylian datasets are overall similar, with some of the models trained from avian and crocodylian datasets having lower accuracies (Fig. 3.4, G – I). Among models trained from archosaurian dataset, the multivariate model trained on variables standardised by *f_length* and univariate models trained on *cah* and *hp* have higher accuracy than their counterparts standardised by *caw*. By comparison, univariate models trained on *appp* and *cl* have higher accuracies when they are standardised by *caw*. Among models trained from avian dataset, the accuracies are substantially higher for univariate models trained on *appp*, *lpre*, and *lpost* standardised by *caw*. Among the models trained from crocodylian dataset, all models have higher

accuracies when variables are standardised by *f_length*, except the univariate models trained on *cah* which both standardisation approaches offer similar accuracies. Accordingly, NaïveBayse models and LDA models trained from the datasets in this study have similar accuracies.

Random Forest models — Random Forest models have overall similar accuracies among the three multivariate models trained in this study (Fig. 3.4, J – L). Standardised by *caw*, accuracy is slightly higher for the multivariate model trained from avian dataset.

Overall accuracies of multivariate models are similar regardless of the type of supervised models. Univariate models have most consistent accuracies when they are trained from archosaurian dataset. For models trained from avian dataset, accuracies are similar except for those trained on *appp*, *lpre*, and *lpost*, which are lower for LDA and NaïveBayse models trained on variables standardised by *f_length*. For models trained from crocodylian dataset, accuracies are comparable among the four types of supervised models when variables are standardized by *f_length*, and are substantially lower when variables are standardized by *caw*.

3.3.3 Predictions on sampled fossil presacrals

Among the 31 sampled fossil archosaur taxa, predictions using majority rule models predicted classification of cervicals and dorsals comparable to the identifications in the literature and/or using the type II DP criterion (see Chapter 2) only in four non-avian dinosaurs and one crocodylian (Table S3.2). Among the three majority rule models, the ones based on archosaurian and avian datasets are more consistent and comparable to the regionalisation from the literature and from the type II DP criterion. By comparison, majority rule model based on crocodylian dataset is not comparable to the regionalisation in the literature and the type II DP criterion. For example, the first three preserved presacrals in *Montanoceratops cerhrhynchos* (AMNH 5464) are regionalised as cervicals both in the literature and by the type II DP criterion. However, these most definitely cervicals are regionalised as dorsals by the supervised statistical models trained in this study. In the original descriptive study of *Ao. fragilis* (AMNH 666), P11 was identified by Gilmore (1920) and documented in the collection as the D1, and by the type II DP criterion as the CD1. By comparison, P11 of *Ao. fragilis* (AMNH 666) is regionalised as D3.

The supervised statistical models in this study generated regionalisations comparable to those seen in the literature and/or resulting from the type II DP criterion in three non-avian dinosaurs and one fossil crocodylian. Our majority rule model produced a regionalisation into

cervicals and dorsals for *Deinonychus antirrhopus* (YPM 5204) identical to that in the original descriptive study (Ostrom 1969), apart from the classification of one presacral: the vertebra identified by Ostrom (1969) as D1 was regionalised as a cervical by our majority rule model. In *Gilmoreosaurus mongoliensis* (AMNH 30671, 30672, 30673, 30678, 30680, and 30681), the two cervicodorsals regionalised as cervicals by the type II DP criterion are regionalised as cervicals by our majority rule model, and D1 is regionalised identically between the two methods. In *Ankylosaurus magniventris* (AMNH 5859), the vertebrae identified by Carpenter (2004) as D1 to D3 are regionalised identically by our majority rule model, but as the last three cervicodorsals by the type II DP criterion. As the type II DP criterion typically takes several dorsals as cervicodorsals (see Chapter 2), the last three cervicodorsal in *Ak. magniventris* (AMNH 5859) identified by the type II DP criterion could have been the first three presacrals after the first sternal connection. In *Alligator mcgrewi* (AMNH 10316) with comparable classification, the presacrals are preserved in articulation. Presacral 9 is regionalised as CD1 by the type II DP criterion, and as D1 by our majority rule model. As extant crocodylians consistently have nine cervicals (Cong et al. 1988; Frey 1988), the closely related fossil crocodylians such as *Al. mcgrewi* (AMNH 10316) would likely have nine cervicals. Our majority rule model therefore identified the cervicodosal transition in *Al. mcgrewi* (AMNH 10316) one presacral anterior to the first sternal connection.

3.4 Discussion

3.4.1 Anatomical features with potential for identifying the cervicodorsal transition

Among the sampled variables, *appp* and *cl* capture the length of presacrals, *caw*, *lpre*, and *lpost* capture the width of presacrals, and *cah* and *hp* capture the height of presacrals. All models developed in this study have similar median of accuracy, except for the models trained on *cah* and *hp* that are standardised by *caw* and the models trained on *appp* and *cl* that are standardised by *f_length*. Among the 14 models with less than 50% accuracy (Fig. 3.3) (Table S3.1), seven of the models are based on variables characterising the width of presacrals, whereas four and three of the models are based on variables characterising the height and length of presacrals, respectively. Sampling variables from the length and height of the presacrals are seemingly preferrable compared to those using the width of presacrals. However, all seven models based on

the width of prescarals have accuracies above 35%, whereas the two and one model(s) using the length and height of presacrals have accuracies below 30%.

As majority rule could increase the accuracy of supervised models to identify the cervicodorsal transition, sampling variables capturing the width of presacrals is recommended, because of the potential to avoid severely low accuracy. This recommendation is consistent with the findings of a morphometric study on the presacrals in extant crocodylians (Iijima and Kubo 2019), in which the standardised centrum width is increased towards the cervicodorsal transition. Unlike centrum width, pre-zygapophyseal width examined by Ijima and Kubo (2019) does not show a clear contrast between cervicals and dorsals. Our univariate models trained on *lpre* from crocodylian dataset are high in accuracy (Fig. 3.4), which suggests a distinct contrast in pre-zygapophyseal width exist between the cervicals and dorsals.

3.4.2 Plausible factors contributing to inconsistent regionalisation in fossil archosaurs

Limitation of training procedure — data sampled from extant archosaurs in this study is relatively small, especially from the extant crocodylians, and criterion for input of majority rule models was set to accuracy at 80%. As supervised learning can be improved by increasing the sizes of high-quality training data with good representations (Ajiboye et al. 2015), continue sampling extant archosaurs may improve the robustness of supervised models, and the models with much higher accuracies may be filtered out input for majority rule models. Further augmenting the training dataset would theoretically reduce the degrees of multicollinearity (Kim 2019), allowing more sample variables to be trained collectively in multivariate models, which in turn may increase accuracy of models (e.g. comparisons between multivariate and univariate models in this study) (Fig. 3.3). However, increasing the size of training dataset does not guarantee the elimination of multicollinearity in empirical studies (Vatcheva et al. 2016), and sampled variables should be examined and filtered every time the training dataset is altered. Furthermore, augmenting training dataset would risk overfitting supervised models with training data, and factors such as sampled variables and rounds of cross-validation should be taken into account (Vabalas et al. 2019).

Influences from biological adaptations — Archosaurs have a deep evolutionary history (Brusatte et al. 2010; Benton 2014; Pol and Leardi 2015; Puértolas Pascual et al. 2015; Nesbitt et

al. 2017), and the vertebral columns of many taxa were likely altered for functional adaptations such as weight bearing (e.g. hyposphene-hypantrum) (Stefanic and Nesbitt 2018), facilitating locomotion (Abourachid et al. 2011; Molnar et al. 2015), promoting head movements (Terray et al. 2020), and respiration (Schachner et al. 2011; Brocklehurst et al. 2018). The logic of the level I extant phylogenetic bracket (Witmer 1995) may not be appropriate to follow in inferring the cervicodorsal transition across Archosauria. With articulated skeletons of fossil archosaurs (Norelli and Makovicky 1999; Brochu 2003; Clark et al. 2004; Salisbury et al. 2006; Xu et al. 2015; Currie et al. 2016), the first sternal connection may be approximated, and supervised models could be trained using data collected from both extant and fossil archosaurs. Regionalisation of presacrals in other fossil archosaurs could be made following the logic of the level II extant phylogenetic bracket (Witmer 1995). If such supervised modelling can accurately and perhaps even precisely identify the cervicodorsal transitions in fossil archosaurs, an anatomical framework may be established for the regionalisation of the axial skeletons, and evolutionary timing of functional adaptations along the vertebral column seen in extant birds and crocodylians (Fujiwara et al. 2009; Molnar et al. 2014; Molnar et al. 2015; Terray et al. 2020) may be traced back to their ancestral precursors. Furthermore, such an anatomical framework would allow presacrals of extant and fossil archosaurs to be regionalised in a consistent manner, and insights from anatomical studies of the presacral vertebral column in deep time may be combined with insights from studies of embryonic development of presacral vertebral column (Mansfield and Abzhanov 2010; Böhmer et al. 2015; Bui and Larsson 2021), which in turn has the potential to perceive the evolutionary transitions of vertebral column since the bygone days of archosaurian history.

Tables

Table 3. 1. Definitions of seven linear measurements on presacrals sampled in this study.

Variable	Definition
Centrum length (*cl*)	Maximal anteroposterior distance between the pedicle and the centrum along the NCS.
Centrum anterior height (*cah*)	Dorsoventral distance from the NCS to the base of the centrum.
Centrum anterior width (*caw*)	Maximal distance between the left and right NCS at their anterior ends.
Height of the pedicle (*hp*)	Maximal dorsoventral distance from the prezygapophyseal facet to the NCS.
Zygapophyseal length (*appp*)	Maximal anteroposterior distance between the prezygapophyseal and the postzygapophyseal facets of the same side.
Prezygapophyseal width (*lpre*)	Maximal distance between the left and right prezygapophyseal facets.
Postzygapophyseal width (*lpost*)	Maximal distance between the left and right postzygapophyseal facets

Table 3. 2. List of archosaur taxa sampled for linear measurements on presacrals (see Table S3.2 for the full list of taxa and the sequential orders of presacrals where available).

Pseudosuchia		**Avemetatarsalia**	
Clade	Number of Taxa	Clade	Number of Taxa
Crocodylia	11	Aves	11
Dyrosauridae	2	Hesperornithidae	1
Poposauroidea	2	Dromaeosauridae	1
Gracilisuchidae	1	Coeluridae	1
Rauisuchidae	1	Allosauroidea	3
Phytosauria	1	Camarasauridae	1
		Ceratopsia	3
		Ornithopoda	3
		Stegosauridae	2
		Ankylosauria	3
		Basal avemetatarsalians	2

Figures

Figure 3.1. Linear measurements taken from presacrals sampled in this study.

Line drawings of dorsal in crocodylian illustrating seven linear measurements sampled in anterior (A) and left lateral (B) views. Abbreviations: *appp*, zygapophyseal length; caw, centrum anterior width; *cah*, centrum anterior height; *cl*, centrum length; *hp*, height of pedicle; *lpre*, prezygapophyseal width; and *lpost*, postzygapophyseal width.

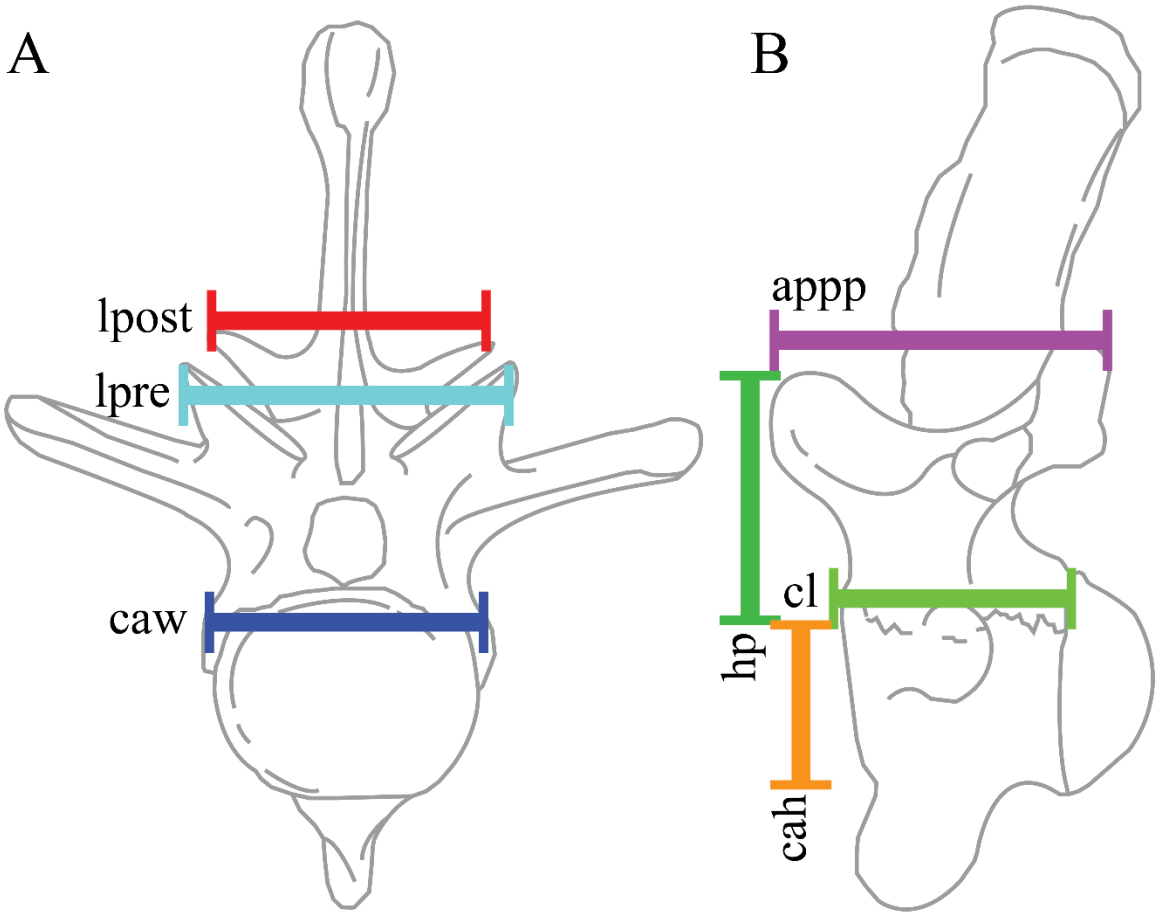
A
lpost
lpre
caw
B
appp
cl
hp
cah

Figure 3.2. Experimental design of constructing supervised models.

Flow chart illustrating the steps taken to construct supervised models. Abbreviations: LDA, linear discriminant analysis.

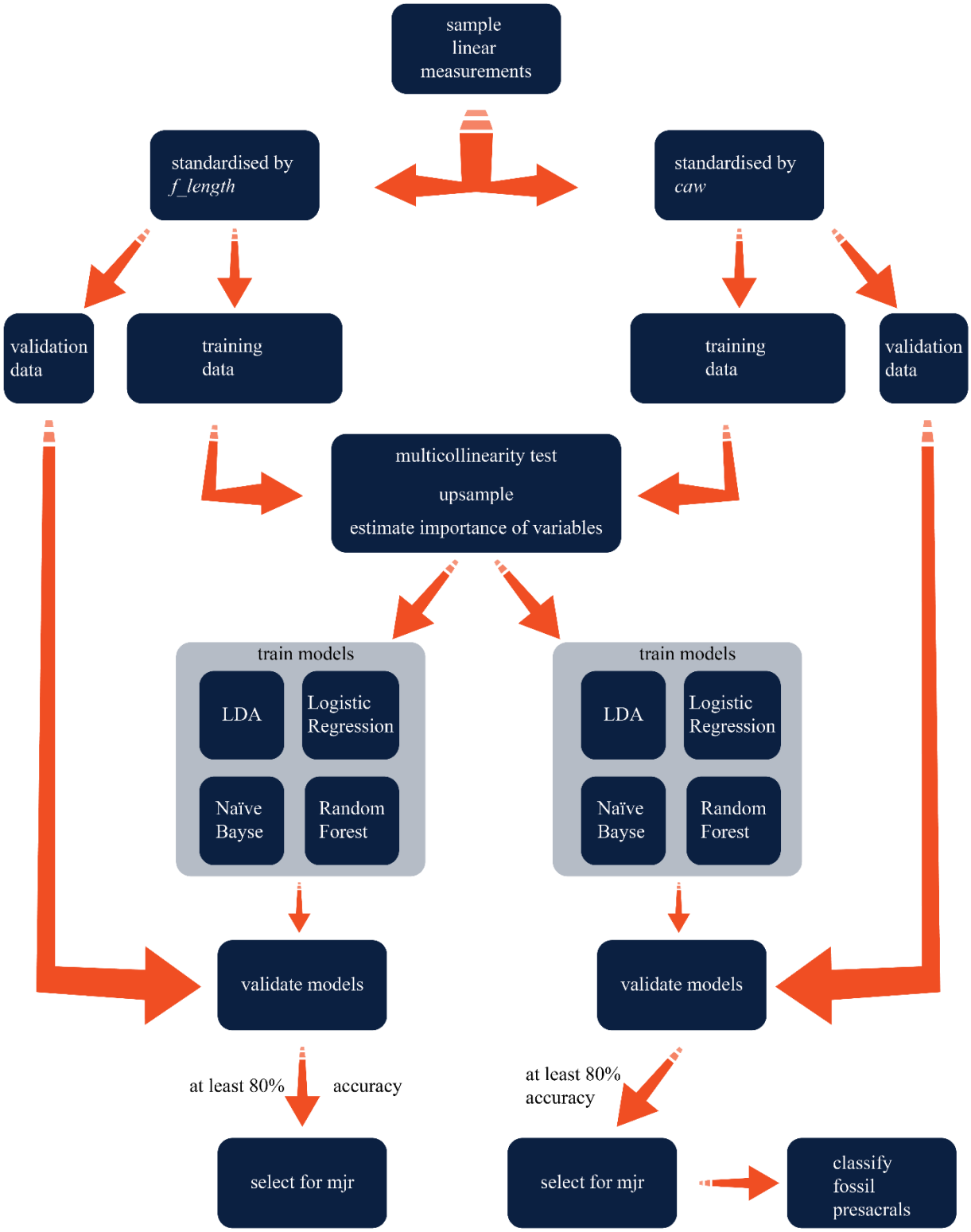
sample linear measurements
standardised by *f_length*
standardised by *caw*
validation data
training data
training data
validation data
multicollinearity test
upsample
estimate importance of variables
train models
LDA
Logistic Regression
Naïve Bayse
Random Forest
train models
LDA
Logistic Regression
Naïve Bayse
Random Forest
validate models
validate models
at least 80% accuracy
at least 80% accuracy
select for mjr
select for mjr
classify fossil presacrals

Figure 3.3. Overall accuracies of 146 supervised models.

Boxplot of model accuracies plotted against variables of multivariate, univariate, and majority rule supervised models. Medians are labelled by horizontal solid lines within box; box ranges represent 25% to 75% quartiles in accuracy; length of whiskers equal interquartile range; and outliers are labelled as solid dots. Models trained on variables standardised by *caw* and *f_length* are coloured orange and navy blue, respectively. Abbreviations: 3var, multivariate models trained on a combination of three independent variables; *appp*, zygapophyseal length; caw, centrum anterior width; *cah*, centrum anterior height; *cl*, centrum length; *hp*, height of pedicle; *lpre*, prezygapophyseal width; and *lpost*, postzygapophyseal width; mjr, majority rule model.

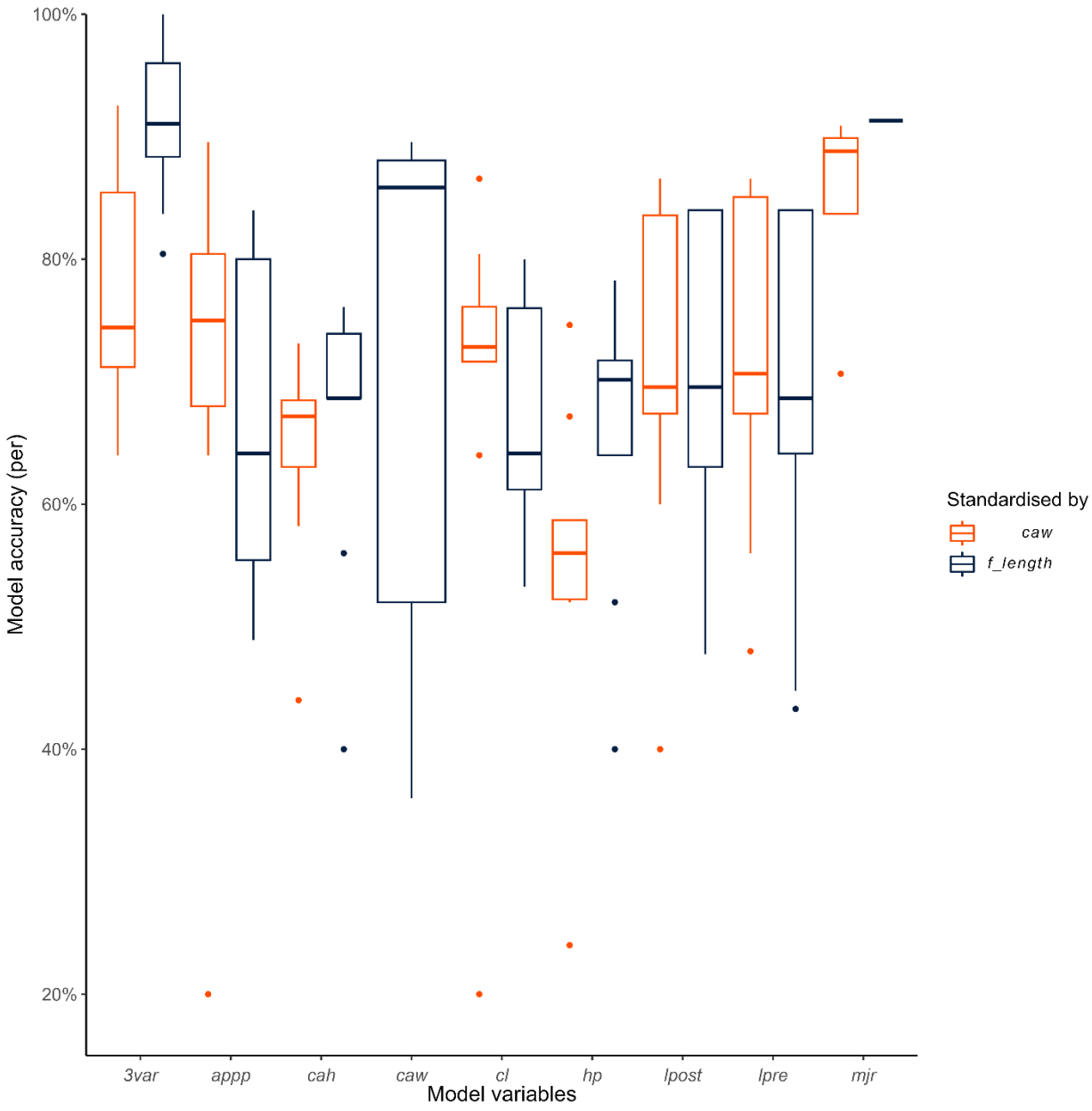
100%
80%
60%
40%
20%
Model accuracy (per)
3var
appp
cah
caw
cl
hp
lpost
lpre
mjr
Model variables
Standardised by
caw
f_length

Figure 3.4. Accuracy of four types of supervised models.

Bar graphs of model accuracies plotted against variables of multivariate and univariate supervised models. Accuracies of LDA models trained on variables from archosaurian (A), avian (B), and crocodylian (C) datasets; accuracies of logistic regression models trained on variables from archosaurian (D), avian (E), and crocodylian (F) datasets; accuracies of NaïveBayse models trained on variables from archosaurian (G), avian (H), and crocodylian (I) datasets; accuracies of Random Forest models trained on variables from archosaurian (J), avian (K), and crocodylian (L) datasets. Models trained on variables standardised by *caw* and *f_length* are coloured orange and navy blue, respectively. Abbreviations: 3var, multivariate models trained on a combination of three independent variables; *appp*, zygapophyseal length; caw, centrum anterior width; *cah*, centrum anterior height; *cl*, centrum length; *hp*, height of pedicle; *lpre*, prezygapophyseal width; and *lpost*, postzygapophyseal width.

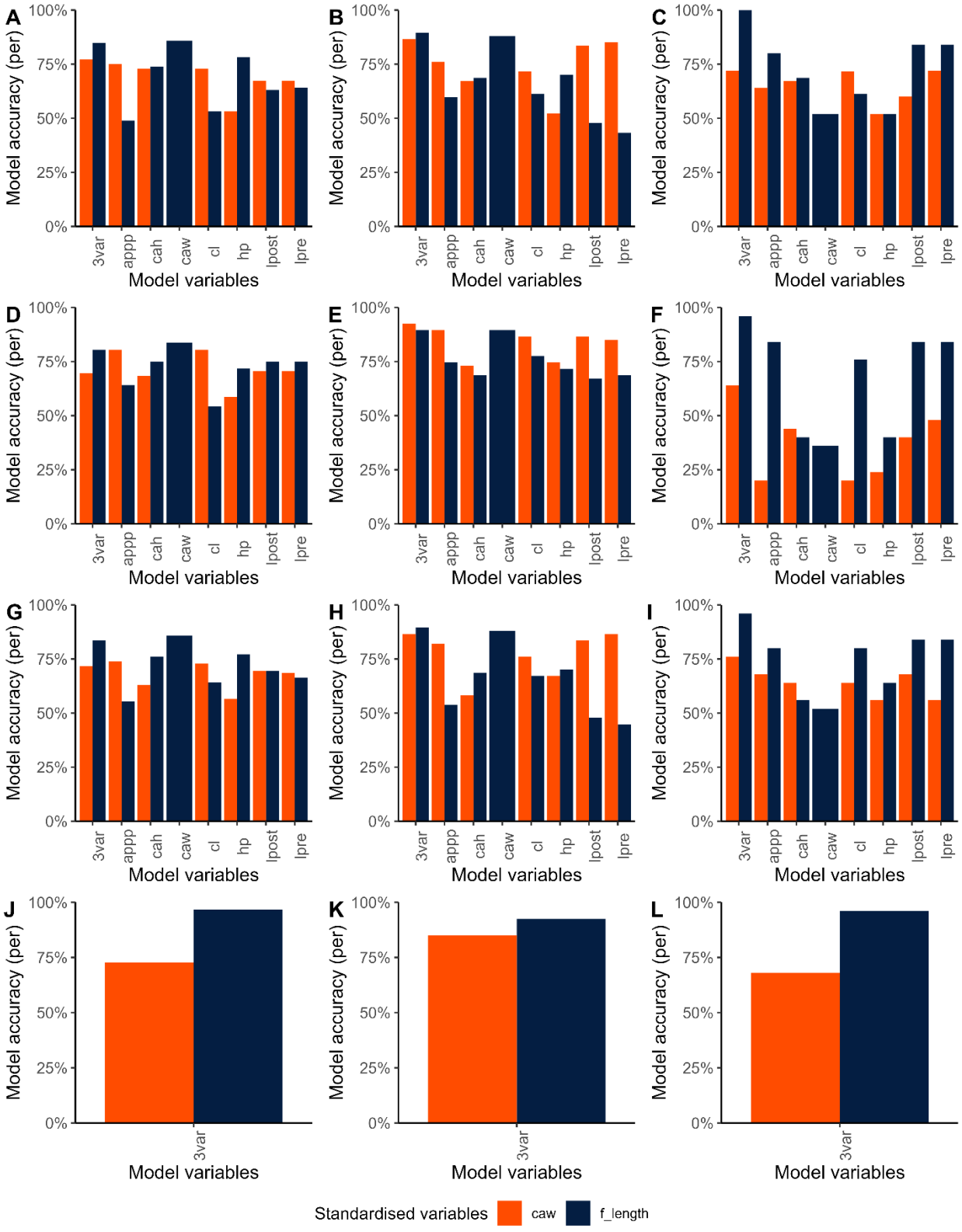
A
B
C
D
E
F
G
H
I
J
K
L
Model accuracy (per)
100%
75%
50%
25%
0%
3var
appp
cah
caw
cl
hp
lpost
lpre
Model variables
Standardised variables
caw
f_length

3.5 Literature Cited

Abourachid, A. et al. 2011. Bird terrestrial locomotion as revealed by 3D kinematics. *Zoology* 114(6), pp. 360–368. doi: 10.1016/j.zool.2011.07.002.

Ajiboye, A.R., Abdullah-Arshah, R., Qin, H. and Isah-Kebbe, H. 2015. Evaluating the effect of dataset size on predictive model using supervised learning technique. *International Journal of Computer Systems & Software Engineering* 1(1), pp. 75–84. doi: 10.15282/ijsecs.1.2015.6.0006.

Baumel, J.J., King, A.S., Breazile, J.E., Evans, H.E. and Vanden Berge, J.C. 1993. *Handbook of avian anatomy: Nomina anatomica avium*. second edition. Cambridge: Nuttall Ornithological Club.

Benton, M.J. 2014. *Vertebrate Palaeontology*. John Wiley & Sons.

Böhmer, C., Plateau, O., Cornette, R. and Abourachid, A. 2019. Correlated evolution of neck length and leg length in birds. *Royal Society Open Science* 6(5), p. 181588. doi: 10.1098/rsos.181588.

Böhmer, C., Rauhut, O.W.M. and Wörheide, G. 2015. Correlation between Hox code and vertebral morphology in archosaurs. *Proceedings of the Royal Society B: Biological Sciences* 282(1810), p. 20150077. doi: 10.1098/rspb.2015.0077.

Brochu, C. 2011. Phylogenetic relationships of *Necrosuchus ionensis* Simpson, 1937 and the early history of caimanines. *Zoological Journal of the Linnean Society* 163(sup 1), pp. S228–S256. doi: 10.1111/j.1096-3642.2011.00716.x.

Brochu, C.A. 2003. Osteology of *Tyrannosaurus Rex*: Insights from a nearly complete skeleton and high-resolution computed tomographic analysis of the skull. *Journal of Vertebrate Paleontology* 22(sup 4), pp. 1–138. doi: 10.1080/02724634.2003.10010947.

Brocklehurst, R.J., Schachner, E.R. and Sellers, W.I. 2018. Vertebral morphometrics and lung structure in non-avian dinosaurs. *Royal Society Open Science* 5(10), p. 180983. doi: 10.1098/rsos.180983.

Brown, B. and Schlaikjer, E.M. 1942. The skeleton of *Leptoceratops* with the description of a new species. *American Museum Novitates* 1169, pp. 1–15.

Brusatte, S.L., Nesbitt, S.J., Irmis, R.B., Butler, R.J., Benton, M.J. and Norell, M.A. 2010. The origin and early radiation of dinosaurs. *Earth-Science Reviews* 101(1–2), pp. 68–100. doi: 10.1016/j.earscirev.2010.04.001.

Bui, H.-N.N. and Larsson, H.C.E. 2021. Development and evolution of regionalization within the avian axial column. *Zoological Journal of the Linnean Society* 191(1), pp. 302–321. doi: 10.1093/zoolinnean/zlaa038.

Carpenter, K. 2004. Redescription of *Ankylosaurus magniventris* Brown 1908 (Ankylosauridae) from the Upper Cretaceous of the Western Interior of North America. *Canadian Journal of Earth Sciences* 41(8), pp. 961–986. doi: 10.1139/e04-043.

Cieri, R.L., Hatch, S.T., Capano, J.G. and Brainerd, E.L. 2020. Locomotor rib kinematics in two species of lizards and a new hypothesis for the evolution of aspiration breathing in amniotes. *Scientific Reports* 10(1), p. 7739. doi: 10.1038/s41598-020-64140-y.

Clark, J.M., Xu, X., Forster, C.A. and Wang, Y. 2004. A Middle Jurassic ‘sphenosuchian’ from China and the origin of the crocodylian skull. *Nature* 430(7003), pp. 1021–1024. doi: 10.1038/nature02802.

Cong, L.Y., Hou, L.H. and Wu, X.C. 1988. *The Gross anatomy of Alligator sinensis Fauvel: Integument, Osteology, and Myology (In Chinese with English summary)*. Beijing, China: China Science Publishing & Media Ltd.

Currie, P.J., Holmes, R.B., Ryan, M.J. and Coy, C. 2016. A juvenile chasmosaurine ceratopsid (Dinosauria, Ornithischia) from the Dinosaur Park Formation, Alberta, Canada. *Journal of Vertebrate Paleontology* 36(2), p. e1048348. doi: 10.1080/02724634.2015.1048348.

Forster, C. 1990. The postcranial skeleton of the ornithopod dinosaur *Tenontosaurus tilletti*. *Journal of Vertebrate Paleontology* 10(3), pp. 273–294. doi: 10.1080/02724634.1990.10011815.

Frey, T. von E. 1988. Anatomie des Körperstammes von *Alligator mississippiensis* Daudin. *Stuttgarter Beitraege zur Naturkunde, Serie A* 424, pp. 1–106.

Fujiwara, S., Kuwazuru, O., Inuzuka, N. and Yoshikawa, N. 2009. Relationship between scapular position and structural strength of rib cage in quadruped animals. *Journal of Morphology* 270(9), pp. 1084–1094. doi: 10.1002/jmor.10744.

Gilmore, C.W. 1920. Osteology of the carnivorous Dinosauria in the United States National Museum: with special reference to the Genera *Antrodemus* (*Allosaurus*) and *Ceratosaurus*. *Bulletin of the United States National Museum* 110, pp. 1–154.

Han, F., Forster, C.A., Xu, X. and Clark, J.M. 2018. Postcranial anatomy of *Yinlong downsi* (Dinosauria: Ceratopsia) from the Upper Jurassic Shishugou Formation of China and the phylogeny of basal ornithischians. *Journal of Systematic Palaeontology* 16(14), pp. 1159–1187. doi: 10.1080/14772019.2017.1369185.

Iijima, M. and Kubo, T. 2019. Comparative morphology of presacral vertebrae in extant crocodylians: taxonomic, functional and ecological implications. *Zoological Journal of the Linnean Society*. doi: 10.1093/zoolinnean/zly096.

Kardong, K.V. 2015. *Vertebrates: comparative anatomy, function, evolution*. Seventh edition. New York, NY: McGraw-Hill Education.

Kim, J.H. 2019. Multicollinearity and misleading statistical results. *Korean Journal of Anesthesiology* 72(6), pp. 558–569. doi: 10.4097/kja.19087.

Kuhn, M. 2008. Building predictive models in R using the *Caret* package. *Journal of Statistical Software* 28, pp. 1–26. doi: 10.18637/jss.v028.i05.

Kursa, M.B. and Rudnicki, W.R. 2010. Feature Selection with the *Boruta* Package. *Journal of Statistical Software* 36(11). doi: 10.18637/jss.v036.i11.

Liaw, A. and Wiener, M. 2002. Classification and regression by randomForest. *R News* 2, pp. 18–22.

Mai, Q. 2013. A review of discriminant analysis in high dimensions: Discriminant analysis in high dimensions. *Wiley Interdisciplinary Reviews: Computational Statistics* 5(3), pp. 190–197. doi: 10.1002/wics.1257.

Majka, M. 2019. Naivebayes: High performance implementation of the Naive Nayes algorithm in R.

Mansfield, J.H. and Abzhanov, A. 2010. Hox expression in the American alligator and evolution of archosaurian axial patterning. *Journal of Experimental Zoology Part B: Molecular and Developmental Evolution* 314B(8), pp. 629–644. doi: 10.1002/jez.b.21364.

Marschner, I. 2011. glm2: Fitting generalized linear models with convergence problems. *The R Journal* 3, pp. 12–15.

Mateus, O., Maidment, S.C.R. and Christiansen, N.A. 2009. A new long-necked "sauropod-mimic" stegosaur and the evolution of the plated dinosaurs. *Proceedings: Biological Sciences* 276(1663), pp. 1815–1821.

McDonald, A.T., Maidment, S.C.R., Barrett, P.M., You, H. and Dodson, P. 2014. Osteology of the basal hadrosauroid *Equijubus normani* (Dinosauria, Ornithopoda) from the Early Cretaceous of China. In: *Hadrosaurs*. Bloomington and Indianapolis: Indiana University Press.

Molnar, J.L., Pierce, S.E., Bhullar, B.-A.S., Turner, A.H. and Hutchinson, J.R. 2015. Morphological and functional changes in the vertebral column with increasing aquatic adaptation in crocodylomorphs. *Royal Society Open Science* 2(11), p. 150439. doi: 10.1098/rsos.150439.

Molnar, J.L., Pierce, S.E. and Hutchinson, J.R. 2014. An experimental and morphometric test of the relationship between vertebral morphology and joint stiffness in Nile crocodiles (*Crocodylus niloticus*). *Journal of Experimental Biology* 217(5), pp. 758–768. doi: 10.1242/jeb.089904.

Müller, R.T., Langer, M.C. and Dias-da-Silva, S. 2018. An exceptionally preserved association of complete dinosaur skeletons reveals the oldest long-necked sauropodomorphs. *Biology Letters* 14(11), p. 20180633. doi: 10.1098/rsbl.2018.0633.

Nesbitt, S.J. 2011. The early evolution of archosaurs: relationships and the origin of major clades. *Bulletin of the American Museum of Natural History* 352, pp. 1–292. doi: 10.1206/352.1.

Nesbitt, S.J. et al. 2017. The earliest bird-line archosaurs and the assembly of the dinosaur body plan. *Nature* 544(7651), pp. 484–487. doi: 10.1038/nature22037.

Nesbitt, S.J., Desojo, J.B. and Irmis, R.B. 2013. Anatomy, phylogeny and palaeobiology of early archosaurs and their kin. *Geological Society, London, Special Publications* 379(1), pp. 1–7. doi: 10.1144/SP379.21.

Norelli, M.A. and Makovicky, P.J. 1999. Important features of the dromaeosaurid skeleton II: Information from newly collected specimens of *Velociraptor mongoliensis*. *American Museum Novitates* (3282), pp. 1–48.

O'Connor, P.M. 2007. The postcranial axial skeleton of *Majungasaurus crenatissimus* (Theropoda: Abelisauridae) from the Late Cretaceous of Madagascar. *Journal of Vertebrate Paleontology* 27(sup2), pp. 127–163. doi: 10.1671/0272-4634(2007)27[127:TPASOM]2.0.CO;2.

Ostrom, J.H. 1969. Osteology of *Deinonychus antirrhopus*, an unusual theropod from the Lower Cretaceous of Montana. *Bulletin of the Peabody Museum of Natural History* 30, pp. 1–165.

Pittman, M., O'Connor, J., Field, D.J., Turner, A.H., Waisum, M. and Xu, X. 2020. Pennaraptora systematics. *Bulletin of the American Museum of Natural History* 440, pp. 7–36.

Pol, D. and Leardi, J.M. 2015. Diversity patterns of Notosuchia (Crocodyliformes, Mesoeucrocodylia) during the Cretaceous of Gondwana. *Publicación Electrónica de la Asociación Paleontológica Argentina*. doi: 10.5710/PEAPA.10.06.2015.108.

Puértolas Pascual, E., Rabal Garcés, R. and Canudo, J. 2015. Exceptional crocodylomorph biodiversity of "La Cantalera" site (lower Barremian; Lower Cretaceous) in Teruel, Spain. *Palaeontologia Electronica*. doi: 10.26879/514.

Qiao, Z., Zhou, L. and Huang, J.Z. 2008. Effective linear discriminant analysis for high dimensional, low sample size data. *Proceedings of the World Congress on Engineering* 2.

R Core Team. 2021. R: A language and environment for statistical computing. R Foundation for Statistical Computing.

Rauhut, O.W.M., Remes, K., Fechner, R., Cladera, G. and Puerta, P. 2005. Discovery of a short-necked sauropod dinosaur from the Late Jurassic period of Patagonia. *Nature* 435(7042), pp. 670–672. doi: 10.1038/nature03623.

Revelle, W. 2022. Psych: Procedures for psychological, psychometric, and personality research.

Romer, A.S. 1956. The axial skeleton. In: *The osteology of reptiles*. Illinois: University of Chicago Press, pp. 275–279.

RStudio Team. 2020. RStudio: Integrated Development for R.

Salisbury, S.W., Molnar, R.E., Frey, E. and Willis, P.M.A. 2006. The origin of modern crocodyliforms: new evidence from the Cretaceous of Australia. *Proceedings of the Royal Society B: Biological Sciences* 273(1600), pp. 2439–2448. doi: 10.1098/rspb.2006.3613.

Schachner, E.R., Farmer, C.G., McDonald, A.T. and Dodson, P. 2011. Evolution of the dinosauriform respiratory apparatus: New evidence from the postcranial axial skeleton. *The Anatomical Record: Advances in Integrative Anatomy and Evolutionary Biology* 294(9), pp. 1532–1547. doi: 10.1002/ar.21439.

Schneider, C.A., Rasband, W.S. and Eliceiri, K.W. 2012. NIH Image to ImageJ: 25 years of image analysis. *Nature Methods* 9(7), pp. 671–675. doi: 10.1038/nmeth.2089.

Sereno, P. and Larsson, H. 2009. Cretaceous crocodyliforms from the Sahara. *ZooKeys* 28, pp. 1–143. doi: 10.3897/zookeys.28.325.

Stefanic, C.M. and Nesbitt, S.J. 2018. The axial skeleton of *Poposaurus langstoni* (Pseudosuchia: Poposauroidea) and its implications for accessory intervertebral articulation evolution in pseudosuchian archosaurs. *PeerJ* 6, p. e4235. doi: 10.7717/peerj.4235.

Terray, L., Plateau, O., Abourachid, A., Böhmer, C., Delapré, A., de la Bernardie, X. and Cornette, R. 2020. Modularity of the neck in birds (Aves). *Evolutionary Biology* 47(2), pp. 97–110. doi: 10.1007/s11692-020-09495-w.

Turner, A.H., Makovicky, P.J. and Norell, M.A. 2012. A review of dromaeosaurid systematics and paravian phylogeny. *Bulletin of the American Museum of Natural History* 371, pp. 1–206. doi: 10.1206/748.1.

Vabalas, A., Gowen, E., Poliakoff, E. and Casson, A.J. 2019. Machine learning algorithm validation with a limited sample size. *PLOS ONE* 14(11), p. e0224365. doi: 10.1371/journal.pone.0224365.

Vatcheva, K.P., Lee, M., McCormick, J.B. and Rahbar, M.H. 2016. Multicollinearity in regression analyses conducted in epidemiologic studies. *Epidemiology (Sunnyvale, Calif.)* 6(2), p. 227. doi: 10.4172/2161-1165.1000227.

Venables, W.N. and Ripley, B.D. 2013. *Modern applied statistics with S-Plus*. Springer Science & Business Media.

Wedel, M.J. 2009. Evidence for bird-like air sacs in saurischian dinosaurs. *Journal of Experimental Zoology Part A: Ecological Genetics and Physiology* 311A(8), pp. 611–628. doi: 10.1002/jez.513.

Witmer, L.M. 1995. The extant phylogenetic bracket and the importance of reconstructing soft tissues in fossils. *Functional morphology in vertebrate paleontology* 1, pp. 19–33.

Wu, X.-C. and Chatterjee, S. 1993. *Dibothrosuchus elaphros*, a crocodylomorph from the Lower Jurassic of China and the phylogeny of the Sphenosuchia. *Journal of Vertebrate Paleontology* 13(1), pp. 58–89. doi: 10.1080/02724634.1993.10011488.

Xu, X. et al. 2015. The taxonomic status of the Late Cretaceous dromaeosaurid *Linheraptor exquisitus* and its implications for dromaeosaurid systematics. *Vertebrata PalAsiatica* 53, pp. 29–62.

3.6 Supplementary Information

Table S3. 1. List of supervised models trained in this study, datasets supervised models trained from, variables supervised models trained on, and model accuracies. Names of supervised models are the same as in the r script (Script S3.1).

Names of supervised models	Datasets	Variable use for standardisation	Variables models trained on	Model accuracy
ar_f_3var	archo	f_length	3var	84.80%
ar_f_cl	archo	f_length	cl	53.30%
ar_f_cah	archo	f_length	cah	73.90%
ar_f_caw	archo	f_length	caw	85.90%
ar_f_hp	archo	f_length	hp	78.30%
ar_f_appp	archo	f_length	appp	48.90%
ar_f_lpre	archo	f_length	lpre	64.10%
ar_f_lpost	archo	f_length	lpost	63.00%
b_f_3var	bird	f_length	3var	89.60%
b_f_cl	bird	f_length	cl	61.20%
b_f_cah	bird	f_length	cah	68.70%
b_f_caw	bird	f_length	caw	88.10%
b_f_hp	bird	f_length	hp	70.10%
b_f_appp	bird	f_length	appp	59.70%
b_f_lpre	bird	f_length	lpre	43.30%
b_f_lpost	bird	f_length	lpost	47.80%
c_f_3var	croc	f_length	3var	100.00%
c_f_cl	croc	f_length	cl	61.20%
c_f_cah	croc	f_length	cah	68.70%
c_f_caw	croc	f_length	caw	52.00%
c_f_hp	croc	f_length	hp	52.00%
c_f_appp	croc	f_length	appp	80.00%
c_f_lpre	croc	f_length	lpre	84.00%
c_f_lpost	croc	f_length	lpost	84.00%
ar_caw_3var	archo	caw	3var	77.20%
ar_caw_cl	archo	caw	cl	72.80%
ar_caw_cah	archo	caw	cah	72.80%
ar_caw_hp	archo	caw	hp	53.30%
ar_caw_appp	archo	caw	appp	75.00%
ar_caw_lpre	archo	caw	lpre	67.40%
ar_caw_lpost	archo	caw	lpost	67.40%
b_caw_3var	bird	caw	3var	86.60%

b_caw_cl	bird	caw	cl	71.60%
b_caw_cah	bird	caw	cah	67.20%
b_caw_hp	bird	caw	hp	52.20%
b_caw_appp	bird	caw	appp	76.10%
b_caw_lpre	bird	caw	lpre	85.10%
b_caw_lpost	bird	caw	lpost	83.60%
c_caw_3var	croc	caw	3var	72.00%
c_caw_cl	croc	caw	cl	71.60%
c_caw_cah	croc	caw	cah	67.20%
c_caw_hp	croc	caw	hp	52.00%
c_caw_appp	croc	caw	appp	64.00%
c_caw_lpre	croc	caw	lpre	72.00%
c_caw_lpost	croc	caw	lpost	60.00%
ar_f_3var	archo	f_length	3var	80.40%
ar_f_cl	archo	f_length	cl	54.30%
ar_f_cah	archo	f_length	cah	75.00%
ar_f_caw	archo	f_length	caw	83.70%
ar_f_hp	archo	f_length	hp	71.70%
ar_f_appp	archo	f_length	appp	64.10%
ar_f_lpre	archo	f_length	lpre	75.00%
ar_f_lpost	archo	f_length	lpost	75.00%
b_f_3var	bird	f_length	3var	89.60%
b_f_cl	bird	f_length	cl	77.60%
b_f_cah	bird	f_length	cah	68.70%
b_f_caw	bird	f_length	caw	89.60%
b_f_hp	bird	f_length	hp	71.60%
b_f_appp	bird	f_length	appp	74.60%
b_f_lpre	bird	f_length	lpre	68.70%
b_f_lpost	bird	f_length	lpost	67.20%
c_f_3var	croc	f_length	3var	96.00%
c_f_cl	croc	f_length	cl	76.00%
c_f_cah	croc	f_length	cah	40.00%
c_f_caw	croc	f_length	caw	36.00%
c_f_hp	croc	f_length	hp	40.00%
c_f_appp	croc	f_length	appp	84.00%
c_f_lpre	croc	f_length	lpre	84.00%
c_f_lpost	croc	f_length	lpost	84.00%
ar_caw_3var	archo	caw	3var	69.60%
ar_caw_cl	archo	caw	cl	80.40%

ar_caw_cah	archo	caw	cah	68.50%
ar_caw_hp	archo	caw	hp	58.70%
ar_caw_appp	archo	caw	appp	80.40%
ar_caw_lpre	archo	caw	lpre	70.70%
ar_caw_lpost	archo	caw	lpost	70.70%
b_caw_3var	bird	caw	3var	92.50%
b_caw_cl	bird	caw	cl	86.60%
b_caw_cah	bird	caw	cah	73.10%
b_caw_hp	bird	caw	hp	74.60%
b_caw_appp	bird	caw	appp	89.60%
b_caw_lpre	bird	caw	lpre	85.10%
b_caw_lpost	bird	caw	lpost	86.60%
c_caw_3var	croc	caw	3var	64.00%
c_caw_cl	croc	caw	cl	20.00%
c_caw_cah	croc	caw	cah	44.00%
c_caw_hp	croc	caw	hp	24.00%
c_caw_appp	croc	caw	appp	20.00%
c_caw_lpre	croc	caw	lpre	48.00%
c_caw_lpost	croc	caw	lpost	40.00%
ar_f_3var	archo	f_length	3var	83.70%
ar_f_cl	archo	f_length	cl	64.10%
ar_f_cah	archo	f_length	cah	76.10%
ar_f_caw	archo	f_length	caw	85.90%
ar_f_hp	archo	f_length	hp	77.20%
ar_f_appp	archo	f_length	appp	55.40%
ar_f_lpre	archo	f_length	lpre	66.30%
ar_f_lpost	archo	f_length	lpost	69.60%
b_f_3var	bird	f_length	3var	89.60%
b_f_cl	bird	f_length	cl	67.20%
b_f_cah	bird	f_length	cah	68.70%
b_f_caw	bird	f_length	caw	88.10%
b_f_hp	bird	f_length	hp	70.10%
b_f_appp	bird	f_length	appp	53.70%
b_f_lpre	bird	f_length	lpre	44.80%
b_f_lpost	bird	f_length	lpost	47.80%
c_f_3var	croc	f_length	3var	96.00%
c_f_cl	croc	f_length	cl	80.00%
c_f_cah	croc	f_length	cah	56.00%
c_f_caw	croc	f_length	caw	52.00%

c_f_hp	croc	f_length	hp	64.00%
c_f_appp	croc	f_length	appp	80.00%
c_f_lpre	croc	f_length	lpre	84.00%
c_f_lpost	croc	f_length	lpost	84.00%
ar_caw_3var	archo	caw	3var	71.70%
ar_caw_cl	archo	caw	cl	72.80%
ar_caw_cah	archo	caw	cah	63.00%
ar_caw_hp	archo	caw	hp	56.50%
ar_caw_appp	archo	caw	appp	73.90%
ar_caw_lpre	archo	caw	lpre	68.50%
ar_caw_lpost	archo	caw	lpost	69.60%
b_caw_3var	bird	caw	3var	86.60%
b_caw_cl	bird	caw	cl	76.10%
b_caw_cah	bird	caw	cah	58.20%
b_caw_hp	bird	caw	hp	67.20%
b_caw_appp	bird	caw	appp	82.10%
b_caw_lpre	bird	caw	lpre	86.60%
b_caw_lpost	bird	caw	lpost	83.60%
c_caw_3var	croc	caw	3var	76.00%
c_caw_cl	croc	caw	cl	64.00%
c_caw_cah	croc	caw	cah	64.00%
c_caw_hp	croc	caw	hp	56.00%
c_caw_appp	croc	caw	appp	68.00%
c_caw_lpre	croc	caw	lpre	56.00%
c_caw_lpost	croc	caw	lpost	68.00%
ar_f_3var	archo	f_length	3var	96.70%
b_f_3var	bird	f_length	3var	92.50%
c_f_3var	croc	f_length	3var	96.00%
ar_caw_3var	archo	caw	3var	72.80%
b_caw_3var	bird	caw	3var	85.10%
c_caw_3var	croc	caw	3var	68.00%
mjr_ar_f	archo	f_length	mjr	91.30%
mjr_ar_caw	archo	caw	mjr	70.70%
mjr_ar_b_caw	archo	caw	mjr	89.60%
mjr_b_caw	bird	caw	mjr	88.10%
mjr_c_caw	croc	caw	mjr	90.90%

Abbreviations: 3var, multivariate models trained on a combination of three independent variables; archo, archosaurian dataset; *appp*, zygapophyseal length; bird, avian dataset; caw, centrum anterior width; *cah*, centrum anterior height; *cl*, centrum length; croc, crocodylian

dataset; f_length, femoral length; *hp*, height of pedicle; *lpre*, prezygapophyseal width; and *lpost*, postzygapophyseal width; mjr, majority rule model.

Table S3. 2. Tables of fossil archosaur taxa sampled in this study, presacral numbers identified in the literature and/or labelled in the collection, regionalisation using the type II DP criterion, and regionalisation using majority rule models.

Taxa	Presacral Number	Type II DP	MJR (archo)	MJR (bird)	MJR (croc)
Hesperornis regalis **(YPM 1207)**	—	—	D	D	D
	—	CD	D	D	D
	—	CD	D	D	D
	—	CD	D	D	D
	—	CD	D	D	D
	—	CD	C	C	C
	—	CD	C	C	C
Deinonychus antirrhopus **(*) ((Ostrom 1969) + collection labels)** **(YPM 5204)**	C4	—	C	C	D
	C5	—	C	C	C
	C7	—	C	C	C
	D1	—	C	C	D
	D6	—	D	D	D
	D7	—	D	D	C
	D9	—	D	D	C
	D10	—	D	D	D
Coelurus agilis **(*) (Collection labels)** **(YPM 2010)**	C5	C	C	C	C
	C8	C	C	C	C
	C9	C	C	C	C
	C10	CD	C	C	C
	D1	CD	C	C	C
Allosaurus fragilis **(*) ((Gilmore 1920) + collection labels)** **(AMNH 666)**	P8	C	C	C	C
	P9	C	D	D	D
	P10	C	C	C	D
	P11	CD	D	D	D
	P12	CD	D	D	D
	P13	CD	D	D	D
	P14	CD	D	D	D
	P15	CD	D	D	D
	P16	D	D	D	D
	P17	D	D	D	D
	P18	D	D	D	D
	P19	D	D	D	D
	P20	D	D	D	D
	P21	D	D	D	C
	P22	D	D	D	C
Allosaurus	—	D	D	C	D
	—	D	D	D	D

sp. **(AMNH 680)**	—	D	D	D	D
Allosaurus	—	CD	C	C	D
sp.	—	CD	D	D	D
(AMNH 813)	—	D	D	C	D
	—	D	D	D	D
Camarasaurus grandis	—	C	C	C	C
(YPM 1905)	—	C	C	C	C
	—	C	C	C	C
	—	C	C	C	C
	—	D	C	C	D
	—	D	C	C	D
	—	D	C	C	D
Montanoceratops cerhrhynchos	P4	C	D	D	D
((Brown and Schlaikjer 1942)	P5	C	D	D	D
+ collection labels)	P6	C	D	D	D
	P7	CD	D	D	D
(AMNH 5464)	P8	CD	D	D	D
	P9	CD	D	D	D
	P10	D	D	D	D
	P11	D	D	D	D
	P12	D	D	D	D
	P13	D	D	D	D
	P14	D	D	D	D
	P15	D	D	D	D
	P16	D	D	D	D
Leptoceratops gracilis	P4	CD	—	C	D
(Collection labels)	P5	CD	C	C	D
(CMN 8889)	P6	CD	D	D	D
	P7	CD	D	D	D
	P8	CD	C	C	C
	P9	CD	C	C	C
	P10	D	D	C	D
	P11	D	D	D	D
	P12	D	D	D	D
	P13	D	D	D	C
	P14	D	D	D	D
	P15	D	D	D	C
	P16	D	D	D	C
	P19	D	C	C	C
	P20	D	C	C	C
	P21	D	C	C	D
	P22	D	C	C	D

Ceratopsidae indet.	—	—	D	D	D
(AMNH 5422)	—	D	D	D	D
	—	D	D	D	D
	—	D	D	D	D
	—	D	D	D	D
	—	D	D	D	D
	—	D	D	D	D
	—	D	D	D	D
***Gilmoreosaurus mongoliensis* (*)**	—	C	C	C	D
	—	CD	C	C	D
(AMNH 30671 30672 30673 30678 30680 30681)	—	CD	C	C	D
	—	D	D	D	D
	—	D	D	D	D
	—	D	D	D	D
***Camptosaurus dispar* (Collection labels)**	P3	—	C	C	C
	P4	C	C	C	C
(YPM 1877)	P5	CD	D	D	D
	P6	CD	D	D	D
	P7	CD	D	D	D
	P8	CD	D	D	D
	P9	CD	D	D	D
	P10	D	D	D	D
***Tenontosaurus tilletti* (Forster 1990)**	C10	CD	D	D	D
	C11	CD	D	D	D
(AMNH 3040)	D1	D	D	D	D
	D2	D	D	D	D
	D3	D	D	D	D
	D4	D	D	D	C
	D5	D	D	D	D
	D6	D	D	D	D
***Ankylosaurus magniventris* (*)**	C3	—	C	C	D
((Carpenter 2004)+ collection labels)	C4	—	C	C	D
	C5	CD	C	C	—
	C6	CD	C	C	—
	C7	CD	C	C	—
	D1	CD	D	D	D
	D2	CD	D	D	D
	D3	CD	D	D	D
	D4	D	D	D	D
	D5	D	D	D	C
	D6	D	D	D	D
	D7	D	D	D	D
	D8	D	D	D	D

	D9	D	D	D	D
	D10	D	D	D	D
	D11	D	D	D	D
***Euoplocephalus tutus* (AMNH 5337)**	—	CD	D	D	D
	—	CD	D	D	D
	—	CD	D	D	D
	—	CD	D	D	D
	—	D	D	D	D
***Sauropelta edwardsi* (YPM 5167 5168 5166 5145 5148)**	—	CD	D	D	D
	—	CD	D	D	C
	—	CD	D	D	D
	—	D	D	D	D
	—	D	D	D	D
***Stegosaurus* sp. (AMNH 536)**	—	D	D	D	C
	—	D	D	D	C
	—	D	D	D	D
	—	D	D	D	C
	—	D	C	C	—
	—	D	D	D	C
	—	D	C	C	—
	—	D	D	D	D
	—	D	D	D	C
	—	D	C	C	—
	—	D	D	D	D
***Stegosaurus stenops* (YPM 1856)**	—	CD	D	D	D
	—	CD	D	D	D
	—	CD	D	D	D
	—	CD	D	D	D
	—	CD	D	D	D
	—	D	C	C	D
	—	D	C	C	D
	—	D	D	D	C
	—	D	D	D	D
	—	D	D	D	D
	—	D	D	D	C
	—	D	D	D	C
***Scutellosaurus lawleri* (MCZ 8800)**	—	—	D	D	D
	—	—	D	D	D
	—	—	D	D	D
	—	—	D	D	D
	—	—	D	D	D
	—	—	D	D	D
Lagerpeton chanarensis	—	—	C	C	—

(MCZ 4137)	—	CD	C	C	—
	—	D	C	C	—
	—	D	C	C	—
	—	D	C	C	—
	—	D	C	C	—
	—	D	C	C	—
	—	D	C	C	—
	—	D	C	C	—
	—	D	C	C	—
***Alligator mcgrewi* (*)**	P4	C	C	C	C
(AMNH 10316)	P5	C	C	C	—
(Articulated skeleton)	P6	C	C	C	—
	P7	C	C	C	—
	P8	C	C	C	D
	P9	CD	D	D	D
	P10	CD	D	D	D
	P11	CD	D	D	D
Alligator olseni	—	C	D	D	D
(MCZ 4753)	—	C	D	D	D
	—	CD	C	C	D
	—	CD	C	C	D
	—	CD	C	C	D
	—	CD	C	C	D
	—	D	D	D	D
	—	D	D	D	D
	—	D	C	C	D
	—	D	C	C	D
Crocodilus grinnelli	C4	C	D	D	D
(Collection labels)	C5	C	C	C	—
(YPM 300)	C6	C	D	D	D
	C7	C	D	D	D
	C8	CD	D	D	D
	D1	CD	D	D	D
	D2	CD	D	D	D
	D3	CD	C	C	D
	D4	D	C	C	D
	D5	D	C	C	D
	D6	D	C	C	D
	D7	D	C	C	D
	D8	D	C	C	D
	D9	D	C	C	D
	D10	D	C	C	D
	D11	D	C	C	D

	D12	D	C	C	D
	D13	D	C	C	D
	D14	D	C	C	D
	D15	D	D	C	D
	D16	D	C	C	D
Necrosuchus ionensis **((Brochu 2011) + collection labels) (AMNH 3219)**	C5	C	—	C	D
	C6	C	—	C	D
	C7	C	C	C	D
	C8	CD	C	C	D
	C9	CD	D	D	D
	D1	CD	D	D	D
	D4	CD	D	D	D
	D5	D	C	C	D
	D6	D	C	C	D
	D7	D	C	C	C
	D8	D	C	C	D
Pristichampsus vorax **(AMNH 29993)** **(Collection labels)**	C3	C	D	D	D
	C4	C	C	C	D
	C5	C	C	C	D
	C6	C	D	D	D
	C7	C	D	D	D
	C8	C	D	D	D
	C9	CD	D	D	D
Diplocynodon ratelii **(AMNH 19135)**	—	C	D	C	D
	—	C	D	C	D
	—	CD	C	C	D
	—	D	C	C	D
	—	D	C	C	C
Hyposaurus totor **(YPM 985)** **(Collection labels)**	P3	C	C	C	C
	P6	C	C	C	C
	P8	CD	D	D	D
	P9	CD	C	C	C
	P10	CD	C	C	C
	P15	D	D	D	D
***Hyposaurus* sp.** **(YPM 764)**	—	—	D	D	C
	—	—	D	D	C
Poposaurus gracilis **(YPM 51700)**	C8	—	C	C	—
	D1	—	C	C	—
	D2	—	C	C	D
	D3	—	C	C	C
	D4	—	C	C	C
	D5	—	C	C	C
	D6	—	D	D	C

	D7	—	D	D	C
	D8	—	C	C	C
	D9	—	D	D	C
	D10	—	D	D	C
	D11	—	D	D	C
	D12	—	C	C	C
	D13	—	D	D	D
Gracilisuchus stipanicicorum **(MCZ 4118_1, MCZ 4118_2)**	s4_1	C	C	C	—
	s4_2	C	C	C	—
	s4_3	C	C	C	—
	s4_4	C	C	C	—
	s1_1	CD	C	C	—
	s1_2	CD	C	C	—
	s1_3	D	C	C	—
Pseudopalatus buceros **(NMMNH P 4256)** **(Articulated skeleton)**	—	—	C	C	D
	—	—	C	C	D
	—	—	C	C	D
	—	—	C	C	D
	—	—	C	C	D
	—	—	C	C	D
	—	—	C	C	D
	—	—	C	C	D
	—	—	C	C	D
	—	—	C	C	D

Taxa marked with * are taxa regionalisation from supervised models are comparable to regionalisation in the literature and/or by the type II DP criterion. "—" indicate regionalisation are not available. Abbreviations: C, cervical; CD, cervicodorsal; D, dorsal; NA, not identifiable; P, presacral.

3.7 Digital Supplementary Data

Digital supplementary data is stored and managed by the author, the documents of which are listed as follow:

(1) raw measurements taken from the sampled extant and fossil archosaur taxa

(2) R script to train the supervised models, to make predictions in sampled archosaur taxa, and visualise results.

Latest version of this script may be found at :

https://github.com/Wani2Y/Bioinformatics/blob/main/Supervised%20modelling%20for%20cervicodorsal%20transition/supervised%20modelling%20using%20linear%20measurements

CHAPTER 4

Deep reptilian evolutionary roots of a major avian respiratory adaptation

A version of this chapter has been published as Wang, Y., Claessens, L.P.A.M., Sullivan, C., 2023. Deep reptilian evolutionary roots of a major avian respiratory adaptation. Commun Biol 6, 3. https://doi.org/10.1038/s42003-022-04301-z

4.1 Introduction

Extant birds and crocodylians are modern representatives of Archosauria, a group of amniotes that first appeared in the Triassic and filled most niches available to large-bodied terrestrial vertebrates throughout the Jurassic and Cretaceous (Nesbitt 2011; Benton 2014). The anterior thoracic vertebral ribs of almost all extant archosaurs bear posteriorly protruding uncinate processes, although these structures are typically lacking in anhimid and megapodid birds (Baumel et al. 1993). Some neognath birds (e.g. *Falco sparverius* (UAMZ 4022)) have additional uncinate processes on the posteriormost cervical ribs as well. In most extant birds, uncinate processes take the form of slender, bony protrusions that are typically fully ossified (Tickle et al. 2009; Codd 2010) and fused to the vertebral ribs (Codd et al. 2008) in mature individuals (Fig. 4.1, A - D), whereas in extant crocodylians the uncinate processes take the form of cartilaginous tabs (Fig. 4.1E, 1F) (Cong et al. 1988; Frey 1988; Claessens 2009a). The rod-like cartilaginous uncinate processes of the rhynchocephalian *Sphenodon punctatus* may not be homologous to those of birds and crocodylians: most extant lepidosauromorphs lack uncinate processes (Romer 1956), and whether uncinate processes were ancestrally present is currently ambiguous for both Lepidosauromorpha and Sauria. Two main hypotheses for the function of avian uncinate processes, which are not mutually exclusive have been proposed: mechanical reinforcement of the ribcage (Welty and Baptista 1972; Hildebrand 1982; Walker and Liem 2001; Claessens 2015) and ventilation (Zimmer 1935; Tickle et al. 2007). The ventilatory hypothesis is bolstered by theoretical analyses suggesting that uncinate processes should act to increase the leverage of the muscles attached to them (e.g. mm. appendicocostales), which in

turn should enhance the bird's ventilatory performance as the expansions/contractions of the thorax move air through the respiratory organs (Zimmer 1935; Tickle et al. 2007). The mechanical leverage provided by uncinate processes likely facilitate the ventilatory motions of the ribcage measured in *in vivo* studies (Claessens 2009b; Brocklehurst et al. 2019). The ventilatory hypothesis has received experimental support, from an electromyographic study carried out on mm. appendicocostales in the Canada goose *Branta canadensis* (Codd et al. 2005), and uncinate processes accordingly represent an important component of the highly specialized avian ventilatory system, along with pneumatic sacs, unidirectional pulmonary airflow, and cross-current gas exchange (Duncker 1972; Claessens 2015; Powell 2015). In extant crocodylians, unidirectional pulmonary airflow is also present (Farmer and Sanders 2010; Schachner et al. 2013), and m. iliocostalis, an epaxial muscle attached to the uncinate processes, has been found empirically to serve an expiratory function in the American alligator *Alligator mississippiensis* (Codd et al. 2019). Though the specifics of function and homologies involving the respiratory organs and the process of gas exchange are not yet fully understood (Perry et al. 2019), an anatomical capacity for unidirectional pulmonary airflow and a ventilatory mechanism incorporating uncinate processes may have been ancestral for Archosauria.

The fossil record has provided clear evidence for uncinate processes in a small number of archosaurs outside the extant avian and crocodylian crown groups. Slender, ossified uncinate processes have been reported in some non-avian members of Pennaraptora (Codd et al. 2008), the clade of theropod dinosaurs containing birds and their closest relatives. Ossified uncinate processes are also known in the ornithomimosaurian theropod, *Pelecanimimus polyodon* (Cuesta et al. 2022). Moreover, triangular calcified uncinate processes are present in the notosuchian *Araripesuchus gomesii* (Turner 2006), and broad calcified uncinate processes termed intercostal plates have been observed in several ornithischian dinosaurs including ankylosaurs, thescelosaurids, ornithopods, and stegosaurs (Maryañska 1977; Zhou 1983; Boyd et al. 2011; Park et al. 2021). However, the notosuchian and ornithischian examples listed above notwithstanding, preserved uncinate processes are rarely found outside Pennaraptora. This could indicate that uncinate processes are unusual structures that evolved independently in crocodylians, *Ar. gomesii*, pennaraptorans, *Pe. polyodon*, and several ornithischians. Alternatively, the ossified uncinate processes in pennaraptorans could have been modified from a

cartilaginous precursor that was widespread in extinct archosaurs, and perhaps even plesiomorphic for Archosauria, but mostly absent in the current fossil record because mineralisation of the cartilage was rare and preservation potential in the absence of mineralisation was low.

In this chapter, we establish features associated with the attachment of uncinate processes to vertebral ribs as osteological correlates in extant birds and crocodylians. We show that these osteological correlates allow the presence of uncinate processes in fossil archosaurs to be inferred, when uncinate processes are not directly preserved. Using these newly identified osteological correlates, we examine the distribution of uncinate processes in extinct members of Archosauria with a focus on members of Dinosauria. Finally, we reconstruct ancestral states based on these results to explore patterns of uncinate process evolution, and consider the implications for the evolution of ventilation on the line to birds.

4.2 Materials and Methods

Dorsal vertebral ribs of extant and fossil archosaurs housed in museum collections were directly examined to determine whether uncinate scars were present, and by extension whether the presence of uncinate processes could be. Two discrete coding approaches were used in mapping the distribution of uncinate processes in Archosauria and reconstructing ancestral states with respect to this feature. Under our preferred approach, uncinate processes were coded as present in a fossil archosaur if at least one specimen possessed either an uncinate scar or a preserved uncinate process. In the absence of such evidence, the condition was coded as uncertain. Our alternative coding approach, which was used to test the stability of the results obtained under our preferred coding approach, differed in that uncinate processes were coded as absent in taxa for which at least five dorsal vertebral ribs were available, regardless of their state of preservation, and showed no sign of uncinate processes or uncinate scars. This resulted in coding uncinate processes as absent in nine taxa. The proterochampsian archosauriform *Chanaresuchus bonapartei* was selected as an outgroup to Archosauria, and uncinate processes was coded as absent for *Ch. bonapartei* because evidence of uncinate processes or uncinate scars

was lacking from a total of 13 well-preserved vertebral ribs observed in two individuals (MCZ 4037, 4038). The ancestral state reconstruction (ASR) was performed using RStudio 4.1.2, using an informal species-level cladogram (supertree) compiled from the results of 23 phylogenetic studies of varying scope across Archosauria (Carrano et al. 2012; Otero and Pol 2013; Arbour and Currie 2016; Arbour and Evans 2017; Leardi et al. 2017; Nesbitt et al. 2017; Raven and Maidment 2017; Han et al. 2018; Jones and Butler 2018; Dollman et al. 2019; Gorscak and O'Connor 2019; Mannion et al. 2019; Pittman et al. 2020; Pol and Goloboff 2020; Yu et al. 2020; Evans et al. 2021; McDonald et al. 2021; Rio and Mannion 2021; Rummy et al. 2022). To add a phylogenetic tree to the informal cladogram, at least one common taxon present in both trees was used as a topological landmark, and the phylogenetic tree was grafted onto the informal cladogram at the phylogenetic position of the common taxon. Branch lengths were estimated based on first and last appearance data (Peters and McClennen 2015). Maximum parsimony, maximum likelihood, and Bayesian inference were used to infer ancestral states. Each of these methods was applied using both our preferred and alternate coding approaches, and both with and without branch length estimates. Detailed procedures, R script, and raw data for the ASR are provided in the Supplementary Data.

4.3 Results

4.3.1 Establishing uncinate scars as osteological correlates

In extant crocodylians and skeletally immature extant birds (Fig. 4.1 C – F), the uncinate processes are anchored to the vertebral ribs by soft connective tissue and can be removed. Removal of an uncinate process from a vertebral rib reveals a rugose area, which is usually slightly concave, on the rib's posterior margin (Fig. 4.1 G – L). We term this rugose area an uncinate scar. In the six skeletally immature extant birds and six extant crocodylians we examined, uncinate scars were consistently present on the vertebral ribs of the anterior thorax. The irregular, rugose surface of an uncinate scar contrasts with the smooth cortex constituting the majority of the vertebral rib's surface and is often perforated by a small number of visible nutrient foramina. The largest uncinate scars, in terms of area, typically occur on the second dorsal vertebral rib and/or the ribs of adjacent vertebral segments.

Typical avian uncinate scars are suboval, heavily rugose, and positioned near the midpoint of the vertebral rib, and tend to taper proximally and/or distally (Fig. 4.1G, 1H). Small prominences protrude from the vertebral ribs at the proximal and distal ends of the uncinate scar, contributing to the scar's concavity and potentially causing the scar to appear in lateral view as a slight embayment along the margin of the vertebral rib. Avian uncinate scars vary considerably in width and degree of tapering, both among taxa and depending on anteroposterior position within the thorax. They can be slender and strip-like in extreme cases. However, the avian uncinate scars examined in this study were all heavily rugose.

Unlike in birds, uncinate scars in crocodylians are positioned close to the distal ends of the vertebral ribs. Nevertheless, crocodylians differ from birds in having a third, intermediate segment between each thoracic vertebral rib segment and the corresponding sternal segments (Claessens 2015), and crocodylian uncinate scars are probably positionally equivalent to avian ones if the intermediate ribs of crocodylians are homologous to the distal parts of the vertebral ribs of birds, as suggested by evidence from embryonic quails (Aoyama et al. 2005; Scaal 2021). Uncinate scars in crocodylians range topographically from being distinctly concave as in birds to being essentially flat and inconspicuous. The degree of rugosity is more variable than in avian uncinate scars, and may be quite light. A distal prominence is sometimes present, but we observed no proximal prominences in the specimens we examined. In some cases, the uncinate scar is interrupted along its length by one or two areas of smooth cortex, where the uncinate process was presumably not directly anchored by connective tissue to the vertebral rib. The separate areas of rugosity forming the interrupted scar are always aligned proximodistally and may be situated within a single concavity (Fig. 4.1J, 1L). The suboval shape of avian uncinate scars and the elongate shape of crocodylian ones presumably reflect the prong-like and tab-like forms of the uncinate processes seen in birds and crocodylians, respectively.

Uncinate scars nearly identical in morphology and position to those of extant crocodylians were found on two incomplete crocodylian vertebral ribs (AMNH 7900) from the Miocene of Florida, United States (Fig. 4.1M, 1L). The precise taxonomic identity of AMNH 7900 is unknown, but the vertebral ribs have the characteristic morphological features seen in extant crocodylians, including the presence of well-developed anterior and posterior intercostal

ridges. This observation demonstrates that uncinate scars are sometimes visible in fossil archosaurs, and represent viable osteological correlates of uncinate processes attachment in extinct taxa.

4.3.2 Uncinate scars outside Aves and Crocodylia

Uncinate scars were found on disarticulated dorsal vertebral ribs representing at least 19 fossil members of the avian and crocodylian stem lineages, and on several more archosaur specimens that could be referred only to suprageneric clades (see Table 1 of Supplementary Information for details). Identification of uncinate scars in fossil archosaurs requires that at least the midshaft portion of the vertebral rib be preserved with minimal surficial damage. The rarity of such good preservation probably accounts in part for the fact that relatively few uncinate scars were identified in this study. The observed uncinate scars vary in form, but are generally consistent among closely related taxa (e.g. within cerapodans). These uncinate scars can be distinguished from attachment sites of hypaxial muscles (e.g. mm. intercostales) based on their anatomical positioning, interpreted in light of the typical distribution of muscle attachment areas on the vertebral ribs of extant archosaurs (see section 2 of Supplementary Information for details). All observed uncinate scars are positioned near the midshafts of vertebral ribs, as in extant birds.

Among theropods examined in this study, the uncinate scars found in the tyrannosaurid *Albertosaurus sarcophagus* (TMP 99.50.41, 99.50.42), the allosaurid *Allosaurus fragilis* (AMNH 5753), and the dromaeosaurid *Saurornitholestes langstoni* (TMP 88.121.39) resemble their avian counterparts. In the tyrannosaurids *Gorgosaurus libratus* (UALVP 10) and *Daspletosaurus torosus* (CMN 8506), along with four indeterminate tyrannosaurid specimens, each uncinate scar is associated with a ridge that lies medially adjacent to the scar's proximal portion, which recedes into the rib shaft in the proximal direction. This feature, which we term the 'proximal ridge', is present in all tyrannosaurids we examined, except *Ab. sarcophagus* (TMP 99.50.41, 99.50.42). Uncinate scars in tyrannosaurids (Fig. 4.2A, 2B) typically approximate the vertebral ribs in width, and the prominent proximal ridges are clearly visible in lateral view. However, an uncinate scar on a small vertebral rib definitely belonging to a juvenile tyrannosaurid (TMP 94.12.960) (Fig. 4.2C, 2D) is a small, suboval concavity, occupying

approximately one fifth of the width of the rib shaft, and the proximal ridge is a minor protuberance. The uncinate scars and associated proximal ridges are clearly best developed in mature tyrannosaurids, which suggests that they may have become enlarged in response to muscular loads imposed on the uncinate processes during development. The uncinate scar and the proximal ridge in the ornithomimisaurian theropod, *Struthiomimus altus* (AMNH 5355) (Fig. 4.2E, 2F) resemble that of TMP 94.12.960.

Among cerapodans examined in this study, the uncinate scars found in the hadrosaurs *Gryposaurus* (AMNH 5350, 5456) and *Bactrosaurus johnsoni* (AMNH 6553), the non-dryomorph iguranodontian *Tenontosaurus tilletti* (AMNH 3040), the ceratopsid *Centrosaurus* sp. (TMP 82.18, 96.176.135, ROM 767) and *Pachyrhinosaurus lakustai* (UALVP 57289), the leptoceratopsid *Leptoceratops gracilis* (CMN 8889), and the thescelosaurids *Parksosaurus warreni* (ROM 804) and *Zephyrosaurus schaffi* (MCZ 4392), along with some indeterminate members of Cerapoda resemble their crocodylian counterparts. The cerapodan uncinate scars (Fig. 4.2 I - Q) comprise one or two slender strips that are lightly sculpted, and sometimes situated in a concavity (Fig. 4.2O) as in crocodylians. In *Centrosaurus* sp. (TMP 82.18.41), what appears to be a mass of calcified connective tissue partially covers the uncinate scar externally (Fig. 4.2Q). Though superficially resembling bite marks left by carnivorous vertebrates, the cerapodan uncinate scars are unlike bite marks in their consistent shape, positioning, and orientation, and in that there are never more than two of them on a given vertebral rib (see section 2 of Supplementary Information for details).

The uncinate scars found in the ankylosaurs *Panoplosaurus mirus* (ROM 1215), *Edmontonia longiceps* (CMN 8531), *Sauropelta edwardsi* (AMNH 3032), and *Euplocephalus tutus* (AMNH 5337), the stegosaur *Stegosaurus* spp. (AMNH 650, 5752, YPM 1856), (Fig 2 R – W), the sauropod *Apatosaurus excelsus* (YPM 1981) (Fig. 4.2G, 2H), an indeterminate aetosaur (NMMNH P50048), and two indeterminate phytosaurs (YPM 6649, NMMNH P60401) (Fig. 4.2X, 2Y) generally resemble avian uncinate scars. However, the uncinate scars in ankylosaurs each extend onto a shelf that projects posterolaterally from the vertebral rib, enabling the scar to exceed the vertebral rib shaft in width. Those in *Stegosaurus* and *Ap. excelsus*, by contrast, are proportionally narrower than their avian counterparts. Of the two phytosaurs we examined, he

uncinate scars found in YPM 6649 resemble avian uncinate scars, whereas the one in NMMNH P60401 is narrow and proximodisally elongated, occupying the majority of the preserved rib's margin. Although the uncinate scar in the examined aetosaur (NMMNH P50048) is incompletely preserved, the preserved portion is wide and tapering as in birds.

4.3.3 Ancestral state reconstruction for uncinate processes in archosaurs

An ancestral state reconstruction of the distribution of uncinate processes in archosaurs, based on mapping available data onto an informal consensus cladogram of Archosauria (supertree), suggests that presence of cartilaginous uncinate processes represents the plesiomorphic conditions for both Dinosauria and Archosauria (Fig. 4.3) (see section 3 and Table 2 – 5 of Supplementary Information for details). Incorporating branch length consistently increased the estimated probability that cartilaginous uncinate processes were ancestral for Archosauria, regardless of the exact approaches used for performing the ancestral state reconstruction and for coding the presence and absence of uncinate processes. Using our preferred coding approach, in which absence of uncinate scars was coded as uncertainty, both maximum parsimony and maximum likelihood consistently recovered the presence of cartilaginous uncinate processes as the most likely condition at Archosauria ($p_{ml} \geq 0.98$) and Dinosauria ($p_{ml} = 1.00$), and the presence of ossified uncinate processes as the most likely condition at Maniraptoriformes ($p_{ml} \geq 0.90$) and Pennaraptora ($p_{ml} \geq 0.99$). Bayesian inference also recovered cartilaginous uncinate processes as the most likely condition at Archosauria ($p_{mb} = 0.65$), but only when branch length estimates were included in the analysis. The ancestral conditions at Dinosauria, Maniraptoriformes, and Pennaraptora could not be recovered with Bayesian inference ($p_{mb} \approx 0.33$) both with and without branch length estimates, which likely reflect the fact that only a small number of archosaurs in the informal consensus cladogram had observed uncinate scars.

Using an alternate coding approach in which uncinate processes were coded as absent in taxa represented by five or more dorsal vertebral ribs that all lacked uncinate scars, nine archosaur taxa were coded as lacking uncinate processes. Under this alternate coding, maximum parsimony recovered identical results as using the preferred coding. Maximum likelihood and Bayesian inference recovered cartilaginous uncinate processes as the most likely condition at

Archosauria (p_{ml} = 0.61, p_{mb} = 0.55), but only when branch length estimates were incorporated. By contrast, maximum likelihood excluding branch length estimates recovered the absence of uncinate process as the most likely condition at Archosauria (p_{ml} = 0.92). Methods of reconstruction notwithstanding, the ancestral condition at Dinosauria could not be recovered with confidence ($p_{mb} \approx 0.33$). Maximum likelihood recovered ossified uncinate processes as the most likely condition at Maniraptoriformes (p_{ml} = 0.90) and Pennaraptora (p_{ml} = 0.99), but only when branch estimates were excluded in the analysis. Bayesian inference could not confidently recover the ancestral conditions at Maniraptoriformes (p_{mb} = 0.33) and Pennaraptora (p_{mb} = 0.33).

As the study sample included only four non-crocodylian pseudosuchian taxa with uncinate scars, the ancestral presence of cartilaginous uncinate processes is less well supported for Archosauria as a whole than for Dinosauria. Including vertebral ribs from more fossil pseudosuchians in future studies would be warranted as a further test of whether uncinate processes were plesiomorphically present in archosaurs.

4.4 Discussion

4.4.1 Potential homology of uncinate processes across Archosauria

Uncinate scars in various fossil archosaurs, together with the relatively few known examples of preserved uncinate processes (Norelli and Makovicky 1999; Boyd et al. 2011; Funston and Currie 2016), provide a strong basis for inferring that cartilaginous uncinate processes were widespread and plesiomorphic in Dinosauria. Although only four non-crocodylian pseudosuchians were found to have uncinate scars (two indeterminate phytosaurs, one indeterminate aetosaur, and the notosuchian *Ar. gomesii*), the relative consistency in morphology and anatomical position of all uncinate scars observed in this study suggests that uncinate processes could well be homologous across Archosauria, as opposed to having evolved independently in multiple lineages. If this is indeed the case, and the correlation in shape between uncinate processes and uncinate scars observed for Aves and Crocodylia holds true outside these groups, then uncinate processes possibly were tab-like in ancestral archosaurs, remained tab-like in pseudosuchians and cerapodans, and became more prong-like in theropods.

This scenario is congruent with the presence of preserved tab-like uncinate processes in some ornithischians (Boyd et al. 2011), and would imply that uncinate processes acquired a prong-like morphology before they became ossified structures on the evolutionary line to birds.

Although phytosaurs were treated as pseudosuchians in this study, they were placed outside Archosauria in several phylogenetic studies (Ezcurra 2016; Stocker et al. 2017). If the latter is correct, the inferred presence of uncinate scars in phytosaurs would suggest a possible pre-archosaurian origin of uncinate processes, but the wider distribution of these structures across Sauropsida remains to be investigated. Although ossified uncinate processes were recovered as the ancestral state for Maniraptoriformes in our analysis, this result is highly dependent on the presence of ossified uncinate processes in the ornithomimosaur *Pe. polyodon* (Cuesta et al. 2022), and may reflect the relatively sparse sampling of non-pennaraptoran maniraptoriforms. Thus, it is possible that uncinate ossification evolved separately in *Pelecanimimus* and Pennaraptora.

4.4.2 Uncinate processes and the evolution of ventilation on the line to birds

Definitive evidence of parabronchi, and by extension cross-current gas exchange, is lacking from the fossil record, and the origin of high-efficiency gas exchange in birds is difficult to pinpoint. However, the presence of unidirectional pulmonary airflow in crocodylians and lepidosaurs (Farmer 2015), in combination with the widespread distribution of uncinate processes in archosaurs, suggests that components of the avian ventilatory system were likely acquired gradually on the evolutionary path towards birds. Inferences can therefore be made regarding the emergence of individual components of the avian ventilatory system, leading to a hypothetical evolutionary scenario amenable to future testing (Fig. 4.3). Tab-like, cartilaginous uncinate processes were likely present in ancestral non-avian dinosaurs and potentially present in ancestral archosaurs, as indicated by our ancestral state reconstruction. Such uncinate processes were presumably quite flexible compared to the ossified ones in pennaraptorans, but their advent could nevertheless have resulted in limited increase in both the mechanical advantage of the ventilatory muscles (Zimmer 1935; Tickle et al. 2007) and the structural stability of the trunk (Welty and Baptista 1972; Hildebrand 1982; Walker and Liem 2001), although whether even the ossified uncinate processes of extant birds have much impact on trunk stability has not yet been

rigorously tested. Furthermore, early uncinate processes likely provided additional surface area for ventilatory muscle attachment. By allowing development of larger muscles, potentially with enhanced moment arms, the uncinate processes may have provided the anatomical capacity to meet higher metabolic demands, because the ventilatory muscles could rotate the vertebral ribs with greater torque to generate inspiratory motions. The potential widespread occurrence of uncinate processes in archosaurs suggests selection pressures may have favoured the enhanced ventilatory performance resulting from the increased muscular volumes and the mechanical leverage conferred by the uncinate processes. Such an inference would be congruent with the hypothesis that low ambient atmospheric oxygen levels in the Triassic Period selected for adaptations that enhanced ventilatory performance, as well as lower barriers to gas exchange, in ancestral archosaurs (Farmer 2015). The emergence of postcranial skeletal pneumaticity in saurischians (Wedel 2009) likely also increased metabolic efficiency by replacing heavy, energetically expensive bone with pneumatic space (Benson et al. 2012; Brocklehurst et al. 2020), allowing energy to be budgeted for other biological demands (e.g. increased activity). Resting metabolic rates in extant birds are positively correlated with uncinate process length (Tickle et al. 2009), suggesting that elevated resting metabolic rates were likely present in fossil maniraptorans with long, ossified uncinate processes (Codd et al. 2008). The inferred increase in metabolism in maniraptorans have been related to the origin of powered flight, but this hypothesis cannot be readily tested at present because the inferred metabolic increase and the origin of avian powered flight are difficult to pinpoint in time (Wang and Zhou 2017). However, this uncertainty does not detract from the possibility that uncinate processes were present as an adaptation for improved ventilatory performance in ancestral archosaurs, and were retained and augmented in a wide range of extant and extinct members of the group. Uncinate processes accordingly may have played an important role in ventilation since the dawn of Archosauria.

Figures

Figure 4.1. Dorsal vertebral ribs with uncinate processes and uncinate scars in extant archosaurs, and dorsal vertebral rib with uncinate scar in an indeterminate fossil crocodylian

Left dorsal vertebral rib of bald eagle *Haliaeetus leucocephalus* (UAMZ 5028) in lateral view (A), and close-up of contact between dorsal vertebral rib and uncinate process in lateral view (B); right dorsal vertebral rib of skeletally immature wild turkey *Meleagris gallopavo* (UAMZ 1824) in lateral view (C), and close-up of contact between dorsal vertebral rib and uncinate process in lateral view (D); left dorsal vertebral rib of alligatorid crocodylian *Caiman crocodilus* (UAMZ unnumbered) in lateral view (E), and close-up of contact between dorsal vertebral rib and uncinate process in lateral view (F); left dorsal vertebral rib of palaeognath bird *Rhea americana* (UAMZ 5019) in posteromedial view (G), and close-up of uncinate scar in posterior view (H); left dorsal vertebral rib of *Caiman crocodilus* (UAMZ unnumbered) in posteromedial view (I), and close-up of uncinate scar in posterior view (J); left dorsal vertebral rib of *Caiman crocodilus* (ROM R7077) in posteromedial view (K), and close-up of uncinate scar in posterior view (L); incomplete right dorsal vertebral rib of indeterminate fossil crocodylian from the Miocene of Florida, USA (AMNH 7900) in posteromedial view (M), and close-up of uncinate scar in posterior view (N). Branching lines indicate multiple rugose areas of a single uncinate scar separated by smooth cortex. Abbreviations: An, anterior; L, lateral; nf, nutrient foramen; P, proximal; u, uncinate process; us, uncinate scar.


A
B
u
C
D
u
E
F
u
G
H
nf
us
I
J
us
K
L
us
M
N
5 mm
us
nf
P
An
P
L
1 cm
1 mm

Figure 4.2. Dorsal vertebral ribs with uncinate scars in fossil archosaurs

Left dorsal vertebral rib referred to Tyrannosauridae indet. (TMP 92.36.1231) (A), and close-up of uncinate scar in posterior view (B); right dorsal vertebral rib of juvenile individual referred to Tyrannosauridae indet. (TMP 94.12.960) (C), and close-up of uncinate scar in posterior view (D); right dorsal vertebral rib of ornithomimisaurian theropod *Struthiomimus altus* (AMNH 5355)(E), and close-up of uncinate scar in posterior view (F); right dorsal vertebral rib of sauropod *Apatosaurus excelsus* (YPM 1981) (G), and close-up of uncinate scar in posterior view (H); right dorsal vertebral rib of hadrosaur *Gryposaurus notabilis* (AMNH 5350)(I), and close-up of uncinate scar in posterior view (J, K); left dorsal vertebral rib of ceratopsid *Pachyrhinosaurus lakustai* (UALVP 57289) (L), and close-up of uncinate scar in posterior view (M); dorsal vertebral rib referred to ceratopsid *Centrosaurus* sp. (TMP 96.176.135) (N), and close-up of uncinate scar in posterior view (O); right dorsal vertebral rib referred to ceratopsid *Centrosaurus* sp. (TMP 82.19.41) (P), and close-up of uncinate scar in posterior view (Q); dorsal vertebral rib of ankylosaur *Sauropelta edwardsi* (AMNH 3032) (R), and close-up of uncinate scar in posterior view (S); dorsal vertebral rib of stegosaur *Stegosaurus stenops* (AMNH 650) (T), and close-up of uncinate scar in posterior view (U); left dorsal vertebral rib referred to stegosaur *Stegosaurus* sp. (AMNH 5752) (V), and close-up of uncinate scar in posterior view (W); pseudosuchian right dorsal vertebral rib referred to Phytosauria indet. (YPM 6649) in posteromedial view (X), and close-up of uncinate scar in posterior view (Y). Abbreviations: ct, calcified tissue; L, lateral; nf?, potential nutrient foramen; P, proximal; pr, proximal ridge; us, uncinate scar.


A
B
pr
us
2 cm
5 mm
C
D
pr
us
1 cm
2 mm
E
F
pr
us
1 cm
2 mm
G
H
us
1 cm
I
J
K
us
nf ?
5 cm
5 mm
L
M
us
1 cm
N
O
us
1 cm
2 mm
P
Q
ct
us
2 cm
2 mm
R
S
us
1 cm
T
U
1 cm
U
us
1 cm
V
W
2 cm
W
us
1 cm
X
Y
2 cm
Y
us
5 mm
P
L

Figure 4.3. Ancestral state reconstruction of uncinate processes in archosaurs

Results of ancestral state reconstruction on simplified version of informal consensus cladogram with branch length estimates, using preferred coding approach described in this study. Detailed description and raw data are provided in the section 3 to 6 of Supplementary Information. Nodes of interest are coloured according to the results from maximum parsimony, and estimated probabilities from maximum likelihood and Bayesian inference are indicated using text. Major clades of Archosauria with evidence of cartilaginous uncinate processes are labelled and shaded blue; clades with evidence of ossified uncinate processes are labelled and shaded pinkish red; clade with evidence of both cartilaginous and ossified uncinate processes is labelled and shaded purple; and clades for which no evidence is available are labelled and shaded grey. Complete results of ancestral state reconstruction are given in section 7 of Supplementary Information. Stages of hypothetical evolutionary scenario are outlined to left of cladogram. Abbreviations: A, Archosauria; D, Dinosauria; M, Maniraptoriformes; MB, Bayesian inference; ML, maximum likelihood; P, Pennaraptora; T, Theropoda.

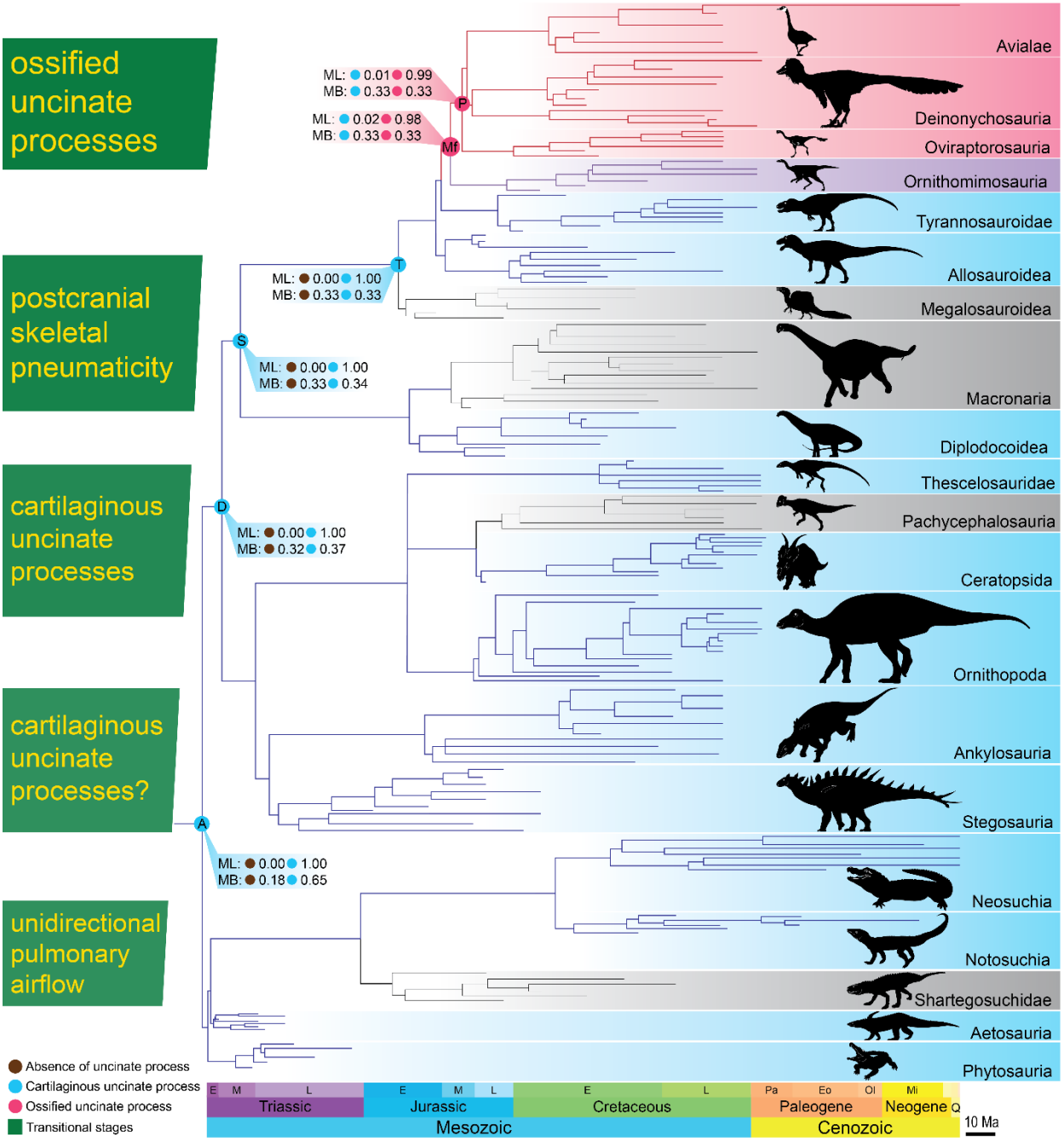
ossified uncinate processes
postcranial skeletal pneumaticity
cartilaginous uncinate processes
cartilaginous uncinate processes?
unidirectional pulmonary airflow
ML: 0.01 0.99
MB: 0.33 0.33
ML: 0.02 0.98
MB: 0.33 0.33
ML: 0.00 1.00
MB: 0.33 0.33
ML: 0.00 1.00
MB: 0.33 0.34
ML: 0.00 1.00
MB: 0.32 0.37
ML: 0.00 1.00
MB: 0.18 0.65
P
Mf
T
S
D
A
Avialae
Deinonychosauria
Oviraptorosauria
Ornithomimosauria
Tyrannosauroidae
Allosauroidea
Megalosauroidea
Macronaria
Diplodocoidea
Thescelosauridae
Pachycephalosauria
Ceratopsida
Ornithopoda
Ankylosauria
Stegosauria
Neosuchia
Notosuchia
Shartegosuchidae
Aetosauria
Phytosauria
Absence of uncinate process
Cartilaginous uncinate process
Ossified uncinate process
Transitional stages
E M L
Triassic
E M L
Jurassic
E L
Cretaceous
Pa Eo Ol
Paleogene
Mi
Neogene
Q
Mesozoic
Cenozoic
10 Ma

4.5 Literature Cited

Aoyama, H., Mizutani-Koseki, S. and Koseki, H. 2005. Three developmental compartments involved in rib formation. *The International Journal of Developmental Biology* 49(2–3), pp. 325–333. doi: 10.1387/ijdb.041932ha.

Arbour, V.M. and Currie, P.J. 2016. Systematics, phylogeny and palaeobiogeography of the ankylosaurid dinosaurs. *Journal of Systematic Palaeontology* 14(5), pp. 385–444. doi: 10.1080/14772019.2015.1059985.

Arbour, V.M. and Evans, D.C. 2017. A new ankylosaurine dinosaur from the Judith River Formation of Montana, USA, based on an exceptional skeleton with soft tissue preservation. *Royal Society Open Science* 4(5), p. 161086. doi: 10.1098/rsos.161086.

Baumel, J.J., King, A.S., Breazile, J.E., Evans, H.E. and Vanden Berge, J.C. 1993. *Handbook of avian anatomy: Nomina anatomica avium*. second edition. Cambridge: Nuttall Ornithological Club.

Benson, R.B., Butler, R.J., Carrano, M.T. and O'Connor, P.M. 2012. Air-filled postcranial bones in theropod dinosaurs: physiological implications and the 'reptile'–bird transition. *Biological Reviews* 87(1), pp. 168–193.

Benton, M.J. 2014. *Vertebrate Palaeontology*. John Wiley & Sons.

Bona, P. and Barrios, F. 2015. The alligatoroidea of Argentina: an update of its fossil record. *Publicación Electrónica de la Asociación Paleontológica Argentina* 15(1), pp. 143–158. doi: 10.5710/PEAPA.15.06.2015.103.

Bourdon, E. and Lindow, B. 2015. A redescription of *Lithornis vulturinus* (Aves, Palaeognathae) from the Early Eocene Fur Formation of Denmark. *Zootaxa* 4032(5), pp. 493–514.

Boyd, C.A. 2015. The systematic relationships and biogeographic history of ornithischian dinosaurs. *PeerJ* 3, p. e1523. doi: 10.7717/peerj.1523.

Boyd, C.A., Cleland, T.P. and Novas, F. 2011. Osteogenesis, homology, and function of the intercostal plates in ornithischian dinosaurs (Tetrapoda, Sauropsida). *Zoomorphology* 130(4), pp. 305–313. doi: 10.1007/s00435-011-0136-x.

Brocklehurst, R.J., Moritz, S., Codd, J., Sellers, W.I. and Brainerd, E.L. 2019. XROMM kinematics of ventilation in wild turkeys (*Meleagris gallopavo*). *Journal of Experimental Biology* 222(23), p. jeb209783. doi: 10.1242/jeb.209783.

Brocklehurst, R.J., Schachner, E.R., Codd, J.R. and Sellers, W.I. 2020. Respiratory evolution in archosaurs. *Philosophical Transactions of the Royal Society B: Biological Sciences* 375(1793), p. 20190140. doi: 10.1098/rstb.2019.0140.

Brown, C.M., Boyd, C.A. and Russell, A.P. 2011. A new basal ornithopod dinosaur (Frenchman Formation, Saskatchewan, Canada), and implications for late Maastrichtian ornithischian diversity in North America. *Zoological Journal of the Linnean Society* 163(4), pp. 1157–1198.

Buscalioni, Á.D., Alcalá, L., Espílez, E. and Mampel, L. 2020. European Goniopholididae from the Early Albian Escucha Formation in Ariño (Teruel, Aragón, Spain). *Spanish Journal of Palaeontology* 28(1), pp. 103–122.

Buscalioni, A.D., Piras, P., Vullo, R., Signore, M. and Barbera, C. 2011. Early eusuchia crocodylomorpha from the vertebrate-rich Plattenkalk of Pietraroia (Lower Albian, southern Apennines, Italy). *Zoological Journal of the Linnean Society* 163, pp. S199–S227. doi: 10.1111/j.1096-3642.2011.00718.x.

Butler, R.J., Brusatte, S.L., Reich, M., Nesbitt, S.J. and Schoch, R.R. 2011. The sail-backed reptile *Ctenosauriscus* from the latest Early Triassic of Germany and the timing and biogeography of the early archosaur radiation.

Butler, R.J. and Galton, P.M. 2008. The ‘dermal armour’ of the ornithopod dinosaur *Hypsilophodon* from the Wealden (Early Cretaceous: Barremian) of the Isle of Wight: a reappraisal. *Cretaceous Research* 29(4), pp. 636–642. doi: 10.1016/j.cretres.2008.02.002.

Butler, R.J., Jones, A.S., Buffetaut, E., Mandl, G.W., Scheyer, T.M. and Schultz, O. 2019. Description and phylogenetic placement of a new marine species of phytosaur (Archosauriformes: Phytosauria) from the Late Triassic of Austria. *Zoological Journal of the Linnean Society* 187(1), pp. 198–228. doi: 10.1093/zoolinnean/zlz014.

Carboneras, C. 1992. Anseriformes. In: *Handbook of birds of the world*. Barcelona: Lynx Edicions, pp. 528–628.

Carrano, M.T., Benson, R.B.J. and Sampson, S.D. 2012. The phylogeny of Tetanurae (Dinosauria: Theropoda). *Journal of Systematic Palaeontology* 10(2), pp. 211–300. doi: 10.1080/14772019.2011.630927.

Carrano, M.T. and Hutchinson, J.R. 2002. Pelvic and hindlimb musculature of *Tyrannosaurus rex* (Dinosauria: Theropoda). *Journal of Morphology* 253(3), pp. 207–228.

Claessens, K.P. 2015. Anatomical transformations and respiratory innovations of the archosaur trunk. In: *Great Transformations in Vertebrate Evolution*. University of Chicago Press. doi: 10.7208/chicago/9780226268392.001.0001.

Claessens, L.P.A.M. 2009a. A cineradiographic study of lung ventilation in *Alligator mississippiensis*. *Journal of Experimental Zoology Part A: Ecological Genetics and Physiology* 311A(8), pp. 563–585. doi: 10.1002/jez.530.

Claessens, L.P.A.M. 2009b. The skeletal kinematics of lung ventilation in three basal bird taxa (emu, tinamou, and guinea fowl). *Journal of Experimental Zoology Part A: Ecological Genetics and Physiology* 311A(8), pp. 586–599. doi: 10.1002/jez.501.

Codd, J.R. 2010. Uncinate processes in birds: Morphology, physiology and function. *Comparative biochemistry and physiology part a: molecular & integrative physiology* 156(3), pp. 303–308. doi: 10.1016/j.cbpa.2009.12.005.

Codd, J.R., Boggs, D.F., Perry, S.F. and Carrier, D.R. 2005. Activity of three muscles associated with the uncinate processes of the giant Canada goose *Branta canadensis maximus*. *Journal of Experimental Biology* 208(5), pp. 849–857. doi: 10.1242/jeb.01489.

Codd, J.R., Manning, P.L., Norell, M.A. and Perry, S.F. 2008. Avian-like breathing mechanics in maniraptoran dinosaurs. *Proceedings of the Royal Society B: Biological Sciences* 275(1631), pp. 157–161. doi: 10.1098/rspb.2007.1233.

Codd, J.R., Rose, K.A.R., Tickle, P.G., Sellers, W.I., Brocklehurst, R.J., Elsey, R.M. and Crossley, D.A. 2019. A novel accessory respiratory muscle in the American alligator (*Alligator mississippiensis*). *Biology Letters* 15(7), p. 20190354. doi: 10.1098/rsbl.2019.0354.

Cong, L.Y., Hou, L.H. and Wu, X.C. 1988. *The Gross anatomy of Alligator sinensis Fauvel: Integument, Osteology, and Myology (In Chinese with English summary)*. Beijing, China: China Science Publishing & Media Ltd.

Cuesta, E., Vidal, D., Ortega, F., Shibata, M. and Sanz, J.L. 2022. *Pelecanimimus* (Theropoda: Ornithomimosauria) postcranial anatomy and the evolution of the specialized manus in Ornithomimosaurs and sternum in maniraptoriforms. *Zoological Journal of the Linnean Society* 194(2), pp. 553–591. doi: 10.1093/zoolinnean/zlab013.

Dollman, K.N., Clark, J.M., Viglietti, P.A., Browning, C. and Choiniere, J.N. 2021. Revised anatomy, taxonomy and biostratigraphy of Notochampsa istedana Broom, 1904, a Lower Jurassic crocodyliform from the Clarens Formation (Stormberg Group), and its implications for early crocodyliform phylogeny. *Journal of Systematic Palaeontology* 19(9), pp. 651–675.

Dollman, K.N., Viglietti, P.A. and Choiniere, J.N. 2019. A new specimen of *Orthosuchus stormbergi* (Nash 1968) and a review of the distribution of Southern African Lower Jurassic crocodylomorphs. *Historical Biology* 31(5), pp. 653–664. doi: 10.1080/08912963.2017.1387110.

Dong, Z.M., Zhou, S.W. and Zhang, X. 1983. Dinosaurs from the Jurassic of Sichuan. *Palaeontologia Sinica* 162, pp. 1–151.

Dumbravă, M., Codrea, V., Solomon, A. and Andrei, R. 2013. Hind leg myology of the Maastrichtian (latest Cretaceous) euornithischian dinosaur *Zalmoxes shquiperorum* from the HaDeg Basin, Romania: preliminary data. *Oltenia. Studii Di comunicări. DtiinDele Naturii* 29(2), pp. 7–18.

Duncker, H.-R. 1972. Structure of avian lungs. *Respiration Physiology* 14(1), pp. 44–63. doi: 10.1016/0034-5687(72)90016-3.

Efimov, M.B. 1975. Late Cretaceous crocodiles of Soviet Central Asia and Kazakhstan. *Paleontologicheskii Zhurnal* 9, pp. 417–420.

Evans, D.C., Brown, C.M., You, H. and Campione, N.E. 2021. Description and revised diagnosis of Asia's first recorded pachycephalosaurid, *Sinocephale bexelli* gen. nov., from the Upper Cretaceous of Inner Mongolia, China. *Canadian Journal of Earth Sciences* 58(10), pp. 981–992.

Ezcurra, M.D. 2016. The phylogenetic relationships of basal archosauromorphs, with an emphasis on the systematics of proterosuchian archosauriforms. *PeerJ* 4, p. e1778. doi: 10.7717/peerj.1778.

Farke, A.A. 2011. Anatomy and taxonomic status of the chasmosaurine ceratopsid *Nedoceratops hatcheri* from the Upper Cretaceous Lance Formation of Wyoming, U.S.A. *PLOS ONE* 6(1), p. e16196. doi: 10.1371/journal.pone.0016196.

Farmer, C.G. 2015. The evolution of unidirectional pulmonary airflow. *Physiology* 30(4), pp. 260–272.

Farmer, C.G. and Sanders, K. 2010. Unidirectional airflow in the lungs of alligators. *Science* 327(5963), pp. 338–340. doi: 10.1126/science.1180219.

Frey, T. von E. 1988. Anatomie des Körperstammes von *Alligator mississippiensis* Daudin. *Stuttgarter Beitraege zur Naturkunde, Serie A* 424, pp. 1–106.

Funston, G.F. and Currie, P.J. 2016. A new caenagnathid (Dinosauria: Oviraptorosauria) from the Horseshoe Canyon Formation of Alberta, Canada, and a reevaluation of the relationships of Caenagnathidae. *Journal of Vertebrate Paleontology* 36(4), p. e1160910.

Galton, P.M. 2009. Notes on Neocomian (Lower Cretaceous) ornithopod dinosaurs from England–*Hypsilophodon*, *Valdosaurus*, "*Camptosaurus*", "*Iguanodon*" – and referred specimens from Romania and elsewhere. *Revue de Paléobiologie* 28(1), pp. 211–73.

Ghetie, V. 1976. *Atlas de anatomie a păsărilor domestice*. Academiei Republicii Socialiste România.

Gorscak, E. and O'Connor, P.M. 2019. A new African titanosaurian sauropod dinosaur from the Middle Cretaceous Galula Formation (Mtuka member), Rukwa Rift Basin, Southwestern Tanzania. *PLOS ONE* 14(2), p. e0211412. doi: 10.1371/journal.pone.0211412.

Griffin, C.T., Stefanic, C.M., Parker, W.G., Hungerbühler, A. and Stocker, M.R. 2017. Sacral anatomy of the phytosaur *Smilosuchus adamanensis*, with implications for pelvic girdle evolution among archosauriformes. *Journal of Anatomy* 231(6), pp. 886–905. doi: 10.1111/joa.12681.

Halliday, T. 2013. A re-evaluation of goniopholidid crocodylomorph material from Central Asia: Biogeographic and phylogenetic implications. *Acta Palaeontologica Polonica* 60(2). doi: 10.4202/app.2013.0018.

Han, F., Forster, C.A., Xu, X. and Clark, J.M. 2018. Postcranial anatomy of *Yinlong downsi* (Dinosauria: Ceratopsia) from the Upper Jurassic Shishugou Formation of China and the phylogeny of basal ornithischians. *Journal of Systematic Palaeontology* 16(14), pp. 1159–1187. doi: 10.1080/14772019.2017.1369185.

Heckert, A.B. and Lucas, S.G. 2003. Stratigraphy and paleontology of the Lower Chinle Group (Adamanian: latest Carnian) in the vicinity of St. Johns, Arizona. *New Mexico Geological Society Guidebook* 54, pp. 281–288.

Heckert, A.B., Lucas, S.G., Hunt, A.P. and Harris, J.D. 2001. A giant phytosaur (Reptilia: Archosauria) skull from the Redonda Formation (Upper Triassic: Apachean) of East-Central New Mexico. *New Mexico Geological Society Guidebook* 52, pp. 171–178.

Heritage, S. 2021. MBASR: Workflow-simplified ancestral state reconstruction of discrete traits with MrBayes in the R environment. *BioRxiv* , pp. 2021–01.

Hildebrand, M. 1982. *Analysis of vertebrate structure*. New York: Wiley Blackwell.

Hone, D.W.E. and Rauhut, O.W.M. 2009. Feeding behaviour and bone utilization by theropod dinosaurs: Theropod feeding behaviour. *Lethaia* 43(2), pp. 232–244. doi: 10.1111/j.1502-3931.2009.00187.x.

Hunt, A.P., Lucas, S.G. and Bircheff, P. 1993. *Biochronological Significance of the Co-occurrence of the Phytosaurs (Reptilia: Archosauria) Angistorhinus and Rutiodon in the Los Esteros Member of the Santa Rosa Formation, Santa Fe County, New Mexico, USA*. New Mexico Museum of Natural History Bulletins.

Hunt, A.P., Lucas, S.G. and Spielmann, J.A. 2006. Sexual dimorphism in a large brachyrostral phytosaur (Archosauria: Crurotarsi) from the Late Triassic of western North America. *New Mexico Museum of Natural History and Science Bulletin* 37, pp. 563–567.

Huxley, T.H. 1877. *The crocodilian remains found in the elgin sandstones: With remarks on the ichnites of Cummingstone*. HM Stationery Office.

Jones, A.S. and Butler, R.J. 2018. A new phylogenetic analysis of Phytosauria (Archosauria: Pseudosuchia) with the application of continuous and geometric morphometric character coding. *PeerJ* 6, p. e5901. doi: 10.7717/peerj.5901.

Junchang, L., Xingsheng, J., Yiming, S., Yihong, L., Guoping, W. and Azuma, Y. 2007. New nodosaurid dinosaur from the Late Cretaceous of Lishui, Zhejiang Province, China. *Acta*

Geologica Sinica - English Edition 81(3), pp. 344–350. doi: 10.1111/j.1755-6724.2007.tb00958.x.

Kurzanov, S.M. 1976. Braincase structure in the carnosaur <i>Itemirus<i/> n. gen. and some aspects of the cranial anatomy of dinosaurs. *Paleontological Journal* 10(36), pp. 1–369.

Leardi, J.M., Pol, D. and Clark, J.M. 2017. Detailed anatomy of the braincase of *Macelognathus vagans* Marsh, 1884 (Archosauria, Crocodylomorpha) using high resolution tomography and new insights on basal crocodylomorph phylogeny. *PeerJ* 5, p. e2801. doi: 10.7717/peerj.2801.

Longrich, N.R. 2010. *Mojoceratops perifania*, a new chasmosaurine ceratopsid from the Late Campanian of Western Canada. *Journal of Paleontology* 84(4), pp. 681–694. doi: 10.1666/09-114.1.

Madzia, D., Boyd, C.A. and Mazuch, M. 2018. A basal ornithopod dinosaur from the Cenomanian of the Czech Republic. *Journal of Systematic Palaeontology* 16(11), pp. 967–979.

Madzia, D., Jagt, J.W.M. and Mulder, E.W.A. 2020. Osteology, phylogenetic affinities and taxonomic status of the enigmatic Late Maastrichtian ornithopod taxon *Orthomerus dolloi* (Dinosauria, Ornithischia). *Cretaceous Research* 108, p. 104334. doi: 10.1016/j.cretres.2019.104334.

Mannion, P.D. 2009. A rebbachisaurid sauropod from the Lower Cretaceous of the Isle of Wight, England. *Cretaceous Research* 30(3), pp. 521–526. doi: 10.1016/j.cretres.2008.09.005.

Mannion, P.D., Upchurch, P., Schwarz, D. and Wings, O. 2019. Taxonomic affinities of the putative titanosaurs from the Late Jurassic Tendaguru Formation of Tanzania: phylogenetic and biogeographic implications for eusauropod dinosaur evolution. *Zoological Journal of the Linnean Society* 185(3), pp. 784–909. doi: 10.1093/zoolinnean/zly068.

Marsh, A.D., Smith, M.E., Parker, W.G., Irmis, R.B. and Kligman, B.T. 2020. Skeletal anatomy of *Acaenasuchus geoffreyi* Long and Murry, 1995 (Archosauria: Pseudosuchia) and its

implications for the origin of the aetosaurian carapace. *Journal of Vertebrate Paleontology* 40(4), p. e1794885.

Marsh, O.C. 1871. Notice of some fossil mammals from the Tertiary Formation. *American Journal of Science* 2, pp. 35–44.

Maryañska, T. 1977. Ankylosauridae (Dinosauria) from Mongolia. *Acta Palaeontologica Polonica* 37, pp. 85–151.

McDonald, A.T., Wolfe, D.G., Fowler, E.A.F. and Gates, T.A. 2021. A new brachylophosaurin (Dinosauria: Hadrosauridae) from the Upper Cretaceous Menefee Formation of New Mexico. *PeerJ* 9, p. e11084. doi: 10.7717/peerj.11084.

Mehl, M.G. 1928. The Phytosauria of the Wyoming. *Journal of the Denison University Laboratories, Denison University* 28, pp. 141–172.

Melstrom, K.M. and Irmis, R.B. 2019. Repeated evolution of herbivorous crocodyliforms during the age of dinosaurs. *Current Biology* 29(14), pp. 2389-2395.e3. doi: 10.1016/j.cub.2019.05.076.

Müller, L. 1927. Ergebnisse der Forschungsreisen Prof. E. Stromers in den Wüsten Ägypteus. In: Abhandlungen der Bayerischen Akademie der Wissenschaften. Mathematisch-Naturwissenschaftliche Abteilung. Oldenbourg Wissenschaftsverlag, pp. 1–97.

Müller, R.T., Langer, M.C., Bronzati, M., Pacheco, C.P., Cabreira, S.F. and Dias-Da-Silva, S. 2018. Early evolution of sauropodomorphs: anatomy and phylogenetic relationships of a remarkably well-preserved dinosaur from the Upper Triassic of southern Brazil. *Zoological Journal of the Linnean Society* 184(4), pp. 1187–1248.

Nesbitt, S.J. 2011. The early evolution of archosaurs: relationships and the origin of major clades. *Bulletin of the American Museum of Natural History* 352, pp. 1–292. doi: 10.1206/352.1.

Nesbitt, S.J. et al. 2017. The earliest bird-line archosaurs and the assembly of the dinosaur body plan. *Nature* 544(7651), pp. 484–487. doi: 10.1038/nature22037.

Nobre, P.H. and Carvalho, I. de S. 2013. Postcranial skeleton of *Mariliasuchus amarali* Carvalho and Bertini, 1999 (Mesoeucrocodylia) from the Bauru Basin, Upper Cretaceous of Brazil. *Ameghiniana* 50(1), pp. 98–113. doi: 10.5710/AMGH.15.8.2012.500.

Norelli, M.A. and Makovicky, P.J. 1999. Important features of the dromaeosaurid skeleton II: Information from newly collected specimens of *Velociraptor mongoliensis*. *American Museum Novitates* (3282), pp. 1–48.

Novas, F.E., Cambiaso, A.V. and Ambrosio, A. 2004. A new basal iguanodontian (Dinosauria, Ornithischia) from the Upper Cretaceous of Patagonia.

Ostrom, J.H. 1969. Osteology of *Deinonychus antirrhopus*, an unusual theropod from the Lower Cretaceous of Montana. *Bulletin of the Peabody Museum of Natural History* 30, pp. 1–165.

Otero, A. and Pol, D. 2013. Postcranial anatomy and phylogenetic relationships of *Mussaurus patagonicus* (Dinosauria, Sauropodomorpha). *Journal of Vertebrate Paleontology* 33(5), pp. 1138–1168. doi: 10.1080/02724634.2013.769444.

Paradis, E., Claude, J. and Strimmer, K. 2004. APE: analyses of phylogenetics and evolution in R language. *Bioinformatics* 20(2), pp. 289–290. doi: 10.1093/bioinformatics/btg412.

Park, J.-Y. et al. 2021. A new ankylosaurid skeleton from the Upper Cretaceous Baruungoyot Formation of Mongolia: its implications for ankylosaurid postcranial evolution. *Scientific Reports* 11(1), p. 4101. doi: 10.1038/s41598-021-83568-4.

Perry, S.F., Lambertz, M. and Schmitz, A. 2019. Respiratory faculties of amphibious and terrestrial craniotes. In: *Respiratory Biology of Animals: evolutionary and functional morphology*. Oxford University Press, pp. 139–163.

Peters, S.E. and McClennen, M. 2015. The Paleobiology Database application programming interface. *Paleobiology* 42(1), pp. 1–7. doi: 10.1017/pab.2015.39.

Pittman, M., O'Connor, J., Field, D.J., Turner, A.H., Waisum, M. and Xu, X. 2020. Pennaraptora systematics. *Bulletin of the American Museum of Natural History* 440, pp. 7–36.

Pol, D. and Goloboff, P.A. 2020. The impact of unstable taxa in coelurosaurian phylogeny and resampling support measures for parsimony analyses.

Pol, D. and Powell, J.E. 2011. A new sebecid mesoeucrocodylian from the Rio Loro Formation (Palaeocene) of north-western Argentina. *Zoological Journal of the Linnean Society* 163(suppl_1), pp. S7–S36.

Powell, F.L. 2015. Respiration. In: *Sturkie's Avian Physiology*. Elsevier, pp. 301–336. doi: 10.1016/B978-0-12-407160-5.00013-0.

Raven, T.J. and Maidment, S.C.R. 2017. A new phylogeny of Stegosauria (Dinosauria, Ornithischia). *Palaeontology* 60(3), pp. 401–408. doi: 10.1111/pala.12291.

Rio, J.P. and Mannion, P.D. 2021. Phylogenetic analysis of a new morphological dataset elucidates the evolutionary history of Crocodylia and resolves the long-standing gharial problem. *PeerJ* 9, p. e12094. doi: 10.7717/peerj.12094.

Ristevski, J., Young, M.T., de Andrade, M.B. and Hastings, A.K. 2018. A new species of *Anteophthalmosuchus* (Crocodylomorpha, Goniopholididae) from the Lower Cretaceous of the Isle of Wight, United Kingdom, and a review of the genus. *Cretaceous Research* 84, pp. 340–383. doi: 10.1016/j.cretres.2017.11.008.

Rivera Sylva, H.E. 2012. Bite marks of a large theropod on an hadrosaur limb bone from Coahuila, Mexico. *Boletín de la Sociedad Geológica Mexicana* 64(1), pp. 155–159. doi: 10.18268/BSGM2012v64n1a11.

Roberto-Da-Silva, L., Müller, R.T., França, M.A.G. de, Cabreira, S.F. and Dias-Da-Silva, S. 2020. An impressive skeleton of the giant top predator *Prestosuchus chiniquensis* (Pseudosuchia: Loricata) from the Triassic of Southern Brazil, with phylogenetic remarks. *Historical Biology* 32(7), pp. 976–995. doi: 10.1080/08912963.2018.1559841.

Romer, A.S. 1956. The axial skeleton. In: *The osteology of reptiles*. Illinois: University of Chicago Press, pp. 275–279.

Rose, K.A., Tickle, P.G., Elsey, R.M., Sellers, W.I., Crossley, D.A. and Codd, J.R. 2021. Scaling of axial muscle architecture in juvenile *Alligator mississippiensis* reveals an enhanced performance capacity of accessory breathing mechanisms. *Journal of Anatomy* 239(6), pp. 1273–1286.

Rummy, P. et al. 2022. A new paralligatorid (Crocodyliformes, Neosuchia) from the mid-Cretaceous of Jilin Province, northeastern China. *Cretaceous Research* 129, p. 105018. doi: 10.1016/j.cretres.2021.105018.

Ryan, M.J., Evans, D.C., Currie, P.J. and Loewen, M.A. 2014. A new chasmosaurine from northern Laramidia expands frill disparity in ceratopsid dinosaurs. *Naturwissenschaften* 101(6), pp. 505–512. doi: 10.1007/s00114-014-1183-1.

Salgado, L. and Gasparini, Z. 2006. Reappraisal of an ankylosaurian dinosaur from the Upper Cretaceous of James Ross Island (Antarctica). *Geodiversitas* 28(1), pp. 119–135.

Scaal, M. 2021. Development of the amniote ventrolateral body wall. *Developmental Dynamics* 250(1), pp. 39–59. doi: 10.1002/dvdy.193.

Schachner, E.R., Hutchinson, J.R. and Farmer, C. 2013. Pulmonary anatomy in the Nile crocodile and the evolution of unidirectional airflow in Archosauria. *PeerJ* 1, p. e60. doi: 10.7717/peerj.60.

Schliep, K.P. 2011. Phangorn: phylogenetic analysis in R. *Bioinformatics* 27(4), pp. 592–593.

Schott, R.K. and Evans, D.C. 2016. Cranial variation and systematics of *Foraminacephale brevis* gen. nov. and the diversity of pachycephalosaurid dinosaurs (Ornithischia: Cerapoda) in the Belly River Group of Alberta, Canada. *Zoological Journal of the Linnean Society* . doi: 10.1111/zoj.12465.

Seeley, H.G. 1883. On the dinosaurs from the Maastricht beds. *Quarterly Journal of the Geological Society* 39(1–4), pp. 246–253.

Sellés, A.G. et al. 2020. A small Cretaceous crocodyliform in a dinosaur nesting ground and the origin of sebecids. *Scientific Reports* 10(1), p. 15293. doi: 10.1038/s41598-020-71975-y.

Shan, H., Wu, X., Cheng, Y. and Sato, T. 2009. A new tomistomine (Crocodylia) from the Miocene of Taiwan. Sues, H.-D. ed. *Canadian Journal of Earth Sciences* 46(7), pp. 529–555. doi: 10.1139/E09-036.

Shufeldt, R.W. 1988. *The myology of the raven (Corvus corax sinuatus): A guide to the study of the muscular system in birds*. Macmillan and Company.

Shuvalov, V.F. 2003. The Cretaceous stratigraphy and palaeobiology of Mongolia. In: *The Age of Dinosaurs in Russia and Mongolia*. Cambridge University Press, pp. 256–278.

Souza, R.G. de, Hörmanseder, B.M., Figueiredo, R.G. and Campos, D. de A. 2020. Description of new dyrosaurid specimens from the Late Cretaceous–Early Paleogene of New Jersey, United States, and comments on Hyposaurus systematics. *Historical Biology* 32(10), pp. 1377–1393.

Stocker, M.R. 2012. A new taxonomic arrangement for *Paleorhinus scurriensis*. *Earth and Environmental Science Transactions of The Royal Society of Edinburgh* 103(3–4), pp. 251–263. doi: 10.1017/S1755691013000340.

Stocker, M.R., Zhao, L.-J., Nesbitt, S.J., Wu, X.-C. and Li, C. 2017. A short-snouted, Middle Triassic phytosaur and its implications for the morphological evolution and biogeography of Phytosauria. *Scientific Reports* 7(1), pp. 1–9.

Tanke, D. and Currie, P.J. 1998. Head-biting behavior in theropod dinosaurs: paleopathological evidence.

Tickle, P., Nudds, R. and Codd, J. 2009. Uncinate process length in birds scales with resting metabolic rate. Lucia, A. ed. *PLoS ONE* 4(5), p. e5667. doi: 10.1371/journal.pone.0005667.

Tickle, P.G., Ennos, A.R., Lennox, L.E., Perry, S.F. and Codd, J.R. 2007. Functional significance of the uncinate processes in birds. *Journal of Experimental Biology* 210(22), pp. 3955–3961. doi: 10.1242/jeb.008953.

Turner, A.H. 2006. Osteology and phylogeny of a new species of *Araripesuchus* (Crocodyliformes: Mesoeucrocodylia) from the Late Cretaceous of Madagascar. *Historical Biology* 18(3), pp. 255–369. doi: 10.1080/08912960500516112.

Walker, W.F. and Liem, K.F. 2001. *Functional Anatomy of the Vertebrates: An Evolutionary Perspective*. New York: Fort Worth : Harcourt College Publishers.

Wang, M. and Zhou, Z. 2017. The evolution of birds with implications from new fossil evidences. *The biology of the avian respiratory system: evolution, development, structure and function* , pp. 1–26.

Wedel, M.J. 2009. Evidence for bird-like air sacs in saurischian dinosaurs. *Journal of Experimental Zoology Part A: Ecological Genetics and Physiology* 311A(8), pp. 611–628. doi: 10.1002/jez.513.

Weinbaum, J.C. 2013. Postcranial skeleton of *Postosuchus kirkpatricki* (Archosauria: Paracrocodylomorpha), from the Upper Triassic of the United States. *Geological Society, London, Special Publications* 379(1), pp. 525–553. doi: 10.1144/SP379.7.

Weishampel, D.B., Dodson, P. and Osmólska, H. 2007. *The Dinosauria*. Univ of California Press.

Welty, J.C. and Baptista, L. 1972. *The life of birds*. London: W. B. Saunders and Co.

Xu, X., Zhou, Z. and Wang, X. 2000. The smallest known non-avian theropod dinosaur. *Nature* 408(6813), pp. 705–708. doi: 10.1038/35047056.

Yu, C., Prieto-Marquez, A., Chinzorig, T., Badamkhatan, Z. and Norell, M. 2020. A neoceratopsian dinosaur from the early Cretaceous of Mongolia and the early evolution of ceratopsia. *Communications Biology* 3(1), pp. 1–8. doi: 10.1038/s42003-020-01222-7.

Yu, G., Smith, D.K., Zhu, H., Guan, Y. and Lam, T.T.-Y. 2017. GGtree: an R package for visualization and annotation of phylogenetic trees with their covariates and other associated data. *Methods in Ecology and Evolution* 8(1), pp. 28–36. doi: 10.1111/2041-210X.12628.

Zhou, S.W. 1983. A nearly complete skeleton of a stegosaur from the Middle Jurassic of Dashanpu, Zigong, Sichuan. *Journal of Chengdu University of Geology* 1, pp. 15–26.

Zhou, Z.H., Wang, X.L., Zhang, F.C. and Xu, X. 2000. Important features of *Caudipteryx* - evidence from two nearly complete new specimens. *Vertebrata PalAsiatica* 38(4), pp. 241–254.

Zimmer, K. 1935. Beiträge zur Mechanik der Atmung bei den Vögeln in Stand-und Flug. *Zoologica* 33, pp. 1–69

4.6 Supplementary Information

4.6.1 Implausibility of alternate interpretations of the uncinate scars

Possible alternate interpretations of the features we interpret as uncinate scars warrant further discussion. Here we exclude muscle scars and bite marks as plausible identifications for these features.

The uncinate scars in most fossil archosaurs (e.g. non-avian theropods) examined in this study superficially resemble muscle scars in having a rugose texture indicative of soft tissue attachment. Clear and distinct muscle scars have been reported from fossil archosaurs (Carrano and Hutchinson 2002; Dumbravă et al. 2013). In the extant and fossil archosaur specimens we surveyed, we were unable to find any definite muscle scars on the posterior margin of the dorsal ribs that were comparable to those reported in the literature. In extant archosaurs, four muscles attach to the dorsal vertebral ribs in the vicinity of the uncinate process: m. iliocostalis, m. obliquus abdominis externus, mm. intercostales externi, mm. appendicocostales, and mm. intercostales interni (Ghetie 1976; Cong et al. 1988; Frey 1988; Shufeldt 1988). With the sole exception of m. obliquus abdominis externus, these muscles form wide sheets with fleshy or tendinous attachment to the dorsal ribs (Cong et al. 1988; Shufeldt 1988; Codd et al. 2019; Rose et al. 2021). Such extensive attachment would not be expected to leave well-defined, relatively small scars like the uncinate scars described in this study. Some of the muscle fibres of m. obliquus abdominis externus do converge on a small area, which might leave a well-defined scar in large-bodied archosaurs (e.g. non-avian dinosaurs). However, m. obliquus abdominus externus attaches to the lateral aspect of the dorsal ribs (Cong et al. 1988; Frey 1988; Shufeldt 1988; Baumel et al. 1993), while the features we identify as uncinate scars are consistently positioned on the posterior aspect of the dorsal ribs. Therefore, the features identified here as uncinate scars are unlikely to represent muscle scars because of their restricted extent, well-defined margins, and posterior anatomical position.

The slender strips that we identify as uncinate scars in ornithischians bear limited resemblance to the groove-like bite marks that have been found on bones of various fossil archosaurs (Hone and Rauhut 2009). However, the slender strips reported in this study do not match the morphology or the distribution that might be expected for bite marks. Morphologically, the slender strips remain uniform in width along their full proximodistal extent,

while the groove-like bite marks inflicted by carnivorous vertebrates such as non-avian theropods tend to be wide at the point of initial tooth-bone contact and taper towards the opposite end (Tanke and Currie 1998; Rivera Sylva 2012). As for distribution, the slender strips are consistently parallel to the long axes of the dorsal ribs and never number more than two, whereas bite marks would likely be far less regular in both orientation and number. As a result, we reject the interpretation that the slender strips found in this study might represent bite marks, along side the interpretation that they might represent sites of muscle attachment and identify them decisively as uncinate scars comparable to those seen in extant archosaurs.

4.6.2 Detailed description of the procedures used for the ancestral state reconstruction

The distribution of uncinate processes was encoded in terms of a discrete character with three states: absence of uncinate processes (0), presence of cartilaginous uncinate processes (1), and presence of ossified uncinate processes (2). A total of five extant taxa and 36 fossil taxa were coded based on direct observation, and 17 taxa were coded based on information provided in the literature (Table 2). In one case, that of *Mariliasuchus amarali* from the Upper Cretaceous of Brazil (Nobre and Carvalho 2013), structures described in the literature as uncinate processes were not accepted as uncinate processes for purposes of this study. The putative uncinate processes described in *Ma. amarali* are positioned between the two rib heads of each rib whereas the uncinate processes of other archosaurs are on the rib shafts. The putative uncinate processes do, however, resemble in both morphology and position the anterolateral process situated between the capitulum and tuberculum on the last cervical rib in extant crocodylians, and most certainly represent anterolateral processes rather than true uncinate processes. Because there is no other evidence for uncinate processes in *Ma. amarali*, the presence of uncinate processes was coded as uncertain (?) for this taxon in the ancestral state reconstruction. The proterochampsian *Chanaresuchus bonapartei* was selected as a representative outgroup to Archosauria, and was assumed to lack uncinate processes based on the absence of uncinate scars on a total of 13 well preserved vertebral ribs observed in two individuals (MCZ 4037, 4038).

Two coding methods were used. Our preferred coding method scored ossified uncinate processes as present (2) if bony uncinate processes were known for a particular taxon; cartilaginous uncinate processes as present (1) if either cartilaginous uncinate processes

(calcified or otherwise) were known, or uncinate scars were present but no uncinate processes were known; and the presence of uncinate processes as uncertain (?) if evidence of uncinate processes or scars was lacking. The alternate coding method was identical, except that absence of evidence was treated as evidence of absence beyond a certain threshold: uncinate processes was scored as absent (0) if more than five dorsal ribs were available for examination and no uncinate processes or uncinate scars were evident. Under the alternate coding method, nine taxa were scored as lacking uncinate processes.

The ancestral state reconstruction was performed on an informal supertree compiled from relevant phylogenetic studies, with a tree from Nesbitt (Nesbitt 2011) as a starting point. To add a phylogenetic tree to the informal supertree, at least one common taxon present in both trees was used as a topological landmark, and the new phylogenetic tree was grafted onto the informal supertree at the phylogenetic position of the common taxon (Table S4.5.5). *Chanaresuchus bonapartei* was chosen as a representative outgroup to Archosauria because multiple specimens could be examined in this study. To ensure that all taxa in which evidence of uncinate processes could be identified were included, five taxa from the original phylogenetic studies were replaced in the informal supertree, as follows: 1) *Aetosaurus ferratus* was replaced by Aetosauria indet. (NMMNH P50048); 2) MBR2747 was replaced by Phytosauridae indet. (YPM 6699); 3) *Allosaurus* was replaced by *Allosaurus fragilis* (AMNH 5753); 4) *Apatosaurus* was replaced by *Apatosaurus excelsus* (YPM 1980 and YPM 1981); and 5) *Crypturellus undulatus* was replaced by *Rhea americana* (UAMZ 5019). Temporal ranges for taxa included in the supertree were estimated based on first and last appearance data, primarily taken from the Paleobiology Database (Peters and McClennen 2015). For taxa without data in the Paleobiology Database, data were taken from the literature (Table S4.5.6). Branch lengths were then estimated using the temporal ranges and the Paleotree package in RStudio 4.1.2. The ancestral state reconstruction was carried out both with and without taking estimated branch lengths into account, using the same informal supertree in both cases. To facilitate the calculations, polytomies were resolved into branches with lengths of one. Polytomies were resolved sequentially, according to the order in which taxa listed first in the tree file were accordingly resolved in relatively basal positions.

The ancestral state reconstruction was performed in RStudio 4.1.2 using the *Phangorn* package for maximum parsimony analysis (Schliep 2011), the *APE* package for maximum

likelihood analysis (Paradis et al. 2004), and the *MBASR* toolkit for Bayesian inference using MRBayes (Heritage 2021). The results of the ancestral state reconstructions were visualized and annotated with *ggtree* (Yu et al. 2017).

Table S4. 1. Specimens with uncinate processes and/or uncinate scars examined in this study

Taxon	Specimen number	Morphology of uncinate processes and/or scars	Number of ribs	Proximal ridge
Caiman crocodilus	ROM R6872	U: tab-like processes US: narrow, irregular strip	1	A
Caiman crocodilus	ROM R7077	U: tab-like processes US: narrow, irregular strip	5	A
Crocodylia indet.	AMNH 7900	US: narrow strip	1	A
Araripesuchus gomesii	AMNH 24450	U: hook-like processes	7	A
Aetosauria indet.	NMMNH P50048	US: suboval concavities	1	A
Phytosauria indet.	YPM 6649	US: suboval concavities	2	A
Phytosauria indet.	NMMNH P60401	US: elongate groove	1	A
Rhea americana	UAMZ 5019	US: suboval concavities	6	A
***Rhea* sp.**		U: hook-like processes US: suboval concavity	6 with U 1 with US	A
Casuarius australis	UAMZ 1369	U: plate-like processes US: suboval concavities	3 iso U 6 with US	A
Ardea herodias	UAMZ4048	U: slender processes US: suboval concavities	6 with U 3 with US	A
Bubo virginianus	UAMZ 6846	U: hook-like processes	2 with U 5 iso U 7 with US	A
Gavia immer	UAMZ 1793	U: hook-like processes US: suboval concavities	3 with U 9 iso U 8 with US	A
Saurornitholestes langstoni	UALVP 55700	U: hook-like processes	5	A
Saurornitholestes langstoni	TMP 88.121.39	US: suboval concavities	2	A
Linheraptor exquisitus	IVPP V 16923	US: hook-like processes	4	A
Struthiomimus altus	AMNH 5355	US: suboval concavity	1	P
Daspletosaurus torosus	CMN 8506	US: suboval concavities	10	P
Gorgosaurus libratus	UALVP 10	US: suboval concavities	6	P

Albertosaurus sarcophagus	TMP 99.50.41	US: irregularly shaped concavity	1	A
Albertosaurus sarcophagus	TMP 99.50.42	US: irregularly shaped concavity	1	A
Allosaurus fragilis	AMNH 5753	US: protruding boss	1	A
Tyrannosauridae indet.	TMP 81.16.285	US: suboval concavity	1	P
Tyrannosauridae indet.	TMP 86.16.285	US: suboval concavity	1	P
Tyrannosauridae indet.	TMP 92.36.1231	US: suboval concavity	1	P
Tyrannosauridae indet.	TMP 94.12.960	US: suboval concavity	1	P
Apatosaurus excelsus	YPM 1981	US: suboval concavities	2	A
Gryposaurus notabilis*	AMNH 5350	US: slender strip	2	A
Gryposaurus latideus	AMNH 5465	US: slender strip	1	A
Bactrosaurus johnsoni	AMNH 6553	US: expanded suboval concavity	1	A
Tenontosaurus tilletti	AMNH 3040	US: suboval concavities	2	A
Zephyrosaurus schaffi	MCZ 4392	US: slender strip	1	A
Parksosaurus warreni	ROM 804	U: tab-like processes	3	A
Hadrosauridae indet.	AMNH 5896	US: slender strip	1	A
Hadrosauridae indet.	TMP 82.13.15	US: slender strip	1	A
***Centrosaurus* sp.**	TMP 82.18.16	US: slender strip	1	A
***Centrosaurus* sp.**	TMP 82.19.41	US: slender strip	1	A
***Centrosaurus* sp.**	TMP 82.18.56	US: slender strip	1	A
***Centrosaurus* sp.**	TMP 82.18.281	US: slender strip	1	A
***Centrosaurus* sp.**	TMP 96.176.135	US: slender strip	1	A
***Centrosaurus* sp.**	ROM 767	US: slender strips	2	A
Pachyrhinosaurus	UALVP 57289	US: slender strip	1	A

lakustai				
Leptoceratops gracilis	CMN 8889	US: suboval concavities	2	A
Ceratopsidae indet.	AMNH 5422	US: slender strip	1	A
Ceratopsia indet.	NMMNH P22797	US: slender strip	1	A
Panoplosaurus mirus	ROM 1215	US: expanded, suboval concavities	2	A
Edmontonia longiceps	CMN 8531	US: expanded, suboval concavities	3	A
Sauropelta edwardsi	AMNH 3032	US: expanded, suboval concavity	1	A
Euplocephalus tutus	AMNH 5337	US: expanded, suboval concavities	2	A
Stegosaurus stenops	YPM 1856	US: suboval concavity	1	A
Stegosaurus stenops	AMNH 650	US: suboval concavity	1	A
***Stegosaurus* sp.**	AMNH 5752	US: suboval concavity	1	A
Dinosauria indet.	NMMNH P50406	US: suboval concavity	1	A

Abbreviation: A, absent; iso, isolated; P, present; U, uncinate; US, uncinate scar.

Table S4. 2. List of character codings used in the ancestral state reconstruction.

Taxa	Specimen or reference used as basis for codings	Preferred coding	Alternate coding
***Chanaresuchus* (based on *Chanaresuchus bonapartei*)**	MCZ 4035, MCZ 4036, MCZ 4037, MCZ 4038	0	0
Caiman crocodilus	ROM R6872, ROM R7707, UAMZ unnumbered	1	1
Alligator mississippiensis	ROM R4410 and ROM R4406	1	1
Alligator sinensis	(Cong et al. 1988)	1	1
***Crocodylus siamensis* (farm crocodile)**	unnumbered specimen dissected at Lingshui Crocodile Farm, Hainan Province, China	1	1
Crocodylus acutus	CMN 10018	1	1
Phytosauria indet.	YPM 6699	1	1
Aetosauria indet.	NMMNH P50048	1	1
Lotosaurus adentus	IVPP V 4910	?	0
Protosuchus richardsoni	AMNH 3024	?	0
Araripesuchus gomesii	AMNH 24450	1	1
Penghusuchus pani	(Shan et al. 2009)	1	1
Lagerpetidae (based on *Lagerpeton chanarensis*)	MCZ 4121	?	0
Rhea americana	UAMZ 5019	2	2
Gallus gallus	(Ghetie 1976)	2	2

Chauna torquata	(Carboneras 1992)	0	0
Lithornis	(Bourdon and Lindow 2015)	2	2
Deinonychus antirrhopus	(Ostrom 1969)	2	2
Velociraptor mongoliensis	(Norelli and Makovicky 1999)	2	2
Saurornitholestes langstoni	TMP1988.121.0039 and UALVP 55700	2	2
Microraptor zhaoianus	(Xu et al. 2000)	2	2
Caudipteryx zoui	(Zhou et al. 2000)	2	2
Oviraptor philoceratops	(Codd et al. 2008)	2	2
Conchoraptor gracilis	(Weishampel et al. 2007)	2	2
Struthiomimus altus	AMNH 5355	1	1
Pelecanimimus polyodon	(Cuesta et al. 2022)	2	2
Gorgosaurus libratus	UALVP 10	1	1
Daspletosaurus torosus	CMN 8506	1	1
Albertosaurus sarcophagus	TMP 99.50.41 and TMP 99.50.43	1	1
Allosaurus fragilis	AMNH 5753	1	1
Apatosaurus excelsus	YPM 1980 and YPM 1981	1	1
Camarasaurus **(based on** ***Camarasaurus grandis*****)**	YPM1905	?	0
Plateosaurus quenstedti	MCZ 2483	?	0
Anchisaurus **(based on**	YPM 1883	?	0

***Anchisaurus colurus*)**			
Parasaurolophus walkeri	ROM 1215	?	0
Edmontosaurus regalis	CMN 2289	?	0
Gryposaurus latidens	AMNH 5465	1	1
Gryposaurus notabilis	AMNH 5350	1	1
Bactrosaurus johnsoni	AMNH 6553	1	1
Camptosaurus dispar	YPM 1877 and YPM 1880	?	0
Tenontosaurus tilleti	AMNH 3040	1	1
Zephyrosaurus schaffi	MCZ 4392	1	1
Parksosaurus warreni	ROM 804	1	1
Thescelosaurus assiniboiensis	(Brown et al. 2011)	1	1
Talenkauen santacrucensis	(Novas et al. 2004)	1	1
Hypsilophodon foxii	(Butler and Galton 2008)	1	1
Pachyrhinosaurus lakustai	UALVP 57289	1	1
***Centrosaurus* sp.**	TMP 82.18.16, TMP 82.19.41, TMP 96.176.135, TMP 82.18.56, and TMP82.18.281	1	1
Chasmosaurus belli	ROM 843	?	0
Protoceratops andrewsi	AMNH 6416	?	0
Leptoceratops gracilis	CMN 8889	1	1
Euoplocephalus tutus	AMNH 5337	1	1
Saichania chulsanensis	(Maryañska 1977)	1	1
Panoplosaurus mirus	ROM 1215	1	1
Sauropelta	AMNH 3032	1	1

edwardsorum			
Stegosaurus stenops	AMNH 650, AMNH 5752, and YPM 1856	1	1
Huayangosaurus taibaii	(Zhou 1983)	1	1

Table S4. 3. List of phylogenetic studies used in compiling the informal supertree

Expansion of informal supertree	Key taxa present in two references	Reference
Basal avemetatarsalians only	NA	Strict consensus, Nesbitt dataset (Nesbitt et al. 2017)
1) Basal avemetatarsalians to silesaurids	*Marasuchus lilloensis*	Strict consensus, Nesbitt dataset (Nesbitt et al. 2017)
2) Basal avemetatarsalians to basal sauropodomorphs		Strict consensus, fifth analysis* (Müller et al. 2018)
1) Basal sauropodomorphs to plateosaurids	*Pantydraco caducus*	Strict consensus, fifth analysis (Müller et al. 2018)
2) Basal sauropodomorphs to basal massopodans	*Thecodontosaurus antiquus*	Strict consensus, (Otero and Pol 2013)
Basal massopodans to basal eusauropods	*Shunosaurus*	Strict consensus (Otero and Pol 2013)
		Strict consensus, with implied weight (Mannion et al. 2019)
Basal somphospondylians to titanosaurs	*Chubutisaurus insignis*	Strict consensus, with implied weight (Mannion et al. 2019)
	Andesaurus delgadoi	Majority rule (Gorscak and O'Connor 2019)
Basal saurischians to basal theropods	*Eoraptor lunensis*	Strict consensus, fifth analysis (Müller et al. 2018)
		Strict consensus (Carrano et al. 2012)
Basal theropods to basal coelurosaurs	*Allosaurus*	Strict consensus (Carrano et al. 2012)
		Strict consensus (Pol and Goloboff 2020)
Basal coelurosaurs to ornithomimosaurs	*Nqwebasaurus thwazi*	Strict consensus (Pol and Goloboff 2020)
		Strict consensus (Cuesta et al.

		2022)
Basal maniraptorans to pennaraptorans**	*Yi qi* *Epidexipteryx hui*	Strict consensus (Pol and Goloboff 2020) Reduced strict consensus (Pittman et al. 2020)
1) Basal dinosauriforms to basal ornithischians **2) Basal dinosauriforms to heterodontosaurids**	*Eoraptor lunensis*	Strict consensus, fifth analysis (Müller et al. 2018) Strict consensus (Han et al. 2018)
Basal ornithischians to stegosaurs	*Scutellosaurus lawleri*	Strict consensus (Han et al. 2018) Strict consensus (Raven and Maidment 2017)
Basal ornithischians to basal ankylosaurs	*Gargoyleosaurus parkpinorum*	Strict consensus (Han et al. 2018) Majority rule (Arbour and Currie 2016)
Basal ankylosaurs to ankylosaurids	Nodosauridae	Majority rule (Arbour and Currie 2016) Strict consensus (Arbour and Evans 2017)
Basal ornithischians to basal neornithischians	*Lesothosaurus diagnosticus* *Agilisaurus louderbacki*	Strict consensus (Han et al. 2018) Strict consensus (Madzia et al. 2018)
Basal ornithopods to basal iguanodontians	*Hypsilophodon foxii* *Rhabdodon* sp.	Strict consensus (Madzia et al. 2018) Majority rule (Madzia et al. 2020)
Basal hadrosauromorphs to hadrosaurids	*Hadrosaurus foulkii*	Majority rule (Madzia et al. 2020) Strict consensus (McDonald et al. 2021)
Basal neornithischians to ceratopsids	*Yinlong downsi*	Strict consensus (Han et al. 2018) Strict consensus (Yu et al. 2020)

Basal neornithischians to pachycephalosaurs	*Wannanosaurus yansiensis*	Strict consensus (Han et al. 2018) Strict consensus (Evans et al. 2021)
Basal archosaurs to phytosaurs* **	*Parasuchus hislopi*	Strict consensus, Nesbitt dataset (Nesbitt et al. 2017) Strict consensus (Butler et al. 2019)
Basal archosaurs to basal pseudosuchians (excluding phytosaurs)	NA	Reduced strict consensus (Roberto-Da-Silva et al. 2020)
Basal pseudosuchians to basal crocodylomorphs	*Postosuchus*	Reduced strict consensus (Roberto-Da-Silva et al. 2020) Strict consensus (Leardi et al. 2017)
Basal crocodylomorphs to basal crocodyliforms	*Dibothrosuchus elaphros*	Strict consensus (Leardi et al. 2017) Strict consensus (Dollman et al. 2019)
1) Basal crocodyliforms to notosuchians **2) Basal crocodyliforms to eusuchians**	*Hisosuchus*	Strict consensus (Dollman et al. 2019) Strict consensus, first analysis (Rummy et al. 2022)
Basal notosuchians to sebecosuchians	*Chimaerasuchus paradoxus*	Strict consensus, first analysis (Rummy et al. 2022) Reduced consensus (Sellés et al. 2020)
Basal neosuchians to gonipholidids	*Sunosuchus junggarensis*	Strict consensus, first analysis (Rummy et al. 2022) Strict consensus, first analysis (Ristevski et al. 2018)
Basal eusuchians to crocodylians	*Bernissartia fagesii*	Strict consensus, first analysis (Rummy et al. 2022) Strict consensus, analysis 1.3 (Rio and Mannion 2021)

*The fifth analysis was chosen because it includes more taxa and internal nodes, and recovering cartilaginous uncinate processes at node Avemetatarsalia is more difficult when many taxa rather than few taxa are present in the basal avemetatarsalian part of the tree (i.e. there are more steps for the ancestral state reconstruction to evaluate, which increases the likelihood of recovering uncinate processes as absent or unknown when all other factors remain the same). ** Placement of Pennaraptora within Maniraptora follows Pittman, et al. [41]. *** We followed Nesbitt, et al. [34] in positioning Phytosauria as the basalmost clade within Pseudosuchia, although recent studies have recovered phytosaurs outside Archosauria [59,60]. See discussion in the main text for the implications of the phylogenetic position of Phytosauria for the reconstructed origin of uncinate processes.

Table S4. 4. First and last appearance data for taxa used in the ancestral state reconstruction.

Taxon*	First appearance time (Ma)	Last appearance time (Ma)
El_Chocón_rebbachisaurid (Marsh et al. 2020)	129.4	100.5
IOW_rebbachisaurid_caudal (Mannion 2009)	129.4	125
CV00214 (Dong et al. 1983)	163.5	152.1
EK_troodontid_IGM_10044**	167.7	66
Archaeopteryx*_Eichstätt **	152.1	125.45
Archaeopteryx*_Thermopolis **	152.1	125.45
Archaeopteryx*_Berlin **	152.1	125.45
Archaeopteryx*_London **	152.1	125.45
Archaeopteryx*_11th **	152.1	125.45
Archaeopteryx*_Munich **	152.1	125.45
Archaeopteryx*_Solnhofen **	152.1	125.45
***Minmi*_sp. (Arbour and Currie 2016)**	145	100.5
***Antarctopelta* (Salgado and Gasparini 2006)**	84.9	70.6
Argentinian_nodosaurid **	157.3	66
***Zhejiangosaurus* (Junchang et al. 2007)**	99.7	94.3
Kaiparowits_orodromine (Boyd 2015)	76.6	74.3
***Camptosaurus_valdensis* (Galton 2009)**	136.4	122.46
***Orthomerus_dolloi* (Seeley 1883)**	70.6	66
***Mercuriceratops_gemini* (Ryan et al. 2014)**	84.9	70.6
***Mojoceratops_kaiseni* (Longrich 2010)**	85.8	70.6
***Nedoceratops_hatcheri* (Farke 2011)**	69	66
***Foraminacephale_brevis* (Schott and Evans 2016)**	85.8	70.6
***Sinocephale_bexelli* (Evans et al. 2021)**	92	66
***Paleorhinus_parvus* (Mehl 1928)**	235	221.5
NMMNHS_P4781 (Hunt et al. 1993)	208.5	201.3
TMM_31100_1332 (Stocker 2012)	228	220
USNM_v_21376 (Jones and Butler 2018)	237	208.5
PEFO_34852 (Griffin et al. 2017)	237	201.3
***Machaeroprosopus_zunii* (Stocker 2012)**	237	208.5
USNM_v_17098 (Heckert and Lucas 2003)	237	227
NMMNHS_P4256 (Hunt et al. 2006)	227	208.5
NMMNHS_P31094 (Heckert et al. 2001)	221	206
Phytosauria_indet. **	237	196.5
***Mystriosuchus_steinbergeri* (Butler et al. 2019)**	216	211

Ornithosuchus_longidens **(Huxley 1877)**	235	205
Waldshut_taxon (Butler et al. 2011)	247.2	242
CM_73372 (Weinbaum 2013)	227	208.5
UCMP_97638 (Melstrom and Irmis 2019)	196.5	183
Notochampsa_istedana **(Dollman et al. 2021)**	182.28	180.1
Lumbrera_form (Pol and Powell 2011)	56	41.2
Hyposaurus_rogersii **(Souza et al. 2020)**	70.6	61.7
PIN_4174_1 (Halliday 2013)	152.1	145
Kansajasuchus_extensus **(Efimov 1975)**	100.5	66
Hulkeopholis_plotos **(Buscalioni et al. 2011)**	117	103
Hulkeopholis_willetti **(Buscalioni et al. 2020)**	140.2	136.4
Dollo_s_*Anteophthalmosuchus* (Ristevski et al. 2018)	129.4	122.46
Paralligator_tersus **(Kurzanov 1976)**	72.1	66
Paralligator_ancestralis **(Shuvalov 2003)**	75	80
UCMP_39978 (Bona and Barrios 2015)	38	7.246
Tomistoma_cairense **(Müller 1927)**	47.8	41.2
Crocodylus_affinis **(Marsh 1871)**	50.3	47.8
Osteolaemus_tetraspis ****	0	0
Mecistops_cataphractus*	0	0
Crocodylus_johnsoni ****	0	0
Crocodylus_novaeguineae ****	0	0
Crocodylus_mindorensis ****	0	0
Crocodylus_moreletii ****	0	0
Crocodylus_rhombifer ****	0	0
Crocodylus_acutus ****	0	0
Crocodylus_intermedius ****	0	0
Crocodylus_porosus ****	0	0
Crocodylus_siamensis ****	0	0
Crocodylus_niloticus ****	0	0
Crocodylus_palustris ****	0	0
Alligator_sinensis ****	0	0
Alligator_mississippiensis ****	0	0
Caiman_lutescens ****	0	0
Caiman_yacare ****	0	0
Gavialis_gangeticus ****	0	0
Melanosuchus_niger ****	0	0
Caiman_latirostris ****	0	0
Caiman_crocodilus ****	0	0

Paleosuchus_palpebrosus* ***	0	0
Paleosuchus_trigonatus* ***	0	0
Tomistoma_schlegelii* ***	0	0
Rhea_americana* ***	0	0
Chauna_torquata* ***	0	0
Anas_platyrhynchos* ***	0	0
Crax_pauxi* ***	0	0
Gallus_gallus* ***	0	0

*For most taxa, first and last appearance data used to estimate branch length were obtained from the Paleobiology Database. ** First and last appearance data of Troodontidae, Nodosauridae, and Mystriosuchinae were used for IGM_10044, Argentinian_nodosaurid, and Phytosauria_indet, respectively. *** same ages used for all *Archaeopteryx*. **** branch lengths of extant taxa were assigned values of zero.

Table S4. 5. Probabilities of the three ancestral states in selected archosaur clades

Clade ASR methods	Archosauria (Node 1027)	Dinosauria (Node 1047)	Saurischia (Node 1048)	Theropoda (Node 1205)	Maniraptoriformes (Node 1286)	Pennaraptora (Node 1318)
MP with preferred coding	S0: 0 S1: 1 S2: 0	S0: 0 S1: 1 S2: 0	S0: 0 S1: 1 S2: 0	S0: 0 S1: 1 S2: 0	S0: 0 S1: 0 S2: 1	S0: 0 S1: 0 S2: 1
MP with preferred coding and branch lengths	S0: 0 S1: 1 S2: 0	S0: 0 S1: 1 S2: 0	S0: 0 S1: 1 S2: 0	S0: 0 S1: 1 S2: 0	S0: 0 S1: 0 S2: 1	S0: 0 S1: 0 S2: 1
ML with preferred coding	S0: 0.02 S1: 0.98 S2: 0	S0: 0 S1: 1 S2: 0	S0: 0 S1: 1 S2: 0	S0: 0 S1: 1 S2: 0	S0: 0 S1: 0.10 S2: 0.90	S0: 0 S1: 0 S2: 1
ML with preferred coding and branch lengths	S0: 0 S1: 1 S2: 0	S0: 0 S1: 1 S2: 0	S0: 0 S1: 1 S2: 0	S0: 0 S1: 1 S2: 0	S0: 0 S1: 0.02 S2: 0.98	S0: 0 S1: 0 S2: 1
MB with preferred coding	S0: 0.33 S1: 0.33 S2: 0.33	S0: 0.33 S1: 0.33 S2: 0.33	S0: 0.33 S1: 0.33 S2: 0.33	S0: 0.33 S1: 0.33 S2: 0.33	S0: 0.33 S1: 0.33 S2: 0.33	S0: 0.33 S1: 0.33 S2: 0.33
MB with preferred coding and branch lengths	S0: 0.23 S1: 0.53 S2: 0.23	S0: 0.33 S1: 0.34 S2: 0.33	S0: 0.33 S1: 0.34 S2: 0.33	S0: 0.33 S1: 0.33 S2: 0.33	S0: 0.33 S1: 0.33 S2: 0.33	S0: 0.33 S1: 0.33 S2: 0.33
MP with alternate coding	S0: 0 S1: 1 S2: 0	S0: 0 S1: 1 S2: 0	S0: 0 S1: 1 S2: 0	S0: 0 S1: 1 S2: 0	S0: 0 S1: 0 S2: 1	S0: 0 S1: 0 S2: 1
MP with alternate coding and branch	S0: 0 S1: 1	S0: 0 S1: 1	S0: 0 S1: 1	S0: 0 S1: 1	S0: 0 S1: 0	S0: 0 S1: 0

lengths	S2: 0	S2: 0	S2: 0	S2: 0	S2: 1	S2: 1
ML with alternate coding	S0: 0.92 S1: 0.08 S2: 0	S0: 0.41 S1: 0.57 S2: 0.01	S0: 0.41 S1: 0.57 S2: 0.02	S0: 0.35 S1: 0.61 S2: 0.04	S0: 0.01 S1: 0.09 S2: 0.90	S0: 0 S1: 0.01 S2: 0.99
ML with alternate coding and branch lengths	S0: 0.26 S1: 0.61 S2: 0.13	S0: 0.34 S1: 0.37 S2: 0.29	S0: 0.34 S1: 0.36 S2: 0.3	S0: 0.34 S1: 0.34 S2: 0.32	S0: 0.33 S1: 0.33 S2: 0.33	S0: 0.33 S1: 0.33 S2: 0.33
MB with alternate coding	S0: 0.33 S1: 0.33 S2: 0.33	S0: 0.33 S1: 0.33 S2: 0.33	S0: 0.33 S1: 0.33 S2: 0.33	S0: 0.33 S1: 0.33 S2: 0.33	S0: 0.33 S1: 0.33 S2: 0.33	S0: 0.33 S1: 0.33 S2: 0.33
MB with alternate coding and branch lengths	S0: 0.24 S1: 0.55 S2: 0.21	S0: 0.33 S1: 0.34 S2: 0.33	S0: 0.33 S1: 0.34 S2: 0.33	S0: 0.33 S1: 0.33 S2: 0.33	S0: 0.33 S1: 0.33 S2: 0.33	S0: 0.33 S1: 0.33 S2: 0.33

Abbreviations: ASR, ancestral state reconstruction; MB, Bayesian inference using Mr. Bayes; ML, Maximum likelihood; MP, Maximum parsimony; S, state.

4.7 Digital Supplementary Data

Digital supplementary data is stored and managed by the author, the documents of which are listed as follow:

(1) raw data of uncinate scar coding and informal consensus cladogram sampled in this study.

(2) R script used to perform the Ancestral State Reconstruction.

Latest version can be found at:

https://github.com/Wani2Y/Bioinformatics/blob/main/Ancestral%20State%20Reconstruction/ancestral%20sate%20of%20uncinate%20process.R

(3) raw results of Ancestral State Reconstruction produced using the R script above

CHAPTER 5

Histological evidence implies divergence of uncinate process attachments in non-avian dinosaurs

5.1 Introduction

Modern birds and crocodylians are living representatives of archosaurs, a group of amniotic vertebrates that originated in the Triassic and occupied the many ecological niches for large-body vertebrates throughout the rest of the Mesozoic era (Nesbitt 2011; Benton 2014). In almost all extant birds except anhimid and megapodid birds, the dorsal vertebral ribs of the anterior thorax carry ossified prongs called uncinate processes (Baumel et al. 1993). The posteriormost cervical ribs at the transition between neck and trunk carry additional uncinate processes in some neognath birds (e.g. *Falco sparverius* (UAMZ 4022)). The avian uncinate processes typically take the form of bony protrusions (Baumel et al. 1993) that are developed from cartilaginous templates through endochondral ossification (Maxwell 2008; Maxwell and Larsson 2009; Tickle and Codd 2009; Codd 2010; Scaal 2021). In extant crocodylians, however, the vertebral ribs of the anterior thorax carry cartilaginous uncinate processes in the forms of polygonal tabs (Cong et al. 1988; Frey 1988; Claessens 2009). Although rod-like cartilaginous uncinate processes are present in the rhynchocephalian *Sphenodon punctatus* (Romer 1956), their homologous relationships with archosaurian uncinate processes are currently ambiguous, because evidence of uncinate process is lacking in most extant and fossil lepidosauromorphs.

In skeletally mature birds, the ossified uncinate processes are typically fused to the vertebral ribs (Codd et al. 2008; Codd 2010), which likely prohibit movements of the uncinate processes relative to the vertebral ribs. In skeletally immature birds, the ossified uncinate processes are connected to the vertebral ribs via soft connective tissues (e.g. *Me. gallopavo* (UAMZ 1824), *Rhea americana* (UAMZ 5019)) (see Chapter 4), which may allow limited movements to occur between the uncinate processes and the vertebral ribs. As in skeletally immature birds, the cartilaginous uncinate processes in crocodylians are connected to the vertebral ribs via soft connective tissues. However, the cartilaginous uncinate processes

themselves are substantially flexible when hydrated, which allows the uncinate processes to rotate and/or bend relative to the vertebral ribs. Synostosis has been proposed as the process governing the fusions between uncinate processes and vertebral ribs in birds as in some other fusions of the avian skeletons (Baumel et al. 1993). However, identities of the connective tissues between uncinate processes and vertebral ribs along with their organisations remain unclear.

At least two functional hypotheses of the uncinate processes have been proposed in the literature, including mechanical supports for the ribcage and ventilation (Zimmer 1935; Welty and Baptista 1972; Hildebrand 1982; Walker and Liem 2001; Tickle et al. 2007; Claessens 2015). The ventilatory hypothesis has received supports in birds from two dimensional mechanical analyses suggesting that uncinate processes function to increase the leverage of the muscles attached to them (e.g. m. appendicocostalis) to rotate the rib segments, which subsequently enhances the bird's capacity to expand/contract the thorax (Zimmer 1935; Tickle et al. 2007). The mechanical analyses have received further support from an electromyographic study conducted on m. appendicocostalis in the Canada goose, *Branta canadensis* correlating the patterns of muscle contractions with the inspiratory phase of ventilation (Codd et al. 2005). In extant crocodylians, empirical evidence has been found that m. iliocostalis, an epaxial muscle attached to the uncinate processes serve an expiratory role (Codd et al. 2019).

The fossil record has provided direct evidence for ossified and cartilaginous uncinate processes in a number of archosaurs outside the avian and crocodylian crown groups. Ossified uncinate processes in the forms of slender rods have been found in non-avian members of Pennaraptora, a clade of theropod dinosaurs containing birds and their closest relatives (Codd et al. 2008). Immediately outside of Pennaraptora, ossified uncinate processes resembling those in pennaraptorans are present in the ornithomimosaurian theropod, *Pelecanimimus polyodon* (Cuesta et al. 2022). Furthermore, broad, mineralised uncinate processes have been found in several members of Ornithsichia, a clade of herbivorous non-avian dinosaurs, including ankylosaurs, thescelosaurids, ornithopods, and stegosaurs (Maryańska 1977; Zhou 1983; Boyd et al. 2011; Park et al. 2021). Outside of Dinosauria, unambiguous evidence of mineralised uncinate processes have only been found in the notosuchian *Araripesuchus gomessi*, a terrestrial relative of extant crocodylians (Turner 2006). As the uncinate processes listed above are from exquisitely

preserved specimens, their occurrence and distribution are likely underrepresented in the fossil record. Removal of uncinate processes from their corresponding vertebral ribs reveals rugose concave scars that is termed uncinate scars, and the presence of uncinate processes has been inferred to be the ancestral condition shared by most archosaurs (see Chapter 4). Accordingly, uncinate processes along with the ventilatory function observed in extant birds and crocoylians may have been inherited from their archosaurian ancestors.

Although uncinate scars can infer the presence of uncinate processes when they are not directly preserved, identifications of uncinate scars require the surficial cortex of the vertebral ribs to be nearly intact. Taphonomic damages accordingly would render unambiguous uncinate scars to plausible ones. Moreover, morphology of known uncinate scars is not always identical to those in extant birds and crocodylians (see Chapter 4), which opens some of the known uncinate scars for alternate identifications.

In this study, we provide detailed description on the histology at the contacts between uncinate processes and vertebral ribs in two extant and at least four fossil archosaurs. Additionally, we provide histological evidence that serves as a basis to infer the presence of uncinate processes along with uncinate scars. Additionally, several configurations that uncinate processes are anchored to their respective vertebral ribs are revealed in the sampled fossil dinosaurs, suggesting the uncinate processes and vertebral rib contacts are not conservative on the evolutionary path to birds.

5.2 Materials and Methods

To establish an extant baseline, two dorsal vertebral ribs were sampled from a skeletally immature domestic turkey, *Meleagris gallopavo* (UAMZ unnumbered) purchased from Save on Food, and a skeletally immature alligatorid crocodylian, *Caiman crocodilus* (UAMZ unnumbered). The vertebral ribs were removed from the ribcage after dissecting away the surrounding muscles. In the case of *Cai. crocodilus* (UAMZ unnumbered), the myosepta were trimmed around the uncinate processes.

The procedure to create thin sections from *Me. gallopavo* (UAMZ unnumbered) and Cai. crocodilus (UAMZ unnumberd) was performed at the Advanced Microscopy Facility at the Department of Biological Sciences, University of Alberta. Vertebral ribs with uncinate processes were placed in 10% neutral buffered formalin (prepared using Fisher formaldehyde F79-1) for 3 days to fix the tissues, which were then placed in Cal-Ex solutions (Fischer Scientific CS510-1D, 5.5% hydrochloric acid and 0.12% disodium EDTA dihydrate, pH 2.0) for decalcifications. To maintain an efficient decalcifying process, the specimens were placed on a mechanical shaker for 8 hours per day, and Cal-Ex solutions were replaced every 48 hours. Specimens of *Me. gallopavo* (UAMZ unnumbered) and *Cai. crocodilus* (UAMZ unnumbered) were decalcified for 14 and 30 days, respectively. The decalcified specimens were rinsed in tap water and were proximodistally cut into several parts, which were fixed in neutral buffered formalin for 48 hours and transferred to 50% ethanol solutions for 1 to 3 hours. The specimens were then processed overnight on program 2 using Leica TP 1020 tissue processor (protocol provided in Supplementary Information). On the following day, the specimens were embedded in paraffin wax using Tissue-Tek II embedding machine. After the paraffin wax was consolidated, specimens were placed on ice for at least an hour before being sectioned at 5 μm thickness using Leica 2025 BioCut rotary microtome. All specimens were sectioned transversely except the first dorsal vertebral rib in *Me. gallopavo* (UAMZ unnumbered), which were sectioned longitudinally in lateromedial direction. Thin sections were mounted on single frosted glass slides (Bio Nuclear Diagnostics Inc., LAB-034) and dried at 37 °C. Most thin sections were applied Hematoxylin and Eosin stain, except one longitudinal thin section of *Me. gallopavo* (UAMZ unnumberd) (T 1 – 3) and two transverse thin sections of *Cai. crocodilus* (UAMZ unnumberd) (T 2 – 3 and T 3 – 6) which were stained using Masson's trichrome (protocol provided in Supplementary Information).

Dorsal vertebral ribs carrying uncinate scars in at least four non-avian dinosaurs were sampled from Tyrrel Museum of Palaeontology and University of Alberta Laboratory for Vertebrate Paleontology. Most fossil specimens available for sectioning were isolated element, and could only be identified to suprageneric level (Table 5.1).

The procedure to create thin sections of fossil vertebral ribs was operated at the Palaeohistology Lab at the Department of Biological Sciences, University of Alberta. Fossil

vertebral ribs were divided into parts with and without uncinate scars. Each specimen was embedded in Eager and polymer EP4101UV crystal clear polyester resin, and placed in Welch DuoSeal vacuum pump to extract air bubbles from the liquid resin. The embedded specimens were cured for at least 48 hours under a fume hood, which were then sectioned at 7 mm thickness using Buehler IsoMet 1000 table saw at the speed between 250 -275 rpm. The thin sections were mounted on plexiglass slides using 3M Scotch-Weld™ Super Fast Instant Adhesive SF100. Subsequently, the sections were first thinned down using a grinding wheel of Hillquist saw and was manually grinded on a glass surface over a mixture of E. T. MetTech silicon carbon grain at 600 and 1000 grits and tap water. Excess silicon carbon grains were removed using an VWR B1500A-DTH sonicator for up to two minutes.

Images of all the histological sections were captured using Nikon DS-FI3 camera mounted on a Nikon Eclipse E600 POL microscope, and Nikon NIS Elements (ver. 4.60) imaging software housed in the Caldwell lab, University of Alberta. Relative anatomical positions of the thin sections sampled in this study were illustrated in Supplementary Figure S5.1.

5.3 Results

5.3.1 A note on terminology

As uncinate scar is defined as the rugose contact between uncinate processes and vertebral ribs (see Chapter 4), uncinate scar in this study refers only to the cortical surface of the vertebral ribs at which uncinate process is attached to via soft connective tissues.

In mammalian bone development, woven bones containing randomly arranged collagen fibres are first laid down, which are then modified into more matured bones (e.g. lamellar bones, compact bones consisted of numerous Haversian systems) (An and Martin 2003; Shapiro and Wu 2019). As woven bones are laid down first, it is sometimes synonymized with primary bones (Mescher and Junqueira 2016). However, fibrolamellar have been observed as primary bone constituting the external cortex in non-avian dinosaurs (Francillon-Vieillot et al. 1990; Cullen et

al. 2014), which is distinguished from woven bones by the presence of bone layers organised in parallel fashion (Shapiro and Wu 2019). Primary bones may therefore be laid down in the forms of woven or fibrolamellar bones. In this study, we broadly classify the cortex of vertebral ribs into primary and mature bones due to three reasons: (1) Primary bones as an umbrella term has been used to describe the bone tissues that are most recently deposited, including woven and fibrolamellar bones (Francillon-Vieillot et al. 1990; Mescher and Junqueira 2016). (2) The external layers of the rib's cortex sampled fossil dinosaurs in this study are laid down in lamellar fashion which house both primary and secondary osteons. However, fibrolamellar bones are not observed in the sampled extant archosaurs. The use of primary and mature bones allows consistent comparisons regarding the skeletal maturity among extant and fossil archosaurs sampled in this study. (3) revisions on the classifications of fibrolamellar bones have been proposed (Prondvai et al. 2014; Shapiro and Wu 2019), and the precise definition of fibrolamellar bones is uncertained at the time of this study.

Two definitions of the Sharpey's fibres are available in the literature (Hall 2005), and we modify from the more restricted definition by Simmons *et al*., (1993). Sharpey's fibres are specifically to the collagen fibres inserted into bones, and collagen fibres accordingly refer to fibres positioned within bones and soft connective tissues. As soft tissues immediately external to the bones are rarely preserved in the fossil record, collagen fibres that can reach the external surface of the cortex are also identified as Sharpey's fibres.

5.3.2 Histology of the uncinate processes and uncinate scars in *Meleagris gallopavo*

The ossified uncinate processes and the vertebral ribs in *Me. gallopavo* (UAMZ unnumbered) is encased by a layer of regular dense connective tissues that we identified as the periosteum, which is consisted of an outer fibrous layer and an inner cellular cambium layer (Fig. 5.1A, C – G) comparable to the periosteum identified in vertebral ribs of dogs (Canalis and Burstein 1985) and mandibles of chicken (Hall 2005). The fibrous layer is predominantly composed of discrete bundles of dense connective tissues oriented towards the uncinate process, which is morphologically distinct from the continuous regular dense connective tissues and the randomly organised irregular dense connective tissues. Blood vessels are present both within and immediate external to the outer layer of the periosteum (Fig. 5.1D, Fig. 5.3, D, E, F). The

cambium layer is rich in nuclei that we interpret as mesenchymal cells (Fig. 5.1, D – G), which presumably contribute to the growth and intramembranous ossification of the uncinate processes and that of the dorsal vertebral ribs. Tissues of the cambium layer can be tightly packed or areolar. Islands of undifferentiated mesenchyme (Fig. 5.1E, 5.1F) are visible within the cambium layer. The cambium layer is thickest at the contact between the uncinate process and vertebral rib, contrasting the minimally developed cambium layer surrounding the uncinate process (Fig. 5.1D).

The uncinate process is not fused to the dorsal vertebral rib, and zones of ossifications are visible on the uncinate processes. On the transverse thin sections (Fig. 5.1A, 5.1B), the midshaft of the uncinate process is fully ossified, which transitions to zones of cartilages proximally and distally. A zone of mineralized cartilage with irregular thickness is at immediate contact with the bone tissues, which is separated from the unmineralized cartilage with comparatively smaller lacunae by visible tidemarks. As the lacunae are not enlarged, we identify this zone as proliferated cartilage migrating towards the uncinate process. Patches of extra cellular matrix are visible within the proliferated cartilage. Further proximally and distally, the proliferated cartilage shifts to a zone of hyaline cartilage, which is consisted of many isogenous aggregate chondrocytes. Small amounts of collagen fibres are likely present, as the external margins of the hyaline cartilage appear to be slightly anisotropic under cross polarized light. However, the centre of the hyaline cartilage are unambiguously anisotropic, and the anisotropic effects we observed are likely from collagen fibres from surrounding soft connective tissues. The collagen fibres of the hyaline cartilages seemingly connect and continue with the fibrous layer of the periosteum surrounding the uncinate process (Fig. 5.1C). Similar results are found on the longitudinal thin sections with three noticeable differences (Fig. 5.1, I – K). A small zone of hypertrophic cartilage can be identified between the mineralised cartilage and proliferated cartilage. Compared to the transverse thin sections, transitions and organizations of tissues between zones appear to be more variable, and hyaline cartilages are only present at the dorsal and ventral aspects of the uncinate process near their contacts to the vertebral rib. Our histological observation is congruent with the findings in embryonic *Me. gallopavo* that uncinate processes ossify from the midshaft towards the proximal and distal ends similar to a typical long bone (Tickle and Codd 2009).

The uncinate process is connected to the dorsal vertebral rib via a thick layer of periosteum, which is predominately consisted of the cambium layer (Fig. 5.1, C – G, Fig. 5.2B, 5.2D). The relatively thin fibrous layer is positioned close to the uncinate process and appears to mesh with the collagen fibres of the hyaline cartilage at the proximal end of the uncinate process. Clusters of mesenchymal tissues surrounding small capillaries are observed between the uncinate scar and uncinate process (Fig. 5.1, C, E – G). By comparison, cambium layer of the periosteum away from the uncinate scar (e.g. anterior and lateral surface) are comparatively thin and lack visible capillaries (Fig. 5.1D, Fig. 5.3, C, G, H).

The cortex of the ossified vertebral rib internal to the cambium layer of the periosteum is consisted of mostly if not exclusively cellular bone. The external primary bone is separated from the mature lamellar bones by distinct cement lines. Many immature osteons with spherical haversian canals are present within the primary bones. The primary bone is more developed on the anterior and posterior aspects of the vertebral rib compared to their lateral and medial counterparts, which is a pattern observed on the transverse thin sections both at and away from the uncinate process. On all sampled thin sections, the layer of primary bone is thickest on the transverse sections through the uncinate process. A large, irregularly shaped canal containing a blood vessel oriented mediolaterally is observed near the site of uncinate process attachment (Fig. 5.1C, Fig. 5.2B, 5.2D), which has not been observed at locations away from the uncinate process. An increase in vascularisation is therefore present at the uncinate scar, potentially supplying and ossifying the uncinate process. At the uncinate scar, meshes of collagen fibres are present within the primary bone on all sampled sections, which can be classified based on orientations into circumferential and radial fibres (Fig. 5.2, B – E). We identify the radial fibres as Sharpey's fibres, as they connect the periosteum to the primary bones both visible from transverse and longitudinal thin sections (Fig. 5.2B, 5.2D, 5.2G, 5.2H). At and adjacent to the uncinate scar, both circumferential and Sharpey's fibres are coarse, forming discrete anisotropic bundles under cross polarized light. Additionally, the Sharpey's fibres at the uncinate attachment seemingly maintain a general orientation towards the uncinate process (Fig. 5.2B, 5.2D), whereas those Sharpey's fibre away from the uncinate process are more radially organised (Fig. 5.3C). Albeit obscured by the cambium layer, the Sharpey's fibres at the uncinate attachment seemingly course from the primary bone to the dense connective tissues surrounding the ossified

uncinate process as indicated by the similar orientations of the Sharpey's fibres (Fig. 5.2B). Bundles of the coarse and distinct Sharpey's fibres could pass into the more mature lamellar bone, though they mostly terminate at the cement lines (Fig. 5.2B). Dorsoventral positions of the thin sections notwithstanding, the primary bone away from the uncinate process sampled in this study contains mostly fine Sharpey's fibres and other collagen fibres, of which individual bundle could not be easily identified (Fig. 5.3C). However, primary bones away from the uncinate scar still contains low quantity of coarse collagen fibres, though they appear as discrete clusters that do not reach the external surface of the cortex.

The primary bone transition into the more compact lamellar bone at the cement line, which predominantly contain fine, circumferentially arranged collagen fibres. Further internally, the cortex of the vertebral rib transitions into medullary cavity containing trabecular bones.

5.3.3 Histology of the uncinate processes and uncinate scars in *Caiman crocodilus*

The cartilaginous uncinate process in *Cai. crocodilus* (UAMZ unnumbered) is completely composed of hyaline cartilage that houses sparsely arranged chondrocytes in the forms of single and isogenous groups of chondrocytes (Fig. 5.4B). The lacunae and presumably the chondrocytes they house have subcircular outlines, except for those positioned near the perichondrium which are more elongated with the long axes oriented parallel to the long axis of the uncinate process (Fig. 5.4C, 5.4D). Collagen fibres are found near the peripheral of the hyaline cartilage near its junction with the perichondrium mostly consisted of dense connective tissues. The precise contact between the hyaline cartilage and the perichondrium could not be identified, but the approximate location can be inferred by the absence of chondrocytes/lacunae and the presence of anisotropic dense regular connective tissues under cross polarized light (Fig. 5.4C, 5.4D).

The perichondrium surrounding the hyaline cartilage is a sheath of dense regular connective tissues the fibres of which are highly organised to be anisotropic and tightly arranged such that the perichondrium is distinguished from the dense irregular connective tissues external to it (Fig. 5.4B, 5.4D, Fig. 5.5B, 5.5C). Blood vessels are found near the contact between the dense irregular connective tissues, which can be classified into two groups based on the fibre

arrangements. The dense regular connective tissues lateral to the uncinate process are arranged predominantly in the similar direction as the fibres of the perichondrium, though the tissues house distinct gaps between parallel bundles. By comparison, the dense irregular connective tissues between the uncinate process and vertebral rib are likely arranged at an angle to the long axis of the uncinate process, as the tissues are arranged in the form of isolated clusters. Fibre orientation notwithstanding, multiple blood vessels are found within the dense irregular connective tissues.

At the uncinate scar, the dense irregular connective tissues transition to a compactly, circumferentially organised dense regular connective tissues that we identify as the fibrous layer of the periosteum (Fig. 5.4E, 5.4F, Fig. 5.5, B – H). Unambiguous fine Shapey's fibres are identified from the fibrous layer of the periosteum from thin sections away from the uncinate scar (Fig. 5.6D). Unlike in *Me. gallopavo* (UAMZ unnumbered), the cambium layer of the periosteum is only observed from sections away from the uncinate process in the form of a series of purple nuclei, which is much less developed compared to the fibrous layer (Fig. 5.6, B – D).

The periosteum is attached to the ossified cortex of the vertebral rib, which is consisted of a thick layer of primary bone separated from a thin layer of mature lamellar bone by cement lines (Fig. 5.4E, 5.4F, Fig. 5.5, D – F). As in *Me. gallopavo*, the cortex of *Cai. crocodilus* lack typical mammalian haversian system, as reported from birds and squamates in the literature. However, the primary bone from the sampled sections in *Cai. crocodilus* is not highly vascularized, and the primary bones overall appear as solid bones. Several irregularly shaped canals are observed within the mature bones near the uncinate scar (Fig. 5.5 C – E). However, blood vessels are not directly observed within these canals, and they may represent secondary remodelling of the mature cortical bones into trabecular bones of the medullary cavity.

The periosteum in vicinity to the uncinate scar is anchored to the primary bone of the rib's cortex by Sharpey's fibres which are typically higher in quantity, coarse, and maintain similar orientations towards the uncinate process. These Sharpey's fibres terminates at the contacts between the primary bones and the fibrous layer of the periosteum (Fig. 5.5G, 5.5H), presumably anchoring the periosteum to the primary bones. However, collections of distinctly

coarse Sharpey's fibres are observed within the primary bones, which pass towards the uncinate process and into the fibrous layer of the periosteum (Fig. 5.5B, 5.5D). On at least two sections (Pt us trunk 3 -5 and Pt us trunk 3-9), coarse Sharpey's fibres are blended with the dense regular connective tissues of the perichondrium surrounding the hyaline cartilage of the uncinate process (Fig. 5.5C, 5.5E, 5.5F). Away from the uncinate scar, collagen fibres within the primary bones are typically fine, and individual bundle is difficult to identified (Fig. 5.6I). However, coarse collagen and Sharpey's fibres can be found away from the uncinate attachment (Fig. 5.6D, 5.6E, 5.6H), but they are relatively low in quantities. Only observed on one thin section, coarse Sharpey's fibres located on the anterior aspect of the vertebral rib are found penetrating through the rib's cortex into the muscle tissues that presumably attached to the vertebral rib (Fig. 5.6F, 5.6G), which are relatively low in quantity as the coarse collagen and Sharpey's fibres away from the uncinate scars observed in this study. The presence of coarse Sharpey's fibres alone therefore does not uniquely indicate sites of uncinate process attachment, and may represent sites of muscle attachments. However, coarse Sharpey's fibres are comparatively lower in quantity at the attachment sites of muscles.

5.3.4 Histological evidence indicative of uncinate attachment

If the observations from *Me. gallopavo* (UAMZ unnumberd) and *Cai. crocodilus* (UAMZ unnumbered) can represent the general conditions in birds and crocodylians, high quantity of coarse Sharpey's fibres can be used as a supporting evidence to infer the presence of uncinate processes.

5.3.5 Histology of the uncinate scars in tyrannosaurid dinosaurs

In all three sampled tyrannosaurids, coarse Sharpey's fibres are observed from thin sections at and adjacent to the uncinate scars, which are positioned within the primary bone as arrays of parallel fibres. These coarse Sharpey's fibres are observed throughout the majority of the primary bone of the posterior aspect of the vertebral rib (Fig. 5.7, D – G, Fig. 5.8, C, 5.8D, Fig. 5.9, C – G). The coarse Sharpey's fibres are oriented towards the uncinate scars, but most appear as radially arranged on thin section at higher magnifications, likely because the vertebral ribs and the uncinate scars in tyrannosaurids are mediolaterally wide compared to those in *Me. gallopavo* (UAMZ unnumbered) and *Cai. crocodilus* (UAMZ unnumbered). The coarse

Sharpey's fibres are most well-preserved at the proximal ridge in TMP 94.12.960 where a distinct cluster of coarse Sharpey's fibres is observed (Fig. 5.8, C – F). Although these coarse Sharpey's fibres are oriented away from the uncinate scar, they could contribute to anchor the soft connective tissues positioned peripheral to the uncinate process, as in some of the coarse Sharpey's fibres observed in *Cai. crocodilus* (UAMZ unnumbered) (Fig. 5.5D). Additionally, clusters of small and round objects with anisotropic peripherals are observed adjacent to the proximal ridge of the uncinate scar in Tyrannosauridae indet. (TMP 94.12.960), which we identify as transverse sections of coarse collagen fibres oriented approximately parallel to the long axis of the vertebral rib (Fig. 5.8E, 5.8F). As these coarse collagen fibres do not contact the external surface of the vertebral ribs on the sampled sections, we could not confidently determine whether they are connected to the uncinate scar or they may contribute to the collagen scaffold of the periosteum.

In two of the sampled tyrannosaurids (TMP 51.81.16.285 and 94.12.960), the high quantity of coarse Sharpey's fibres adjacent to the uncinate scars gradually transition to low quantity of coarse Sharpey's fibres in the primary bone away from the uncinate scar (Fig. 5.7H, Fig. 5.8G). In *Albertosaurus sarcophagus* (TMP 99.52.42), the uncinate scar lacks a proximal ridge (Fig. 5.9B). Coarse Sharpey's fibres are observed at the uncinate scar, but they are less distinct compared to TMP 51.81.16.285 and TMP 94.12.960. The condition observed in *Ab. sarcophagus* (TMP 99.52.42) is likely impacted by taphonomic factors, as the thin sections contain high number of small fractures.

Sharpey's fibres within the primary bone away from the uncinate scars typically appear as radially arranged arrays of fine collagens (Fig. 5.10). Individual bundles of fibres are difficult to be identified, as in the sampled extant archosaurs. However, high quantity of coarse Sharpey's fibres are observed on thin sections at a position distal to the uncinate scar in Tyrannosauridae indet. (TMP 51.81.16.285) (Fig. 5.10F), which are positioned at a bony ridge. Coarse Sharpey's fibres anchoring skeletal muscles to bone have been observed in *Cai. crocodilus* (UAMZ unnumbered), and the bony ridges can indicate attachment sites of skeletal muscles (Holliday 2009; Liparini and Schultz 2013). Therefore, the coarse Sharpey's fibres at the bony ridge distal to the uncinate scar in TMP 51.81.16.285 may represent attachments of trunk muscles.

In addition to coarse Sharpey's fibres at the uncinate scars, multiple irregularly shaped canals are observed on the cortex near the uncinate scar in TMP 51.81.16.285 (Fig. 5.7B), which morphologically resemble the pathway for blood vessels in *Me. gallopavo* (UAMZ unnumbered) described above. Accordingly, we identify the irregularly shaped canals in TMP 51. 81. 16. 285 as pathway for blood vessels, which represents an increase in vascularisation of the cortex at the uncinate scar. Irregularly shaped pathways for blood vessels are also observed in the skeletally less mature, smaller sized Tyrannosauridae indet. (TMP 94.12.960), though the pathways are only found at the proximal ridge of the uncinate scar (Fig. 5.8B, 5.8C). However, proximal ridge and irregularly shaped pathway are absent from the sampled *Ab. sarcophagus* (TMP 99.52.42).

The primary bone on the sampled thin sections in TMP 51.81.16.285 and TMP 94.12.960 is thick on positions away from the uncinate scars, which become thinner or absent near the uncinate scars (Fig. 5.7B, 5.8B, 5.9B). The variable thickness of the primary bone in the sampled tyrannosaurids may represent different rates of bone growth, and the osteons potentially mature faster near the uncinate scars. Alternatively, primary bone may mature at similar rates, but are deposited less frequently near the uncinate scar, resulting in thinner layers of primary. Although a proximal ridge is absent in *Ab. sarcophagus* (TMP 99.52.42), the primary bone is thinner at the uncinate scar compared to regions away from it, as in TMP 51.81.16.285 and TMP 94.12.960.

Comparisons among the three sampled tyrannosaurids indicate that an increase in vascularization could be associated with the presence of a proximal ridge, as angiogenesis and osteogenesis are two closely associated processes in bone development and maintenance (Dai and Rabie 2007; Filipowska et al. 2017). The increase in vascularization may take place at the proximal ridge early in postnatal development, which subsequently expands to the cortex near the uncinate scar to facilitate the maturing of the bony cortex.

5.3.6 Histology of the uncinate scars in hadrosaurid dinosaur

Two groups of coarse Sharpey's fibres are observed on the primary bone at the posterior aspects of the vertebral rib adjacent to the uncinate scar, each of which is oriented towards the uncinate scar (Fig. 5.11 C, 5.11E, 5.11I, Fig. 5.12B, 5.12E). At lateral and medial margins of the uncinate scar, one to two groups of coarse Sharpey's fibres are observed the orientation of which

are further towards the uncinate scar and can be distinguished from the adjacent coarse Sharpey's fibres under cross polarized light (Fig. 5.11L, Fig. 5.12F, 5.12K). Based on the fibre orientations, the coarse Sharpey's fibres at the margins of uncinate scars likely anchor to the uncinate process, whereas those coarse Sharpey's fibres may be attached to the uncinate process, the soft connective tissues peripheral to the uncinate process, and hypaxial muscles (e.g. mm. intercostales).

Unlike the cortex adjacent to the uncinate scar, coarse Sharpey's fibre is absent at the uncinate scar on the thin sections sampled in Hadrosauridae indet. (UALVP 60005). Instead, one to three layers of lamellar bones are observed except for thin sections sampled from the distal end of the uncinate scar which lacks lamellar or primary bone (Fig. 5.11I, 5.11J, Fig. 5.12B, 5.12E). Within the lamellar bones at the uncinate scar, two groups of collagen fibres are arranged perpendicularly (Fig. 5.11I, 5.11J, 5.11M, Fig. 5.12D, 5.12G, 5.12H). The first group is oriented parallel to the concave surface of the uncinate scar on the transverse thin sections, whereas the second group is oriented parallel to the proximodistal axis of the vertebral rib which appears on the transverse thin sections as clusters of black dots surrounded by anisotropic outlines. At several locations, these two groups of collagen fibres are observed within or immediately internal to the lamellar bone (Fig. 5.11M, Fig. 5.12H). Although some of the collagen fibres seem to be organised at the lamellar bone towards the uncinate scar, they all terminate at or within the lamellar bone without reaching the external surface of the cortex (Fig. 5.12D). Lacking a direct contact to the surface of the cortex and a distinct orientation towards the uncinate scar, the two groups of collagen fibres within the lamellar bones may not directly attach to the uncinate process. Instead, the first and second groups of collagen fibres are likely collagen fibres inherited or modified from the scaffold of the periosteum, respectively.

Only fine Sharpey's fibres and collagen fibres are observed on the lateral and medial aspects of the vertebral rib away from the uncinate scar (Fig. 5.12 L, 5.12M), which are organised somewhat radially though a dominant orientation is not crystal clear.

An increase of vascularization is present in the cortex adjacent to the uncinate scar, as large canals that we identify as pathways for blood vessels are observed within the cortex

adjacent to the uncinate scar, and they can be positioned within the lamellar bones. These pathways for blood vessels generally have spherical outlines (Fig. 5.11A, 5.11I, Fig. 5.12B, 5.12E, 5.12G), though irregular shaped pathways are also observed (Fig. 5.11D, 5.11E). Unlike the sampled tyrannosaurids, the pathways for blood vessels are assembled closer to the uncinate scar, and seemingly do not appear on the posterior, medial, and lateral aspects of the vertebral rib away from the uncinate scar (Fig. 5.12E). Although the pattern of vascularization at the uncinate scar is not consistent between sampled tyrannosaurid and Hadrosauridae indet. (UALVP 60005), evidence of increase vascularization at the uncinate scar is found in Tyrannosauridae and Hadrosauridae.

Within the lamellar bone, strands of undulating tissues are observed passing towards the uncinate scar, which are isotropic under cross polarized light and morphologically resemble the canaliculi of Williamson in the actinopterygian fish (Sire and Meunier 1994). However, these strands of tissues at higher magnifications appear as hollow tubes surrounded by meshes of fibres (Fig. 5.11G, 5.11H, Fig. 5.12I), and they can reach the external surface of the uncinate scar (Fig. 5.11G). Instead of canaliculi of Williamson, we identify the undulating strands of tissues as pathways for small capillaries that supply nutrients to the lamellar bone and plausibility soft tissues anchored to the uncinate scar.

Variations are observed proximodistally throughout the uncinate scar in Hadrosauridae indet. (UALVP 60005). Proximal to the uncinate scar, a large and irregularly shaped pathway for blood vessel surrounded by lamellar bone is observed (Fig. 5.11B – E), and the diameter of which seemingly increases as the sectioning position approaches the uncinate scar. The primary bone external to the irregularly shaped pathway is reduced in thickness, potentially due to the formation of the lamellar bone (Fig. 5.11, D – F). At the uncinate scar, the large pathway for blood vessel reduces in diameter and transitions to a position medial to or within the lamellar bone (Fig. 5.11I, Fig. 5.12B, 5.12E, 5.12G). At the distal end of the uncinate scar, the large pathway for blood vessel and lamellar bones are absent (Fig. 5.12J). The observations from the serial thin sections in Hadrosauridae indet. (UALVP 60005) may indicate that the uncinate scar we identify based on surface morphology is a pathway for blood vessel instead of attachment site for uncinate process, echoing one of the improbable identifications (see Chapter 4). However, the

high quantity of coarse Sharpey's fibres is an indicator of uncinate attachment shared with thin sections sampled in *Me. gallopavo* (UAMZ unnumbered) and *Cai. crocodilus* (UAMZ unnumberd). Additionally, nutrient foramens can be found at the external surface of the uncinate scars in extant birds and crocodylians (see Chapter 4). We therefore reason that the pattern of serial thin sections observed in Hadrosauridae indet. (UALVP 60005) represent an increase in blood supply for soft tissues around the uncinate scar.

5.3.7 Histology of the uncinate scars in ceratopsid dinosaurs

In the three sampled ceratopsids, coarse Sharpey's fibres are observed in the primary bones of the cortex adjacent to the uncinate scar, which are oriented towards the uncinate scar (Fig. 5.13, C – N, Fig. 5.14, C, E – L, Fig. 5.15, C - K). Unlike the sampled tyrannosaurids and Hadrosauridae indet. (UALVP 60005), the coarse Sharpey's fibres in *Pachyrhinosaurus lakustai* (PSC 2014.060) and *Centrosaurus* sp. (TMP 96.1776.135) are concentrated at the lateral and/or medial margins of the uncinate scars. However, coarse Sharpey's fibres do occupy the majority of the primary bones on the posterior aspect of the sampled vertebral rib in *Centrosaurus* sp. (TMP 82.18.16) (Fig. 5.15D, 5.15F, 5.15H). Additionally, the coarse Sharpey's fibres are long strands organised in two crossed arrays oriented towards the uncinate scar. The high quantity of coarse Sharpey's fibres observed in *Centrosaurus* sp. (TMP 82.18.16) likely represent a ontogenetic variant in less skeletally mature *Centrosaurus*, because the sampled thin sections in *Centrosaurus* sp. (TMP 82.18.16) have relatively thick primary bone and fewer secondary osteons throughout the cortex. Among the three sampled ceratopsids, orientations of the coarse Sharpey's fibres vary between arrays that are inclined towards the uncinate scar at an actual angle (Fig. 5.13C, 5.13E, 5.13J, Fig. 5.14H), and strands that are arranged nearly parallel to the margins of the uncinate scars (Fig. 5.14 E, 5.14F).

As in Hadrosauridae indet. (UALVP 60005), one or several layers of lamellar bones are observed at the uncinate scar in all three sampled ceratopsids, which contains a group of collagen fibres parallel to the concave surface of the uncinate scar and another group approximately parallel to the long axis of the vertebral rib (Fig. 5.13B, 5.13J, Fig. 5.14B, 5.14J, Fig. 5.15E). However, the coarse Sharpey's fibres adjacent to the uncinate scars can either pass through layers of lamellar bones and reach the external surface of the uncinate scar (Fig. 5.13C, 5.13E,

Fig. 5.14F), or terminate at the internal surface of the lamellar bone (Fig. 5.13J, Fig. 5.15L). The former configuration is not observed in Hadrosauridae indet. (UALVP 60005). The presence of slowly deposited lamellar bones (Hall 2005) at the uncinate scar surrounded by high quantity of actively developing primary bones in the less skeletally mature *Centrosaurus* sp. (TMP 82.18.16) suggest that the relatively slow bone growth at the uncinate scar likely occurs before reaching subadulthood comparable to *Pa. lakustai* (PSC 2014.060) and *Centrosaurus* sp. (TMP 96.1776.135).

Collagen and Sharpey's fibres away from uncinate scars are generally fine and are radially organised in the sampled ceratopsids (Fig. 5.16C, 5.16D, 5.16I). Coarse collagen fibres that do not reach the external surface of the cortex (Fig. 5.16G) and coarse Sharpey's fibres (Fig. 5.16B, 5.16J) are occasionally observed as isolated clusters within the primary bones. A large pathway for blood vessels formed by lamellar bones is observed in *Centrosaurus* sp. (TMP 96.1776.135) (Fig. 5.16F), which can be distinguished from the lamellar bone at the uncinate scar by the absence of collagen fibres approximately parallel to the long axis of the vertebral rib.

The cortex adjacent to the uncinate scar generally shows no signs of increase in vascularization. Therefore, the sampled ceratopsids share a similar condition in vascularization of the cortex adjacent to the uncinate scar with the sampled *Cai. crocodilus* (UAMZ unnumbered), as opposite to the sampled *Me. gallopavo* (UAMZ unnumbered), tyrannosaurids, and Hadrosauridae indet. (UALVP 60005).

Thin sections at various locations through the uncinate scars in *Pa. lakustai* (PSC 2014.060) and *Centrosaurus* sp. (TMP 82.18.16) show minor changes in the concave morphology of the uncinate scars in transverse sections. By comparison, the transverse sections of the uncinate scars in *Centrosaurus* sp. (TMP 96.1776.135) can be narrow and deep (Fig. 5.14B) or wide and shallow, the latter of which can have either a smooth (Fig. 5.14G) or angular outlines (Fig. 5.14E). Only one layer of lamellar bone is observed at the uncinate scar in *Centrosaurus* sp. (TMP 82.18.16, TMP 96.1776.135), which have similar thickness among the sampled thin sections. Variations of the lamellar bones are observed proximodistally throughout the uncinate scar in *Pa. lakustai* (PSC 2014.060). Approximately three layers of lamellar bones

separated by cement lines are observed from thin sections near the proximal end of the uncinate scar (Fig. 5.13B – E), whereas lamellar bones are not distinct on the thin sections positioned further distally (Fig. 5.13F, 5.13K). This could potentially be resulted from taphonomic damages at the uncinate scar. Alternatively, the lamellar bones may still in development, because collagen fibres parallel to the concave surface of the uncinate scar are present where distinct lamellar bones are absent (Fig. 5.13J , 5.13K).

In summary, comparatively high quantity of coarse Sharpey's fibres are observed at uncinate scars in the sampled extant and fossil archosaurs. Evidence of increase vascularization adjacent to uncinate scars are observed in the sampled *Me. gallopavo* (UAMZ unnumbered) and tyrannosaurids, and hadrosaurid. Formation of lamellar bones at the uncinate scars are found in sampled cerapodans.

5.4 Discussion

5.4.1 Refining and augmenting the distribution of uncinate process using histological evidence

Coarse Sharpey's fibres are found in relatively high quantity near the uncinate scars in sampled extant and fossil archosaurs, which can be used as feature to infer the presence of uncinate processes along with uncinate scar. Compared to the surficial uncinate scars, coarse Sharpey's fibres are positioned within the cortex of the vertebral ribs, which do not rely on nearly complete preservations of the cortical surfaces as in inference using uncinate scars. A wide range of fossil archosaurs may be sampled for the distribution of uncinate processes.

However, coarse Sharpey's fibres alone could not unambiguously infer the presence of uncinate processes. Coarse Sharpey's fibres have been observed in the cortex away from the uncinate scar and may reach the cortical surface (Fig. 5.6G, Fig. 5.10F, Fig. 5.16B, 5.16J), though usually in relatively low quantity.

Therefore, we propose that presence of high quantity of coarse Sharpey's fibres should be used as a criterion in conjunction with uncinate scar, to distinguish attachment sites of uncinate processes from other surficial scars (e.g. attachment sites of muscles).

5.4.2 Evolutionary divergence of uncinate process attachments in dinosaurs on the line to birds

The origin of the highly specialised avian respiratory system is difficult to pinpoint, as direct evidence of parabronchi indicative of the presence of cross-current gas exchange is lacking in the fossil record. However, evidence of unidirectional pulmonary airflow has been found in extant crocodylians and lepidosaurs (Farmer and Sanders 2010; Farmer 2015). Along with the widespread postcranial pneumaticity in saurischian dinosaurs (O'Connor 2006; Wedel 2006) and the ancestral presence of uncinate processes in archosaurs (see Chapter 4), anatomical components comparable to the avian ventilatory system may be acquired gradually on the evolutionary path towards birds. A hypothetical evolutionary scenario has been proposed regarding the emergence of cartilaginous uncinate processes, postcranial skeletal pneumaticity, and ossified uncinate processes leading to birds (see Chapter 4). Taphonomic biases notwithstanding, direct evidence of mineralised or even partially ossified cartilaginous uncinate processes have been found in ornithischian dinosaurs (Boyd et al. 2011), but rarely if at all in saurischian dinosaurs. Therefore, the hypothetical scenario based on uncinate scars likely has oversimplified the evolution transitions of uncinate processes in archosaurs into two steps: emergence of cartilaginous uncinate processes and ossified uncinate processes, respectively. With histological evidence provided in this study, we interpret that an increase in vascularisation and development of lamellar bone at uncinate scars are modifications of the vertebral ribs related to the attachments of uncinate processes. Though only two extant and no less than four fossil dinosaurs have been sampled in this study, occurrence of the modifications of cortex at attachment sites of uncinate processes can be used as points of reference for an improved version of the hypothetical evolutionary scenario of uncinate processes leading to birds.

Cartilaginous uncinate processes are likely present in ancestral archosaurs, which most likely increased in mechanical advantages for ventilatory muscles to expand the ribcage and potentially strengthen the structural stability of the trunk as predicted by two-dimensional

biomechanical models (Zimmer 1935; Tickle et al. 2007). If *Cai. crocodilus* (UAMZ unnumberd) can represent the ancestral condition of archosaurs, the cartilaginous uncinate processes carried by the ancestral archosaurs would be anchored to the vertebral ribs by a group of coarse Sharpey's fibres positioned on the rib's posterior aspect near midshaft. Development of lamellar bones at the uncinate scars are likely acquired on the paths to cerapodans, as observed in the sampled cerapodans. Lamellar bones are laid down at a relatively slow rates compared to primary bones (Hall 2005), and more precisely arranged lamellar bone can withstand greater mechanical stress in favoured directions before yielding to elastic deformations (Weiner and Wagner 1998; Currey 2003). The presence of lamellar bones at the uncinate scars in cerapodans may therefore be osteogenic adaptations to meet the demands of mechanical stresses imposed on the uncinate processes by ventilatory muscles. An increase in vascularisation at the uncinate scars in the form of several canals as observed in Hadrosauridae indet. (UALVP 60005) may be acquired after ornithopods diverge from ceratopsians, potentially as an adaptation in ornithopods. Alternatively, the increased vascularization may be acquired in ancestral cerapodans, which was subsequently retained in ornithopods and secondarily lost in ceratopsians. The ancestral condition of cerapodans notwithstanding, an increase in vascularisation at the attachment sites of uncinate process provides an anatomical condition in which mineralisation of the cartilaginous uncinate processes may take place via invading blood vessels or cartilage canals (Dai and Rabie 2007; Sivaraj and Adams 2016; Filipowska et al. 2017). This in turn may explain the comparative high number of mineralised uncinate processes preserved in ornithopods (Butler and Galton 2008; Boyd et al. 2011). An increase in vascularisation at uncinate scars in the form of multiple irregularly shaped canals was likely acquired in tyrannosaurids, which may be independent from that in ornithopods unless increased vascularisation at uncinate scars is an ancestral condition for Dinosauria. If the condition observed in the sampled tyrannosaurids represent the general condition of theropods carrying cartilaginous uncinate processes, the high number of vascular canals likely provide an anatomical condition for uncinate processes to be ossified in *Pelecanimimus polyodon* and penneraptorans leading to birds (Codd et al. 2008; Cuesta et al. 2022). As an increase in vascularisation at uncinate scar is not unique to tyrannosaurids, and by our inferred extension theropods, other osteogenic factors were likely present to promote the evolutionary step from mineralisation to ossification of uncinate processes. Further sampling is admitted warranted to test the hypothetical scenario presented

here. We can nevertheless conclude with the histological evidence in this study that attachment sites of uncinate processes are most definitely not conservative, but instead have likely been subjected to natural selections and remained as a functional anatomical component favoured by natural selection on the evolutionary paths to extant birds.

Table

Table 5. 1. Number of histology sections sampled from individual taxon in this study.

Taxa	Number of sections	Orientation of the sections *	Position relative to uncinate scar
***Meleagris gallopavo* (UALVP unnumbered)**	5	Longitudinal	At uncinate scar
	5	Transverse	At uncinate scar
	4	Transverse	Away from uncinate scar
***Caiman crocodilus* (UALVP unnumbered)**	2	Longitudinal	Away from uncinate scar
	12	Transverse	At uncinate scar
	2	Transverse	Away from uncinate scar
Tyrannosauridae indet. (TMP 51.81.16.285)	10	Transverse	At uncinate scar
	2	Transverse	Away from uncinate scar
***Albertosaurus sarcophagus* (TMP 99.52.42)**	8	Transverse	At uncinate scar
Tyrannosauridae indet. (TMP 94.12.960)	6	Transverse	At uncinate scar
	4	Transverse	Away from uncinate scar
Hadrosauroidea indet. (TMP 6005)	6	Transverse	At uncinate scar
	2	Transverse	Near uncinate scar
***Pachyrhinosaurus lakustai* (PSC 2014.060)**	7	Transverse	At uncinate scar
	4	Transverse	Away from uncinate scar
***Centrosaurus* sp. (TMP 82.18.16)**	7	Transverse	At uncinate scar
	1	Longitudinal	At uncinate scar
***Centrosaurus* sp. (TMP 96.1776.135)**	7	Transverse	At uncinate scar

* Longitudinal and transverse refer to sections parallel and perpendicular to the long axis of the vertebral ribs, respectively.

Figures

Figure 5.1. Histological thin sections of vertebral ribs through uncinate process in *Meleagris gallopavo* (UAMZ unnumbered).

Transverse thin section T 1 – 1 of dorsal vertebral rib and right dorsal vertebral rib in lateral view showing the approximate anatomical position of thin section (A); close-up of the thin section T 1 – 1 showing zones of ossifications within uncinate process (B), contact between uncinate process and vertebral rib at the uncinate scar (C), periosteum lateral to uncinate process (D); thick cambium layer of periosteum (E), mesenchymal tissues (F), and capillaries (G) near uncinate scar; a right dorsal vertebral rib of *Me. gallopavo* (UAMZ 1824) in lateral view showing the approximate anatomical position of thin section T 1 – 4 (H); overview of longitudinal thin section T 1 – 4 (I), and close-up of longitudinal thin section T 1 – 4, showing zones of ossification within uncinate process (J), and contact between uncinate process and vertebral rib at uncinate scar (K). Panels A – G, H – J are captured under normal light, and panel K is captured under cross polarised light. Single capitalised letters indicate the approximate locations of close-ups. Red triangles point at tidemarks between mineralised and unmineralized cartilages. Dark cyan triangles point at cement lines between primary and mature bones. Abbreviations: bm mature bones, bp primary bones, bv pathways containing blood vessels, ca capillaries, me mesenchymal tissues, pc cambium layer of the periosteum, pf fibrous layer of the periosteum, up uncinate process, vr vertebral rib, zb zone of bones, zh, zone of hyaline cartilage, zm, zone of mineralised cartilages, zp, zone of proliferated cartilages, zy zone of hypertrophic.

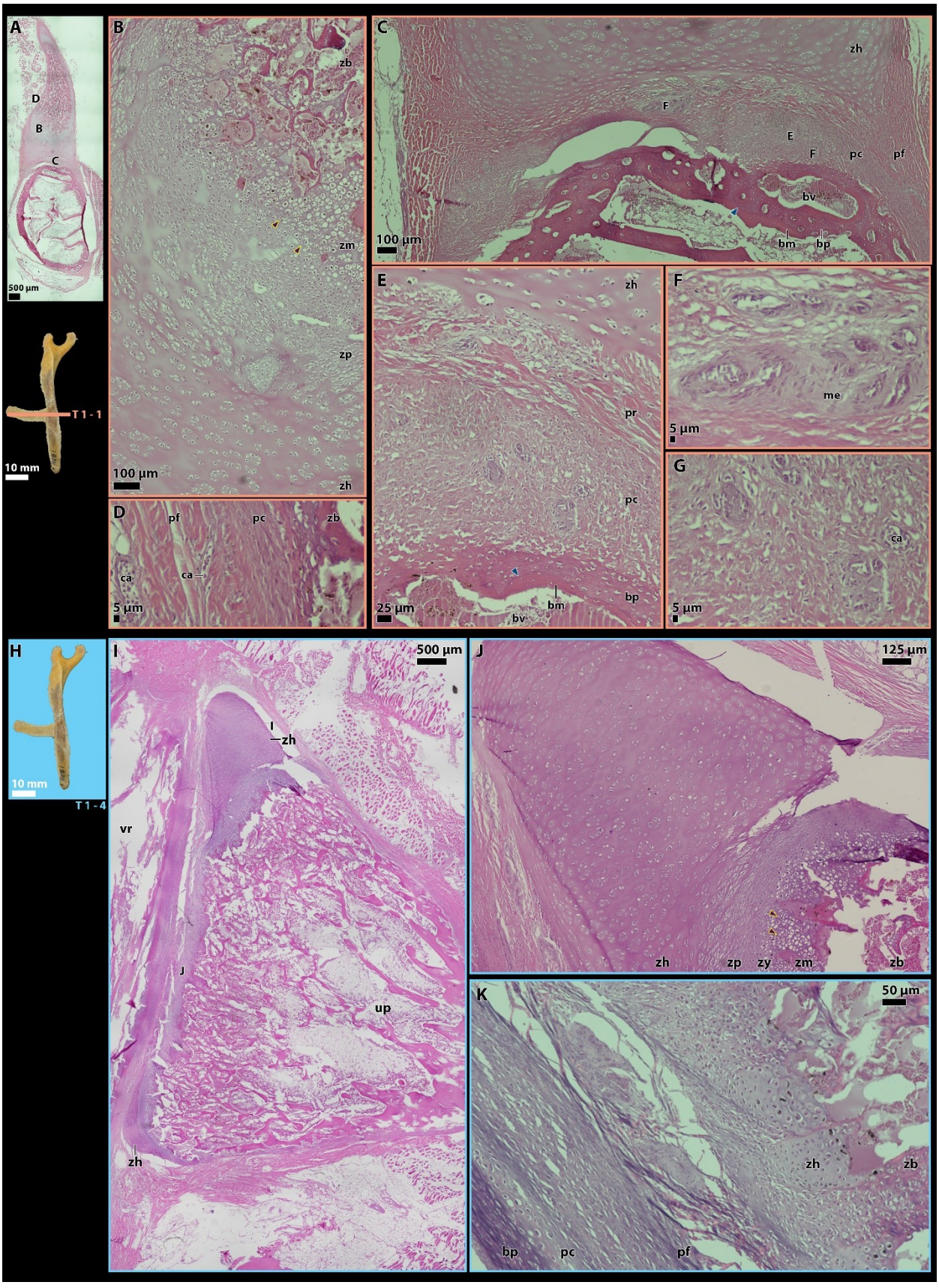
A
D
B
C
500 µm
T1 - 1
10 mm
B
zb
zm
zp
100 µm
zh
C
zh
F
E
F
pc
pf
bv
100 µm
bm
bp
D
pf
pc
zb
ca
ca
5 µm
E
zh
pr
pc
bp
25 µm
bm
bv
F
me
5 µm
G
ca
5 µm
H
10 mm
T1 - 4
I
500 µm
I
zh
vr
J
up
zh
J
125 µm
zh
zp
zy
zm
zb
K
50 µm
zh
zb
bp
pc
pf

Figure 5.2. Histological thin sections of vertebral ribs through uncinate process in *Meleagris gallopavo* (UAMZ unnumbered).

Transverse thin section T 1 – 4 of dorsal vertebral rib and a right dorsal vertebral rib in lateral view showing approximate anatomical position of thin sections (A); close-up of transverse thin section T 1 – 4, showing orientations of collagen and Sharpey's fibres near uncinate scar (B), circumferential collagen fibres near uncinate scar (C, D), coarse Sharpey's fibres anchoring cambium layer of periosteum to primary bones (E); longitudinal thin section T 1 – 4 and a right dorsal vertebral rib of *Me. gallopavo* (UAMZ 1824) in lateral view, showing approximate anatomical position of thin section (F); close-up of longitudinal thin section T 1 – 4, showing orientation of Sharpey's fibres within primary bones of vertebral rib (G) and close-up of Sharpey's fibres within primary bones of vertebral rib at different extinction angles (H). Panel A and F are captured under normal light, and the rests are captured under cross polarised light. Single capitalised letters indicate the approximate locations of close-ups. Black and white triangles point at collagen and Sharpey's fibres appearing as dark and light fibres at specific extinction angles, respectively. Abbreviations: bm mature bones, bp primary bones, bv pathways containing blood vessels, ca capillaries, pc cambium layer of the periosteum, pf fibrous layer of the periosteum, up uncinate process, vr vertebral rib.

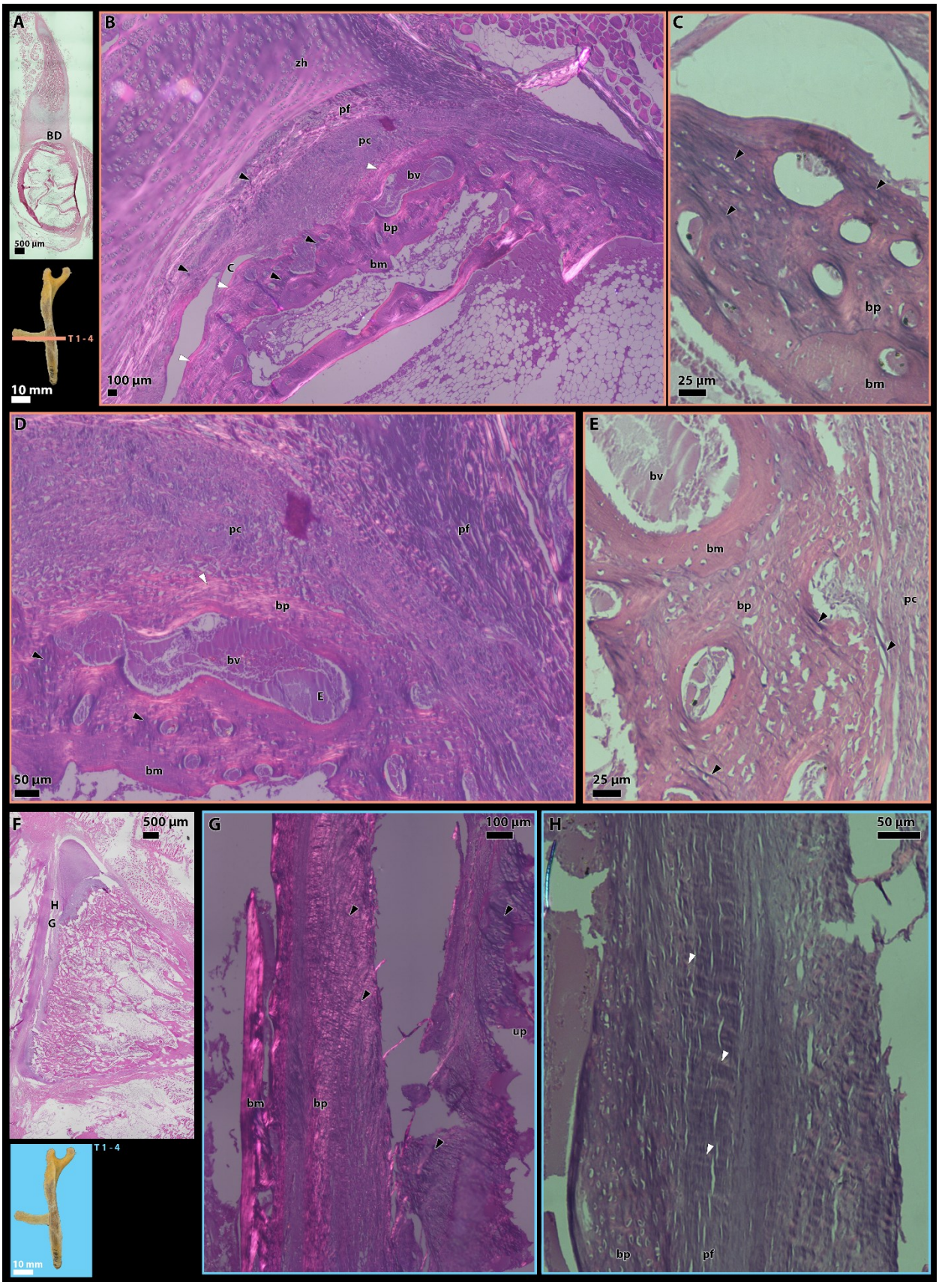
A
BD
500 µm
T1 - 4
10 mm
B
zh
pf
pc
bv
bp
bm
C
100 µm
C
bp
bm
25 µm
D
pc
pf
bp
bv
E
bm
50 µm
E
bv
bm
bp
pc
25 µm
F
500 µm
H
G
T1 - 4
10 mm
G
100 µm
up
bm
bp
H
50 µm
bp
pf

Figure 5.3. Histological thin sections of vertebral ribs away from uncinate process in *Meleagris gallopavo* (UAMZ unnumbered).

Transverse thin section T 1 – 1 of dorsal vertebral rib and a right dorsal vertebral rib in lateral view showing approximate anatomical position of thin sections (A); close-up of transverse thin section T 1 – 1, showing coarse collagen fibres from lateral aspect of vertebral rib (B), fine collagen fibres from anterior aspect of vertebral rib (C), and blood vessels and capillaries with thin (D), medium (E), and thick (F) walls; transverse thin section T 2 – 2, showing tissues (G) and fibres (H) of periosteum and cortex of vertebral rib near its distal end. Panel A, D, E, F, G are captured under normal light, and panel B, C, H are captured under cross polarised light. Single capitalised letters indicate the approximate locations of close-ups. Black triangles point at collagen fibres at specific extinction angles. Abbreviations: bm mature bones, bp primary bones, bv pathways containing blood vessels, ca capillaries, pc cambium layer of the periosteum, pf fibrous layer of the periosteum.

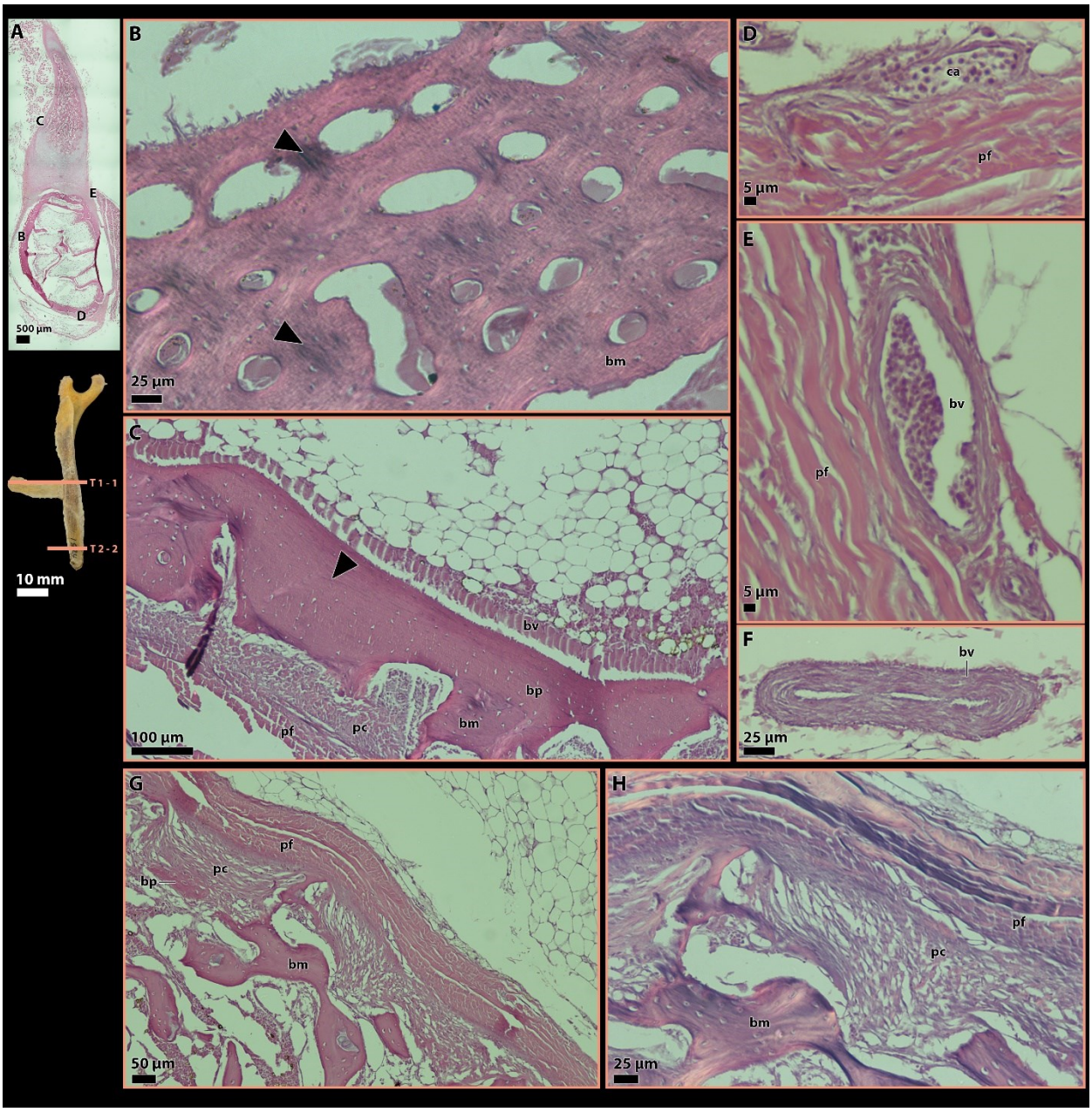
A
C
E
B
D
500 µm
T1 - 1
T2 - 2
10 mm
B
25 µm
bm
C
bv
bp
pf
pc
bm
100 µm
D
ca
pf
5 µm
E
bv
pf
5 µm
F
bv
25 µm
G
pf
pc
bp
bm
50 µm
H
pf
pc
bm
25 µm

Figure 5.4. Histological thin sections of vertebral rib through uncinate process in *Caiman crocodilus* (UAMZ unnumbered).

Transverse thin section T 2 – 2 and first right dorsal vertebral rib in lateral view, showing the approximate anatomical position of thin sections (A); close-up of transverse thin section T 2 – 1, showing cartilaginous uncinate process and surrounding soft connective tissues (B), approximate junction between cartilaginous uncinate process and perichondrium (C, D), contact between uncinate process and vertebral rib at uncinate scar (E), contact between primary and mature bones near uncinate scar (F). All panels except panel D are captured under normal light, and panel D is captured under cross polarised light. Single capitalised letters indicate the approximate locations of close-ups. Sky blue triangles point at approximate locations of perichondrium, and dark cyan triangles point at cement lines between primary and mature bones. Abbreviations: bm mature bones, bp primary bones, bv pathway for blood vessels, cdi dense irregular connective tissues, pf fibrous layer of periosteum, ph perichondrium, up uncinate process.

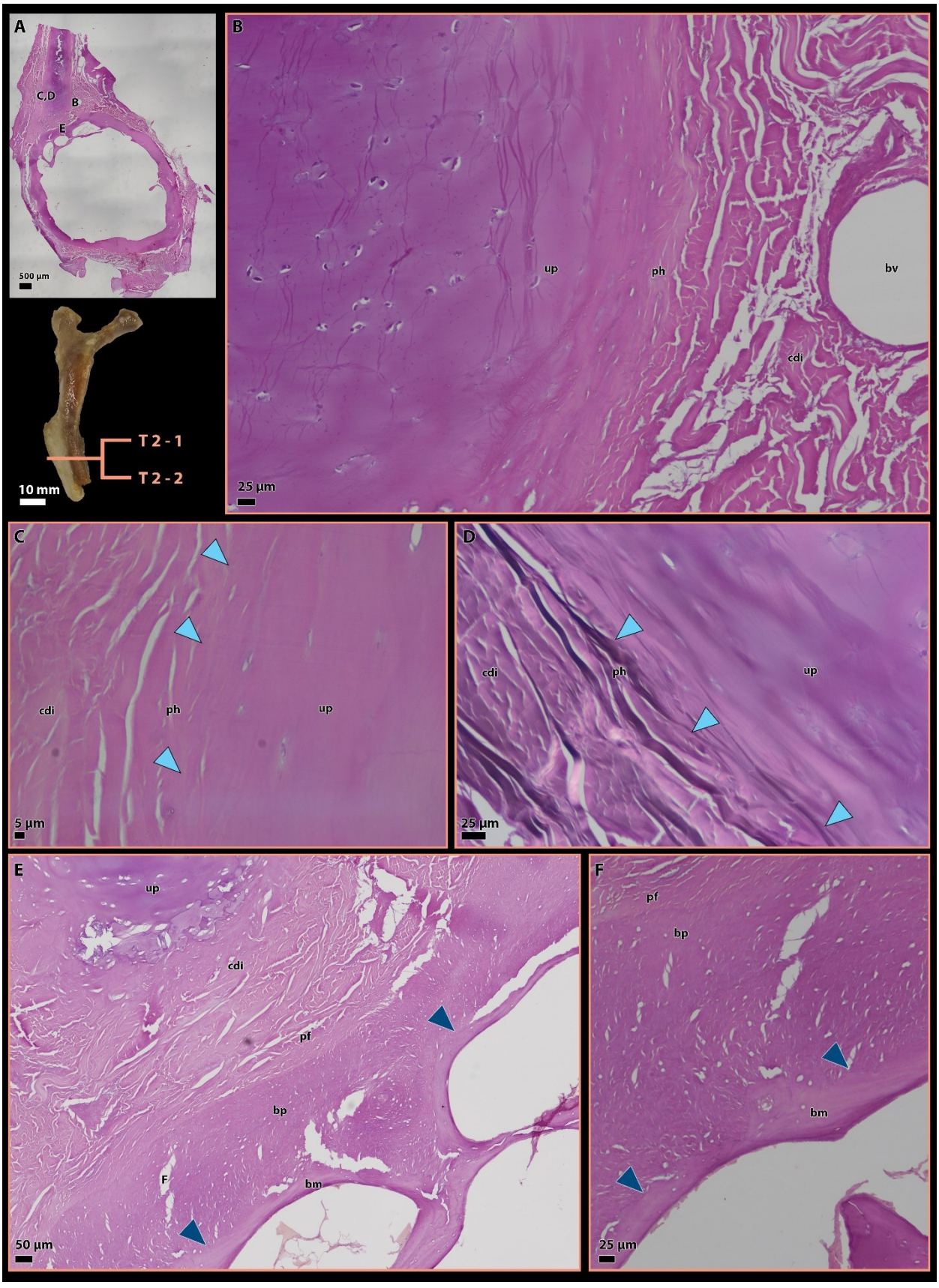
A
C,D
B
E
500 µm
T2-1
T2-2
10 mm
B
up
ph
bv
cdi
25 µm
C
cdi
ph
up
5 µm
D
cdi
ph
up
25 µm
E
up
cdi
pf
bp
F
bm
50 µm
F
pf
bp
bm
25 µm

Figure 5.5. Histological thin sections of vertebral ribs through uncinate processes in *Caiman crocodilus* (UAMZ unnumbered).

First and second right dorsal vertebral ribs in lateral views, showing the approximate anatomical positions of thin sections (A); transverse thin section T 2 – 1, showing Sharpey's fibres within primary bones near uncinate scar (B); transverse thin section T 3 – 5, showing collagen and Sharpey's fibres within primary bones near uncinate scar (C), and close-up of contact between cartilaginous uncinate process and vertebral rib at two angels of extinctions (D, E), coarse Sharpey's fibres blending with periosteum and perichondrium (F), Sharpey's fibres anchoring periosteum to primary bones of vertebral rib (G); transverse thins section T 2 – 3, showing Sharpey's fibres terminating at contacts with periosteum of vertebral rib (H). Panel A is captured under normal light, and the rests are captured under cross polarised light. Single capitalised letters indicate the approximate locations of close-ups. Black and white triangles point at collagen and Sharpey's fibres appearing as dark and light fibres at specific extinction angles, respectively. Abbreviations: bm mature bones, bp primary bones, bv pathway for blood vessels, cdi dense irregular connective tissues, pf fibrous layer of periosteum, up uncinate process.

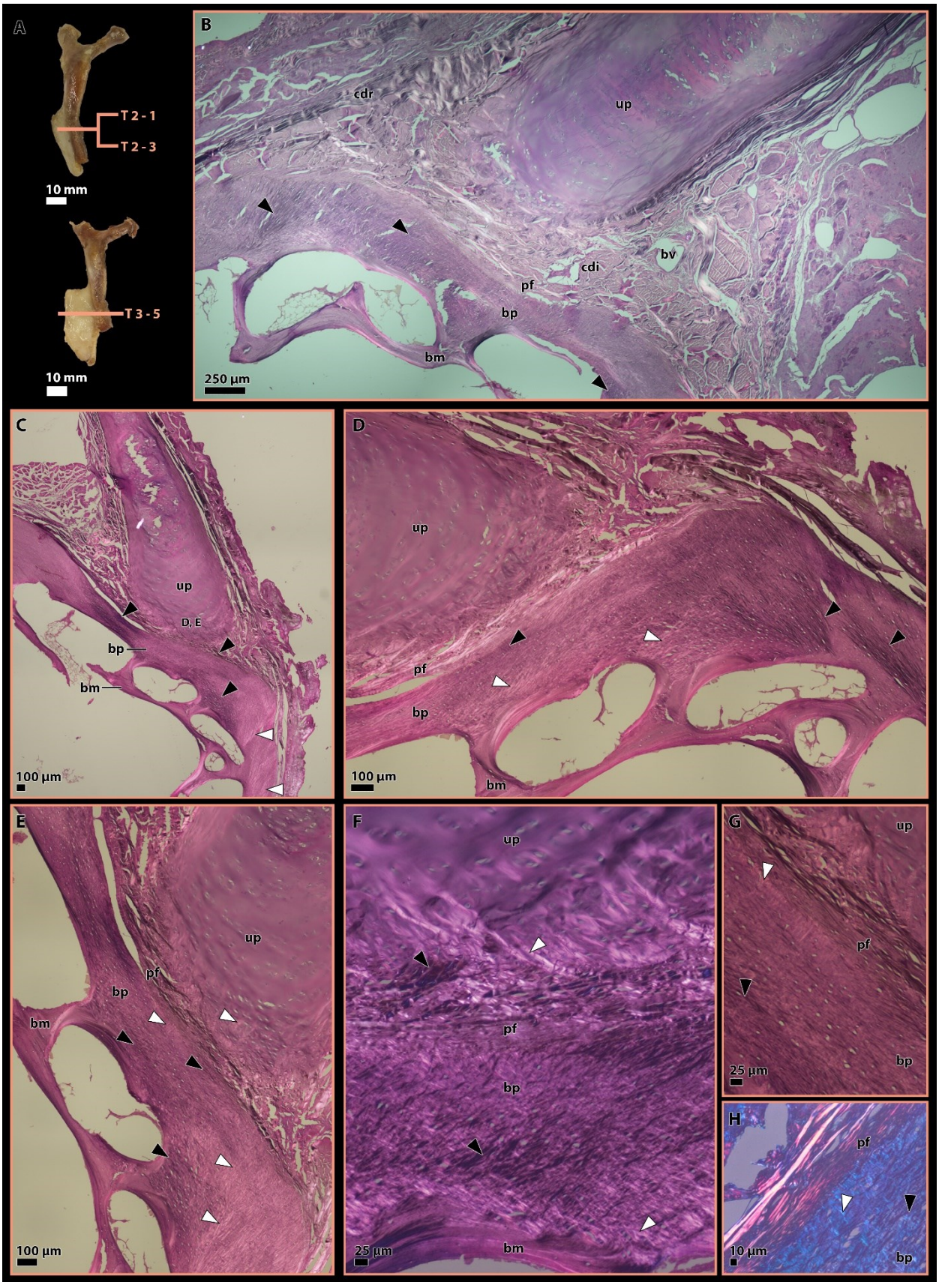
A
T2-1
T2-3
10 mm
T3-5
10 mm
B
cdr
up
bv
cdi
pf
bp
bm
250 µm
C
up
D, E
bp
bm
100 µm
D
up
pf
bp
100 µm
bm
E
up
pf
bp
bm
100 µm
F
up
pf
bp
25 µm
bm
G
up
pf
25 µm
bp
H
pf
10 µm
bp

Figure 5.6. Histological thin sections of vertebral ribs away from uncinate process in *Caiman crocodilus* (UAMZ unnumbered).

Transverse thin section T 4 – 2 and first and second right dorsal vertebral rib in lateral view, showing the approximate anatomical position of thin sections (A); close-up of transverse thin section T 4 – 2, showing periosteum of vertebral rib proximal to uncinate scar (B), cambium layer of periosteum (C), fine Sharpey's fibres within periosteum and collagen fibres within primary bones of vertebral rib (D), and collagen fibres in primary bones proximal to uncinate scar (E); transverse thin section T 2 – 1, showing coarse Sharpey's fibres in primary bones from anterior aspect of first vertebral rib (F), and close-up of coarse Sharpey's fibres penetrating into muscles (G), coarse collagen fibres within primary bones (H); transverse thin section T 3 – 9, showing collagen and Sharpey's fibres within primary bones from anteromedial aspect of second right dorsal vertebral rib. Panels A – C are captured under normal light, and the rests are captured under cross polarised light. Single capitalised letters indicate the approximate locations of close-ups. Black and white triangles point at collagen and Sharpey's fibres appearing as dark and light fibres at specific extinction angles, respectively. Abbreviations: bm mature bones, bp primary bones, mu muscle, pc cambium layer of periosteum, pf fibrous layer of periosteum.

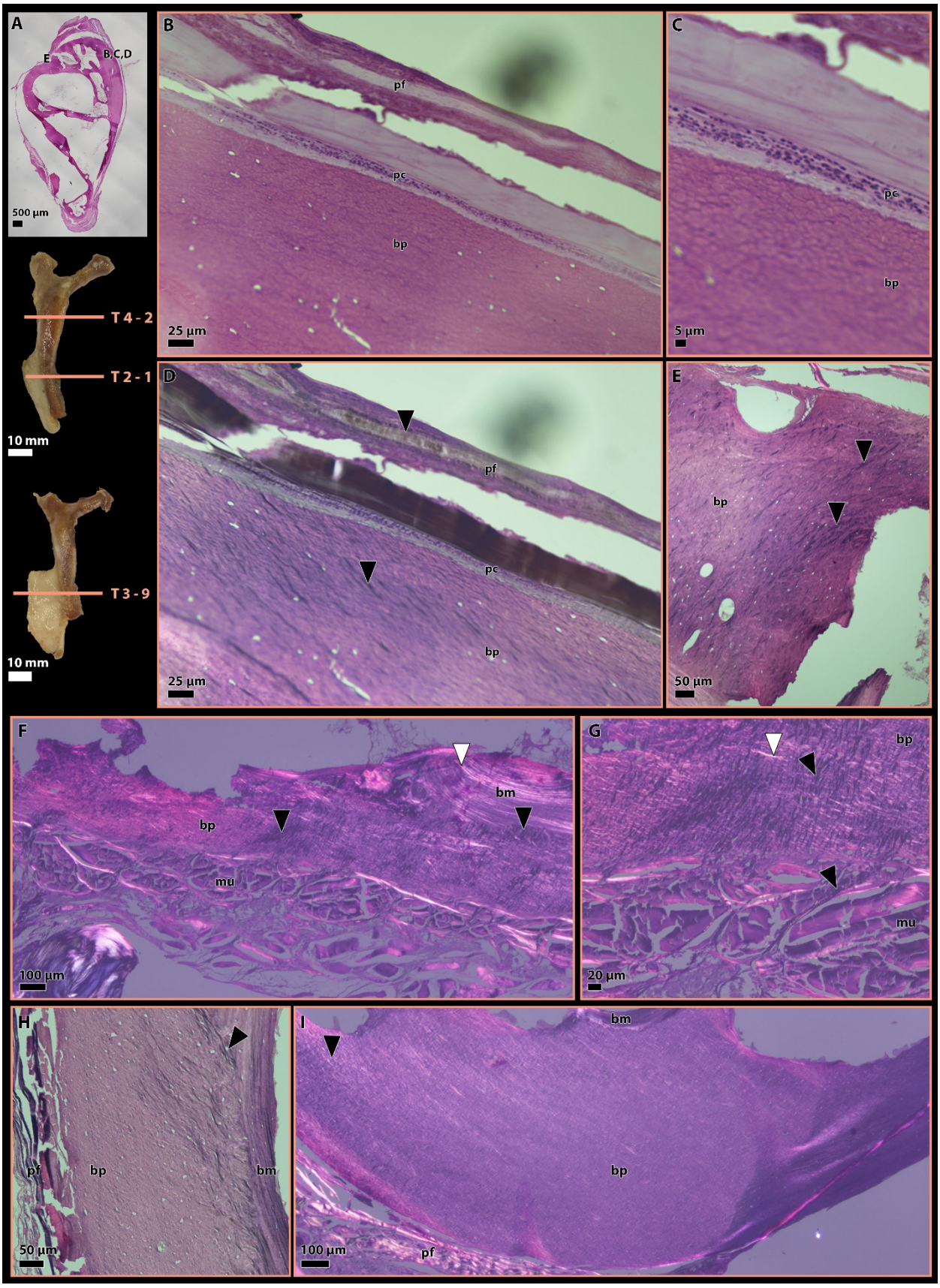
A
E
B,C,D
500 µm
T4-2
T2-1
10 mm
T3-9
10 mm
B
pf
pc
bp
25 µm
C
pc
bp
5 µm
D
pf
pc
bp
25 µm
E
bp
50 µm
F
bm
bp
mu
100 µm
G
bp
mu
20 µm
H
pf
bp
bm
50 µm
I
bm
bp
100 µm
pf

Figure 5.7. Histological thin sections of vertebral rib near uncinate scar in Tyrannosauridae indet. (TMP 51.81.16.285).

Left dorsal vertebral rib in anterior view, showing approximate anatomical position of thin section (A); transverse thin section T 2 – 3, showing an increase in vascularisation of cortex adjacent to uncinate scar (B), and close-up of proximal ridge of uncinate scar (C), coarse Sharpey's fibres at proximal ridge of uncinate scar (D), coarse Sharpey's fibres throughout the primary bones at and adjacent to uncinate scar (E), coarse Sharpey's fibres adjacent to proximal ridge of uncinate scar (F), and further close-up on a single bundle of coarse Sharpey's fibres (G); close-up of transverse thin section T 2 – 3, showing transitions from high quantity of coarse Sharpey's fibres at uncinate scar to relatively low quantity at lateral aspect of rib's cortex. Panels A – C are captured under normal light, and the rests are captured under cross polarised light. Single capitalised letters indicate the approximate locations of close-ups. Black triangles point at collagen and Sharpey's fibres appearing as dark fibres at specific extinction angles. Abbreviations: bm mature bones, bp primary bones, op primary osteon, pr proximal ridge, us uncinate scar.

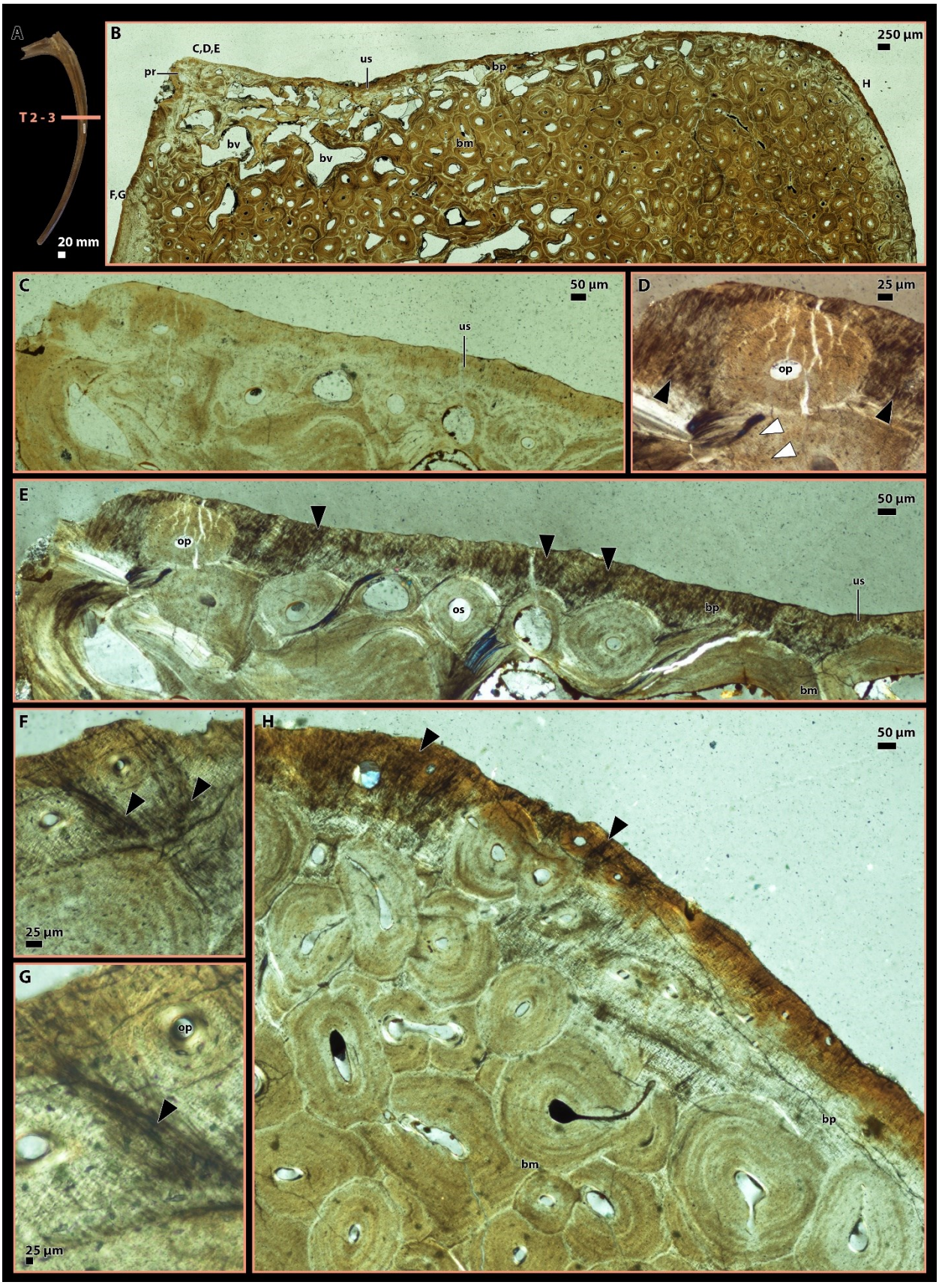
A
T2-3
20 mm
B
C,D,E
pr
us
bp
H
bv
bv
bm
F,G
250 µm
C
50 µm
us
D
25 µm
op
E
50 µm
op
os
bp
us
bm
F
25 µm
G
op
25 µm
H
50 µm
bp
bm

Figure 5.8. Histological thin sections of vertebral rib near uncinate scar in Tyrannosauridae indet. (TMP 94.12.960).

Right dorsal vertebral rib in posterior view, showing the approximate anatomical positions of the thin sections (A); transverse thin section T 4 – 2, showing an increase in vascularisation of cortex at proximal ridge (B), and close-up of coarse Sharpey's fibres at adjacent to uncinate scar (C); transverse thin section T 4 – 3, showing coarse Sharpey's fibres at proximal ridge of uncinate scar (D), close-up of coarse Sharpey fibres adjacent to uncinate scar (E) and further close-up on transverse sections of coarse collagen fibres (F); transverse thin section T 3 – 2, showing transitions of coarse Sharpey's fibres from high quantity at uncinate scar to relatively loo quantity at lateral aspect of rib's cortex. Panel A and B are captured under normal light, and the rest are captured under cross polarised light. Single capitalised letters indicate the approximate locations of close-ups. Black and white triangles point at collagen and Sharpey's fibres appearing as dark and light fibres at specific extinction angles, respectively. Abbreviations: bp primary bones, bv blood vessel, cct transverse sections of coarse collagen fibres, os, secondary osteon, pr proximal ridge, us uncinate scar.

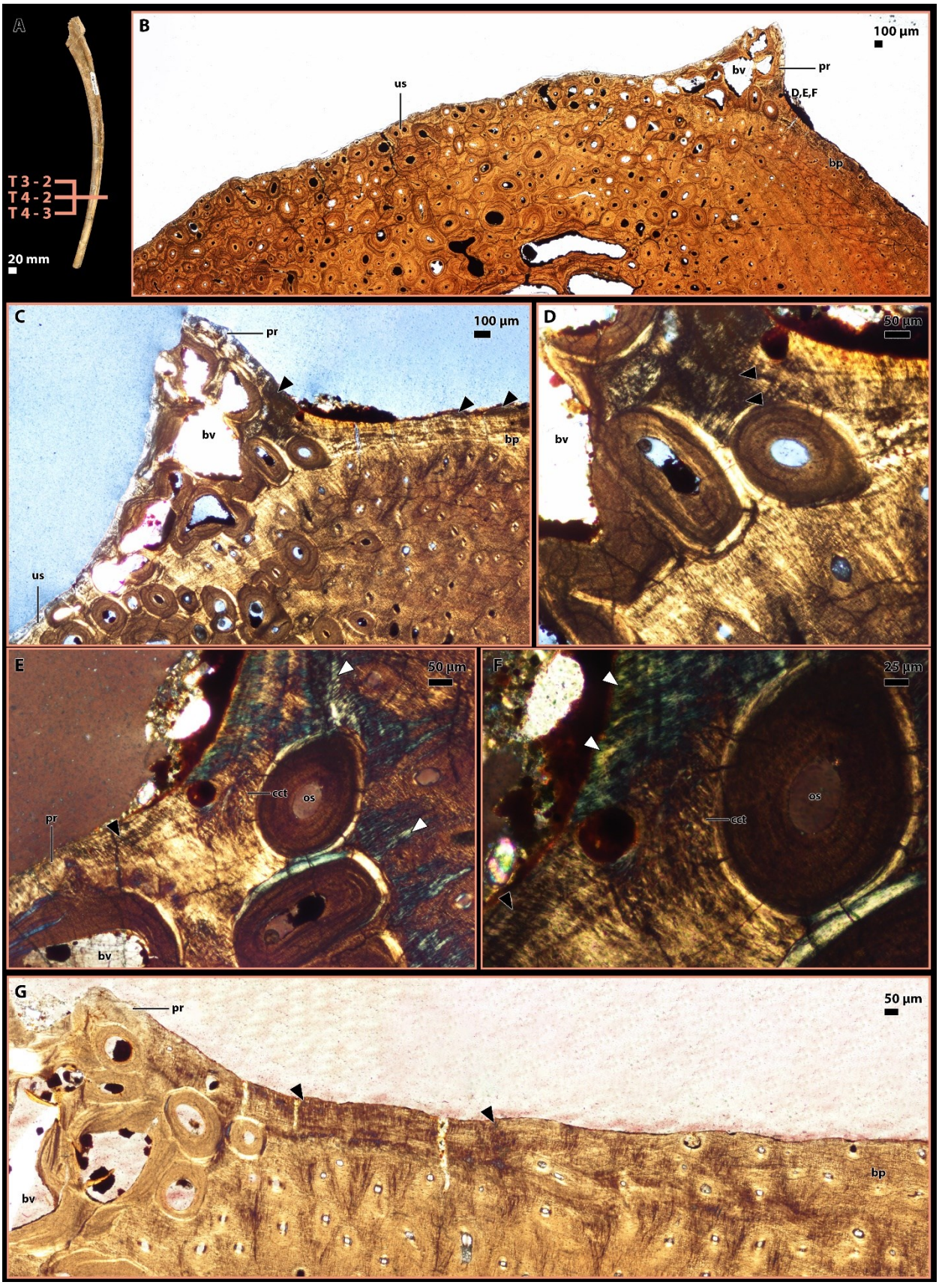
A
T3-2
T4-2
T4-3
20 mm
B
100 µm
us
bv
pr
D,E,F
bp
C
100 µm
pr
bv
bp
us
D
50 µm
bv
E
50 µm
cct
os
pr
bv
F
25 µm
os
cct
G
50 µm
pr
bv
bp

Figure 5.9. Histological thin sections of vertebral rib near uncinate scar in *Albertosaurus sarcophagus* (TMP 99.52.42).

Right dorsal vertebral rib in posterior view, showing the approximate anatomical positions of thin sections (A); transverse thin section T 2 – 4, showing higher quantity of secondary osteons at uncinate scar (B); transverse thin section T 2 – 3, showing coarse Sharpey's fibres at uncinate scar (C), close-up of coarse Sharpey's fibres at uncinate scar (D), and further close-up on several bundles of coarse Sharpey's fibres (E); transverse thin sections T 2 – 5, showing coarse Sharpey's fibres at uncinate scar (F), and close-up of bundles of coarse Sharpey's fibres (G). Panel A is captured under normal light and the rest are captured under cross polarised light. Single capitalised letters indicate the approximate locations of close-ups. Black triangles point at coarse Sharpey's fibres at specific extinction angles. Abbreviations: bp primary bones, os secondary osteons, us uncinate scar.

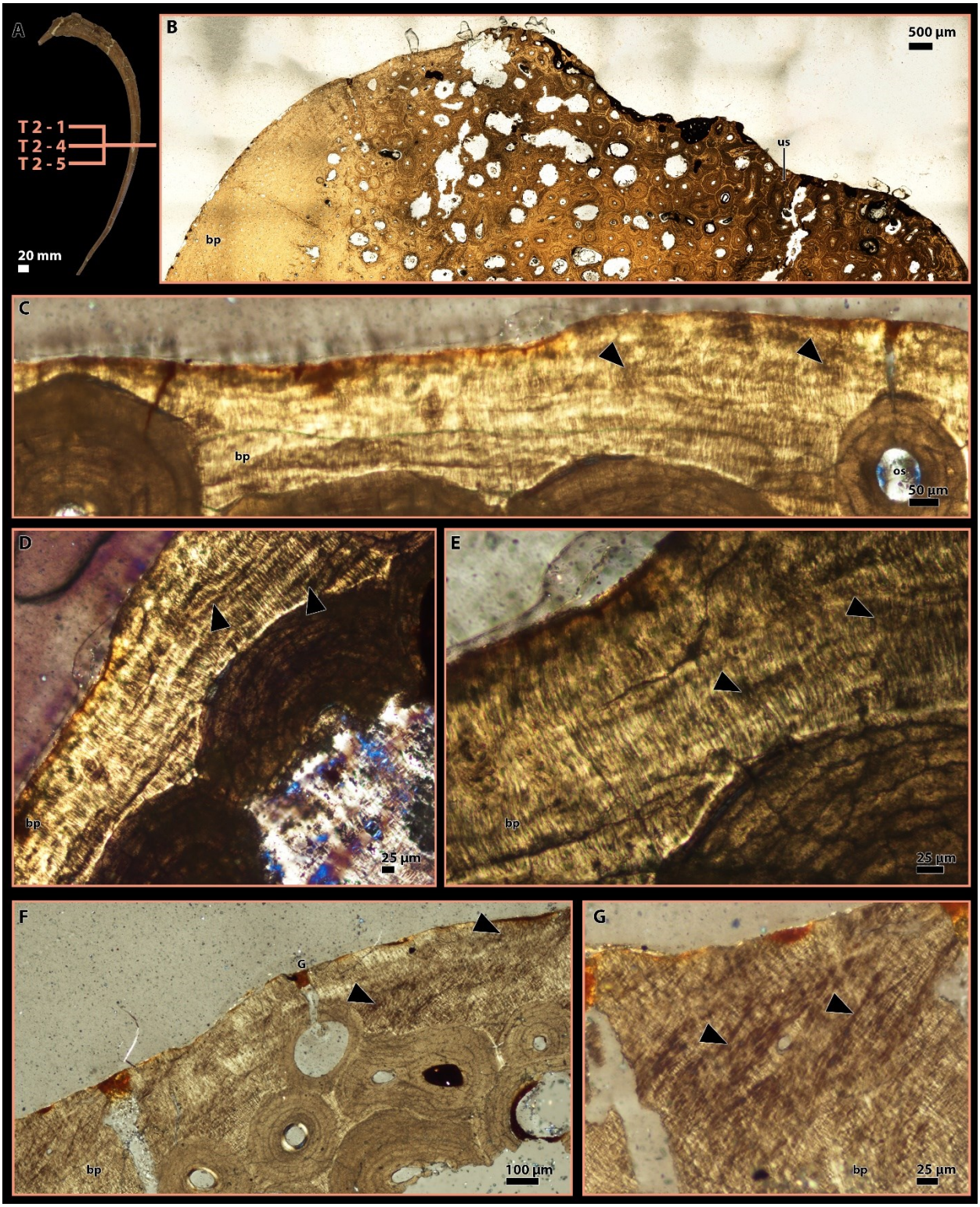
A
T2-1
T2-4
T2-5
20 mm
B
500 µm
us
bp
C
bp
os
50 µm
D
bp
25 µm
E
bp
25 µm
F
G
bp
100 µm
G
bp
25 µm

Figure 5.10. Histological thin sections of vertebral ribs away from uncinate scars in three sampled tyrannosaurids.

Left dorsal vertebral rib of Tyrannosaurid indet. (TMP 51.81.16.285) in anterior view, showing approximate anatomical positions of transverse thin sections (A); transverse thin section T 2 – 3, showing primary and mature bones (B) and fine collagen and Sharpey's fibres within primary bones (C); transverse thin section T 1 – 2, showing fine (D) and coarse (E) Sharpey's fibres within primary bones; transverse thin section T 1 – 1, showing coarse Sharpey's fibres within primary bones distal to uncinate scar (F); right dorsal vertebral rib of Tyrannosauridae indet. (TMP 94.12.960) in posterior view, showing approximate anatomical positions of thin sections (G); transverse thin section T 3 – 2, showing coarse Sharpey's fibres away from uncinate scar (H); transverse thin section T 4 – 4, showing fine collagen and Sharpey's fibres away from uncinate scar (I); right dorsal vertebral rib of *Albertosaurus sarcophagus* (TMP 99.52.42) in posterior view, showing approximate anatomical positions of thin sections (J); transverse thin section T 2 – 1, showing fine collagen and Sharpey's fibres away from uncinate scar (K); transverse thin section T 2 – 3, showing coarse collagen fibres away from uncinate scar (L). Panel A, B, G, J are captured under normal light, and the rests are captured under cross polarised light. Single capitalised letters indicate the approximate locations of close-ups. Black triangles point at coarse Sharpey's fibres at specific extinction angles. Abbreviations: bm, mature bones, bp primary bones.

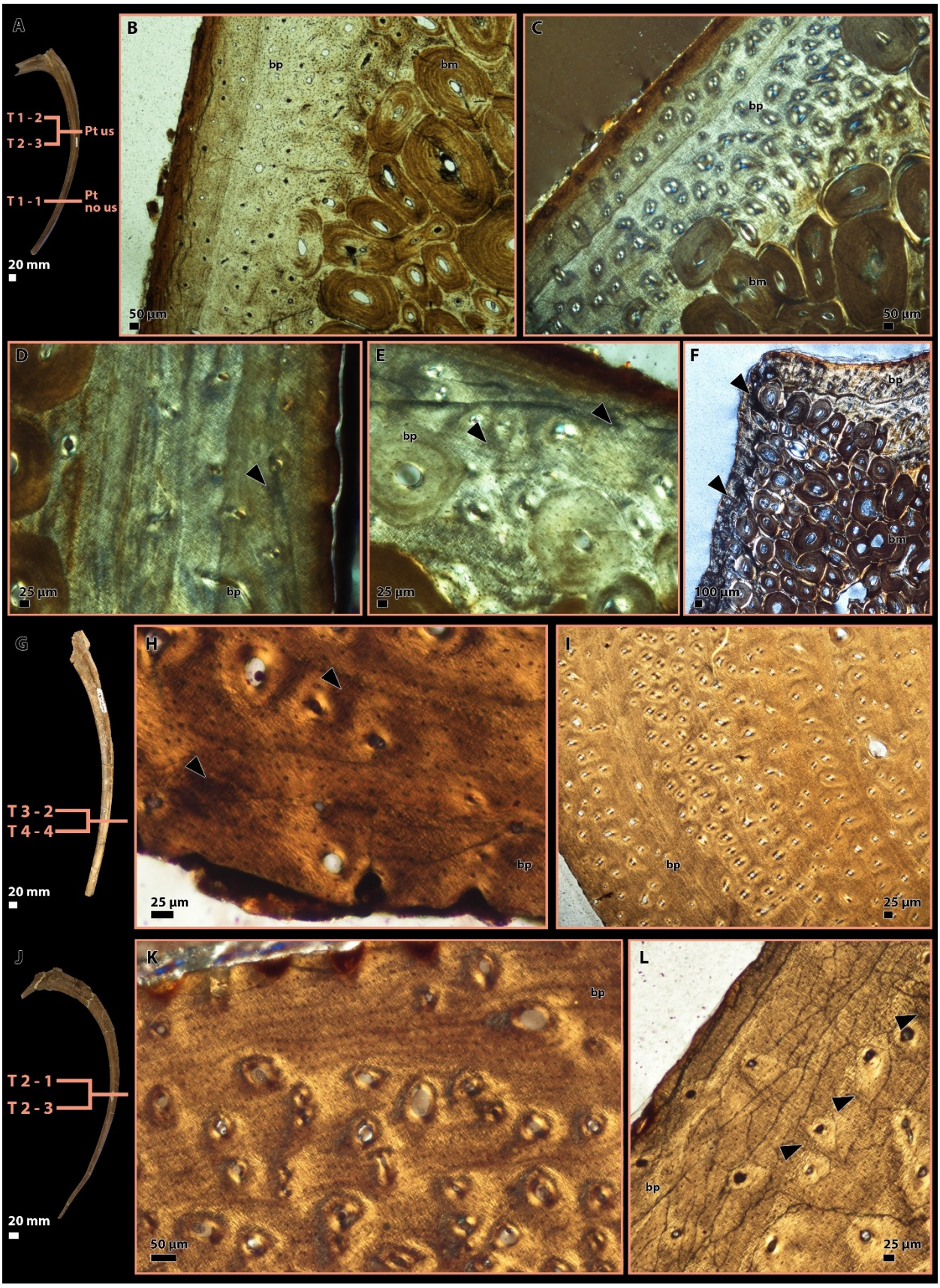
A
T1-2
T2-3
Pt us
T1-1
Pt no us
20 mm
B
bp
bm
50 µm
C
bp
bm
50 µm
D
25 µm
bp
E
bp
25 µm
F
bp
bm
100 µm
G
T3-2
T4-4
20 mm
H
bp
25 µm
I
bp
25 µm
J
T2-1
T2-3
20 mm
K
bp
50 µm
L
bp
25 µm

Figure 5.11. Histological thin sections of vertebral rib near uncinate scar in Hadrosauridae indet. (UALVP 60005).

Dorsal vertebral rib of Hadrosauridae indet. (UALVP 60005) in medial view, showing the approximate anatomical positions of thin sections (A); transverse thin section T 1 – 1, showing primary and mature bones adjacent to uncinate scar (B), and close-up of coarse Sharpey's fibres near uncinate scar (C); transverse thin section T 1 – 2, showing primary and mature bones adjacent to uncinate scar (D), coarse Sharpey's fibres adjacent to uncinate scar (E), close-up of coarse Sharpey's fibres (F), two capillaries within lamellar bones near uncinate scar with connections between capillaries and pathway for blood vessel (G), one capillary within lamellar bones (H), and ; transverse thin section T 2 – 2, showing coarse Sharpey's fibres adjacent to uncinate scar (I), close-up of lamellar bones at uncinate scar (J), and close-up of three capillaries within lamellar bones at uncinate scar (K), coarse Sharpey's fibres next to uncinate scar (L), collagen fibres within lamellar bones (M). Panels B, D, and K are captured under normal light, and the rests are captured under cross polarised light. Single capitalised letters indicate the approximate locations of close-ups. Black and white triangles point at collagen and Sharpey's fibres appearing as dark and light fibres at specific extinction angles, respectively. Red triangles point at capillaries within lamellar bones. Abbreviations: bm mature bones, bp primary bones, bv blood vessel, cct transverse sections of coarse collagen fibres, lb lamellar bones, us uncinate scar.

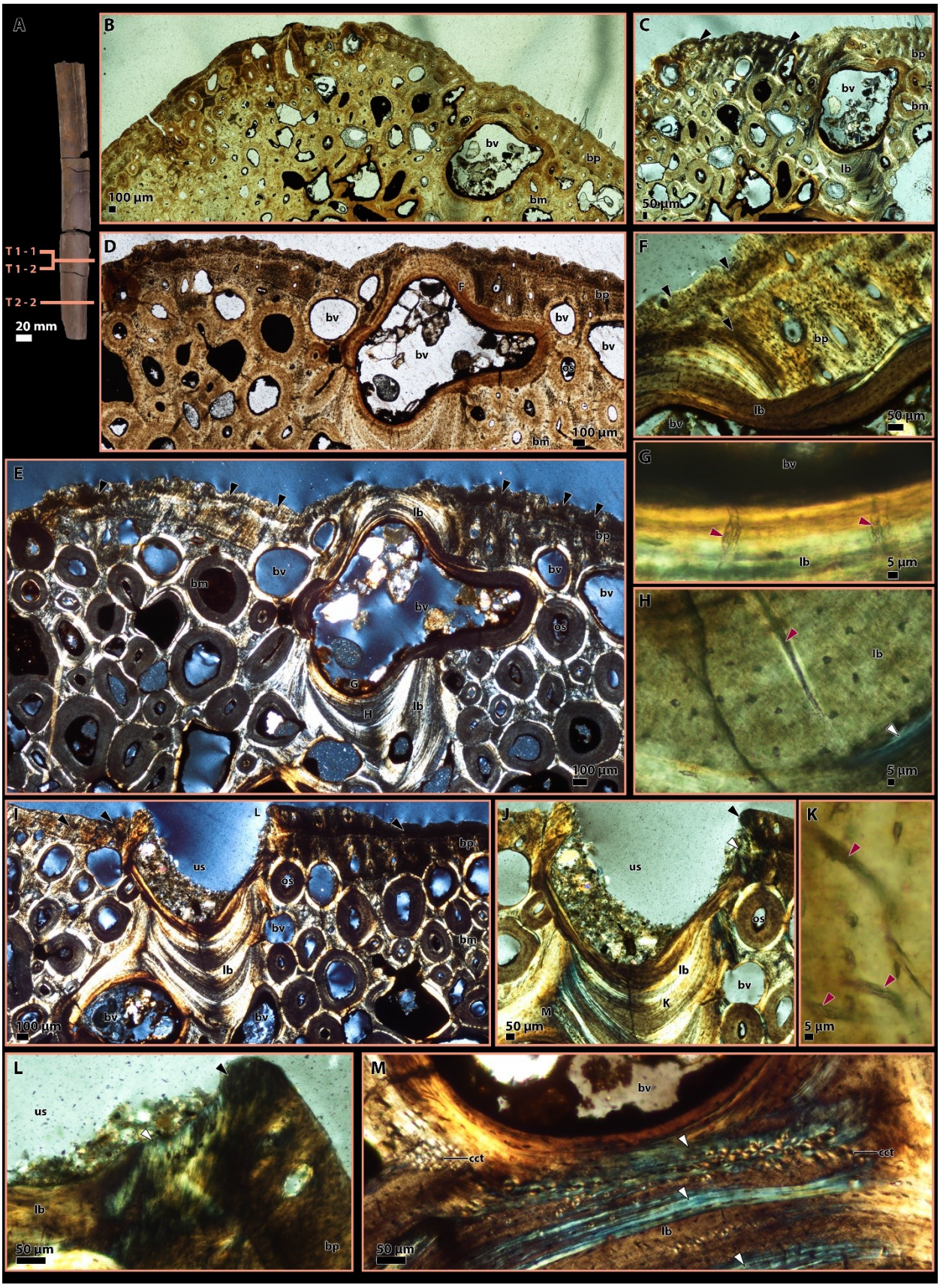
A
T1-1
T1-2
T2-2
20 mm
B
bv
bp
bm
100 µm
C
bp
bv
bm
lb
50 µm
D
F
bp
bv
bv
bv
bv
os
bm
100 µm
F
bp
lb
bv
50 µm
G
bv
lb
5 µm
E
lb
bp
bm
bv
bv
bv
bv
os
G
H
lb
100 µm
H
lb
5 µm
I
L
bp
us
os
bv
bm
lb
bv
bv
100 µm
J
us
os
lb
bv
K
M
50 µm
K
5 µm
L
us
lb
50 µm
bp
M
bv
cct
cct
lb
50 µm

Figure 5.12. Histological thin sections of vertebral rib near uncinate scar in Hadrosauridae indet. (UALVP 6005).

Dorsal vertebral rib of Hadrosauridae indet. (UALVP 60005) in medial view, showing the approximate anatomical positions of thin sections (A); transverse thin section T 2 – 3, showing coarse Sharpey's fibres and lamellar bones adjacent to uncinate scar (B), and coarse Sharpey's fibres near uncinate scar (C), and coarse collagen fibres terminated at lamellar bones adjacent to uncinate scar (D); transverse thin section T 2 – 4, showing coarse Sharpey's fibres and lamellar bones adjacent to uncinate scar (E), close-up of coarse collagen and Sharpey's fibres adjacent to uncinate scar (F); transverse thin section T 3 – 1, showing coarse collagen fibres within lamellar bones at uncinate scar (G), close-up of transverse sections of coarse collagen fibres (H), and one capillary within lamellar bone at uncinate scar (I); transverse thin section T 4 – 1 at distal end of uncinate scar, showing low quantity of coarse Sharpey's fibres (J), and close-up of coarse Sharpey's fibres adjacent to uncinate scar (K); transverse thin section T 1 – 2, showing fine collagen and Sharpey's fibres away from uncinate scar (L); transverse thin section of T 2 – 4, showing Sharpey's fibres away from uncinate scar (M). Panel A is captured under normal light and the rests are captured under cross polarised light. Single capitalised letters indicate the approximate locations of close-ups. Black and white triangles point at collagen and Sharpey's fibres appearing as dark and light fibres at specific extinction angles, respectively. Red triangle points at capillary within lamellar bones. Abbreviations: bm mature bones, bp primary bones, bv blood vessel, cct transverse sections of coarse collagen fibres, lb lamellar bones, us uncinate scar.

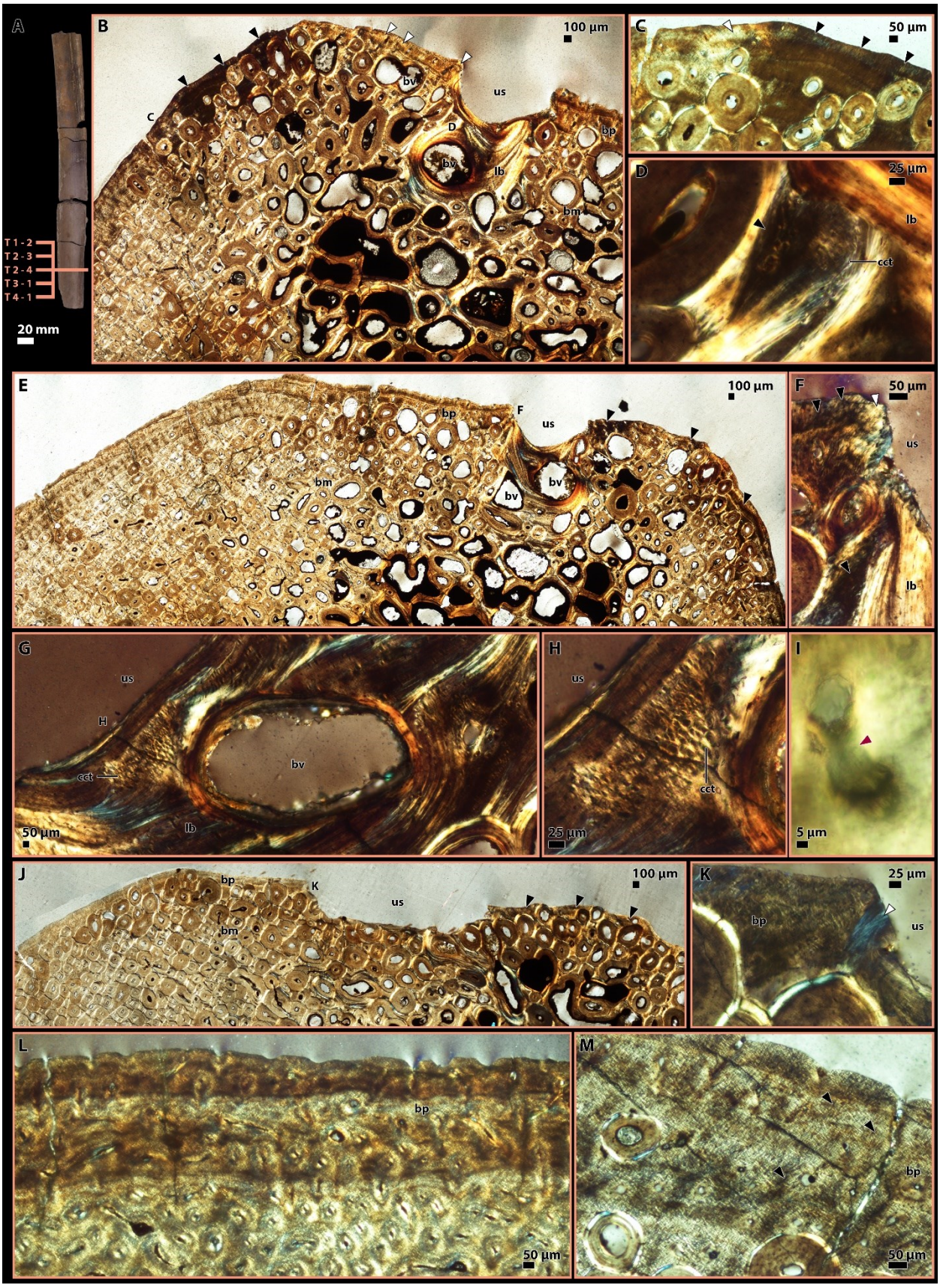
A
T1-2
T2-3
T2-4
T3-1
T4-1
20 mm
B
100 µm
bv
us
C
D
bp
bv
lb
bm
C
50 µm
D
25 µm
lb
cct
E
100 µm
bp
F
us
bm
bv
bv
F
50 µm
us
lb
G
us
H
bv
cct
50 µm
lb
H
us
cct
25 µm
I
5 µm
J
100 µm
bp
K
us
bm
K
25 µm
bp
us
L
bp
50 µm
M
bp
50 µm

Figure 5.13. Histological thin sections of vertebral rib near uncinate scar in *Pachyrhinosaurus lakustai* (PSC 2014.060).

Left dorsal vertebral rib of *Pa. lakustai* (PSC 2014.060), showing the approximate anatomical positions of thin sections (A); transverse thin section T 2 – 1, showing lamellar bones at uncinate scar (B), and close-up of coarse Sharpey's fibres at uncinate scar (C); transverse thin section T 2 – 4, showing lamellar bones and coarse Sharpey's fibres adjacent to uncinate scar (D), and close-up of coarse Sharpey's fibres at uncinate scar (E); transverse thin section T 3 – 1, showing coarse Sharpey's fibres adjacent to uncinate scar (F), and close-ups of coarse Sharpey's fibres next to uncinate scar (G, H); transverse thin section T 3 – 2, showing coarse Sharpey's fibres at uncinate scar (I), and close-up of bundles of coarse Sharpey's fibres (J); transverse thin section T 3 – 3, showing coarse Sharpey's fibres adjacent to uncinate scar (K), and close-up of bundles of coarse Sharpey's fibres (L); transverse thin section T 4 – 1 at distal end of uncinate scar, showing absence of lamellar bones (M), and close-up of coarse Sharpey's fibres adjacent to uncinate scar (N). Panel A and B are captured under normal light, and the rest are captured under cross polarised light. Single capitalised letters indicate the approximate locations of close-ups. Black and white triangles point at collagen and Sharpey's fibres appearing as dark and light fibres at specific extinction angles, respectively. Abbreviations: bm mature bones, bp primary bones, bv blood vessel, lb lamellar bones, us uncinate scar.

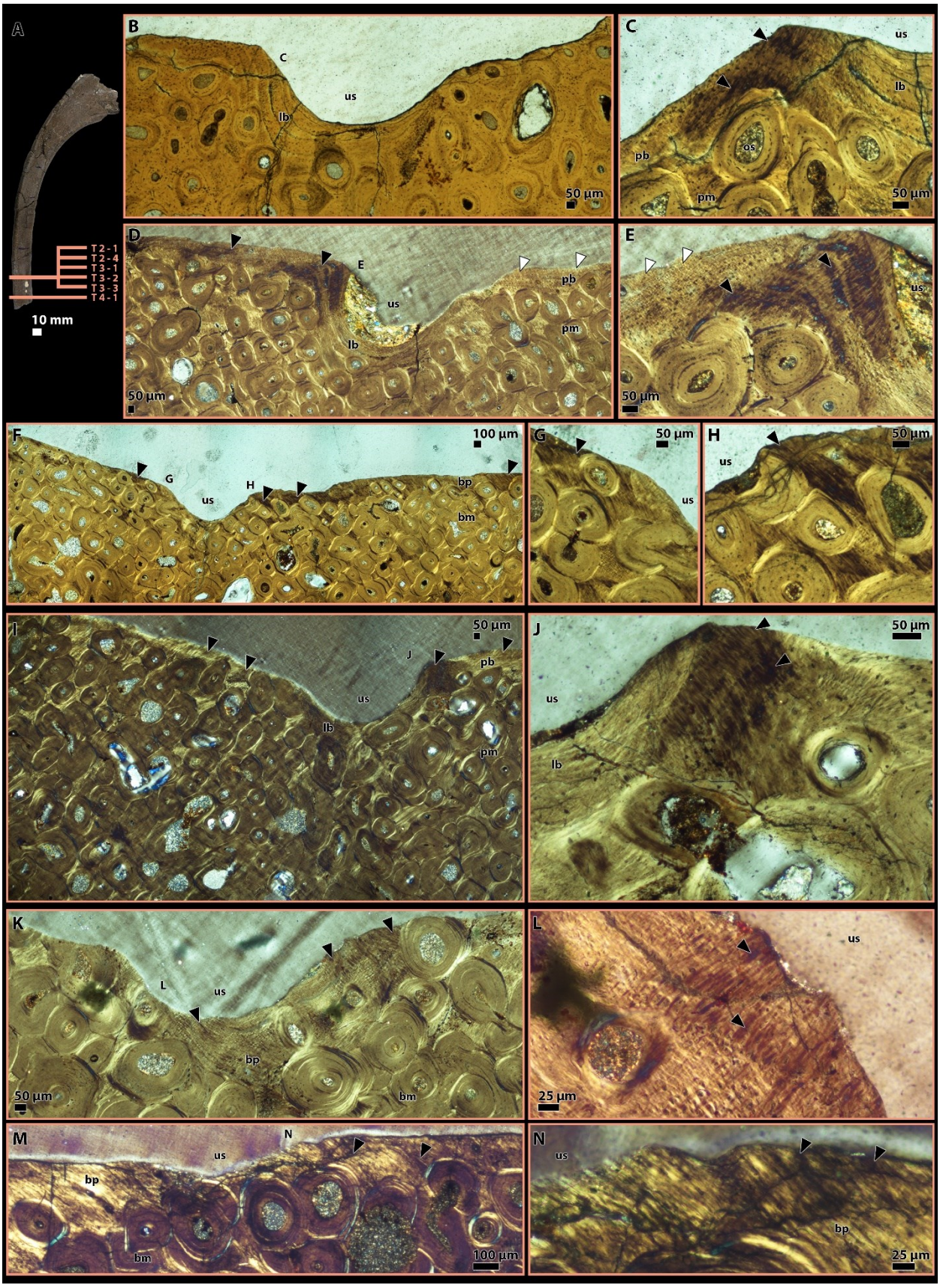
A
T2-1
T2-4
T3-1
T3-2
T3-3
T4-1
10 mm
B
C
us
lb
50 µm
pb
os
pm
D
E
bp
bm
F
100 µm
G
H
I
J
K
L
25 µm
M
N

Figure 5.14. Histological thin sections of vertebral rib near uncinate scar in *Centrosaurus* sp. (TMP 96.1776.135).

Dorsal vertebral rib of *Centrosaurus* sp. (TMP 96.1776.135), showing the approximate anatomical positions of thin sections (A); transverse thin section T 2 – 1, showing the coarse Sharpey's fibres at uncinate scar (B), and close-up of bundles of coarse Sharpey's fibres next to uncinate scar (C); transverse thin section T 3 – 4, showing lamellar bones at uncinate scar (D), coarse Sharpey's fibres at and adjacent to uncinate scar (E), and close-up of coarse Sharpey's fibres at uncinate scar (F); transverse thin section T 4 – 1, showing coarse Sharpey's fibres adjacent to uncinate scar (I), and close-up of bundles of coarse Sharpey's fibres at uncinate scar (H); transverse thin section T 4 – 2, showing coarse Sharpey's fibres adjacent to uncinate scar at two extinction angle (I, K), and close up of transverse sections of collagen fibres (J) and coarse Sharpey's fibres (L) at uncinate scar. Panel A and D are captured under normal light, and the rest are captured under cross polarised light. Single capitalised letters indicate the approximate locations of close-ups. Black and white triangles point at collagen and Sharpey's fibres appearing as dark and light fibres at specific extinction angles, respectively. Abbreviations: bm mature bones, bp primary bones, bv blood vessel, cct transverse sections of coarse collagen fibres, lb lamellar bones, us uncinate scar.

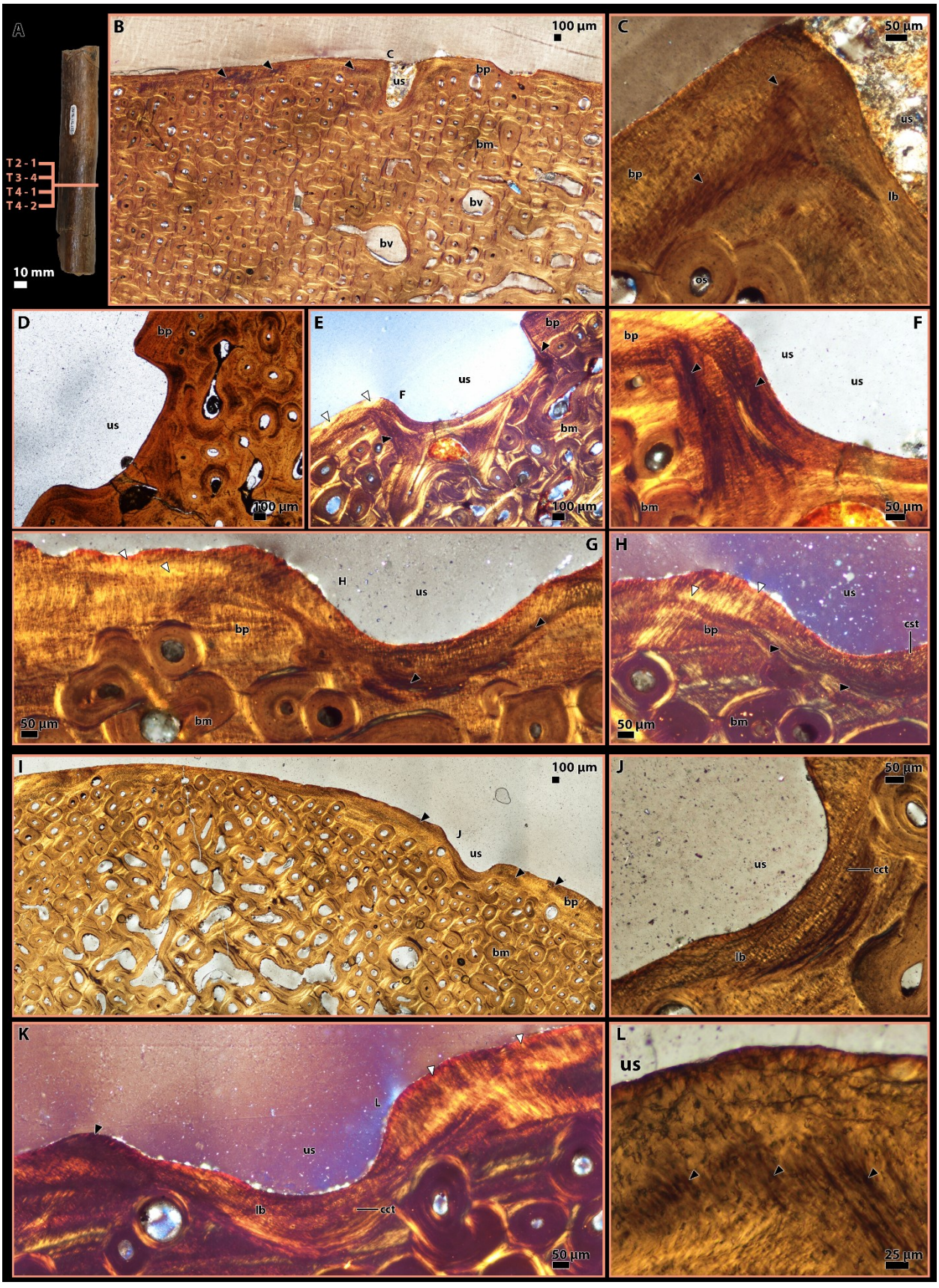
A
T2-1
T3-4
T4-1
T4-2
10 mm
B
100 µm
C
bp
us
bm
bv
bv
C
50 µm
us
bp
lb
os
D
bp
us
100 µm
E
bp
us
F
bm
100 µm
F
bp
us
us
bm
50 µm
G
H
us
bp
50 µm
bm
H
us
bp
cst
50 µm
bm
I
100 µm
J
us
bp
bm
J
50 µm
us
cct
lb
K
L
us
lb
cct
50 µm
L
us
25 µm

Figure 5.15. Histological thin sections of vertebral rib near uncinate scar in *Centrosaurus* sp. (TMP 82.18.16).

Left dorsal vertebral rib in posterior view, showing the approximate anatomical positions of thin sections (A); transverse thin section T 2 – 2, showing thick primary bones adjacent to uncinate scar (B), high quantity of coarse Sharpey's fibres adjacent to uncinate scar (D), and close-ups of coarse Sharpey's fibres at two extinction angels (C, E); transverse thin section T 2 – 4, showing high quantity of coarse Sharpey's fibres adjacent to uncinate scar (F), and close-up of lamellar bones and coarse Sharpey's fibres (G); transverse thin section T 2 – 7, showing high quantity of coarse Sharpey's fibres adjacent to uncinate scar (H), lamellar bones and coarse Sharpey's fibres at uncinate scar (I), further close-ups of coarse Sharpey's fibres at uncinate scar (J, K) and coarse collagen fibres terminated at uncinate scar (L). Panel A and D are captured under normal light, and the rest are captured under cross polarised light. Single capitalised letters indicate the approximate locations of close-ups. Black and white triangles point at collagen and Sharpey's fibres appearing as dark and light fibres at specific extinction angles, respectively. Abbreviations: bm mature bones, bp primary bones, bv blood vessel, cct transverse sections of coarse collagen fibres, lb lamellar bones, us uncinate scar.

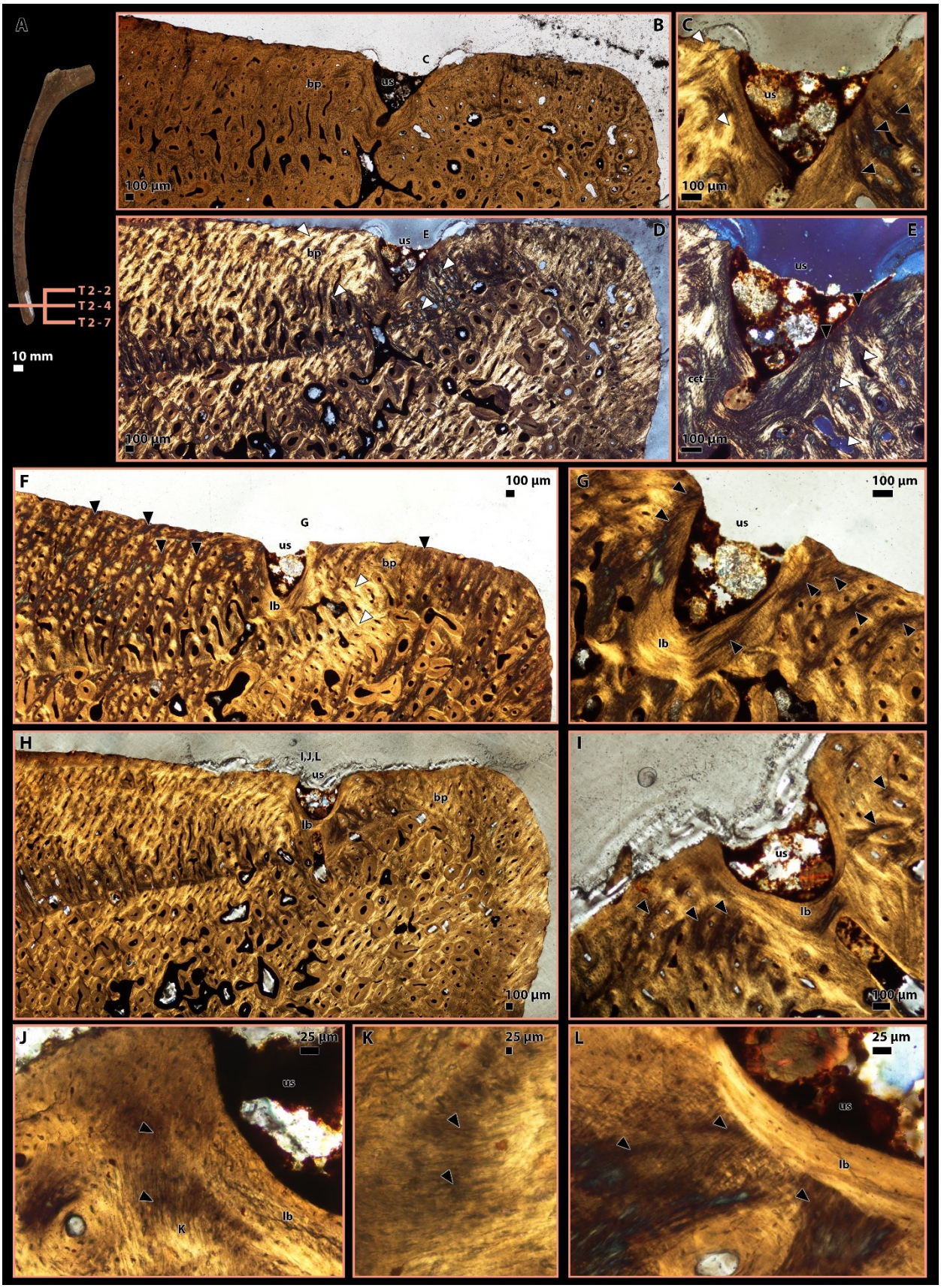
A
T2-2
T2-4
T2-7
10 mm
B
C
bp
us
100 µm
C
us
100 µm
D
E
bp
us
100 µm
E
us
cct
100 µm
F
G
us
bp
lb
100 µm
G
us
lb
100 µm
H
I,J,L
us
bp
lb
100 µm
I
us
lb
100 µm
J
25 µm
us
lb
K
K
25 µm
L
25 µm
us
lb

Figure 5.16. Histological thin sections of vertebral ribs away from uncinate scars in sampled ceratopsians.

Left dorsal vertebral rib of *Pa. lakustai* (PSC 2014.060), showing the approximate anatomical positions of thin sections (A); transverse thin section T 1 – 1, showing coarse Sharpey's fibres (B); transverse thin section T 1 – 2, showing fine collagen and Sharpey's fibres (C); transverse thin section T 2 – 1, showing fine Sharpey's fibres (D); dorsal vertebral rib of *Centrosaurus* sp. (TMP 96.1776.135), showing the approximate anatomical positions of thin sections (E); transverse thin section T 3 – 4, showing one pathway for blood vessel within mature bones (F); transverse thin section T 4 – 1, showing coarse collagen fibres within mature bones (G); Left dorsal vertebral rib of *Centrosaurus* sp. (TMP 82.18.16) in posterior view, showing the approximate anatomical positions of thin sections (H); transverse thin section T 2 – 2, showing collagen and Sharpey's fibres within primary bones (I); transverse thin section T 2 – 4, showing coarse Sharpey's fibres. Black and white triangles point at collagen and Sharpey's fibres appearing as dark and light fibres at specific extinction angles, respectively. Abbreviations: bm mature bones, bp primary bones, bv blood vessel, lb lamellar bones, us uncinate scar.

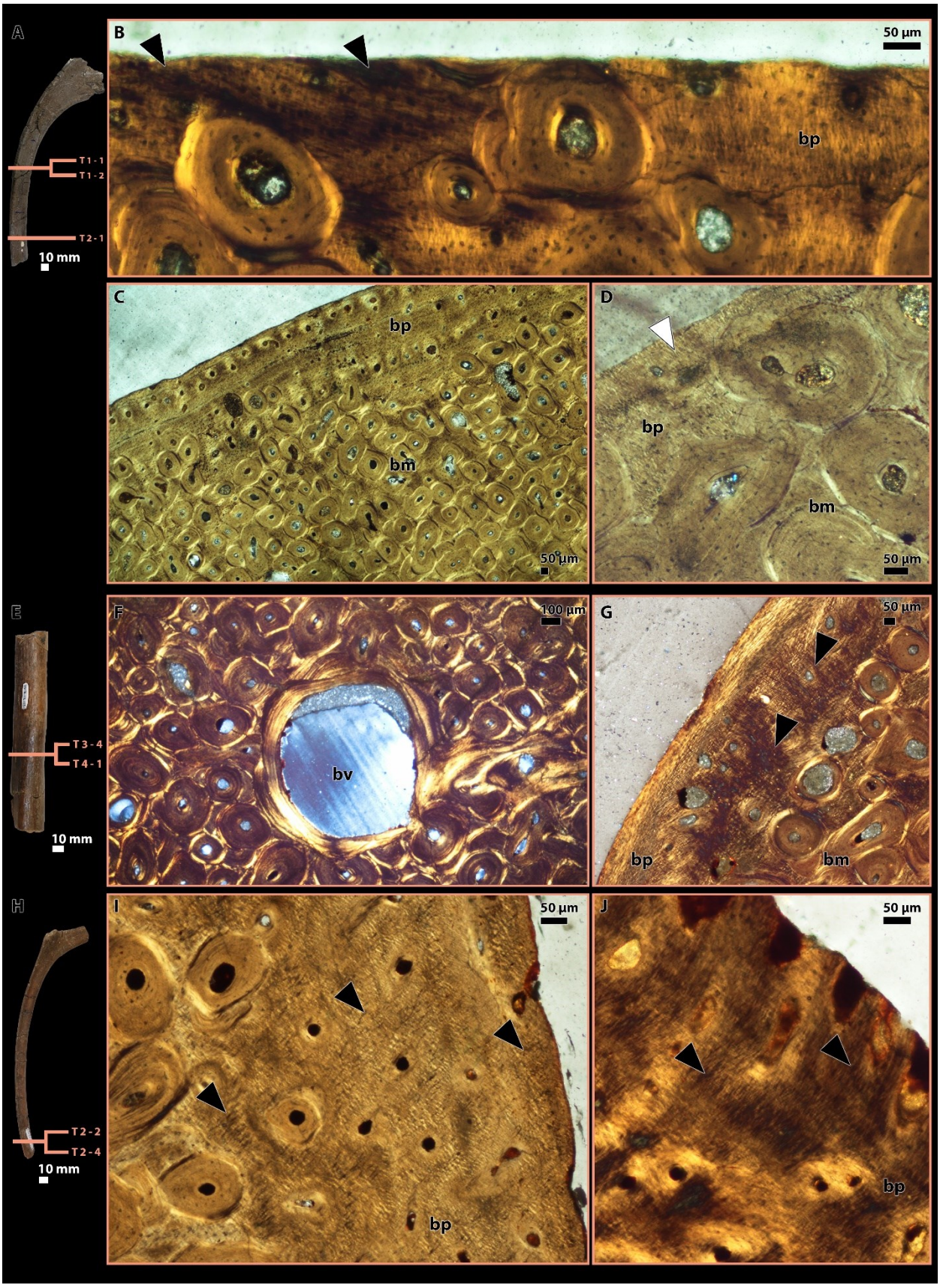
A
T1-1
T1-2
T2-1
10 mm
B
50 µm
bp
C
bp
bm
50 µm
D
bp
bm
50 µm
E
T3-4
T4-1
10 mm
F
100 µm
bv
G
50 µm
bp
bm
H
T2-2
T2-4
10 mm
I
50 µm
bp
J
50 µm
bp

5.5 Literature Cited

An, Y.H. and Martin, K.L. eds. 2003. *Handbook of Histology Methods for Bone and Cartilage*. Totowa, NJ: Humana Press. doi: 10.1007/978-1-59259-417-7.

Baumel, J.J., King, A.S., Breazile, J.E., Evans, H.E. and Vanden Berge, J.C. 1993. *Handbook of avian anatomy: Nomina anatomica avium*. second edition. Cambridge: Nuttall Ornithological Club.

Benton, M.J. 2014. *Vertebrate Palaeontology*. John Wiley & Sons.

Boyd, C.A., Cleland, T.P. and Novas, F. 2011. Osteogenesis, homology, and function of the intercostal plates in ornithischian dinosaurs (Tetrapoda, Sauropsida). *Zoomorphology* 130(4), pp. 305–313. doi: 10.1007/s00435-011-0136-x.

Butler, R.J. and Galton, P.M. 2008. The 'dermal armour' of the ornithopod dinosaur *Hypsilophodon* from the Wealden (Early Cretaceous: Barremian) of the Isle of Wight: a reappraisal. *Cretaceous Research* 29(4), pp. 636–642. doi: 10.1016/j.cretres.2008.02.002.

Canalis, R.F. and Burstein, F.D. 1985. Osteogenesis in vascularized periosteum: interactions with underlying bone. *Archives of Otolaryngology - Head and Neck Surgery* 111(8), pp. 511–516. doi: 10.1001/archotol.1985.00800100059007.

Claessens, K.P. 2015. Anatomical transformations and respiratory innovations of the archosaur trunk. In: *Great Transformations in Vertebrate Evolution*. University of Chicago Press. doi: 10.7208/chicago/9780226268392.001.0001.

Claessens, L.P.A.M. 2009. A cineradiographic study of lung ventilation in *Alligator mississippiensis*. *Journal of Experimental Zoology Part A: Ecological Genetics and Physiology* 311A(8), pp. 563–585. doi: 10.1002/jez.530.

Codd, J.R. 2010. Uncinate processes in birds: Morphology, physiology and function. *Comparative biochemistry and physiology part a: molecular & integrative physiology* 156(3), pp. 303–308. doi: 10.1016/j.cbpa.2009.12.005.

Codd, J.R., Boggs, D.F., Perry, S.F. and Carrier, D.R. 2005. Activity of three muscles associated with the uncinate processes of the giant Canada goose *Branta canadensis maximus*. *Journal of Experimental Biology* 208(5), pp. 849–857. doi: 10.1242/jeb.01489.

Codd, J.R., Manning, P.L., Norell, M.A. and Perry, S.F. 2008. Avian-like breathing mechanics in maniraptoran dinosaurs. *Proceedings of the Royal Society B: Biological Sciences* 275(1631), pp. 157–161. doi: 10.1098/rspb.2007.1233.

Codd, J.R., Rose, K.A.R., Tickle, P.G., Sellers, W.I., Brocklehurst, R.J., Elsey, R.M. and Crossley, D.A. 2019. A novel accessory respiratory muscle in the American alligator (*Alligator mississippiensis*). *Biology Letters* 15(7), p. 20190354. doi: 10.1098/rsbl.2019.0354.

Cong, L.Y., Hou, L.H. and Wu, X.C. 1988. *The Gross anatomy of Alligator sinensis Fauvel: Integument, Osteology, and Myology (In Chinese with English summary)*. Beijing, China: China Science Publishing & Media Ltd.

Cuesta, E., Vidal, D., Ortega, F., Shibata, M. and Sanz, J.L. 2022. *Pelecanimimus* (Theropoda: Ornithomimosauria) postcranial anatomy and the evolution of the specialized manus in Ornithomimosaurs and sternum in maniraptoriforms. *Zoological Journal of the Linnean Society* 194(2), pp. 553–591. doi: 10.1093/zoolinnean/zlab013.

Cullen, T.M., Evans, D.C., Ryan, M.J., Currie, P.J. and Kobayashi, Y. 2014. Osteohistological variation in growth marks and osteocyte lacunar density in a theropod dinosaur (Coelurosauria: Ornithomimidae).

Currey, J.D. 2003. The many adaptations of bone. *Journal of Biomechanics* 36(10), pp. 1487–1495. doi: 10.1016/S0021-9290(03)00124-6.

Dai, J. and Rabie, A.B.M. 2007. VEGF: an essential mediator of both angiogenesis and endochondral ossification. *Journal of Dental Research* 86(10), pp. 937–950. doi: 10.1177/154405910708601006.

Farmer, C.G. 2015. Unidirectional flow in lizard lungs: a paradigm shift in our understanding of lung evolution in Diapsida. *Zoology* 118(5), pp. 299–301. doi: 10.1016/j.zool.2015.06.001.

Farmer, C.G. and Sanders, K. 2010. Unidirectional airflow in the lungs of alligators. *Science* 327(5963), pp. 338–340. doi: 10.1126/science.1180219.

Filipowska, J., Tomaszewski, K.A., Niedźwiedzki, Ł., Walocha, J.A. and Niedźwiedzki, T. 2017. The role of vasculature in bone development, regeneration and proper systemic functioning. *Angiogenesis* 20(3), pp. 291–302. doi: 10.1007/s10456-017-9541-1.

Francillon-Vieillot, H. et al. 1990. Microstructure and mineralization of vertebrate skeletal tissues. In: *Skeletal Biomineralization: Patterns, Processes and Evolutionary Trends*. New York: Van Nostrand Reinhold, pp. 471–530.

Frey, T. von E. 1988. Anatomie des Körperstammes von *Alligator mississippiensis* Daudin. *Stuttgarter Beitraege zur Naturkunde, Serie A* 424, pp. 1–106.

Hall, B.K. 2005. *Bones and cartilage: developmental and evolutionary skeletal biology*. Elsevier Academic Press.

Hildebrand, M. 1982. *Analysis of vertebrate structure*. New York: Wiley Blackwell.

Holliday, C.M. 2009. New Insights Into Dinosaur Jaw Muscle Anatomy. *The anatomical record: advances in integrative anatomy and evolutionary biology* 292(9), pp. 1246–1265. doi: 10.1002/ar.20982.

Liparini, A. and Schultz, C.L. 2013. A reconstruction of the thigh musculature of the extinct pseudosuchian *Prestosuchus chiniquensis* from the *Dinodontosaurus* Assemblage Zone (Middle

Triassic Epoch), Santa Maria 1 Sequence, southern Brazil. *Geological Society, London, Special Publications* 379(1), pp. 441–468. doi: 10.1144/SP379.20.

Maryañska, T. 1977. Ankylosauridae (Dinosauria) from Mongolia. *Acta Palaeontologica Polonica* 37, pp. 85–151.

Maxwell, E.E. 2008. Comparative embryonic development of the skeleton of the domestic turkey (*Meleagris gallopavo*) and other galliform birds. *Zoology* 111(3), pp. 242–257. doi: 10.1016/j.zool.2007.08.004.

Maxwell, E.E. and Larsson, H.C.E. 2009. Comparative ossification sequence and skeletal development of the postcranium of palaeognathous birds (Aves: Palaeognathae). *Zoological Journal of the Linnean Society* 157(1), pp. 169–196. doi: 10.1111/j.1096-3642.2009.00533.x.

Mescher, A.L. and Junqueira, L.C.U. 2016. *Junqueira's basic histology: text and atlas*. Fourteenth edition. New York: Mcgraw-Hill Education.

Nesbitt, S.J. 2011. The early evolution of archosaurs: relationships and the origin of major clades. *Bulletin of the American Museum of Natural History* 352, pp. 1–292. doi: 10.1206/352.1.

O'Connor, P.M. 2006. Postcranial pneumaticity: An evaluation of soft-tissue influences on the postcranial skeleton and the reconstruction of pulmonary anatomy in archosaurs. *Journal of Morphology* 267(10), pp. 1199–1226. doi: 10.1002/jmor.10470.

Park, J.-Y. et al. 2021. A new ankylosaurid skeleton from the Upper Cretaceous Baruungoyot Formation of Mongolia: its implications for ankylosaurid postcranial evolution. *Scientific Reports* 11(1), p. 4101. doi: 10.1038/s41598-021-83568-4.

Prondvai, E., Stein, K.H.W., de Ricqlès, A. and Cubo, J. 2014. Development-based revision of bone tissue classification: the importance of semantics for science: Development-based bone tissue classification. *Biological Journal of the Linnean Society* 112(4), pp. 799–816. doi: 10.1111/bij.12323.

Romer, A.S. 1956. The axial skeleton. In: *The osteology of reptiles*. Illinois: University of Chicago Press, pp. 275–279.

Scaal, M. 2021. Development of the amniote ventrolateral body wall. *Developmental Dynamics* 250(1), pp. 39–59. doi: 10.1002/dvdy.193.

Shapiro, F. and Wu, J. 2019. Woven bone overview: Structural classification based on its integral role in developmental, repair and pathological bone formation throughout vertebrate groups. *European Cells and Materials* 38, pp. 137–167. doi: 10.22203/eCM.v038a11.

Simmons, D.J., Menton, D.N., Miller, S. and Lozano, R. 1993. Periosteal attachment fibers in the rat calvarium. *Calcified Tissue International* 53(6), pp. 424–427. doi: 10.1007/BF03549786.

Sire, J.-Y. and Meunier, F.J. 1994. The canaliculi of Williamson in holostean bone (osteichthyes, actinopterygii): a structural and ultrastructural study. *Acta Zoologica* 75(3), pp. 235–247. doi: 10.1111/j.1463-6395.1994.tb01211.x.

Sivaraj, K.K. and Adams, R.H. 2016. Blood vessel formation and function in bone. *Development* 143(15), pp. 2706–2715. doi: 10.1242/dev.136861.

Tickle, P.G. and Codd, J.R. 2009. Ontogenetic development of the uncinate processes in the domestic turkey (*Meleagris gallopavo*). *Poultry Science* 88(1), pp. 179–184. doi: 10.3382/ps.2008-00349.

Tickle, P.G., Ennos, A.R., Lennox, L.E., Perry, S.F. and Codd, J.R. 2007. Functional significance of the uncinate processes in birds. *Journal of Experimental Biology* 210(22), pp. 3955–3961. doi: 10.1242/jeb.008953.

Turner, A.H. 2006. Osteology and phylogeny of a new species of *Araripesuchus* (Crocodyliformes: Mesoeucrocodylia) from the Late Cretaceous of Madagascar. *Historical Biology* 18(3), pp. 255–369. doi: 10.1080/08912960500516112.

Walker, W.F. and Liem, K.F. 2001. *Functional Anatomy of the Vertebrates: An Evolutionary Perspective*. New York: Fort Worth : Harcourt College Publishers.

Wedel, M.J. 2006. Origin of postcranial skeletal pneumaticity in dinosaurs. *Integrative Zoology* 1(2), pp. 80–85. doi: 10.1111/j.1749-4877.2006.00019.x.

Weiner, S. and Wagner, H.D. 1998. The material bone: Structure-mechanical function relations. *Annual Review of Materials Science* 28(1), pp. 271–298. doi: 10.1146/annurev.matsci.28.1.271.

Welty, J.C. and Baptista, L. 1972. *The life of birds*. London: W. B. Saunders and Co.

Zhou, S.W. 1983. A nearly complete skeleton of a stegosaur from the Middle Jurassic of Dashanpu, Zigong, Sichuan. *Journal of Chengdu University of Geology* 1, pp. 15–26.

Zimmer, K. 1935. Beiträge zur Mechanik der Atmung bei den Vögeln in Stand-und Flug. *Zoologica* 33, pp. 1–69.

5.6 Supplementary Information

5.6.1 Hematoxylin and Eosin staining procedure

Safety: This procedure is to be done in the fume hood except for the Tap water wash. Wear nitrile gloves.

Toluene 1	5 minutes	De-wax
Toluene 2	5 minutes	De-wax
100% Ethanol	2 minutes	
100% Ethanol	2 minutes	
90% Ethanol	2 minutes	
70% Ethanol	2 minutes	
50% Ethanol	2 minutes	
Dist. Water	2 minutes	
Hematoxylin Gill III*	2 minutes	
Dist. Water	Rinse (Carry to sink in square dish of water)	
Tap Water	15 minutes	Running Slowly – Cold only
70% Ethanol	2 minutes	
Eosin*	30 seconds	
100% Ethanol	2 minutes	Discard to waste bottle after use.
100% Ethanol	2 minutes	Transfer to 100% Ethanol 1 after use
Toluene 1	2 minutes	
Toluene 2	2 minutes plus time to coverslip the slides. Slides must be kept in Toluene during coverslipping so they never dry out.	

Coverslip with DPX in the Fume Hood. Wear Nitrile gloves.

Slides should be kept in 37 degree oven overnight for the DPX to solidify.

*Hematoxylin needs to be filtered before use regularly.

As of 2010:

*Hematoxylin: Surgipath/Leica - Gill III Cat. # 3801542

*Eosin: Surgipath/Leica Cat. # 3801602

5.6.2 Masson's Trichrome staining procedure

Procedure takes about 1.5 hours including the cover-slipping of 8 slides with DPX

PPE: Fume hood, gloves, glasses

1.TOLUENE 1 and TOLUENE 2 (Top Shelf) 5 minutes each

2.Ethanol Series: 100%, 100%, 90%, 70%, 50% ethanol - 2 minutes each

3.Water - 2min.

4. Stain nuclei with Hematoxylin Gill III (Surgipath) 1 min

5. Wash well in cold running tap water in sink 15 min

6. Rinse in distilled water. 1 min total

7. Stain in Ponceau-acid fuchsin – did not filter 2 min

8. Rinse in distilled water 1 min total

Three Pots of d. water rinses best and less contamination for next solution

9. Differentiate in 1% Phosphomolybdic Acid-1 5 min

10. Do not Rinse. Transfer to Acetic Aniline Blue 3 min

11. Rinse in distilled water 1 min total

Three Pots of d. water rinses best and less contamination for next solution

12. 1% Phosphomolybdic Acid-2 – use fresh solution 5 min

13. Place in 1% aqueous acetic acid 3 min

14. Dehydrate in 95% alcohol (discard after use) 2 min

15. 100% Ethanol Lower Shelf 2 min

16. 100% Ethanol Lower Shelf 2 min

17. Toluene Lower Shelf 2 min

18. Toluene Lower Shelf 2 min plus cover-slipping time

19. Coverslip with DPX in the Fume Hood. Wear Nitrile gloves. The slides stay in Toluene while cover-slipping

5.6.3 Supplementary Figure S5.1. Dorsal vertebral ribs of sampled extant and fossil archosaurs.

Right dorsal vertebral rib of *Meleagris gallopavo* (UAMZ 1824) in lateral views, showing the approximate anatomical positions of all sampled thin sections (A, B); First and second right dorsal vertebral ribs of *Caiman crocodilus* (UAMZ unnumbered), showing the approximate anatomical positions of all sampled thin sections (C, D); left dorsal vertebral rib of Tyrannosauridae indet. (TMP 51.81.16.285) in anterior view, showing the approximate anatomical positions of all sampled thin sections (E); right dorsal vertebral rib of Tyrannosauridae indet. (TMP 94.12.960) in posterior view, showing the approximate anatomical positions of all sampled thin sections (F); right dorsal vertebral rib of *Albertosaurus sarcophagus* (TMP 99.52.42) in posterior view, showing the approximate anatomical positions of all sampled thin sections (G); dorsal vertebral rib of Hadrosauridae indet. (UALVP 60005) in medial view, showing the approximate anatomical positions of all sampled thin sections (H); left dorsal vertebral rib of *Pachyrhinosaurus lakustai* (PSC 2014.060) in posterior view, showing the approximate anatomical positions of all sampled thin sections (I), dorsal vertebral rib of *Centrosaurus* sp. (TMP 96.1776.135), showing the approximate anatomical positions of all sampled thin sections (J); left dorsal vertebral rib of *Centrosaurus* sp. (TMP 82.18.16) in posterior view, showing the approximate anatomical positions of all sampled thin sections (K).

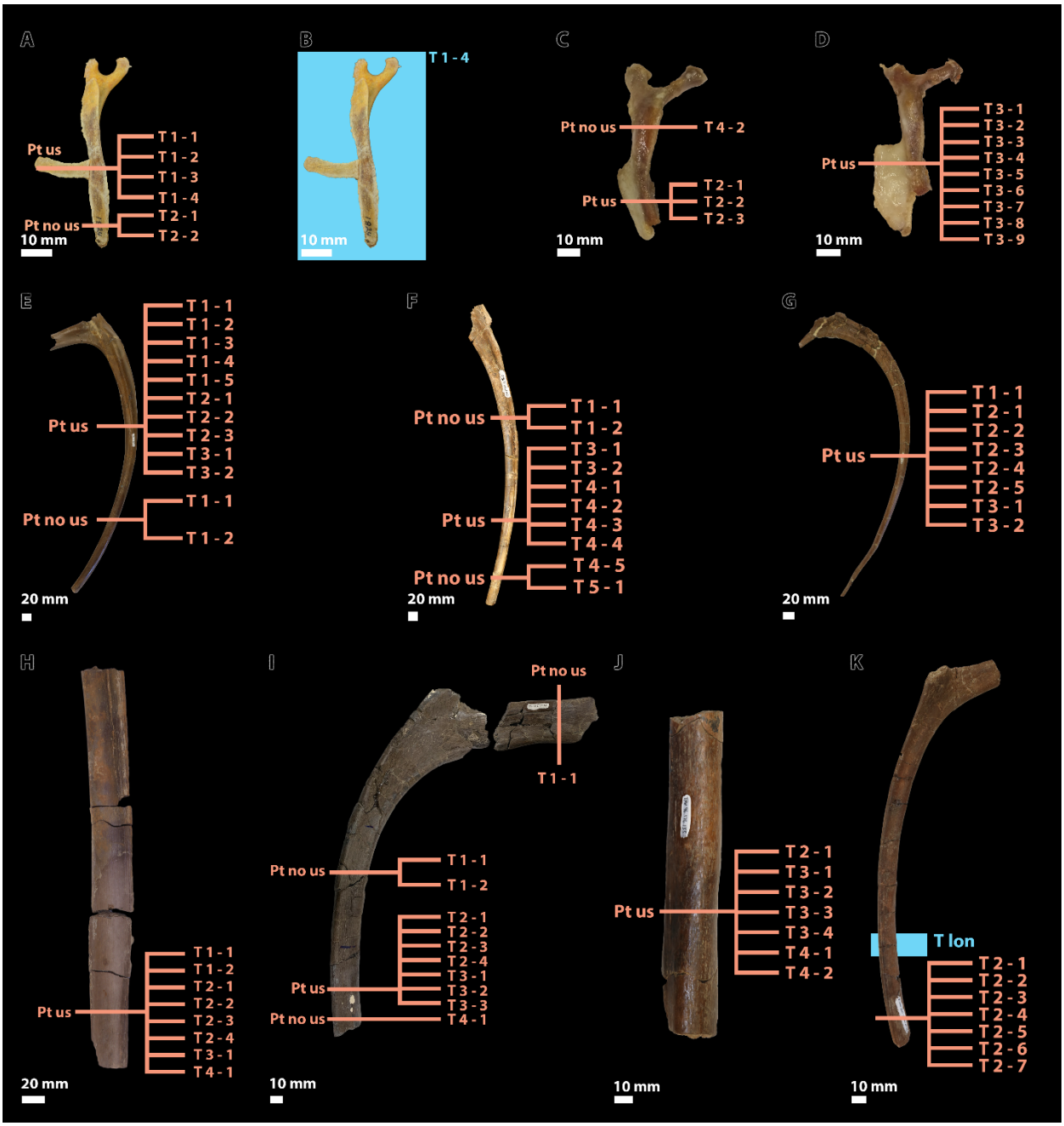
A
Pt us
T 1 - 1
T 1 - 2
T 1 - 3
T 1 - 4
Pt no us
T 2 - 1
T 2 - 2
10 mm
B
T 1 - 4
10 mm
C
Pt no us
T 4 - 2
Pt us
T 2 - 1
T 2 - 2
T 2 - 3
10 mm
D
Pt us
T 3 - 1
T 3 - 2
T 3 - 3
T 3 - 4
T 3 - 5
T 3 - 6
T 3 - 7
T 3 - 8
T 3 - 9
10 mm
E
Pt us
T 1 - 1
T 1 - 2
T 1 - 3
T 1 - 4
T 1 - 5
T 2 - 1
T 2 - 2
T 2 - 3
T 3 - 1
T 3 - 2
Pt no us
T 1 - 1
T 1 - 2
20 mm
F
Pt no us
T 1 - 1
T 1 - 2
T 3 - 1
T 3 - 2
T 4 - 1
T 4 - 2
Pt us
T 4 - 3
T 4 - 4
Pt no us
T 4 - 5
T 5 - 1
20 mm
G
Pt us
T 1 - 1
T 2 - 1
T 2 - 2
T 2 - 3
T 2 - 4
T 2 - 5
T 3 - 1
T 3 - 2
20 mm
H
Pt us
T 1 - 1
T 1 - 2
T 2 - 1
T 2 - 2
T 2 - 3
T 2 - 4
T 3 - 1
T 4 - 1
20 mm
I
Pt no us
T 1 - 1
Pt no us
T 1 - 1
T 1 - 2
T 2 - 1
T 2 - 2
T 2 - 3
T 2 - 4
T 3 - 1
Pt us
T 3 - 2
T 3 - 3
Pt no us
T 4 - 1
10 mm
J
Pt us
T 2 - 1
T 3 - 1
T 3 - 2
T 3 - 3
T 3 - 4
T 4 - 1
T 4 - 2
10 mm
K
T lon
T 2 - 1
T 2 - 2
T 2 - 3
T 2 - 4
T 2 - 5
T 2 - 6
T 2 - 7
10 mm

CHAPTER 6

Muscle scars of trunk and pelvic muscles hint at ventilatory and locomotory adaptations in fossil dinosaurs on the line to birds

6.1 Introduction

Extant birds and crocodylians are the living representatives of archosaurs, a diverse group of amniotes once occupied many terrestrial ecological niches for large body vertebrates (Benton 2014; Kardong 2015). Most extant birds are capable of power flight whereas crocodylians are consistently semi-aquatic, and the difference in their ecology likely constrain aspects of the anatomy.

Skeletal muscles of birds and crocodylians has been dissected and documented in detail since the 1800s (Romer 1923; George and Berger 1966; Cong et al. 1988; Frey 1988; Shufeldt 1988; Baumel et al. 1993; Rose et al. 2021), which forms a solid foundation to compare muscle architectures and interpret their functions. Electromyographic studies are one of the methods to test these functional interpretations (Fedde et al. 1964; Codd et al. 2005; Codd et al. 2019). However, anatomical terminologies, and by extension the homologies they represent, are not always clear and consistent in the literature at least for the thorax and the pelvis (e.g. that attachment sites of mm. intercostales interni in crocodylians) (Cong et al. 1988; Rose et al. 2021), which hinders the comparisons of muscle architectures between archosaurs. Scholars have re-examined the homologies of some skeletal muscles including those of the thorax and the pelvis (Harris 2004; Organ 2006; Wilson 2006; Tsuihiji 2007), but these revisions tend not to focus on the detailed documentation of the attachment sites and muscle morphology. More precise study of these aspects, especially on the trunk muscles attaching to the ribcage and the intrinsic pelvic muscles, will provide sufficient detail of osteological correlate boundaries to draw qualitative and quantitative data in a comparative context.

Details of the muscle attachment sites are crucial because they can leave visible muscle scars on the skeletons. As skeletal elements are commonly documented in the fossil record, the

muscle architectures and their functions can be inferred in the long extinct archosaurs by applying various levels of the extant phylogenetic bracket (Witmer 1995). Pelvic and hindlimb muscles are especially well studied, likely due to its relevance to locomotion (Hutchinson and Gatesy 2000; Carrano and Hutchinson 2002; Maidment and Barrett 2011; Persons IV and Currie 2011; Rhodes et al. 2020). By comparisons, studies of the thorax are scarce with focuses on the epaxial muscles (Organ 2006; Schwarz-Wings 2009). Trunk muscles attaching to the rib segments have received little, if any attention, despite its relevance to ventilation.

Integrations between locomotion and ventilation are known from studies using electromyography and functional morphology in extant crocodylians, birds, and mammals (Berger et al. 1970; Carrier 1996; Carrier and Farmer 2000). A recent X-ray Reconstruction of Moving Morphology (XROMM) study of *Varanus* and *Tegu* have shown evidence of vertebral ribs participating in locomotion without clear ventilatory airflow (pure locomotion in Cieri et al. 2020). Compared to other extant amniotes, birds and crocodylians possess unique adaptations in ventilation (e.g. pneumatic sacs in birds and hepatic piston in crocodylians), which may be associated with the evolutionary transitions of the locomotory strategies (e.g. gaits, postures).

In this chapter, we directly established osteological correlates for the thoracic and pelvic muscles that are less well-documented in the literature. The correlates were used to reconstruct the thoracic and pelvic muscles in fossil archosaurs where possible. Plausible evolutionary scenarios of locomotion and ventilation were proposed.

6.2 Materials and Methods

Two extant birds and three extant crocodylians were dissected at the University of Alberta in Canada and Hainan Lingshui Crocodile Farm in China. to examine the configuration of the skeletal muscles of the thorax and pelvis. To compare the variations of muscle architectures between archosaurs of different locomotor modes, *Corvus corax* and *Dromaius novaehollandiae* were selected to represent volant and bipedally cursorial archosaurs, whereas *Caiman crocodilus* and farm crocodiles (hybrids between *Crocodylus siamensis* and *Crocodylus*

porosus) were selected to represent quadrupedal archosaurs. Additionally, a varanid lizard, *Varanus exanthematicus* was dissected to represent the outgroup of Archosauria. We focused on the trunk and deep pelvic muscles in this study because epaxial muscles and superficial pelvic muscles have been well documented in the literature (Haughton 1867; George and Berger 1966; Cong et al. 1988; Hutchinson 2001b; Organ 2006). For each muscle, general morphology and sites of attachments were documented and compared among the studied subjects and with the literature. Comparisons with *Va. exanthematicus* were made only where birds and crocodylians have different configurations. Images of skeletal muscles were captured using Canon EOS 80D DSLR camera and composited in Adobe Photoshop.

Extant baseline was established based on osteological correlates identified during physical examinations. Distinct and rugose scars, when present at the sites of attachments, were identified as osteological correlates. For the purpose of documenting the trunk muscles in detail, a typical vertebral rib was deconstructed into three elements proximodistally: (1) the separated capitulum and tuberculum constituting the proximal end before merging into the rib shaft, (2) a rib shaft constituting the medial aspect of the body of the vertebral rib, and (3) a costal flange constituting the lateral aspect of the vertebral rib, from which the anterior and posterior intercostal ridges extend into the intercostal space (see Supplementary Information for detailed definition). Muscle homologies follow existing conventions (George and Berger 1966; Cong et al. 1988; Frey 1988; Baumel et al. 1993; Hutchinson 2001b; Hutchinson 2002; Organ 2006; Tsuihiji 2007; Rhodes et al. 2021). Where multiple names of homologous muscles exist, the homology was examined based on muscular morphology and topology. Osteological correlates identified in this study are summarised in Table 6.1.

Vertebral ribs of fossil archosaurs housed in collections of North America and China (Table 6.2) were directly examined using the extant baseline established above, to reconstruct their muscle configurations where possible. Articulated specimens and long, non-tapering dorsal vertebral ribs were prioritized to avoid potential morphological variations within the ribcage.

Unlike the thoracic muscles, the attachment sites of pelvic muscles can be confidently measured and standardized for quantitative comparisons of muscle configurations and for

inference on cursoriality in theropods leading to birds. Phylogenetic relationships among sampled theropods were depicted on a cladogram modified from the literature (Hendrickx et al. 2015). Areas of pelvic muscle attachments in *Co. corax* and *Dr. novaehollandiae* were measured in ImageJ (Schneider et al. 2012) using the procedure of (Rhodes et al. 2021). Functions of pelvic muscles in *Co. corax* were determined based on the consensus in the literature (Hudson 1937; Verstappen et al. 1998; Meilak et al. 2021). The body masses of *Dr. novaehollandiae* and *Co. corax* were obtained from the average value of both sexes in the CRC Handbook of Avian Body Masses (Dunning Jr 2007), and the body masses of the remaining theropods followed Rhodes et al. (2021). All measurements were log-transformed to account for allometry. A Phylogenetic Generalized Least Squares (PGLS) regression was performed to examine the relationship between body mass and pelvic muscles or hip sizes. This method performs bivariate comparisons while accounting for phylogenetic autocorrelation due to the relationships among the taxa analyzed (Garland and Ives, 2000). Jenks Natural Breaks optimization was then performed using '*ClassInt*" package (Bivand et al. 2013). with the inferred values of major extensor muscles, to classify the cursoriality of representing archosaurs on the line to birds. Raw data are available in the digital Supplementary Information.

6.3 Results

Descriptions of trunk and pelvic muscles are organized in anterior-to-posterior and superficial-to-deep order. Distinct osteological correlates were observed from pelvic muscles but were absent from trunk muscles. As skeletal muscles do not necessarily leave unambiguous scars (Bryant and Seymour 1990), topology of the sites of attachment and the anatomical features of the trunk skeleton were used to established osteological correlates. Osteological correlates are provided in Table 6.1.

6.3.1 Trunk muscles

m. iliocostalis (IC). IC is a segmented epaxial muscle in birds and crocodylians, but it is attached also to the vertebral ribs as the hypaxial muscles. IC in this study refers only to the partition associated with the thoracic and lumbar regions, although it continues anteriorly into the cervical region (i.e. m. iliocostalis cervicis in Cong et al. 1988). To distinguish fibres attached to the vertebrae from those attached to the vertebral ribs, IC is partitioned into dorsal (dIC) and ventral (vIC) portions separated at the contact between the transverse process and the tuberculum.

IC in *Co. corax* (Fig. 6.1A, 6.1D) *and Dr. novaehollandiae* (Fig. 6.1B, 6.1D) has a triangular outline between the last cervical vertebra and the ilium in dorsal view. dIC has a tendinous origin from the anterior aspect of the iliac crest, which receive additional fibres originated from the dorsolateral aspects of the transverse process of each dorsal vertebra. Tendons of dIC originated from the ilium are positioned lateral to the muscle fascicle whereas those originated from the dorsal vertebrae are positioned medial to the muscle fascicle. Passing anteriorly from the ilium, portions of the fibres insert on the dorsolateral aspect of the transverses process of the first or second adjacent dorsal vertebra. The remaining fibres blend with those originated from the transverse process and pass further anteriorly, the insertion of which could not be confidently identified. Fibres of vIC originate from a sheet of parallel tendons immediately ventral to the origin of dIC, which receive additional fibres with fleshy origins from the anterolateral aspect of the tuberculum. Passing anteriorly, fibres insert on the first and second adjacent vertebral rib at the posterolateral aspect of the tuberculum. In both *Co. corax* and *Dr. novaehollandiae*, the direction insertion of vIC on the tuberculum likely contribute to the formation of its flange-like projections into the intercostal space.

IC in crocodylians (Fig. 6.1C, 6.1D) is a robust muscle with a crescentic outline in dorsal view, and it externally covers up the dorsal half of the trunk. The transition between dIC and vIC is indistinct, and the two parts could not be easily dissected away as in birds, but dIC and vIC can be identified based on sites of attachments. dIC in crocodylians share a similar configuration as in birds. However, vIC is highly developed in crocodylian, covering the lateral aspect of the trunk between dIC and OE. Fibres of vIC originate from the anterior aspect of the iliac crest,

which pass anteriorly to insert on the lateral aspect of the costal flange and envelope the posterodorsal aspect of the uncinate processes. Between the adjacent vertebral ribs, fibres of vIC also attach to a tendinous sheet dorsal to the uncinate processes, which can be exposed by reflecting the fleshy fibres of vIC. However, the tendinous sheet is variable in size, and may be poorly developed.

The vIC in *Va. exanthematicus* (Fig. 6.2E) attaches approximately to the midpoint of the vertebral ribs, as in crocodylians, and the reduced vIC in birds is likely a derived condition.

m. obliquus externus (OE). OE, the most superficial abdominal muscle, originates from the anterolateral aspect of the pubis in *Co. corax* and *Dr. novaehollandiae*, and from the contact between the pubis and ischium in crocodylians. In both *Co. corax* (Fig. 6.2A, 6.2D) and crocodylians (Fig. 6.1C, Fig. 6.2C, 6.2D), fibres of OE pass anterodorsally to insert on the lateral aspect of the costal flange near its contact with the uncinate process. Additionally, the anteriormost portion of OE is attached to the distal end of the last cervical rib. By comparison, fibres of OE in *Dr. novaehollandiae* insert on the costal flange near the intracostal joint between the vertebral and sternal ribs (Fig. 6.2B, 6.2D), which may be related to the absence of uncinate process. OE in *Va. exanthematicus* (Fig. 6.2E. 6.2F) insert on the midpoint of the vertebral rib, which suggest the condition observed in *Co. corax* and crocodylians represent that of the typical archosaurs.

m. scalenus (SN). In this study, SN refers to the portion near the cervicodorsal transition and is associated with the trunk, though it continues anteriorly into the cervical region (Cong et al. 1988; Tsuihiji 2007).

SN is a robust muscle positioned in the intercostal spaces between the penultimate cervical and the first dorsal vertebral ribs. SN in *Co. corax* (Fig. 6.3A, 6.3D) is constituted of two fascicles as described by Shufeldt (1988). Between the penultimate and the last cervical ribs, fibres originate from the ventrolateral aspect of the transverse process, which pass posteroventrally to insert on the anterolateral aspect of the tuberculum, the costal flange, and the rib shaft. Between the last cervical and the first dorsal vertebral ribs, SN insert on the lateral

aspect of the costal flange. Unlike *Co. corax*, SN in *Dr. novaehollandiae* (Fig. 6.3B, 6.3D) is constituted of three adjoined fascicles between the penultimate and the last cervical ribs. The proximal fascicle connects the ventrolateral aspect of the transverse process to the lateral aspect of the costal flange of the succeeding cervical vertebral rib, whereas the distal two fascicles connect the intercostal ridges of the adjacent cervical ribs.

SN in crocodylians is constituted of a uniform fascicle and is robust enough to cover the cervical ribs laterally (Fig. 6.3C, 6.3D). Fibre configuration is analogous to the SN between the last cervical and the first dorsal vertebral ribs in *Dr. novaehollandiae*.

m. levator costarum (LC). LC is a triangular hypaxial muscle positioned ventromedial to IC and occupies the proximal most portion of the intercostal spaces between the first and the last dorsal vertebral ribs. In *Co. corax* (Fig. 6.3A, Fig. 6.4A, 6.4E), *Dr. novaehollandiae* (Fig. 6.4B, 6.4C, 6.4E), and crocodylians (Fig. 6.4D, 6.4E), fibres originate from the posteroventral aspect of the transverse process, which pass posteroventrally and insert on the succeeding vertebral rib on the anterior aspect of the capitulum, tuberculum, and the proximal part of the anterior intercostal ridge. Except for the posteriorly positioned dorsal vertebral ribs in crocodylians (e.g. the fifth dorsal vertebral rib), a smooth concavity is present between the capitulum and tuberculum to receive the majority of the fibres.

Among the extant archosaurs examined in this study, LC has greater volumes in the anteriorly positioned intercostal spaces in *Co. corax* and *Dr. novaehollandiae*, whereas LC remains approximately the same volume in all intercostal spaces in crocodylians. At the origin of LC, a thin sheet of parallel tendinous fibres was observed in *Dr. novaehollandiae* and crocodylians, and the absence of clear tendinous origin in *Co. corax* may be related to its small body size.

mm. intercostales externi (IE). IE is a rectangular hypaxial muscle that occupies the intercostal spaces between the first and the last dorsal vertebral ribs in birds and crocodylians.

In birds examined in this study, IE is positioned ventral to LC and vIC. Fibres of IE originate from the posterior intercostal ridge and insert on the anterior intercostal ridge of the

succeeding vertebral rib. In *Co. corax* (Fig. 6.4A, Fig. 6.5A, 6.5B, 6.5E), IE has approximately the same volume in all intercostal spaces. Fibres of IE in *Co. corax* can be divided at the uncinate process into a proximal part that pass posteriorly and a distal part that pass posteroventrally. Fine, parallel fibres of tendons can extend to positions near the attachments of the succeeding vertebral rib. In *Dr. novaehollandiae* (Fig. 6.5C, 6.5E), IE has similar volumes in all except the last intercostal space where IE is comparatively smaller. Unlike *Co. corax*, fibres of IE in *Dr. novaehollandiae* pass consistently posteroventrally within a given intercostal space. The tendinous fibres of IE are well-developed compared to *Co. corax*, forming a jaggy transition to the muscle fibres. However, the tendon-muscle transitions in *Dr. novaehollandiae* are always anterior to the midpoint of the intercostal space.

In crocodylians (Fig. 6.4D, Fig. 6.5D, 6.5E), IE is positioned lateral to LC and medial to vIC. Fibres of IE and vIC are blended smoothly. However, sections of IE were clearly exposed in our dissections based on its position medial to the tendinous sheet of vIC and the direct attachment on the anterior/posterior intercostal ridge. The blending of fibres between IE and vIC can be observed at the distal end of the vertebral rib where the attachment of fibres transition from the costal flange to the uncinate process. Further distally, IE are separated from II between intermediate ribs by a weak fascia. Fibres of IE originate from the posterior aspect of the tuberculum and posterior intercostal ridge, which insert on the succeeding vertebral rib on the anterior aspect of the tuberculum and the anterior intercostal ridge. As in *Co. corax*, fibres pass posteriorly on the proximal section and posteroventrally on the distal section. The IE we identified is comparable to parts of the IE in the literature (m. intercostales externi proprius in Frey 1988; dorsal external intercostalis in Murakami et al. 1991; intercostales externi dorsales in Rose et al. 2021). Murakami et al. (1991) and Rose et al. (2021) identified the muscle fascicle immediately ventral to the IE as mm. intercostales externi dorsalis longi. However, fibres of this fascicle are continuous with those of II in the crocodylians examined in this study, which can not be distinguished morphologically. Mm intercostales externi dorsalis longi is therefore not recognized as a distinct muscle in this study.

m. appendicocostalis (APC). APE is a hypaxial muscle with a triangular or strap-like outline that connects the uncinate process to the next rib segment(s).

In the extant birds examined in this study, APC is consistently positioned lateral to IE. In *Co. corax* (Fig. 6.2A, Fig. 6.6A, 6.6B, 6.6E), fibres of APC originate from the posteromedial aspect of the uncinate process, which pass posteroventrally and insert on the succeeding vertebral rib. The exact sites of attachments are combinations of the lateral aspects of the costal flange, the lateral aspect of uncinate process, and the ligamentum triangulare between the uncinate process and the vertebral rib, which varies according to the muscle volume. On the *Co. corax* we examined, APC is most developed in the intercostal spaces between the second and the fourth dorsal vertebral ribs, which reduced in volume anteriorly and posteriorly. Unlike *Co. corax*, *Dr. novaehollandiae* (Fig. 6.2B, Fig. 6.6C, 6.6E) does not have uncinate process. Instead, fibres originate from a distinct tendon on the posterior intercostal ridge of the vertebral rib near its midshaft, which is lateral to the tendons of IE. Passing posteriorly, muscle fibres insert on the anterior intercostal ridge of the succeeding vertebral rib, which takes up approximately fifth or fourth of the rib's proximodistal length. APC in *Dr. novaehollandiae* can therefore be construed as an unipennate muscle because its tendon runs along the posterior intercostal ridge, forming an acuate angle to the muscle fibres. Volume of APC is approximately the same on all intercostal space. APC we identified in *Dr. novaehollandiae* is probably equivalent to m. costosternalis externus in anhimids and megapodids, a group of modern birds lack uncinate process (Beddard 1898; George and Berger 1966; Baumel et al. 1993). However, other parts of m. costosternalis (COT) are associated with the sternum and sternal ribs (George and Berger 1966), which could not capture the anatomical position of APC or its close relationships with IE. We therefore use APC instead of m. costosternalis externus in this study. Observations on *D. novaehollandidae* proof that APC can still developed even the uncinate process is secondarily loss.

In crocodylians (Fig. 6.6D, 6.6E), APC is positioned ventral to IE and lateral to II. fibres of APC originate from the posteroventral aspects of the uncinate process and lateral aspects of the intermediate rib. Tendinous fibres can be observed only at the origin, and the majority of APC is constituted of muscle fibres. Passing posteroventrally, fibres attach on the lateral aspect of the succeeding intermediate rib, and occasionally attached laterally to the distal ends of the succeeding vertebral ribs. Uncinate process is absent on the posterior intercostal spaces, and APC is poorly developed as thin sheets of muscles. In this case, fibres originate from the lateral aspect of the vertebral rib near its distal end and the lateral aspect of the intermediate rib. APC

identified in this study is probably equivalent to ventral parts of IE in the literature (mm. intercostales externi ventralis in Rose et al. 2021). We identify APC as a distinct muscle because its fibres are separated from those of IE by fascia, and fibres of IE are associated with those of II (see description of IE above). In addition, studies of intercostal nerves suggest the innervation patterns can distinguish APC from IE (Murakami et al. 1991). Developmental evidence in extant birds suggest the dorsal and ventral parts of avian dorsal vertebral ribs have different embryonic origins (Aoyama et al. 2005; Scaal 2021), and the intermediate ribs in crocodylians may be homologous to the ventral parts of vertebral ribs in birds (Claessens 2015). The sites of attachments are therefore comparable between the birds and crocodylians examined in this study, and we use APC in this study to emphasise on its potential homology across Archosauria.

mm. intercostales interni (II). Positioned ventral to LC and medial to IE, II is a hypaxial muscle that typically occupies parts of the intercostal spaces between the first and the last dorsal rib segments. IE and II are separated by fascia and intercostal nerves.

In *Co. corax* (Fig. 6.7A, 6.7F), II can be divided at the uncinate process into proximal and distal parts, and the distal parts are better developed. Fibres of the proximal part originate freshly from the anterior aspects of the tuberculum and rib shaft, which pass anteriorly and insert on the preceding vertebral rib on the posterior aspects of the tuberculum and rib shaft. Fibres of the distal parts originate tendinously from the anterior aspect of the rib shaft immediately medial to the costal flange. The tendinous origins form a sheet that transitions to muscle fibres near the midpoint of the intercostal space, which pass anteroventrally and insert on the posterior aspects of the preceding vertebral rib on the rib shaft medial to the costal flange. Distal part of II at the last intercostal space lack well-developed tendinous origin, and the attachments are mostly fleshy. Though the exact tendon to muscle fibre ratio varies between intercostal spaces, distal parts of II in the *Co. corax* we examined consistently occupies the entire intercostal space. II in *Dr. novaehollandiae* (Fig. 6.7B, 6.7C, 6.7F) has the same attachment sites as in *Co. corax*, and the fibres pass anteroventrally on all intercostal spaces. However, four distinct features were observed in *Dr. novaehollandiae*: (1) II is present between the last cervical and the first dorsal vertebral ribs. (2) II only occupies the proximal two-thirds of the intercostal space. (3) tendinous fibres make up more than half the volume of II. (4) the proximal most portions of II form several

discrete, spindle-like fascicles instead of a continuous sheet. In *Dr. novaehollandiae*, straps of muscles that share the same fibre orientations as IE are occasionally developed immediately distal or medial to II. We interpreted these straps as variations of II because a consistent pattern is absent within the same individual.

In crocodylians (Fig. 6.5D, Fig. 6.7D, 6.7E, 6.7F), II connects the adjacent dorsal vertebral and intermediate ribs. Between the adjacent vertebral ribs, fibres originated freshly from the anterior aspect of the rib shaft medial to the costal flange. Passing anteroventrally at an acute angle, fibres attach tendinously to the preceding vertebral ribs. Between the intermediate ribs, fibres pass anteroventrally to connect the anterior and posterior margins of the adjacent segments. At the junction between vertebral and intermediate ribs, the intercostal nerves transition from being positioned lateral to II to being positioned medial to it, which is consistent with observations in the literature (Murakami et al. 1991). Unlike in *Co. corax* and *Dr. novaehollandiae*, the attachments of II are positioned more medially, and the insertions are the tendinous ends. II is inconsistently identified in the literature. Cong et al. (1988) and Frey (1988) consider II to occupy the intercostal spaces between vertebral, intermediate, and sternal ribs, whereas Murakami et al. (1991) and Rose et al. (2021) identify II between the intermediate and sternal ribs. In the crocodylians we examined, fibres of II between the intermediate ribs do transition smoothly into m. subcostalis (SC) between the sternal ribs. II and SC can however be distinguished morphologically. Although SC and II examined in this study may be homologous, we distinguish SC from II for the ease of descriptive comparisons between birds and crocodylians as they are attached to sternal and intermediate ribs, respectively.

m. costoplumonare (CP). CP is the deepest hypaxial muscle ventral to the fixed lung, which was only observed in *Dr. novaehollandiae* (Fig. 6.8A, 6.8B). Fibres originate medially from the rib shafts of the dorsal vertebral ribs near the intracostal joints, which converge medially and attach to an aponeurosis adhered to the ventral surface of the lung. CP is therefore a broad sheet of muscle between the lung and the other abdominal organs (e.g. liver). Though CP was not observed in *Co. corax*, it has been reported from galliforms, anseriforms, and columbrids with similar configuration (Fedde et al. 1964; George and Berger 1966; Ghetie 1976). CP in birds, m. diaphramaticus in crocodylians, the diaphragm in mammals, and the non-muscular

intracoelomic septum in squamates are positioned approximately between the lungs and the livers, which hint at a homologous relationships between these muscles and the intracoelomic septum (Klein and Owerkowicz 2006). The intracoelomic septa might independently have become muscular to facilitate respiration in ancestral amniotes, as these muscles are generally associated with respiration (Fedde et al. 1964; Carrier and Farmer 2000; Evans and Miller 2013).

m. costosternalis (COT). COT is a muscle with multiple strips and positioned ventral to IE with two configurations in birds. In *Co. corax*, fibres originate from the anterolateral process of the sternum, which pass posteriorly and attach on the anterior aspect of the first sternal rib. In *Dr. novaehollandiae* (Fig. 6.9A, 6.9B), fibres originate from the anterolateral process of the sternum, which pass posterolaterally into five strips and insert on the lateral aspects of the five sternal ribs. Claessens (2009) describe a strip of COT (m. costosternalis pars major in Claessens 2009) attaching to the last cervical rib in basal birds, which was not observed in our *Dr. novaehollandiae*.

deWet et al. (1967) identify COT as m. costosternalis pars major, which is illustrated lateral to the sternal ribs. By comparison, George and Berger (1966) suggest that COT is homologous to m. triangularis sterni which is positioned anterior and posterior to the sternal ribs in *Co. corax* described by Shufeldt (1988), which is not consistent with our observations. Illustrations of Ghetie et al. (1976) agree with Shufeldt (1988) but divide m. triangularis sterni into mm. subcostalis lateralis and mm. subcostalis medialis in galliforms and anseriforms. Zusi and Bentz (1984) identify a muscle termed costosternalis pars major in trochilid birds that share similar configuration as m. triangularis sterni in *Co. corax* identified by Shufeldt (1988). In crocodylians, Cong et al. (1988) identify m. sternocostalis as a muscle originate from the sternum and insert on the first three sternal ribs ventrally, which is topologically similar to COT. Unfortunately, we could not confirm the presence of m. sternocsotalis in our dissections. From our dissections and the literature, non-volant birds and crocodylians seemingly have COT lateral/external to the ribcage, whereas most volant birds have COT medial to the ribcage. COT and other muscles connecting the sternum and the sternal ribs are probably homologous with SC judging from their close proximity to sternal ribs, and the different configurations likely

represent adaptations to respiratory demands as COT is active during inspirations (dewet et al. 1967; Claessens 2009).

m. subcostalis (SC). SC is constituted of multiple strips occupying the intercostal spaces between adjacent sternal ribs.

SC has similar fibre orientations in extant birds examined in this study. Fibres originate from the posterior margin of a sternal rib, which pass posteroproximally and insert on the anterior margin of the succeeding sternal rib. In *Co. corax* (Fig. 6.10A, 6.10D), SC takes up the entirety of the intercostal space between the first and second sternal ribs, which gradually reduce in volume in the subsequent four intercostal spaces. In the last intercostal space between the fifth and the sixth sternal ribs, only a membrane of transparent connective tissues is present. In *D. novaehollnadiae* (Fig. 6.10B, 6.10D), SC takes up approximately 60% of the intercostal space between the first three sternal ribs. A mesh of loose connective tissues and fatty tissues take up the last two intercostal spaces between the third and the fifth sternal ribs.

In crocodylians (Fig. 6.6D, Fig. 6.10C, 6.10D), fibres of SC originate from multiple tendons on the anterior margin of the sternal rib, which pass anteromedially and insert on the posterior margin of the preceding sternal rib. In at least one *Cai. crocodilus* (UAMZ unnumbered), fibres of SC between the first and the second sternal ribs have additional attachment on the ventral aspect of the first sternal rib. This fascicle of SC is topologically comparable to m. sternocostalis described by Cong et al. (1988) but the attachment is not on the sternum as m. sternocostalis would be. Unlike *Co. corax* and *Dr. novaehollandiae*, SC takes up the entirety of all intercostal spaces between adjacent sternal ribs, though the volume of SC is reduced in the intercostal space posterior to the fifth sternal ribs. The SC in crocodylians is typically identified as the ventral portion of II between adjacent sternal ribs in the literature (Cong et al. 1988; Frey 1988; Rose et al. 2021). A smooth transition between II and SC without distinct separation of fascia was observed in our dissection. However, SC can be distinguished from II in at least two ways. Fibres of SC originate from multiple tendons whereas those of II originate freshly. Moreover, fascicles of SC are more developed in the anterior half of the intercostal space between adjacent sternal ribs, whereas those of II are evenly distributed within

a given intercostal space. Therefore, SC in crocodylians is identified as a distinct muscle in this study.

6.3.2 Pelvic muscles

m. iliofemoralis internus (IFI)/ m. puboischiofemoralis internus 1 (PIFI1). IFI in birds and PIFI1 in crocodylians are homologous deep pelvic muscles that connect the femur to the pelvis (Rowe 1986, p.198; Gatesy and Middleton 1997; Hutchinson 2001b; Hutchinson 2001a; Rhodes et al. 2021)

IFI is consistently smaller than the closely positioned ITCR or ITM in *Co. corax* and *Dr. novaehollandiae*. Fibres originate from the preacetabular blade of the ilium at its ventral border, which pass laterally to insert on the posteromedial aspect of the femur. An oval or round scar marking the origin of IFI is present immediately anterior to the acetabulum and its insertion is near the base of the femoral neck on the medial side (Fig. 6.11D, 6.11I). The configuration of the IFI in *Co. corax* is consistent with the literature (Hudson 1937; Gatesy and Middleton 1997; Verstappen et al. 1998; Allen et al. 2015; Allen et al. 2015; Klinkhamer et al. 2017). However, the origin of IFI in *Dr. novaehollandiae* is much smaller than it is usually illustrated in the literature (Patak and Baldwin 1998; Lamas et al. 2014).

In crocodylians, fibres of PIFI1 (Fig. 6.11E, 6.11G, 6.11J) originate from an area on the medial aspect of the ilium and ischium outlined by the sacral ribs and the acetabulum. Laterally, the fibres insert on the femur medial to the fourth trochanter, between the dorsally positioned m. puboischiofemoralis externus 3 and the ventrally positioned m. adductor femoris 1 (Fig. 6.11). Configuration of PIFI1 is consistent with the literature (Romer 1923; Gatesy and Middleton 1997; Klinkhamer et al. 2017).

mm. iliotrochanterici cranialis et medius (ITCR+ITM)/ m. puboischiofemoralis internus 2 (PIFI2). ITCR+ITM together in birds have been interpreted as the homologue of PIFI2 in crocodylians, both of which are deep muscles positioned anteriorly on the ilium (Rowe 1986; Hutchinson 2001a; Hutchinson 2001b; Hutchinson 2002).

In extant birds examined in this study, the ITCR is positioned anterior to ITM (Fig. 6.11B, 6.11C, 6.11H, 6.11I). Fibres of both ITCR and ITM originate along the ventrolateral edge of the preacetabular blade of the ilium. Posterolaterally the muscle fibres of ITCR and ITM pass to insert on the anterolateral aspect of the femur with ITCR inserting further distally. The two are fused or closely associated along much of their length in the specimens of *Co. corax* and *Dr. novaehollandiae* examined (Fig. 6.11, A – C).

Two types of muscle scars are present. In *Co. corax*, the osteological correlates of the origins of ITCR and ITM are along the narrow ridge formed by the ventrolateral margin of the preacetabular portion of the ilium (Fig. 6.11A, 6.11B). The origin of ITCR extends along the majority of the preacetabular iliac blade to the anteroventral corner of the ilium, whereas the origin of ITM occupies the small remaining space between the origin of ITCR and the acetabulum, which are consistent with literature (Hudson 1937; Verstappen et al. 1998). The origins of ITCR and ITM in *Dr. novaehollandiae* are indicated by clear, adjacent, tri-oval scars on the lateral side of the preacetabular hook (i.e. "ventral preacetabular hook" sensu Carrano and Hutchinson 2002), which are positioned ventral to the origin of m. iliotrochantericus caudalis (Fig. 6.11, A – C). The origin of ITCR occupies the anterior portion, from the anterior apex of the ilium to the ventral apex of the preacetabular hook, and the origin of ITM extends from this point to about halfway to the acetabulum (Fig. 6.11, A – C). Both muscle attachments extend slightly onto abdominal soft tissues. Intermuscular lines outline the origins of ITCR and ITM and separate them from the origin of m. iliotrochantericus caudalis, and a faint intermuscular line divides the origins of ITCR and ITM from each other (Fig. 6.11A, 11C). Dorsally, neither origin extends much, if at all, beyond the acetabulum, nor do they extend beyond the notch at the anterior end of the ilium separating the preacetabular hook from the rest of the preacetabular portion of the ilium. The origin of m. iliotrochantericus caudalis in *Dr. novaehollandiae* noteworthily occupies the majority of the preacetabular blade laterally, which is a configuration consistent with many other birds (Hudson 1937; Hudson et al. 1959; Halvorson 1972; Shufeldt 1988; Verstappen et al. 1998; Paxton et al. 2010). However, in other studies of *Dr. novaehollandiae*, the origins of ITCR and ITM are displaced dorsally and appear to restrict available space for the origin of m. iliotrochantericus caudalis on the preacetabular iliac blade (Patak and Baldwin 1998; Lamas et al. 2014).

PIFI2 is a triangular muscle sheet in crocodylians. Fibres originate from the last six dorsal vertebrae at the ventrolateral aspect of the centra, which converge posterolaterally into a broad, strap-like tendon inserting onto the proximolateral aspect of the femur. The configuration of PIFI2 is consistent with literature (Gatesy and Middleton 1997; Klinkhamer et al. 2017).

m. obturatorius lateralis (OL)/ m. puboischiofemoralis externus 1 (PIFE1). OL in birds and PIFE1 in crocodylians are homologous, deep pelvic muscles (Gatesy and Middleton 1997; Patak and Baldwin 1998; Verstappen et al. 1998; Gangl et al. 2004; Lamas et al. 2014).

In *Co. corax* examined in this study, fibres of OL originate fleshly from the anterodorsal margin of the obturator foramen and from a small area at the centre of ventral margin of the ilioischiadic foramen, which pass laterally to insert onto the posterior aspect of the femoral trochanter (Fig. 6.12A, 6.12B, 6.12G). The OL was absent in the specimen of *Dr. novaehollandiae* examined, which matches observations of Lamas et al. (2014) but contradicts to those of Haughton (1867) and Patak and Baldwin (1998) In *Co. corax*, these two bellies share a common, predominantly muscular insertion on the femoral head, medial to and closely associated with the insertion tendon of OM (Fig. 6.12C, 6.12D, 6.12H). This condition is consistent with literature on *Corvus* (Hudson 1937) but differs from other corvids (Verstappen et al. 1998; Meilak et al. 2021).

PIFE1 in crocodylians originates from the anterior surface of the pubic apron and has a tendinous insertion on the greater trochanter of the femoral head, similar to the OL in *Co. corax* (Fig. 6.12E, 6.12B, 6.12G). The configuration of PIFE1 is consistent with literature (Gatesy and Middleton 1997; Hutchinson 2001a; Allen et al. 2015; Klinkhamer et al. 2017).

m. obturatorius medialis (OM)/m. puboischiofemoralis externus 2 (PIFE2).
The OM of birds and its crocodylian homologue, PIFE2, are deep pelvic muscles (Gatesy and Middleton 1997; Patak and Baldwin 1998; Verstappen et al. 1998; Gangl et al. 2004; Lamas et al. 2014).

In *Co. corax*, fibres of OM originate from the medial side of the puboischiadic membrane and the surrounding osseous ring except its anterior edge and pass anterolaterally to join the

tendon of OL before inserting onto the femoral trochanter (Fig. 6.12A, 6.12B, 6.12G). This is consistent with the literature (Hudson 1937; Verstappen et al. 1998). However, the OM in *D. novaeholldandiae* has two heads: an ilium-ischium part (OMII) that originates from the medial aspect of the ilioischiadic membrane, and an ischium-pubis part (OMIP) that arises from the medial surface of the puboischiadic membrane (Fig. 6.12C, 6.12D, 6.12H). The osteological correlates for both heads of the OM include the thin, delicate ridge of bone lining the dorsal, posterior, and ventral margins of their respective fenestrae. Both the OMII and OMIP insert via separate but adjacent tendons on the femoral trochanter (Fig. 6.12A, 6.12B). The configuration of OM in *Dr. novaehollandiae* is consistent with the literature (Lamas et al. 2014).

The origin of PIFE2 in crocodylians is the posterior surface of the pubic apron (Fig. 6.12E, 6.12F, 6.12I). It shares a common insertion with PIFE1 on the greater trochanter of the femoral head. Observations were consistent with previous studies (Gatesy and Middleton 1997; Verstappen et al. 1998; Hutchinson 2001a; Hutchinson 2001b; Hutchinson 2002).

In *Co. corax*, the area of origin of ISF is relatively large compared to other pelvic muscles, occupying much of the ischium laterally. It extends to the ilioischiadic foramen anterodorsally, to the puboischiadic fenestra ventrally, to the posterior margin of the ilium posteriorly, and abuts the origins of m. iliofibularis (ILFB) and m. flexor cruris lateralis pars pelvica (FCLP) (Fig. 6.13A, 6.13D). Away from the origin, muscle fibres of ISF converge into a broad and flat tendon that inserts on the posterolateral aspect of the femur between the common insertion of OL and OM proximally and the insertion of m. caudofemoralis pars caudalis (CFC) distally. Unlike *Co. corax*, the ISF in *Dr. novaehollandiae* (Fig. 6.13B, 6.13C) is small relative to other pelvic muscles, as in many other palaeonagths (Gangl et al. 2004; Zinoviev 2006; Lamas et al. 2014). Fibres originate from the lateral aspect of the ischium and the obturator flange, which converge laterally into a flat tendon that superficially crosse the tendons of OM before inserting onto the posterolateral aspect of the femur (Fig. 6.13B). The insertion is closely positioned posteroventrally to that of m. iliofemoralis externus (IFE) and m. iliotrochantericus caudalis (ITC), and adjacent to the proximal end of the origin of m. femorotibialis lateralis (FMTL).

Muscle scars of ISF are distinct between *Co. corax* and *Dr. novaehollandiae*. The origin of ISF in *Co. corax* is not clearly defined but can be approximated by the posteroventral margin of the ilioischiadic foramen, dorsal margin of the puboischiadic fenestra, and posterior edge of the ilium that form most of its border (Fig. 6.13D, 6.13E). The insertion in *Co. corax* is a low, dorsoventrally elongated ridge on the posterolateral aspect of the femur. In *Dr. novaehollandiae*, the origin is an elongated, teardrop-shaped area demarcated by faint intermuscular lines along the lateral side of the obturator flange and proximal portion of the ischial shaft (Fig. 6.13D, 6.13E). The insertion of ISF is marked by a posteriorly opening concavity near the trochanter on the posterolateral side of the femur.

6.3.3 Hypaxial muscles in fossil archosaurs

Osteological correlates identified five trunk muscles in 33 fossil archosaurs and 11 taxonomically indetermined archosaur specimens (Table 6.2). Of the five trunk muscles, OE is identified using uncinate or uncinate scar (see Chapter 4), but little more can be added beyond the positions of the attachment.

Ventral portions of m. iliocostalis (vIC). Attachments of vIC are identified at the tuberculum in *Edmontonia longiceps* (CMN 8531) (Fig. 6.14A) and *Prosaurolophus maximus* (TMP 98.50.1) (Fig. 6.14B). As in *Co. corax* and *Dr. novaehollandiae* (Fig. 6.1B), tubercula in *Em. longiceps* form bony ridges extending anteriorly and posteriorly into the adjacent intercostal spaces, whereas only the tubercula of anterior dorsal vertebral ribs bear bony ridges extending posteriorly in *Pr. maximus*. In *Co. corax* and *Dr. novaehollandiae*, the bony ridges of tuberculum are narrow rectangles that confluent with the costal flange. By comparison, the bony ridges in *Em. longiceps* and *Pr. maximus* are well-developed with triangular or crescent outline, and they are separated from the costal flange. The ventral extensions of vIC in *Em. longiceps* and *Pr. maximus* are unknown due to the variations observed in extant birds and crocodylians and the lack of an unambiguous osteological correlate on the costal flange.

m. levator costarum (LC). Attachments of LC were identified between the capitulum and the tuberculum in 16 fossil archosaurs and additional four taxonomically indetermined specimens of non-avian dinosaurs.

As in extant archosaurs examined in this study, a smooth concavity is present between the capitulum and tuberculum in fossil pseudosuchians, *Coelophysis bauri* (NMMNH P 42351) (Fig. 6.15A), and *Protoceratops andrewsi* (AMNH 6416). LC in these fossil archosaurs likely resemble their extant counterparts. However, a bony capitulotubercular lamina is developed to connect the capitulum and the tuberculum in the several cerapodans (e.g. *Edmontosaurus regalis* (CMN 2289) and *Leptoceratops gracilis* (CMN 8889)), sauropods, tyrannosaurids (Fig. 6.15B, Fig. 6.16A), and dromaeosaurids (Fig. 6.15C) examined in this study. The proximal ends of most dorsal vertebral ribs in *Li. exquisitus* were not fully prepared for examinations at the time of this study. Distinct scars are present in large-bodied tyrannosaurids (e.g. *Gorgosaurus libratus* (UALVP 10)), confirming the capitulotubercular laminae are sites of muscle attachment. Among fossil archosaurs with capitulotubercular laminae, the proximal margins of the capitulotubercular laminae in cerapodans are slightly concave and smaller in size, whereas the capitulotubercular laminae are large with a nearly straight proximal margin in saurischians (e.g. *Saurornitholestes langstoni* (TMP1988.121.0039)). In several vertebral ribs of tyrannosaurids (e.g. *Go. libratus* (UALVP 10)) (Fig. 6.15B), a shallow concavity is present on the anterior surface of the capitulotubercular laminae. Among the archosaurs sampled in this study, LC is likely most developed in tyrannosaurids.

mm. intercostales externi (IE). Attachments of IE were identified based on the anterior and posterior intercostal ridges of the costal flange in 26 fossil archosaurs and seven taxonomically indeterminate archosaur specimens (Table 6.2). The posterior intercostal ridges tend to be more developed than the anterior counterparts. However, the sizes and orientations of the intercostal ridges of the vertebral ribs vary within a given ribcage (e.g. *Go. libratus* (TMP 91.36.500) (Fig. 6.16A, 6.16B) and *Pr. maximus* (TMP 98.50.1) (Fig. 6.14B)).

Despite the observed variations, general and qualitative comparisons can be made between taxa of major archosaur clades examined in this study. Intercostal ridges are generally

well-developed in larger vertebral ribs, which is exemplified by comparisons between a young *Go. libratus* (TMP 91.36.500) (Currie 2003) and a most definitely juvenile tyrannosaurid (TMP 94.12.960) (Fig. 6.16A, 6.16B). Configurations of IE along with the intercostal ridges are likely related to body sizes. However, body size alone can not account for all variations of the intercostal ridges. A relatively small vertebral rib of *Struthiomimus altus* (AMNH 5355) carry well-developed intercostal ridges, whereas decent sized vertebral ribs of ornithischians (e.g. *Triceratops horridus* (AMNH 5033), *Ed. regalis* (CMN 2289)) carry less developed intercostal ridges. The dimensions of the intercostal ridges, and by extension the configurations of IE are likely influenced by phylogenetic constraints and functional demands.

mm. intercostales interni (II). Attachments of II were identified only in *Gorgosaurus libratus* (TMP1991.36.500) (Fig. 6.16A) and two taxonomically indeterminate tyrannosaurids (Fig. 6.16C, 6.16D). The muscle scar is a slender rugosity positioned on the anterior aspect of the rib shaft immediately medial to the costal flange. Extending parallel to the long axis of the vertebral rib, muscle scars of II terminate before reaching the midshaft in all vertebral ribs examined in this study. If the muscle scars outline the exact attachments on the vertebral ribs, II is likely reduced in tyrannosaurids as in *Dr. novaehollandiae*.

m. appendicocostalis (APC). Attachments of APC were identified based on preserved cartilaginous uncinate processes in the notosuchian, *Araripesuchus gomesii* (AMNH 24450) and the thescelosaurid, *Parkosaurus warreni* (ROM 804) (Boyd et al. 2009). With ossified uncinate processes, attachments of APC were identified in the dromaeosaurids, *Saurornitholestes langstoni* (UALVP 55700) (Fig. 6.17A) (Currie and Evans 2019) *Li. exquisitus* (IVPP V 16923) (Xu et al. 2015) (Fig. 6.17B). In the sampled dromaeosaurids, the dorsal vertebral ribs adjacent to the uncinate processes are slender compared to extant archosaurs examined in this study, a sheet of membranous connective tissues (e.g. ligamentum triangulare) may be present to receive fibres of APC. In archosaurs without preserved uncinate process, approximate attachments of APC were identified on the costal flange lateral to the uncinate scars (see Chapter 4) in 24 fossil archosaurs and additional nine taxonomically indeterminate vertebral ribs of archosaurs.

6.3.4 Phylogenetic inferences on the area of attachment in pelvic muscles

Results of the Phylogenetic Generalized Least Square (PGLS) regressions recovered similar results as (Rhodes et al. 2021) with the revised measurements taken directly from *Co. corax* and *Dr. novaehollandiae* (Fig. 6.18) (see digital supplementary Information, Data S1). The divergences from Rhodes et al. (2021) are found only within Aves where the regression model now fits well ($p < 0.05$) with each of the three dependent/response variables—the area of all hip muscles ($R^2_{adj} = 0.8966$, $p = 0.0351$), major extensors ($R^2_{adj} = 0.9266$, $p = 0.0248$), and ilium length ($R^2_{adj} = 0.8842$, $p = 0.0394$). Regressions for non-avian theropods were virtually unchanged as these data weren't modified, whereas regressions for bipeds in all three dependent variables yielded different values. Between regressions including only non-avian theropods and that includes all bipeds, the phylogenetically corrected residuals of the latter contain higher variations, greater extreme values, and conflicting signals in the residuals. The most extreme example is in the PGLS regression of major extensors in bipeds in which *Corvus* has a phylogenetically corrected residual +388.5% its fitted value, suggesting that ravens have nearly 4 times the major extensors expected for a biped of its body size (see digital supplementary Information, Data S1). In context with the odd pattern of phylogenetically corrected residuals in the other PGLS regressions, the noise introduced by the avian data may represent the anatomical and behavioural distinctions between non-avian theropods and birds (Hutchinson and Gatesy 2000; Bishop et al. 2018; Rhodes et al. 2021).

Jenks Natural Breaks optimization recovered nearly the same distribution of cursoriality as Rhodes et al. (2021) The revised data from *Dr. novaehollandiae* drops it one class regarding the proportion of major extensors, but it remains as having among the highest degree of "average" cursoriality in the dataset (Fig. 6.19). Sensu Rhodes et al. (2021, Fig. 6.14), "average" cursoriality is derived from the average score of major extensors (according to their class in Jenks Natural Breaks optimization), leg proportions, ankle joint/fusion, functional digits, and foot symmetry rated on a categorical scale from 1–5. However, *Co. corax*, with the major extensors constituting mere 12% of the area of all pelvic muscles, was classified as the lowest tier alongside the non-theropod saurian (Fig. 6.19). The same pattern as Rhodes et al. (2021) was found comparing the four- and five-class models, although the latter performed much better ($\Delta AIC_C = 22.18$) (see digital supplementary Information, Data S1). For "average" cursoriality,

the raven was in the second-lowest category, grouping with *Falcarius*, *Saurornitholestes*, and *Sinovenator* (Fig. 6.19C). These results remained the same whether four or five classes were used, neither of which was notably better (ΔAIC_C = 1.15) (see digital supplementary Information, Data S1).

6.4 Discussion

6.4.1 Implications on the origin of uncinate process. Uncinate processes are directly found in several fossil archosaurs (Turner and Calvo 2005; Codd et al. 2008; Boyd et al. 2011), and indirect evidence of uncinate processes are found in at least 19 archosaurs (see Chapter 4). The anatomical data presented in this chapter show that uncinate process is positioned near the attachments of several trunk muscles (i.e. OE, IE, II, APC, and vIC in crocodylians). Embryonic studies have provided empirical evidence on the significance of muscle activities for the formations of skeletal features. Embryonic studies have provided empirical evidence on the significance of muscle activities for the formations of skeletal features (deltoid tuberosity in mice in Blitz et al. 2009; retroverted hallax in birds in Francisco Botelho et al. 2015). Activities of trunk muscles (e.g. IE) during embryonic development may induce the presence of bony ridges/eminences by exerting mechanical stimuli on the cartilaginous template (Shwartz et al. 2013), which may in turn alter the distributions of cell population (Mammoto and Ingber 2010) and contribute to the formation of uncinate process.

The cartilaginous and ossified uncinate processes in extant crocodylians and birds accordingly may offer a portal to study the developmental processes that govern the formations and ossifications of uncinate processes. In addition, key stages of uncinate process formation independent of muscle activities can be explored in *Dr. novaehollandiae* and anhimids (George and Berger 1966) where uncinate process is lost but APC is retained.

6.4.2 Possible functional transformations of trunks muscles in archosaurs

Three of the trunk muscles and their osteological correlates show great disparities among archosaurs examined in this study. vIC is attached mostly to the tuberculum of the dorsal vertebral ribs in *Co. corax* and *Dr. novaehollandiae*, whereas vIC laterally covers the dorsal vertebral ribs and attaches to the uncinate processes in crocodylians. IC in crocodylians has been identified as an expiratory muscle in an *in vivo* electromyographic study performed on *Al. mississippiensis* (Codd et al. 2019). If vIC in *Co. corax* and *Dr. novaehollandiae* share the same function as in *Al. mississippiensis*, their reduced vIC likely generate less torques to contract the thorax. Alternatively, vIC in *Co. corax* and *Dr. novaehollandiae* may assume an inspiratory role and flex the axial skeleton along with some epaxial inspiratory muscles such as m. longissimus dorsi (Baumel et al. 1990). Assuming the observations of *Co. corax* and *Dr. novaehollandiae* represent the general conditions in birds, the reductions of vIC imply a functional shift in its function in archosaurs on the line to birds. Evidence of pneumatic sacs are known from saurischian dinosaurs (O'Connor 2006; Wedel 2009), and a semi-rigid lung in saurischian dinosaurs are inferred leading to a completely immobile lung in birds by the morphology of vertebral ribs (Schachner et al. 2011; Brocklehurst et al. 2018). Recruitment of pneumatic sacs as part of the respiratory organs would increase the compliance of the respiratory tract (Perry and Duncker 1980), which likely reduce the needs for skeletal muscles to generate expiratory airflow by contracting the thorax. The reduction of vIC likely contribute to a decrease in body mass, along with the pneumatization of the skeleton, which may contribute to the anatomical capacity for flight.

LC and its osteological correlates suggest LC is more developed in several tyrannosaurids and cerapodans as the vertebral ribs of these taxa carry capitulotubercular laminae, which offer additional area of attachment. LC is considered an inspiratory muscle in birds and crocodylians (George and Berger 1966; Cong et al. 1988), though empirical evidence is well documented only from the domestic chicken, *Gallus domesticus* (Fedde et al. 1964). In non-avian dinosaurs, the well-developed LC could rotate the vertebral ribs at a higher rate to ventilate air into and out of the respiratory organs, assuming all other variables are equal. The well-developed LC could be an adaptation to meet the metabolic demands of oxygen from increased body mass (Burness et al. 2001; Hudson et al. 2013) As capitulotubercular laminae are present in large-bodied

cerapodans and non-avian saurischians, the improved inspiratory capacity of LC might be present in basal dinosaurs and even be one of the adaptations to increase body mass. The capitulotubercular laminae in dromaeosaurids is probably inherited from the phylogenetically more basal theropods and not developed independently, as the sizes of dromaeosaurids examined in this study could approximate the sizes of extant paleognaths (e.g. *Dr. novaehollandiae*). The lost of capitulotubercular laminae in extant birds potentially took place after Dromaeosauridae branched off Eumaniraptora.

In *Dr. novaehollandiae* and crocodylians, insertions of APC are positioned adequately ventral to the origins, whereas insertions of APC in *Co. corax* are positioned approximately the same positions as the origins on the dorsal vertebral ribs. If the changes in APC configuration coincide with the development of an ossified uncinate process, APC in maniraptoran dinosaurs may already have similar configurations as in extant birds carrying ossified uncinate processes, instead of *Dr. novaehollandiae* and anhimids and megapodids. Zimmer (1935) and Tickle et al. (2007) quantitatively estiamte the mechanical leverages of APC provided by ossified uncinate processes in birds. The variations in APC attachments may represent a different functional strategy to inspire air in *Dr. novaehollandiae*, anhimids, and megapodids.

6.4.3 Trunk muscle studies and their potentials for addressing Carrier's constraints

Birds and crocodylians represent archosaurs with distinct strategies in terrestrial locomotion. Extant birds have fully-erect/parasagittal gaits where the hindlimbs are positioned parasagittally ventral to the pelvic girdle, and the acetabulum of the pelvic girdle is oriented laterally (Bakker 1971; Baumel et al. 1993; Sullivan 2007). By comparison, crocodylians have semi-erect gaits where the femur is extended ventral laterally from the laterally oriented acetabulum (Cong et al. 1988; Gatesy 1991).

Carrier (1987) identified conflicts between simultaneous demands of locomotion and ventilation in lizards and early tetrapods, termed Carrier's constraints, in which locomotion is achieved by undulating the body from a sprawling gait and ventilation is achieved largely by costal ventilation (Perry et al. 2019). The 'locomotion components' of the ribcage have been captured *in vivo* in *Va. exanthematicus* and *Salvator merianae* (pure locomotion in Cieri et al.

2020), confirming the involvement of the trunk in locomotion in squamates with sprawling gaits. Similar constraints are likely present in crocodylians with semi-erect gaits although crocodylians can use a repertoire of gaits (Gatesy 1991; Renous et al. 2002). In addition to propel the body directly, the trunk muscles function to adjust the position of the centre of mass in *Coturnix coturnix*, a bipedal bird with parasagittal gaits (Abourachid et al. 2011), and possibly other bipedal birds and theropod dinosaurs. The involvement of trunk muscles in locomotion could be common in archosaurs, and Carrier's constraints may be present, regardless of gaits and postures.

In extant birds and mammals, locomotion and ventilation are integrated in various synchronised patterns (Tucker 1972; Art et al. 1990; Funk et al. 1993; Boggs 1997; Stickford and Stickford 2014). Such integrations have been suggested in fossil dinosaurs (Carrier and Farmer 2000). As LC and APC are both considered inspiratory muscles (Fedde et al. 1964; George and Berger 1966; Cong et al. 1988; Codd et al. 2005), the enlarged LC and the development of APC in some fossil theropods and cerapodans as inferred by the osteological correlates may enhance the anatomical capacity to inspire in archosaurs, which, along with the shifts in acetabulum orientation (Gatesy 1991; Sullivan 2007), could alleviate the impacts of Carrier's constraints.

6.4.4 Pelvic muscle identification and its bearing on studies of locomotion

The pelvis and its associated soft tissues are integral for locomotion in archosaurs (Hutchinson and Gatesy 2000; Allen et al. 2021). The majority of our observations were consistent with existing literature on pelvic musculature in crocodylians and neognath birds (Gatesy 1997; Verstappen et al. 1998; Allen et al. 2015; Klinkhamer et al. 2017). However, there were some conflicts between our dissection and previous studies on emus. Fortunately, a recent study (Lamas et al. 2014) using updated myological terms consistent with recently standardized nomenclature (Baumel et al. 1993) allowed easier comparisons between homologous muscles across Archosauria (Hutchinson 2002). Nevertheless, some conflicts remained, and addressing these issues will clarify conditions for identification, reconstruction, and analysis.

The IFI is the smallest muscle in the deep dorsal group and its origin and insertion are close to the hip joint (Fig. 6.11D). Haughton (1867) describes the absence of IFI in *Dr. novaehollandiae*, whereas IFI is identified and/or illustrated in at least two other anatomical

studies (Patak and Baldwin 1998; Lamas et al. 2014). The IFI was observed in this study and is smaller than what is illustrated in the literature. The absolute and relative sizes of the ITCR and ITM are usually represented more accurately, although the position of the origins on the ilium tend to be displaced dorsally compared to our specimen (Haughton 1867; Patak and Baldwin 1998; Lamas et al. 2014). The origins of ITCR and ITM are along the anteroventral edge of the ilium, even expanding slightly onto abdominal soft tissues, as the origin of ITC occupies the majority of the lateral surface of the preacetabular iliac blade (Fig. 6.11A, 11B, 11H, 11I). Partial fusion of the ITCR and ITM was noted in our specimen, but this is not uncommon in paleognaths birds (Gangl et al. 2004; Lamas et al. 2014).

Opposite the acetabulum, the paired heads of the OM cover the entire medial surfaces of the ilioischiadic and puboischiadic membranes (Fig. 6.12 A – D). The OL was absent in the specimen examined, corroborating Lamas et al. (2014) but contradicting Haughton (1867). This condition is unusual for birds as the typical avian condition is that the OL is present and the OM has a single head originating from the medial side of the puboischiadic membrane (Hudson 1937; Baumel et al. 1993; Verstappen et al. 1998). Ratites do exhibit variation in the presence or fusion of certain pelvic muscles including the OL (Mellett 1994; Gangl et al. 2004; Smith et al. 2006; Lamas et al. 2014; Hutchinson et al. 2015).

Although Patak and Baldwin (1998) described the OL, it was not illustrated and its brief description is entirely applicable to the ISF in our specimen. The muscle we identified as ISF has a fleshy origin from the lateral side of the ischium and obturator flange and a separate insertion from the obturator musculature on the posterolateral aspect of the femoral shaft (Fig. 6.12A). This is topologically and morphologically consistent with the ISF in ostriches (Gangl et al. 2004; Zinoviev 2006; Lamas et al. 2014). Furthermore, this is topologically inconsistent with the OL (in ostriches or other birds), which originates from the margin of the obturator foramen and lacks an independent insertion, instead sharing a common insertion with the OM (Hudson 1937; McKitrick 1991; Verstappen et al. 1998; Gangl et al. 2004). To make matters more confusing, a synonym of ISF is OL, but this superficial similarity in names stems from traditional attempts to conform to mammalian terminology (Shufeldt 1988; Verstappen et al. 1998) and does not reflect the fact that they are separate, non-homologous muscles within Archosauria (Hutchinson 2002).

Moreover, ostriches possess both the ISF and OL as separate, distinct muscles, as do most other birds and the vast majority of other archosaurs (Gangl et al. 2004; Zinoviev 2006; Lamas et al. 2014). Although Lamas et al. (2014) resolved the concerns of the ISF, it is depicted as originating from the posterior side of the antitrochanter and inserting relatively distal, underneath the origin of m. femorotibialis lateralis (FMTL), compared to the condition of the specimen we examined (Fig. 6.13). These conditions suggest that the OL and ISF in *Dr. novaehollandiae* have high variability in their presence and morphology, have suffered from confusion in their identification (possibly hindered by historical synonyms), or both.

The muscle identified as the ISF by Patak and Baldwin (1998) and described as m. ilioischiofemoralis, originating from the lateral side of the ilioischiadic membrane, is in fact the CFP (Fig. 6.13B). This issue was also resolved and discussed by Lamas et al. (2014). This apparent frameshift in the names of the OL, ISF, and CFP may stem from the aforementioned confusion caused by traditional terminology. This issue is compounded by not including all muscles in illustrations and brief descriptions that may not clearly communicate the conditions of certain muscles.

Overall, our observations are largely in line with Lamas et al. (2014) with only a few minor divergences. These inconsistencies may simply be due to individual variation among the specimens examined. However, clarity and precision are strongly encouraged for future work to facilitate both descriptive and visual communication. Following a framework that accounts for homologies across the taxonomic range of study benefits identification and comparison with other works. Clear visuals, whether photographs, illustrations, or simple diagrams, further expedite these steps. Inconsistencies in nomenclature can cause confusion and make soft tissue reconstruction challenging, even on a skeletonized specimen of an extant species with reasonably clear osteological correlates. These parameters directly affect studies reliant on osteological correlates for data collection or analysis.

These points are underscored by comparing our observations with the reconstruction of pelvic musculature of *Dr. novaehollandiae* in (Rhodes et al. 2021). The area of attachment measured on the revised diagram was significantly different (> ±5%) for four-fifths of the

muscles. Most notably affected were the origins of ITC (378% of original area), IFI (9% of original area), and ISF (560% of original area). Altogether, the area of attachment for all pelvic muscles increased to 118% of the original diagram. While this did not alter the broader interpretations of Rhodes et al. (2021), revised areas of attachment caused the emu to drop into a lower class in the Jenks Natural Breaks optimization on the proportion of major extensors (Fig. 6.19). This result seems more sensible, especially with the addition of *Co. corax*, given that the staircase pattern formed by extant birds corresponds well to relative running ability and decreases from ostrich to emu to chicken to raven. The "average" cursoriality for extant birds reflects a similar relationship. The ostrich and emu are well established as being well adapted for running (Patak and Baldwin 1998; Smith et al. 2006, p.200; Lamas et al. 2014; Hutchinson et al. 2015). The chicken and many other galliforms are decent runners with an intermediate cursoriality and lower speed ranges than paleognaths (Gatesy and Biewener 1991; Dial 2003; Anten-Houston et al. 2017).

Considering extinct taxa offers a few broader comparisons. The proportion of major extensors in the revised emu diagram and the derived troodontid are nearly identical (<1%), perhaps not surprising for taxa both considered adept runners (Fig. 6.19) (Patak and Baldwin 1998; Carrano 1999; Lamas et al. 2014). Unfortunately, area of attachment cannot ascertain if *Sinovenator* and *Corvus* also engaged in similar terrestrial locomotory behaviours (i.e., preference for out-of-phase hopping over running). Pelvic and hind limb morphology and myology are only two aspects that do not fully capture the palaeoecological diversity of a species or a clade, and they are influenced by many factors (Gatesy and Middleton 1997; Dececchi et al. 2019). Nevertheless, locomotion is a fundamental component of palaeobiology and offers insight into adaptations and diversity among extant and extinct animals alike.

Tables

Table 6. 1. Osteological correlates of hypaxial and pelvic muscles in sampled extant archosaurs.

Muscle	Origin/Intion		
	Corvus corax	*Dromaius novaehollandiae*	crocodylians
dIC	Ori: Anterior aspect of iliac crest Dorsolateral aspect of transverse process	Ori: Anterior aspect of iliac crest Dorsolateral aspect of transverse process	Ori: Anterior aspect of iliac crest Dorsolateral aspect of transverse process
	Int: Dorsolateral aspect of transverse process	Int: Dorsolateral aspect of transverse process	Int: Dorsolateral aspect of transverse process
vIC	Ori: Anterior aspect of iliac crest Dorsolateral aspect of tuberculum	Ori: Anterior aspect of iliac crest Dorsolateral aspect of tuberculum	Ori: Anterior aspect of iliac crest Dorsolateral aspect of tuberculum
	Int: Posterolateral aspect of tuberculum	Int: Posterolateral aspect of tuberculum	Int: Posterolateral aspect of tuberculum Lateral aspect of costal flange Uncinate process
OE	Ori: Anterolateral aspect of pubis	Ori: Anterolateral aspect of pubis	Ori: Anterolateral aspect of pubis
	Int: Lateral aspect of costal flange adjacent to uncinate scar	Int: Lateral aspect of costal flange adjacent to intracostal joint Distal end of last cervical vertebral rib	Int: Lateral aspect of costal flange adjacent to uncinate scar
SN	Ori: Ventrolateral aspect of transverse process	Ori: Ventrolateral aspect of transverse process Posterior intercostal ridge of last two cervical ribs	Ori: Ventrolateral aspect of transverse process Posterior intercostal ridge of cervical ribs
	Int: Lateral aspect of costal flange of last two cervical ribs	Int: Lateral aspect of costal flange of last two cervical ribs Anterior intercostal ridge of last two cervical ribs	Int: Lateral aspect of costal flange of cervical ribs Anterior intercostal ridge of cervical ribs
LC	Ori: Posteroventral aspect of transverse	Ori: Posteroventral aspect of transverse process	Ori: Posteroventral aspect of transverse

	process		process
	Int: Anteiror aspects of capitulum and tuberculum of dorsal vertebral ribs Proximal aspect of anteiror intercostal ridge of dorsal vertebral ribs	Int: Anteiror aspects of capitulum and tuberculum of dorsal vertebral ribs Proximal aspect of anteiror intercostal ridge of dorsal vertebral ribs	Int: Anteiror aspects of capitulum and tuberculum of dorsal vertebral ribs Proximal aspect of anteiror intercostal ridge of dorsal vertebral ribs
IE	Ori: Posterior intercostal ridge of dorsal vertebral ribs	Ori: Posterior intercostal ridge of dorsal vertebral ribs	Ori: Posterior intercostal ridge of dorsal vertebral and intermediate ribs
	Int: Anterior intercostal ridge of dorsal vertebral ribs	Int: Anterior intercostal ridge of dorsal vertebral ribs	Int: Anterior intercostal ridge of dorsal vertebral and intermediate ribs
APC	Ori: Posteromedial aspect of uncinate processes	Ori: Posterior intercostal ridge of dorsal vertebral ribs near midshaft	Ori: Posteroventral aspect of uncinate processes
	Int: Lateral aspect of costal flange of dorsal vertebral ribs Lateral aspect of uncinate process Ligamentum triangulare	Int: Anteiror intercostal ridge of dorsal vertebral ribs near intracostal joint	Int: Lateral aspect of intermediate ribs
II	Ori: Anterior aspects of tuberculum of dorsal vertebral ribs Anterior aspects of ribshafts medial to costal flange of dorsal vertebral ribs	Ori: Anterior aspects of tuberculum of dorsal vertebral ribs Anterior aspects of ribshafts medial to costal flange of dorsal vertebral ribs	Ori: Anterior aspects of ribshafts medial to costal flange of dorsal vertebral ribs Anterior margins of intermediate ribs
	Int: Posterior aspects of tuberculum of dorsal vertebral ribs Posterior aspects of ribshafts medial to costal flange of dorsal vertebral ribs	Int: Posterior aspects of tuberculum of dorsal vertebral ribs Posterior aspects of ribshafts medial to costal flange of dorsal vertebral ribs	Int: Posterior aspects of ribshafts medial to costal flange of dorsal vertebral ribs Posterior margins of intermediate ribs
CP	—	Ori: Medial aspects of ribshafts of dorsal	—

		vertebral ribs adjacent to intracostal joint	
	—	Int: Aponeurosis ventral to lung	—
COT	Ori: Anterolateral process of sternum	Ori: Anterolateral aspect of sternum	—
	Int: Anterior aspect of first sternal rib	Int: Lateral aspects of sternal ribs	—
SC	Ori: Posterior margin of sternal ribs	Ori: Posterior margin of sternal ribs	Ori: Anterior margin of sternal ribs
	Int: Anterior margin of sternal ribs	Int: Anterior margin of sternal ribs	Int: Posterior margin of sternal ribs
IFI/PIFI1	Ori: Small scar on ventrolateral aspect of preacetabular blade of ilium, near and anterior to acetabulum, ventral to origin of ITM	Ori: Small scar on ventrolateral aspect of preacetabular blade of ilium, near and anterior to acetabulum	Ori: Medial side of ilium between sacral ribs and acetabulum
	Int: Medial aspect of femur near base of neck	Int: Medial aspect of femur near base of neck, between origins of FMTIM and FMTM	Int: Narrow, arcuate area medial and adjacent to fourth trochanter of femur
ITCR/PIFI2	Ori: Anteroventral edge of preacetabular blade of ilium	Ori: Anterior portion of lateral side of preacetabular hook, between anterior apex of ilium and ventral apex of preacetabular hook	Ori: Ventral aspects of centra of last six dorsal vertebrae
	Int: Proximolateral aspect of femur, distal to insertion of ITM, proximal to origin of FMTL	Int: Proximolateral aspect of femur, distal to insertion of ITM, proximal to origin of FMTL	Int: Two insertions on proximolateral aspect of femur, both proximal and adjacent to insertion of IF
ITM	Ori: Small area between origin of ITCR and acetabulum, dorsal to origin of IFI	Ori: Posterior portion of lateral side of preacetabular hook, posterior to origin of ITCR and anterior to origin of IFI	—

	Int: Proximolateral aspect of femur, proximal to insertion of ITCR, distal to insertion of ITC	Int: Proximolateral aspect of femur, proximal to insertion of ITCR, distal to insertion of ITC	—
OL/PIFE1	Ori: Two heads, larger from dorsal margin of obturator foramen and smaller from ventral margin of ilioischiadic foramen	—	Ori: Anterior (dorsal) surface of pubic apron
	Int: Posterolateral aspect of femoral trochanter, shared with OM	—	Int: Posterolateral aspect of greater trochanter on femoral head, shared with PIFE2 and PIFE3
OM/PIFE2	Ori: Medial aspects of puboischiadic membrane and adjacent osseous ring	Ori: Two heads, larger from medial aspect of puboischiadic membrane and adjacent osseus ring, smaller from medial aspect of ilioischiadic membrane and adjacent osseous ring	Ori: Posterior (ventral) surface of pubic apron
	Int: Posterolateral aspect of femoral trochanter, shared with OL	Int: Two insertions on proximolateral aspect of femoral trochanter	Int: Posterolateral aspect of greater trochanter on femoral head, shared with PIFE1 and PIFE3
ISF/ISTR	Ori: Lateral aspect of ischium between ilioischiadic and puboischiadic foramina	Ori: Obturator flange on proximolateral aspect of ischium	Ori: Posteromedial edge of ischium
	Int: Posterolateral aspect of femur, distal to insertion of OL+OM	Int: Posterolateral aspect of femur, distal to insertion of OM, proximal to insertion of IFE	Int: Posterolateral aspect of femur, proximal to origin of FMTE, posterior to insertion of PIFI2, anterior to insertion of PIFE1–3

Abbreviations: APC, m. appendicocostalis; mm. caudofemorales pars pelvica, CFP; COT, m. costosternalis; CP, m. costoplumonare; dIC, dorsal part of m. iliocostalis; IC, m. iliocostalis; IE, mm. intercostales externi; IFI, m. iliofemoralis internus; II, mm. intercostales interni; Int,

Insertion; ISF, m. ischiofemoralis; ISTR, m. ischiotrochantericus; ITCR, m. iliotrochantericus cranialis; ITM, m. iliotrochantericus medius; LC, m. levator costarum; OE, m. obliquus externuss; OL, m. obturatorius lateralis; OM, m. obturatorius medialis; Ori, Origin; PIFI1, m. puboischiofemoralis internus 1; PIFI2, m. puboischiofemoralis internus 2; SC, m. subcostalis; SN, m. scalenus; vIC, ventral part of m. iliocostalis; U, uncinate process.

Table 6. 2. Osteological correlates of trunk muscles in sampled fossil archosaurs.

Taxa	OE	vIC	LC	IE	APC	II
Deinonychus antirrhopus YPM 5250	—	—	Int: CTL	Ori: PIR Int: AIR	—	—
Linheraptor exquisitus IVPP V 16923	Int:CF next to up/us	—	—	—	Ori: up process Int: up process and the adjacent CF	—
Saurornitholestes langstoni UALVP 55700	Int:CF next to up/us	—	Int: CTL	Ori: PIR Int: AIR	Ori: up process Int: up process and the adjacent CF	—
TMP 88.121.39	Int:CF next to up/us	—	Int: CTL	Ori: PIR Int: AIR	Int: CF adjacent to the us	—
Struthiomimus altus AMNH 5355	Int:CF next to up/us	—	Int: CTL	Ori: PIR Int: AIR	Int: CF adjacent to the us	—
Daspletosaurus torosus CMN 8506	Int:CF next to up/us	—	Int: CTL	Ori: PIR Int: AIR	Int: CF adjacent to the us	—
TMP 94.143.1	—	—	Int: CTL	Ori: PIR Int: AIR	—	—
Gorgosaurus libratus UALVP 10	Int:CF next to up/us	—	Int: CTL	Ori: PIR Int: AIR	Int: CF adjacent to the us	—
TMP 91.36.500	Int:CF next to up/us	—	Int: CTL	Ori: PIR Int: AIR	Int: CF adjacent to the us	Ori: Longitudinal scar anteromedial to the CF

Albertosaurus sarcophagus TMP 99.50.41	Int:CF next to up/us	—	—	Ori: PIR Int: AIR	—	—
Albertosaurus sarcophagus TMP 99.50.43	Int:CF next to up/us	—	—	—	—	—
Albertosaurus sarcophagus AMNH 5428	—	—	Int: CTL	Ori: PIR Int: AIR	—	—
Allosaurus fragilis AMNH 5753	Int:CF next to up/us	—	—	—	Int: CF adjacent to the us	—
Allosaurus sp. MCZ 3897	—	—	Int: CTL	Ori: PIR Int: AIR	—	—
Tyrannosauridae indet. TMP 81.16.285	Int:CF next to up/us	—	—	Ori: PIR Int: AIR	Int: CF adjacent to the us	—
Tyrannosauridae indet. TMP 92.36.1231	Int:CF next to up/us	—	Int: CTL	Ori: PIR Int: AIR	Int: CF adjacent to the us	Ori: Longitudinal scar anteromedial to the CF
Tyrannosauridae indet. TMP 94.12.960	Int:CF next to up/us	—	—	Ori: PIR Int: AIR	Int: CF adjacent to the us	—
Coelophysis bauri NMMNH P 42351	—	—	Int: Anterior aspects of cm and tm	Ori: PIR Int: AIR	—	—
Apatosaurus excelsus YPM 1981	Int:CF next to up/us	—	—	Ori: PIR Int: AIR	Int: CF adjacent to the us	—
Barosaurus lentus YPM 429	—	—	Int: CTL	—	—	—
Camarasaurus sp. AMNH 625	—	—	—	Ori: PIR Int: AIR	—	—

Edmontosaurus regalis CMN 2289	—	—	Int: CTL	Ori: PIR Int: AIR	—	—
Gryposaurus notabilis AMNH 5350	Int:CF next to up/us	—	Int: CTL	Ori: PIR Int: AIR	Int: CF adjacent to the us	—
Gryposaurus latideus AMNH 5465	Int:CF next to up/us	—	—	Ori: PIR Int: AIR	Int: CF adjacent to the us	—
Bactrosaurus johnsoni AMNH 6553	Int:CF next to up/us	—	—	—	Int: CF adjacent to the us	—
Prosaurolophus maximus TMP 98.50.1	—	Int: Bony ridges of the tm	Int: CTL	Ori: PIR Int: AIR	—	—
Tenontosaurus telletti AMNH 3040	Int:CF next to up/us	—	—	Ori: PIR Int: AIR	Int: CF adjacent to the us	—
Zephyrosaurus schaffi MCZ 4392	Int:CF next to up/us	—	—	Ori: PIR Int: AIR	Int: CF adjacent to the us	—
Parkosaurus warreni ROM 804	Int:CF next to up/us	—	—	—	Ori: up process Int: up process and the adjacent CF	—
Hadrosauridae indet. AMNH 5896	Int:CF next to up/us	—	Int: CTL	Ori: PIR Int: AIR	Int: CF adjacent to the us	—
TMP 82.13.15	Int:CF next to up/us	—	—	—	Int: CF adjacent to the us	—
Leptoceratops gracilis CMN 8889	Int:CF next to up/us	—	Int: CTL	Ori: PIR Int: AIR	Int: CF adjacent to the us	—
Centrosaurus sp. TMP 82.18.16	Int:CF next to up/us	—	—	Ori: PIR Int: AIR	Int: CF adjacent to the us	—

Centrosaurus sp. TMP 82.19.41	Int:CF next to up/us	—	—	Ori: PIR Int: AIR	Int: CF adjacent to the us	—
Centrosaurus sp. TMP 82.18.56	Int:CF next to up/us	—	—	Ori: PIR Int: AIR	Int: CF adjacent to the us	—
Centrosaurus sp. TMP 82.18.281	Int:CF next to up/us	—	—	Ori: PIR Int: AIR	Int: CF adjacent to the us	—
Centrosaurus sp. TMP 96.176.135	Int:CF next to up/us	—	—	—	Int: CF adjacent to the us	—
Centrosaurus sp. ROM 767	Int:CF next to up/us	—	—	—	Int: CF adjacent to the us	—
Protoceratops andrewsi AMNH 6416	—	—	Int: Anterior aspects of cm and tm	—	—	—
Ceratopsidae indet. AMNH 5422	Int:CF next to up/us	—	—	Ori: PIR Int: AIR	Int: CF adjacent to the us	—
Ceratopsia indet.. NMMNH P22797	Int:CF next to up/us	—	—	—	Int: CF adjacent to the us	—
Panoplosaurus mirus ROM 1215	Int:CF next to up/us	—	—	Ori: PIR Int: AIR	Int: CF adjacent to the us	—
Edmontonia longiceps CMN 8531	Int:CF next to up/us	Int: Bony ridges of the tm	Int: CTL	Ori: PIR Int: AIR	Int: CF adjacent to the us	—
Sauropelta edwardsi AMNH 3032	Int:CF next to up/us	—	—	—	Int: CF adjacent to the us	—
Euplocephalus tutus AMNH 5337	Int:CF next to up/us	—	—	—	Int: CF adjacent to the us	—
Ankylosaurus magniventris AMNH 5895	—	—	—	Ori: PIR Int: AIR	—	—

Stegosaurus stenops YPM 1856	Int:CF next to up/us	—	—	—	Int: CF adjacent to the us	—
Stegosaurus stenops AMNH 650	Int:CF next to up/us	—	—	Ori: PIR Int: AIR	Int: CF adjacent to the us	—
Stegosaurus sp. AMNH 5752	Int:CF next to up/us	—	—	Ori: PIR Int: AIR	Int: CF adjacent to the us	—
Phytosauridae indet. YPM 6649	Int:CF next to up/us	—	—	Ori: PIR Int: AIR	Int: CF adjacent to the us	—
Aetosauria indet. NMMNH P50048	Int:CF next to up/us	—	—	—	Int: CF adjacent to the us	—
Gracilisuchus stipanicicorum MCZ 4116	—	—	Int: Anterior aspects of cm and tm	Ori: PIR Int: AIR	—	—
Gracilisuchus stipanicicorum MCZ 4118	—	—	Int: Anterior aspects of cm and tm	Ori: PIR Int: AIR	—	—
Lotosaurus adentus IVPP V 4910	—	—	Int: Anterior aspects of cm and tm	Ori: PIR Int: AIR	—	—
Junggarsuchus sloni IVPP V 14010	—	—	Int: Anterior aspects of cm and tm	Ori: PIR Int: AIR	—	—
Araripesuchus gomesii AMNH 24450	Int:CF next to up/us	—	Int: Anterior aspects of cm and tm	Ori: PIR Int: AIR	Ori: up process Int: intermedia te rib	—

Abbreviation: AIR, anterior intercostal ridge; CF, costal flange; cm, capitulum; CTL, Capitulotubercular lamina; PIR, posterior intercostal ridge; tm, tuberculum; up, uncinate process; us, uncinate scar.

Figures

Figure 6.1. m. iliocostalis (IC) in extant archosaurs.

dIC and vIC in *Corvus corax* (A), *Dromaius novaehollandiae* (B), and farm crocodile (C) in left lateral views. Schematic drawings of osteological correlates of dIC and vIC (D). Scale bars equal 1 cm. Abbreviations: dIC, dorsal part of m. iliocostalis; OE, m. obliquus externuss; vIC, ventral part of m. iliocostalis.

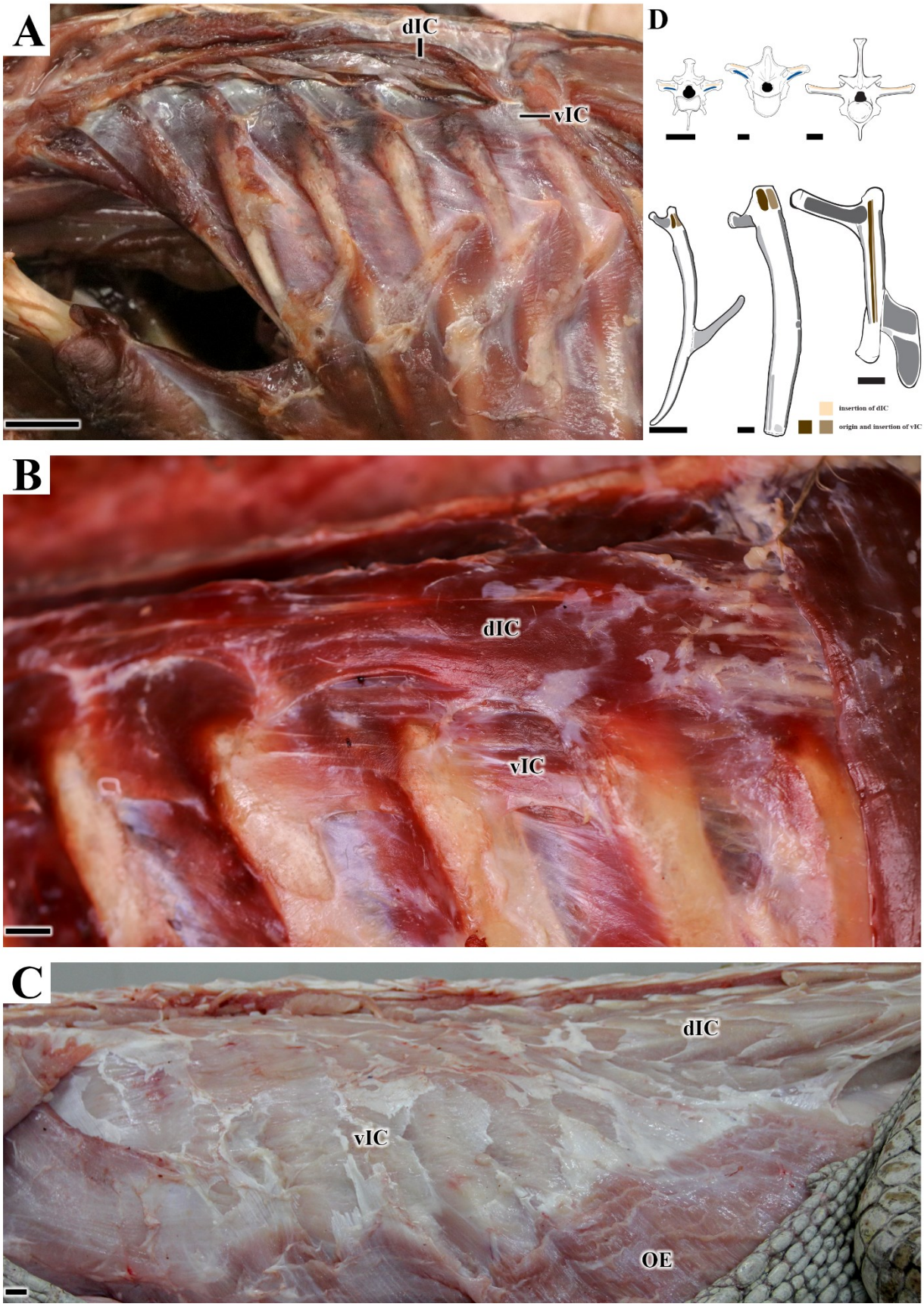
A
dIC
vIC
D
insertion of dIC
origin and insertion of vIC
B
dIC
vIC
C
dIC
vIC
OE

Figure 6.2. m. obliquus externuss (OE) in extant archosaurs.

Insertions of OE in *Corvus corax* (A), *Dromaius novaehollandiae* (B), and farm crocodile (C) in left lateral views. Schematic drawings of osteological correlates of OE (D); insertions of OE and vIC in *Varanus exanthematicus* in left lateral views (E), with OE reflected to show insertions at vertebral ribs near midshafts. Scale bars equal 1 cm. Abbreviations: APC, m. appendicocostalis; IE, mm. intercostales externi; LT, ligamentum triangulare; OE, m. obliquus externuss; vIC, ventral part of m. iliocostalis.

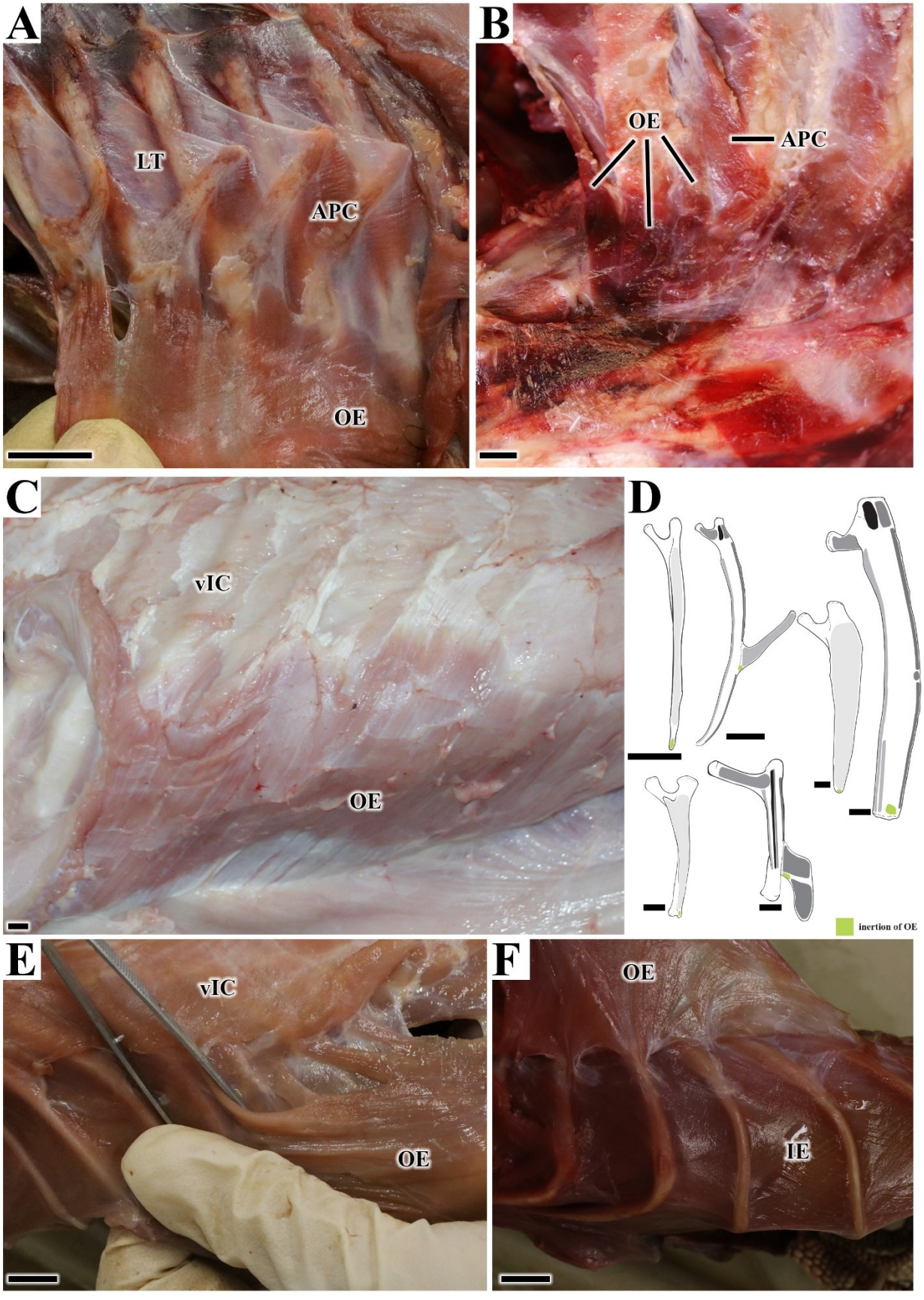
A
LT
APC
OE
B
OE
APC
C
vIC
OE
D
inertion of OE
E
vIC
OE
F
OE
IE

Figure 6.3. m. scalenus (SN) in extant archosaurs.

SN in *Corvus corax* (A), *Dromaius novaehollandiae* (B), and *Caiman crocodilus* (C) in left lateral views. Schematic drawings of osteological correlates of SN (D). Scale bars equal 1 cm. Abbreviations: LC, m. levator costarum; SN, m. scalenus.

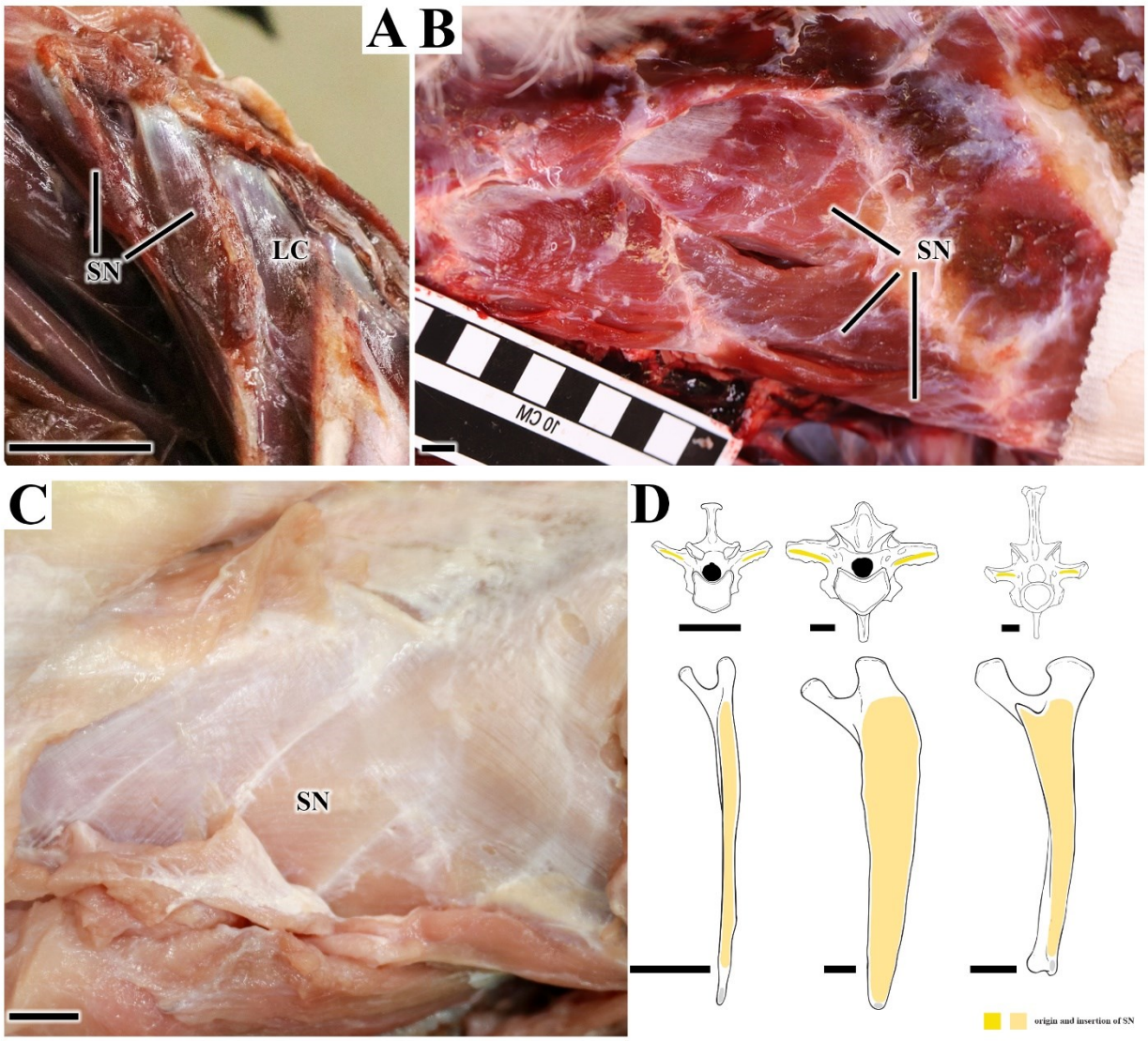
A B
SN
LC
SN
10 CM
C
SN
D
origin and insertion of SN

Figure 6.4. m. levator costarum (LC) in extant archosaurs.

LC in *Corvus corax* in right lateral view (A), *Dromaius novaehollandiae* in right lateral views (B, C), in *Caiman crocodilus* in left lateral view (D). Osteological correlates of LC (E). Scale bars equal 1cm. Abbreviations: dIC, dorsal part of m. iliocostalis; IE, mm. intercostales externi; II, mm. intercostales interni; SN, m. scalenus; vIC, ventral part of m. iliocostalis; U, uncinate process.

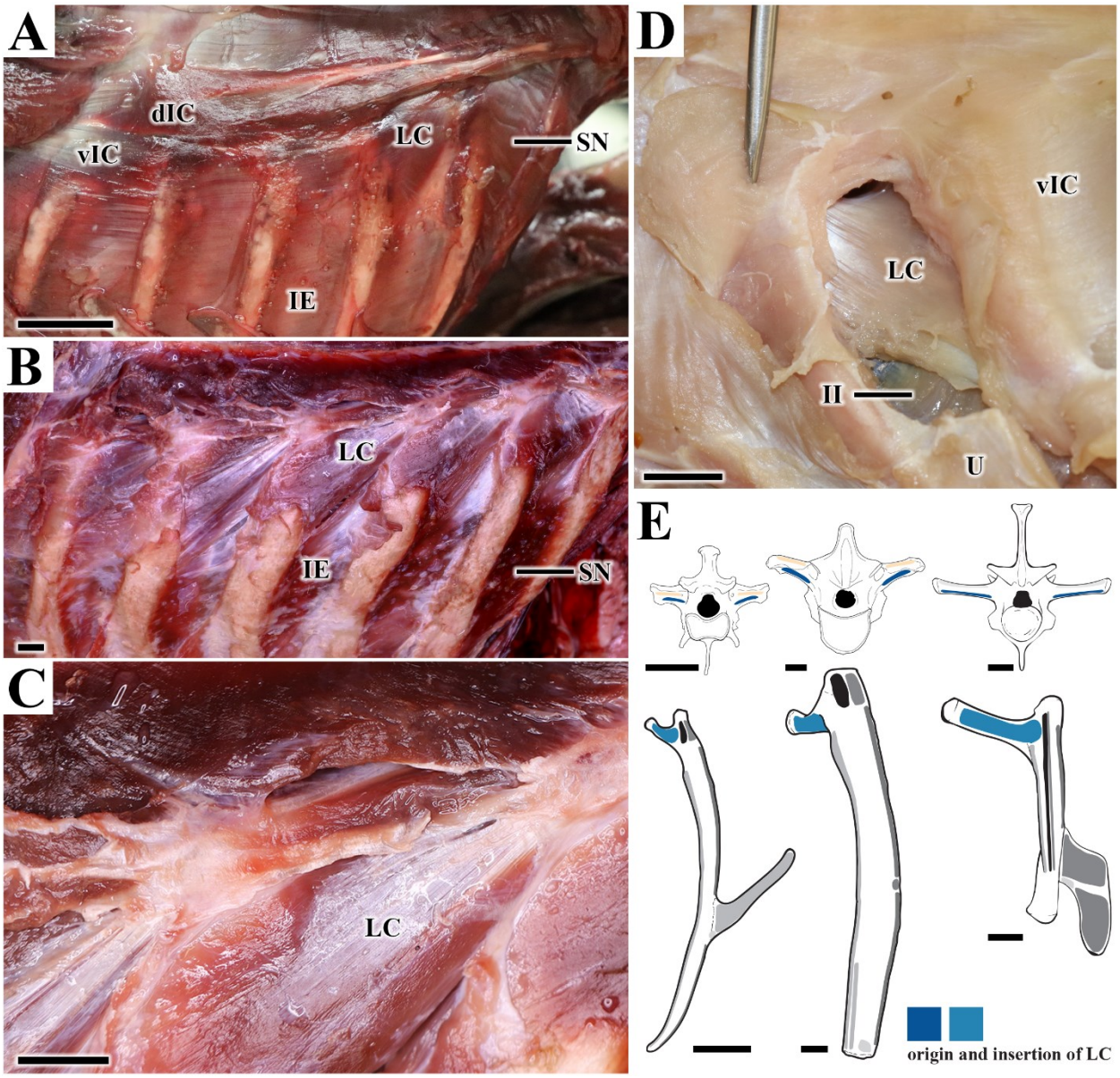
A
dIC
vIC
LC
SN
IE
B
LC
IE
SN
C
LC
D
vIC
LC
II
U
E
origin and insertion of LC

Figure 6.5. mm. intercostales externi (IE) in extant archosaurs.

IE in *Corvus corax* in right lateral views (A, B), *Dromaius novaehollandiae* in right lateral view (C), and in *Caiman crocodilus* in left lateral view (D). Osteological correlates of IE (E). Scale bars equal 1cm. Abbreviations: APC, m. appendicocostalis; IE, mm. intercostales externi; II, mm. intercostales interni; OE, m. obliquus externuss; SC, m. subcostalis; vIC, ventral part of m. iliocostalis; U, uncinate process. Blue star indicate portion of vIC attached to cartilaginous uncinate process posteromedially.

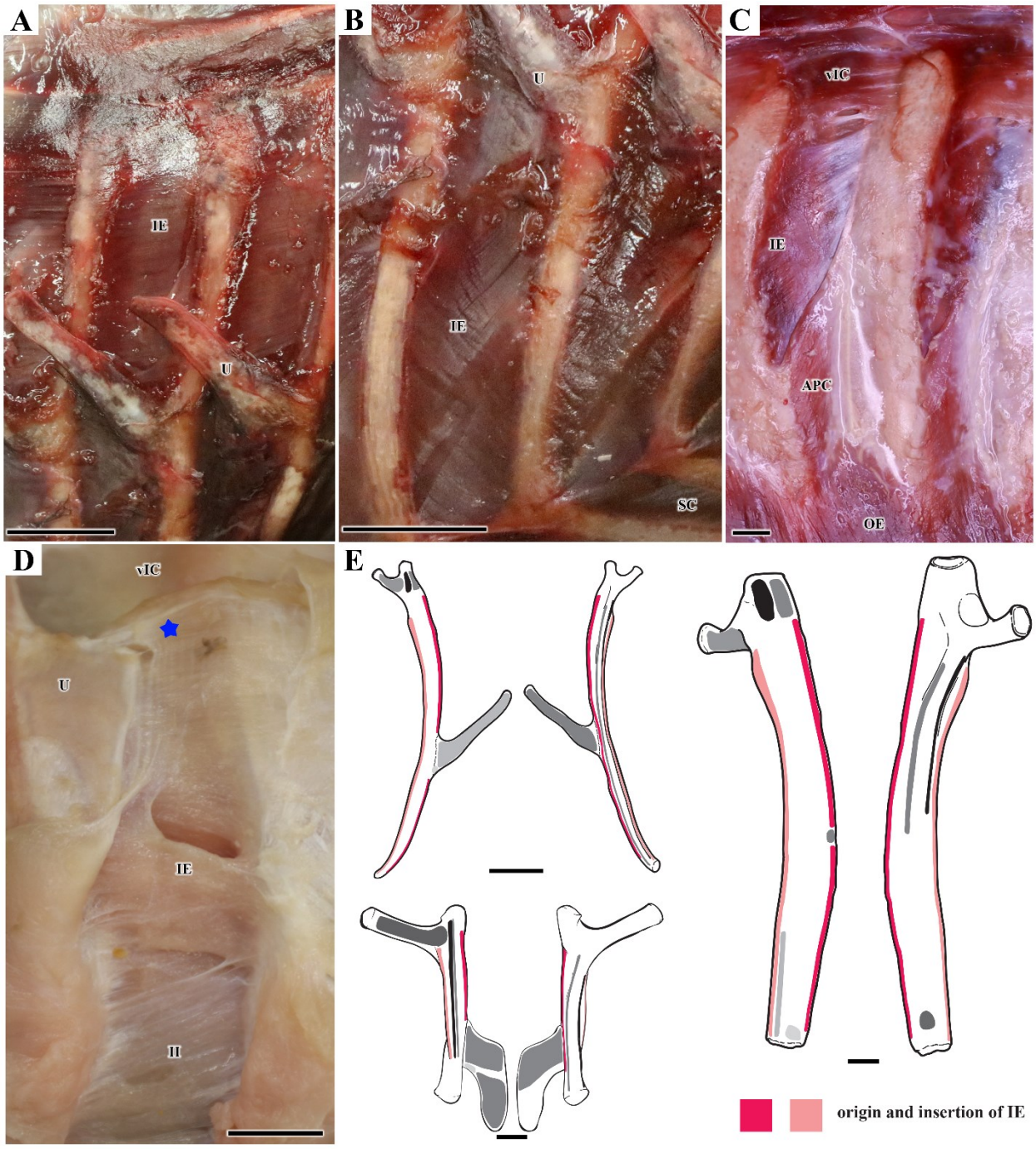
A
IE
U
B
U
IE
SC
C
vIC
IE
APC
OE
D
vIC
U
IE
II
E
origin and insertion of IE

Figure 6.6. m. appendicocostales (APC) in extant archosaurs.

APC in *Corvus corax* in left lateral views (A, B), in *Dromaius novaehollandiae* in right lateral view (C), and in *Caiman crocodilus* in left lateral view (D). Osteological correlates of APC (E). Scale bars equal 1cm. Abbreviations: APC, m. appendicocostalis; IE, mm. intercostales externi; LT, ligamentum triangulare; OE, m. obliquus externuss; SC, m. subcostalis; vIC, ventral part of m. iliocostalis; U, uncinate process.

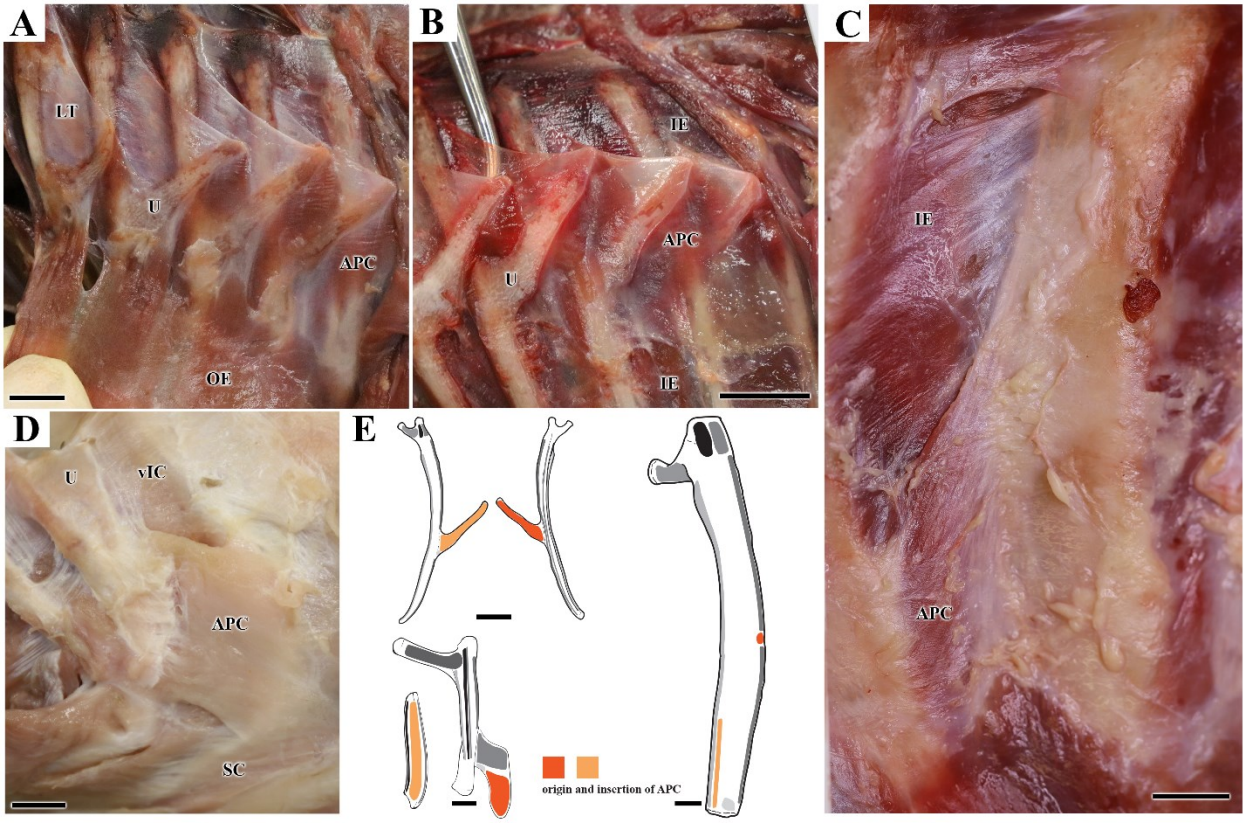
A
LT
U
APC
OE
B
IE
APC
U
IE
C
IE
APC
D
U
vIC
APC
SC
E
origin and insertion of APC

Figure 6.7. mm. intercostales interni (II) in extant archosaurs.

II in *Corvus corax* in right lateral views (A), in *Dromaius novaehollandiae* in right lateral view (B, C), and in *Caiman crocodilus* in left lateral views (D, E). Osteological correlates (F). Scale bars equal 1cm. Abbreviations: dIC, dorsal part of m. iliocostalis; IE, mm. intercostales externi; II, mm. intercostales interni; IN, intercostal nerve; LC, m. levator costarum; ; U, uncinate process.

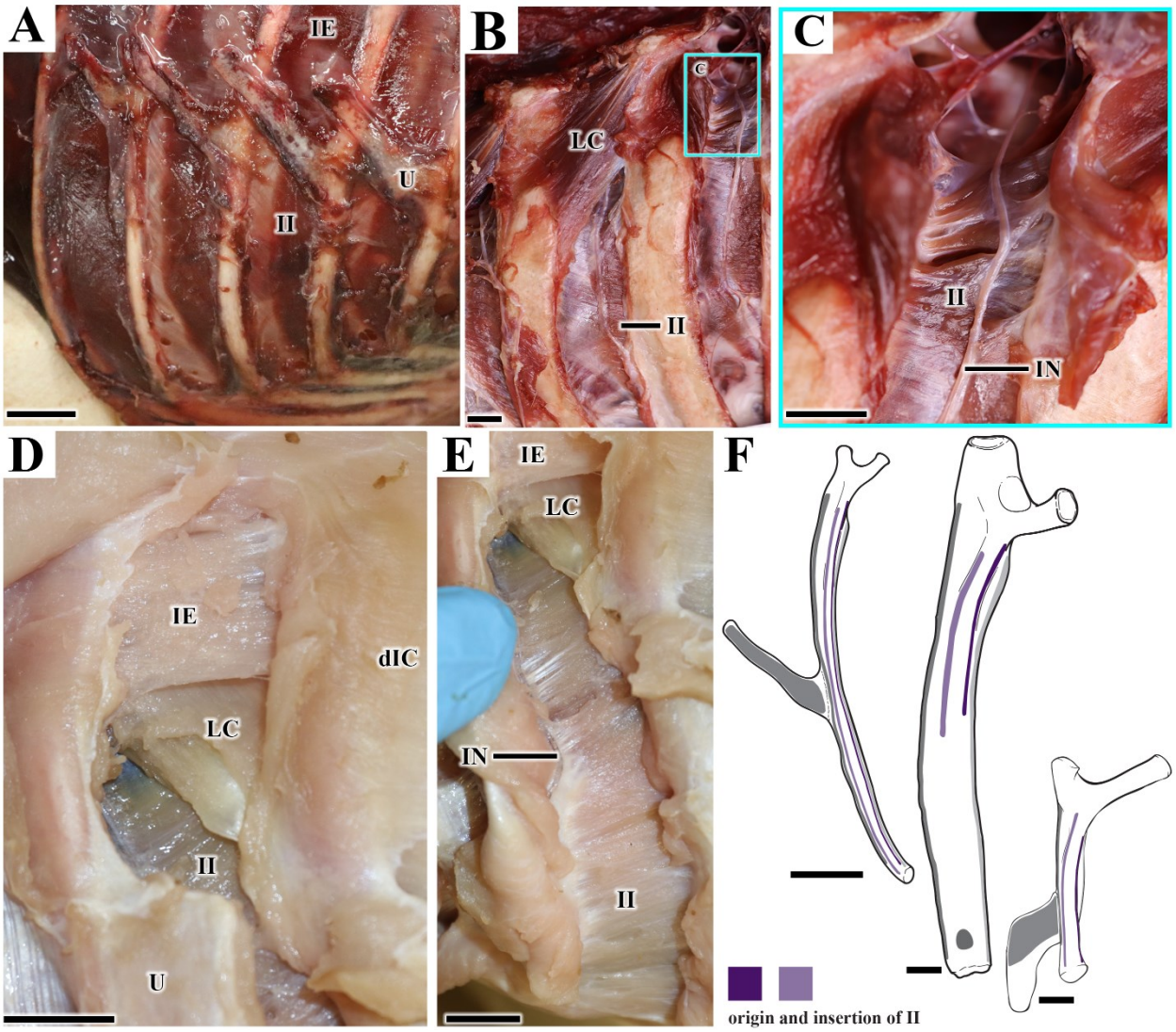
A
IE
U
II
B
C
LC
II
C
II
IN
D
IE
dIC
LC
II
U
E
IE
LC
IN
II
F
origin and insertion of II

Figure 6.8. m. costoplumonare (CP) in *Dromaius novaehollandiae* (UAMZ unnumbered).

Four strips of CP connecting PA to dorsal vertebral ribs in right medial view (A). Osteological correlate of PA (B). Scale bars equal 1cm. Abbreviations: CP, m. costoplumonare; PA, pulmonary aponeurosis.

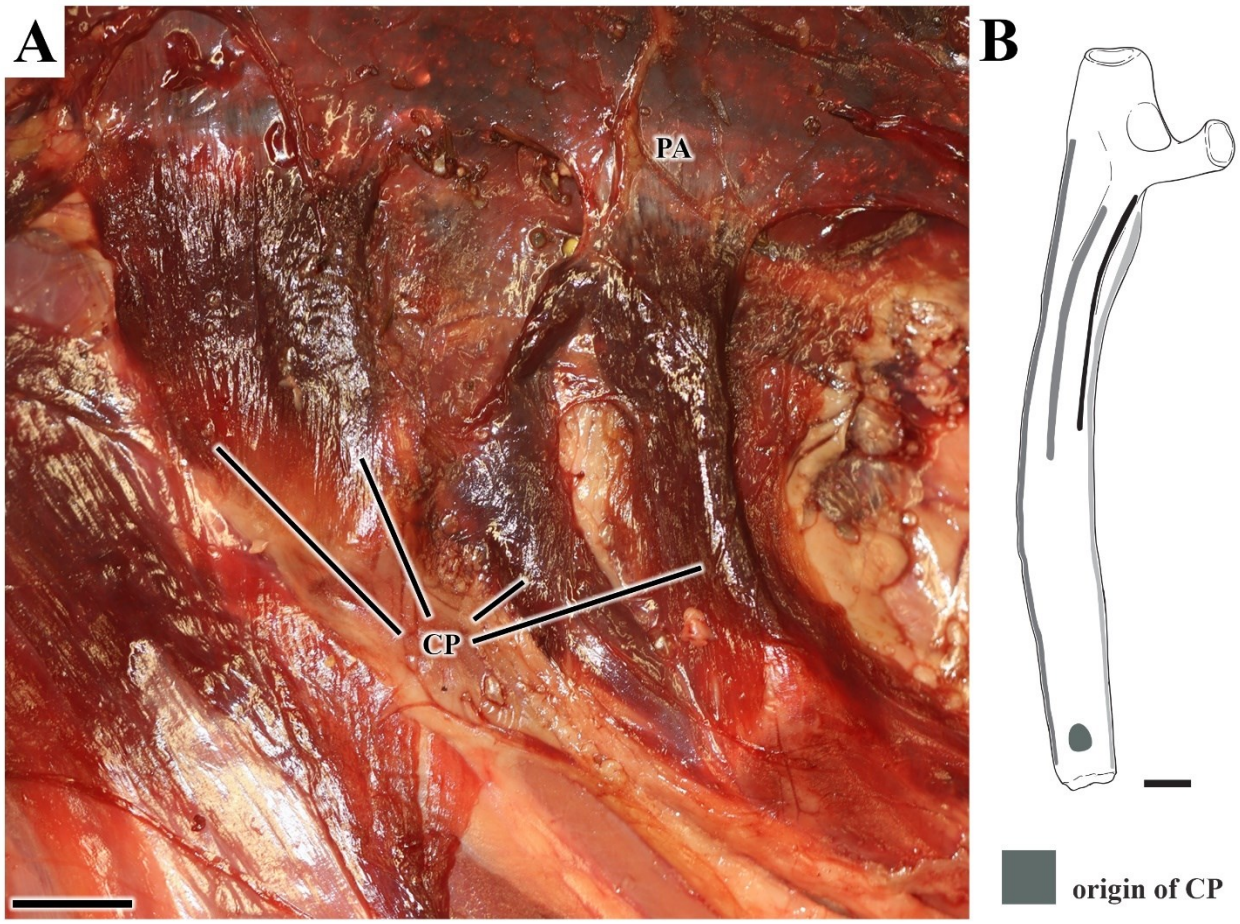
A
PA
CP
B
origin of CP

Figure 6.9. m. costosternalis (COT) in *Dromaius novaehollandiae* (UAMZ unnumbered).

Three strips of COT in right lateral view (A). Osteological correlates of COT (B). Scale bars equal 1cm. Abbreviation: COT, m. costosternalis.

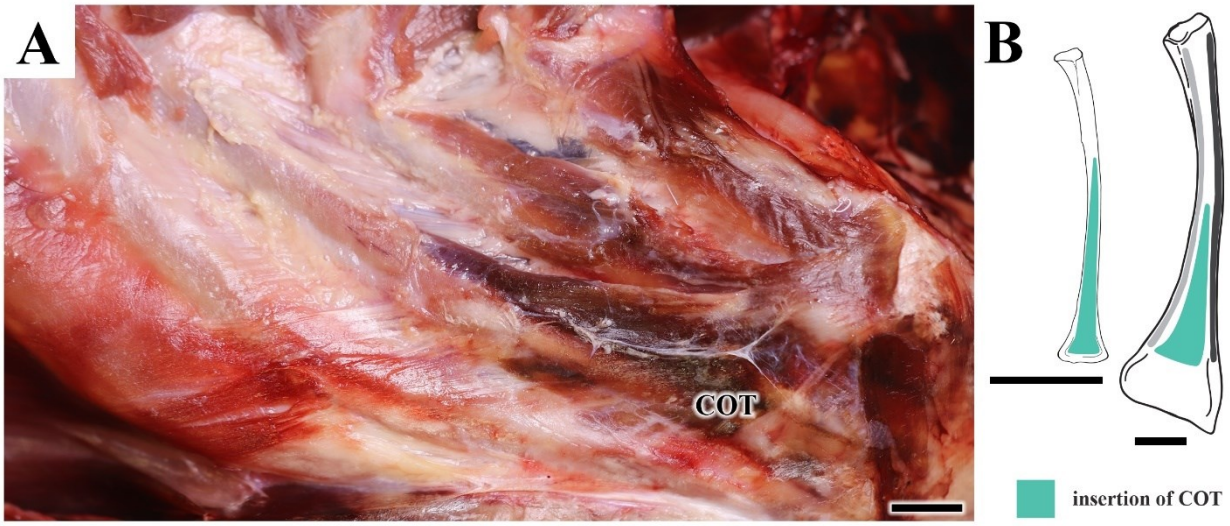
A
COT
B
insertion of COT

Figure 6.10. m. subcostales (SC) in extant archosaurs.

SC in *Corvus corax* (A), *Dromaius novaehollandiae* (B), and *Caiman crocodilus* (C) in left lateral views. Osteological correlates of SC (D). Scale bars equal 1 cm. Abbreviations: COT, m. costosternalis; IE, mm. intercostales externi; SC, m. subcostalis.

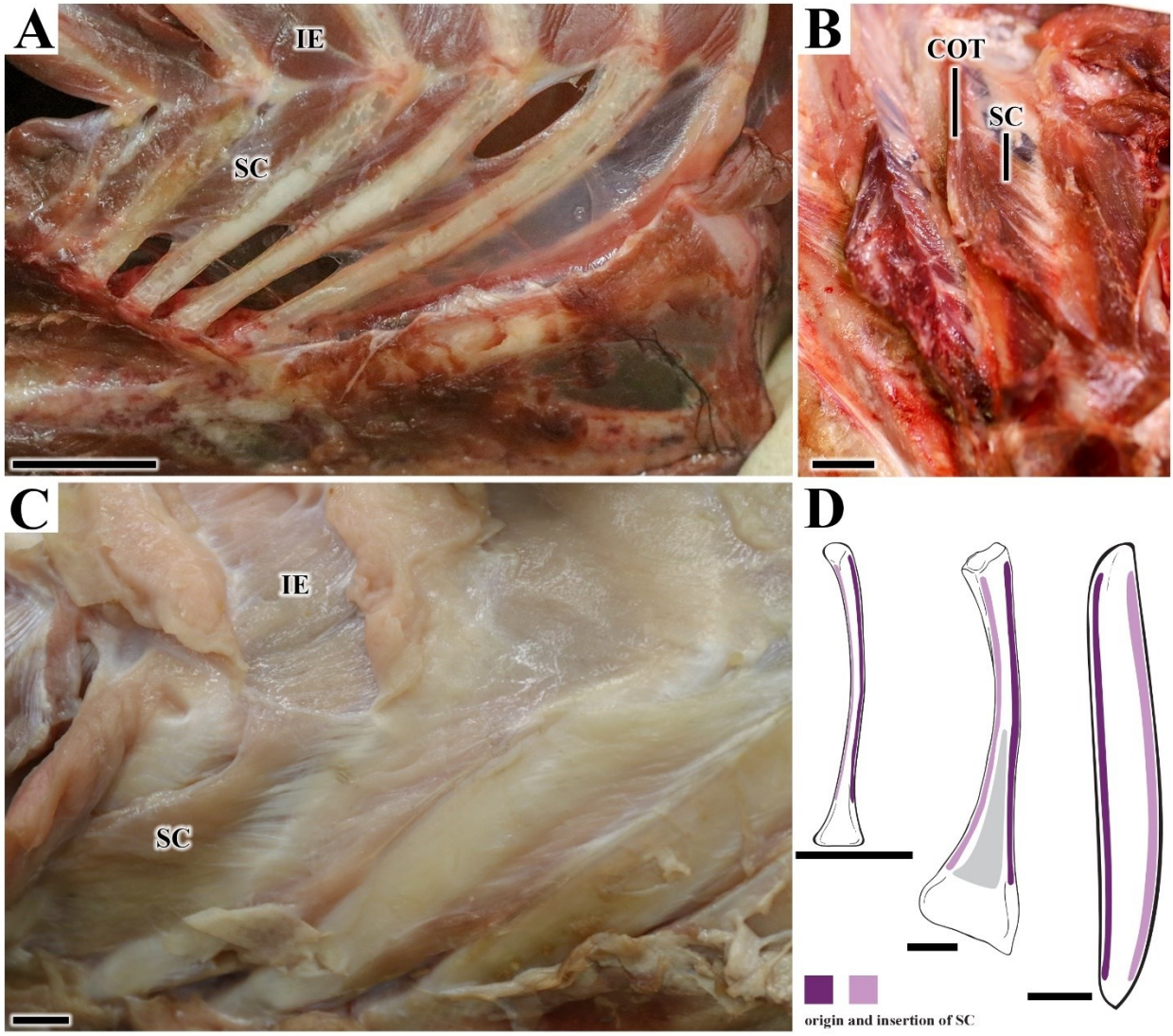
A
IE
SC
B
COT
SC
C
IE
SC
D
origin and insertion of SC

Figure 6.11. Pelvic muscles of the deep dorsal group in extant archosaurs.

m. iliofemoralis internus (IFI)/m. puboischiofemoralis internus 1 (PIFI1) and mm. iliotrochanterici cranialis et medius (ITCR+ITM)/m. puboischiofemoralis internus 2 (PIFI2) in extant archosaurs shown in context with m. iliofemoralis (IF)/mm. iliotrochantericus caudalis et iliofemoralis externus (ITC+IFE). ITCR and ITM in *Corvus corax* in left lateral view (A). ITCR and ITM in *Dromaius novaehollandiae* in context with overlying ITC and IFE (B), ITCR and ITM exposed (C), and IFI (D) in right lateral views. PIFI1–2 in *Caiman crocodilus* in ventral view (E), PIFI2 intact in right lateral view (F), and PIFI2 cut to expose underlying PIFI1 in right lateral view (G). Osteological correlates in *Co. corax* (H), *Dr. novaehollandiae* (I), and *Cai. crocodilus* (J) on a left pelvis in lateral and medial views and a left femur in anterior, lateral, posterior, and medial views (left to right). Scale bars equal 1 cm. Abbreviations: IFE, m. iliofemoralis externus; IFI, m. iliofemoralis internus; ITCR, m. iliotrochantericus cranialis; ITM, m. iliotrochantericus medius; PIFI1, m. puboischiofemoralis internus 1; PIFI2, m. puboischiofemoralis internus 2.

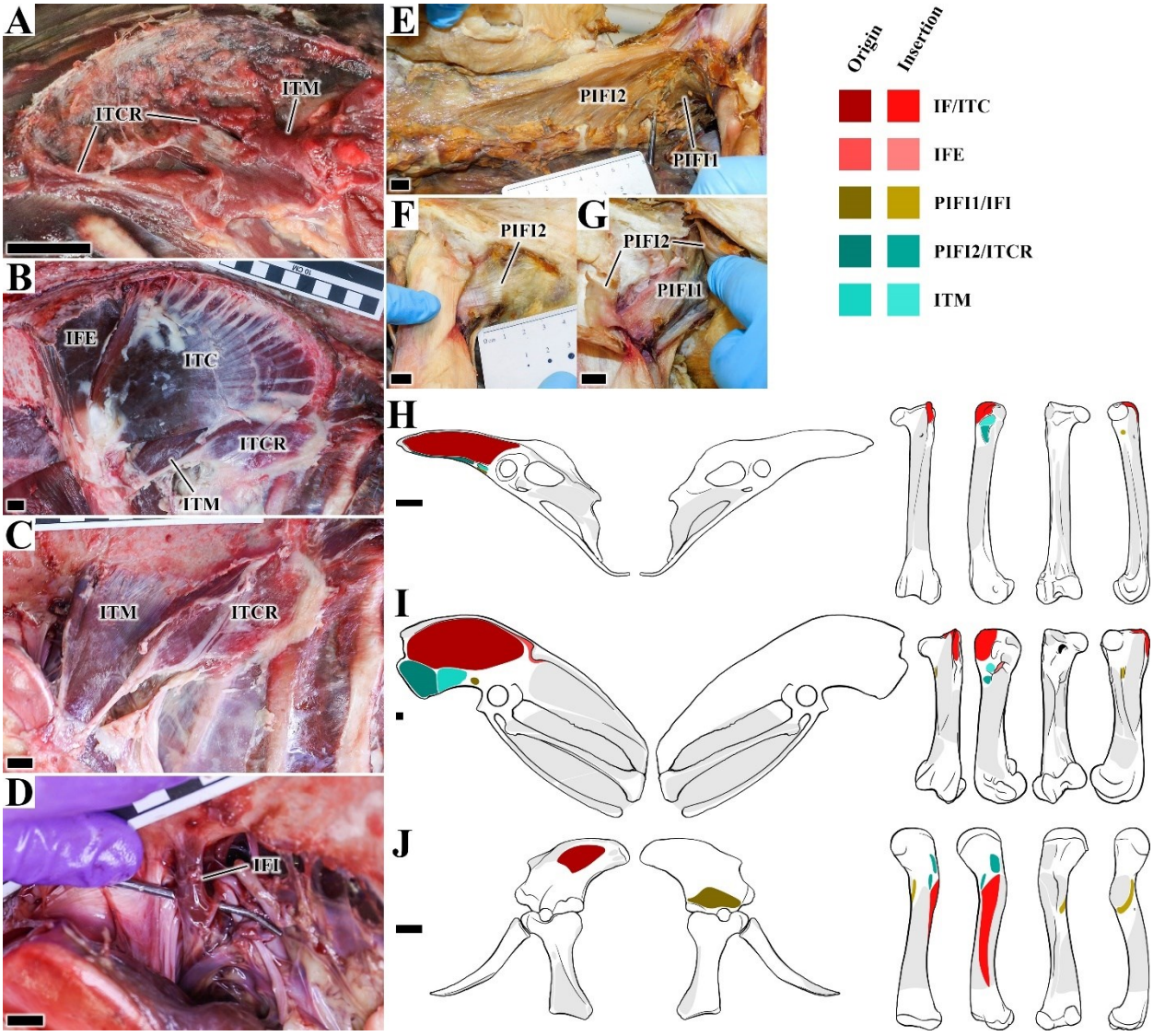
A
ITCR
ITM
B
IFE
ITC
ITCR
ITM
C
ITM
ITCR
D
IFI
E
PIFI2
PIFI1
F
PIFI2
G
PIFI2
PIFI1
Origin
Insertion
IF/ITC
IFE
PIFI1/IFI
PIFI2/ITCR
ITM
H
I
J

Figure 6.12. Deep pelvic muscles in extant archosaurs

mm. obturatorii lateralis et medialis (OL+OM)/mm. puboischiofemorales externi 1–2 (PIFE1–2) in extant archosaurs shown in context with m. puboischiofemoralis externus 3 (PIFE3). Insertion tendons of OL and OM in *Corvus corax* in left lateral view (A) and origin of OM in medial view (B). Insertion tendons of OMII and OMIP in *Dromaius novaehollandiae* under tendon of ISF in posterior view (C) and origins of OMII and OMIP in ventromedial view (D). PIFE1 in *Caiman crocodilus* in anterior view (E) and PIFE2 in ventral view (F). Osteological correlates in *Co. corax* (G) and *Dr. novaehollandiae* (H) on a left pelvis in lateral and medial views and a left femur in anterior, lateral, posterior, and medial views (left to right). Osteological correlates in *Cai. crocodilus* also include the pubes in anterodorsal and posteroventral views (I). Scale bars equal 1 cm. Abbreviations: ISF, m. ischiofemoralis; OL, m. obturatorius lateralis; OM, m. obturatorius medialis; OMII, ilium-ischium part of m. obturatorius medialis; OMIP, ischium-pubis part of m. obturatorius medialis; PIFE1, m. puboischiofemoralis externus 1; PIFE2, m. puboischiofemoralis externus 2.

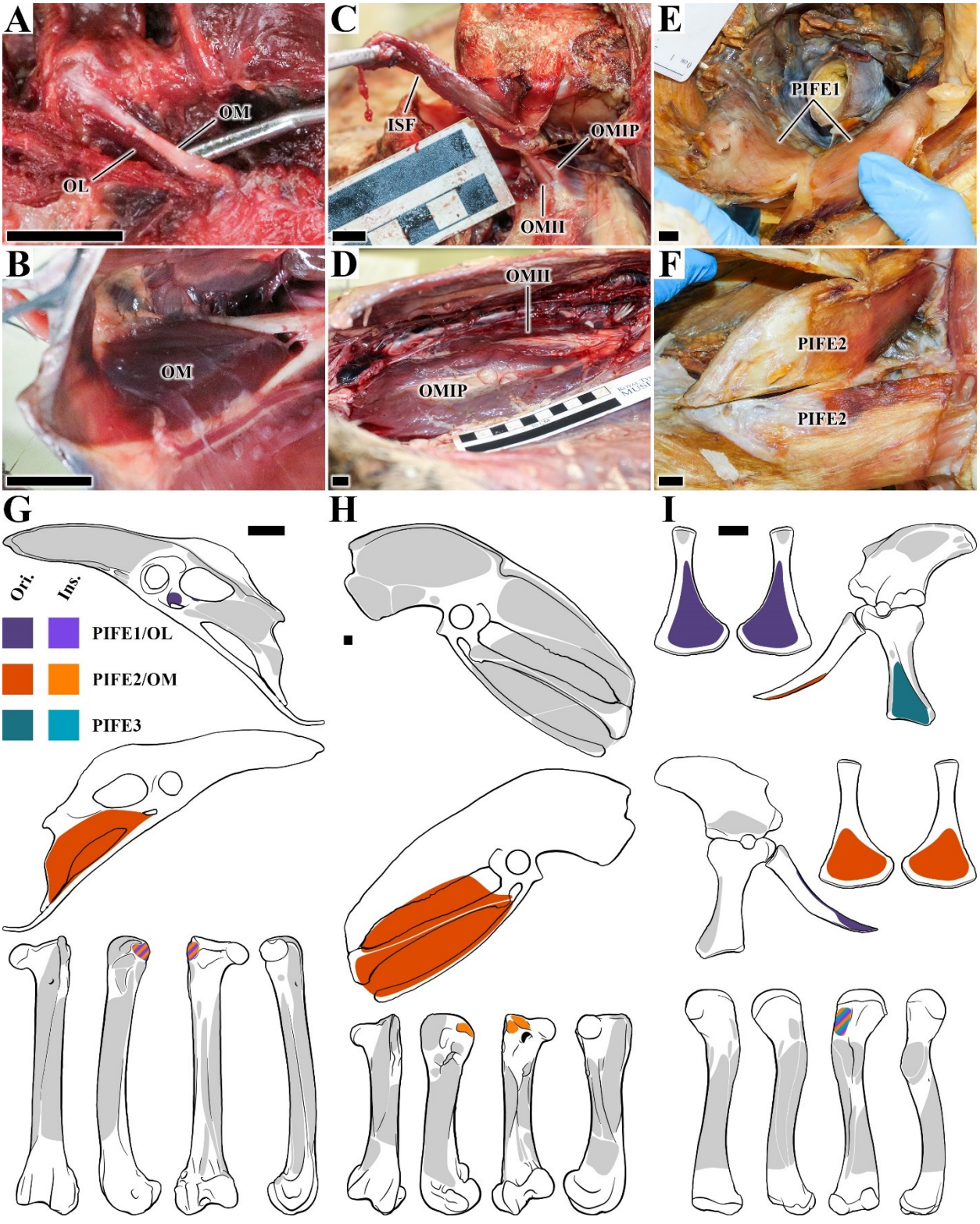
A
OM
OL
C
ISF
OMIP
OMII
E
PIFE1
B
OM
D
OMII
OMIP
F
PIFE2
PIFE2
G
Ori.
Ins.
PIFE1/OL
PIFE2/OM
PIFE3
H
I

Figure 6.13. Deep pelvic muscles in extant archosaurs.

m. ischiofemoralis (ISF) in extant birds in context of surrounding musculature including m. iliofibularis (ILFB), m. flexor cruris medialis (FCM), m. flexor cruris lateralis pars pelvica (FCLP) et accessoria (FCLA), mm. puboischiofemorales medialis (PIFM) et lateralis (PIFL), and mm. caudofemorales pars pelvica (CFP) et caudalis (CFC). ISF in *Corvus corax* in left lateral view (A) and ISF in *Dromaius novaehollandiae* in right lateral view (B) with close-up (C). Osteological correlates in *Co. corax* (D) and *Dr. novaehollandiae* (E) on a left pelvis in lateral and medial views and a left femur in anterior and lateral (top) and posterior and medial (bottom) views. Scale bars equal 1 cm. Abbreviations: CFC, mm. caudofemorales pars cadalis; FCLP, m. flexor cruris lateralis pars pelvica; FCM, m. flexor cruris medialis; ILFB, m. iliofibularis; ISF, m. ischiofemoralis; PIFL, mm. puboischiofemorales lateralis; PIFM, mm. puboischiofemorales medialis.

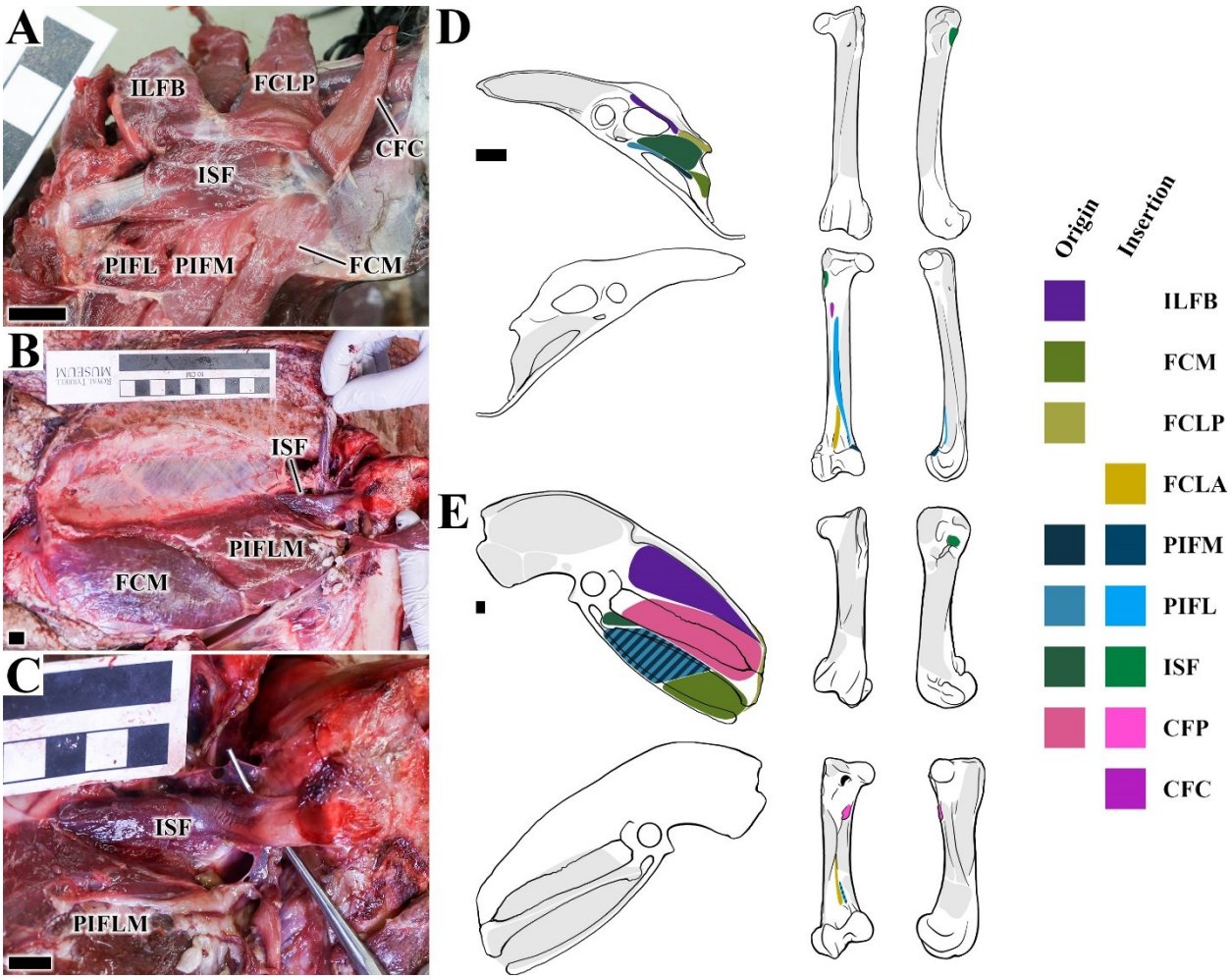
A
ILFB
FCLP
CFC
ISF
PIFL
PIFM
FCM
B
ISF
PIFLM
FCM
C
ISF
PIFLM
D
E
Origin
Insertion
ILFB
FCM
FCLP
FCLA
PIFM
PIFL
ISF
CFP
CFC

Figure 6.14. Osteological correlates of vIC and IE in ornithischian dinosaurs.

Dorsal vertebral ribs of *Edmontonia longiceps* (CMN8531) in right medial view (A), and dorsal vertebral ribs of *Prosaurolophus maximus* (TMP 1998.50.1) in right lateral view (B). Scale bars equal 1cm. Abbreviations: F, flange like projections of the tuberculum; IE, IE, mm. intercostales externi.

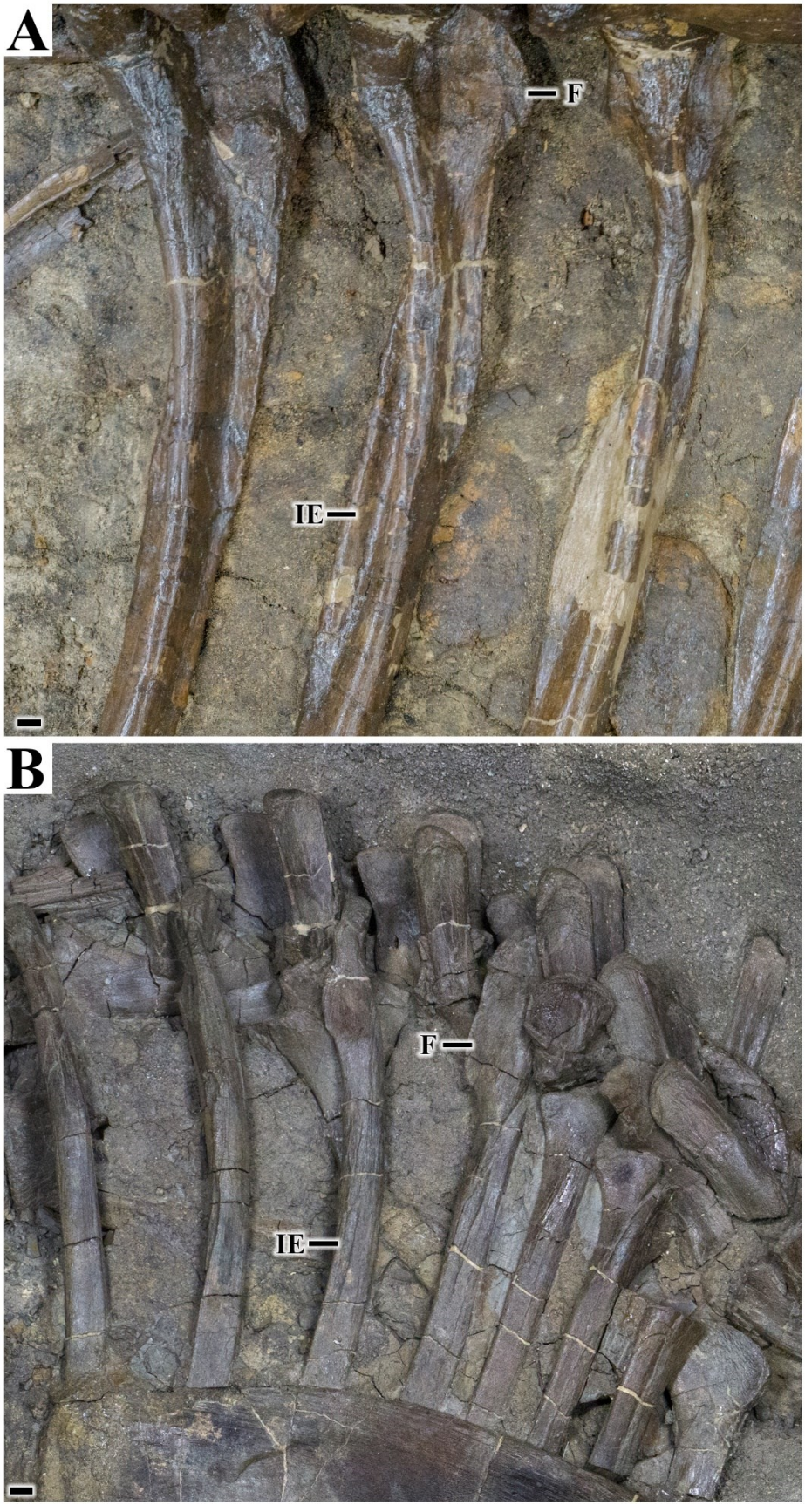
A
F
IE
B
F
IE

Figure 6.15. Osteological correlates of m. levator costarum (LC) in theropods mapped on a cladogram illustrating the phylogenetic relationships of sampled fossil theropods.

Dorsal vertebral ribs and the osteological correlates in *Coelophysis bauri* (NMMNH P42351) in left lateral view with osteological correlate to the right (A); proximal end of dorsal vertebral rib of *Gorgosaurus libratus* (UALVP 10.74) with muscle scar at the osteological correlate in right anterior view (B); proximal part of dorsal vertebral rib of *Deinonychus antirrhopus* (YPM 5250) with the osteological correlate in right anterior view (C). Scale bars equal 1cm. Abbreviations: CTL, capitulotubercular lamina; LC, m. levator costarum.

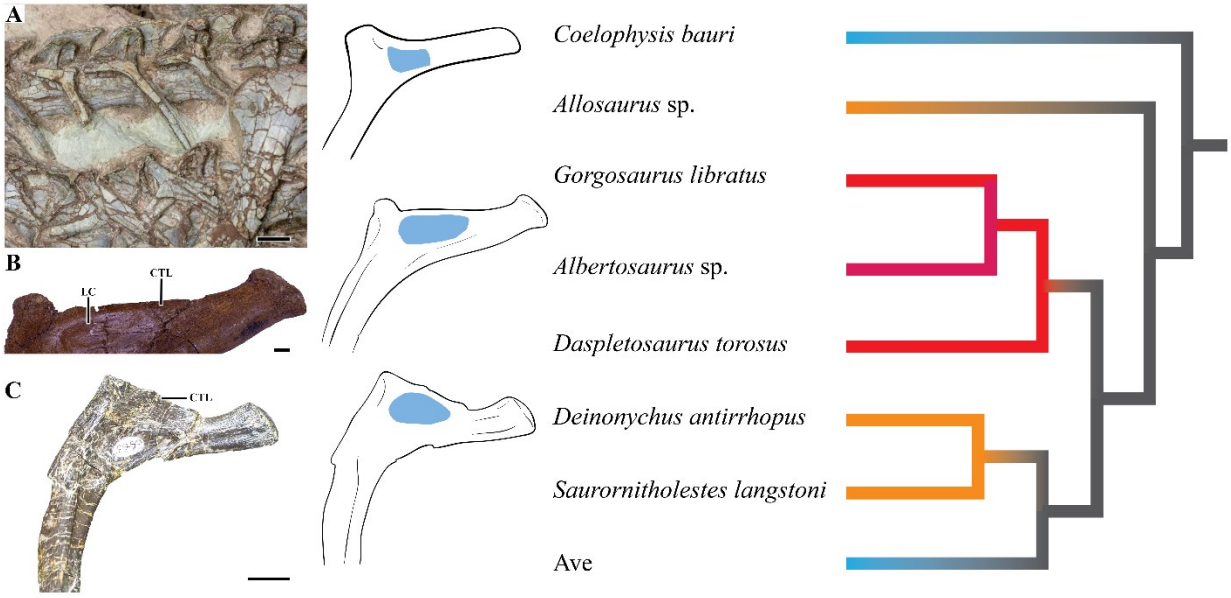
A
B
CTL
LC
C
CTL
Coelophysis bauri
Allosaurus sp.
Gorgosaurus libratus
Albertosaurus sp.
Daspletosaurus torosus
Deinonychus antirrhopus
Saurornitholestes langstoni
Ave

Figure 6.16. Osteological correlates of LC, IE, and II in tyrannosaurid dinosaurs.

Dorsal vertebral ribs of *Gorgosaurus libratus* (TMP 1991.36.500) with osteological correlates for CTL, II, and IE in right anterolateral (A) and with osteological correlates for IE lateral (B) views; Dorsal vertebral rib of Tyrannosauridae indet. (TMP 1992.36.1231) with osteological correlates for CTL and II in left anterior view (C), and close-up on CTL and muscle scar of II (D). Scale bar equals 1cm. Abbreviations: CTL, capitulotubercular lamina; IE, mm. intercostales externi; II, mm. intercostales interni; LC, m. levator costarum.

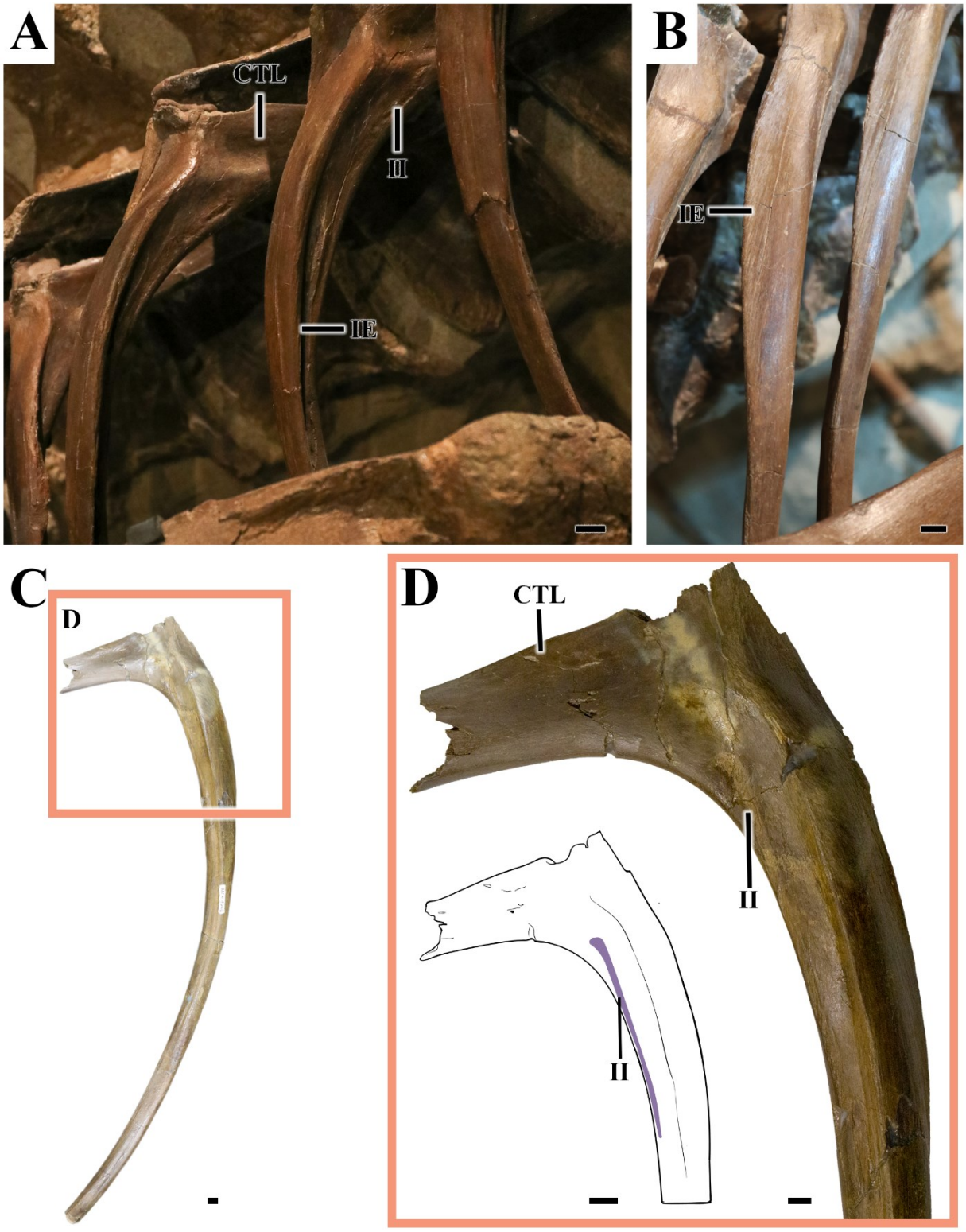
A
CTL
II
IE
B
IE
C
D
D
CTL
II
II

Figure 6.17. Osteological correlates of APC in dromaeosaurid dinosaurs.

Dorsal vertebral ribs carrying mineralised/ossified uncinate processes for APC in *Saurornitholestes langstoni* (UALVP 55700) (A), and in *Linheraptor exquisitus* (IVPP V 16923) in right lateral views (B). Osteological correlates of APC with interpreted LT (C). Scale bars equal 1cm. Abbreviations: APC, m. appendicocostalis; LT, ligamentum triangulare.

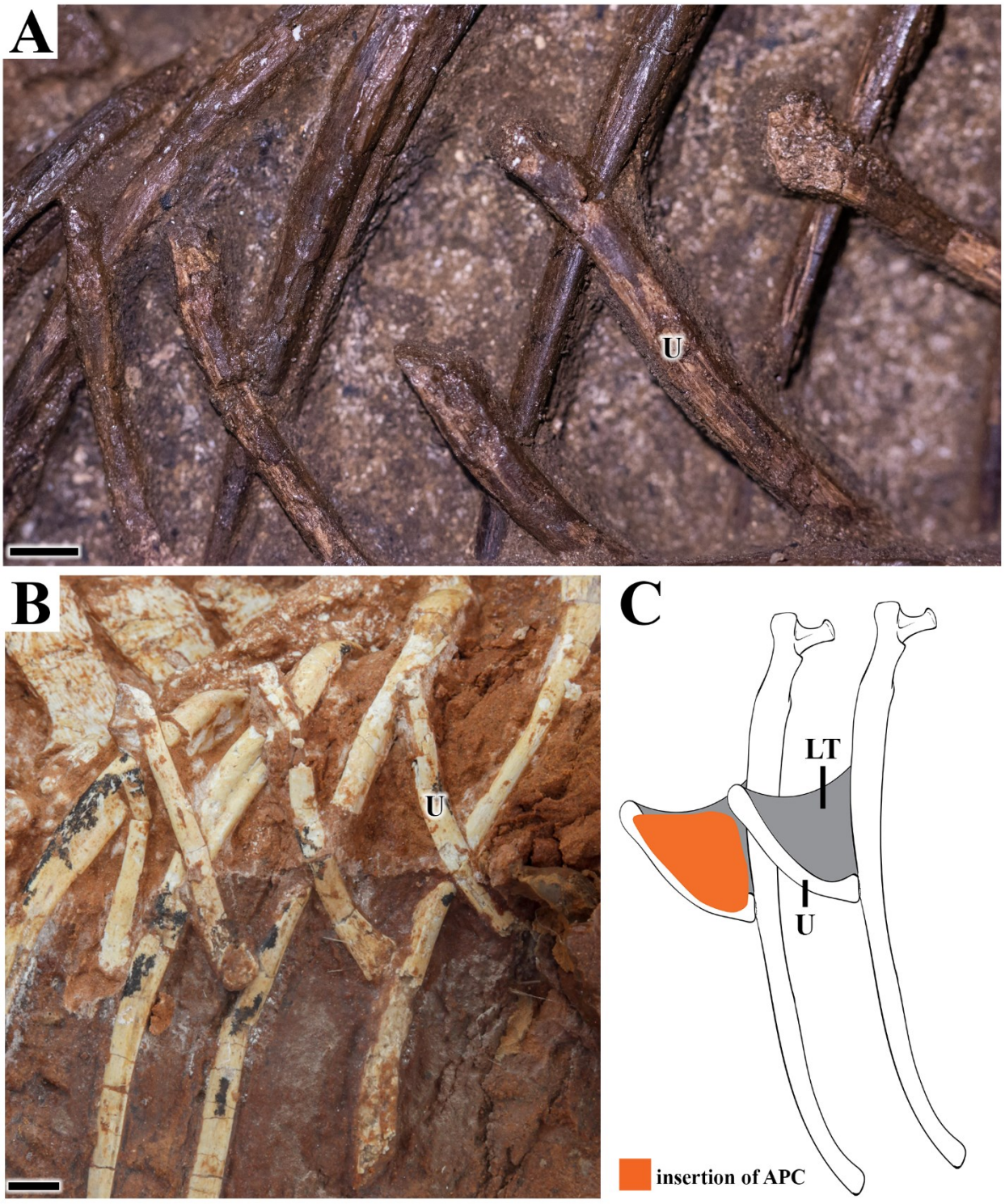
A
U
B
U
C
LT
U
insertion of APC

Figure 6.18. Results of Phylogenetic Generalized Least Squares (PGLS) regressions on pelvic muscles.

Phylogenetic Generalized Least Squares (PGLS) regressions on area of attachment for all hip muscles, major extensors, and ilium length, normalized to body mass (all log-transformed). Regressions for each major taxonomic group (A), non-avian theropods (B), and bipeds (C). Phylogenetically corrected residuals for non-avian theropods (D) and bipeds (E).

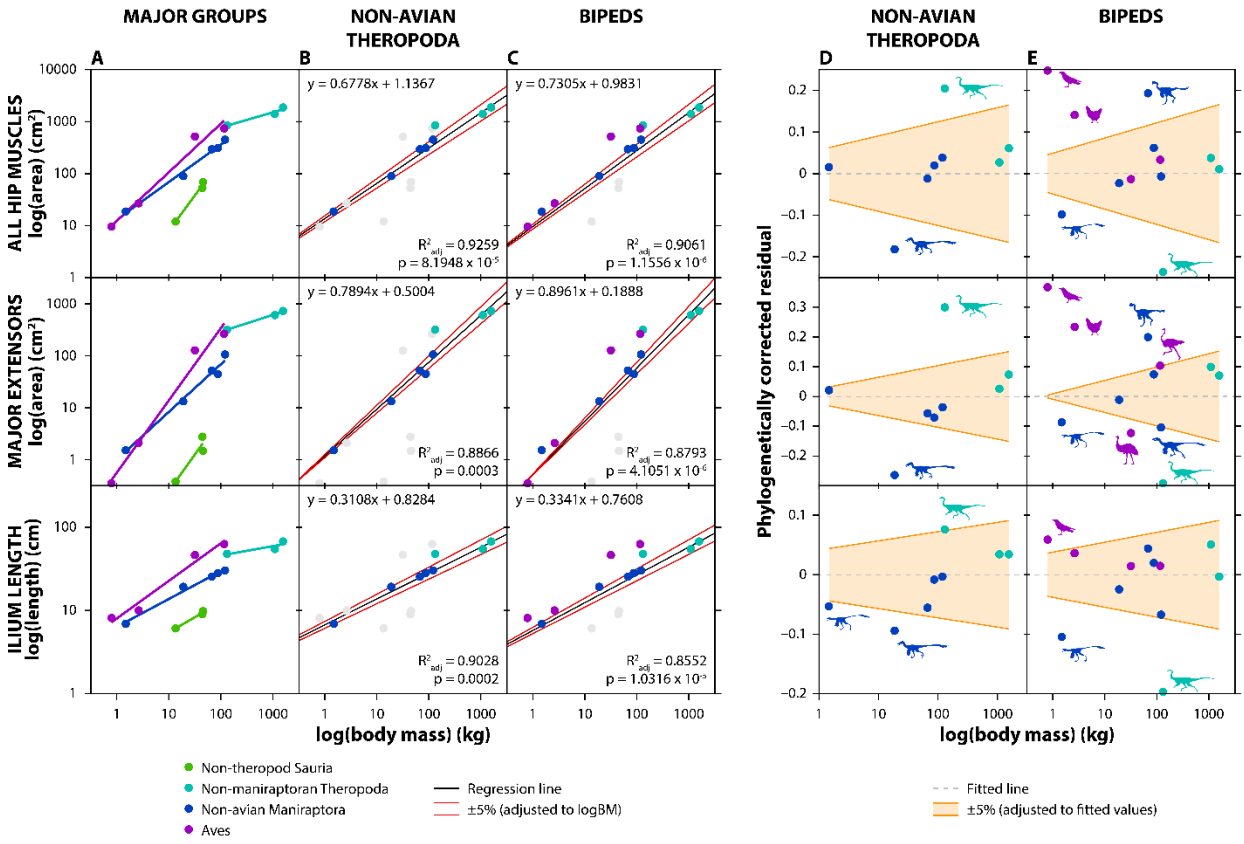
MAJOR GROUPS
NON-AVIAN THEROPODA
BIPEDS
NON-AVIAN THEROPODA
BIPEDS
A
B
C
D
E
ALL HIP MUSCLES log(area) (cm²)
MAJOR EXTENSORS log(area) (cm²)
ILIUM LENGTH log(length) (cm)
y = 0.6778x + 1.1367
y = 0.7305x + 0.9831
y = 0.7894x + 0.5004
y = 0.8961x + 0.1888
y = 0.3108x + 0.8284
y = 0.3341x + 0.7608
R²adj = 0.9259
p = 8.1948 x 10⁻⁵
R²adj = 0.9061
p = 1.1556 x 10⁻⁶
R²adj = 0.8866
p = 0.0003
R²adj = 0.8793
p = 4.1051 x 10⁻⁶
R²adj = 0.9028
p = 0.0002
R²adj = 0.8552
p = 1.0316 x 10⁻⁵
log(body mass) (kg)
Phylogenetically corrected residual
log(body mass) (kg)
Non-theropod Sauria
Non-maniraptoran Theropoda
Non-avian Maniraptora
Aves
Regression line
±5% (adjusted to logBM)
Fitted line
±5% (adjusted to fitted values)

Figure 6.19. Pelvic musculature compared to other aspects of cursoriality.

Proportion of major extensors (Table S2 in the digital supplementary information) grouped according to 5-class Jenks Natural Breaks optimization (A). Heat map of major extensors (from A), relative limb element proportions (sensu Carrano, 1999), morphology of the ankle joint (ball-and-socket; hinge-like with unspecialized metatarsals; subarctometatarsus; arctometatarsus; tarsometatarsus), number of weight-bearing digits (fewer = higher), and foot symmetry (B). Average cursoriality inferred from heat map (C).

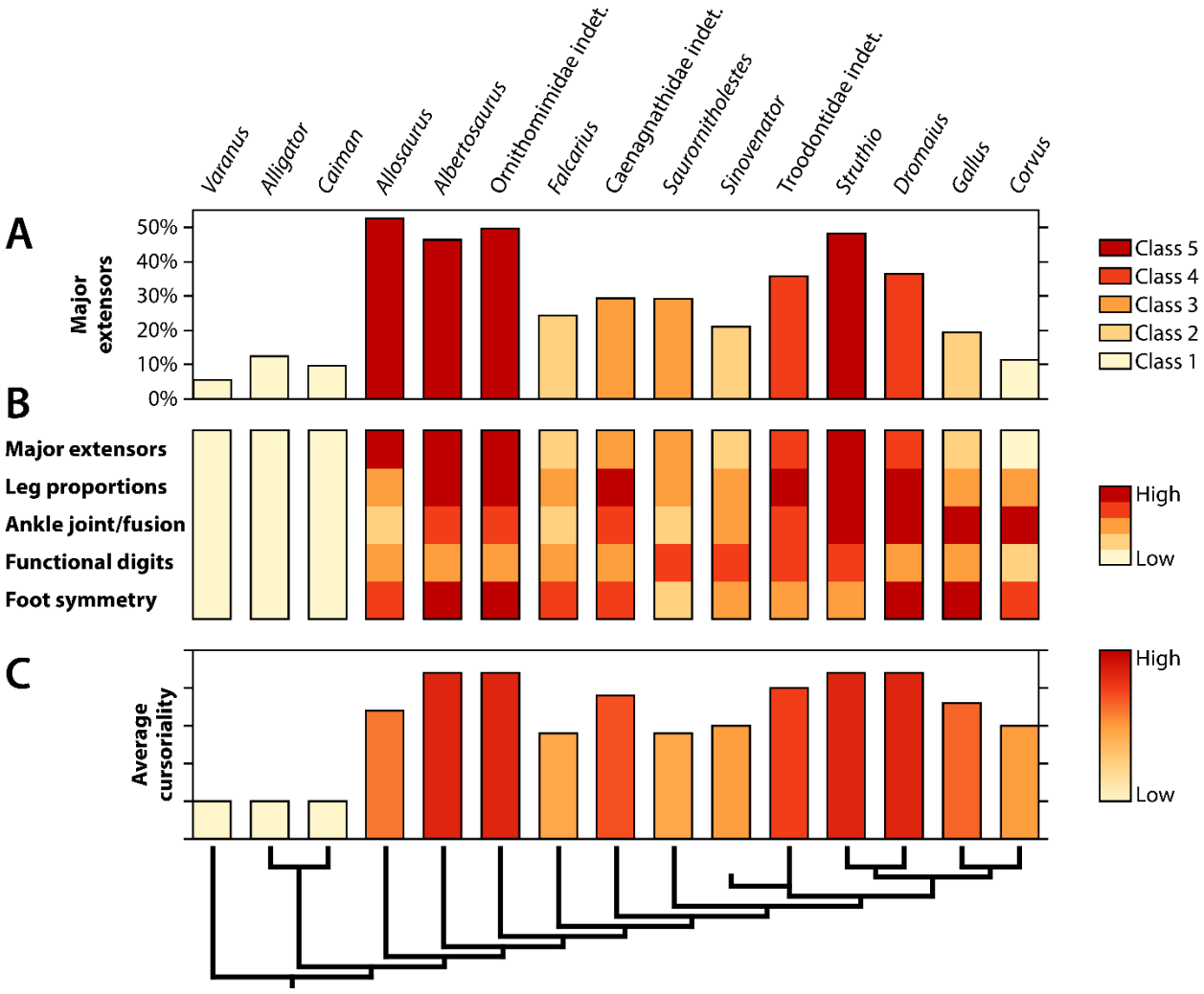
Varanus
Alligator
Caiman
Allosaurus
Albertosaurus
Ornithomimidae indet.
Falcarius
Caenagnathidae indet.
Saurornitholestes
Sinovenator
Troodontidae indet.
Struthio
Dromaius
Gallus
Corvus
A
Major extensors
50%
40%
30%
20%
10%
0%
Class 5
Class 4
Class 3
Class 2
Class 1
B
Major extensors
Leg proportions
Ankle joint/fusion
Functional digits
Foot symmetry
High
Low
C
Average cursoriality
High
Low

6.5 Literature Cited

Abourachid, A. et al. 2011. Bird terrestrial locomotion as revealed by 3D kinematics. *Zoology* 114(6), pp. 360–368. doi: 10.1016/j.zool.2011.07.002.

Allen, V., Molnar, J., Parker, W., Pollard, A., Nolan, G. and Hutchinson, J.R. 2015. Comparative architectural properties of limb muscles in Crocodylidae and Alligatoridae and their relevance to divergent use of asymmetrical gaits in extant Crocodylia. *Journal of Anatomy* 225(6), pp. 569–582. doi: 10.1111/joa.12245.

Allen, V.R., Kilbourne, B.M. and Hutchinson, J.R. 2021. The evolution of pelvic limb muscle moment arms in bird-line archosaurs. *Science Advances* 7(12), p. eabe2778.

Anten-Houston, M.V., Ruta, M. and Deeming, D.C. 2017. Effects of phylogeny and locomotor style on the allometry of body mass and pelvic dimensions in birds. *Journal of Anatomy* 231(3), pp. 342–358. doi: 10.1111/joa.12647.

Aoyama, H., Mizutani-Koseki, S. and Koseki, H. 2005. Three developmental compartments involved in rib formation. *The International Journal of Developmental Biology* 49(2–3), pp. 325–333. doi: 10.1387/ijdb.041932ha.

Art, T., Desmecht, D., Amory, H. and Lekeux, P. 1990. Synchronization of Locomotion and Respiration in Trotting Ponies. *Journal of Veterinary Medicine Series A* 37(1–10), pp. 95–103. doi: 10.1111/j.1439-0442.1990.tb00880.x.

Bakker, R.T. 1971. Dinosaur physiology and the origin of mammals. *Evolution* 25(4), pp. 636–658.

Baumel, J.J., King, A.S., Breazile, J.E., Evans, H.E. and Vanden Berge, J.C. 1993. *Handbook of avian anatomy: Nomina anatomica avium*. second edition. Cambridge: Nuttall Ornithological Club.

Baumel, J.J., Wilson, J.A. and Bergren, D.R. 1990. The ventilatory movements of the avian pelvis and tail: function of the muscles of the tail region of the pigeon (*Columba livia*). *Journal of Experimental Biology* 151, pp. 263–277.

Beddard, F.E. 1898. *The structure and classification of birds*. Longmans, Green, and Company.

Benton, M.J. 2014. *Vertebrate Palaeontology*. John Wiley & Sons.

Berger, M., Roy, O.Z. and Hart, J.S. 1970. The co-ordination between respiration and wing beats in birds. *Zeitschrift für vergleichende Physiologie* 66(2), pp. 190–200. doi: 10.1007/BF00297778.

Bishop, P.J. et al. 2018. Cancellous bone and theropod dinosaur locomotion. Part I—an examination of cancellous bone architecture in the hindlimb bones of theropods. *PeerJ* 6, p. e5778. doi: 10.7717/peerj.5778.

Bivand, R., Ono, H., Dunlap, R. and Stigler, M. 2013. ClassInt: Choose univariate class intervals. *URL http://CRAN. R-project. org/package= classInt. R package version 0.1–21*

Blitz, E. et al. 2009. Bone ridge patterning during musculoskeletal assembly is mediated through SCX regulation of Bmp4 at the tendon-skeleton junction. *Developmental Cell* 17(6), pp. 861–873. doi: 10.1016/j.devcel.2009.10.010.

Boggs, D.F. 1997. Coordinated control of respiratory pattern during locomotion in birds. *American Zoologist* 37(1), pp. 41–53. doi: 10.1093/icb/37.1.41.

Boyd, C.A., Brown, C.M., Scheetz, R.D. and Clarke, J.A. 2009. Taxonomic revison of the basal neornithischian taxa *Thescelosaurus* and *Bugenasaura*. *Journal of Vertebrate Paleontology* 29(3), pp. 758–770. doi: 10.1671/039.029.0328.

Boyd, C.A., Cleland, T.P. and Novas, F. 2011. Osteogenesis, homology, and function of the intercostal plates in ornithischian dinosaurs (Tetrapoda, Sauropsida). *Zoomorphology* 130(4), pp. 305–313. doi: 10.1007/s00435-011-0136-x.

Brocklehurst, R.J., Schachner, E.R. and Sellers, W.I. 2018. Vertebral morphometrics and lung structure in non-avian dinosaurs. *Royal Society Open Science* 5(10), p. 180983. doi: 10.1098/rsos.180983.

Bryant, H.N. and Seymour, K.L. 1990. Observations and comments on the reliability of muscle reconstruction in fossil vertebrates. *Journal of Morphology* 206(1), pp. 109–117.

Burness, G.P., Diamond, J. and Flannery, T. 2001. Dinosaurs, dragons, and dwarfs: The evolution of maximal body size. *Proceedings of the National Academy of Sciences* 98(25), pp. 14518–14523. doi: 10.1073/pnas.251548698.

Carrano, M.T. 1999. What, if anything, is a cursor? Categories versus continua for determining locomotor habit in mammals and dinosaurs. *Journal of Zoology* 247(1), pp. 29–42. doi: 10.1111/j.1469-7998.1999.tb00190.x.

Carrano, M.T. and Hutchinson, J.R. 2002. Pelvic and hindlimb musculature of *Tyrannosaurus rex* (Dinosauria: Theropoda). *Journal of Morphology* 253(3), pp. 207–228.

Carrier, D.R. 1987. The evolution of locomotor stamina in tetrapods: Circumventing a mechanical constraint. *Paleobiology* 13(3), pp. 326–341.

Carrier, D.R. 1996. Function of the intercostal muscles in trotting dogs: Ventilation or locomotion? *The Journal of Experimental Biology* 199, pp. 1455–1465.

Carrier, D.R. and Farmer, C.G. 2000. The integration of ventilation and locomotion in archosaurs. *American Zoologist* 40, pp. 87–100.

Cieri, R.L., Hatch, S.T., Capano, J.G. and Brainerd, E.L. 2020. Locomotor rib kinematics in two species of lizards and a new hypothesis for the evolution of aspiration breathing in amniotes. *Scientific Reports* 10(1), p. 7739. doi: 10.1038/s41598-020-64140-y.

Claessens, K.P. 2015. Anatomical transformations and respiratory innovations of the archosaur trunk. In: *Great Transformations in Vertebrate Evolution*. University of Chicago Press. doi: 10.7208/chicago/9780226268392.001.0001.

Claessens, L.P.A.M. 2009. The skeletal kinematics of lung ventilation in three basal bird taxa (emu, tinamou, and guinea fowl). *Journal of Experimental Zoology Part A: Ecological Genetics and Physiology* 311A(8), pp. 586–599. doi: 10.1002/jez.501.

Codd, J.R., Boggs, D.F., Perry, S.F. and Carrier, D.R. 2005. Activity of three muscles associated with the uncinate processes of the giant Canada goose *Branta canadensis maximus*. *Journal of Experimental Biology* 208(5), pp. 849–857. doi: 10.1242/jeb.01489.

Codd, J.R., Manning, P.L., Norell, M.A. and Perry, S.F. 2008. Avian-like breathing mechanics in maniraptoran dinosaurs. *Proceedings of the Royal Society B: Biological Sciences* 275(1631), pp. 157–161. doi: 10.1098/rspb.2007.1233.

Codd, J.R., Rose, K.A.R., Tickle, P.G., Sellers, W.I., Brocklehurst, R.J., Elsey, R.M. and Crossley, D.A. 2019. A novel accessory respiratory muscle in the American alligator (*Alligator mississippiensis*). *Biology Letters* 15(7), p. 20190354. doi: 10.1098/rsbl.2019.0354.

Cong, L.Y., Hou, L.H. and Wu, X.C. 1988. *The Gross anatomy of Alligator sinensis Fauvel: Integument, Osteology, and Myology (In Chinese with English summary)*. Beijing, China: China Science Publishing & Media Ltd.

Currie, P.J. 2003. Cranial anatomy of tyrannosaurid dinosaurs from the Late Cretaceous of Alberta,Canada. *Acta Palaeontologica Polonica* 48(2), pp. 191–226.

Currie, P.J. and Evans, D.C. 2019. Cranial Anatomy of New Specimens of *Saurornitholestes langstoni* (Dinosauria, Theropoda, Dromaeosauridae) from the Dinosaur Park Formation (Campanian) of Alberta. *The Anatomical Record* 303(4), pp. 691–715. doi: 10.1002/ar.24241.

Dececchi, T.A., Mloszewska, A.M., Holtz, T.R., Habib, M.B. and Larsson, H.C.E. 2019. The fast and the frugal: Divergent locomotory strategies drive limb lengthening in theropod dinosaurs. doi: 10.1101/785238.

dewet, P.D., Fedde, M.R. and Kitchell, R.L. 1967. Innervation of the respiratory muscles of *Gallus domesticus*. *Journal of Morphology* 123(1), pp. 17–34. doi: 10.1002/jmor.1051230103.

Dial, K.P. 2003. Evolution of avian locomotion: Correlates of flight style, locomotor modules, nesting biology, body size, development, and the origin of flapping flight. *The Auk* 120(4), pp. 941–952. doi: 10.1093/auk/120.4.941.

Dunning Jr, J.B. 2007. *CRC handbook of avian body masses*. CRC press.

Evans, H.E. and Miller, M.E. 2013. *Miller's anatomy of the dog*. Fourth edition. St. Louis, Missouri: Elsevier.

Fedde, M.R., Burger, R.E. and Kitchell, R.L. 1964. Anatomic and electromyographic studies of the costo-pulmonary muscles in the cock. *Poultry Science* 43(5), pp. 1177–1184. doi: 10.3382/ps.0431177.

Francisco Botelho, J., Smith-Paredes, D., Soto-Acuña, S., Mpodozis, J., Palma, V. and Vargas, A.O. 2015. Skeletal plasticity in response to embryonic muscular activity underlies the development and evolution of the perching digit of birds. *Scientific Reports* 5(1), p. 9840. doi: 10.1038/srep09840.

Frey, T. von E. 1988. Anatomie des Körperstammes von *Alligator mississippiensis* Daudin. *Stuttgarter Beitraege zur Naturkunde, Serie A* 424, pp. 1–106.

Funk, G.D., Sholomenko, G.N., Valenzuela, I.J., Steeves, J.D. and Milsom, W.K. 1993. Coordination of wing beat and respiration in Canada geese during free flight. *Journal of Experimental Biology* 175, pp. 317–323.

Gangl, D., Weissengruber, G.E., Egerbacher, M. and Forstenpointner, G. 2004. Anatomical description of the muscles of the pelvic limb in the ostrich (*Struthio camelus*). *Anatomia, Histologia, Embryologia* 33(2), pp. 100–114.

Gatesy, S.M. 1991. Hind limb movements of the American alligator (*Alligator mississippiensis*) and postural grades. *Journal of Zoology* 224(4), pp. 577–588.

Gatesy, S.M. 1997. An electromyographic analysis of hindlimb function in *Alligator* during terrestrial locomotion. *Journal of Morphology* 234(2), pp. 197–212. doi: 10.1002/(SICI)1097-4687(199711)234:2<197::AID-JMOR6>3.0.CO;2-9.

Gatesy, S.M. and Biewener, A.A. 1991. Bipedal locomotion: effects of speed, size and limb posture in birds and humans. *Journal of Zoology* 224(1), pp. 127–147. doi: 10.1111/j.1469-7998.1991.tb04794.x.

Gatesy, S.M. and Middleton, K.M. 1997. Bipedalism, flight, and the evolution of theropod locomotor diversity. *Journal of Vertebrate Paleontology* 17(2), pp. 308–329.

George, J.C. and Berger, A.J. 1966. *Avian myology*. New York and London: Academic Press.

Ghetie, V. 1976. *Atlas de anatomie a păsărilor domestice*. Academiei Republicii Socialiste România.

Halvorson, D.B. 1972. Differences in naming muscles of the pelvic limb of chicken. *Poultry Science* 51(3), pp. 727–738. doi: 10.3382/ps.0510727.

Harris, J.D. 2004. Confusing dinosaurs with mammals: tetrapod phylogenetics and anatomical terminology in the world of homology. *The Anatomical Record Part A: Discoveries in Molecular,*

Cellular, and Evolutionary Biology: An Official Publication of the American Association of Anatomists 281(2), pp. 1240–1246.

Haughton, S. 1867. The muscular anatomy of the emu (*Dromaius novaehollandiae*). *Proceedings of the Royal Irish Academy* 9, pp. 487–497.

Hendrickx, C., Araújo, R. and Mateus, O. 2015. The non-avian theropod quadrate I: standardized terminology with an overview of the anatomy and function. *PeerJ* 3, p. e1245. doi: 10.7717/peerj.1245.

Hudson, G.E. 1937. Studies on the muscles of the pelvic appendage in birds. *The American Midland Naturalist* 18, pp. 1–108.

Hudson, G.E., Lanzillotti, P.J. and Edwards, G.D. 1959. Muscles of the pelvic limb in galliform birds. *The American Midland Naturalist* 61(1), pp. 1–67. doi: 10.2307/2422340.

Hudson, L.N., Isaac, N.J.B. and Reuman, D.C. 2013. The relationship between body mass and field metabolic rate among individual birds and mammals. *Journal of Animal Ecology* 82(5), pp. 1009–1020. doi: 10.1111/1365-2656.12086.

Hutchinson, J.R. 2001a. The evolution of femoral osteology and soft tissues on the line to extant birds (Neornithes). *Zoological Journal of the Linnean Society* 131(2), pp. 169–197. doi: 10.1111/j.1096-3642.2001.tb01314.x.

Hutchinson, J.R. 2001b. The evolution of pelvic osteology and soft tissues on the line to extant birds (Neornithes). *Zoological Journal of the Linnean Society* 131(2), pp. 123–168. doi: 10.1111/j.1096-3642.2001.tb01313.x.

Hutchinson, J.R. 2002. The evolution of hindlimb tendons and muscles on the line to crown-group birds. *Comparative Biochemistry and Physiology Part A: Molecular & Integrative Physiology* 133(4), pp. 1051–1086. doi: 10.1016/S1095-6433(02)00158-7.

Hutchinson, J.R. and Gatesy, S.M. 2000. Adductors, abductors, and the evolution of archosaur locomotion. *Paleobiology* 26(4), pp. 734–751. doi: 10.1666/0094-8373(2000)026<0734:AAATEO>2.0.CO;2.

Hutchinson, J.R., Rankin, J.W., Rubenson, J., Rosenbluth, K.H., Siston, R.A. and Delp, S.L. 2015. Musculoskeletal modelling of an ostrich (*Struthio camelus*) pelvic limb: influence of limb orientation on muscular capacity during locomotion. *PeerJ* 3, p. e1001. doi: 10.7717/peerj.1001.

Kardong, K.V. 2015. *Vertebrates: comparative anatomy, function, evolution*. Seventh edition. New York, NY: McGraw-Hill Education.

Klein, W. and Owerkowicz, T. 2006. Function of intracoelomic septa in lung ventilation of amniotes: lessons from lizards. *Physiological and Biochemical Zoology* 79(6), pp. 1019–1032. doi: 10.1086/507656.

Klinkhamer, A.J., Wilhite, D.R., White, M.A. and Wroe, S. 2017. Digital dissection and three-dimensional interactive models of limb musculature in the Australian estuarine crocodile (*Crocodylus porosus*). *PLOS ONE* 12, p. e0175079.

Lamas, L.P., Main, R.P. and Hutchinson, J.R. 2014. Ontogenetic scaling patterns and functional anatomy of the pelvic limb musculature in emus (*Dromaius novaehollandiae*). *PeerJ* 2, p. e716. doi: 10.7717/peerj.716.

Maidment, S.C. and Barrett, P.M. 2011. The locomotor musculature of basal ornithischian dinosaurs. *Journal of Vertebrate Paleontology* 31(6), pp. 1265–1291.

Mammoto, T. and Ingber, D.E. 2010. Mechanical control of tissue and organ development. *Development* 137(9), pp. 1407–1420.

McKitrick, M.C. 1991. Phylogenetic analysis of avian hindlimb musculature.

Meilak, E.A., Gostling, N.J., Palmer, C. and Heller, M.O. 2021. On the 3D nature of the magpie (aves: *pica pica*) functional hindlimb anatomy during the take-off jump. *Frontiers in Bioengineering and Biotechnology* 9

Mellett, F.D. 1994. The pelvic limb of the ostrich (*Struthio camelus*). *Journal of the South African Veterinary Association* 65(1), pp. 5–9.

Murakami, G., Keniichi, A. and Tatsuo, S. 1991. Arrangement and innervation of the iliocostalis and longissimus muscles of the brown caiman (*Caiman crocodilus* fuscus: Alligatoridae, Crocodilia). *The American Journal of Anatomy* 192, pp. 241–256.

O'Connor, P.M. 2006. Postcranial pneumaticity: An evaluation of soft-tissue influences on the postcranial skeleton and the reconstruction of pulmonary anatomy in archosaurs. *Journal of Morphology* 267(10), pp. 1199–1226. doi: 10.1002/jmor.10470.

Organ, C.L. 2006. Thoracic epaxial muscles in living archosaurs and ornithopod dinosaurs. *The Anatomical Record Part A: Discoveries in Molecular, Cellular, and Evolutionary Biology* 288A(7), pp. 782–793. doi: 10.1002/ar.a.20341.

Patak, A.E. and Baldwin, J. 1998. Pelvic limb musculature in the emu *Dromaius novaehollandiae* (Aves: Struthioniformes: Dromaiidae): Adaptations to high-speed running. *Journal of Morphology* 238(1), pp. 23–37.

Paxton, H., Anthony, N.B., Corr, S.A. and Hutchinson, J.R. 2010. The effects of selective breeding on the architectural properties of the pelvic limb in broiler chickens: A comparative study across modern and ancestral populations. *Journal of Anatomy* 217(2), pp. 153–166.

Perry, S.F. and Duncker, H.-R. 1980. Interrelationship of static mechanical factors and anatomical structure in lung evolution. *Journal of Comparative Physiology B* 138(4), pp. 321–334. doi: 10.1007/BF00691567.

Perry, S.F., Lambertz, M. and Schmitz, A. 2019. Respiratory faculties of amphibious and terrestrial craniotes. In: *Respiratory Biology of Animals: evolutionary and functional morphology*. Oxford University Press, pp. 139–163.

Persons IV, W.S. and Currie, P.J. 2011. The tail of *Tyrannosaurus*: Reassessing the size and locomotive importance of the M. caudofemoralis in non-avian theropods. *The Anatomical Record: Advances in Integrative Anatomy and Evolutionary Biology* 294(1), pp. 119–131.

Renous, S., Gasc, J. -P., Bels, V.L. and Wicker, R. 2002. Asymmetrical gaits of juvenile *Crocodylus johnstoni*, galloping Australian crocodiles. *Journal of Zoology* 256(3), pp. 311–325. doi: 10.1017/S0952836902000353.

Rhodes, M.M., Funston, G.F. and Currie, P.J. 2020. New material reveals the pelvic morphology of Caenagnathidae (Theropoda, Oviraptorosauria). *Cretaceous Research* 114, p. 104521. doi: 10.1016/j.cretres.2020.104521.

Rhodes, M.M., Henderson, D.M. and Currie, P.J. 2021. Maniraptoran pelvic musculature highlights evolutionary patterns in theropod locomotion on the line to birds. *PeerJ* 9, p. e10855. doi: 10.7717/peerj.10855.

Romer, A.S. 1923. Crocodilian pelvic muscles and their avian and reptilian homologues. *Bulletin of the American Museum of Natural History* 48, pp. 533–552.

Rose, K.A., Tickle, P.G., Elsey, R.M., Sellers, W.I., Crossley, D.A. and Codd, J.R. 2021. Scaling of axial muscle architecture in juvenile *Alligator mississippiensis* reveals an enhanced performance capacity of accessory breathing mechanisms. *Journal of Anatomy* 239(6), pp. 1273–1286.

Rowe, T. 1986. Homology and evolution of the deep dorsal thigh musculature in birds and other Reptilia. *Journal of Morphology* 189(3), pp. 327–346.

Scaal, M. 2021. Development of the amniote ventrolateral body wall. *Developmental Dynamics* 250(1), pp. 39–59. doi: 10.1002/dvdy.193.

Schachner, E.R., Farmer, C.G., McDonald, A.T. and Dodson, P. 2011. Evolution of the dinosauriform respiratory apparatus: New evidence from the postcranial axial skeleton. *The Anatomical Record: Advances in Integrative Anatomy and Evolutionary Biology* 294(9), pp. 1532–1547. doi: 10.1002/ar.21439.

Schneider, C.A., Rasband, W.S. and Eliceiri, K.W. 2012. NIH Image to ImageJ: 25 years of image analysis. *Nature Methods* 9(7), pp. 671–675. doi: 10.1038/nmeth.2089.

Schwarz-Wings, D. 2009. Reconstruction of the thoracic epaxial musculature of diplodocid and dicraeosaurid sauropods. *Journal of Vertebrate Paleontology* 29(2), pp. 517–534. doi: 10.1671/039.029.0229.

Shufeldt, R.W. 1988. *The myology of the raven (Corvus corax sinuatus): A guide to the study of the muscular system in birds*. Macmillan and Company.

Shwartz, Y., Blitz, E. and Zelzer, E. 2013. One load to rule them all: Mechanical control of the musculoskeletal system in development and aging. *Differentiation* 86(3), pp. 104–111. doi: 10.1016/j.diff.2013.07.003.

Smith, N.C., Wilson, A.M., Jespers, K.J. and Payne, R.C. 2006. Muscle architecture and functional anatomy of the pelvic limb of the ostrich (*Struthio camelus*). *Journal of Anatomy* 209(6), pp. 765–779.

Stickford, A.S.L. and Stickford, J.L. 2014. Ventilation and locomotion in humans: Mechanisms, implications, and perturbations to the coupling of these two rhythms. *Springer Science Reviews* 2(1–2), pp. 95–118. doi: 10.1007/s40362-014-0020-4.

Sullivan, C. 2007. *Function and evolution of the hind limb in Triassic archosaurian reptiles*. PhD Dissertation, Harvard University.

Tickle, P.G., Ennos, A.R., Lennox, L.E., Perry, S.F. and Codd, J.R. 2007. Functional significance of the uncinate processes in birds. *Journal of Experimental Biology* 210(22), pp. 3955–3961. doi: 10.1242/jeb.008953.

Tsuihiji, T. 2007. Homologies of the longissimus, iliocostalis, and hypaxial muscles in the anterior presacral region of extant Diapsida. *Journal of Morphology* 268(11), pp. 986–1020.

Tucker, V.A. 1972. Respiration during flight in birds. *Respiration Physiology* 14, pp. 75–82.

Turner, A.H. and Calvo, J.O. 2005. A new sebecosuchian crocodyliform from the Late Cretaceous of Patagonia. *Journal of Vertebrate Paleontology* 25(1), pp. 87–98.

Verstappen, M., Aerts, P. and Van Damme, R. 1998. Terrestrial locomotion in the black-billed magpie: kinematic analysis of walking, running and out-of-phase hopping. *Journal of Experimental Biology* 203(14), pp. 2159–2170.

Wedel, M.J. 2009. Evidence for bird-like air sacs in saurischian dinosaurs. *Journal of Experimental Zoology Part A: Ecological Genetics and Physiology* 311A(8), pp. 611–628. doi: 10.1002/jez.513.

Wilson, J.A. 2006. Anatomical nomenclature of fossil vertebrates: standardized terms or 'lingua franca'? *Journal of Vertebrate Paleontology* 26(3), pp. 511–518.

Witmer, L.M. 1995. The extant phylogenetic bracket and the importance of reconstructing soft tissues in fossils. *Functional morphology in vertebrate paleontology* 1, pp. 19–33.

Xu, X. et al. 2015. The taxonomic status of the Late Cretaceous dromaeosaurid *Linheraptor exquisitus* and its implications for dromaeosaurid systematics. *Vertebrata PalAsiatica* 53, pp. 29–62.

Zimmer, K. 1935. Beiträge zur Mechanik der Atmung bei den Vögeln in Stand-und Flug. *Zoologica* 33, pp. 1–69.

Zinoviev, A.V. 2006. Notes on the hind limb myology of the ostrich (*Struthio camelus*). *Ornithologia* 33, pp. 53–62.

Zusi, R.L. and Bentz, G.D. 1984. Myology of the purple-throated Carib (*Eulampis jugularis*) and other hummingbirds (Aves: Trochilidae). *Smithsonian Contributions to Zoology* (385), pp. 1–70. doi: 10.5479/si.00810282.385.

6.6 Supplementary Information

Figure S6.1. A summary of osteological correlates of hypaxial muscles in archosaurs. Osteological correlates in *Co. corax*, including the last cervical vertebra (A), the last cervical vertebral rib (B), the second dorsal vertebra (C), the second dorsal vertebral rib (D), the first sternal rib (E), the second sternal rib (F), and the sternum (G). Osteological correlates in *Dr. novaehollandiae*, including the last cervical vertebra (H), the last cervical vertebral rib (I), the second dorsal vertebra (J), the second dorsal vertebral rib (K), the second sternal rib (L), and the sternum (M). Osteological correlates in crocodylians, including the last cervical vertebra (N), the last cervical rib (O), the second dorsal vertebra (P), the second dorsal vertebral rib (Q), the third intermediate rib (R), and the third sternal rib (S). Scale bars equal 1cm.

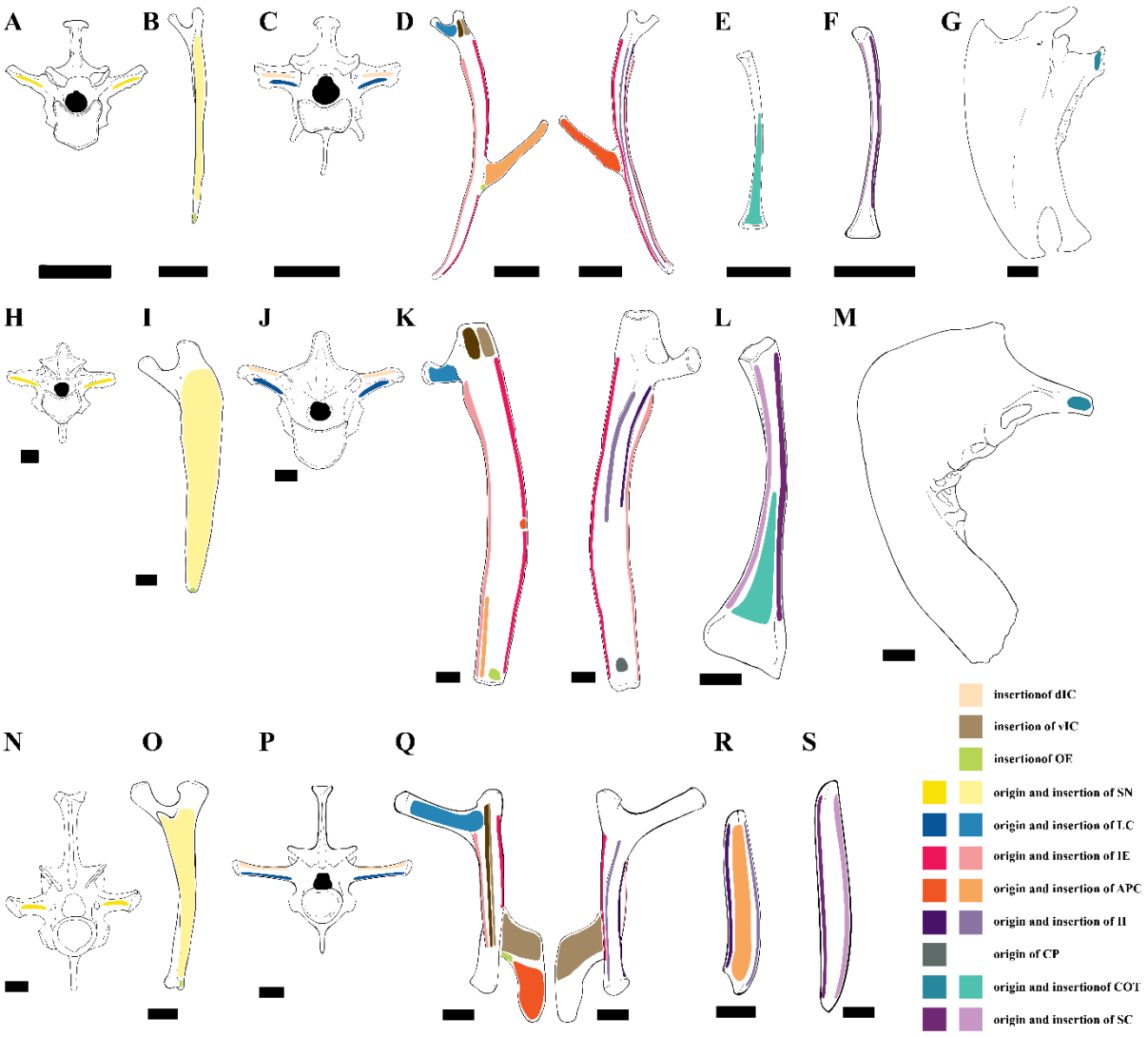
A
B
C
D
E
F
G
H
I
J
K
L
M
N
O
P
Q
R
S
insertionof dIC
insertion of vIC
insertionof OF
origin and insertion of SN
origin and insertion of LC
origin and insertion of IE
origin and insertion of APC
origin and insertion of II
origin of CP
origin and insertionof COT
origin and insertion of SC

6.7 Digital Supplementary Data

Raw data and r script to perform the Phylogenetic Generalized Least Squares (PGLS) regressions. Documents are stored and managed digitally by author and collaborators. R script is written and managed by Matthew Rhodes.

CHAPTER 7

Estimating ventilatory motions of ribcages with tidal volumes in paleognath birds and crocodylians

7.1 Introduction

Extant birds and crocodylians are members of archosaurs, a group of sauropsid amniotes first appeared in the Triassic Period, and occupied many ecological niches available for large bodied vertebrates throughout the Mesozoic era (Brusatte et al. 2010; Nesbitt 2011; Benton 2014).

Birds and crocodylians generate airflow into and out of the respiratory organs by expansion and contraction of the ribcage, a process often referred to as costal ventilation, which drives inspiration and expiration of air. In extant birds, the respiratory organs are compartmentalised into an immobile lung and high compliance air-sacs that facilitate high efficient cross-current gas exchanges and unidirectional airflow through the lung-air sac system, respectively (Duncker 1972; Maina 2002; Powell 2015). Additionally, vertebral ribs of the anterior thorax in most extant birds carry bony prongs extending posteriorly from the rib's midshaft called uncinate processes (Baumel et al. 1993), which potentially increase the leverage of the associated muscles (mm. appendicocostales) to expand the ribcage (Zimmer 1935; Tickle et al. 2007). An electromyographic study carried out on the Canada goose, *Branta canadensis* provided *in vivo* experimental support for the theoretical function of uncinate processes and suggested that they enhance the bird's ability to inspire air (Codd et al. 2005). In extant crocodylians, unidirectional air flow is also present in the less compartmentalised bronchoalveolar lung (Farmer and Sanders 2010). As in birds, dorsal vertebral ribs in extant crocodylians carry uncinate processes, though they are in the forms of cartilaginous tabs (Cong et al. 1988; Frey 1988), and m. iliocostalis, an epaxial muscle attached to the cartilaginous uncinate processes, may have an expiratory function based on experimental evidence (Codd et al. 2019). In addition to costal ventilation, extant crocodylians further enhance their ability to generate airflow by an adaptation called the "hepatic piston", which refers to the craniocaudal

movements of the liver by the skeletal muscle, m. diaphragmaticus (Carrier and Farmer 2000a; Farmer and Carrier 2000a). At least three electromyographic studies on m. diaphragmaticus (Gans and Clark 1976; Farmer and Carrier 2000a; Munns et al. 2012) and one cineradiographic study of the kinematics of the skeleton (Claessens 2009a) have suggested that the "hepatic piston" has an inspiratory function. Furthermore, anatomical and histological evidence suggest that the pubis can rotate relative to the rest of the pelvic girdle in crocodyliforms leading to modern crocodylians (Claessens and Vickaryous 2012), which may have enhanced the craniocaudal movement of the "hepatic piston". Aside from the "hepatic piston" and pubic rotation in crocodylians, both birds and crocodylians rely on costal ventilation.

Kinematics of vertebrate skeletons are typically described in terms of rotation of a mobile skeletal element relative to a fixed skeletal element about a centre of rotation situated at an idealised anatomical joint near their area of contact (e.g. within a synovial joint) (Neumann 2017). Accordingly, the capacity for movement at a given joint can be quantified as osteological range of motion (oROM), which can be measured *in vivo* (Sullivan 2007; Baier and Gatesy 2013; Kambic et al. 2014; Brocklehurst et al. 2017; Brocklehurst et al. 2019) and/or *ex vivo* (Hutson and Hutson 2012; Manafzadeh 2020; Herbst et al. 2022). As soft tissues can constrain the movement of joints (Manafzadeh and Padian 2018), traditional *ex vivo* oROM estimates based only on bones (Bramwell et al. 1997; Senter and Robins 2005) are likely exaggerated (Hutson and Hutson 2012; Kambic et al. 2017; Tsai et al. 2020). In studies of archosaur locomotion, oROM of a given joint (e.g. femoroacetabular joint) is mapped in a three dimensional joint space, and anatomically impossible poses are then excluded, defining a finite plausible oROM (Gatesy et al. 2009; Manafzadeh and Padian 2018; Demuth et al. 2020; Griffin et al. 2022). The recent implementation of AutoBend (Jones et al. 2021) and APSE (Bishop et al. 2023) further reduce the cost of time and computation power for oROM study.

In contrast to the relatively wide taxonomic scope of studies of archosaur locomotion, *in vivo* ventilatory motions of the ribcage have only been captured in the American alligator *Alligator mississippiensis* (Claessens 2009a; Brocklehurst et al. 2017), three palaeognath birds (Claessens 2009b), and the wild turkey *Melagris gallopavo* (Brocklehurst et al. 2019). Three-dimensional *ex vivo* study of the kinematics during ventilation has not been explored. However,

methods used in oROM studies of archosaur locomotion mostly focus on one joint, and may not be applicable in studies of ventilation, as the ribcage consists of multiple bones (i.e. vertebrae, rib segments, and sternum) connected by joints (Cong et al. 1988; Baumel et al. 1993) forming a system comparable to a closed kinematic chain (Levin 2013; Levin et al. 2017). Accordingly, kinematics of the ribcage would need to be estimated as a one working unit.

In extant birds and crocodylians, normal, rhythmical changes in lung volume during ventilation called tidal volume vary between different activities and environments, such as under general anesthesia, at rest without general anesthesia, during locomotion, during recovery, and at high altitude (Schmidt-Nielsen et al. 1969; Berger et al. 1970a; Brackenbury et al. 1982; Kiley et al. 1982; Farmer and Carrier 2000b; York et al. 2017). As costal ventilation is achieved by expansion/contraction of the ribcage, variations in tidal volumes in the situations listed above likely result from changes in the kinematics of the ribcage. Accordingly, tidal volume represents one of the factors in respiration that could be used to guide estimation of plausible oROM in archosaurs.

In this study, we construct three-dimensional models of a palaeognath and a crocodylian using skeletal elements, and we estimate oROM of the ribcage during three types of ventilatory motion. Then the estimated oROM is scaled down to a plausible range according to tidal volume measurements available in the literature. Finally, scaled oROM is compared among anatomical joints, among ventilatory motions, and between the palaeognath and the crocodylian.

7.2 Materials and Methods

Skeletal elements of a skeletally mature *Struthio camelus* (UAMZ 7159) and a *Caiman crocodilius* (UAMZ unnumbered) housed at the University of Alberta were chosen to represent Palaeognathae and Crocodylia, respectively. In this study, we used a five-step procedure to construct kinematic models and estimate ventilatory oROM (see Supplementary Information for detailed description of the procedure):

Meshing — Elements of ribcages were digitalised using a structured light scanner (Polyga Carbon series) housed in the Sullivan Lab at the University of Alberta, which includes presacral vertebrae at and adjacent to the ribcage, left rib segments, and the *Su. camelus* (UAMZ 7159) sternum. The sixth sternal rib, the cartilaginous uncinate processes and sternum of *Cai. crocodilus* (UAMZ unnumbered) were not completely preserved. A simple rod, ten compressed cubes and a low poly mesh were created in Autodesk Maya 2022 using reference in the literature (Cong et al. 1988; Baier and Gatesy 2013), to represent the last sternal rib, the cartilaginous uncinate processes and the sternum, respectively. Raw scans were smoothed, decimated, and remeshed using ZBrush 2018. An inclined plane was created to represent m. diaphragmaticus in *Cai. crocodilus* (UAMZ unnumbered). Landmarks were placed on the internal aspects of the ribcage, and a geometric mesh was created to represent the thoracic volume. A wrap deformer was created such that the thoracic volume would change according to the ventilatory motions of the ribcages.

Digital articulation — Three kinematic models with working unit as metre were created in Autodesk Maya 2022 to represent palaeognath bird (Palaeognath), crocodylian with m. diaphragmaticus (Crocodylian W), and crocodylian without m. diaphragmaticus (Crocodylian WOD), respectively. For all scenes, the last cervical vertebrae were positioned at the origin of the scenes, and the remaining skeletal elements were articulated digitally to represent the state of the ribcage at maximal expiration. A maximal gap of 1 cm was allowed between skeletal elements at the joint surface, to represent the space occupied by soft tissues.

Joint coordinate systems (JCS) — JCS in this study refers to the joint systems used in Maya that express rotations in Euler angles around three perpendicular axes (i.e. x-axis, y-axis, and z-axis). Although the setup used in this study is not identical to the practices in XROMM (Brainerd et al. 2010; Gatesy et al. 2010; Brocklehurst et al. 2017; Brocklehurst et al. 2019), the orientations of JCS are comparable.

Maya joints (Mjoints) were placed anterior to the centra near the centres of the articular facet to represent intervertebral joints; near the centres of parapophysis, diapophysis, capitulum and tuberculum to represent costal joints; and near the midpoints between articular facets of rib

segments to represent intracostal joints. A single Mjoint was placed near the centroid of the sternum in *Su. camelus*, and near the junction between prosternum and mesosternum.

Three types of JCS orientations were created to describe kinematics and compare descriptive capacities of different setups existed in the literature: (1) CBP (Caliper-Bucket-Pump) setup (Fig. 1A) aligned the x-axis lateromedially to describe pump-handle motions, the y-axis craniocaudally to describe caliper motions, and z-axis ventrodorsally to describe bucket-handle motions; (2) AB (Anatomical Bone) setup (Fig. 1B) aligned JCS with the long axis of the bones such that x-axis describes the axial rotation, y-axis describes abduction/adduction, and z-axis describes protraction/retraction; (3) AJ (Anatomical Joint) setup (Fig. 1C) aligned JCS with a vector between joint surfaces, and describe rotations similar to AB setup. Accordingly, motions described by the CBP setup are comparable to those for costal joints captured in *Iguana iguana* by Brainerd et al. (2015), AB setup is comparable to parapophysis-diapophysis JCS by Brocklehurst et al. (2019). The AB and AJ setups differ in that the AB setup accounted for the long axis of bones, whereas the AJ setup only considers the positions of articular facets. In crocodylian models, the protraction/retraction are comparable is not equivalent to elevations/depressions due to the orientations of the sternal ribs. However, protraction/retraction were used so that comparisons between rib segments and between models can use the same sets of terms. The rotation order for each joint was set to xyz with Script 7.1.

Estimation of plausible oROM — To simplify the models, ventilatory motions were expressed as oROM around axes of JCS, and translations were excluded except in the case of the sternum, which was allowed to translate cranially and dorsally. To estimate oROM, bones were manually rotated to expand the ribcage and find positions to represent states of the ribcages at maximal inspiration. For a given intervertebral, costal, and intracostal joint, bones were allowed to rotate close to collision without moving the sternal ribs from the sternum to a point that can be interpreted as disarticulation. All oROMs were scaled until changes in thoracic volume between maximal expiration and inspiration approximated the tidal volumes taken from the literature (Schmidt-Nielsen et al. 1969; Perry 1988) (Table 7.1). The scaled rotations accordingly represent the plausible oROM. The scaling process caused the last sternal rib to collide with the sternum in

Palaeognath model during the ventilatory motions, and oROM of the last sternal rib in Palaeognath model was manually adjusted to avoid collisions.

Three versions of ventilatory motions were created: (1) vertebra-rib-sternum (VRS) version represents ventilation with vertebrae, rib segments, and sternum; (2) rib-sternum (RS) represents ventilation with rib segments and sternum; and (3) rib (R) represents ventilation with only rib segments. For the CBP, AB, and AJ setups of each version of ventilation, both oROM and plausible oROM were recorded as animation keyframes.

To describe oROM and plausible oROM from maximal expiration to maximal inspiration in a ventilatory cycle, the ratio of duration of inspiration to expiration was set to 1:2 for Palaeognath model and 1:1 for crocodylian models, which are based on respiratory studies in neognath and crocodylians (Table S7.1). To test the potential impacts of different kinematic assumptions, rotations were prescribed both as linear angular motions and motions with a constant angular acceleration estimated from oROM and duration of ventilation (see Supplementary Information for detailed description).

Visualise — For Palaeognath model, Crocodylian W model, and Crocodylian WOD model, oROM and plausible oROM were tabulated into 36 tables. Comparisons and visualisation were performed using Script 7.2 in Rstudio 4.1.2 (RStudio Team 2020).

7.3 Results

Following the rationales of terminologies used in Chapter 2 and Chapter 3, presacral vertebrae, cervical vertebrae, dorsal vertebrae are termed presacrals, cervicals, and dorsals, respectively. Anatomical joints are termed intervertebral joints between articulated presacrals, costal joints between articulated presacrals and vertebral rib. In Palaeognath model, intracostal joints refers to the antomical joints between articulated vertebral and sternal ribs. In the Crocodylian W and Crocodylian WOD models, intracostal joints were further categorised into dorsal intracostal joints between vertebral and intermediate ribs and ventral intracostal joints

between intermediate and sternal ribs. Anatomical joints are also referred to by the sequential number of the presacral regions (i.e. IV#, C#, DIR#, IR#, VIR#, and SR#) where necessary.

Ventilatory motions are described using the AB setups, as they closely resemble anatomical rotations of bones. Comparisons with the CBP and AJ setups following the description using the AB setups.

7.3.1 Scaling of oROM

To increase the thoracic volumes by the amount of tidal volume (approximately 10%) in Palaeognath model (Table 7.1), plausible oROM were 30%, 37%, and 39% of the estimated oROM for VRS, RS, and R versions, respectively. To increase the thoracic volume by approximately 6.7% in Crocodylian W model, plausible oROM in Crocodylian W model were 4.5%, 5.3%, and 5.4% of the estimated oROM for VRS, RS, and R versions, respectively. By comparison, plausible oROM in Crocodylian WOD were 19%, 28%, and 37% of the estimated oROM for VRS, RS, and R versions, respectively. Before scalling for plausible oROM, the geometric plane representing m. diaphragmaticus in Crocodylian W model translate caudally for 13 cm, and ventrally for 1.7 or 2.2 cm. After scaling for plausible oROM, m. diaphragmaticus only translates caudally for 7 mm and ventrally for 1 mm. The remaining portion of the result section focus on plausible oROM.

7.3.2 Ventilatory motions in Palaeognath model

Ventilatory motions described using the AB setup — All intervertebral joints have less than two degrees of plausible oROM, and the greatest amounts of rotation occurred at IV25, followed by IV19 and IV20 (Fig. 2). The greater amounts of plausible oROM recovered at IV25 may be unrealistic, as IV25 is attached to and therefore constrained by the pelvis which was not modelled in this study. By comparisons, plausible oROM are below one degree for intervertebral joitns from IV21 to IV24. Although signs of plausible oROM suggest that IV21 and IV24 flex and IV22 and IV23 extend toward maximal inspiration, the amounts the rotations are nearly negligible. The directions and amounts of rotations recovered from the intervertebral joints suggest ventilatory flexions of the dorsal vertebrae are achieved by flexions of the last cervicals while the dorsals remain relatively immobile.

At costal joints between presacrals and vertebral ribs, the VRS version recovered plausible oROM approximately five degrees of axial rotation, abduction, and protraction at maximal inspiration, except for the first dorsal vertebral rib at the C21, the axial rotation of which is substantially lower (Fig. 3, A – C). Likewise, the RS version also recovered low amount of axial rotation at C21 at less than two degrees. However, the amounts of protraction at costal joints gradually decrease from C19 to C25 (Fig. 4 A – C). By comparison, axial rotation at C21 is not distinctly lower than those of adjacent costal joints. Like the RS version, the R version recovered smaller amounts of protraction at costal joints from the posterior portion of the ribcage, and at the last costal joint C25, the vertebral rib is almost never protracted for inspiration. The plausible oROM across costal joints suggested that caudally positioned vertebral ribs may be needed only when the bird ventilate with the vertebral column and/or the sternum. Across all sampled costal joints among the VRS, RS, and R versions, axial rotation and abduction have overall similar amounts of rotations, suggesting that they could be the primary contributors to the kinematics of inspiration in palaeognath birds.

At intracostal joints between vertebral ribs and sternal ribs, the VRS version recovered greatest amounts of axial rotation near the anteroposterior midpoint at IR23, and the axial rotation at IR21 and IR25 are nearly negligible (Fig. 6A). Unlike the costal joints described above, sternal ribs are adducted at least five degrees and are retracted for inspiration, and adduction of the anterior sternal ribs have greater amounts of rotations (Fig. 6B, 6C). The RS and R versions recovered axial rotation and adduction comparable to VRS version, except for IR24 that has near zero axial rotation (Fig. 8A). In the RS and R versions, the posterior sternal ribs have lower amounts of adduction compared to their counterparts in the VRS motions. Although all sternal ribs are retracted for inspiration in the VRS version, protraction are recovered at IR23 in the RS version, and from IR23 to IR25 in the R version. Accordingly, the discrepancies at intracostal joints from IR23 to IR25 may be related to the flexion of the presacrals. Except for axial rotation, the kinematics of intracostal joints are in opposite directions the those recovered from costal joints. This is likely related to translations of the intracostal joints driven by vertebral ribs and the needs of sternal ribs to remain articulated with the sternum. Accordingly, sternal ribs, compared to their vertebral counterparts, in palaeognath may not act to expand the thorax.

Comparisons between three types of JCS setups — Of the costal joints, the AB setup recovered all ventilatory motions as positive rotations with overall similar amounts of rotations for inspirations. The AJ setup (Fig. 3, D – F, Fig. 4, D – F, Fig. 5, D – F) recovered results comparable to those from the AB setup only for abduction and protraction, whereas axial rotation recovered by the AJ setup are lower in magnitude, and show less consistency in terms of magnitude and sign of rotations among the VRS, RS, and R versions. For example, C23 and C24 in the VRS version have axial rotation in opposite directions to the remaining costal joints, whereas C22, C23, and C24 in the RS version and C20, C23, and C24 in the R version rotate in opposite direction to the remaining costal joints. Caliper and bucket-handle motions of the CBP setup (Fig. 3, G – I, Fig. 4, G – I, Fig. 5, G – I) are comparable to the abduction and protraction in the AB setup both in terms of amounts of rotations and signs. The pump-handle motions in the CBP setup have higher amounts of rotations and display patterns that are not recovered in both the AB and AJ setup. Plausible oROM and oROM are similar in magnitudes for pump-handle motions of C25 in the VRS version, of C24 and C25 in the RS version, of costal joints from C22 to C25 in the R version (Fig. 3G, Fig. 4G, Fig. 5G).

Of the intracostal joints, the AB setup recovered all axial rotation as positive rotations and all adduction as negative rotations. Retractions recovered by the AB setup have inconsistent signs at IR23, IR24, and IR25 between ventilatory motions. The AJ setup recovered similar axial rotation as the AB setup except for IR21 where the axial rotation are in opposite directions to other intracostal joints. All intracostal joints of the AJ setup but IR21 recovered adduction, although the plausible oROM is near negligible. Pump-handle and bucket-handle motions of the CBP setup are recovered with rotations in the same direction, whereas caliper motions recovered inconsistent patterns between ventilatory motions. JCS setups and ventilatory motions notwithstanding, pump-handle motions have the greatest amounts of rotations at intracostal joints.

Accordingly, abduction/caliper motions and protraction/bucket-handle motions of the costal joints in palaeognath are comparable both in terms of sings and amounts of rotations among three JCS setups, and the lateral and anterior expansions of the thorax could seemingly be captured regardless of which of the three JCS is used.

7.3.2 ventilatory motions in crocodylian model

Ventilatory motions described using the AB setup — All intervertebral joints have less than one degree of plausible oROM (Fig. 9). The magnitude of rotations is overall low in both Crocodylian W and Crocodylian WOD models. According to the signs of rotations recovered from intervertebral joints, intervertebral joints from IV8 to IV12 (last two cervicals to first three dorsals) act to flex the dorsal vertebral column, whereas IV13 to IV18 act to extend the dorsal vertebral column. The last cervicals in Crocodylian W and Crocodylian WOD models do not have greater amounts of rotations compared to the intervertebral joints of the dorsals. This may be artifacts introduced in the process of digital articulation, as the last cervical in Crocodylian W and Crocodylian WOD models were oriented caudodorsally whereas the last cervical in Palaeognath model was oriented posteriorly.

In Crocodylian W model, most costal and intracostal joints in recovered less than negligible amount (less than one degree) rotations regardless of JCS and version of ventilatory motions (Fig. 10, A – C, Fig. 11, A – C, Fig. 12, A – C), and exceptions such as axial rotation of C8 in the RS and R versions recovered ventilatory rotations only between one to two degrees.

In Crocodylian WOD model, influences of m. diaphragmaticus is absence, and patterns of ventilatory motions can be discerned. In the VRS version, protraction are overall recovered to have greatest amounts of rotations that peak at C11, C12, C13, which are dorsal costal joints from the anterior portion of the ribcage. Abductions of the costal joints are around one degree for all costal joints except C8 and C9, C12, and C13. At C8 and C9, adduction instead of abduction are recovered, and at C12 and C13, the amounts of abduction are distinctly smaller than adjacent costal joints. The parapophysis migrates onto the diapophysis/transverse process on the third dorsal that C12 is located. Changes in parapophyseal position likely influence the orientations of JCS in the AB setup, which may contribute to the small amounts of abduction recovered at C12 and C13. VRS version recovered overall smaller amounts of axial rotation from costal joints of the anterior ribcage. At the costal joints of the first two dorsals (C10 and C11), axial rotation have opposite directions compared to the remaining costal joints. Compared to VRS version, the RS and R versions recovered similar amounts of protraction from all costal joints, and costal joints of the first four dorsals (C10 to C13) all recovered smaller amounts of abduction compared

to the remaining costal joints. All axial rotation recovered by RS version have the same sign, though the amounts of rotations are uneven as in the VRS version. The VRS version recovered greater amounts of protraction from cranial portion of the ribcage and greater amounts of abduction from caudal portion of the ribcage. Such craniocaudal difference suggests that the ribcage of crocodylians may be functionally segregated into two craniocaudal units, prioritising protraction and abduction, respectively.

Of the dorsal intracostal joints, VRS version recovered uneven amounts of ventilatory motions of all three JCS (Fig. 13, A – C, Fig. 14, A – C, Fig. 15, A – C). Only protraction are consistently recovered from all dorsal intracostal joints. By comparison, the first four dorsal intracostal joints (DIR10 – DIR13) recovered adduction instead o abduction. Unlike costal joints, abduction/adduction are recovered to have overall least amounts of rotations at dorsal intracostal joints in VRS version. RS and R versions overall recovered comparable amounts of rotations from all three JCS. However, DIR11 and DIR 12 recovered adduction as in VRS version.

Of the ventral intracostal joints (Fig. 16, A – C, Fig. 17, A – C, Fig. 18, A – C), VRS version recovered comparable amounts of retraction of all except VIR 16 which has substantially smaller amounts of retraction. By comparison, the VRS version recovered discernable amount of adduction only at ventral instracostal joints from the posterior portion of the ribcage. Constrasting the abduction recovered at the costal and dorsal intracostal joints from the caudal portion of the ribcage, the sternal ribs are adducted at the ventral intracostal joints, which likely act to keep rib segments connected to the sternum. The RS and R versions recovered similar patterns for adduction at ventral instracostal joints as in the VRS version. Although the RS version recovered retraction from all but the last ventral intracostal joints, R version does not recover retraction with a discernable pattern. Unlike palaeognath, the sternal ribs in crocodylians are oriented so that retraction at the ventral intracostal joints would depress the sternal ribs. Therefore, retraction of ventral intracostal joints recovered from the VRS and RS versions may expand the thorax dorsoventrally. However, sternum in the R version is immobile, and ventral intracostal joints could not be expected to show a distinct pattern for retraction. This would suggest that sternal movements may be needed for sternal ribs to contribute to inspiration. The consistent adduction of sternal ribs along with the potential to expand the ribcage in tandem with

sternal movements indicate that sternal ribs may act both to increase the thoracic volume, and to keep rib segments connected to the sternum.

Comparisons between three types of JCS setups — Of the costal joints, the AB setup consistently abduction and protraction from costal joints of dorsals (Fig. 10 A – C, Fig. 11 A – C, Fig. 12 A – C). Although the AJ setup could not recover consistent patterns for abduction and protraction, the axial rotation the AJ setup (Fig. 10B, Fig. 11B, Fig. 12B) recovered from all costal joints have the same sign representing the directions of axial rotation. CBP setup recovered consistent patterns for pump-handle and caliper motions for costal joints of all dorsals (Fig. 10G, 10H, Fig. 11G, 11H, Fig. 12G, 12H), and caliper motions and abduction recovered by the CBP and the AB setups have comparable amounts of rotations, although in opposite directions of rotations. Unlike the Palaeognath model, plausible oROM of pump-handle motions recovered by the CBP setup is substantially smaller than the oROM, and pump-handle motions does not exceed axial rotation recovered by the AB and AJ setups.

Of the dorsal intracostal joints, consistent pattern shared by at least two types of JCS is seemingly absent. However, signs and by extension, the directions of joint orientation can still be compared between the AB and AJ setups. The AB setup recovered protraction from most dorsal intracostal joints (Fig. 13A, 13B, Fig. 14A, 14B, Fig. 15A, 15B) whereas the AJ setups recovered retraction from most dorsal intracostal joints with the amounts of rotations comparable to those recovered by the AB setup (Fig. 13D, 13E, Fig. 14D, 14E, Fig. 15D, 15E). Similar contrast in terms of signs can be seen from comparisons of abduction/adduction recovered by the AB and AJ setups. Of the ventral intracostal joints, consistent pattern shared by all three JCS is seemingly absent.

Accordingly, abduction/caliper motions are comparable in terms of amounts of rotations for costal joints between the AB and CBP setups. The lateral expansions of the dorsal thorax could seemingly be captured by either the AB or CBP setups.

7.3.3 ventilatory motions between two kinematic assumptions

With an assumed constant angular acceleration, ventilatory motions of Mjoints and by extension motions of anatomical joints in ways comparable to bell curves (Fig. 19, Fig. 20). By comparison, describing the ventilatory motions in as linear motions recover motions as straight lines from zero at maximal expiration to plausible oROM at maximal inspiration. For comparisons among rotations around JCS (e.g. axial rotation vs abduction), using an assumed angular acceleration recovered similar pattern as describing the rotations as linear motions.

7.4 Discussion

7.4.1 Comparisons with *in vivo* observations

Lateral expansions of the thorax in relatively uniform fashion and caudal motions of sternal ribs have been observed in palaeognath birds (Claessens 2009b). Caudal motions of the sternal ribs are likely represented by the retraction recovered at the intracostal joints in our Palaeognath model. As for lateral expansions of the thorax, Claessens (2009b) observed that the lateral expansion is greatest on the cranial aspects of the thorax. The Palaeognath model presented in this study recovered abduction at costal joints and adduction at intracostal joints. Accordingly, lateral expansions of palaeognath thorax are likely contributed mostly by abduction at costal joints. Unlike observations made by Claessens (2009b), abduction and the comparable caliper motions have similar plausible oROM across all costal joints of dorsals in the Palaeognath model (Fig. 3B, 3E, 3H, Fig. 4B, 4E, 4H, Fig. 5B, 5E, 5H). Two possible factors may contribute to the discrepancies between plausible oROM estimated in this study and those observed by Claessens (2009b). Firstly, ventilation in palaeognath birds is observed when the birds are walking or running in Claessens (2009b), whereas the tidal volume used to estimate plausible oROM is taken from resting individuals of *Su. camelus* under normal condition (Schmidt-Nielsen et al. 1969). Palaeognath birds with physiological demands from locomotion likely require more oxygen (Powell 2015), which would conceivably be archived by further expanding the thorax beyond the plausible oROM at rest. Secondly, skeletal muscles of the thorax have different volume (George and Berger 1966; Baumel et al. 1993) (see Chapter 6), and muscles that have been identified as inspiratory muscles such as m. levator costarum and mm.

intercostales externi have greater volumes on the anterior portion of thorax. The greater volume of skeletal muscles likely has higher physiological cross-section area which is related to the maximal muscle forces plausible for the muscle (Neumann 2017). With the increased muscle volume and maximal muscle forces, inspiratory muscles of the cranial thorax may contribute more muscle work in expanding the thorax compared to the inspiratory muscles of caudal thorax, which may contribute to the greater amount of expansion estimated from the cranial thorax. Although the discrepancies between the plausible oROM presented in this study and the ventilatory motions observed by Claessens (2009b) does not negate the viability of using tidal volumes to estimate plausible oROM during ventilation. We will need to test the effects of estimating oROM using tidal volumes from a wide range of activities, to reliably construe a general pattern in ventilatory oROM.

Compared to the observations made in a cineradiographic study on the American alligator *Alligator mississippiensis* (Claessens 2009a), m. diaphragmaticus in the Crocodylian W model presented in this study only translated slightly caudally and ventrally, which is smaller than the minimal 1.4 length of presacrals estimated by Claessens (2009a), and is much smaller than the cineradiographic records (supplementary video S2) created by Claessens (2009a). Claessens (2009a) estimated 0.8 the length presacrals as the minimal translations of m. diaphragmaticus, which is likely still higher than the 7 mm recovered from the estimation of plausible oROM using Crocodylian W model. The representation of m. diaphragmaticus in the Crocodylian W model was a concave plane and may not accurately capture the morphology of the *in vivo* m. diaphragmaticus, which along with the possible errors introduced from using deformers as a method to scale tidal volumes may account for the discrepancies between the plausible oROM of m. diaphragmaticus estimated using Crocodylian W model and those observed by Claessens (2009a).

Cranial motions have been reported as the primary ventilatory motions of vertebral ribs from the cranial portion of the ribcage, and lateral expansions of the thorax occurs more obviously on the vertebral ribs positioned further caudally (Claessens 2009a). For all three version of ventilatory motions in Crocodylian WOD model, protraction are recovered with greatest amounts of rotations, and abduction have greater amounts of rotations at costal joints

from the caudal portions of the ribcage (Fig. 10B, 10C, Fig. 11B, 11C, Fig. 12B, 12C). Accordingly, plausible oROM estimated from Crocodylian WOD model matches the qualitative descriptions in some *in vivo* observations. As anatomical landmarks other than joints (e.g. distal ends of intermediate ribs) are sometimes used to described kinematics (Baumel et al. 1990; Claessens 2009a), ventilatory motions of the skeleton would need to be compare in details with additional landmarks.

Ventilatory motions of anatomical joints of the ribcage have been measured in at least *Al. mississippiensis* and *Me. gallopavo* (Brocklehurst et al. 2017; Brocklehurst et al. 2019), in which the kinematics of a given ventilatory cycle resemble the bell curves ventilatory motions with an assumed constant angular accelerations presented in this study (Fig. 19, Fig. 20). Accordingly, assuming a constant angular acceleration may describe the ventilatory motions in a more realistic manner.

As the JCS setups in this study share similar rationale as those recorded by Brocklehurst et al. (2017) and Brocklehurst et al. (2019), the plausible oROM estimated in this study could be quantitatively compared with the *in vivo* measurements. In *Me. gallopavo*, the ventilatory motions as measured by pump-handle, caliper, and bucket-handle motions are of similar magnitudes below one degree of rotation (Brocklehurst et al. 2019). In our Palaeognath model however, pump-handle motions have recovered greater amounts of rotations than caliper and bucket-handle motions, and all plausible oROM are greater than one degree. In *Al. mississippiensis* examined by Brocklehurst et al. (2017), however, pump-handle, caliper, and bucket handle motions are comparable and at some joints (e.g. (Costovertebral joint 4 in Brocklehurst et al. 2017)) have greater amounts of rotations than the plausible oROM estimated in Crocodylian W and Crocodylian WOD models presented in this study. The causes of quantitative discrepancies could not be inferred confidently.

7.4.2 Implications for understanding transitions in the evolution of archosaur ventilation

Birds and crocodylians use costal ventilation to generate airflow through the respiratory organs for gas exchange (Brainerd and Owerkowicz 2006; Perry et al. 2019), which is achieved by motions of the vertebrae, rib segments, and sternum (Claessens 2009b; Claessens 2009a; Brocklehurst et al. 2017; Brocklehurst et al. 2019).

A great number of anatomical features can be extracted from ribcages of birds and crocodylians. As a whole, birds such as *Su. camelus* have deep and narrow ribcages whereas crocodylians have wide and shallow ribcages (Cong et al. 1988; Baumel et al. 1993; Claessens 2015). Along the vertebral column, the parapophysis drifts dorsally and migrates onto the diapophysis/transverse process in crocodylians, which has been used to infer the pulmonary morphology and ventilatory mechanics (Schachner et al. 2009; Brocklehurst et al. 2018; Brocklehurst et al. 2019). Birds, crocodylians, and presumably most extinct archosaurs carry uncinate processes (Cong et al. 1988; Codd et al. 2008; Codd 2010; Boyd et al. 2011) (see Chapter 3 and 4), which theoretically improve archosaur's ability to ventilate (Zimmer 1935; Tickle et al. 2007). However, which one(s) of the ventilatory motions that uncinate processes enhance muscles to perform remains unclear.

In Palaeognath model presented in this study, all ventilatory motions have comparable plausible oROM, whereas protraction in Crocodylian W and Crocodylian WOD models have the greatest plausible oROM. If morphological features of the ribcages can be correlated with the types of ventilatory motions they prioritise, abduction and protraction may be prioritised in archosaurs with an avian-like and crocodylian-like ribcages, respectively. However, caution may be warranted when attempting to establish such correlation. Firstly, compliance and material properties of the respiratory organs (Scheid and Piiper 1969; Perry 1988; Maina 2007; Farmer 2017) may have a greater bearing on how the ribcage would be expanded. Furthermore, discrepancies between plausible oROM estimated in this study and the *in vivo* observations are not fully resolved, and patterns observed from kinematic models in this study warrant further examinations and validations, using tidal volumes under various biological conditions (e.g. during locomotion, recovery after exercise). Challenges in research notwithstanding, well-

preserved ribcages are found in exquisitely preserved fossil archosaurs (Xu et al. 2015; Currie et al. 2016). and plausible oROM could be estimated in fossil taxa following the rationale of extant phylogenetic bracket (Witmer 1995), especially in pennaraptorans with ossified sternum. Plausible oROM may then be compared in both extant and fossil archosaurs, for insights into evolutionary transitions of ventilatory mechanics at key moment of archosaurian history.

Tables

Table 7. 1. Scaling factors used to estimate plausible oROM

scaling percentage	**Crocodylian W model**					
	max_ex (m^3)	max_in (m^3)	volume difference (m^3)	delta/ex (%)	delta/in (%)	MT
5.4%	0.0012	0.0012	0.0001	6.6028	6.1938	r
5.3%	0.0012	0.0012	0.0001	6.6495	6.2349	rs
4.5%	0.0012	0.0012	0.0001	6.5797	6.1735	vrs
scaling percentage	Crocodylian WOD model					
	max_ex (m^3)	max_in (m^3)	volume difference (m^3)	delta/ex (%)	delta/in (%)	
37.0%	0.0034	0.0037	0.0002	6.6546	6.2394	r
28.0%	0.0034	0.0037	0.0002	6.6098	6.2000	rs
19.0%	0.0034	0.0037	0.0002	6.5927	6.1850	vrs
scaling percentage	Palaeognath model					
	max_ex (m^3)	max_in (m^3)	volume difference (m^3)	delta/ex (%)	delta/in (%)	
39%	0.0785	0.0870	0.0085	10.7866	9.7364	r version
37%	0.0785	0.0871	0.0085	10.8781	9.8109	rs version
30%	0.0785	0.0871	0.0086	10.9872	9.8995	vrs version

Abbreviations: r, rib only; rs, rib-sternum; vrs, vertebra-rib-sternum.

Figures

Figure 7.1. Axes of three types of joint coordinate system (JCS).

Line drawings of vertebra, vertebral rib, and sternal rib of *Struthio camelus* (UAMZ 7159) illustrating the axes of CBP setup (A) of the JCS in this study; line drawing of vertebra, vertebral rib, and sternal rib of *Struthio camelus* (UAMZ 7159) illustrating the axes of AB setup (B) of the JCS in this study; and line drawings of vertebra, vertebral rib, and sternal rib of *Struthio camelus* (UAMZ 7159) illustrating the axes of AJ setup (C) of the JCS in this study. Scale bars equal 1 cm. red arrows represent pump-handle motions and axial rotation; green arrows represent caliper motions and abduction/adduction; and blue arrows represent bucket-handle motions and protraction/retraction. Directions of arrows indicate directions of positive rotations.

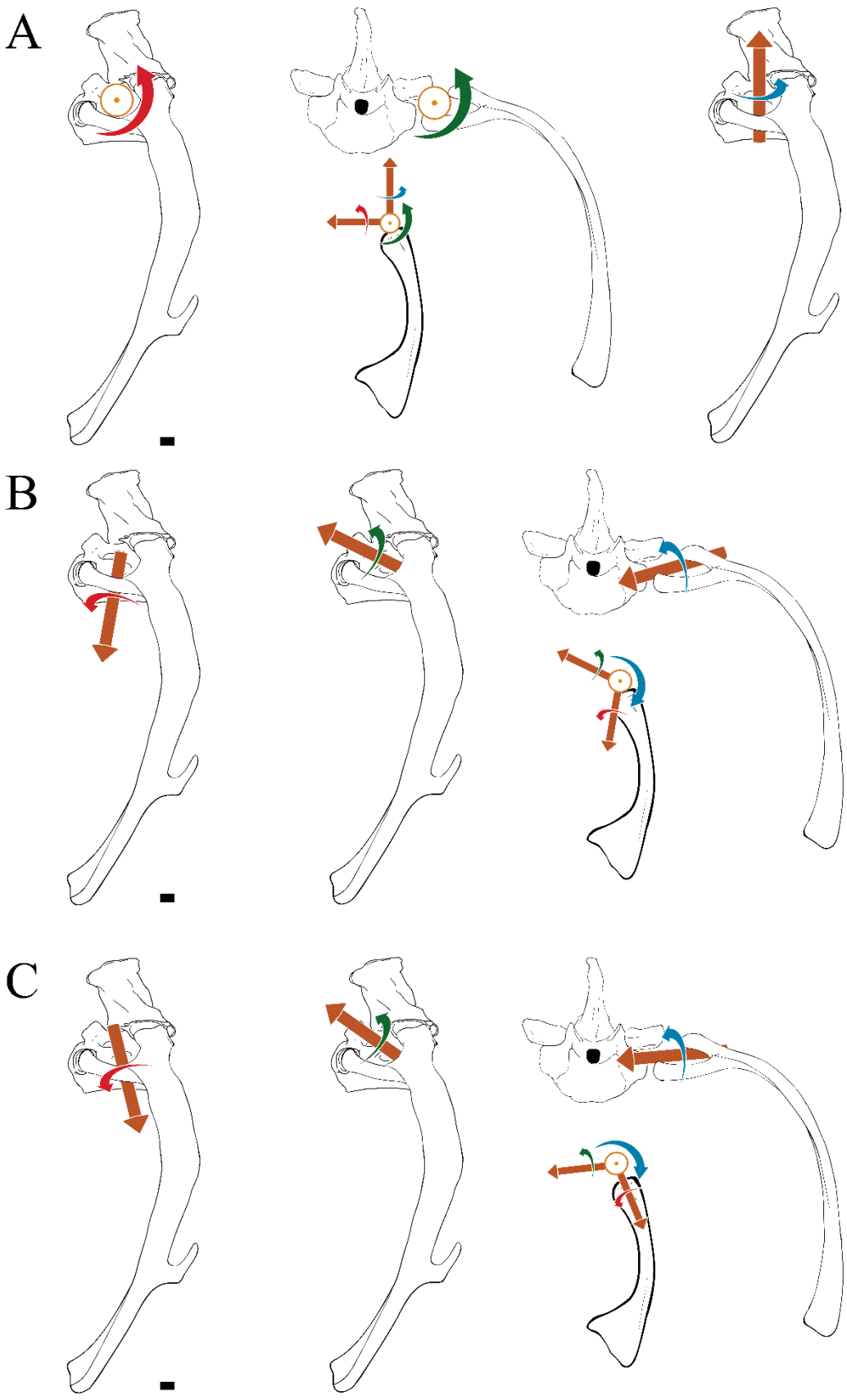
A
B
C

Figure 7.2. oROM and plausible oROM of intervertebral joints in Palaeognath model.

Bar graph of oROM and plausible oROM of intervertebral joints estimated using tidal volume. Orange at high and low opacity represent plausible oROM and oROM.

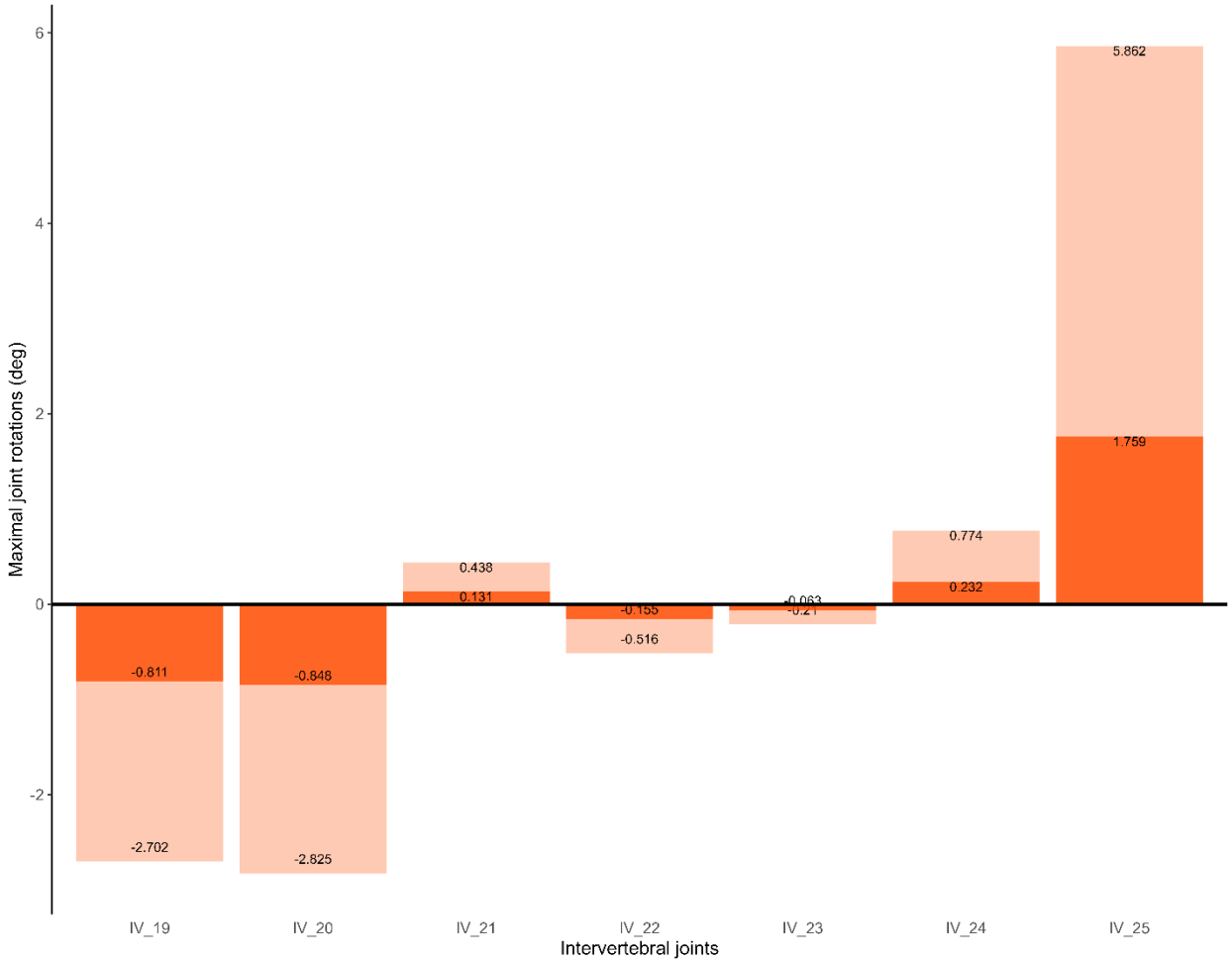
Maximal joint rotations (deg)
6
4
2
0
-2
5.862
1.759
0.774
0.232
0.438
0.131
-0.155
-0.516
-0.063
-0.21
-0.811
-2.702
-0.848
-2.825
IV_19
IV_20
IV_21
IV_22
IV_23
IV_24
IV_25
Intervertebral joints

Figure 7.3. oROM and plausible oROM of costal joints in VRS version of ventilatory motions in Palaeognath model.

Bar graph of oROM and plausible oROM estimated from tidal volume in Palaeognath model. Axial rotations (A), abduction (B), and protraction (C) using AB setup; axial rotation (D), abduction (E), and protraction (F) using AJ setup; and pump-handle motions (G), caliper motions (H), and bucket-handle motions (I) using CBP setup. Orange at high and low opacity refer to plausible oROM and oROM using AB setups; Yellow at high and low opacity refer to plausible oROM and oROM using AJ setup; navy blue at high and low opacity refer to plausible oROM and oROM using CBP setups.

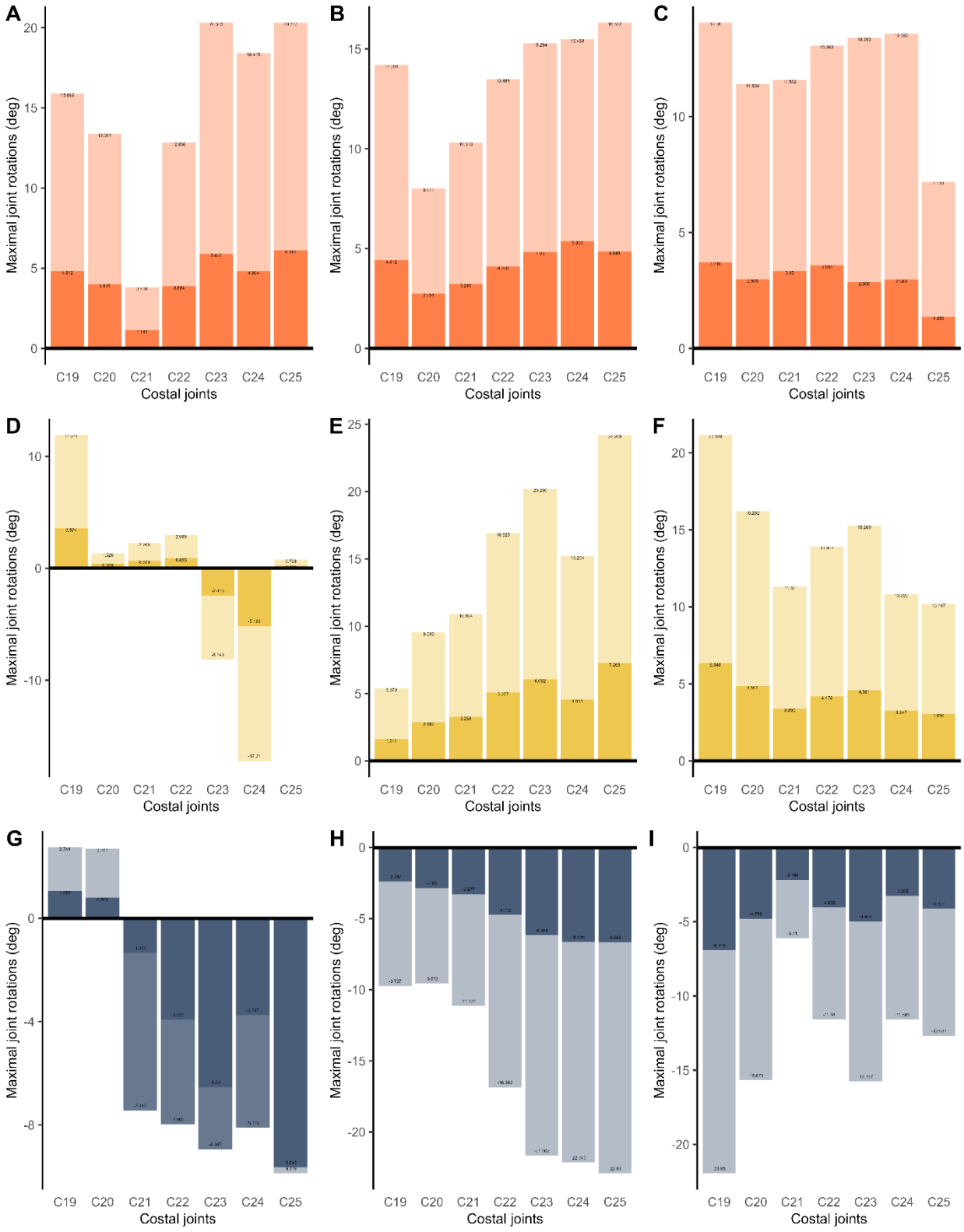
A
B
C
D
E
F
G
H
I
Maximal joint rotations (deg)
C19 C20 C21 C22 C23 C24 C25
Costal joints

Figure 7.4. oROM and plausible oROM of costal joints in RS version of ventilatory motions in Palaeognath model.

Bar graph of oROM and plausible oROM estimated from tidal volume in Palaeognath model. Axial rotations (A), abduction (B), and protraction (C) using AB setup; axial rotation (D), abduction (E), and protraction (F) using AJ setup; and pump-handle motions (G), caliper motions (H), and bucket-handle motions (I) using CBP setup. Orange at high and low opacity refer to plausible oROM and oROM using AB setups; Yellow at high and low opacity refer to plausible oROM and oROM using AJ setup; navy blue at high and low opacity refer to plausible oROM and oROM using CBP setups.

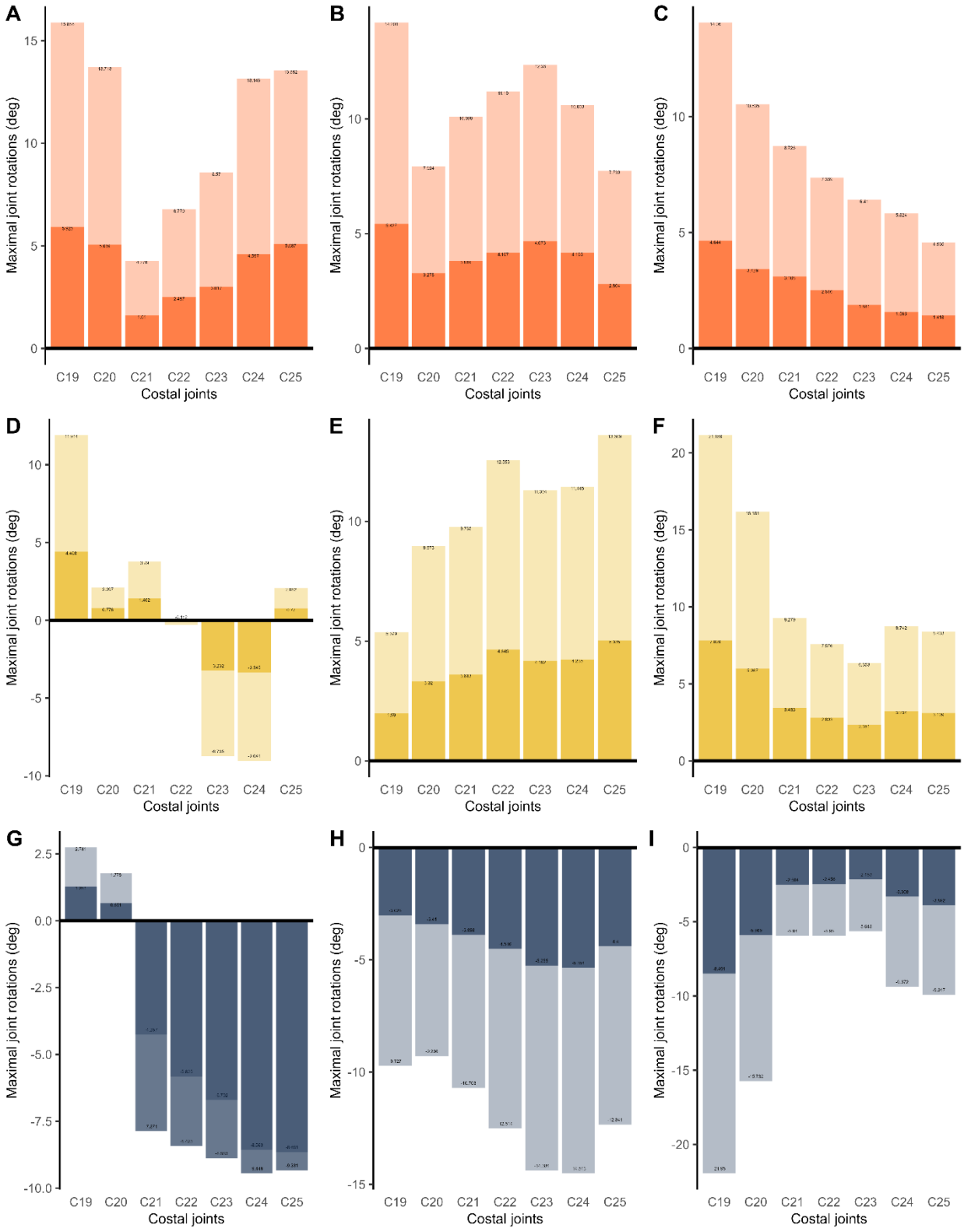
A
B
C
D
E
F
G
H
I
Maximal joint rotations (deg)
Costal joints
C19
C20
C21
C22
C23
C24
C25

Figure 7.5. oROM and plausible oROM of costal joints in R version of ventilatory motions in Palaeognath model.

Bar graph of oROM and plausible oROM estimated from tidal volume in Palaeognath model. Axial rotations (A), abduction (B), and protraction (C) using AB setup; axial rotation (D), abduction (E), and protraction (F) using AJ setup; and pump-handle motions (G), caliper motions (H), and bucket-handle motions (I) using CBP setup. Orange at high and low opacity refer to plausible oROM and oROM using AB setups; Yellow at high and low opacity refer to plausible oROM and oROM using AJ setup; navy blue at high and low opacity refer to plausible oROM and oROM using CBP setups.

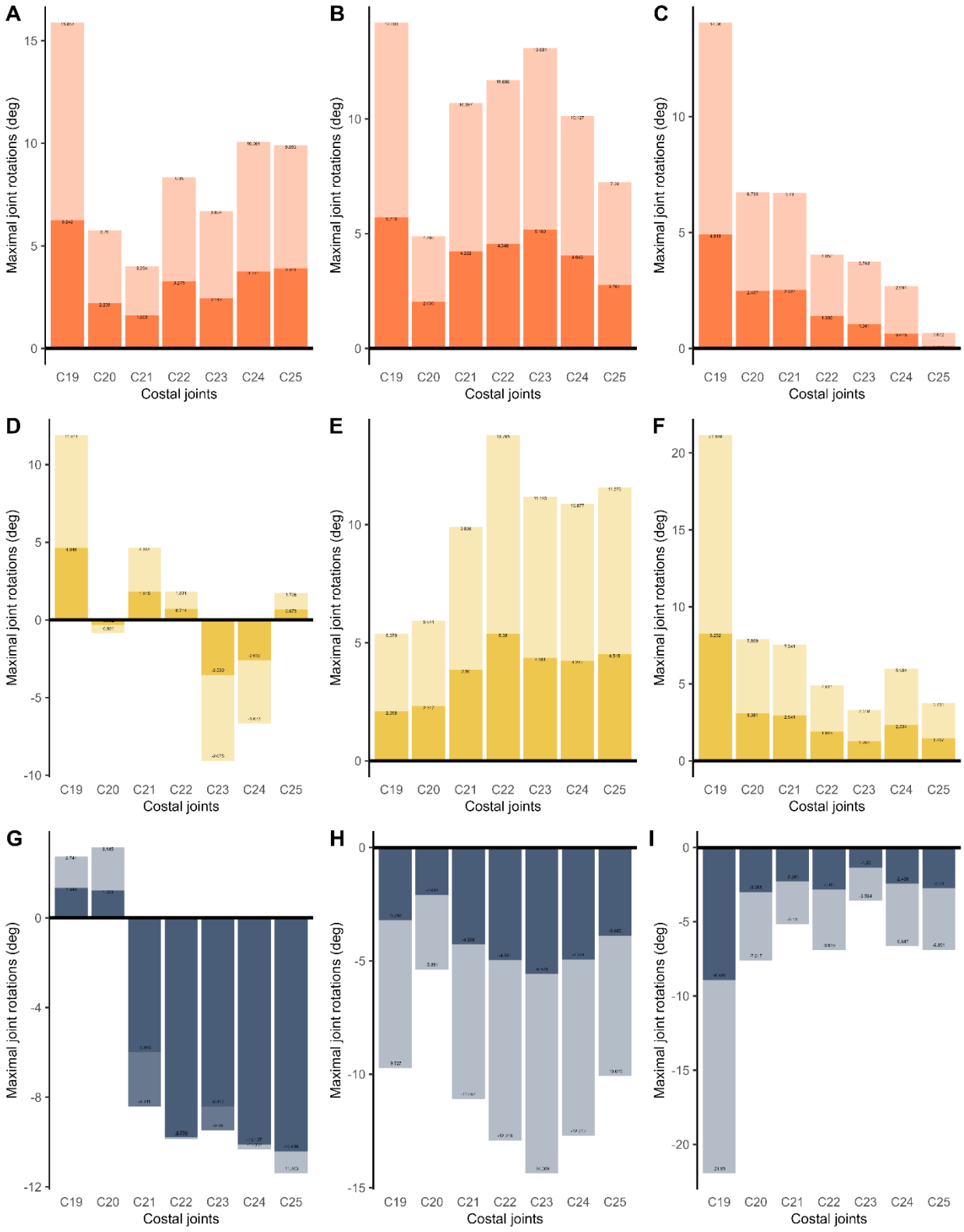
A
B
C
D
E
F
G
H
I
Maximal joint rotations (deg)
Costal joints
C19
C20
C21
C22
C23
C24
C25

Figure 7.6. oROM and plausible oROM of intracostal joints in VRS version of ventilatory motions in Palaeognath model.

Bar graph of oROM and plausible oROM estimated from tidal volume in Palaeognath model. Axial rotations (A), abduction (B), and protraction (C) using AB setup; axial rotation (D), abduction (E), and protraction (F) using AJ setup; and pump-handle motions (G), caliper motions (H), and bucket-handle motions (I) using CBP setup. Orange at high and low opacity refer to plausible oROM and oROM using AB setups; Yellow at high and low opacity refer to plausible oROM and oROM using AJ setup; navy blue at high and low opacity refer to plausible oROM and oROM using CBP setups.

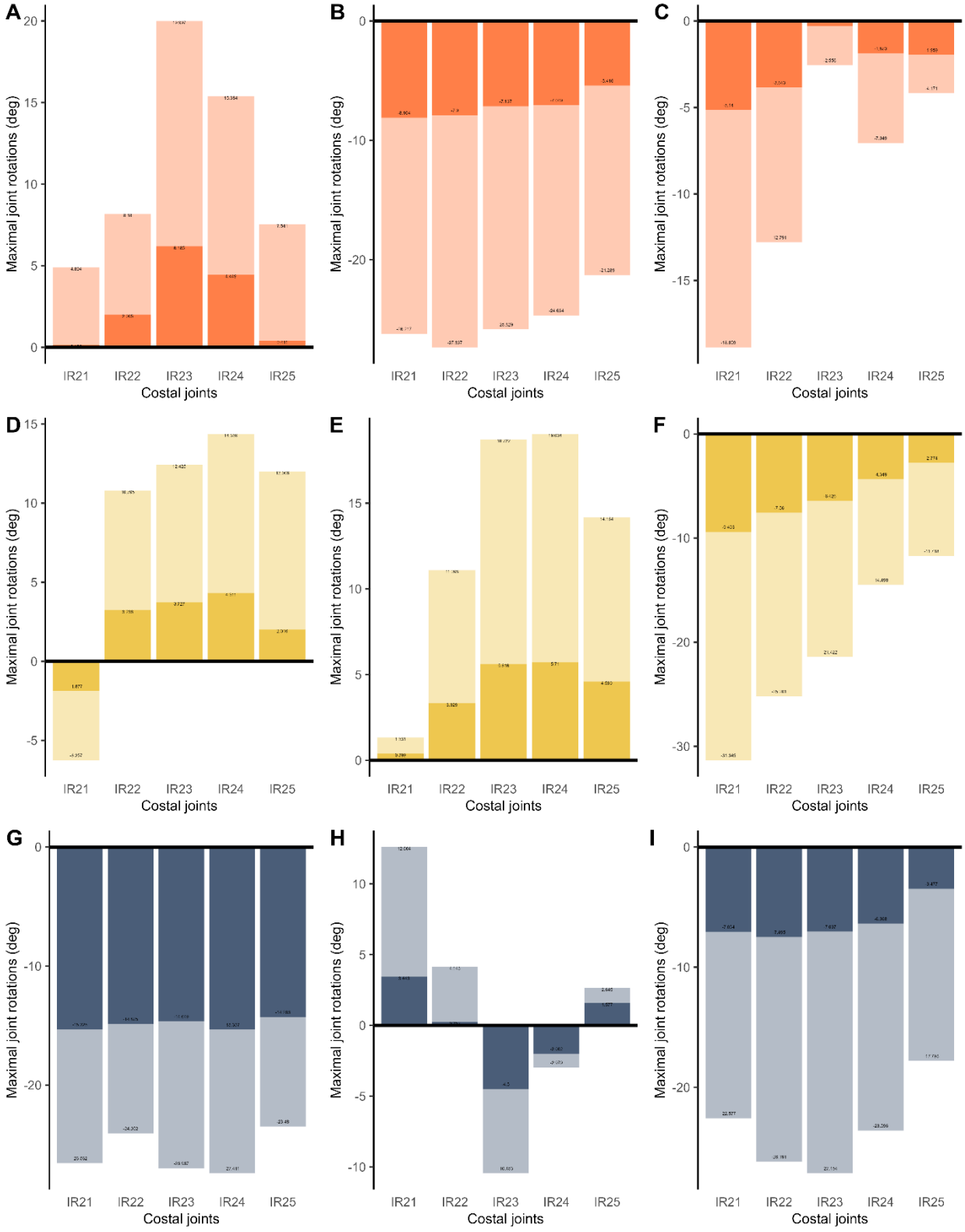
A
B
C
D
E
F
G
H
I
Maximal joint rotations (deg)
IR21
IR22
IR23
IR24
IR25
Costal joints

Figure 7.7. oROM and plausible oROM of intracostal joints in RS version of ventilatory motions in Palaeognath model.

Bar graph of oROM and plausible oROM estimated from tidal volume in Palaeognath model. Axial rotations (A), abduction (B), and protraction (C) using AB setup; axial rotation (D), abduction (E), and protraction (F) using AJ setup; and pump-handle motions (G), caliper motions (H), and bucket-handle motions (I) using CBP setup. Orange at high and low opacity refer to plausible oROM and oROM using AB setups; Yellow at high and low opacity refer to plausible oROM and oROM using AJ setup; navy blue at high and low opacity refer to plausible oROM and oROM using CBP setups.

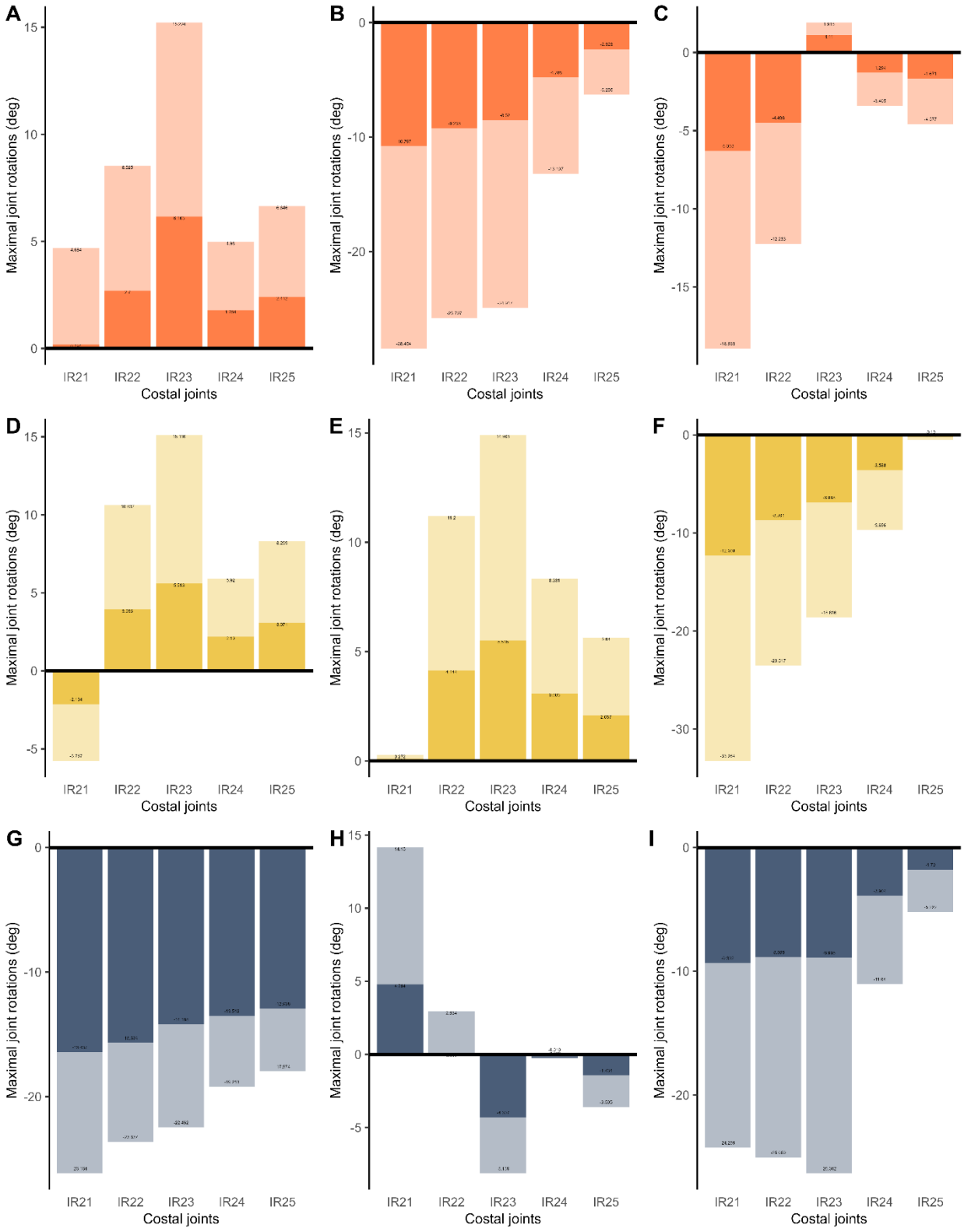
A
B
C
D
E
F
G
H
I
Maximal joint rotations (deg)
IR21
IR22
IR23
IR24
IR25
Costal joints

Figure 7.8. oROM and plausible oROM of intracostal joints in R version of ventilatory motions in Palaeognath model.

Bar graph of oROM and plausible oROM estimated from tidal volume in Palaeognath model. Axial rotations (A), abduction (B), and protraction (C) using AB setup; axial rotation (D), abduction (E), and protraction (F) using AJ setup; and pump-handle motions (G), caliper motions (H), and bucket-handle motions (I) using CBP setup. Orange at high and low opacity refer to plausible oROM and oROM using AB setups; Yellow at high and low opacity refer to plausible oROM and oROM using AJ setup; navy blue at high and low opacity refer to plausible oROM and oROM using CBP setups.

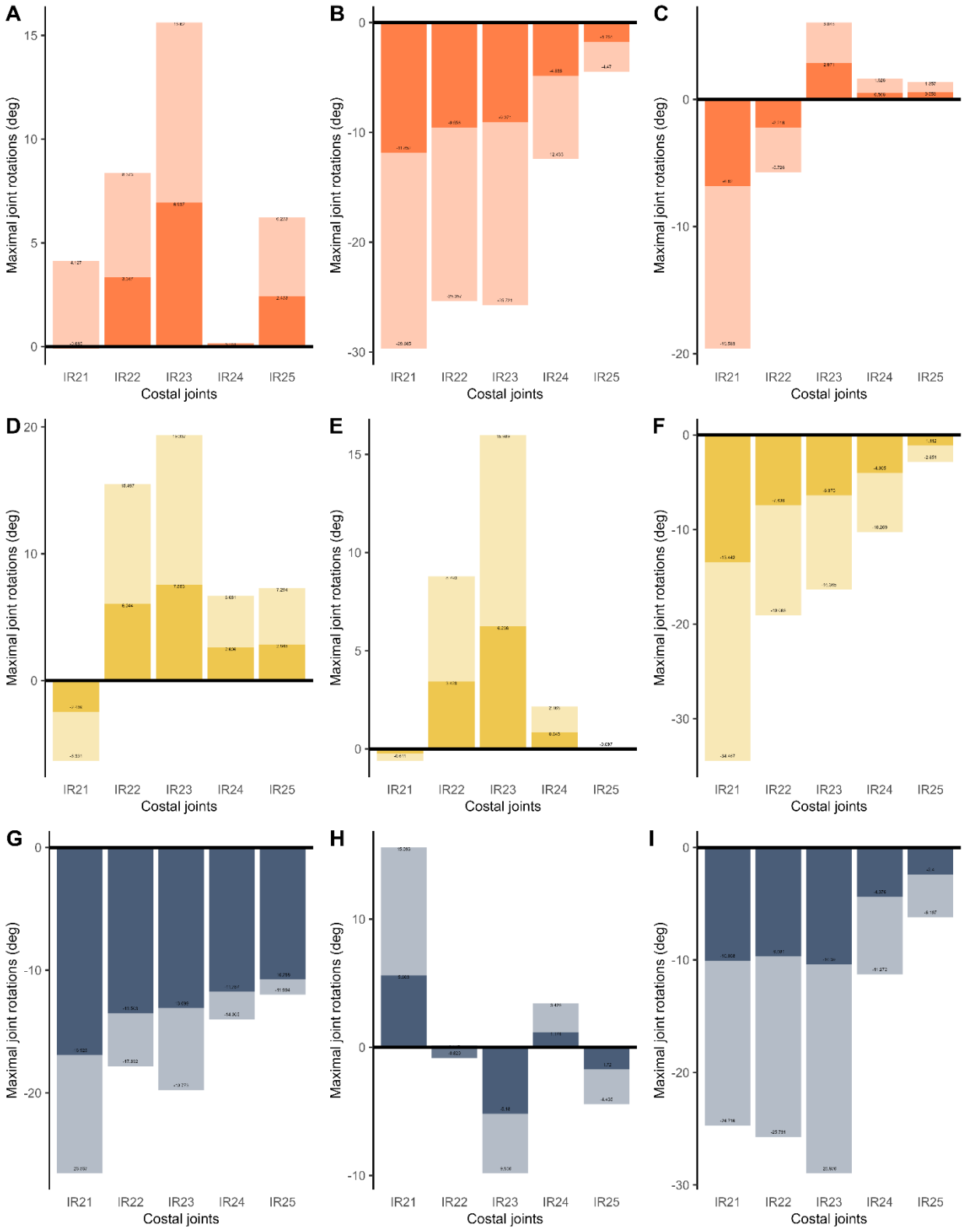
A
B
C
D
E
F
G
H
I
Maximal joint rotations (deg)
IR21
IR22
IR23
IR24
IR25
Costal joints

Figure 7.9. oROM and plausible oROM of intervertebral joints in VRS version of ventilatory motions in Crocodylian W and Crocodylian WOD model.

Bar graph of oROM and plausible oROM estimated from tidal volume in Crocodylian W and Crocodylian WOD models. Orange at high, medium, and low opacity refer to plausible oROM in Crocodylian W model, Crocodylian WOD mode, and oROM, respectively.

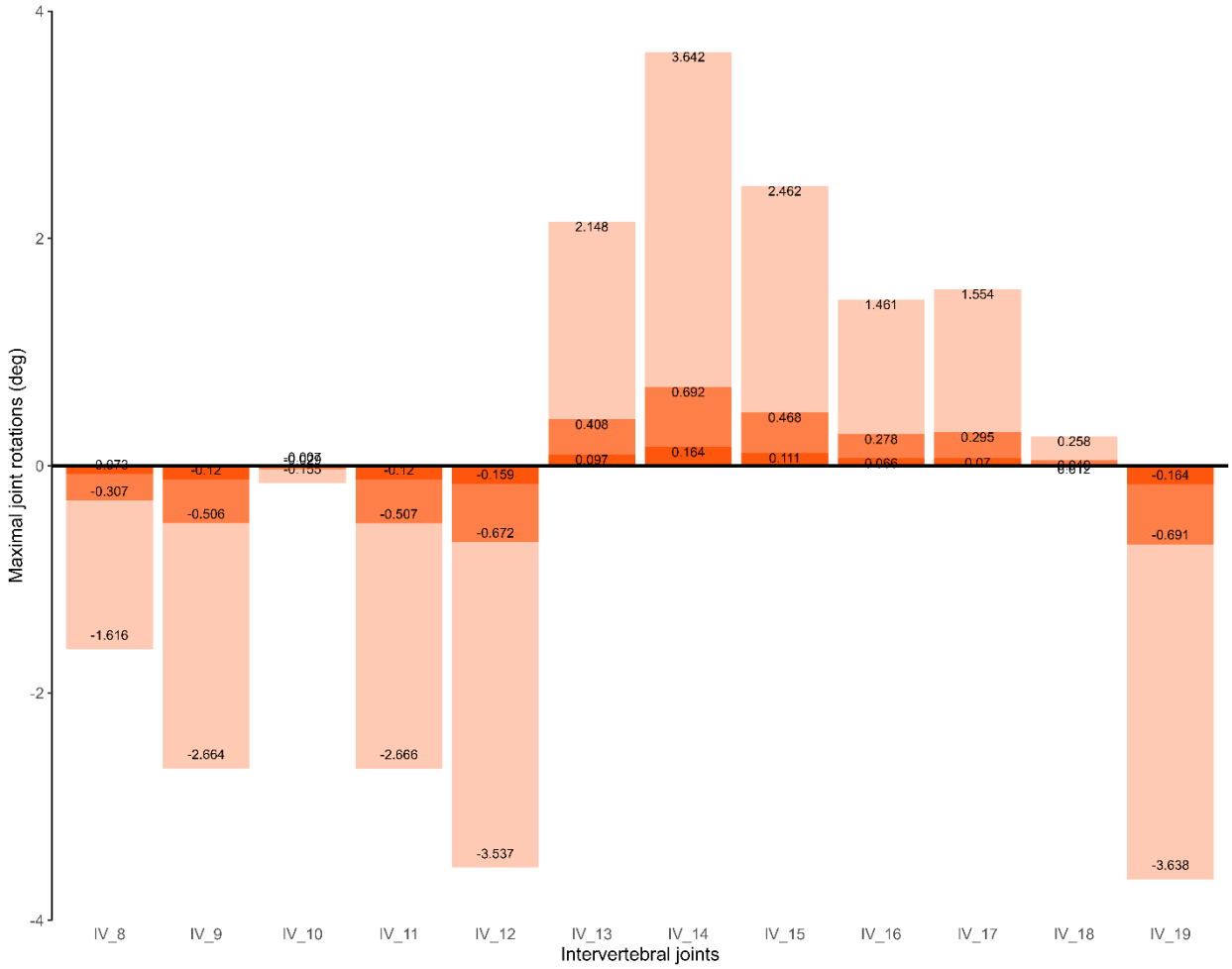
Maximal joint rotations (deg)
4
2
0
-2
-4
3.642
2.462
2.148
1.461
1.554
0.692
0.468
0.408
0.278
0.295
0.258
0.164
0.111
0.097
-0.159
-0.164
-0.307
-0.506
-0.507
-0.672
-0.691
-1.616
-2.664
-2.666
-3.537
-3.638
IV_8
IV_9
IV_10
IV_11
IV_12
IV_13
IV_14
IV_15
IV_16
IV_17
IV_18
IV_19
Intervertebral joints

Figure 7.10. oROM and plausible oROM of costal joints in VRS version of ventilatory motions in Crocodylian W and Crocodylian WOD models.

Bar graph of oROM and plausible oROM estimated from tidal volume in Palaeognath model. Axial rotations (A), abduction (B), and protraction (C) using AB setup; axial rotation (D), abduction (E), and protraction (F) using AJ setup; and pump-handle motions (G), caliper motions (H), and bucket-handle motions (I) using CBP setup. Orange at high, medium, and low opacity refer to plausible oROM in Crocodylian W model, plausible oROM in Crocodylian WOD model, and oROM using AB setups; Yellow at high, medium, and low opacity refer to Crocodylian W model, plausible oROM in Crocodylian WOD model, and oROM using AJ setup; navy blue at high, medium, and low opacity refer to Crocodylian W model, plausible oROM in Crocodylian WOD model, and oROM using CBP setups.

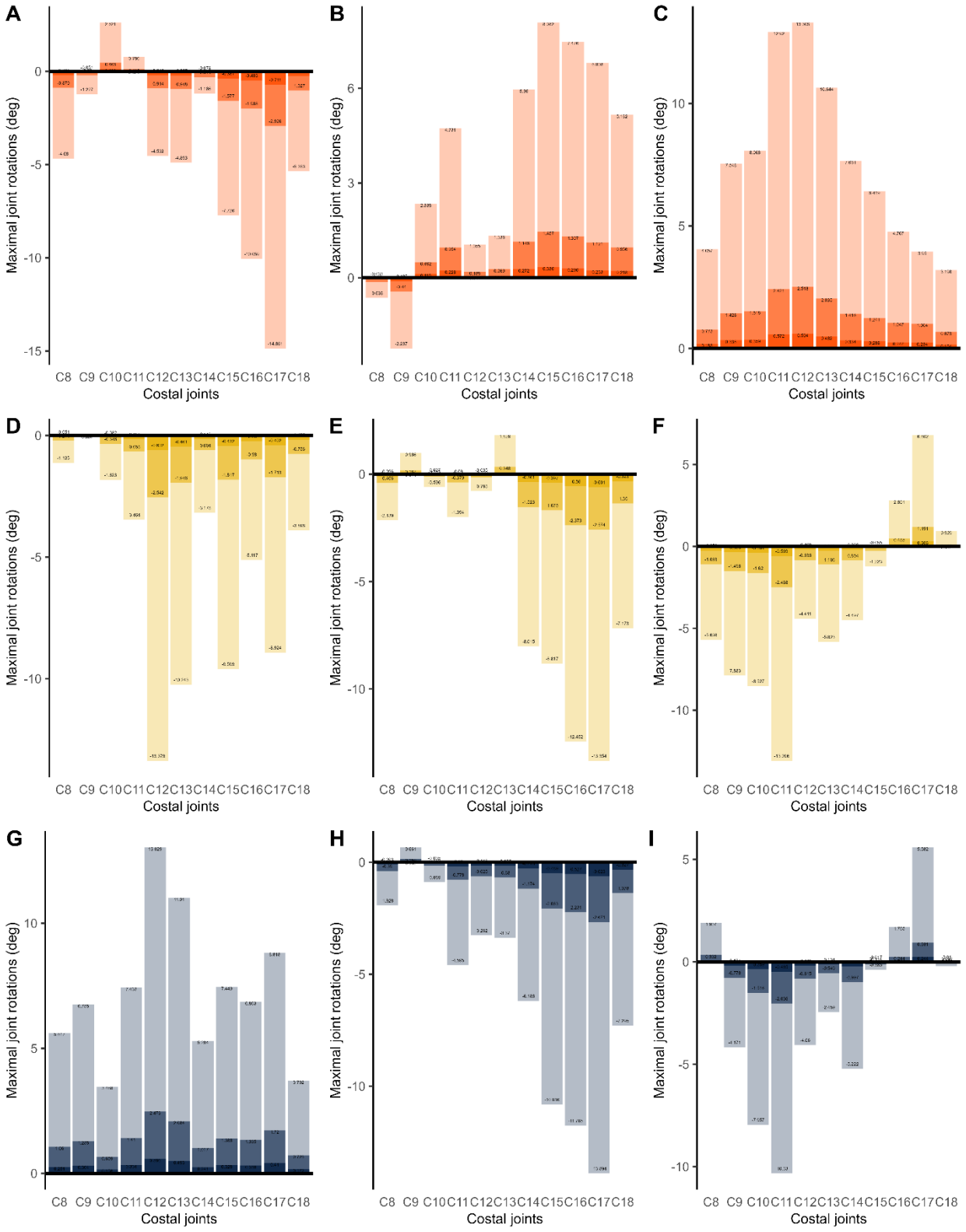
A
B
C
D
E
F
G
H
I
Maximal joint rotations (deg)
C8 C9 C10 C11 C12 C13 C14 C15 C16 C17 C18
Costal joints

Figure 7.11. oROM and plausible oROM of costal joints in RS version of ventilatory motions in Crocodylian W and Crocodylian WOD models.

Bar graph of oROM and plausible oROM estimated from tidal volume in Palaeognath model. Axial rotations (A), abduction (B), and protraction (C) using AB setup; axial rotation (D), abduction (E), and protraction (F) using AJ setup; and pump-handle motions (G), caliper motions (H), and bucket-handle motions (I) using CBP setup. Orange at high, medium, and low opacity refer to plausible oROM in Crocodylian W model, plausible oROM in Crocodylian WOD model, and oROM using AB setups; Yellow at high, medium, and low opacity refer to Crocodylian W model, plausible oROM in Crocodylian WOD model, and oROM using AJ setup; navy blue at high, medium, and low opacity refer to Crocodylian W model, plausible oROM in Crocodylian WOD model, and oROM using CBP setups.

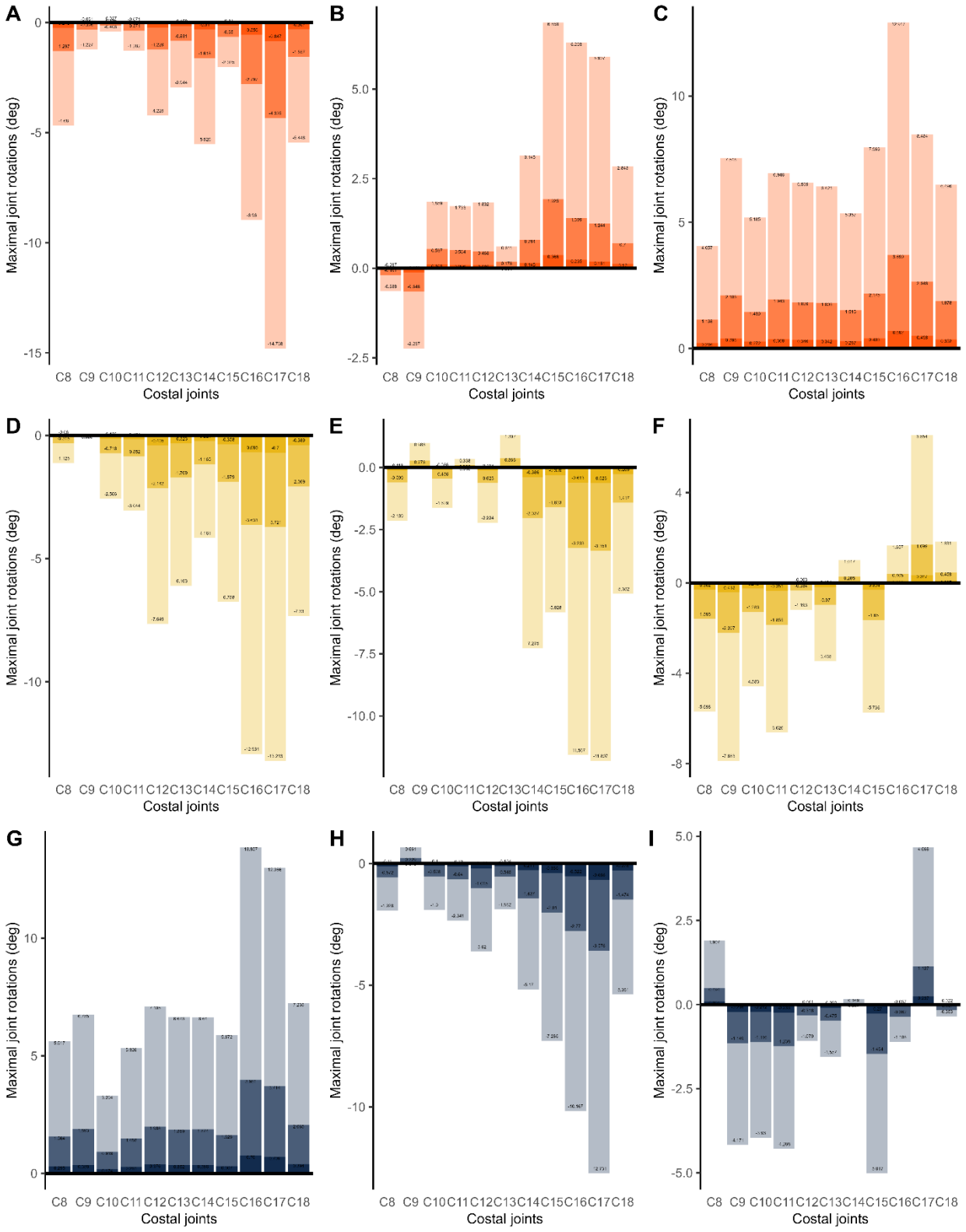
A
B
C
D
E
F
G
H
I
Maximal joint rotations (deg)
Costal joints
C8 C9 C10 C11 C12 C13 C14 C15 C16 C17 C18

Figure 7.12. oROM and plausible oROM of costal joints in R version of ventilatory motions in Crocodylian W and Crocodylian WOD models.

Bar graph of oROM and plausible oROM estimated from tidal volume in Palaeognath model. Axial rotations (A), abduction (B), and protraction (C) using AB setup; axial rotation (D), abduction (E), and protraction (F) using AJ setup; and pump-handle motions (G), caliper motions (H), and bucket-handle motions (I) using CBP setup. Orange at high, medium, and low opacity refer to plausible oROM in Crocodylian W model, plausible oROM in Crocodylian WOD model, and oROM using AB setups; Yellow at high, medium, and low opacity refer to Crocodylian W model, plausible oROM in Crocodylian WOD model, and oROM using AJ setup; navy blue at high, medium, and low opacity refer to Crocodylian W model, plausible oROM in Crocodylian WOD model, and oROM using CBP setups.

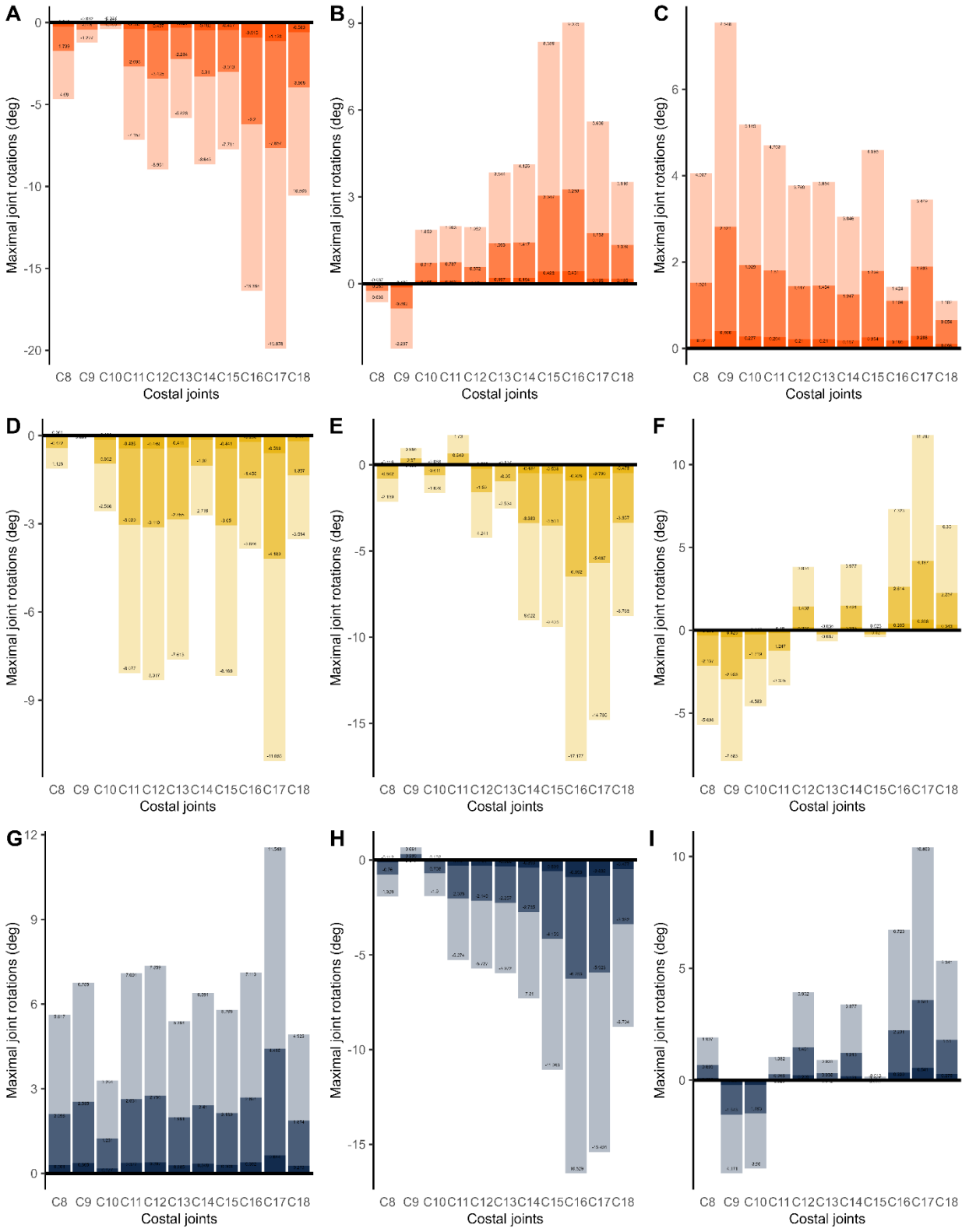
A
B
C
D
E
F
G
H
I
Maximal joint rotations (deg)
C8 C9 C10 C11 C12 C13 C14 C15 C16 C17 C18
Costal joints

Figure 7.13. oROM and plausible oROM of dorsal intracostal joints in VRS version of ventilatory motions in Crocodylian W and Crocodylian WOD models.

Bar graph of oROM and plausible oROM estimated from tidal volume in Palaeognath model. Axial rotations (A), abduction (B), and protraction (C) using AB setup; axial rotation (D), abduction (E), and protraction (F) using AJ setup; and pump-handle motions (G), caliper motions (H), and bucket-handle motions (I) using CBP setup. Orange at high, medium, and low opacity refer to plausible oROM in Crocodylian W model, plausible oROM in Crocodylian WOD model, and oROM using AB setups; Yellow at high, medium, and low opacity refer to Crocodylian W model, plausible oROM in Crocodylian WOD model, and oROM using AJ setup; navy blue at high, medium, and low opacity refer to Crocodylian W model, plausible oROM in Crocodylian WOD model, and oROM using CBP setups.

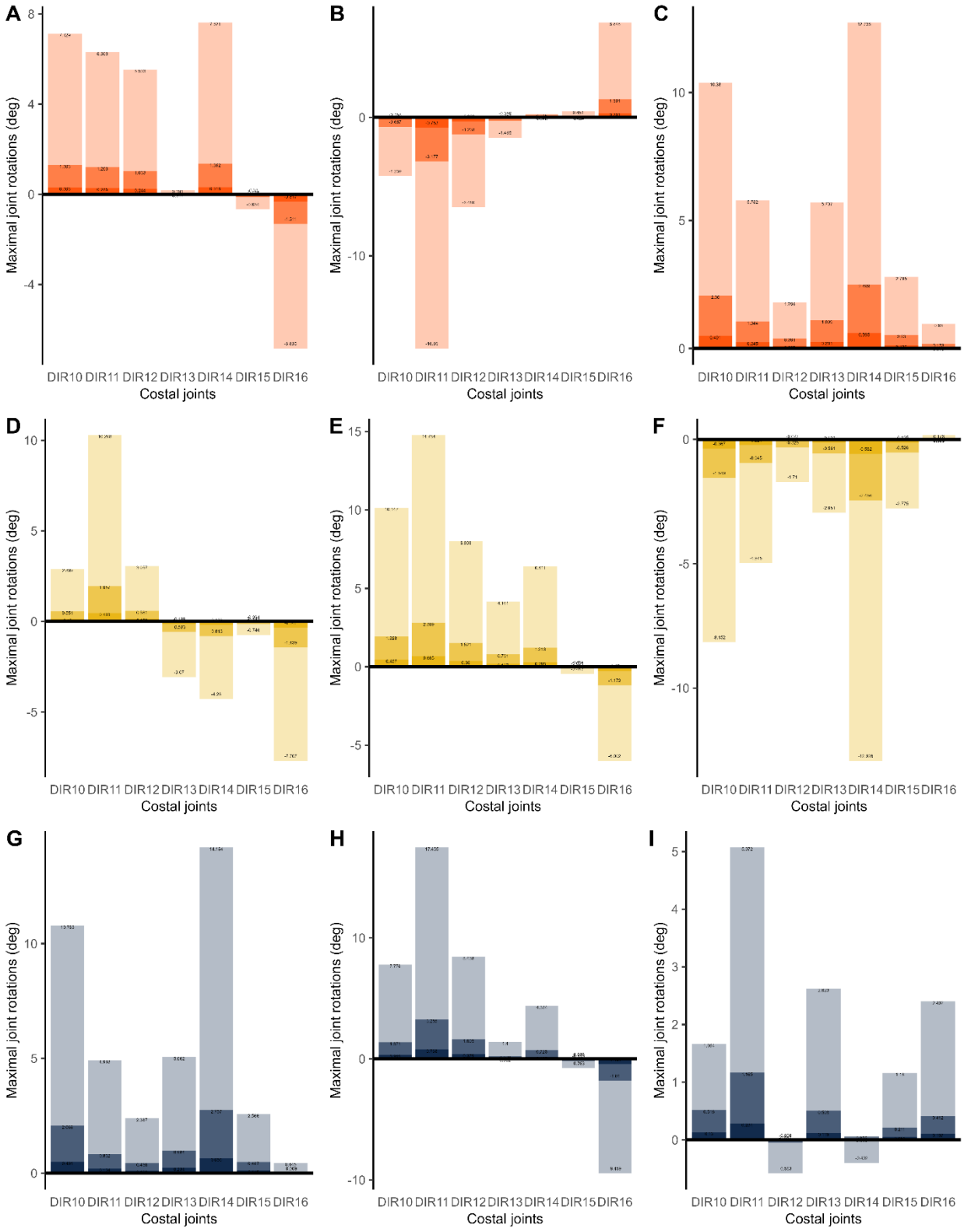
A
B
C
D
E
F
G
H
I
Maximal joint rotations (deg)
DIR10 DIR11 DIR12 DIR13 DIR14 DIR15 DIR16
Costal joints

Figure 7.14. oROM and plausible oROM of dorsal intracostal joints in RS version of ventilatory motions in Crocodylian W and Crocodylian WOD models.

Bar graph of oROM and plausible oROM estimated from tidal volume in Palaeognath model. Axial rotations (A), abduction (B), and protraction (C) using AB setup; axial rotation (D), abduction (E), and protraction (F) using AJ setup; and pump-handle motions (G), caliper motions (H), and bucket-handle motions (I) using CBP setup. Orange at high, medium, and low opacity refer to plausible oROM in Crocodylian W model, plausible oROM in Crocodylian WOD model, and oROM using AB setups; Yellow at high, medium, and low opacity refer to Crocodylian W model, plausible oROM in Crocodylian WOD model, and oROM using AJ setup; navy blue at high, medium, and low opacity refer to Crocodylian W model, plausible oROM in Crocodylian WOD model, and oROM using CBP setups.

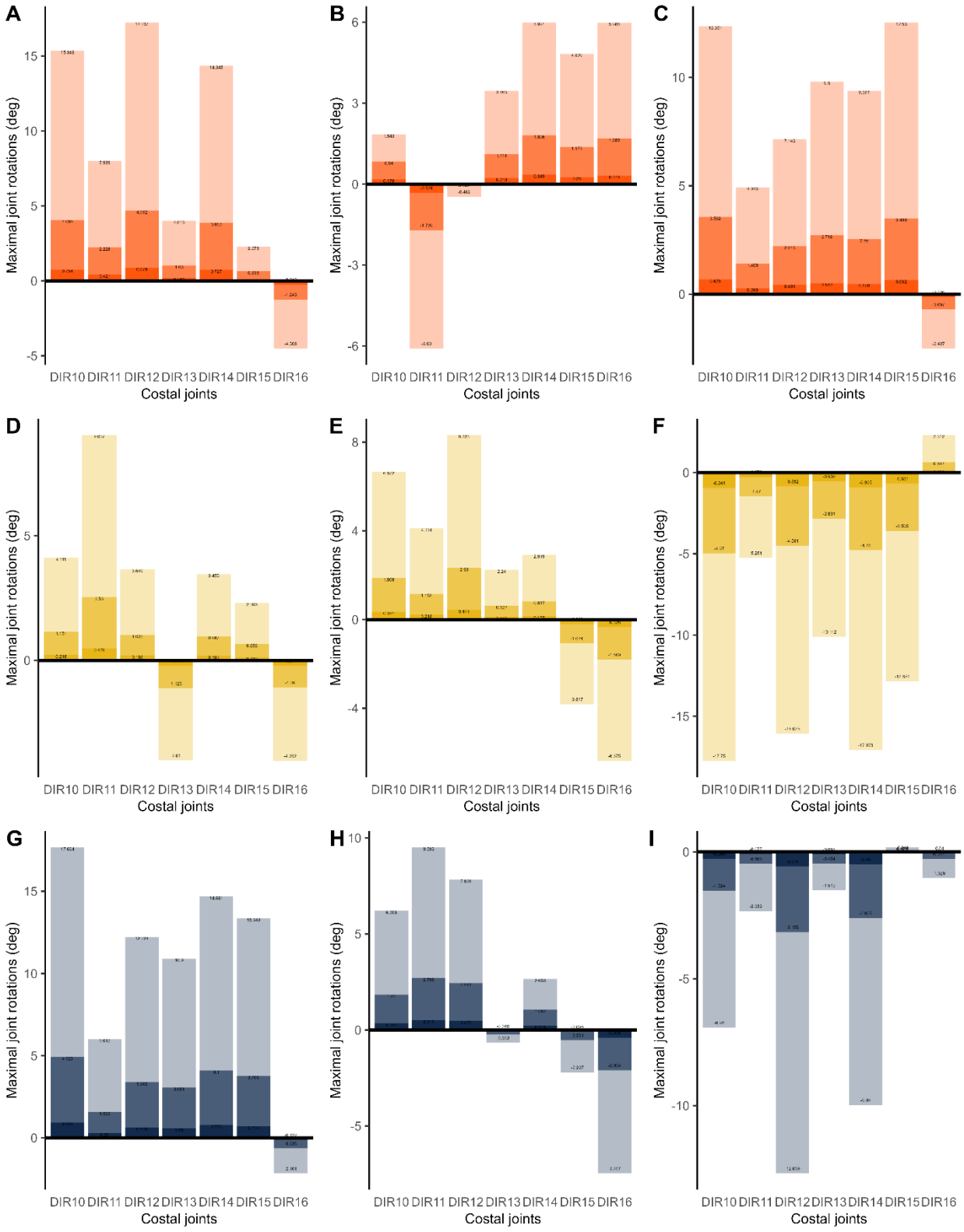
A
B
C
D
E
F
G
H
I
Maximal joint rotations (deg)
DIR10 DIR11 DIR12 DIR13 DIR14 DIR15 DIR16
Costal joints

Figure 7.15. oROM and plausible oROM of dorsal intracostal joints in R version of ventilatory motions in Crocodylian W and Crocodylian WOD models.

Bar graph of oROM and plausible oROM estimated from tidal volume in Palaeognath model. Axial rotations (A), abduction (B), and protraction (C) using AB setup; axial rotation (D), abduction (E), and protraction (F) using AJ setup; and pump-handle motions (G), caliper motions (H), and bucket-handle motions (I) using CBP setup. Orange at high, medium, and low opacity refer to plausible oROM in Crocodylian W model, plausible oROM in Crocodylian WOD model, and oROM using AB setups; Yellow at high, medium, and low opacity refer to Crocodylian W model, plausible oROM in Crocodylian WOD model, and oROM using AJ setup; navy blue at high, medium, and low opacity refer to Crocodylian W model, plausible oROM in Crocodylian WOD model, and oROM using CBP setups.

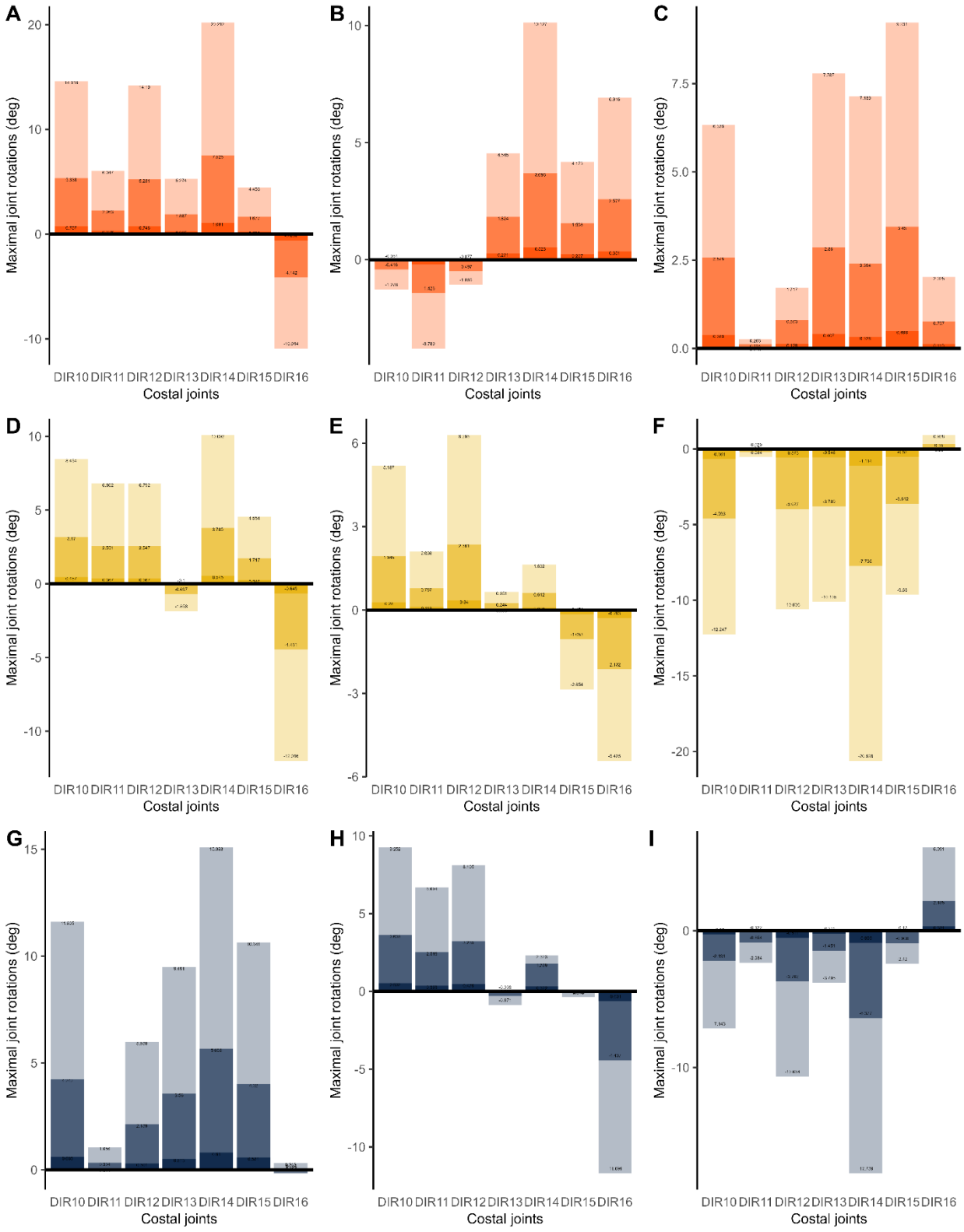
A
B
C
D
E
F
G
H
I
Maximal joint rotations (deg)
DIR10 DIR11 DIR12 DIR13 DIR14 DIR15 DIR16
Costal joints

Figure 7.16. oROM and plausible oROM of ventral intracostal joints in VRS version of ventilatory motions in Crocodylian W and Crocodylian WOD models.

Bar graph of oROM and plausible oROM estimated from tidal volume in Palaeognath model. Axial rotations (A), abduction (B), and protraction (C) using AB setup; axial rotation (D), abduction (E), and protraction (F) using AJ setup; and pump-handle motions (G), caliper motions (H), and bucket-handle motions (I) using CBP setup. Orange at high, medium, and low opacity refer to plausible oROM in Crocodylian W model, plausible oROM in Crocodylian WOD model, and oROM using AB setups; Yellow at high, medium, and low opacity refer to Crocodylian W model, plausible oROM in Crocodylian WOD model, and oROM using AJ setup; navy blue at high, medium, and low opacity refer to Crocodylian W model, plausible oROM in Crocodylian WOD model, and oROM using CBP setups.

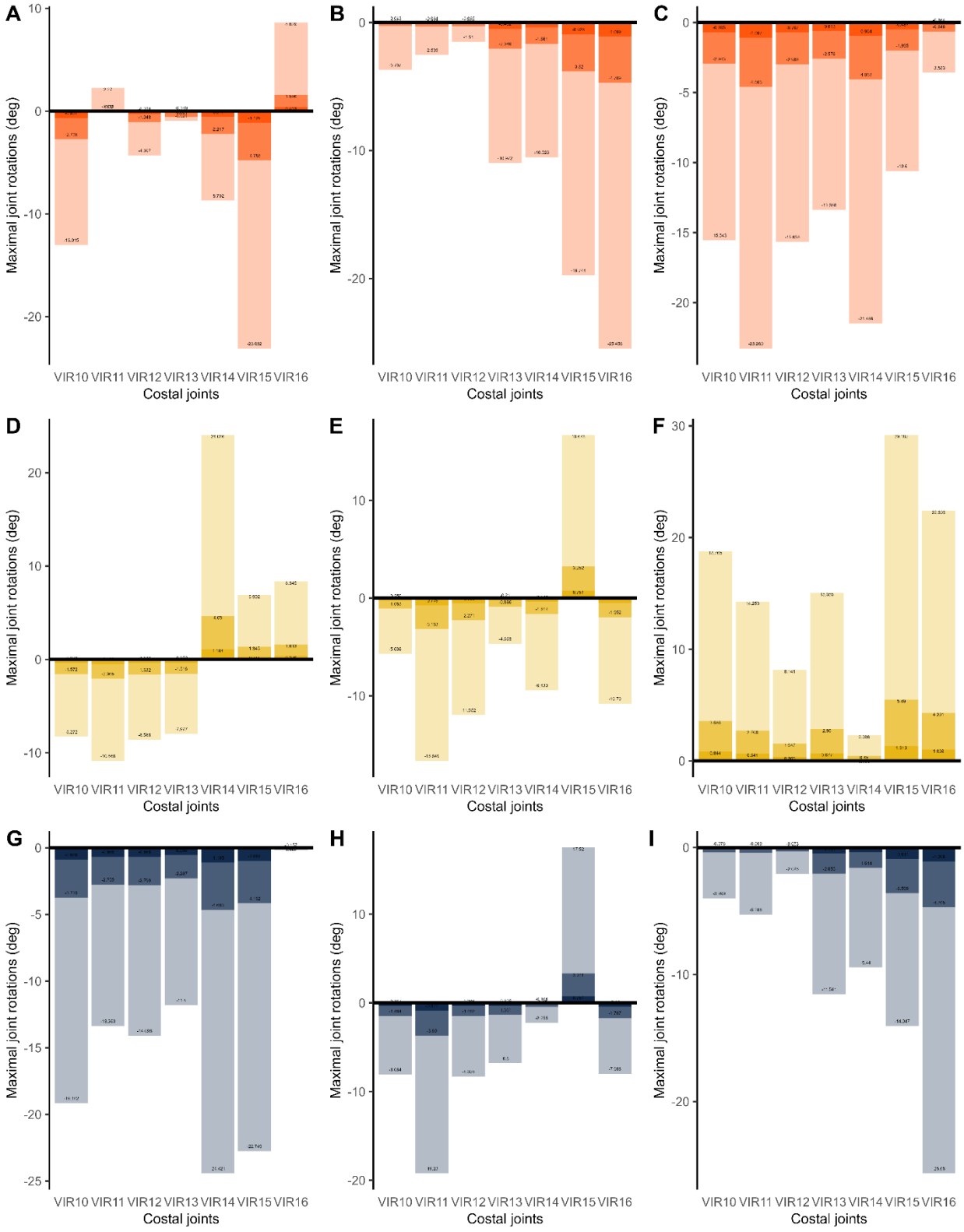
A
B
C
D
E
F
G
H
I
Maximal joint rotations (deg)
VIR10 VIR11 VIR12 VIR13 VIR14 VIR15 VIR16
Costal joints

Figure 7.17. oROM and plausible oROM of ventral intracostal joints in RS version of ventilatory motions in Crocodylian W and Crocodylian WOD models.

Bar graph of oROM and plausible oROM estimated from tidal volume in Palaeognath model. Axial rotations (A), abduction (B), and protraction (C) using AB setup; axial rotation (D), abduction (E), and protraction (F) using AJ setup; and pump-handle motions (G), caliper motions (H), and bucket-handle motions (I) using CBP setup. Orange at high, medium, and low opacity refer to plausible oROM in Crocodylian W model, plausible oROM in Crocodylian WOD model, and oROM using AB setups; Yellow at high, medium, and low opacity refer to Crocodylian W model, plausible oROM in Crocodylian WOD model, and oROM using AJ setup; navy blue at high, medium, and low opacity refer to Crocodylian W model, plausible oROM in Crocodylian WOD model, and oROM using CBP setups.

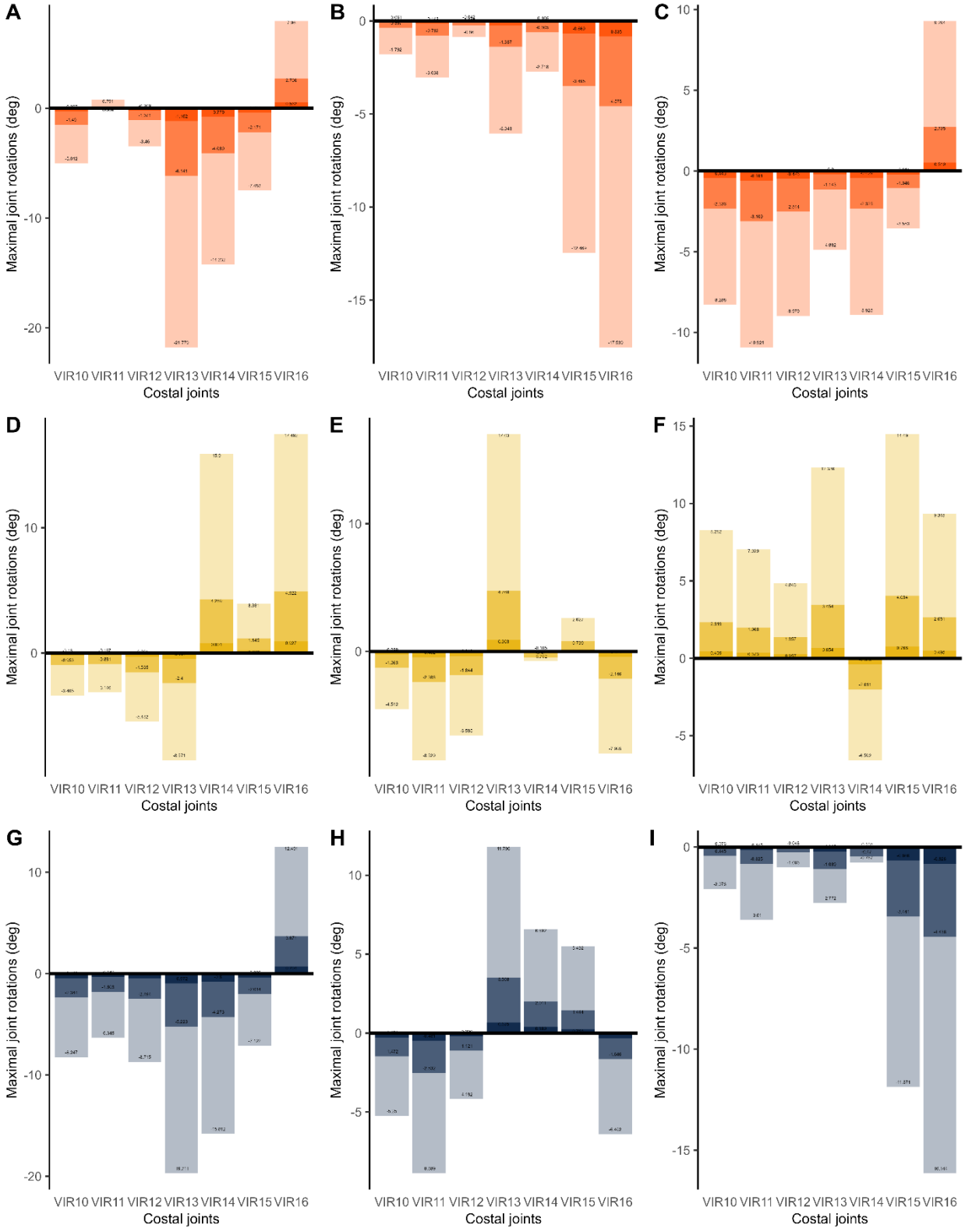
A
B
C
D
E
F
G
H
I
Maximal joint rotations (deg)
VIR10 VIR11 VIR12 VIR13 VIR14 VIR15 VIR16
Costal joints

Figure 7.18. oROM and plausible oROM of ventral intracostal joints in R version of ventilatory motions in Crocodylian W and Crocodylian WOD models.

Bar graph of oROM and plausible oROM estimated from tidal volume in Palaeognath model. Axial rotations (A), abduction (B), and protraction (C) using AB setup; axial rotation (D), abduction (E), and protraction (F) using AJ setup; and pump-handle motions (G), caliper motions (H), and bucket-handle motions (I) using CBP setup. Orange at high, medium, and low opacity refer to plausible oROM in Crocodylian W model, plausible oROM in Crocodylian WOD model, and oROM using AB setups; Yellow at high, medium, and low opacity refer to Crocodylian W model, plausible oROM in Crocodylian WOD model, and oROM using AJ setup; navy blue at high, medium, and low opacity refer to Crocodylian W model, plausible oROM in Crocodylian WOD model, and oROM using CBP setups.

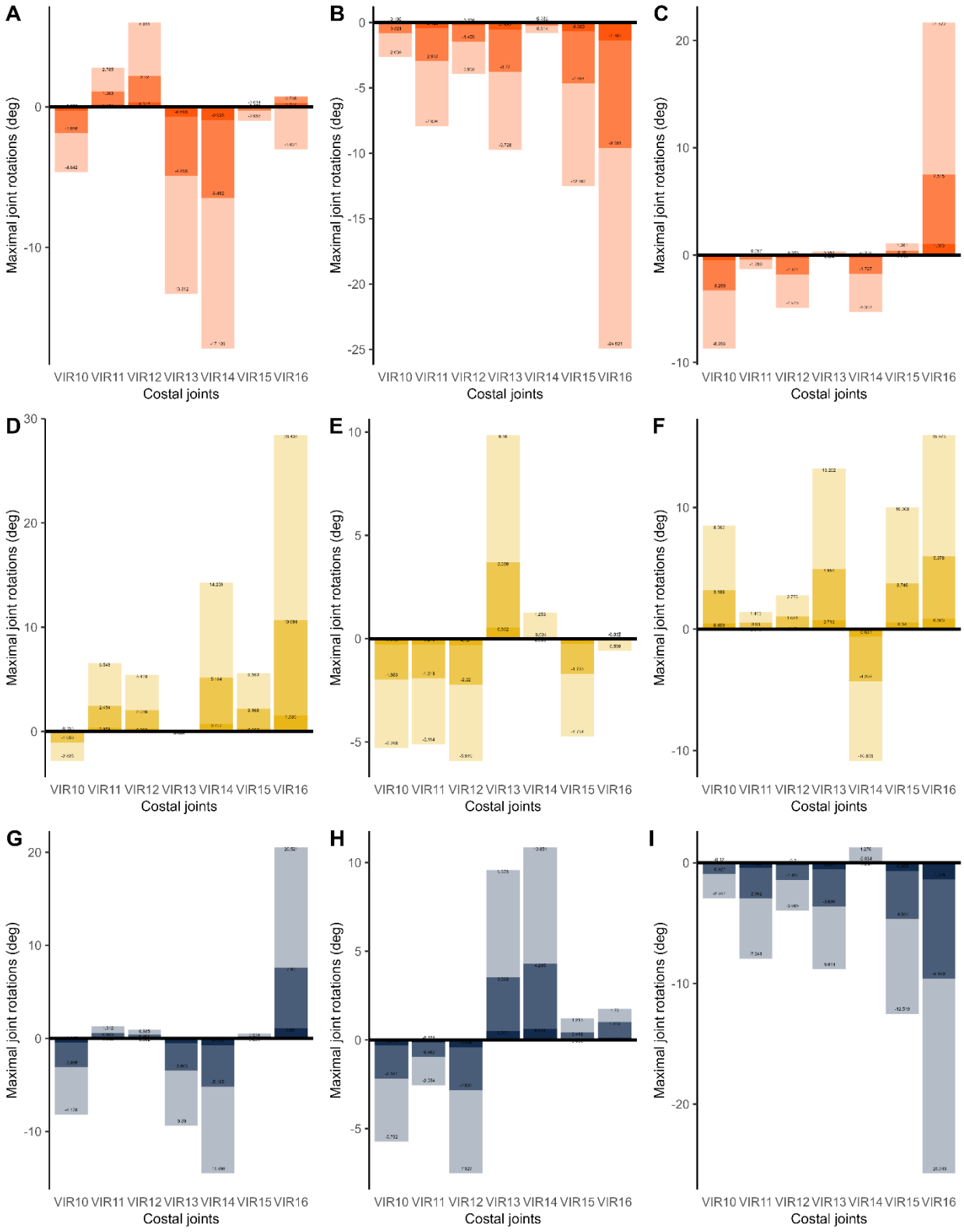
A
B
C
D
E
F
G
H
I
Maximal joint rotations (deg)
VIR10 VIR11 VIR12 VIR13 VIR14 VIR15 VIR16
Costal joints

Figure 7.19. Ventilatory motions plots, oROM, and plausible oROM of R version ventilatory motions at costal joint C23 in Palaeognath model.

Line plot of axial rotation/pump-handle motions based on oROM plotted against percentage of a ventilatory cycle (A); line plot of abduction/caliper motions based on oROM plotted against percentage of a ventilatory cycle (B); line plot of protraction/bucket-handle motions based on oROM plotted against percentage of a ventilatory cycle (C); line plot of axial rotation/pump-handle motions based on plausible oROM plotted against percentage of a ventilatory cycle (D); line plot of abduction/caliper motions based on plausible oROM plotted against percentage of a ventilatory cycle (E); line plot of protraction/bucket-handle motions based on plausible oROM plotted against percentage of a ventilatory cycle (F); bar graph of oROM and plausible oROM representing axial rotation/pump-handle motions at C23 (G); bar graph of oROM and plausible oROM representing abduction/caliper motions at C23 (H); bar graph of oROM and plausible oROM representing protraction/bucket-handle motions at C23 (I). solid lines represent motions described as linear angular motions, and dotted dash lines represent motions described with an assumed angular accelerations. Orange at high and low opacity represents plausible oROM and oROM using AB setup; yellow at high and low opacity represents plausible oROM and oROM using AJ setup; navy blue at high and low opacity represents plausible oROM and oROM using CBP setup. Abbreviations: AB, anatomical bone; AJ, anatomical joint; CBP, caliper, bucket-handle, pump-handle; JCS, joint coordinate system.

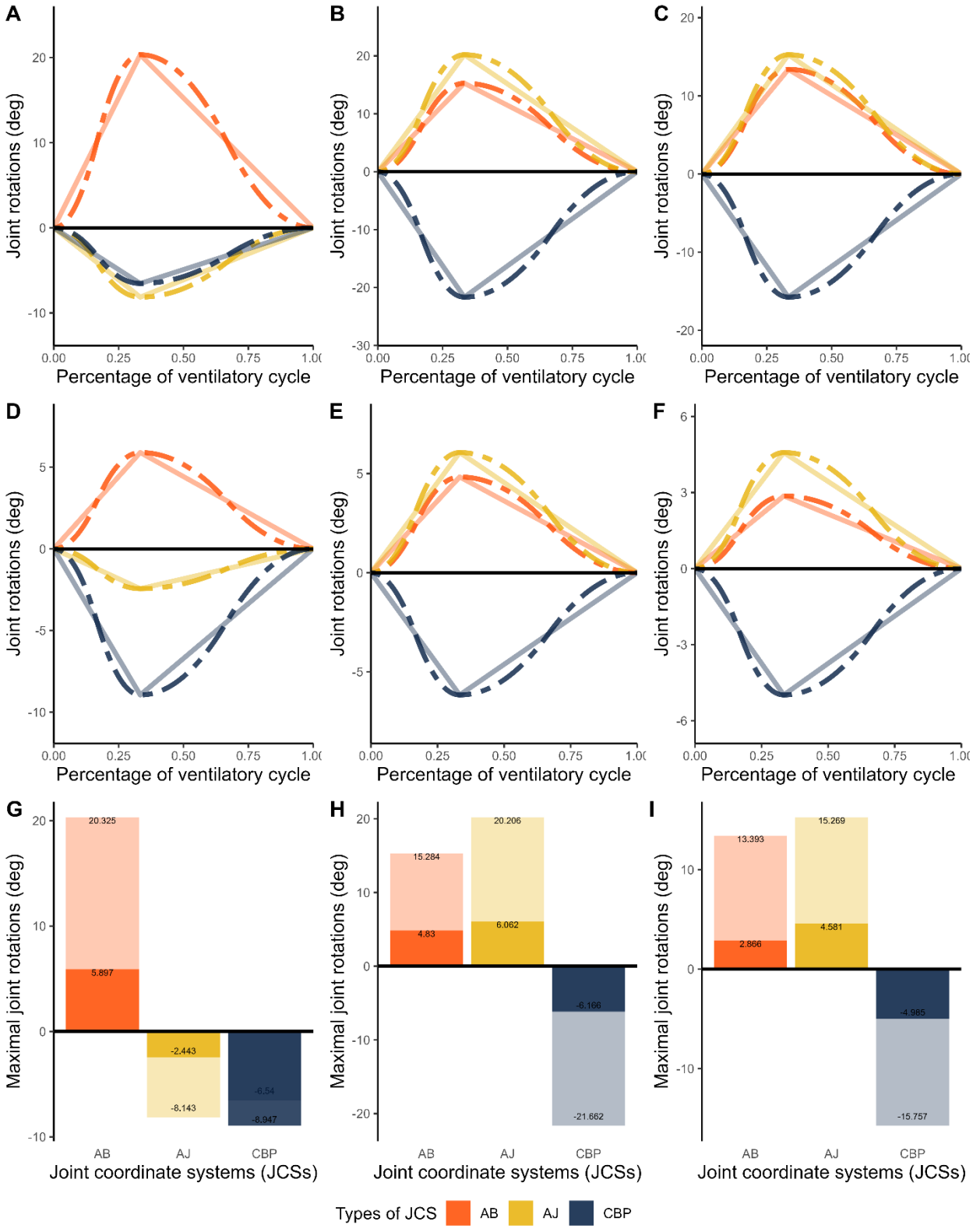
A
B
C
D
E
F
G
H
I
Joint rotations (deg)
Percentage of ventilatory cycle
Maximal joint rotations (deg)
Joint coordinate systems (JCSs)
AB
AJ
CBP
20.325
5.897
-2.443
-8.143
-6.54
-8.947
15.284
4.83
20.206
6.062
-6.166
-21.662
13.393
2.866
15.269
4.581
-4.985
-15.757
Types of JCS

Figure 7.20. Ventilatory motions plots, oROM, and plausible oROM of VRS version ventilatory motions at costal joint C11 in Crocodylian W and Crocodylian WOD model.

Line plot of axial rotation/pump-handle motions based on oROM plotted against percentage of a ventilatory cycle (A); line plot of abduction/caliper motions based on oROM plotted against percentage of a ventilatory cycle (B); line plot of protraction/bucket-handle motions based on oROM plotted against percentage of a ventilatory cycle (C); line plot of axial rotation/pump-handle motions based on plausible oROM plotted against percentage of a ventilatory cycle (D); line plot of abduction/caliper motions based on plausible oROM plotted against percentage of a ventilatory cycle (E); line plot of protraction/bucket-handle motions based on plausible oROM plotted against percentage of a ventilatory cycle (F); bar graph of oROM and plausible oROM representing axial rotation/pump-handle motions at C23 (G); bar graph of oROM and plausible oROM representing abduction/caliper motions at C23 (H); bar graph of oROM and plausible oROM representing protraction/bucket-handle motions at C23 (I). solid lines represent motions described as linear angular motions, and dotted dash lines represent motions described with an assumed angular acceleration. Orange at high, medium, and low opacity refer to plausible oROM in Crocodylian W model, plausible oROM in Crocodylian WOD model, and oROM using AB setups; Yellow at high, medium, and low opacity refer to Crocodylian W model, plausible oROM in Crocodylian WOD model, and oROM using AJ setup; navy blue at high, medium, and low opacity refer to Crocodylian W model, plausible oROM in Crocodylian WOD model, and oROM using CBP setups. Abbreviations: AB, anatomical bone; AJ, anatomical joint; CBP, caliper, bucket-handle, pump-handle; JCS, joint coordinate system.

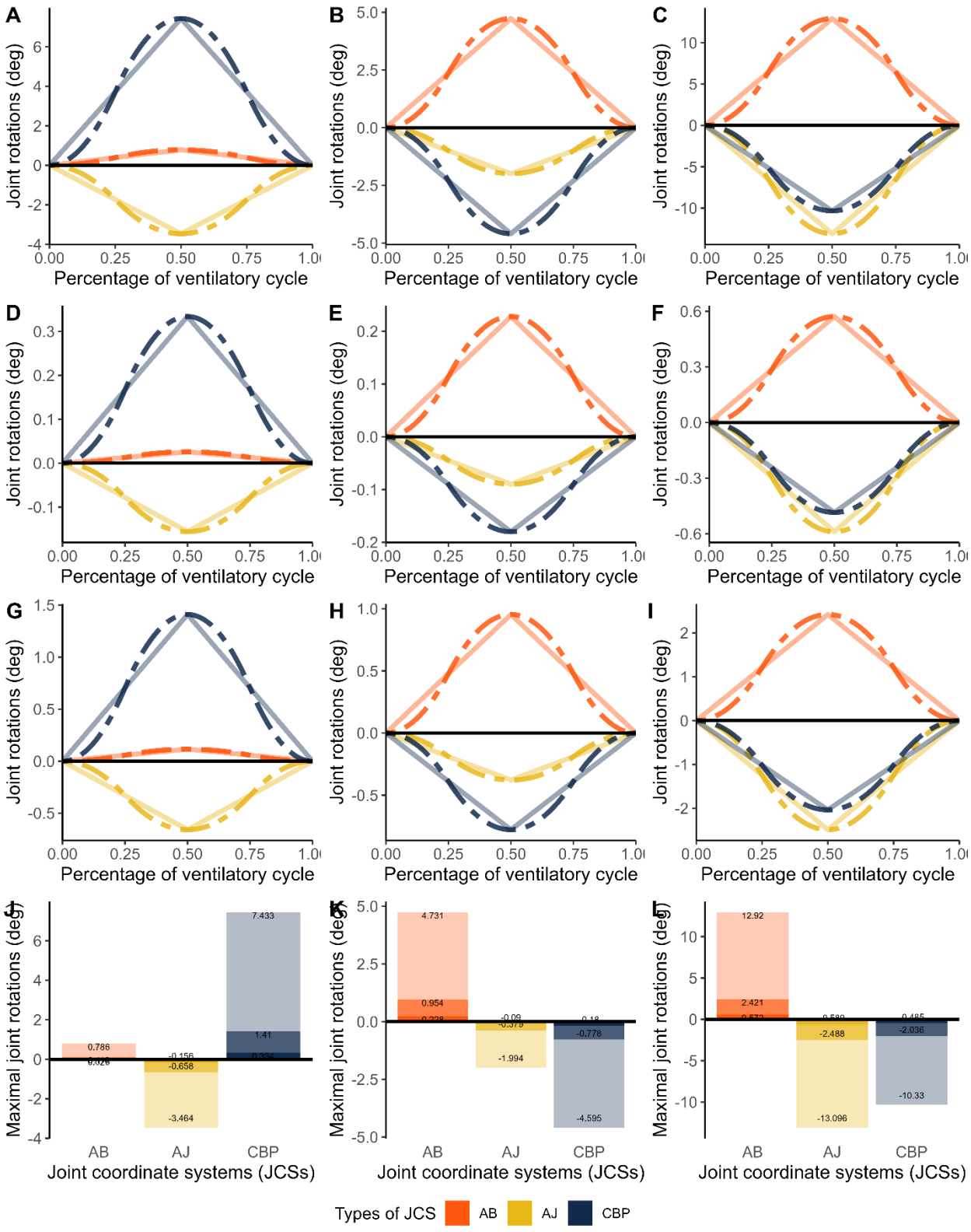
A
B
C
D
E
F
G
H
I
J
K
L
Joint rotations (deg)
Percentage of ventilatory cycle
Maximal joint rotations (deg)
Joint coordinate systems (JCSs)
AB
AJ
CBP
0.786
-0.156
-0.658
-3.464
7.433
1.41
4.731
0.954
-0.09
-1.994
-0.778
-4.595
12.92
2.421
-2.488
-13.096
-2.036
-10.33
Types of JCS

7.5 Literature Cited

Baier, D.B. and Gatesy, S.M. 2013. Three-dimensional skeletal kinematics of the shoulder girdle and forelimb in walking *Alligator*. *Journal of Anatomy* 223(5), pp. 462–473. doi: 10.1111/joa.12102.

Baumel, J.J., King, A.S., Breazile, J.E., Evans, H.E. and Vanden Berge, J.C. 1993. *Handbook of avian anatomy: Nomina anatomica avium*. second edition. Cambridge: Nuttall Ornithological Club.

Baumel, J.J., Wilson, J.A. and Bergren, D.R. 1990. The ventilatory movements of the avian pelvis and tail: function of the muscles of the tail region of the pigeon (*Columba livia*). *Journal of Experimental Biology* 151, pp. 263–277.

Benton, M.J. 2014. *Vertebrate Palaeontology*. John Wiley & Sons.

Berger, M., Hart, J.S. and Roy, O.Z. 1970a. Respiration, oxygen consumption and heart rate in some birds during rest and flight. *Zeitschrift für vergleichende Physiologie* 66(2), pp. 201–214. doi: 10.1007/BF00297779.

Berger, M., Roy, O.Z. and Hart, J.S. 1970b. The co-ordination between respiration and wing beats in birds. *Zeitschrift für vergleichende Physiologie* 66(2), pp. 190–200. doi: 10.1007/BF00297778.

Bishop, P.J., Brocklehurst, R.J. and Pierce, S.E. 2023. Intelligent sampling of high-dimensional joint mobility space for analysis of articular function. *Methods in Ecology and Evolution* 14(2), pp. 569–582. doi: 10.1111/2041-210X.14016.

Boggs, D.F. 1997. Coordinated control of respiratory pattern during locomotion in birds. *American Zoologist* 37(1), pp. 41–53. doi: 10.1093/icb/37.1.41.

Boggs, D.F., Jenkins, F.A. and Dial, K.P. 1997a. The effects of the wingbeat cycle on respiration in black-billed magpies (pica pica). *The Journal of Experimental Biology* 200, pp. 1403–1412.

Boggs, D.F., Seveyka, J.J., Kilgore, D.L. and Dial, K.P. 1997b. Coordination of Respiratory Cycles with Wingbeat Cycles in the Black-Billed Magpie (*Pica pica*). *The Journal of Experimental Biology* 200, pp. 1413–1420.

Boyd, C.A., Cleland, T.P. and Novas, F. 2011. Osteogenesis, homology, and function of the intercostal plates in ornithischian dinosaurs (Tetrapoda, Sauropsida). *Zoomorphology* 130(4), pp. 305–313. doi: 10.1007/s00435-011-0136-x.

Brackenbury, J.H., Gleeson, M. and Avery, P. 1982. Respiration in exercising fowl. III. ventilation. *Journal of Experimental Biology* 96(1), pp. 315–324. doi: 10.1242/jeb.96.1.315.

Brainerd, E.L., Baier, D.B., Gatesy, S.M., Hedrick, T.L., Metzger, K.A., Gilbert, S.L. and Crisco, J.J. 2010. X-ray reconstruction of moving morphology (XROMM): precision, accuracy and applications in comparative biomechanics research. *Journal of Experimental Zoology Part A: Ecological Genetics and Physiology* 9999A, p. n/a-n/a. doi: 10.1002/jez.589.

Brainerd, E.L., Moritz, S. and Ritter, D.A. 2015. XROMM analysis of rib kinematics during lung ventilation in the green iguana, *Iguana iguana*. *Journal of Experimental Biology* 219, p. jeb.127928. doi: 10.1242/jeb.127928.

Brainerd, E.L. and Owerkowicz, T. 2006. Functional morphology and evolution of aspiration breathing in tetrapods. *Respiratory Physiology & Neurobiology* 154(1–2), pp. 73–88. doi: 10.1016/j.resp.2006.06.003.

Bramwell, C.D., Whitfield, G.R. and Parrington, F.R. 1997. Biomechanics of *Pteranodon*. *Philosophical Transactions of the Royal Society of London. B, Biological Sciences* 267(890), pp. 503–581. doi: 10.1098/rstb.1974.0007.

Brocklehurst, R.J., Moritz, S., Codd, J., Sellers, W.I. and Brainerd, E.L. 2017. Rib kinematics during lung ventilation in the American alligator (*Alligator mississippiensis*): an XROMM analysis. *Journal of Experimental Biology* 220(17), pp. 3181–3190. doi: 10.1242/jeb.156166.

Brocklehurst, R.J., Moritz, S., Codd, J., Sellers, W.I. and Brainerd, E.L. 2019. XROMM kinematics of ventilation in wild turkeys (*Meleagris gallopavo*). *Journal of Experimental Biology* 222(23), p. jeb209783. doi: 10.1242/jeb.209783.

Brocklehurst, R.J., Schachner, E.R. and Sellers, W.I. 2018. Vertebral morphometrics and lung structure in non-avian dinosaurs. *Royal Society Open Science* 5(10), p. 180983. doi: 10.1098/rsos.180983.

Brusatte, S.L., Nesbitt, S.J., Irmis, R.B., Butler, R.J., Benton, M.J. and Norell, M.A. 2010. The origin and early radiation of dinosaurs. *Earth-Science Reviews* 101(1–2), pp. 68–100. doi: 10.1016/j.earscirev.2010.04.001.

Carrier, D.R. and Farmer, C.G. 2000a. The evolution of pelvic aspiration in archosaurs. *Paleobiology* 26(2), pp. 271–293. doi: 10.1666/0094-8373(2000)026<0271:TEOPAI>2.0.CO;2.

Carrier, D.R. and Farmer, C.G. 2000b. The integration of ventilation and locomotion in archosaurs. *American Zoologist* 40, pp. 87–100.

Claessens, K.P. 2015. Anatomical transformations and respiratory innovations of the archosaur trunk. In: *Great Transformations in Vertebrate Evolution*. University of Chicago Press. doi: 10.7208/chicago/9780226268392.001.0001.

Claessens, L.P.A.M. 2009a. A cineradiographic study of lung ventilation in *Alligator mississippiensis*. *Journal of Experimental Zoology Part A: Ecological Genetics and Physiology* 311A(8), pp. 563–585. doi: 10.1002/jez.530.

Claessens, L.P.A.M. 2009b. The skeletal kinematics of lung ventilation in three basal bird taxa (emu, tinamou, and guinea fowl). *Journal of Experimental Zoology Part A: Ecological Genetics and Physiology* 311A(8), pp. 586–599. doi: 10.1002/jez.501.

Claessens, L.P.A.M. and Vickaryous, M.K. 2012. The evolution, development and skeletal identity of the crocodylian pelvis: Revisiting a forgotten scientific debate. *Journal of Morphology* 273(10), pp. 1185–1198. doi: 10.1002/jmor.20059.

Codd, J.R. 2010. Uncinate processes in birds: Morphology, physiology and function. *Comparative biochemistry and physiology part a: molecular & integrative physiology* 156(3), pp. 303–308. doi: 10.1016/j.cbpa.2009.12.005.

Codd, J.R., Boggs, D.F., Perry, S.F. and Carrier, D.R. 2005. Activity of three muscles associated with the uncinate processes of the giant Canada goose *Branta canadensis maximus*. *Journal of Experimental Biology* 208(5), pp. 849–857. doi: 10.1242/jeb.01489.

Codd, J.R., Manning, P.L., Norell, M.A. and Perry, S.F. 2008. Avian-like breathing mechanics in maniraptoran dinosaurs. *Proceedings of the Royal Society B: Biological Sciences* 275(1631), pp. 157–161. doi: 10.1098/rspb.2007.1233.

Codd, J.R., Rose, K.A.R., Tickle, P.G., Sellers, W.I., Brocklehurst, R.J., Elsey, R.M. and Crossley, D.A. 2019. A novel accessory respiratory muscle in the American alligator (*Alligator mississippiensis*). *Biology Letters* 15(7), p. 20190354. doi: 10.1098/rsbl.2019.0354.

Cohn, J.E. and Shannon, R. 1968. Respiration in unanathesitized geese. *Respiration Physiology* 5, pp. 259–268.

Cong, L.Y., Hou, L.H. and Wu, X.C. 1988. *The Gross anatomy of Alligator sinensis Fauvel: Integument, Osteology, and Myology (In Chinese with English summary)*. Beijing, China: China Science Publishing & Media Ltd.

Currie, P.J., Holmes, R.B., Ryan, M.J. and Coy, C. 2016. A juvenile chasmosaurine ceratopsid (Dinosauria, Ornithischia) from the Dinosaur Park Formation, Alberta, Canada. *Journal of Vertebrate Paleontology* 36(2), p. e1048348. doi: 10.1080/02724634.2015.1048348.

Demuth, O.E., Rayfield, E.J. and Hutchinson, J.R. 2020. 3D hindlimb joint mobility of the stem-archosaur Euparkeria capensis with implications for postural evolution within Archosauria. *Scientific Reports* 10(1), p. 15357. doi: 10.1038/s41598-020-70175-y.

Duncker, H.-R. 1972. Structure of avian lungs. *Respiration Physiology* 14(1), pp. 44–63. doi: 10.1016/0034-5687(72)90016-3.

Farmer, C.G. 2017. Pulmonary Transformations of Vertebrates. In: *The Biology of the Avian Respiratory System*. Cham: Springer International Publishing, pp. 99–112. doi: 10.1007/978-3-319-44153-5_3.

Farmer, C.G. and Carrier, D.R. 2000a. Pelvic aspiration in alligators. *The Journal of Experimental Biology* 203, pp. 1679–1687.

Farmer, C.G. and Carrier, D.R. 2000b. Respiration and gas exchange during recovery from exercise in the American alligator. *Respiration Physiology* 120(1), pp. 81–87. doi: 10.1016/S0034-5687(00)00098-0.

Farmer, C.G. and Sanders, K. 2010. Unidirectional airflow in the lungs of alligators. *Science* 327(5963), pp. 338–340. doi: 10.1126/science.1180219.

Frey, T. von E. 1988. Anatomie des Körperstammes von *Alligator mississippiensis* Daudin. *Stuttgarter Beitraege zur Naturkunde, Serie A* 424, pp. 1–106.

Funk, G.D., Sholomenko, G.N., Valenzuela, I.J., Steeves, J.D. and Milsom, W.K. 1993. Coordination of wing beat and respiration in Canada geese during free flight. *Journal of Experimental Biology* 175, pp. 317–323.

Gans, C. and Clark 1976. Studies on ventilation of *Caiman crocodilus* (Crocodylia: Reptilia). *Respiration Physiology* 26, p. 1.

Gatesy, S.M., Baier, D.B., Jenkins, F.A. and Dial, K.P. 2010. Scientific rotoscoping: a morphology-based method of 3-D motion analysis and visualization. *Journal of Experimental Zoology Part A: Ecological Genetics and Physiology* 9999A, p. n/a-n/a. doi: 10.1002/jez.588.

Gatesy, S.M., Bäker, M. and Hutchinson, J.R. 2009. Constraint-based exclusion of limb poses for reconstructing theropod dinosaur locomotion. *Journal of Vertebrate Paleontology* 29(2), pp. 535–544. doi: 10.1671/039.029.0213.

George, J.C. and Berger, A.J. 1966. *Avian myology*. New York and London: Academic Press.

Griffin, B., Martin-Silverstone, E., Demuth, O., Pêgas, R., Palmer, C. and Rayfield, E. 2022. Constraining pterosaur launch: range of motion in the pectoral and pelvic girdles of a medium-sized ornithocheiraean pterosaur. *Biological Journal of the Linnean Society* 137(2), pp. 250–266. doi: 10.1093/biolinnean/blac063.

Herbst, E.C., Eberhard, E.A., Richards, C.T. and Hutchinson, J.R. 2022. *In vivo* and *ex vivo* range of motion in the fire salamander *Salamandra salamandra*. *Journal of Anatomy* 241(4), pp. 1066–1082. doi: 10.1111/joa.13738.

Hutson, J.D. and Hutson, K.N. 2012. Using the American alligator and a repeated-measures design to place constraints on *in vivo* shoulder joint range of motion in dinosaurs and other fossil archosaurs. *Journal of Experimental Biology* , p. jeb.074229. doi: 10.1242/jeb.074229.

Jones, K.E., Brocklehurst, R.J. and Pierce, S.E. 2021. AutoBend: an automated approach for estimating intervertebral joint function from bone-only digital models. *Integrative Organismal Biology* 3(1), p. obab026. doi: 10.1093/iob/obab026.

Kadono, H., Okada, T. and Ono, K. 1963. Electromyographic studies on the respiratory muscles of the chicken. *Poultry Science* 42(1), pp. 121–128. doi: 10.3382/ps.0420121.

Kambic, R.E., Biewener, A.A. and Pierce, S.E. 2017. Experimental determination of three-dimensional cervical joint mobility in the avian neck. *Frontiers in Zoology* 14(1), p. 37. doi: 10.1186/s12983-017-0223-z.

Kambic, R.E., Roberts, T.J. and Gatesy, S.M. 2014. Long-axis rotation: a missing degree of freedom in avian bipedal locomotion. *Journal of Experimental Biology* , p. jeb.101428. doi: 10.1242/jeb.101428.

Kiley, J.P., Kuhlmann, W.D. and Fedde, M.R. 1982. Ventilatory and blood gas adjustments in exercising isothermic ducks. *Journal of comparative physiology* 147(1), pp. 107–112. doi: 10.1007/BF00689298.

Levin, S., de Solórzano, S.L. and Scarr, G. 2017. The significance of closed kinematic chains to biological movement and dynamic stability. *Journal of Bodywork and Movement Therapies* 21(3), pp. 664–672. doi: 10.1016/j.jbmt.2017.03.012.

Levin, S.M. 2013. Closed kinematic chain mechanisms comprise the fundamental mechanics of biologic movement and stability.

Lord, R.D., Bellrose, F.C. and Cochran, W.W. 1962. Radiotelemetry of the Respiration of a Flying Duck. *Science* 137(3523), pp. 39–40. doi: 10.1126/science.137.3523.39.

Maina, J.N. 2002. *Functional Morphology of the Vertebrate Respiratory Systems*. Science Publishers.

Maina, J.N. 2007. Spectacularly robust! Tensegrity principle explains the mechanical strength of the avian lung. *Respiratory Physiology & Neurobiology* 155(1), pp. 1–10. doi: 10.1016/j.resp.2006.05.005.

Maina, J.N., Singh, P. and Moss, E.A. 2009. Inspiratory aerodynamic valving occurs in the ostrich, Struthio camelus lung: A computational fluid dynamics study under resting unsteady

state inhalation. *Respiratory Physiology & Neurobiology* 169(3), pp. 262–270. doi: 10.1016/j.resp.2009.09.011.

Manafzadeh, A.R. 2020. A practical guide to measuring ex vivo joint mobility using XROMM. *Integrative Organismal Biology* 2(1), p. obaa041. doi: 10.1093/iob/obaa041.

Manafzadeh, A.R. and Padian, K. 2018. ROM mapping of ligamentous constraints on avian hip mobility: Implications for extinct ornithodirans. *Proceedings of the Royal Society B: Biological Sciences* 285(1879), p. 20180727. doi: 10.1098/rspb.2018.0727.

Munns, S.L., Owerkowicz, T., Andrewartha, S.J. and Frappell, P.B. 2012. The accessory role of the diaphragmaticus muscle in lung ventilation in the estuarine crocodile *Crocodylus porosus*. *Journal of Experimental Biology* 215(5), pp. 845–852. doi: 10.1242/jeb.061952.

Nesbitt, S.J. 2011. The early evolution of archosaurs: relationships and the origin of major clades. *Bulletin of the American Museum of Natural History* 352, pp. 1–292. doi: 10.1206/352.1.

Neumann, D.A. 2017. *Kinesiology of the musculoskeletal system-e-book: foundations for rehabilitation*. third. Elsevier Health Sciences.

Perry, S.F. 1988. Functional morphology of the lungs of the nile crocodile, *Crocodylus niloticus:* non-respiratory parameters. *Journal of Experimental Biology* 134(1), pp. 99–117. doi: 10.1242/jeb.134.1.99.

Perry, S.F., Lambertz, M. and Schmitz, A. 2019. Respiratory faculties of amphibious and terrestrial craniotes. In: *Respiratory Biology of Animals: evolutionary and functional morphology*. Oxford University Press, pp. 139–163.

Powell, F.L. 2015. Respiration. In: *Sturkie's Avian Physiology*. Elsevier, pp. 301–336. doi: 10.1016/B978-0-12-407160-5.00013-0.

RStudio Team 2020. RStudio: Integrated Development for R.

Schachner, E.R., Lyson, T.R. and Dodson, P. 2009. Evolution of the respiratory system in nonavian theropods: evidence from rib and vertebral morphology. *The Anatomical Record: Advances in Integrative Anatomy and Evolutionary Biology* 292(9), pp. 1501–1513. doi: 10.1002/ar.20989.

Scheid, P. and Piiper, J. 1969. Volume, ventilation and compliance of the respiratory system in the domestic fowl. *Respiration Physiology* 6(3), pp. 298–308. doi: 10.1016/0034-5687(69)90029-2.

Schmidt-Nielsen, K., Kanwisher, J., Lasiewski, R.C., Cohn, J.E. and Bretz, W.L. 1969. Temperature regulation and respiration in the ostrich. *The Condor* 71(4), pp. 341–352. doi: 10.2307/1365733.

Schneider, C.A., Rasband, W.S. and Eliceiri, K.W. 2012. NIH Image to ImageJ: 25 years of image analysis. *Nature Methods* 9(7), pp. 671–675. doi: 10.1038/nmeth.2089.

Senter, P. and Robins, J.H. 2005. Range of motion in the forelimb of the theropod dinosaur Acrocanthosaurus atokensis, and implications for predatory behaviour. *Journal of Zoology* 266(3), pp. 307–318. doi: 10.1017/S0952836905006989.

Sullivan, C. 2007. *Function and evolution of the hind limb in Triassic archosaurian reptiles*. PhD Dissertation, Harvard University.

Tickle, P.G., Ennos, A.R., Lennox, L.E., Perry, S.F. and Codd, J.R. 2007. Functional significance of the uncinate processes in birds. *Journal of Experimental Biology* 210(22), pp. 3955–3961. doi: 10.1242/jeb.008953.

Tsai, H.P., Turner, M.L., Manafzadeh, A.R. and Gatesy, S.M. 2020. Contrast-enhanced XROMM reveals in vivo soft tissue interactions in the hip of Alligator mississippiensis. *Journal of Anatomy* 236(2), pp. 288–304. doi: 10.1111/joa.13101.

Witmer, L.M. 1995. The extant phylogenetic bracket and the importance of reconstructing soft tissues in fossils. *Functional morphology in vertebrate paleontology* 1, pp. 19–33.

Xu, X. et al. 2015. The taxonomic status of the Late Cretaceous dromaeosaurid *Linheraptor exquisitus* and its implications for dromaeosaurid systematics. *Vertebrata PalAsiatica* 53, pp. 29–62.

York, J.M. et al. 2017. Respiratory mechanics of eleven avian species resident at high and low altitude. *Journal of Experimental Biology* 220(6), pp. 1079–1089. doi: 10.1242/jeb.151191.

Zimmer, K. 1935. Beiträge zur Mechanik der Atmung bei den Vögeln in Stand-und Flug. *Zoologica* 33, pp. 1–69.

7.6 Supplementary Information

7.6.1 Detailed description of the procedure used to construct kinematic models in this study

In this section, individual presacral and presacral ribs is referred by the sequential number of the respective regions (i.e. P#, C#, D#, PR#, IR#, SR#) where necessary.

Sampling for digitalisation — For the palaeognath model, 20 elements were sampled from *Struthio camelus* (UAMZ 7159), including seven vertebrae from P19 to P25, left PR19 to PR25, five left SR21 to SR25, and the sternum. For both crocodylian with m. diaphragmaticus (crocodylian W) and crocodylian without m. diaphragmaticus (crocodylian WOD), 33 elements were sampled from *Caiman crocodilus* (UAMZ unnumbered), including 12 vertebrae from P8 to P19, left PR9 to PR18, left IR10 to IR16, and left SR10 to SR15.

Meshing — the sampled elements were scanned over several sessions using a light reflected scanner (Polyga Carbon series) controlled by the program FlexScan 3D housed in the Sullivan Lab at the University of Alberta. Scanner was calibrated using 10mm calibration board, and the spatial coverage of each scanning sessions was at least 85%. For clean up in FlexScan 3D, erosion of the edges of holes were performed once or twice followed by one to two iterations of smoothing for each scanned bone.

Some areas of the sampled bones were not completely captured by the scanner: (1) internal surfaces of the neural canals of all sampled vertebrae, as they are underexposed and filtered out by the scanner; (2) anterior and posterior rugose surface of the neural spines near their proximal ends in *Su. camelus* (UAMZ 7159), as the rugose textures created many noisy polygons when captured by the scanner; (3) distal articular facet of PR13 and PR18, articular facet of capitulum of PR15, and articular facet of tuberculum of PR14 in *Cai. crocodilus* (UAMZ unnumbered), as remnants of soft tissues were present at the time of scanning; (4) proximal end of IR11 as it was damaged during dissection performed in Chapter 6.

Meshes of ribcages were exported from FlexScan 3D as .obj files, and were refined in ZBrush 2018. For each mesh, the .obj file was imported in ZBrush as tool, Dyna mesh was

performed once to fill holes with blur set to zero, resolution of mesh set to 1024. The mesh was decimated using decimation master in ZBrush, the levels of decimation were set differently for individual mesh, such that the key morphological features such as outline of the articular facets were preserved. Masking key area before decimation can limit the amount of anatomical features lost in the process of decimation. However, the unmasked portion would lose more anatomical features, and masking was therefore not used in this study. With target polygon count set to 100, ZRemesher was then used to change the mesh from being composed of triangular geometry to evenly distributed quadrangulate geometry. Of the sampled meshes, Dyna mesh and ZRemesher were used twice for PR10 of *Cai. crocodilus* (UAMZ unnumbered), to fill all holes. Then, meshes were exported as .obj files.

As left SR16, the cartilaginous uncinate processes and the sternum in *Cai. crocodilus* (UAMZ unnumbered) were not preserved, a simple rod was created using geometric primitive in Maya to represent SR16; five compressed cubes were created from using primitive geometric in Maya to represent the cartilaginous uncinate processes; a low poly mesh was created using reference images of crocodylian sternum from the literature to represent the cartilaginous sternum (Cong et al. 1988; Baier and Gatesy 2013). The scales of these interpreted meshes were adjusted such that they approximate the approximate size of the sternum in *Cai. crocodilus* (UAMZ unnumberd).

Three scenes were created in Autodesk Maya 2022 with working unit set to metre for palaeognath, crocodylian W, crocodylian WOD kinematic models, and ribcage meshes were imported as bone meshes (Bmesh) for digital articulation.

Digital articulation — For all kinematic models, Bmesh of the last cervical vertebra (P19 and P8) was positioning such that the cranial side of the vertebra was aligned with the Z-axis of the world, and the dorsal side of the vertebra was aligned with the Y-axis of the world. The remaining vertebra, rib segments, and sternum were positioned such that the ribcage represent maximal expiration. Using operations such as centre pivots and freeze transformation may facilitate the process of digital articulation. A maximal gap of 1 cm was allowed between articular facets of Bmesh, which were estimated using the distance tool in Maya (Bonus tool add-

on in Maya can perform similar functions). Variations are likely present between trials of using distance tool, as placement of the locators could not guaranteed to be the same. All Bmeshes of the left side were mirrored to the right side. After all Bmeshes were digitally articulated, free transformation was performed to set the translation and rotation values at zero. History of each mesh was deleted to avoid complications in Bmesh attribute.

Creating thoracic volume and m. diaphragmaticus — A incline plane was created from geometric primitive in Maya to represent m. diaphragmaticus (Dmesh), which was then scaled and placed at the position representing maximal expiration according to anatomical landmarks from the literature (Claessens 2009a).

Landmarks were placed on the ventral aspects of the vertebrae, medial aspects of the left rib segments, and dorsal aspects of the sternum. A low poly mesh was then created based on the landmarks using create polygon tool. Vertices of the low poly mesh were moved manually to limit the amount of overlapping with Bmeshes of the ribcage. The low poly mesh was then mirrored into a closed mesh, which was then duplicated and scaled to 95% to 96% of its size called lung mesh (Lmesh). Lmesh was then remeshed and retopoligised in Maya, such that deformations of the Lmesh appear natural. The exact threshold for remesh and retopology are subjected to hardware of computers, and a clear threshold at which optimal results may be obtained was not found in this study. If edge flows of the remesh and retopoligised Lmesh appear unnatural, the subsequent deformation used for estimating plausible oROM may be affected. If needed, tools such as live retopology can be used to create a new Lmesh.

A deformer was setup to drive the deformation of Lmesh. The low poly mesh created from landmarks in this step was used as a hulk to drive deformation of the slightly smaller Lmesh. A wrap deformer in Maya was used, such that motions of vertices of the hulk would deform Lmesh.

To have vertices of the hulk follow ventilatory motions of Bmeshes, Vertices of the hulk were assigned to cluster deformers that were parent constrained to the nearest Bmeshes. For vertices positioned between two Bmeshes (e.g. vertices positioned within an intercostal space),

clusters of the vertices were parent constrained by both adjacent Bmeshes. The resulting deformation should expand smoothly, and reassigning vertices to clusters may be required to achieve desirable effects.

For crocodylian W model, the Lmesh was created also using landmarks from the Dmesh. As Lmesh does not reach the posterior aspects of the ribcage, additional edge loops were created near the posterior end of Lmesh, such that ventilatory motions of the posterior ribcage can drive deformations of Lmesh. Setup of deformer could be done after oROM is estimated.

Joint coordinate systems (JCS) — Three types of JCS were created using Maya joints (Mjoints) to describe anatomical rotations of Bmeshes around three axes using Euler angles. Intervertebral joints and sternum have the same setup across all three types of JCS. For intervertebral joints, Mjoints were placed at the anterior aspect of the centrum near the centres of the centrum. To place an intervertebral joint, a landmark was placed at the left lateral most aspect of the centrum, and a mirror landmark was created across Z-axis of the world using mirror tool in Maya. The intervertebral joint was placed in the midpoint between two landmarks. For sternum, Mjoints was placed at near its centroid. Orientation of intervertebral joints and sternum follow the CBP setup. For costal joints and intracostal joints, three types of JCS were setup as follow:

(1) CBP (Caliper-Bucket-Pump) setup

CBP setup describes ventilatory motions around x-axis as pump-handle motions, around y-axis as caliper motions, and around z-axis as bucket-handle motion.

For costal joints, Mjoints were placed at the centre among parapophysis, diapophysis, capitulum, and tuberculum. To place a costal joint, landmarks were placed near the centres on the articular facets of parapophysis, diapophysis, capitulum, and tuberculum. Maya tools such as snap to vertices and geometric constraints may facilitate placements of landmarks. The costal joint was then positioned to the centre of landmarks by point constraint of the costal joints under all four landmarks. Constraint was removed after the placement of costal joint was completed.

For intracostal joints, Mjoints were placed at the centres between articular facets of rib segments. To place an intracostal joint, four landmarks were placed at two ends of the long axes

of each articular facet (e.g. long axis of the surface at the distal end of a dorsal vertebral rib and at the proximal end of the articulated sternal rib). The intracostal joint was then positioned to the centre of the four landmarks. Constraints, if used, were removed after the intracostal joint was placed.

To orient a costal/intracostal joint in CBP manner, a child joint was created by duplicating the costal/intracostal joint, which was then translated dorsally along the Y-axis of the world and parented under the costal/intracostal joint. The costal/intracostal joint was then oriented using Orient Joint Option in Maya with Z-axis as the primary axis, Y-axis as the secondary axis, and negative Z-axis as the secondary axis world orientation. Child joint was removed after the costal/intracostal joint was oriented. X-axis of the costal/intracostal joint was scaled to -1. As channel box values in Maya do not take scale into account, a new attribute was created for costal/intracostal joints to scale the values from x-axis in the channel box by -1.

(2) AB (Anatomical Bone) setup

Taking the long axis of Bmeshes as morphological features in considerations, AB setup describes ventilatory motions around x-axis as axial rotation, around y-axis as abduction/adduction, and around z-axis as protraction/retraction.

For costal joints, Mjoints were placed at the midpoint between capitulum and tuberculum. To place a costal joint, landmarks were placed near the centres on the articular facets of capitulum and tuberculum. The costal joint was then positioned to the midpoint of two landmarks by point constraint of the costal joints. Constraint was removed after the placement of costal joint was completed.

For intracostal joints, Mjoints were placed at the midpoints on the proximal articular facets of rib segments. To place an intracostal joint, two landmarks were placed at the ends of the long axis on the articular facet (e.g. long axis of the surface at the proximal end of the articulated sternal rib). The intracostal joint was then placed in the midpoint of two landmarks. Constraints, if used, were removed after the intracostal joint was placed.

To orient a costal/intracostal joint in AB manner, a child joint was created and placed near the centre of the articular facet at the distal end of the rib segment. The child joint was parented under the costal/intracostal joint. The costal/intracostal joint was then oriented using Orient Joint Option in Maya with X-axis as the primary axis, Y-axis as the secondary axis, and positive Z-axis as the secondary axis world orientation.

(3) AJ (Anatomical Joint) setup

Only account for the positions of articular facets of rib segmetns, AJ setup describes ventilatory motions around x-axis as axial rotation, around y-axis as abduction/adduction, and around z-axis as protraction/retraction.

Placements of costal and intracostal joints were the same as CBP setup. To orient a costal joint in palaeognath model, a child joint was created at the midpoint between capitulum and tuberculum. The costal joint was then oriented using Orient Joint Option in Maya with X-axis as the primary axis, Y-axis as the secondary axis, and positive Z-axis as the secondary axis world orientation. To orient an intracostal joint in palaeognath model, a child joint was created at the midpoint on the articular facet of the sternal rib. The intracostal joint was then oriented using Orient Joint Option in Maya with X-axis as the primary axis, Z-axis as the secondary axis, and positive Y-axis as the secondary axis world orientation. To orient a costal joint in crocodylian W and crocodylian WOD, the procedure was the same as orienting a costal joint in palaeognath model. To orient a dorsal intracoastal joint, a child joint was created at the midpoint on the articular facet along the long axis of intermediate rib, and the child joint was parented under the costal joint. The dorsal intracostal joint was then oriented using Orient Joint Option in Maya with X-axis as the primary axis, Y-axis as the secondary axis, and positive Z-axis as the secondary axis world orientation. To orient a ventral intracostal joint, a child joint was created at the midpoint on the articular facet along the long axis of sternal rib, and the child joint was parented under the ventral intraocostal joint. The ventral intracostal joint was then oriented using Orient Joint Option in Maya with X-axis as the primary axis, Y-axis as the secondary axis, and positive Y-axis as the secondary axis world orientation.

Rigging and setting up connections — To connect Mjoints with CBP, AB, and AJ setups, joint locators (JLocators) were then placed and oriented in the same way as the Mjoints with AJ setup. All Mjoints with CBP, AB, and AJ setups were parent constrained under the JLocators.

Duplicates of joints from AJ setup were created to drive motions of the ribcage in Maya. NURB curves were created as controller to record oROM as animation key frames. Pivot points and orientations of Bmeshes and NURB controllers were matched to those of the Mjoints duplicated from AJ setup. Maya tools such as Match Transformation may facilitate this process. Then, freeze transformation were applied to Bmeshes. To have clean channel boxes for the NURB controllers, we could create groups that house the NURB controllers, and Match Transformation of the group to Mjoints.

Bmehes were then parent constrained to Mjoints, which were parent constrained to NURB controllers. Accordingly, we can use NURB controller to drive movement of individual Bmesh. Bmeshes of vertebrae would need to drive motions of rib segments, so that translations were not required for rib segments. To achieve this effect, NURB controllers of the ventral rib segments (e.g. sternal ribs) were hierarchically parent constrained to the dorsal rib segments (e.g. vertebral rib), and then parent constrained to the NURB controller of the corresponding vertebral Bmeshes. NURB controller of the posterior vertebral Bmeshes were then hierarchically parent constrained to those of the anterior vertebral Bmeshes. To have clean connections, empty groups can be created as parent objects to house NURB controllers, and parent constrains can be placed on the group. Note that NURB controller of the ventral Bmeshes (e.g. sternal ribs) under this setup would inherit transformations driven by the those of the dorsal Bmeshes (e.g. vertebrae), which is why JLocators were used to record pure rotations of the ventral Bmeshes.

Rotation orders of all objects in the scene were set to xyz with Script 7.1.

Estimate plausible oROM — NURB controller were manually rotate such that the ribcage was expanded to a state representing maximal inspiration, and the manual rotations were recorded as animation keyframes representing oROM. Bmeshes were allowed to approached

other Bmeshes without direct contact. Xray view in Maya may facilitate the estimations. For crocodylian W model, Dmesh was manually translated to a position representing maximal inspiration by referencing the literature (Claessens 2009a).

To estimate plausible oROM, oROM of all Bmeshes were scaled until changes of the thoracic volume approximated the tidal volumes taken from the literature (Schmidt-Nielsen et al. 1969; Perry 1988; Maina et al. 2009) (Table 7.1). Noted that tidal volume used for crocodylian W and crocodylian WOD models were computed from V_{Lr} and V_{Lm} reported by Perry (1988). Volumes of Lmesh were estimated using the MEL command *ComputePolysetVolume*. Multiple trial and error may be needed to approximate the tidal volume, and we did not recover the exact value of tidal volumes documented in the literature.

Three versions of ventilatory motions were created: (1) vertebra-rib-sternum (VRS) version represents ventilation with vertebrae, rib segments, and sternum; (2) rib-sternum (RS) represents ventilation with rib segments and sternum; and (3) rib (R) represents ventilation with only rib segments. For CBP, AB, AJ setups of each version of ventilation, both oROM and plausible oROM were recorded as animation keyframes and were saved in .atom format. JLocators were also keyframed with the same values as NURB controller, so that pure rotations of the Mjoints of CBP, AB, and AJ can be recorded and exported.

To describe oROM and plausible oROM from maximal expiration to maximal inspiration in a ventilatory cycle, the ratio of duration of inspiration to expiration as expressed by animation keyframes in Maya was set to 1:2 for paleognath and 1:1 for crocodylian, which are based on respiratory studies in neognath and crocodylians (Table S7.1). To test the potential impacts of different kinematic assumptions, rotations were prescribed both as linear angular motions and motions with a constant angular acceleration estimated from oROM and duration of ventilation. Linear angular motions were prescribed as equal steps each of the size determined by the following formula:

$$S_s = (ROM)/(t)$$

S_s: the increments of angular rotation between successive keyframes.

ROM: oROM or plausible oROM.

t: duration of inspiration and/or expiration as expressed by animation keyframes.

Motions with a constant angular acceleration was prescribed using kinematic equations as follow:

$$S_s = (\omega_{(f+1)}^2 - \omega_f^2) / (2 * \alpha)$$

$$\omega_f = \alpha * f$$

$$\alpha = (ROM)/t^2$$

S_s: the increments of angular rotation between successive keyframes.

ω_f: angular velocity at a given point in time during ventilation.

α = angular acceleration.

ROM: oROM or plausible oROM.

Table S7. 1. Durations of inspiration and expiration estimated from the literature

Taxa	Active level	Condition	Inspiration (s)	Expiration (s)	I:E ratio
Domestic goose (Cohn and Shannon 1968)	resting	unanathetized	2.44	2.41	1.01
			2.52	2.54	0.99
Canada geese (Funk et al. 1993)	in flight	unanathetized	1.99	4.86	0.41
			1.85	4.92	0.38
			1.67	5.13	0.33
			1.79	4.72	0.38
Mallard duck * (Lord et al. 1962)	resting	unanathetized	1.5	3	0.50
	in flight	unanathetized	0.4	0.4	1.00
Chicken (Kadono et al. 1963)	resting	unanathetized	0.96	1.1	0.87
			1.1	0.89	1.24
			0.95	1.22	0.78
			1.11	1.2	0.93
			0.91	0.96	0.95
			0.5	0.92	0.54
			0.99	0.85	1.16
			0.95	0.97	0.98
			1.09	0.87	1.25
			1.26	1.27	0.99
			1.05	1.13	0.93
			0.96	1.12	0.86
			0.9	1.22	0.74
			1.09	1.23	0.89
			1.02	1.24	0.82
			0.99	1.21	0.82
			1.29	1.16	1.11
			1.27	1.19	1.07
			1.28	0.98	1.31
			1.1	1.28	0.86
			1.38	1.14	1.21
			1.02	1.13	0.90
			0.9	1.19	0.76
			0.48	0.55	0.87
			0.44	0.42	1.05
			0.38	0.48	0.79
			0.39	0.43	0.91
			0.46	0.48	0.96
			0.4	0.45	0.89

			0.4	0.46	0.87
			0.39	0.44	0.89
			0.39	0.42	0.93
			0.38	0.5	0.76
			0.36	0.43	0.84
			0.89	0.71	1.25
			0.83	0.76	1.09
			0.66	1.24	0.53
			0.58	1.29	0.45
			0.46	0.5	0.92
			0.44	0.47	0.94
			0.4	0.5	0.80
			0.48	0.54	0.89
			0.81	0.91	0.89
			0.81	1.02	0.79
			0.73	0.72	1.01
			0.75	0.85	0.88
			0.29	0.37	0.78
			0.24	0.41	0.59
			0.3	0.41	0.73
			0.29	0.46	0.63
			0.27	0.5	0.54
			0.27	0.49	0.55
			0.48	0.48	1.00
			0.49	0.45	1.09
			0.47	0.43	1.09
			0.46	0.45	1.02
			0.44	0.41	1.07
			0.45	0.5	0.90
			0.46	0.51	0.90
			0.44	0.59	0.75
Black duck (Berger et al. 1970b)	in flight	unanathetized	0.21	0.75	0.28
			0.22	0.84	0.26
			0.22	0.95	0.23
			0.13	0.89	0.15
			0.22	0.87	0.25
			0.35	1.39	0.25
			0.41	1.38	0.30
			0.42	1.28	0.33
			0.43	0.78	0.55
			0.46	0.74	0.62
			0.49	0.69	0.71
			0.46	0.88	0.52

			0.36	0.66	0.55
Evening grosbeak (Berger et al. 1970b)	in flight	unanathetized	0.06	0.14	0.43
			0.07	0.14	0.50
			0.06	0.09	0.67
			0.06	0.09	0.67
			0.07	0.14	0.50
Magpie (Boggs 1997)	in flight	unanathetized	0.19	0.24	0.79
			0.24	0.26	0.92
			0.19	0.23	0.83
Magpie (Boggs et al. 1997a)	in flight	unanathetized	0.19	0.21	0.90
			0.23	0.34	0.68
			0.15	0.18	0.83
Magpie (Boggs et al. 1997b)	in flight	unanathetized	0.24	0.26	0.92
			0.12	0.25	0.48
American alligator (Carrier and Farmer 2000b)	in walk	unanathetized	2.19	1.62	1.35
			1.74	1.95	0.89
			1.69	2.17	0.78
American alligator (Farmer and Carrier 2000a)	recovering	unanathetized	2.74	8.46	0.32
			3.27	10.39	0.31
			3.85	9.11	0.42
			3.97	7.98	0.50
American alligator (Farmer and Carrier 2000a)	in walk	unanathetized	2.22	1.76	1.26
			1.76	1.94	0.91
			1.63	2.26	0.72
American alligator (Farmer and Carrier 2000a)	in walk	unanathetized	1.98	2.14	0.93
			0.9	1.28	0.70
			1.46	1.74	0.84
			1.86	1.35	1.38

* indicates taxon where durations of inspiration and expiration were described. Durations of inspiration and expiration in other taxa were measured from figures using ImageJ (Schneider et al. 2012).

7.7 Digital Supplementary Data

Digital supplementary data is stored and managed by the author, the documents of which are listed as follow:

(1) three Maya scenes for the Palaeognath, Crocodylian W, and Crocodylian WOD mdoels.

(2) oROM and plausible oROM estimated for VRS, RS, and R versions of ventilatory motions in this study.

(3) raw figures of oROM and plausible oROM for each anatomical joints in VRS, RS, and R versions of ventilatory motions, using AB, AJ, and CBP setups.

(4) two R scripts to organise and visualise the oROM and plausible oROM estimated in this study.

Latest version of this script may be found at:

https://github.com/Wani2Y/Bioinformatics/tree/main/visualise%20oROM%20from%20Maya%20animation

CHAPTER 8

Inferring ventilatory contributions of hypaxial muscles in a palaeognath and a crocodylian using muscle moment arms

8.1 Introduction

Extant birds and crocodylians are modern representatives of Archosauria, a group of amniotes that first appeared in the Triassic and filled most niches available to large-bodied terrestrial vertebrates throughout the Jurassic and Cretaceous (Brusatte et al. 2010; Nesbitt 2011; Benton 2014).

As in other amniotes, birds and crocodylians fuel their biological activities by oxygen obtained via airflow into and out of the respiratory organs (Powell 2015; Perry et al. 2019). In both birds and crocodylians, airflow through the respiratory organs is mostly generated by the rhymic movements of the ribcage, a process traditionally referred to as costal ventilation (Janis and Keller 2001; Perry et al. 2019) that is classified into inspiration that draws air in and expiration that pump air out. In extant birds, respiratory organs are compartmentalised into a lung fixed to the vertebral column and nine pneumatic sacs responsible for highly efficient cross-current gas exchanges and unidirectional airflow through the lung-air sac system, respectively (Duncker 1972; Maina 2002; Powell 2015). Additionally, vertebral ribs of the anterior thorax in most extant birds carry bony prongs extending caudally from the rib's midshaft called uncinate processes (Baumel et al. 1993), which theoretically provide additional leverage for the associated muscles (m. appendicocostales) to expand the ribcage (Zimmer 1935; Tickle et al. 2007). Inspiratory function of m. appendicocostales, and by extension that of the uncinate processes have received experimental support from an electromyographic study conducted on the Canada goose, *Branta canadensis* (Codd et al. 2005).

Like birds, unidirectional airflow is present in the less compartmentalised bronchoalveolar lung in crocodylians (Farmer and Sanders 2010), though a capacity for cross-current gas exchange may be lacking. Dorsal vertebral ribs in crocodylians also carry uncinate

processes, though they are cartilaginous tabs extending caudally from the rib's distal ends (Cong et al. 1988; Frey 1988). M. iliocostalis, an epaxial muscle attached to the cartilaginous uncinate processes has received experimental support for an expiratory function (Codd et al. 2019). In addition to costal ventilation, the capacity to generate ventilatory airflow in crocodylian is further enhanced by the so called "hepatic piston", which refers to the craniocaudal movements of the liver driven by rotation of the pubis relative to the ilium and ischium transmitted via the skeletal muscle, m. diaphragmaticus (Carrier and Farmer 2000a; Farmer and Carrier 2000a). The "hepatic piston" in crocodylians likely act to inspire air into the lung, as suggested by three electromyographic studies on m. diaphragmaticus (Gans and Clark 1976; Farmer and Carrier 2000a; Munns et al. 2012) and a cineradiographic study on the ventilatory motions of the trunk (Claessens 2009a). Anatomical and histological evidence suggest that the mobile pubis, and its inspiratory function may have appeared in early crocodyliforms on the evolutionary path to extant crocodylians (Claessens and Vickaryous 2012). Besides "hepatic pistion" in crocodylians, costal ventilation is the primary mechanism for ventilation in both birds and crocodylians.

A large volume of existing studies notwithstanding, ventilation in archosaurs focus primarily on three aspects: (1) volumetric estimations of tidal volumes between inspiration and expiration, and their correlations to other biological aspects such as locomotion (Berger et al. 1970; Butler 1981; Funk et al. 1993; Carrier 1996; Carrier and Farmer 2000b) and ecological adaptations (Schmidt-Nielsen et al. 1969; Brackenbury et al. 1982; Kiley et al. 1982; Farmer and Carrier 2000b; York et al. 2017); (2) muscle activations during ventilation indicative of the inspiratory and expiratory functions of skeletal muscles (Fedde et al. 1964; dewet et al. 1967; Gans and Clark 1976; Baumel et al. 1990; Codd et al. 2005; Codd et al. 2019); (3) anatomical features indicative of pulmonary morphologies (Schachner et al. 2009; Schachner et al. 2011; Brocklehurst et al. 2018) and those relevant to the origin of an avian-like ventilation (e.g. pneumatic sac, uncinate processes) (O'Connor 2006; Codd et al. 2008; Wedel 2009; Codd 2010). By comparison, the mechanical process of costal ventilation and ventilatory functions of muscles have remained largely unexplored in archosaurs, and kinetic studies on the relationships between muscles and motions are lacking. Existing mechanical studies of archosaur ventilation are mostly if not exclusively two-dimensional in scope, and the focus is on one intercostal space between two series of rib segments (Zimmer 1935; Tickle et al. 2007).

With the advent of three-dimensional techniques to capture skeletal motions (Brainerd et al. 2010; Gatesy et al. 2010), *in vivo* ventilatory motions in archosaurs have been captured at least in the domestic turkey *Meleagris gallopavo* and the American alligator *Alligator mississippiensis* as rotations around three perpendicular axes in three-dimensional space (Brocklehurst et al. 2017; Brocklehurst et al. 2019). Additionally, ventilatory motions may be inferred using *ex vivo* skeletons (see Chapter 7). Accordingly, functional interpretations of muscle based on two-dimensional analysis and muscle activations listed above could be difficult to connected with the three-dimensional nature of ventilatory motions.

In this study, we constructed two three-dimensional models of palaeognath and crocodylian, to estimate changes in moment arms of trunk muscles during ventilation. Then, the capacity of various trunk muscles to contribute to ventilation is inferred based on signs and values of muscle moment arms, and variations of muscle functions within the trunk are explored. Finally, the functional significance of uncinate processes is evaluated in three-dimensional terms.

8.2 Materials and methods

Following the rationales of terminologies used in Chapter 7, presacral vertebrae, costal joints refer to the anatomical joints between articulated presacrals and vertebral rib. In Palaeognath model, intracostal joints refers to the antomical joints between articulated vertebral and sternal ribs. In Crocodylian model, intracostal joints were further categorised into dorsal intracostal joints between vertebral and intermediate ribs and ventral intracostal joints between intermediate and sternal ribs. Anatomical joints are also referred to by the sequential number of the presacral regions (i.e. IV#, C#, DIR#, IR#, and VIR#) where necessary. For pseudo-muscle units, “PC#” is used to differentiate from their counterparts that have attachment sites on the uncinate processes. Muscle abbreviations follow those used in Chapter 6, and the following sections assume muscles were activated when describing moment arms. All inferred ventilatory functions of Palaeognath and Crocodylian models are provided in Table 8.1 and 8.2, respectively.

Ribcages of a skeletally mature *Struthio camelus* (UAMZ 7159) and a *Caiman crocodilius* (UAMZ unnumbered) housed at the University of Alberta were chosen to represent palaeognath and crocodylian, respectively. In this study, we used a three-step procedure to construct two models (i.e. Palaeognath model and Crocodylian model) and infer muscle functions during ventilation (see Supplementary Information for detailed description of the procedure):

Kinematic modeling and estimate ventilatory motions — Elements of ribcages were digitised using a light reflected scanner (Polyga Carbon series) housed in the Sullivan Lab at the University of Alberta, and then digitally articulated in Autodesk Maya following the procedure described in Chapter 7. Joint coordinate systems (JCS) were created using Anatomical Bone (AB) setup (Fig. 1), such that ventilatory motions were described as axial rotation, abduction/adduction, and protraction/retraction of the skeletal elements. As the uncinate processes are anchored to the dorsal vertebral ribs with limited mobility (see Chapter 5), uncinate processes in this study were assumed to be immobile relative to the dorsal vertebral ribs. Ventilatory motions based on osteological range of motion (oROM) and plausible oROM were estimated, which were described as both linear angular motions and motions with a constant angular acceleration following the procedure in Chapter 7. Only the Vertebrae-Rib-Sternum (VRS) versions from the Palaeognath kinematic, Crocodylian W and Crocodylian WOD models were used in this study. Assisted by Script 8.1 and Script 8.2, kinematic models and ventilatory motions were transferred to models in Software for Interactive Musculoskeletal Modeling (SIMM), such that the exact coordinates of digital ribcages, JCS, and ventilatory motions are identical between Maya and SIMM. All five costal joints between vertebrae and vertebral ribs and five intracostal joints between vertebral and sternal ribs were examined in Palaeognath model. In Crocodylian model, only the first, second, fourth, and sixth costal joints, only the second, fourth, and seventh dorsal intracostal joitns between the vertebral and intermediate ribs, and only the second, fourth, and sixth ventral intracostal joints between the intermediate and sternal ribs were sampled for functional interpretations.

Representing trunk muscles — Trunk muscles were represented as vectors connecting bony elements of the ribcage. However, many hypaxial muscles (e.g. mm. intercostales externi) have broad insertions on the ribs, and cannot be accurately represented as single vectors. Instead,

such muscles were represented by vectors for multiple "muscle units" evenly spaced throughout the areas of origin and insertion indicated by osteological correlates (see Chapter 6 for osteological correlates), with each vector representing a bundle of similarly oriented fibres (Fig. 2). A total of 136 and 300 muscle units were created for the kinetic Palaeognath and Crocodylian models using Script 8.3. As this study focused on hypaxial trunk muscles, only 67 and 84 muscle units were examined as a basis for functional interpretations. Where appropriate, wrap objects were added in SIMM to prevent vectors of muscle units from passing through bony elements. To evaluate the functional significance of uncinate processes from the perspective of moment arms, pseudo-muscle units were created for ventral part of m. iliocostalis and m. appendicocostalis, which were attached directly to the vertebral ribs, neglecting the presence of uncinate processes. Accordingly, the pseudo-muscle units represent hypothetical muscles without the additional mechanical leverage that may be provided by the uncinate processes.

Analysing moment arm plots — For a given ventilatory cycle, changes in moment arms of sampled muscle units were plotted in SIMM, which were organised in RStudio 4.1(RStudio Team 2020) using Script 8.4 and Script 8.5, such that magnitudes of moment arms and changes of moment arms throughout a ventilatory cycle can be compared between three kinematic motions and among anatomical joints. As signs of moment arms are indicative of the directions in which the muscles would drive the skeletal elements to rotate, ventilatory functions of each muscle unit were inferred by comparing the signs of moment arms to those of the kinematic motions. Muscle units with moment arms of the same and opposite signs as those of kinematic motions were inferred to have inspiratory and expiratory functions, respectively. Muscle units with moment arms that change signs during a ventilatory cycle were inferred to have mixed ventilatory functions. Only the VRS version of plausible oROM from Palaeognath and Crocodylian W kinematic models were used to infer ventilatory function.

As many vertebral ribs carry attachment sites cranially and caudally for ventral part of m. iliocostalis, mm. intercostales externi, and mm. intercostales interni (see Chapter 6), the simultaneous contractions of muscle units cranial and caudal to a given vertebral ribs may result in inspiratory or expiratory function. Combinations of muscle moment arms were computed, and the signs of combined moment arms were used to inferred whether the combinations of cranial

and caudal units of ventral part of m. iliocostalis, mm. intercostales externi, and mm. intercostales interni would rotate vertebral ribs for inspiration or expiration. The third and fourth costal joints were sampled as representative in Palaeognath and Crocodylian models, respectively.

Results were visualised using the R package GGplot2 (Wickham 2009).

8.3 Results

8.3.1 Inferred ventilatory functions of sampled trunk muscles

Ventral part of m. iliocostalis (vIC) (Fig. 3)**.** vIC is only sampled in Crocodylian model, and all five units of vIC at C10, C11, C13, and C15 provide axial rotations for inspiration. All units of vIC adduct vertebral ribs for expirations, except unit 1 at C11 and unit 4 at C13 which abduct vertebral ribs. All five units of vIC at C10 and C11 protract vertebral ribs for inspiration, whereas all five units of vIC at C13 and C15 retract vertebral ribs for expiration. Accordingly, alterations of muscle attachment sites provided by the uncinate processes do not change the ventilatory functions for vIC at C10 and C11. Accordingly, vIC likely have expiratory function in crocodylians, as most units adduct vertebral ribs, and caudal units of vIC also retract vertebral ribs.

Maximal moment arms of vIC are similar in magnitude between abduction/adduction and protraction/retraction, both of which are higher than the moment arms for axial rotations. Of the five units of vIC, moment arms for axial rotation are similar in magnitudes, whereas units of vIC positioned further distally have larger moment arms to generate craniocaudal motions. Moment arms for abduction/adduction are somewhat variable, though unit 5 attached to uncinate processes tend to have largest moment arms. Moment arms for axial rotation and protraction/retraction do not vary significantly among costal joints, whereas moment arms for abduction/adduction are substantially larger at C10.

M. levator costarum (LC). LC is represented as two units in Palaeognath (Fig. 4) and one unit in Crocodylian (Fig. 5) models. In Palaeognath model, both unit 1 and unit 2 of LC at all costal joints from C21 to C25 provide axial rotations for inspiration. Only the two units of LC at C22 abduct vertebral ribs for inspiration, and all remaining units at C21 to C25 except unit 2 at C21 would adduct vertebral ribs. Unit 2 at C21 is inferred to have mixed function, as the moment arm changes sign near maximal inspiration. All units at C21 to C25 act to protract vertebral ribs for inspiration.

Comparing only the maximal magnitude, moment arms are overall largest for protraction/retraction and are smallest for axial rotation. Moment arms for protraction/retraction gradually decrease from C21 to C2. For abduction/adduction, moment arms are largest near the centre of the ribcage at C23, and gradually reduce cranially and caudally. Moment arms for axial rotation do not vary significantly among costal joints.

In Crocodylian model, unit 1 of LC at both C10 and C11 provide axial rotation for inspiration, whereas those at C13 and C15 rotate axially for expiration. Unit 1 of LC at all sampled costal joints abduct vertebral ribs for inspiration, except unit 1 at C10 that act to adduct vertebral rib. As in Palaeognath model, unit 1 of LC at all sampled costal joints consistently protract vertebral ribs for inspiration.

For LC in Crocodylian model, maximal moment arms are largest for protraction/retraction and smallest for abduction/adduction. For protraction/retraction, moment arms gradually decrease from C10 to C15, as in Palaeognath model. Moment arm for axial rotation do no vary significantly among sampled costal joints. For abduction/adduction, moment arm is largest at C11, and are substantially smaller in magnitude at remaining costal joints.

LC accordingly would mostly act to protract vertebral ribs for inspiration in palaeognaths and crocodylians.

Mm. intercostales externi (IE). IE is represented as five units in Palaeognath (Fig. 6) and four units in Crocodylian (Fig. 7) models. In Palaeognath model, all units of IE at C21 to C25 provide axial rotation for inspiration. All five units of IE from C23 to C25 act to abduct

vertebral ribs for inspiration, whereas all five units of IE at C21 act to adduct vertebral rib. Unit 1 IE at C22 have mixed function due to a change in sign of moment arm, and the remaining four units of IE at C22 act to abduct vertebral ribs as their counterparts from C23 to C25. All five units at costal joints from C21 to C25 act to protract vertebral ribs.

Comparing only the maximal magnitude, moment arms in Palaeognath model are largest for protraction/retraction, and smallest for axial rotation. For protraction/retraction, maximal moment arms are generally largest for units positioned distally on vertebral ribs, except for IE at C22 where moment arms for protraction/retraction are similar for unit 4 and unit 5. Similar to moment arms for protraction/retraction, moment arms for abduction/adduction are generally larger for units positioned distally. By comparison, moment arms for axial rotations are smaller for units positioned distally on vertebral rib. Moment arms do not vary among sampled costal joints.

In Crocodylian model, all four units of IE at C10 and C11 provide axial rotations for inspirations, whereas all four units of IE at C13 and C15 act to rotate vertebral ribs axially for expiration. All five units of IE at C15 abduct vertebral rib for inspiration, whereas all five units of IE at C10 adduct vertebral rib for expiration. At C11 and C13, unit 1 and unit 2 of IE abduct vertebral ribs for inspiration, and unit 3 and unit 4 of IE adduct vertebral ribs for expiration. As in Palaeognath model, all units of IE at all four sampled costal joints act to protract vertebral ribs for inspiration.

Estimating only the maximal magnitude, moment arms are largest for protraction/retraction, followed by both abduction/adduction and axial rotation of similar magnitudes. Moment arms for protraction/retraction are generally larger for units positioned further distally on vertebral rib, whereas a clear pattern is seemingly absent for abduction/adduction and axial rotation.

IE accordingly has most consistent inspiratory function to protract vertebral ribs, and only units of IE from caudal aspects of the trunk would abduct vertebral ribs for inspiration.

M. appendicocostalis (APC). APC is represented as two units in Palaeognath (Fig. 8) and three units in Crocodylian (Fig. 9) models. In Palaeognath model, all units of APC rotate axially, abduct, and protract vertebral ribs for inspiration, except for unit 2 at C24 which adduct vertebral rib for expiration.

Comparing only the maximal magnitude, moment arms are largest for protraction/retraction and smallest for axial rotation. Moment arms do not vary between C23 and C24. Between unit 1 and unit 2 of APC, unit 1 has comparatively larger moment arms for axial rotation and abduction/adduction, whereas unit 2 has larger moment arms for protraction/retraction. The contrasts between unit 1 and unit 2 may represent difference in orientation, as unit 1 is more dorsoventrally oriented, and unit 2 is more craniocaudally oriented.

In Crocodylian model, APC in crocodylians connects vertebral and intermediate ribs, and intermediate ribs may be rotated at the dorsal intracostal joint relative to their corresponding vertebral ribs. Accordingly, moment arms estimated at the costal joints take vertebral ribs and intermediate ribs a combined unit, and moment arms estimated at the dorsal intracostal joints consider ventilatory motions of the intermediate ribs relative to the vertebral ribs. All three units of APC at C11 provide axial rotation for expiration, whereas those at C13 and C15 axially rotate vertebral and intermediate ribs for inspiration. All three units of APC at C11, C13, and C15 abduct and protract vertebral and intermediate ribs for inspiration. At dorsal intracostal joints, all three units of APC at DIR10 and DIR11 provide axial rotations for inspiration, whereas all three units of APC at DIR 16 axially rotate for expiration. All three units of APC at DIR10 and DIR11 adduct intermediate ribs for expiration, and the three units of APC at DIR16 abduct intermediate rib for inspiration. All three units of APC at DIR11, DIR13 and DIR16 protract intermediate ribs for inspiration, as at the costal joints.

Estimating only the maximal magnitude, moment arms are largest for protraction/retraction, and smallest for axial rotation at both costal and dorsal intracostal joints. Among the three units of APC at costal joints, units positioned distally have relatively larger moment arms for abduction/adduction and axial rotation, whereas moment arms are similar in magnitude for protraction/retraction. At dorsal intracostal joints, the distally positioned units of

APC have marginally larger moment arms for protraction/retraction, and a clear pattern in absent for axial rotation and abduction/adduction.

Accordingly, APC is likely an inspiratory muscle that primarily abduct and protract rib segments at costal joints and protract intermediate ribs at dorsal intracostal joints.

Mm. intercostales interni (II). II is represented as five units in Palaeognath (Fig. 10) and eight units of Crocodylian (Fig. 11) models. In Palaeognath model, all five units of II at costal joints from C21 to C25 retract and axially rotate vertebral ribs for expiration. All unit 1 of II at costal joints from C21 to C25 abduct vertebral ribs for inspiration, whereas unit 5 of II adduct vertebral ribs for expiration. Unit 2 of II at cranial costal joints abduct vertebral ribs for inspiration and those at caudal costal joints adduct vertebral ribs for expiration.

Comparing only the maximal magnitude, moment arms are largest for protraction/retraction and smallest for axial rotation. Units of II positioned distally have larger moment arms for protraction/retraction, which do not vary significantly from C21 to C24. By comparison, a distinct pattern is absent for axial rotation and abduction/adduction.

Of the eight units of II in Crocodylian model, first five units connect adjacent vertebral ribs, and the last three units connect adjacent intermediate ribs. Unit 1 to unit 5 of II at C10 and C11 retract and axially rotate vertebral ribs for expiration, whereas their counterparts at C13 and C15 axially rotate vertebral ribs for inspiration. All five units of II at C13 and C15 adduct vertebral ribs for expiration, whereas all five units of II at C11 abduct vertebral rib for inspiration. At C10, unit 1 of II adducts vertebral rib and the remaining four units abduct vertebral rib for expiration and inspiration, respectively. At DIR11 and DIR13, all but two units of II rotate axially, adduct, and retract intermediate ribs for expiration. Unit 8 at DIR11 and unit 6 at DIR13 provide axial rotations and abduct intermediate rib for inspiration, respectively.

Estimating only the maximal magnitude, moment arms are largest for protraction/retraction and smallest for axial rotation at costal and dorsal intracostal joints. Among the five units of II at costal joints, units positioned distally on vertebral ribs have larger moment arms for protraction/retraction and smaller moment arms for axial rotations. For

abduction/adduction, units of II at C10 and C11 positioned distally have larger moment arms, but units of II at C13 and C15 are similar in magnitude and lack a distinct pattern. Among the three units of II at dorsal intracostal joint, units positioned distally have larger moment arms for protraction/retraction and smaller moment arms for axial rotation, as in units of II at C10 and C112. A distinct pattern is lacking for abduction/adduction, as in units of II at C13 and C15.

Accordingly, II is most likely an expiratory muscle that mostly retract rib segments.

M. costosternalis (COT). COT is only sampled in Palaeognath model (Fig. 12), and all three units at IR21, IR22, and IR 23 act to rotate axially, adduct, and protract the sternal ribs for expiration.

Comparing only the maximal magnitude, moment arms for protraction/retraction are largest and moment arms for abduction/adduction are smallest. For both protraction/retraction and axial rotation, moment arms are larger at caudally positioned intracostal joint, whereas the opposite is found for abduction/adduction.

M. subcostalis (SC). SC is represented as one unit in Palaeognath (Fig. 13) and three units in Crocodylian (Fig. 14) models. In Palaeognath model, unit 1 of SC at all costal joints from IR21 to IR25 provide axial rotations for inspiration and protract sternal ribs for expiration. All unit 1 of SC adduct sternal ribs for expiration except that at IR21 which abducts sternal rib for inspiration.

Comparing only the maximal magnitude, moment arms are largest for protraction/retraction, and are larger on units of SC at caudally positioned intracostal joints. For both axial rotation and abduction/adduction, moment arms are similar from IR21 to IR 24 and is increased at IR25.

In Crocodylian model, all three units of SC at VIR11, VIR13, and VIR15 retract and axially rotate sternal ribs for expiration. Unit 1 of SC at VIR11 adducts sternal rib for expiration, and unit 2 and 3 positioned further distally abduct the sternal rib for inspiration. At VIR13, the proximal two units abduct for inspiration and the distal most unit 3 adduct for expiration. At

VIR15, the proximal most unit 1 abduct for inspiration, and the two units positioned further distally adduct sternal ribs for expiration.

Overall, LC, IE, APC are inferred as inspiratory muscles act to protract rib segments. APC additionally would abduct rib segments at costal joints. vIC, II, COT, and SC are inferred as expiratory muscles act to retract rib segments. Trunk muscles likely abduct or adduct rib segments according to the relative anatomical positions of the muscles and joints. Of the sampled moment arms, protraction/retraction has the largest maximal magnitude, and by extension the greatest mechanical leverage compared to axial rotation and abduction/adduction. Ventilatory functions of muscles contributed to axial rotations are more variable compared to those contributed to abduction/adduction and protraction/retraction, which suggests axial rotations may have other functional significance other than rotating rib segments for inspiration and expiration.

8.3.3 Impacts of uncinate processes on ventilatory function of APC

In Palaeognath model, both units of APC (Fig. 8) and IE (Fig. 6) act almost exclusively for inspiration, which suggest they have the same ventilatory function. Accounting for the mechanical leverage to rotate vertebral ribs, unit 1 of APC positioned midshaft of vertebral rib has maximal moment arms for axial rotation, abduction/adduction, and protraction/retraction similar to unit 3 of IE which is positioned distally on vertebral rib. Similarly, unit 2 of APC positioned midshaft of vertebral rib has maximal moment arms for protraction/retraction comparable to unit 4 of IE which is positioned further distally on vertebral rib. Compared to the pseudo-muscle unit of APC that pass through uncinate process and attach to vertebral rib, however, maximal moment arms of unit 1 for protraction/retraction are similar between units of APC and that of pseudo-muscle unit. Maximal moment arms for axial rotations are larger in unit 1 of APC, whereas maximal moment arms for abduction/adduction are larger in the unit of pseudo-muscle unit. Unit 2 of APC at both C23 and C24 have slightly larger maximal moment arms for axial rotation and protraction/retraction than those of pseudo-muscle unit, whereas moment arms for abduction/adduction is substantially smaller in unit 2 of APC. As unit 1 of APC is oriented somewhat dorsoventrally and unit 2 of APC is oriented craniocaudally, the maximal moment arms in Palaeognath model suggest that uncinate processes may enhance the ability of

craniocaudally oriented muscles to protract vertebral ribs at the costs of lowering muscle's ability to abduct vertebral ribs in palaeognath birds.

In Crocodylian model, units of APC (Fig. 9) have maximal moment arms for protraction/retraction comparable to unit 4 of IE (Fig. 7) position at the distal end of vertebral ribs, which are marginally larger than pseudo-muscle units that pass through uncinate processes and attach to vertebral ribs. For abduction/adduction, units of APC have substantially larger moment arms compared to the pseudo-muscle unit. Accordingly, uncinate processes likely enhance muscle's ability to both abduct and protract rib segments in crocodylians.

8.3.4 Impacts on inferring ventilatory function using different oROM and kinematic descriptions.

Estimating moment arms using oROM show more drastic changes in moment arm magnitudes throughout the ventilatory cycle. For several muscle units (e.g. unit 1 of LC and unit 2 of vIC at C13 in Crocodylian model) (Fig. 15), moment arms change sign near maximal inspiration only when estimations are based on oROM, which would likely lead to incorrect inference on ventilatory function of the muscle units. Accordingly, estimating muscle moment arms based on oROM may be exaggerated, and plausible oROM may provide more accurate inference on muscle's ventilatory functions.

Although describing ventilatory motions as rotations with a constant angular acceleration may recover ventilatory motions comparable to *in vivo* studies (see Chapter 7), moment arms estimated based on linear angular rotations and angular rotations with an assumed angular acceleration do not vary significantly. Therefore, linear angular rotations may be preferrable for functional interpretations.

8.3.5 Combined effects of cranial and caudal muscle units attached to the same vertebral rib.

Combined effects of vIC (del_vIC) (Fig. 16)**.** Units of del_vIC are inferred to have the same ventilatory functions as units of vIC at C13, except for unit 3 which have mixed function for abduction/adduction. However, the mixed function of unit 3 is likely accounted for by its near

zero moment arm throughout the ventilatory cycle. Compared to vIC, the maximal moment arms of del_vIC are substantially smaller, indicating that the capacity of vIC, when contract simultaneously, would have less capacity to retract vertebral ribs for expiration.

Combined effects of IE (del_IE). At C23 in Palaeognath (Fig. 17) and C13 in Crocodylian (Fig. 18) models, units of del_IE are inferred to have similar functions as units of IE to protract vertebral ribs for inspiration, except unit 4 of del_IE in Crocodylian model which is inferred to retract vertebral rib. Unlike inference from units of IE, all units of del_IE in Palaeognath and Crocodylian models adduct vertebral ribs for expiration, except unit 4 and unit 5 of del_IE in Palaeognath model, which have mixed function and abduct vertebral rib for inspiration, respectively. Accordingly, simultaneous activations of IE near the centre of ribcage may have tendencies to protract and adduct vertebral ribs. However, the maximal moment arms of del_IE are overall small, such that the tendencies to adduct vertebral ribs could be compensated by activations of other inspiratory muscles such as APC.

Combined effects of II (del_II). At C23 in Palaeognath (Fig. 19) and C13 in Crocodylian (Fig. 20) models, units of del_IE are inferred to have similar functions as units of II to retract and adduct vertebral ribs except unit 5 of II in both Palaeognath and Crocodylian models which have mixed function and protract vertebral rib, respectively. Accordingly, simultaneous contractions of II near the centre of the ribcage would have tendencies to retract and adduct rib segments.

8.4 Discussion

8.4.1 ribcage morphology indicative of overall ventilatory functions

Of the trunk muscles inferred in this study, protraction/retraction consistently has largest maximal moment arms. Except for all units of vIC in Crocodylian model, trunk muscles are inferred to have the same ventilatory function for protraction/retraction among sampled costal and intracostal joints. Accordingly, craniocaudal motions of the ribcage are likely prioritised to generate ventilatory airflow in palaeognath and crocodylians, which echoes with the dominant

craniocaudal motions observed upon inspiration in *in vivo* experiments in extant birds and crocodylians (Claessens 2009a; Claessens 2009b; Brocklehurst et al. 2017; Brocklehurst et al. 2019). In addition, maximal moment arms for protraction/retraction do not vary significantly in Paleognath model, suggesting that if forces provided by trunk muscles are of similar magnitude, ventilatory motions are relatively uniforms throughout the ribcage. Such an inference would be consistent with the *in vivo* observations in extant birds (Claessens 2009b; Brocklehurst et al. 2019).

Unlike protraction/retraction, inferred ventilatory function for abduction/adduction generated by sampled trunk muscles are variable according to the craniocaudal positions of rib segments that the trunk muscles attach to, except for unit 1 of APC and unit 1 of COT in Palaeognath model, and all units of APC in Crocodylian model which consistently abduct/adduct rib segments. In basal birds, lateral expansions of the thorax observed in a cineradiographic study are most noticeable if not significant from the cranial and middle portions of the thorax (Claessens 2009b), whereas in crocodylians, lateral expansions observed in a cineradiographic and an XROMM studies are more obvious from the middle and caudal portions of the thorax. The variable ventilatory motions observed in these *in vivo* studies may be related to the different ventilatory function for abduction/adduction inferred in this study.

From an anatomical perspective, dorsal vertebral ribs from the middle portions of the ribcages are positioned lateral to the costal segments both cranial and caudal to them in *Su. camelus* (UAMZ 7159), *Cai. crocodilus* (UAMZ unnumbered), and many other extant archosaurs (Ghetie 1976; Cong et al. 1988; Baumel et al. 1993) (also see Chapter 6). Trunk muscles originated from the cranial and caudal of the ribcage would pass somewhat laterally and insert on the adjacent costal segments, the activation of which would most definitely adduct the costal segments medially. Whether a trunk muscle would abduct or adduct a given costal segment may be influenced if not determined by the mediolateral positions of adjacent costal segments. Brocklehurst et al. (2017) observe that the lateral expansions of the thorax as represented by caliper motions become an important component of the ventilatory motions after parapophysis of a vertebra migrates dorsally onto the diapophysis/transverse process. Unlike crocodylians, parapophysis generally does not migrate onto the diapophysis in birds (Ghetie

1976; Baumel et al. 1993), although lateral expansions of the thorax have been observed from the cranial portion of the thorax in basal birds (Claessens 2009b).

Accordingly, a palaeognath-like ribcage may limit the bird's ability to expand the thorax laterally by the relative positions of parapophysis and costal segments.

8.4.2 Functional significance of uncinate processes

Uncinate processes have received two primary functional hypotheses: (1) reinforcement of the ribcage (Welty and Baptista 1972; Hildebrand 1982; Walker and Liem 2001) and (2) ventilation (Zimmer 1935; Tickle et al. 2007). Only the ventilatory hypothesis has been analysed from a mechanical perspective using two-dimensional geometric models. Both Zimmer (1935) and Tickle et al. (2007) represent dorsal vertebral ribs by straight lines or solid beams, and fibres of APC pass caudoventrally from the distal end of uncinate processes to protract the vertebral rib. Unlike the geometric models by Zimmer (1935) and Tickle et al. (2007), muscle units of APC in Palaeognath model presented in this study have marginally larger maximal moment arms to protract vertebral ribs compared to pseudo-muscle units of IE attached directly to vertebral ribs only when fibres of APC (e.g. unit 2) is oriented nearly craniocadually. Instead, muscle units of APC have comparatively larger maximal moment arms for axial rotations and smaller maximal moment arms for abduction/adduction. The discrepancies between our inferences and those modelled by Zimmer (1935) and Tickle et al. (2007) may be attributed to three plausible factors. Firstly, fibres of IE are represented as vectors nearly perpendicular to vertebral ribs by Zimmer (1935) and Tickle et al. (2007), whereas muscles units of IE are oriented caudoventrally in our Palaeognath model based on observations from an emu *Dromaius novaehollandiae* (see Chapter 6), which are similar to the orientation APC. Representation IE by Zimmer (1935) and Tickle et al. (2007) has been observed from the intercostal space dorsal to uncinate processes in a common raven *Corvus corax* (see Chapter 6) and from the literature (Ghetie 1976; Shufeldt 1988). The different representations of IE would likely affect the comparative results. Secondly, vertebral ribs are represented as straight elements by Zimmer (1935) and Tickle et al. (2007), whereas the natural curvatures of vertebral ribs are captured by our Palaeognath models. The different curvature may alter attachment sites of muscle units, which in turn may impact the computation of moment arms. Lastly, uncinate processes in *Su. camelus* (UAMZ 7159) are overall short and

do not extend dorsally as in uncinate processes modelled by Zimmer (1935) and Tickle et al. (2007). The units of APC in our Palaeognath model would not pass caudoventrally at a steep angle as represented in the geometric models by Zimmer (1935) and Tickle et al. (2007).

Unlike the Palaeognath model, our Crocodylian model represents uncinate processes and the orientation of the APC in approximately the same manner as the geometric models by Zimmer (1935) and Tickle et al. (2007). Maximal moment arms estimated from units of APC to protract vertebral ribs are not comparable to the units positioned further distally at the distal ends of vertebral rib, and units of APC have decently larger moment arms to abduct vertebral ribs laterally.

Comparisons among functional inferences on APC from Palaeognath model, Crocodylian model, and geometric models by Zimmer (1935) and Tickle et al. (2007) suggest that uncinate processes and the caudoventrally oriented APC likely enhance the capacity to expand the thorax laterally, while maintaining similar capacity to protract vertebral ribs. The comparisons also suggest that uncinate processes and the craniocaudally oriented APC likely constraint palaeognath bird's capacity to abduct vertebral rib, while promote palaeognath bird's capacity to protract vertebral ribs. Although uncinate processes most definitely enhances archosaurs' capacities to ventilate, the exact ways of ventilatory enhancement may be tied to the overall ribcage morphology and the configurations of trunk muscles.

8.4.3 Implications for studies of ventilation in deep time

Vertebrae and vertebral ribs in fossil archosaurs have various features and curvatures (Brochu 2003) (also see Chapter 4), which have been used to infer the pulmonary morphology in fossil dinosaurs, and when an immobile lung may have evolved on the evolutionary line toward birds (Schachner et al. 2011; Brocklehurst et al. 2018). Direct and indirect evidence of uncinate processes have also been used to infer that uncinate process, along with their enhancement in ventilation may have evolved long before the origin of birds (Codd et al. 2008) (also see Chapter 4).

Palaeognath and Crocodylian models presented in this study further hint at a correlation between the configurations of bony elements and ventilatory functions of trunk muscles. Bony elements of ribcages in fossil archosaurs can be well preserved in three dimension (Brochu 2003; Turner 2006; Xu et al. 2015; Currie et al. 2016; Drysdale et al. 2018), and articulated versions of ribcages in fossil archosaurs may be reconstructed with reasonable constraints on soft tissues (Claessens 2015). Accordingly, three-dimensional models can be created from well-preserved fossil archosaurs, and we may gain insights into how ventilatory functions of the ribcage changes on the evolutionary paths to extant birds and crocodylians.

Tables

Table 8. 1. Ventilatory functions of sampled hypaxial muscles inferred by moment arms in Palaeognath model.

Costal Joints							
muscle	muscle unit	muscle action	C21	C22	C23	C24	C25
LC	unit 1	axial rotation	Ins	Ins	Ins	Ins	Ins
		abduction/adduction	Exp	Ins	Exp	Exp	Exp
		protraction/retraction	Ins	Ins	Ins	Ins	Ins
	unit 2	axial rotation	Ins	Ins	Ins	Ins	Ins
		abduction/adduction	Mix	Ins	Exp	Exp	Exp
		protraction/retraction	Ins	Ins	Ins	Ins	Ins
IE	unit 1	axial rotation	Ins	Ins	Ins	Ins	Ins
		abduction/adduction	Exp	Mix	Ins	Ins	Ins
		protraction/retraction	Ins	Ins	Ins	Ins	Ins
	unit 2	axial rotation	Ins	Ins	Ins	Ins	Ins
		abduction/adduction	Exp	Ins	Ins	Ins	Ins
		protraction/retraction	Ins	Ins	Ins	Ins	Ins
	unit 3	axial rotation	Ins	Ins	Ins	Ins	Ins
		abduction/adduction	Exp	Ins	Ins	Ins	Ins
		protraction/retraction	Ins	Ins	Ins	Ins	Ins
	unit 4	axial rotation	Ins	Ins	Ins	Ins	Ins
		abduction/adduction	Exp	Ins	Ins	Ins	Ins
		protraction/retraction	Ins	Ins	Ins	Ins	Ins
	unit 5	axial rotation	Ins	Ins	Ins	Ins	Ins
		abduction/adduction	Exp	Ins	Ins	Ins	Ins
		protraction/retraction	Ins	Ins	Ins	Ins	Ins
APC	unit 1	axial rotation	-	-	Ins	Ins	-
		abduction/adduction	-	-	Ins	Ins	-
		protraction/retraction	-	-	Ins	Ins	-
	unit 2	axial rotation	-	-	Ins	Ins	-
		abduction/adduction	-	-	Ins	Exp	-
		protraction/retraction	-	-	Ins	Ins	-
II	unit 1	axial rotation	Exp	Exp	Exp	Exp	-
		abduction/adduction	Ins	Ins	Ins	Ins	-
		protraction/retraction	Exp	Exp	Exp	Exp	-
	unit 2	axial rotation	Exp	Exp	Exp	Exp	-
		abduction/adduction	Ins	Ins	Mix	Exp	-
		protraction/retraction	Exp	Exp	Exp	Exp	-
	unit 3	axial rotation	Exp	Exp	Exp	Exp	-
		abduction/adduction	Ins	Mix	Exp	Exp	-
		protraction/retraction	Exp	Exp	Exp	Exp	-
	unit 4	axial rotation	Exp	Exp	Exp	Exp	-

		abduction/adduction	Mix	Exp	Exp	Exp	-
		protraction/retraction	Exp	Exp	Exp	Exp	-
	unit 5	axial rotation	Exp	Exp	Exp	Exp	-
		abduction/adduction	Exp	Exp	Exp	Exp	-
		protraction/retraction	Exp	Exp	Exp	Exp	-
del_IE	unit 1	axial rotation	-	-	Exp	-	-
		abduction/adduction	-	-	Exp	-	-
		protraction/retraction	-	-	Ins	-	-
	unit 2	axial rotation	-	-	Exp	-	-
		abduction/adduction	-	-	Exp	-	-
		protraction/retraction	-	-	Ins	-	-
	unit 3	axial rotation	-	-	Exp	-	-
		abduction/adduction	-	-	Exp	-	-
		protraction/retraction	-	-	Ins	-	-
	unit 4	axial rotation	-	-	Exp	-	-
		abduction/adduction	-	-	Mix	-	-
		protraction/retraction	-	-	Ins	-	-
	unit 5	axial rotation	-	-	Exp	-	-
		abduction/adduction	-	-	Ins	-	-
		protraction/retraction	-	-	Ins	-	-
del_II	unit 1	axial rotation	-	-	Exp	-	-
		abduction/adduction	-	-	Exp	-	-
		protraction/retraction	-	-	Exp	-	-
	unit 2	axial rotation	-	-	Exp	-	-
		abduction/adduction	-	-	Exp	-	-
		protraction/retraction	-	-	Exp	-	-
	unit 3	axial rotation	-	-	Mix	-	-
		abduction/adduction	-	-	Exp	-	-
		protraction/retraction	-	-	Exp	-	-
	unit 4	axial rotation	-	-	Ins	-	-
		abduction/adduction	-	-	Exp	-	-
		protraction/retraction	-	-	Exp	-	-
	unit 5	axial rotation	-	-	Ins	-	-
		abduction/adduction	-	-	Mix	-	-
		protraction/retraction	-	-	Exp	-	-
Intracostal Joints							
muscle	muscle unit	muscle action	IR21	IR22	IR23	IR24	IR25
COT	unit 1	axial rotation	Exp	Exp	Exp	-	-
		abduction/adduction	Exp	Exp	Exp	-	-
		protraction/retraction	Exp	Exp	Exp	-	-
SC	unit 1	axial rotation	Ins	Ins	Ins	Ins	Ins
		abduction/adduction	Ins	Exp	Exp	Exp	Exp
		protraction/retraction	Exp	Exp	Exp	Exp	Exp

Abbreviations: APC, m. appendicocostalis; del_IE, combination of mm. intercostales externus attached anterior and posterior to the vertebral rib; COT, m. costosternalis; del_II, combination of mm. intercostales internus attached anterior and posterior to the vertebral rib; Exp, expiration; IE, mm. intercostales externi; II, mm. intercostales interni; Ins, inspiration; LC, m. levator costarum; SC, m. subcostalis; vIC, ventral part of m. iliocostalis.

Table 8. 2. Ventilatory functions of sampled hypaxial muscles inferred by moment arms in Crocodylian model.

Costal Joints						
muscle	muscle unit	muscle action	C10	C11	C13	C15
vIC	unit 1	axial rotation	Ins	Ins	Ins	Ins
		abduction/adduction	Exp	Ins	Exp	Exp
		protraction/retraction	Ins	Ins	Exp	Exp
	unit 2	axial rotation	Ins	Ins	Ins	Ins
		abduction/adduction	Exp	Exp	Exp	Exp
		protraction/retraction	Ins	Ins	Exp	Exp
	unit 3	axial rotation	Ins	Ins	Ins	Ins
		abduction/adduction	Exp	Exp	Exp	Exp
		protraction/retraction	Ins	Ins	Exp	Exp
	unit 4	axial rotation	Ins	Ins	Ins	Ins
		abduction/adduction	Exp	Exp	Ins	Exp
		protraction/retraction	Ins	Ins	Exp	Exp
	unit 5	axial rotation	Ins	Ins	Ins	Ins
		abduction/adduction	Exp	Exp	Exp	Exp
		protraction/retraction	Ins	Ins	Exp	Exp
LC	unit 1	axial rotation	Ins	Ins	Exp	Exp
		abduction/adduction	Exp	Ins	Ins	Ins
		protraction/retraction	Ins	Ins	Ins	Ins
IE	unit 1	axial rotation	Ins	Ins	Exp	Exp
		abduction/adduction	Exp	Ins	Ins	Ins
		protraction/retraction	Ins	Ins	Ins	Ins
	unit 2	axial rotation	Ins	Ins	Exp	Exp
		abduction/adduction	Exp	Ins	Ins	Ins
		protraction/retraction	Ins	Ins	Ins	Ins
	unit 3	axial rotation	Ins	Ins	Exp	Exp
		abduction/adduction	Exp	Exp	Exp	Ins
		protraction/retraction	Ins	Ins	Ins	Ins
	unit 4	axial rotation	Ins	Ins	Exp	Exp
		abduction/adduction	Exp	Exp	Exp	Ins
		protraction/retraction	Ins	Ins	Ins	Ins
APC_vr	unit 1	axial rotation	-	Exp	Ins	Ins
		abduction/adduction	-	Ins	Ins	Ins
		protraction/retraction	-	Ins	Ins	Ins
	unit 2	axial rotation	-	Exp	Ins	Ins
		abduction/adduction	-	Ins	Ins	Ins
		protraction/retraction	-	Ins	Ins	Ins
	unit 3	axial rotation	-	Exp	Ins	Ins
		abduction/adduction	-	Ins	Ins	Ins

		protraction/retraction	-	Ins	Ins	Ins
II_vr	unit 1	axial rotation	Exp	Exp	Ins	Ins
		abduction/adduction	Exp	Ins	Exp	Exp
		protraction/retraction	Exp	Exp	Exp	Exp
	unit 2	axial rotation	Exp	Exp	Ins	Ins
		abduction/adduction	Ins	Ins	Exp	Exp
		protraction/retraction	Exp	Exp	Exp	Exp
	unit 3	axial rotation	Exp	Exp	Ins	Ins
		abduction/adduction	Ins	Ins	Exp	Exp
		protraction/retraction	Exp	Exp	Exp	Exp
	unit 4	axial rotation	Exp	Exp	Ins	Ins
		abduction/adduction	Ins	Ins	Exp	Exp
		protraction/retraction	Exp	Exp	Exp	Exp
	unit 5	axial rotation	Exp	Exp	Ins	Ins
		abduction/adduction	Ins	Ins	Exp	Exp
		protraction/retraction	Exp	Exp	Exp	Exp
del_vIC	unit 1	axial rotation	-	-	Ins	-
		abduction/adduction	-	-	Exp	-
		protraction/retraction	-	-	Exp	-
	unit 2	axial rotation	-	-	Ins	-
		abduction/adduction	-	-	Exp	-
		protraction/retraction	-	-	Exp	-
	unit 3	axial rotation	-	-	Ins	-
		abduction/adduction	-	-	Mix	-
		protraction/retraction	-	-	Exp	-
	unit 4	axial rotation	-	-	Ins	-
		abduction/adduction	-	-	Ins	-
		protraction/retraction	-	-	Exp	-
	unit 5	axial rotation	-	-	Ins	-
		abduction/adduction	-	-	Exp	-
		protraction/retraction	-	-	Exp	-
del_IE	unit 1	axial rotation	-	-	Ins	-
		abduction/adduction	-	-	Exp	-
		protraction/retraction	-	-	Ins	-
	unit 2	axial rotation	-	-	Ins	-
		abduction/adduction	-	-	Exp	-
		protraction/retraction	-	-	Ins	-
	unit 3	axial rotation	-	-	Exp	-
		abduction/adduction	-	-	Exp	-
		protraction/retraction	-	-	Ins	-
	unit 4	axial rotation	-	-	Ins	-
		abduction/adduction	-	-	Exp	-
		protraction/retraction	-	-	Exp	-

del_II	unit 1	axial rotation	-	-	Ins	-
		abduction/adduction	-	-	Exp	-
		protraction/retraction	-	-	Exp	-
	unit 2	axial rotation	-	-	Ins	-
		abduction/adduction	-	-	Exp	-
		protraction/retraction	-	-	Exp	-
	unit 3	axial rotation	-	-	Exp	-
		abduction/adduction	-	-	Exp	-
		protraction/retraction	-	-	Exp	-
	unit 4	axial rotation	-	-	Exp	-
		abduction/adduction	-	-	Exp	-
		protraction/retraction	-	-	Exp	-
	unit 5	axial rotation	-	-	Exp	-
		abduction/adduction	-	-	Exp	-
		protraction/retraction	-	-	Ins	-
Dorsal Intracostal Joints						
muscle	muscle unit	muscle action	DIR11	DIR13	DIR16	-
APC_ir	unit 1	axial rotation	Ins	Ins	Exp	-
		abduction/adduction	Exp	Exp	Ins	-
		protraction/retraction	Ins	Ins	Ins	-
	unit 2	axial rotation	Ins	Ins	Exp	-
		abduction/adduction	Exp	Exp	Ins	-
		protraction/retraction	Ins	Ins	Ins	-
	unit 3	axial rotation	Ins	Ins	Exp	-
		abduction/adduction	Exp	Exp	Ins	-
		protraction/retraction	Ins	Ins	Ins	-
II_ir	unit 6	axial rotation	Exp	Exp	-	-
		abduction/adduction	Exp	Ins	-	-
		protraction/retraction	Exp	Exp	-	-
	unit 7	axial rotation	Exp	Exp	-	-
		abduction/adduction	Exp	Exp	-	-
		protraction/retraction	Exp	Exp	-	-
	unit 8	axial rotation	Ins	Exp	-	-
		abduction/adduction	Exp	Exp	-	-
		protraction/retraction	Exp	Exp	-	-
Ventral Intracostal Joints						
muscle	muscle unit	muscle action	VIR11	VIR13	VIR15	-
SC	unit 1	axial rotation	Exp	Exp	Exp	-
		abduction/adduction	Exp	Ins	Ins	-
		protraction/retraction	Exp	Exp	Exp	-
	unit 2	axial rotation	Exp	Exp	Exp	-
		abduction/adduction	Ins	Ins	Exp	-
		protraction/retraction	Exp	Exp	Exp	-

unit 3	axial rotation	Exp	Exp	Exp	-
	abduction/adduction	Ins	Exp	Exp	-
	protraction/retraction	Exp	Exp	Exp	-

Abbreviations: APC_ir, m. appendicocostalis acted on dorsal intracostal joint; APC_vr, m. appendicocostalis acted on costal joint; del_IE, combination of mm. intercostales externus attached anterior and posterior to the vertebral rib; del_II, combination of mm. intercostales internus attached anterior and posterior to the vertebral rib; del_VIC, combination of m. iliocostalis attached anterior and posterior to the vertebral rib; Exp, expiration; IE, mm. intercostales externi; II_ir, mm. intercostales interni acted on dorsal intracostal joint; II_vr, mm. intercostales interni acted on costal joint; Ins, inspiration; LC, m. levator costarum; SC, m. subcostalis; vIC, ventral part of m. iliocostalis.

Figures

Figure 8.1. Joint coordinate system (JCS) used in SIMM models.

Line drawings of vertebra, vertebral rib, and sternal rib of *Struthio camelus* (UAMZ 7159) illustrating the AB setup of the JCS system for axial rotation at dorsal costal joint in lateral view (A), for abduction/adduction at dorsal costal joint in lateral view (B), for protraction/retraction at dorsal costal joint in anterior view (C), and all three axes at intracostal joint in anterolateral view (D). Scale bar equals 1 cm.

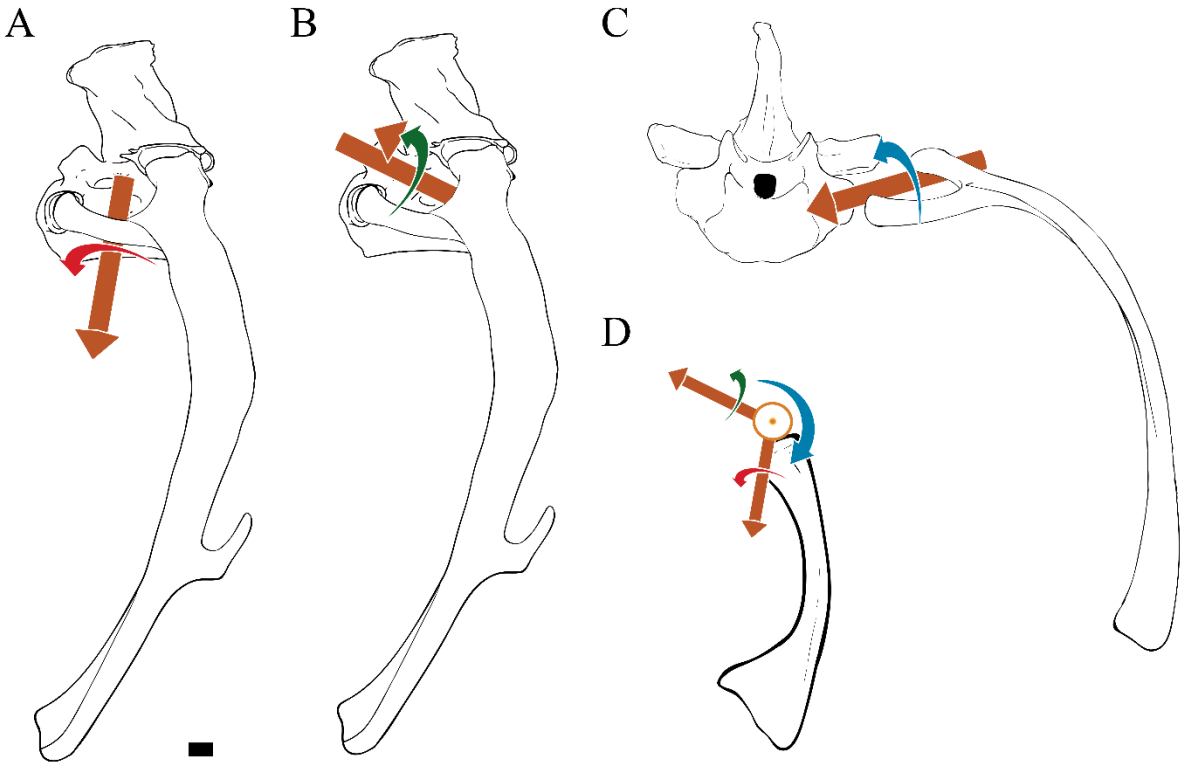
A
B
C
D

Figure 8.2. Muscle units in SIMM models reported in this study.

Line drawings of vertebral rib and sternal rib of *Struthio camelus* (UAMZ 7159) in lateral and anterolateral views (A), illustrating the approximate anatomical positions of all muscle units reported from Palaeognath model; line drawings of vertebral rib, intermediate rib, and sternal rib of *Caiman crocodilus* (UAMZ unnumbered) in lateral, lateral, and ventral views (B), illustrating the approximate anatomical positions of all muscle units reported from Crocodylian model. Drawings are oriented such that proximal ends of rib segments face the top side. Scale bars equal 1 cm. See digital Supplementary Data for precise coordinates used in SIMM models. Abbreviations: APC, m. appendicocostalis; COT, m. costosternalis; IE, mm. intercostales externi; II, mm. intercostales interni; LC, m. levator costarum; SC, m. subcostalis; vIC, ventral part of m. iliocostalis.

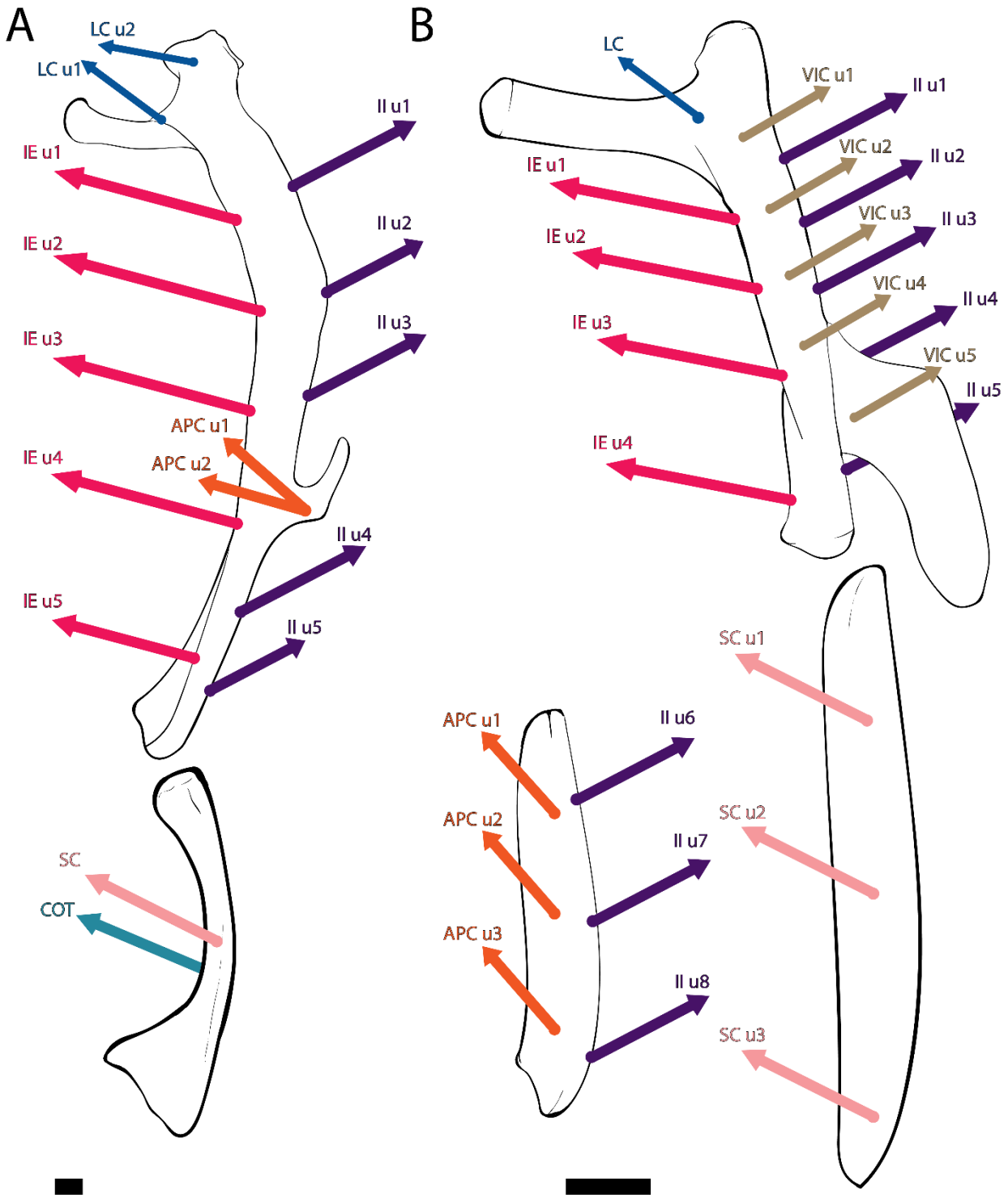
A
LC u2
LC u1
II u1
IE u1
II u2
IE u2
II u3
IE u3
APC u1
APC u2
IE u4
II u4
IE u5
II u5
SC
COT
B
LC
VIC u1
II u1
VIC u2
II u2
IE u1
VIC u3
II u3
IE u2
VIC u4
II u4
IE u3
VIC u5
II u5
IE u4
SC u1
APC u1
II u6
SC u2
APC u2
II u7
APC u3
II u8
SC u3

Figure 8.3. Maximal muscle moment arms of costal joints for ventral part of m. iliocostalis (vIC) in Crocodylian model at maximal inspiration.

Bar graphs of moment arms for five units of vIC estimated in Paleognath model. Moment arms about x-axis for axial rotations at C10, C11, C13, C15, and the pseudo-muscle units at C10 and C11 (A); moment arms about y-axis for abduction/adduction at C10, C11, C13, C15, and the pseudo-muscle units at C10 and C11 (B); moment arms about z-axis for protraction/retraction at C10, C11, C13, C15, and the pseudo-muscle units at C10 and C11 (C). Colours at high and low opacity refer to moment arms estimated using plausible oROM and oROM, respectively. Abbreviations: C, costal joint; PC, pseudo-muscle units at costal joint; oROM, osteological range of motions.

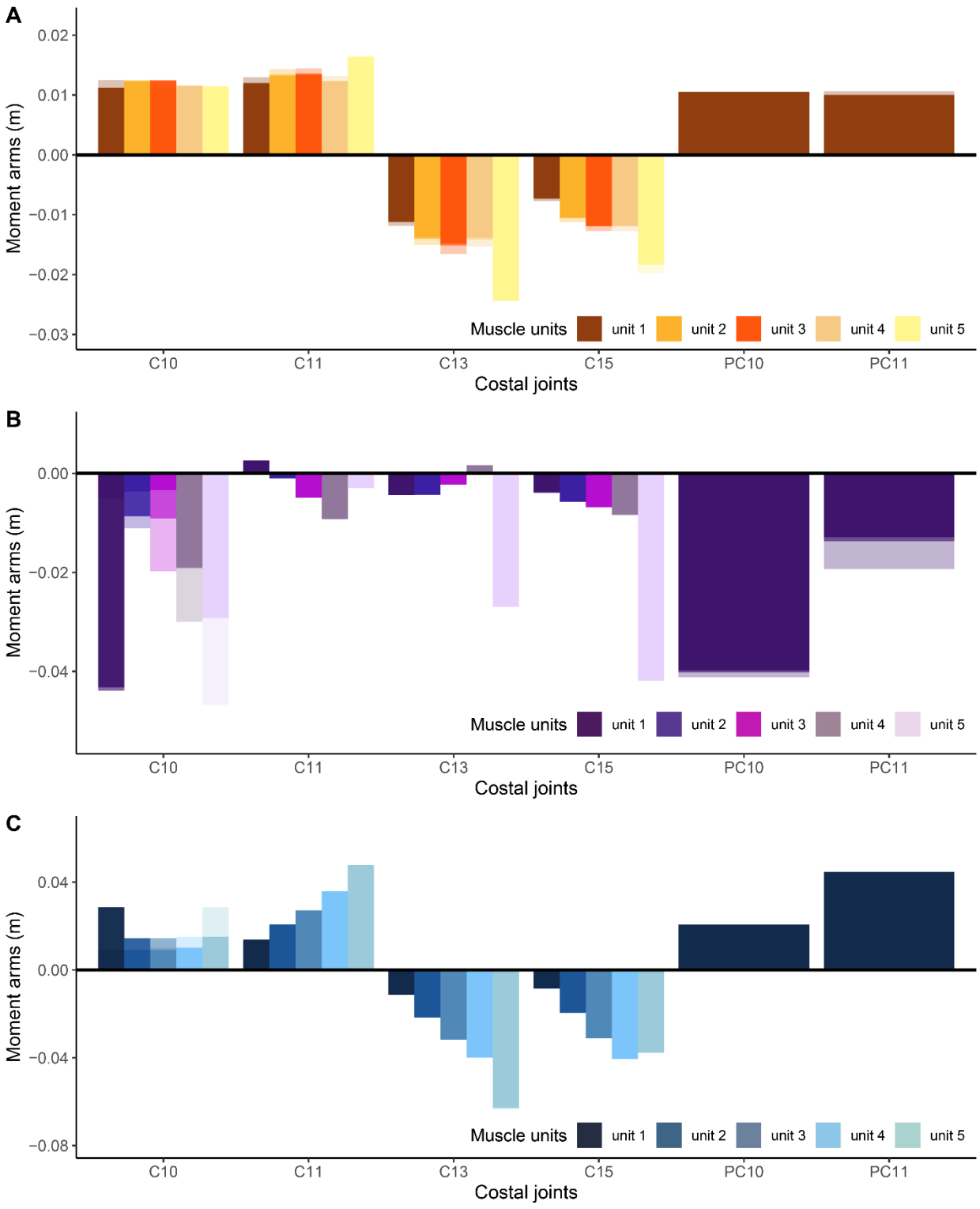
A
0.02
0.01
0.00
−0.01
−0.02
−0.03
Moment arms (m)
Muscle units
unit 1
unit 2
unit 3
unit 4
unit 5
C10
C11
C13
C15
PC10
PC11
Costal joints
B
0.00
−0.02
−0.04
Moment arms (m)
Muscle units
unit 1
unit 2
unit 3
unit 4
unit 5
C10
C11
C13
C15
PC10
PC11
Costal joints
C
0.04
0.00
−0.04
−0.08
Moment arms (m)
Muscle units
unit 1
unit 2
unit 3
unit 4
unit 5
C10
C11
C13
C15
PC10
PC11
Costal joints

Figure 8.4. Maximal muscle moment arms at costal joints for m. levator costarum (LC) in Palaeognath model.

Bar graphs of moment arms for two units of LC estimated in Paleognath model. Moment arms about x-axis for axial rotations at first five dorsal costal joints (A); moment arms about y-axis for abduction/adduction at first five dorsal costal joints (B); moment arms about z-axis for protraction/retraction at first five dorsal costal joints (C). Colours at high and low opacity refer to moment arms estimated using plausible oROM and oROM, respectively. Abbreviations: C, costal joint; oROM, osteological range of motions.

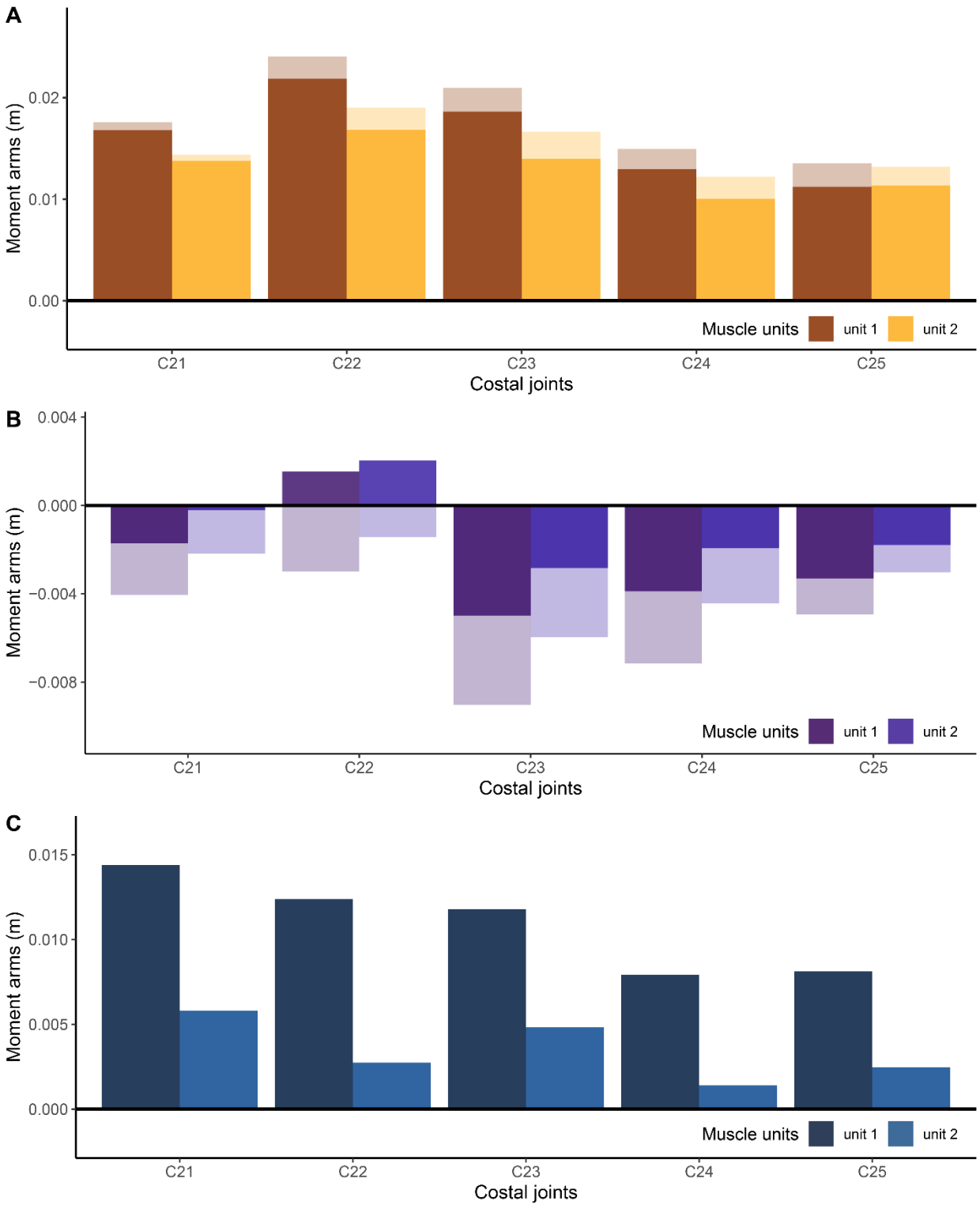
A
Moment arms (m)
0.02
0.01
0.00
Muscle units
unit 1
unit 2
C21
C22
C23
C24
C25
Costal joints
B
0.004
0.000
−0.004
−0.008
Moment arms (m)
Muscle units
unit 1
unit 2
C21
C22
C23
C24
C25
Costal joints
C
0.015
0.010
0.005
0.000
Moment arms (m)
Muscle units
unit 1
unit 2
C21
C22
C23
C24
C25
Costal joints

Figure 8.5. Maximal muscle moment arms at costal joints for m. levator costarum (LC) in Crocodylian model.

Bar graphs of moment arms for LC estimated in Crocodylian model. Moment arms about x-axis for axial rotations at C10, C11, C13, C15 (A); moment arms about y-axis for abduction/adduction at C10, C11, C13, C15 (B); moment arms about z-axis for protraction/retraction at C10, C11, C13, C15 (C). Colours at high and low opacity refer to moment arms estimated using plausible oROM and oROM, respectively. Abbreviations: C, costal joint; oROM, osteological range of motions.

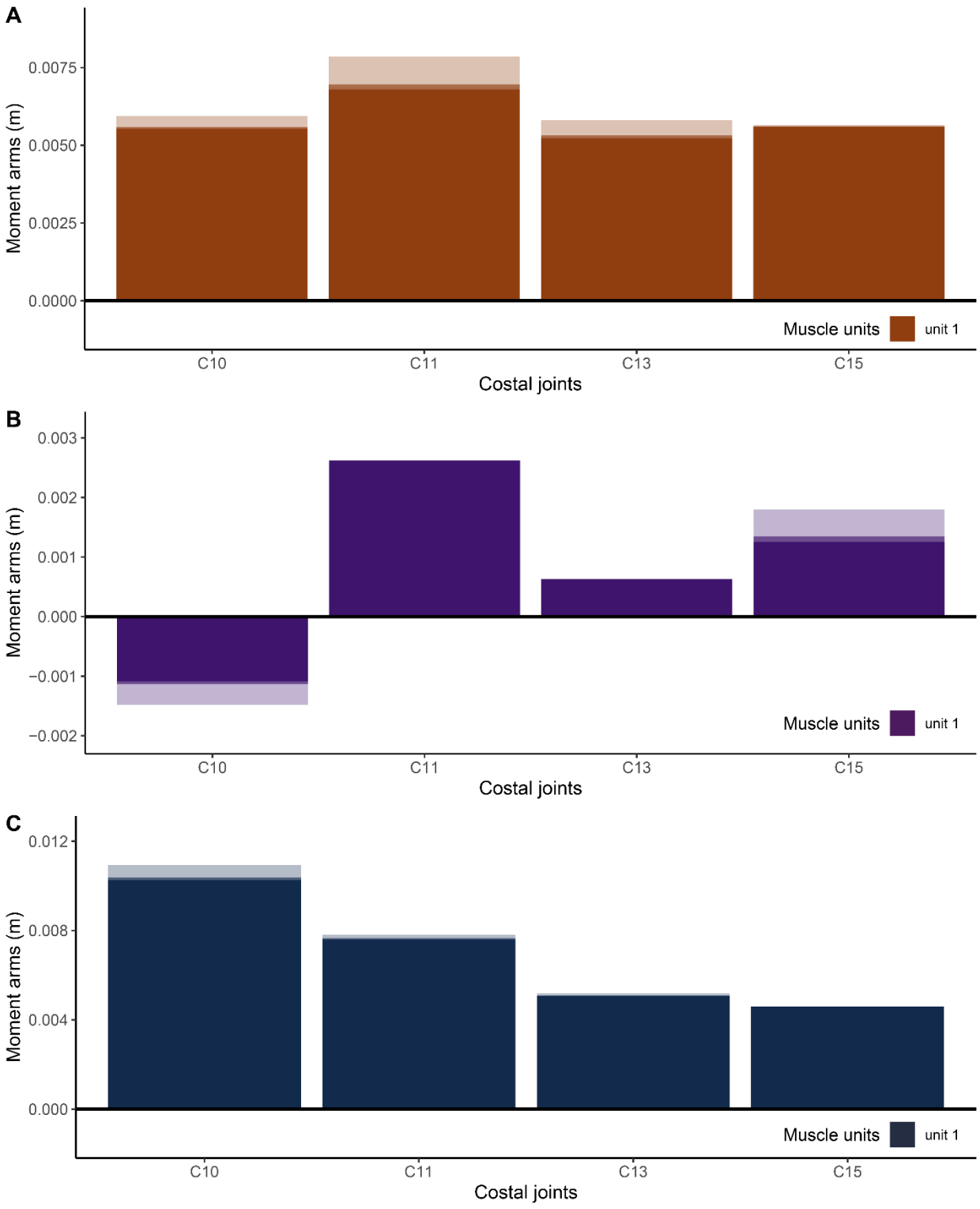
A
Moment arms (m)
0.0075
0.0050
0.0025
0.0000
Muscle units
unit 1
C10
C11
C13
C15
Costal joints
B
Moment arms (m)
0.003
0.002
0.001
0.000
−0.001
−0.002
Muscle units
unit 1
C10
C11
C13
C15
Costal joints
C
Moment arms (m)
0.012
0.008
0.004
0.000
Muscle units
unit 1
C10
C11
C13
C15
Costal joints

Figure 8.6. Maximal muscle moment arms at costal joints for mm. intercostales externi (IE) in Palaeognath model.

Bar graphs of moment arms for five units of IE estimated in Paleognath model. Moment arms about x-axis for axial rotations at first five dorsal costal joints (A); moment arms about y-axis for abduction/adduction at first five dorsal costal joints (B); moment arms about z-axis for protraction/retraction at first five dorsal costal joints (C). Colours at high and low opacity refer to moment arms estimated using plausible oROM and oROM, respectively. Abbreviations: C, costal joint; oROM, osteological range of motions.

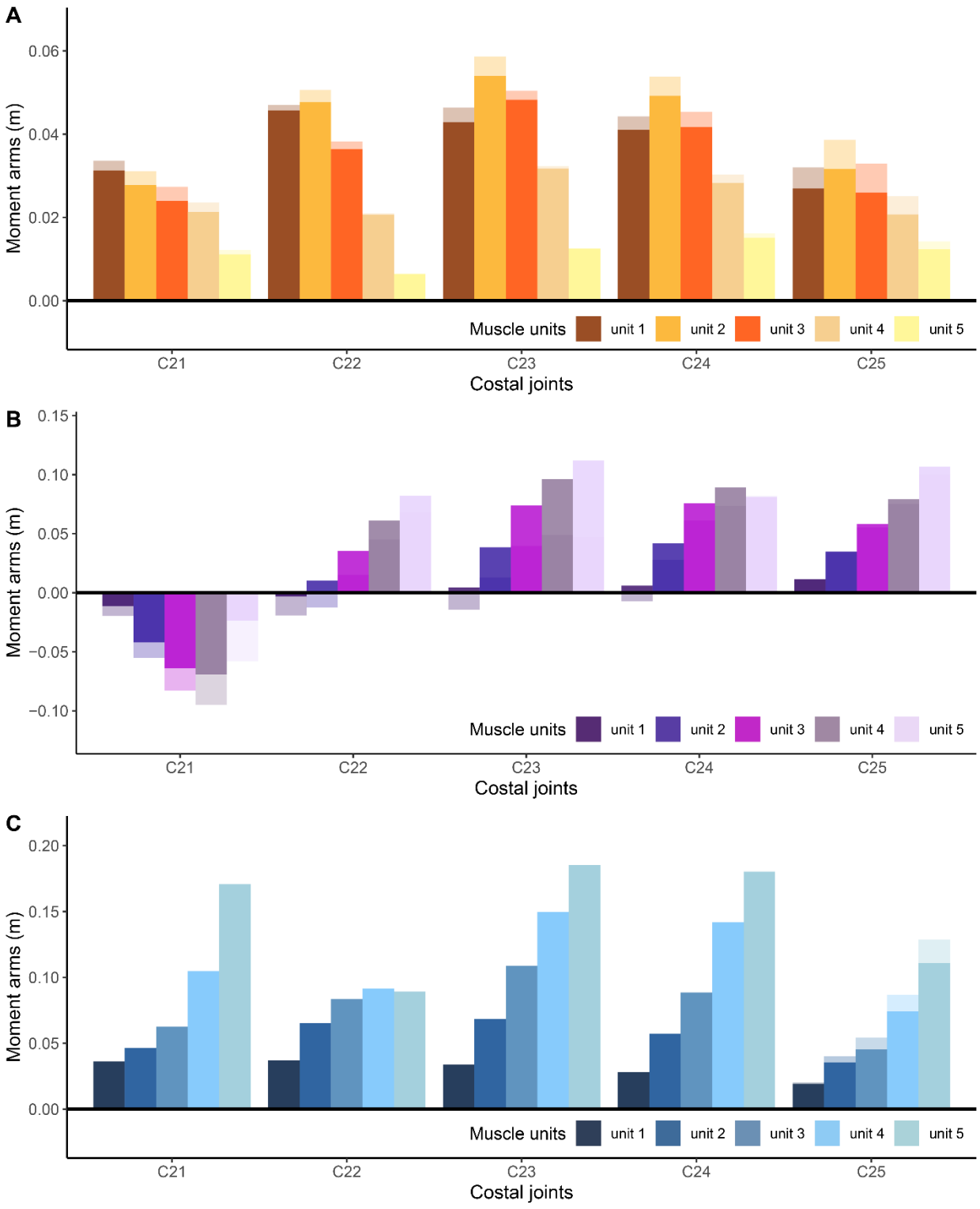
A
0.06
0.04
0.02
0.00
Moment arms (m)
Muscle units
unit 1
unit 2
unit 3
unit 4
unit 5
C21
C22
C23
C24
C25
Costal joints
B
0.15
0.10
0.05
0.00
−0.05
−0.10
Moment arms (m)
Muscle units
unit 1
unit 2
unit 3
unit 4
unit 5
C21
C22
C23
C24
C25
Costal joints
C
0.20
0.15
0.10
0.05
0.00
Moment arms (m)
Muscle units
unit 1
unit 2
unit 3
unit 4
unit 5
C21
C22
C23
C24
C25
Costal joints

Figure 8.7. Maximal muscle moment arms at costal joints for mm. intercostales externi (IE) in Crocodylian model.

Bar graphs of moment arms for four units of IE estimated in Paleognath model. Moment arms about x-axis for axial rotations at C10, C11, C13, C15 (A); moment arms about y-axis for abduction/adduction at C10, C11, C13, C15 (B); moment arms about z-axis for protraction/retraction at C10, C11, C13, C15 (C). Colours at high and low opacity refer to moment arms estimated using plausible oROM and oROM, respectively. Abbreviations: C, costal joint; oROM, osteological range of motions.

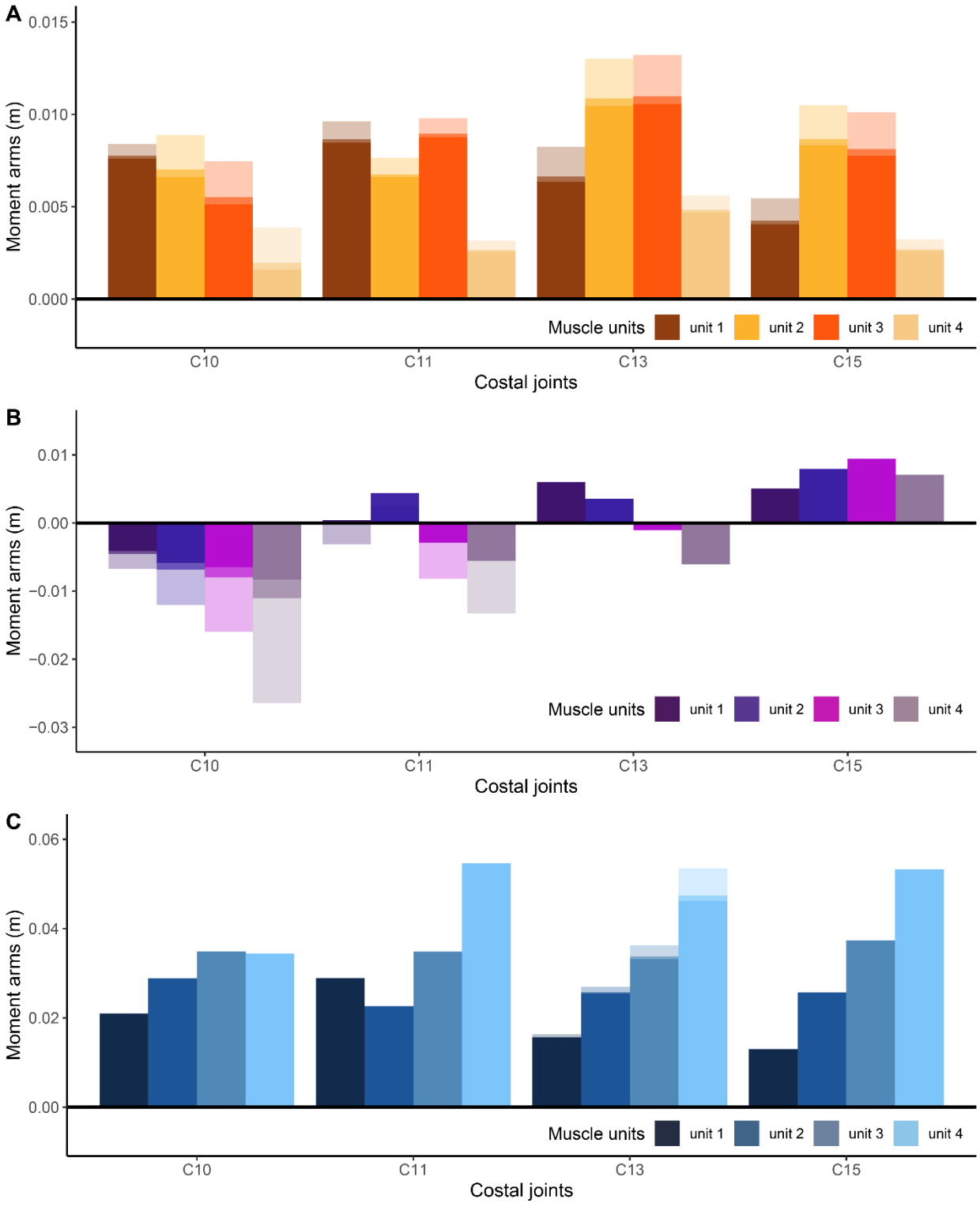
A
0.015
0.010
0.005
0.000
Moment arms (m)
Muscle units
unit 1
unit 2
unit 3
unit 4
C10
C11
C13
C15
Costal joints
B
0.01
0.00
−0.01
−0.02
−0.03
Moment arms (m)
Muscle units
unit 1
unit 2
unit 3
unit 4
C10
C11
C13
C15
Costal joints
C
0.06
0.04
0.02
0.00
Moment arms (m)
Muscle units
unit 1
unit 2
unit 3
unit 4
C10
C11
C13
C15
Costal joints

Figure 8.8. Maximal muscle moment arms at costal joints for m. appendicocostalis (APC) in Palaeognath model.

Bar graphs of moment arms for two units of IE estimated in Paleognath model. Moment arms about x-axis for axial rotations at C23, C24 and pseudo-muscle units at C23 and C24 (A); moment arms about y-axis for abduction/adduction at C23, C24 and pseudo-muscle units at C23 and C24 (B); moment arms about z-axis for protraction/retraction at C23, C24 and pseudo-muscle units at C23 and C24 (C). Colours at high and low opacity refer to moment arms estimated using plausible oROM and oROM, respectively. Abbreviations: C, costal joint; PC, pseudo-muscle unit at costal joint; oROM, osteological range of motions.

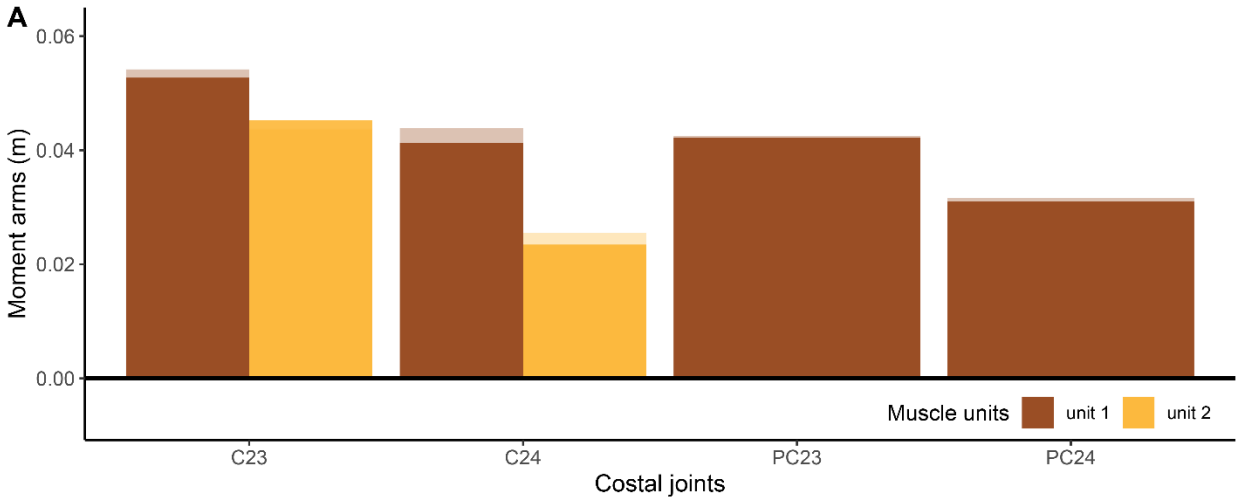
A
0.06
0.04
0.02
0.00
Moment arms (m)
Muscle units
unit 1
unit 2
C23
C24
PC23
PC24
Costal joints

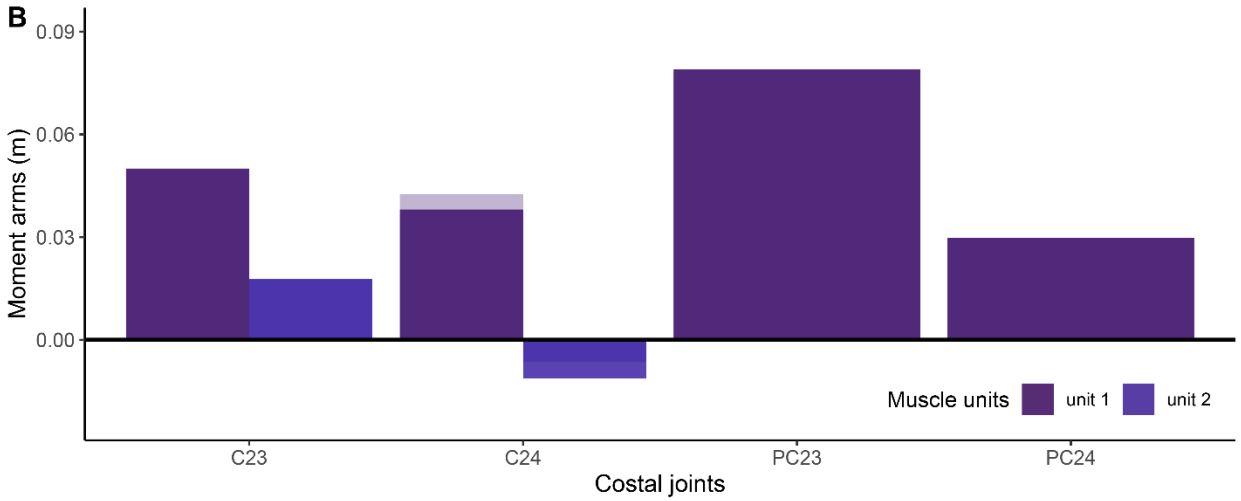
B
0.09
0.06
0.03
0.00
Moment arms (m)
Muscle units
unit 1
unit 2
C23
C24
PC23
PC24
Costal joints

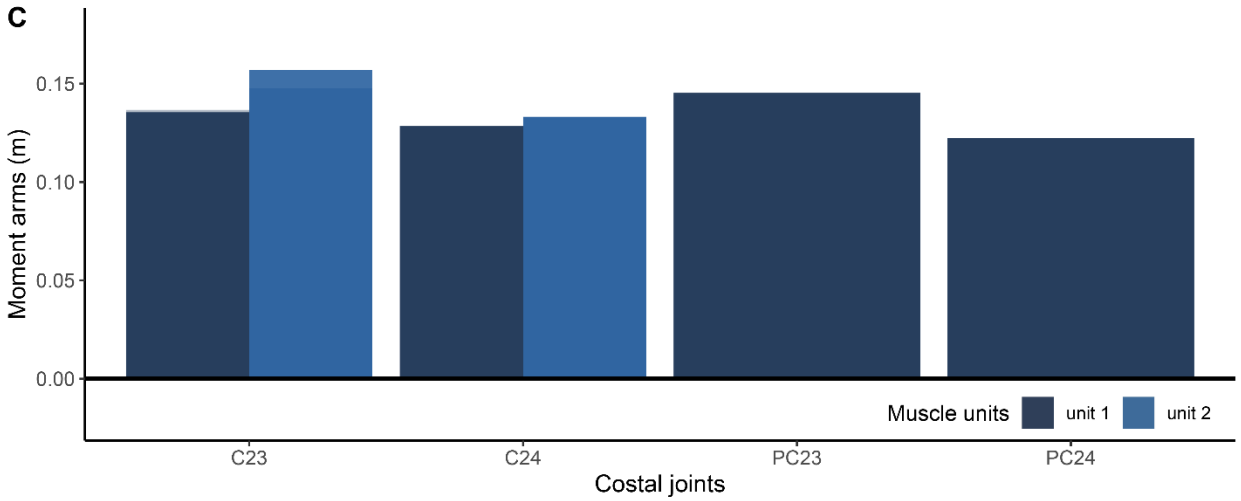
C
0.15
0.10
0.05
0.00
Moment arms (m)
Muscle units
unit 1
unit 2
C23
C24
PC23
PC24
Costal joints

Figure 8.9. Maximal muscle moment arms at costal joints and dorsal intracostal joints for m. appendicocostalis (APC) in Crocodylian model.

Bar graphs of moment arms for three units of IE estimated in Crocodylian model. Moment arms about x-axis for axial rotations at C11, C13, C15, DIR11, DIR13, and DIR16 (A); moment arms about y-axis for abduction/adduction at C11, C13, C15, DIR11, DIR13, and DIR16 (B); moment arms about z-axis for protraction/retraction at C11, C13, C15, DIR11, DIR13, and DIR16 (C). Colours at high and low opacity refer to moment arms estimated using plausible oROM and oROM, respectively. Abbreviations: C, costal joint; DIR, dorsal intracostal joint; oROM, osteological range of motions.

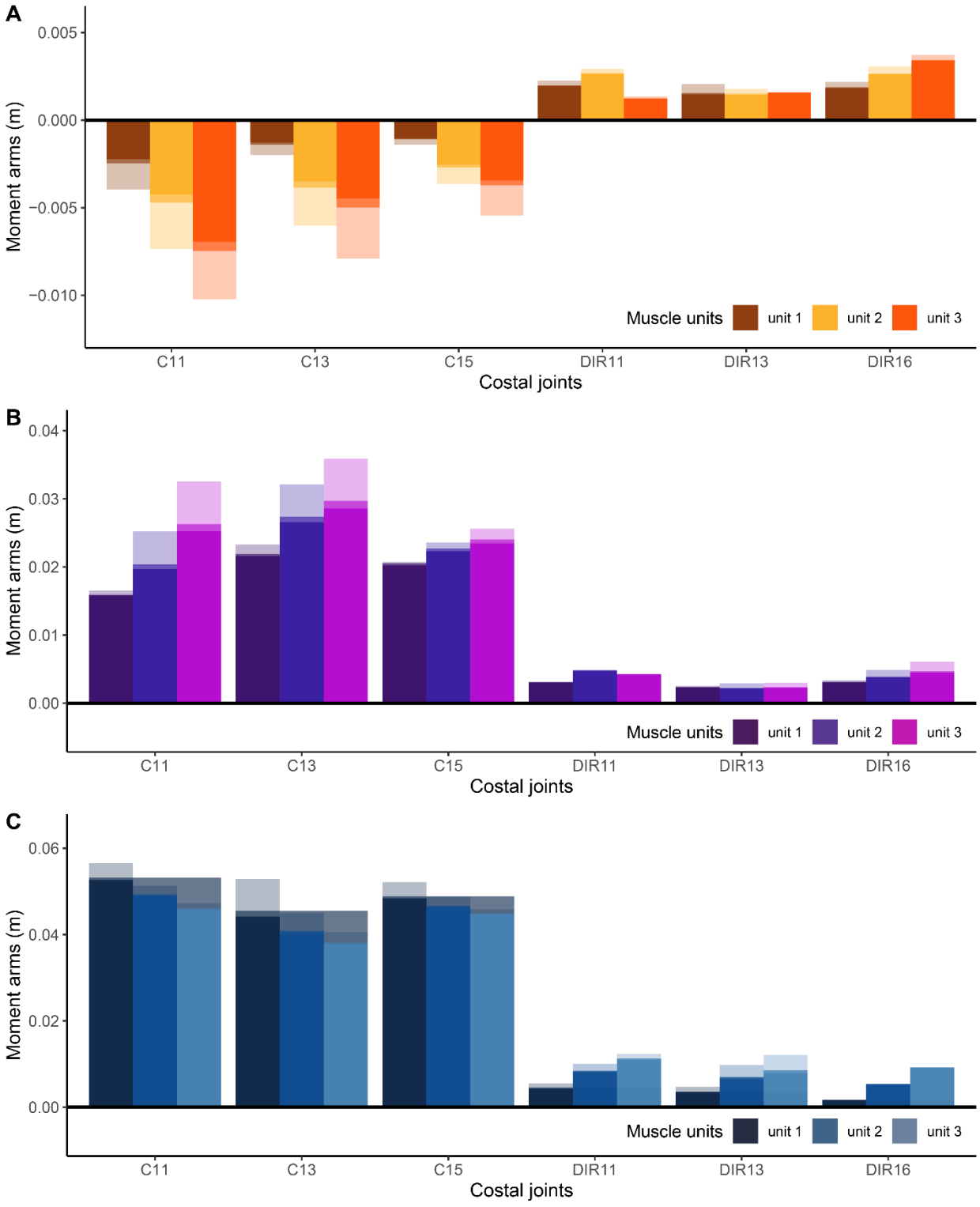
A
0.005
0.000
−0.005
−0.010
Moment arms (m)
Muscle units
unit 1
unit 2
unit 3
C11
C13
C15
DIR11
DIR13
DIR16
Costal joints
B
0.04
0.03
0.02
0.01
0.00
Moment arms (m)
Muscle units
unit 1
unit 2
unit 3
C11
C13
C15
DIR11
DIR13
DIR16
Costal joints
C
0.06
0.04
0.02
0.00
Moment arms (m)
Muscle units
unit 1
unit 2
unit 3
C11
C13
C15
DIR11
DIR13
DIR16
Costal joints

Figure 8.10. Maximal muscle moment arms at costal joints for mm. intercostales interni (II) in Palaeognath model.

Bar graphs of moment arms for five units of II estimated in Paleognath model. Moment arms about x-axis for axial rotations at first four dorsal costal joints (A); moment arms about y-axis for abduction/adduction at first four dorsal costal joints (B); moment arms about z-axis for protraction/retraction at first four dorsal costal joints (C). Colours at high and low opacity refer to moment arms estimated using plausible oROM and oROM, respectively. Abbreviations: C, costal joint; oROM, osteological range of motions.

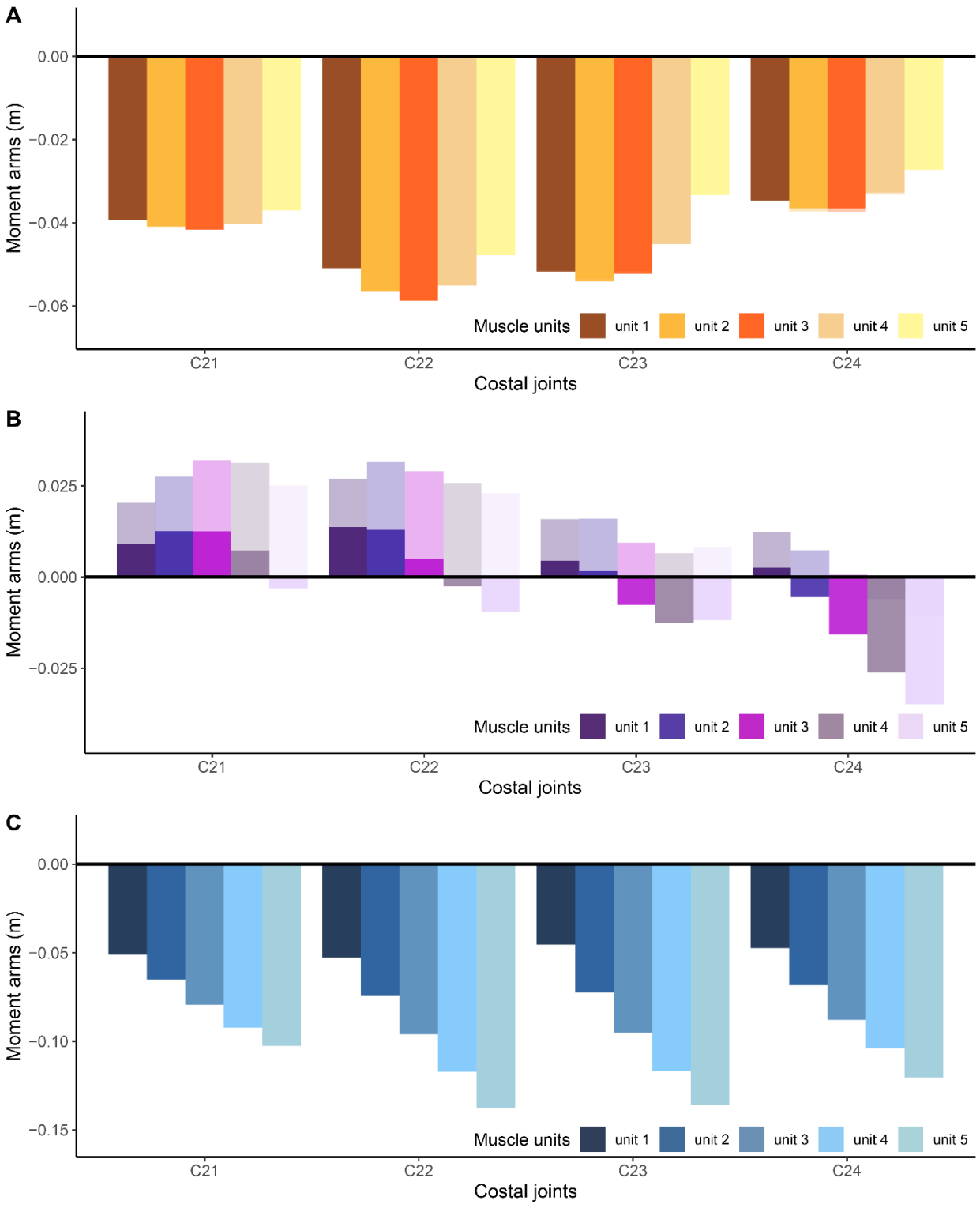
A
0.00
−0.02
−0.04
−0.06
Moment arms (m)
Muscle units
unit 1
unit 2
unit 3
unit 4
unit 5
C21
C22
C23
C24
Costal joints
B
0.025
0.000
−0.025
Moment arms (m)
Muscle units
unit 1
unit 2
unit 3
unit 4
unit 5
C21
C22
C23
C24
Costal joints
C
0.00
−0.05
−0.10
−0.15
Moment arms (m)
Muscle units
unit 1
unit 2
unit 3
unit 4
unit 5
C21
C22
C23
C24
Costal joints

Figure 8.11. Maximal muscle moment arms at costal joints and dorsal intracostal joints for mm. intercsotalis internus (II) in Crocodylian model.

Bar graphs of moment arms for five units of II estimated in Crocodylian model. Moment arms about x-axis for axial rotations at C11, C13, C15, DIR11, DIR13, and DIR16 (A); moment arms about y-axis for abduction/adduction at C11, C13, C15, DIR11, DIR13, and DIR16 (B); moment arms about z-axis for protraction/retraction at C11, C13, C15, DIR11, DIR13, and DIR16 (C). Colours at high and low opacity refer to moment arms estimated using plausible oROM and oROM, respectively. Abbreviations: C, costal joint; DIR, dorsal intracostal joint; oROM, osteological range of motions.

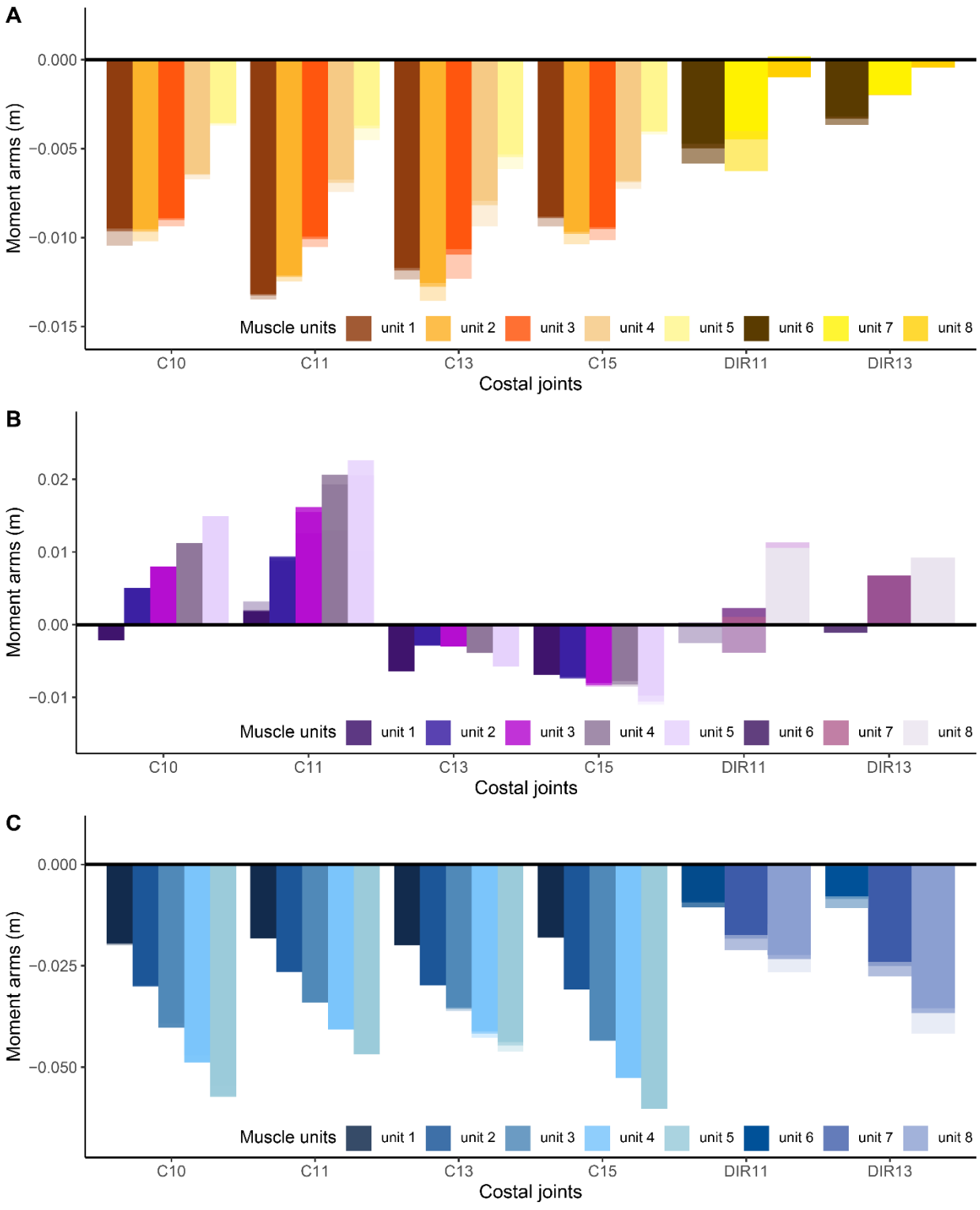
A
0.000
−0.005
−0.010
−0.015
Moment arms (m)
Muscle units
unit 1
unit 2
unit 3
unit 4
unit 5
unit 6
unit 7
unit 8
C10
C11
C13
C15
DIR11
DIR13
Costal joints
B
0.02
0.01
0.00
−0.01
Moment arms (m)
Muscle units
unit 1
unit 2
unit 3
unit 4
unit 5
unit 6
unit 7
unit 8
C10
C11
C13
C15
DIR11
DIR13
Costal joints
C
0.000
−0.025
−0.050
Moment arms (m)
Muscle units
unit 1
unit 2
unit 3
unit 4
unit 5
unit 6
unit 7
unit 8
C10
C11
C13
C15
DIR11
DIR13
Costal joints

Figure 8.12. Maximal muscle moment arms at intracostal joints for m. costosternalis (COT) in Palaeognath model.

Bar graphs of moment arms for COT estimated in Paleognath model. Moment arms about x-axis for axial rotations at first three intracostal joints (A); moment arms about y-axis for abduction/adduction at first three intracostal joints (B); moment arms about z-axis for protraction/retraction at first three intracostal joints (C). Colours at high and low opacity refer to moment arms estimated using plausible oROM and oROM, respectively. Abbreviations: IR, intracostal joint; oROM, osteological range of motions.

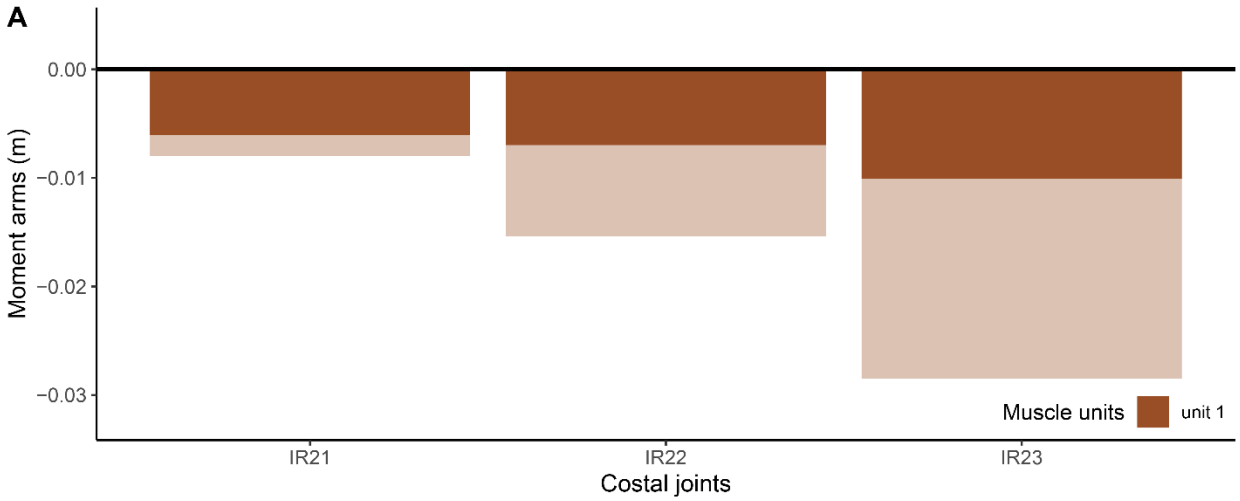
A
0.00
−0.01
−0.02
−0.03
Moment arms (m)
Muscle units
unit 1
IR21
IR22
IR23
Costal joints

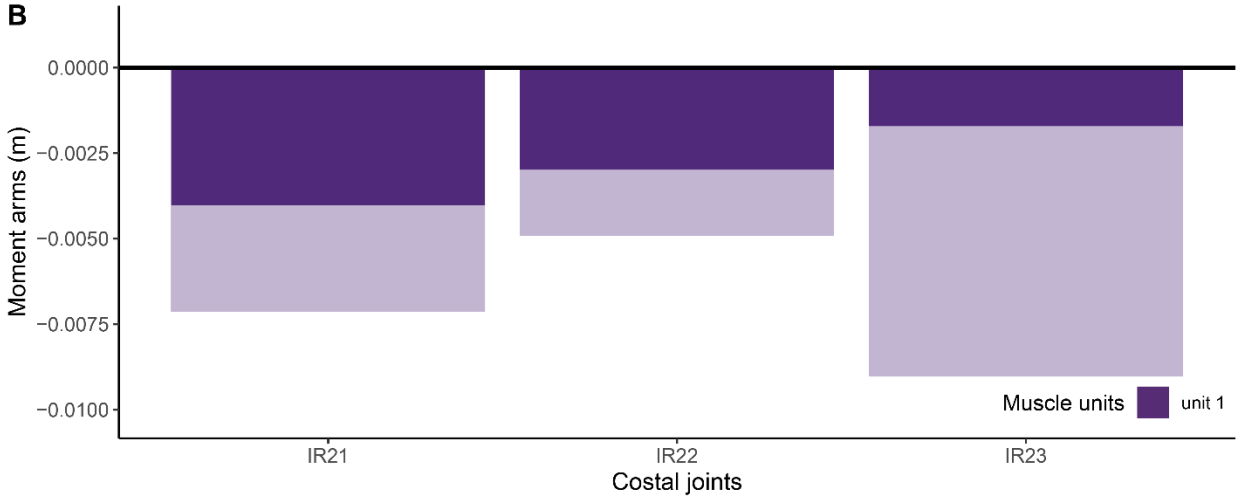
B
0.0000
−0.0025
−0.0050
−0.0075
−0.0100
Moment arms (m)
Muscle units
unit 1
IR21
IR22
IR23
Costal joints

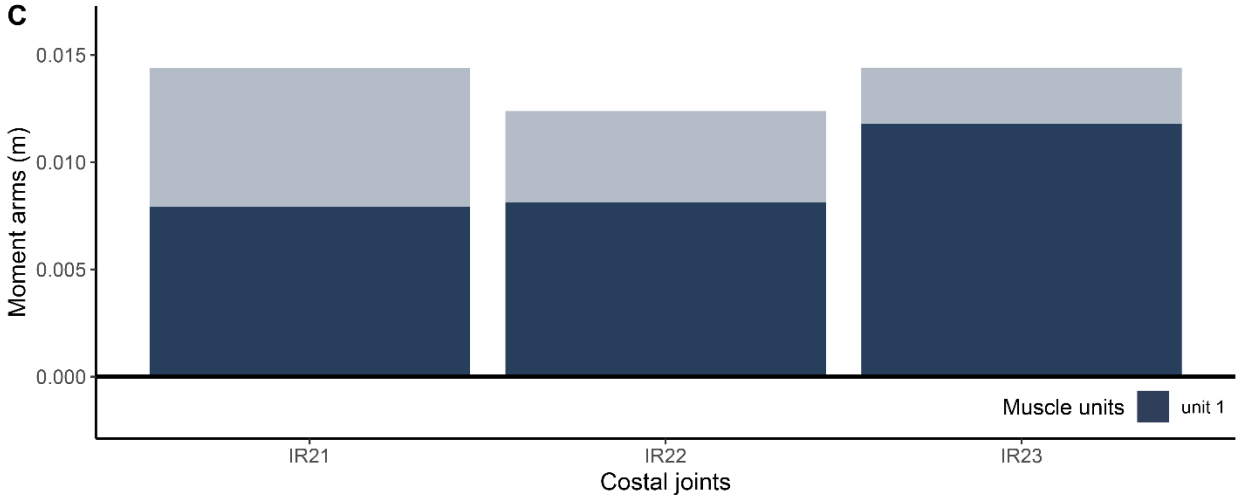
C
0.015
0.010
0.005
0.000
Moment arms (m)
Muscle units
unit 1
IR21
IR22
IR23
Costal joints

Figure 8.13. Maximal muscle moment arms of intracostal joints for m. subcostalis (SC) in Palaeognath model.

Bar graphs of moment arms for SC estimated in Paleognath model. Moment arms about x-axis for axial rotations at first five intracostal joints (A); moment arms about y-axis for abduction/adduction at first five intracostal joints (B); moment arms about z-axis for protraction/retraction at first five intracostal joints (C). Colours at high and low opacity refer to moment arms estimated using plausible oROM and oROM, respectively. Abbreviations: IR, intracostal joint; oROM, osteological range of motions.

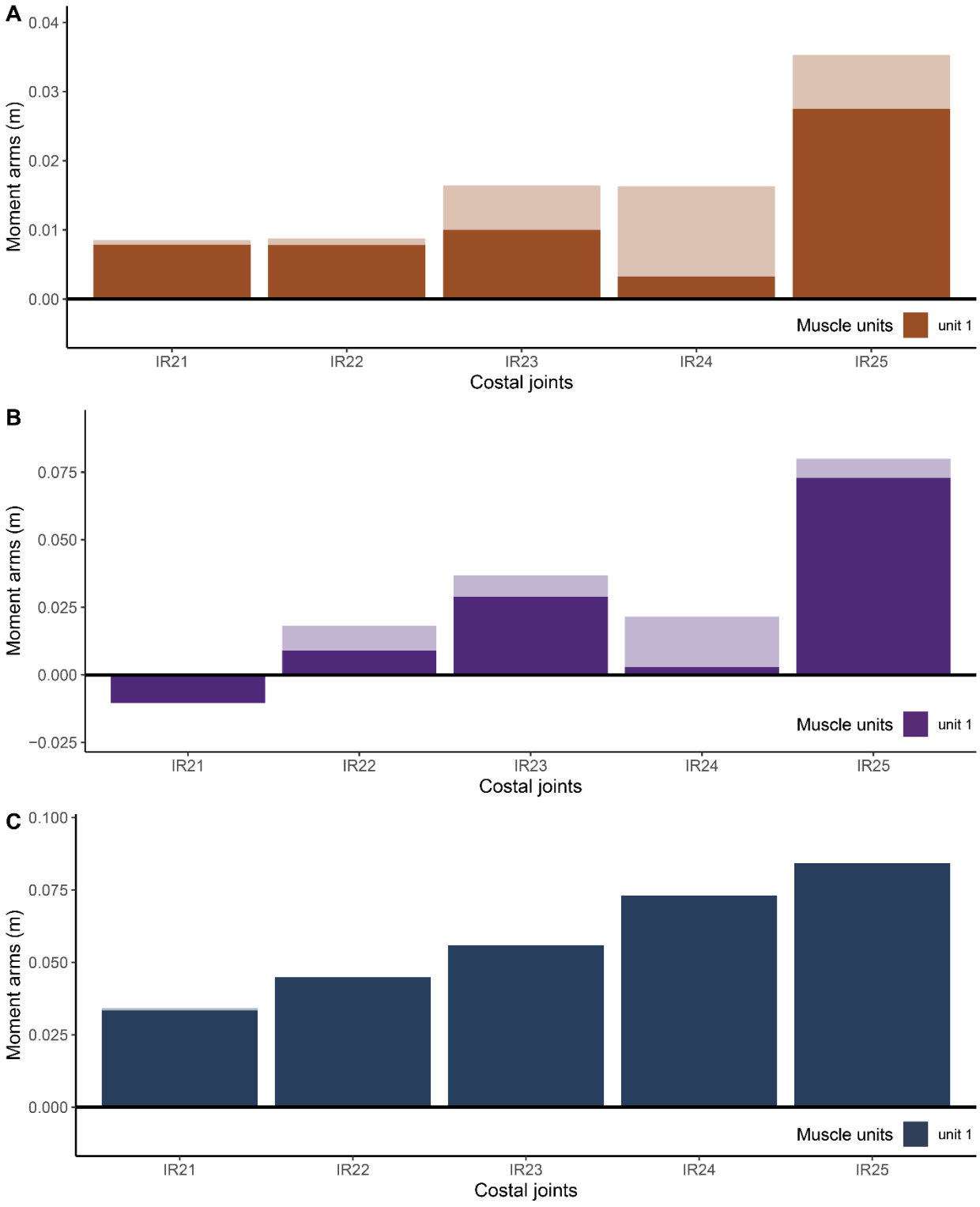
A
0.04
0.03
0.02
0.01
0.00
Moment arms (m)
Muscle units
unit 1
IR21
IR22
IR23
IR24
IR25
Costal joints
B
0.075
0.050
0.025
0.000
−0.025
Moment arms (m)
Muscle units
unit 1
IR21
IR22
IR23
IR24
IR25
Costal joints
C
0.100
0.075
0.050
0.025
0.000
Moment arms (m)
Muscle units
unit 1
IR21
IR22
IR23
IR24
IR25
Costal joints

Figure 8.14. Maximal muscle moment arms of ventral intracostal joints for m. subcostalis (SC) in Crocodylian model.

Bar graphs of moment arms for SC estimated in Crocodylian model. Moment arms about x-axis for axial rotations at VIR11, VIR13, and VIR15 (A); moment arms about y-axis for abduction/adduction at VIR11, VIR13, and VIR15 (B); moment arms about z-axis for protraction/retraction at VIR11, VIR13, and VIR15 (C). Colours at high and low opacity refer to moment arms estimated using plausible oROM and oROM, respectively. Abbreviations: VIR, ventral intracostal joint; oROM, osteological range of motions.

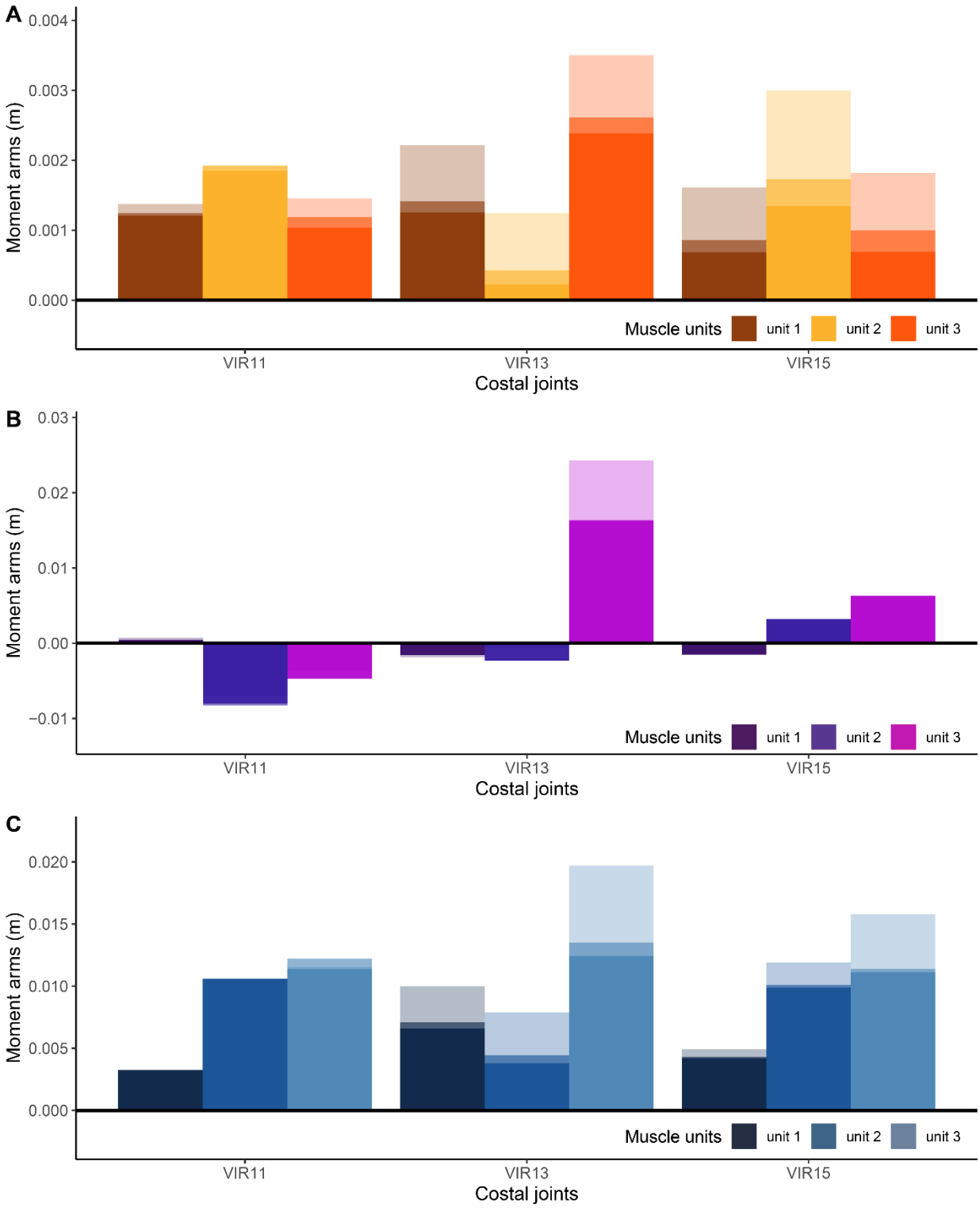
A
0.004
0.003
0.002
0.001
0.000
Moment arms (m)
Muscle units
unit 1
unit 2
unit 3
VIR11
VIR13
VIR15
Costal joints
B
0.03
0.02
0.01
0.00
−0.01
Moment arms (m)
Muscle units
unit 1
unit 2
unit 3
VIR11
VIR13
VIR15
Costal joints
C
0.020
0.015
0.010
0.005
0.000
Moment arms (m)
Muscle units
unit 1
unit 2
unit 3
VIR11
VIR13
VIR15
Costal joints

Figure 8.15. Muscle moment arms at C15 for m. levator costarum (LC) in Crocodylian model.

Changes of moment arms throughout a ventilatory cycle at C15 about x-axis for axial rotation from oROM (A), plausible oROM in Crocodylian W model (B), and plausible oROM in Crocodylian WOD model (C); Changes of moment arms throughout a ventilatory cycle at C15 about y-axis for abduction/adduction from oROM (E), plausible oROM in Crocodylian W model (F), and plausible oROM in Crocodylian WOD model (G); Changes of moment arms throughout a ventilatory cycle at C15 about z-axis for protraction/retraction from oROM (I), plausible oROM in Crocodylian W model (K), and plausible oROM in Crocodylian WOD model (L); Bar graphs of maximal moment arms for LC estimated in Crocodylian model (D, H, M). Colours at high and low opacity refer to moment arms estimated using plausible oROM and oROM, respectively. Abbreviations: C, ventral costal joint; oROM, osteological range of motions.

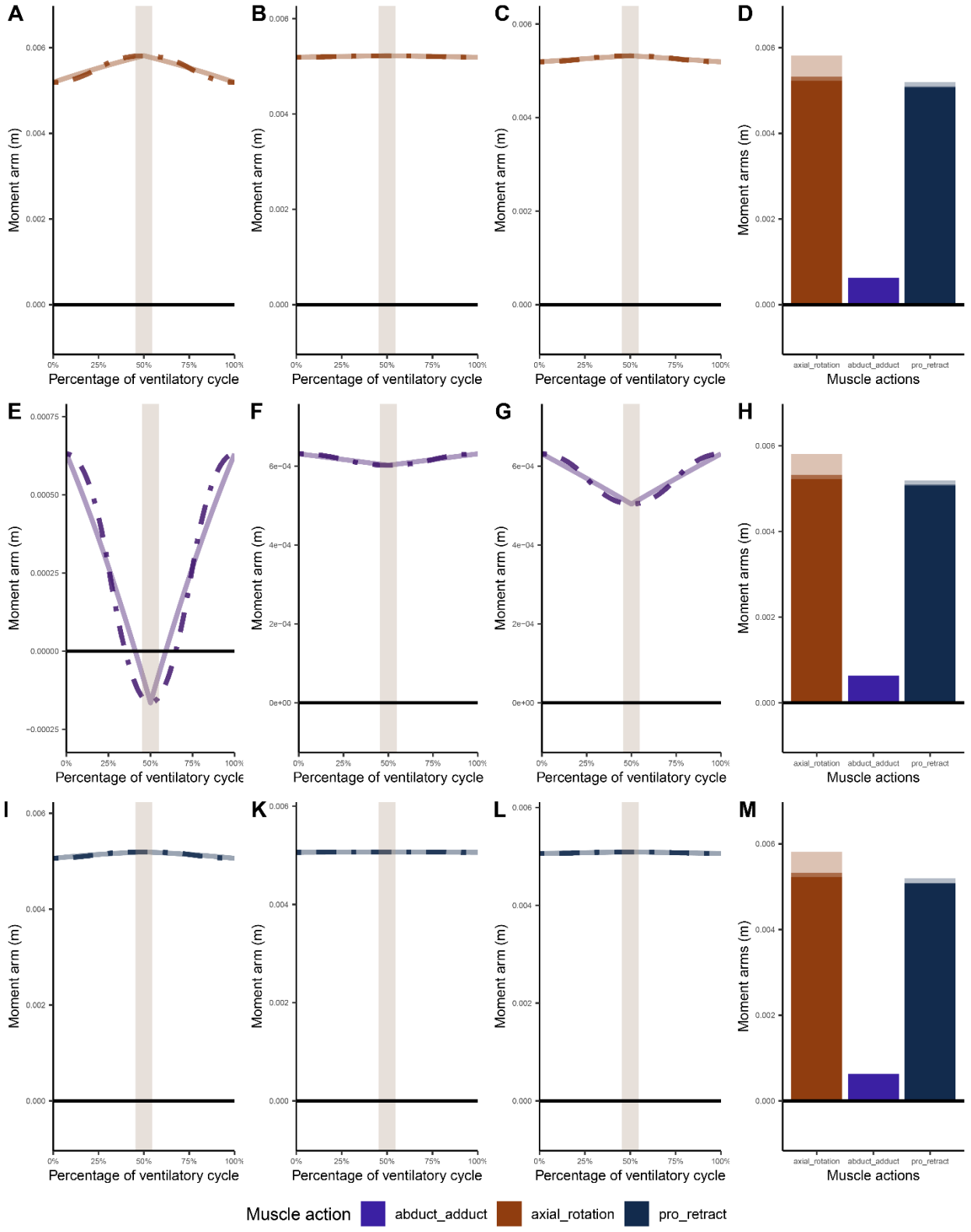
A
B
C
D
E
F
G
H
I
K
L
M
Moment arm (m)
Moment arms (m)
Percentage of ventilatory cycle
Muscle actions
axial_rotation
abduct_adduct
pro_retract
Muscle action

Figure 8.16. Muscle moment arms at C13 for combined effects of ventral part of m. iliocostalis (del_vLC) in Crocodylian model.

Changes of moment arms throughout a ventilatory cycle at C13 about x-axis for axial rotation from oROM (A), plausible oROM in Crocodylian W model (B), and plausible oROM in Crocodylian WOD model (C); Changes of moment arms throughout a ventilatory cycle at C13 about y-axis for abduction/adduction from oROM (E), plausible oROM in Crocodylian W model (F), and plausible oROM in Crocodylian WOD model (G); Changes of moment arms throughout a ventilatory cycle at C13 about z-axis for protraction/retraction from oROM (I), plausible oROM in Crocodylian W model (K), and plausible oROM in Crocodylian WOD model (L); Bar graphs of maximal moment arms for del_vIC estimated in Crocodylian model (D, H, M). Colours at high and low opacity refer to moment arms estimated using plausible oROM and oROM, respectively. Abbreviations: C, costal joint; oROM, osteological range of motions.

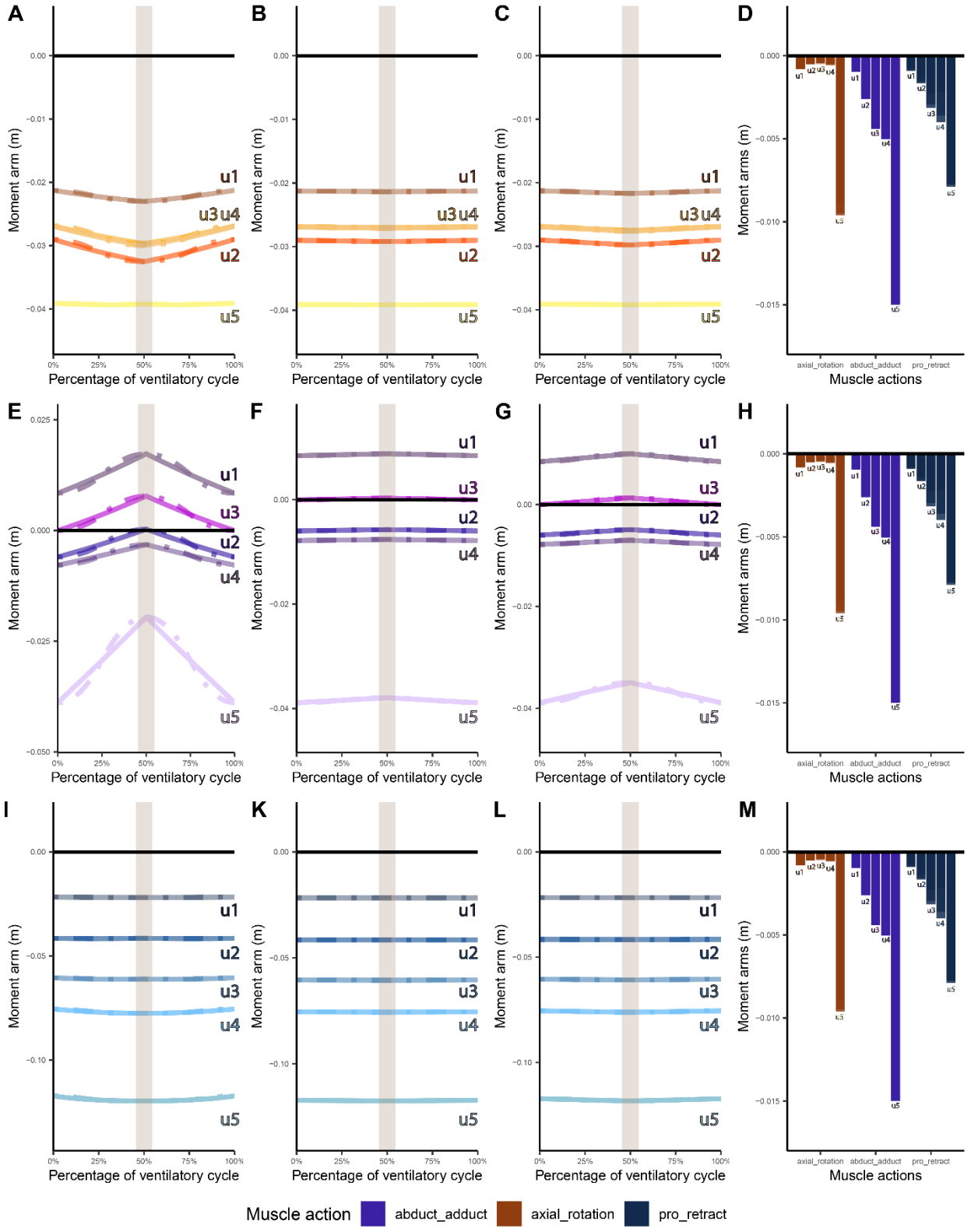
A
B
C
D
E
F
G
H
I
K
L
M
Moment arm (m)
Moment arms (m)
Percentage of ventilatory cycle
Muscle actions
axial_rotation
abduct_adduct
pro_retract
u1
u2
u3
u4
u5
u3 u4
Muscle action
abduct_adduct
axial_rotation
pro_retract

Figure 8.17. Muscle moment arms at C23 for combined effects of mm. intercostales externi (del_IE) in Palaeognath model.

Changes of moment arms throughout a ventilatory cycle at C23 about x-axis for axial rotation from oROM (A) and plausible oROM (B); Changes of moment arms throughout a ventilatory cycle at C23 about y-axis for abduction/adduction from oROM (D) and plausible oROM (E); Changes of moment arms throughout a ventilatory cycle at C23 about z-axis for protraction/retraction from oROM (G) and plausible oROM (H); Bar graphs of maximal moment arms for del_IE estimated in Palaeognath model (C, F, I). Colours at high and low opacity refer to moment arms estimated using plausible oROM and oROM, respectively. Abbreviations: C, costal joint; oROM, osteological range of motions.

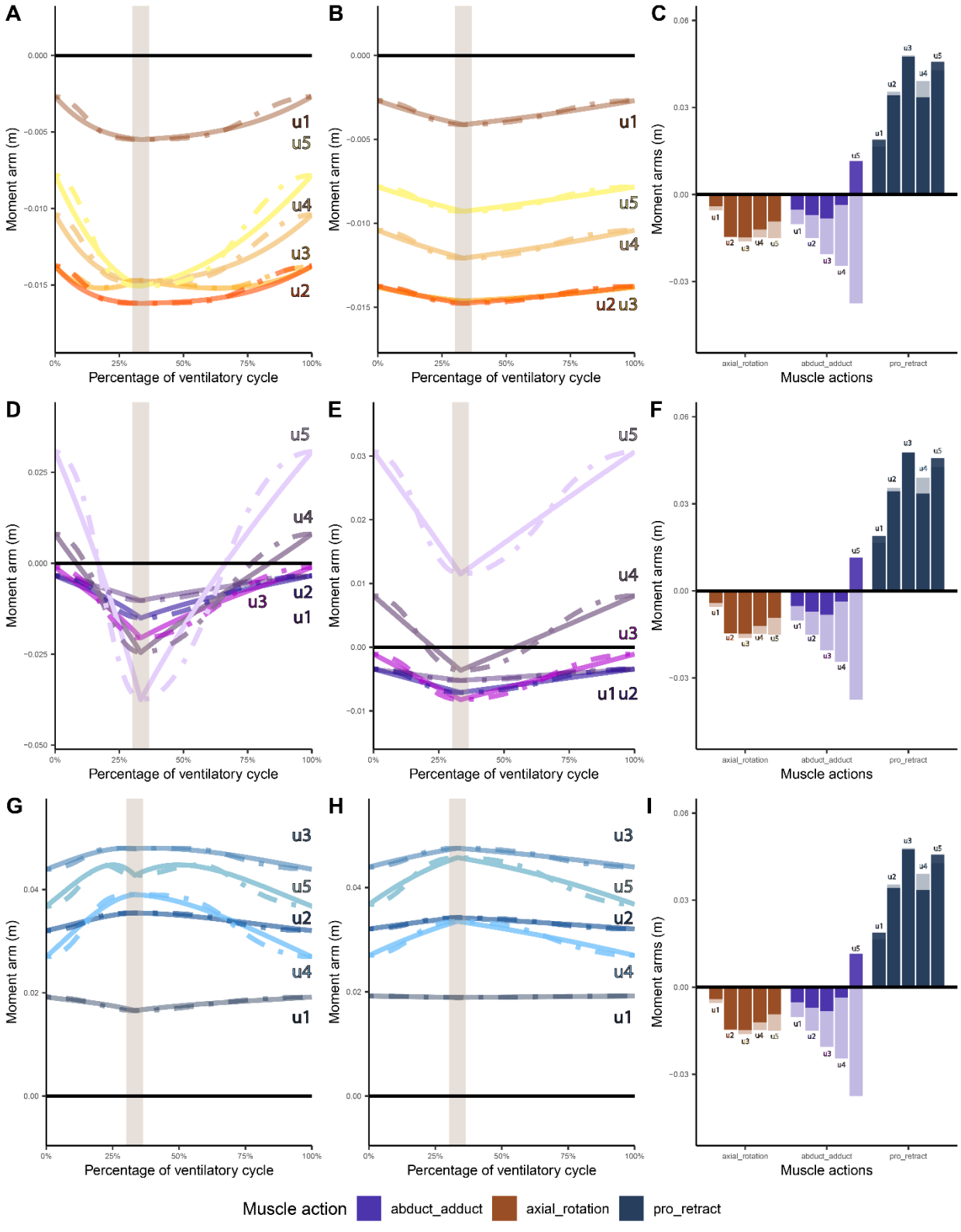
A
B
C
D
E
F
G
H
I
Moment arm (m)
Moment arms (m)
Percentage of ventilatory cycle
Muscle actions
axial_rotation
abduct_adduct
pro_retract
u1
u2
u3
u4
u5
Muscle action
abduct_adduct
axial_rotation
pro_retract

Figure 8.18. Muscle moment arms at C13 for combined effects of mm. intercostales externi (del_IE) in Crocodylian model.

Changes of moment arms throughout a ventilatory cycle at C13 about x-axis for axial rotation from oROM (A), plausible oROM in Crocodylian W model (B), and plausible oROM in Crocodylian WOD model (C); Changes of moment arms throughout a ventilatory cycle at C13 about y-axis for abduction/adduction from oROM (E), plausible oROM in Crocodylian W model (F), and plausible oROM in Crocodylian WOD model (G); Changes of moment arms throughout a ventilatory cycle at C13 about z-axis for protraction/retraction from oROM (I), plausible oROM in Crocodylian W model (K), and plausible oROM in Crocodylian WOD model (L); Bar graphs of maximal moment arms for del_IE estimated in Crocodylian model (D, H, M). Colours at high and low opacity refer to moment arms estimated using plausible oROM and oROM, respectively. Abbreviations: C, costal joint; oROM, osteological range of motions.

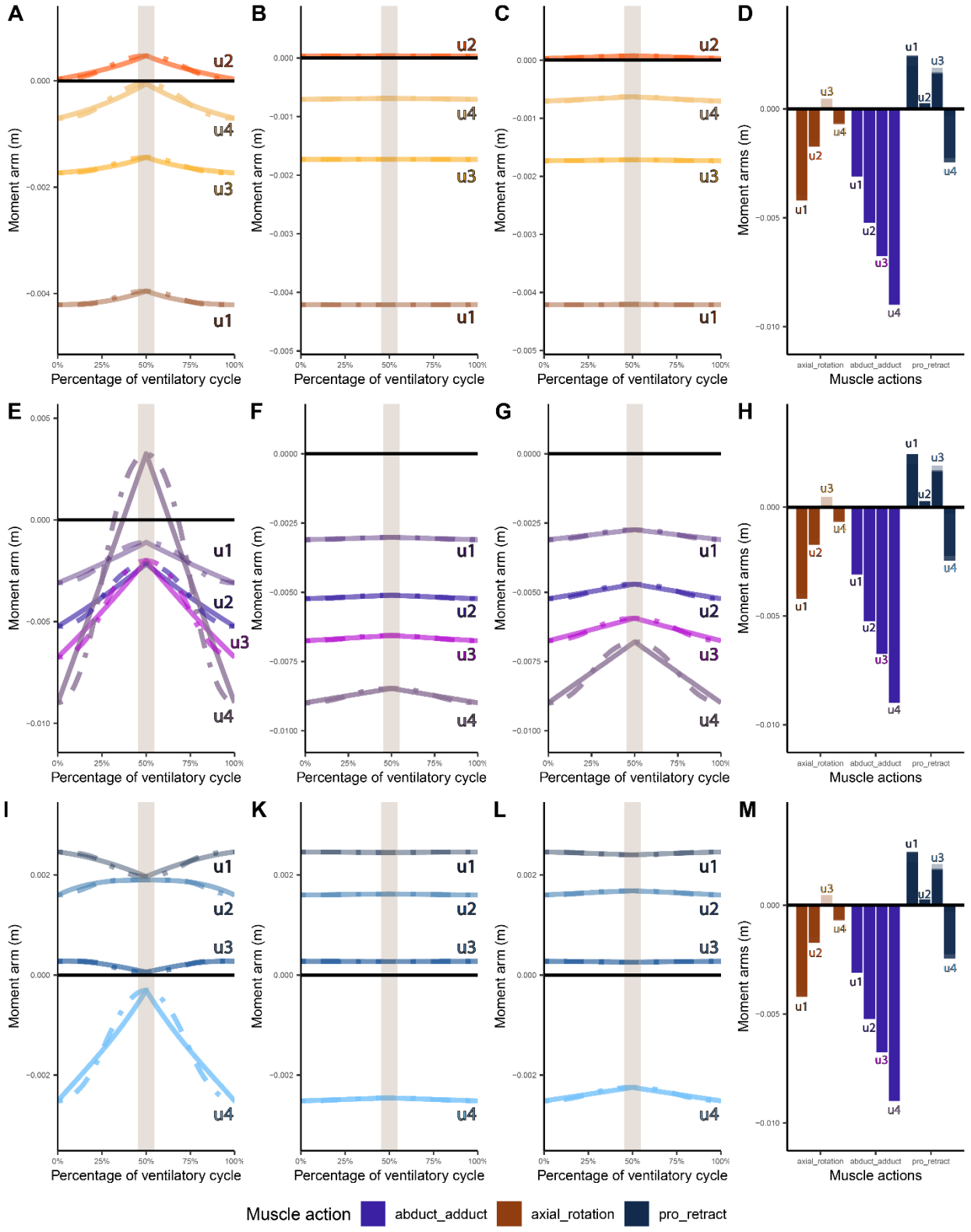
A
B
C
D
E
F
G
H
I
K
L
M
Moment arm (m)
Moment arms (m)
Percentage of ventilatory cycle
Muscle actions
axial_rotation
abduct_adduct
pro_retract
u1
u2
u3
u4
Muscle action
abduct_adduct
axial_rotation
pro_retract

Figure 8.19. Muscle moment arms at C23 for combined effects of mm. intercostales interni (del_II) in Palaeognath model.

Changes of moment arms throughout a ventilatory cycle at C23 about x-axis for axial rotation from oROM (A) and plausible oROM (B); Changes of moment arms throughout a ventilatory cycle at C23 about y-axis for abduction/adduction from oROM (D) and plausible oROM (E); Changes of moment arms throughout a ventilatory cycle at C23 about z-axis for protraction/retraction from oROM (G) and plausible oROM (H); Bar graphs of maximal moment arms for del_II estimated in Palaeognath model (C, F, I). Colours at high and low opacity refer to moment arms estimated using plausible oROM and oROM, respectively. Abbreviations: C, costal joint; oROM, osteological range of motions.

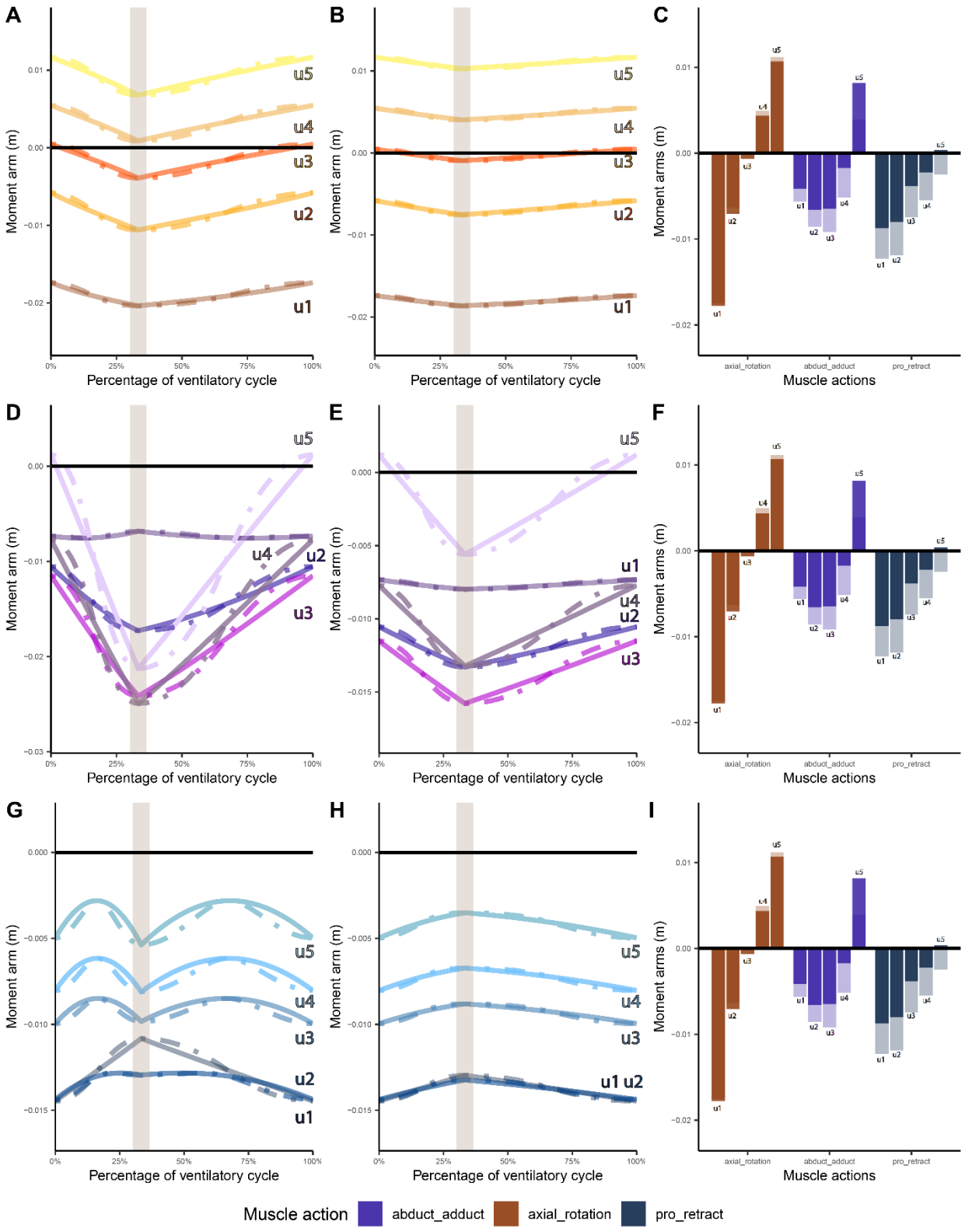
A
B
C
D
E
F
G
H
I
Moment arm (m)
Moment arms (m)
Percentage of ventilatory cycle
Muscle actions
axial_rotation
abduct_adduct
pro_retract
u1
u2
u3
u4
u5
Muscle action
abduct_adduct
axial_rotation
pro_retract

Figure 8.20. Muscle moment arms at C13 for combined effects of mm. intercostales interni (del_II) in Crocodylian model.

Changes of moment arms throughout a ventilatory cycle at C13 about x-axis for axial rotation from oROM (A), plausible oROM in Crocodylian W model (B), and plausible oROM in Crocodylian WOD model (C); Changes of moment arms throughout a ventilatory cycle at C13 about y-axis for abduction/adduction from oROM (E), plausible oROM in Crocodylian W model (F), and plausible oROM in Crocodylian WOD model (G); Changes of moment arms throughout a ventilatory cycle at C13 about z-axis for protraction/retraction from oROM (I), plausible oROM in Crocodylian W model (K), and plausible oROM in Crocodylian WOD model (L); Bar graphs of maximal moment arms for del_II estimated in Crocodylian model (D, H, M). Colours at high and low opacity refer to moment arms estimated using plausible oROM and oROM, respectively. Abbreviations: C, costal joint; oROM, osteological range of motions.

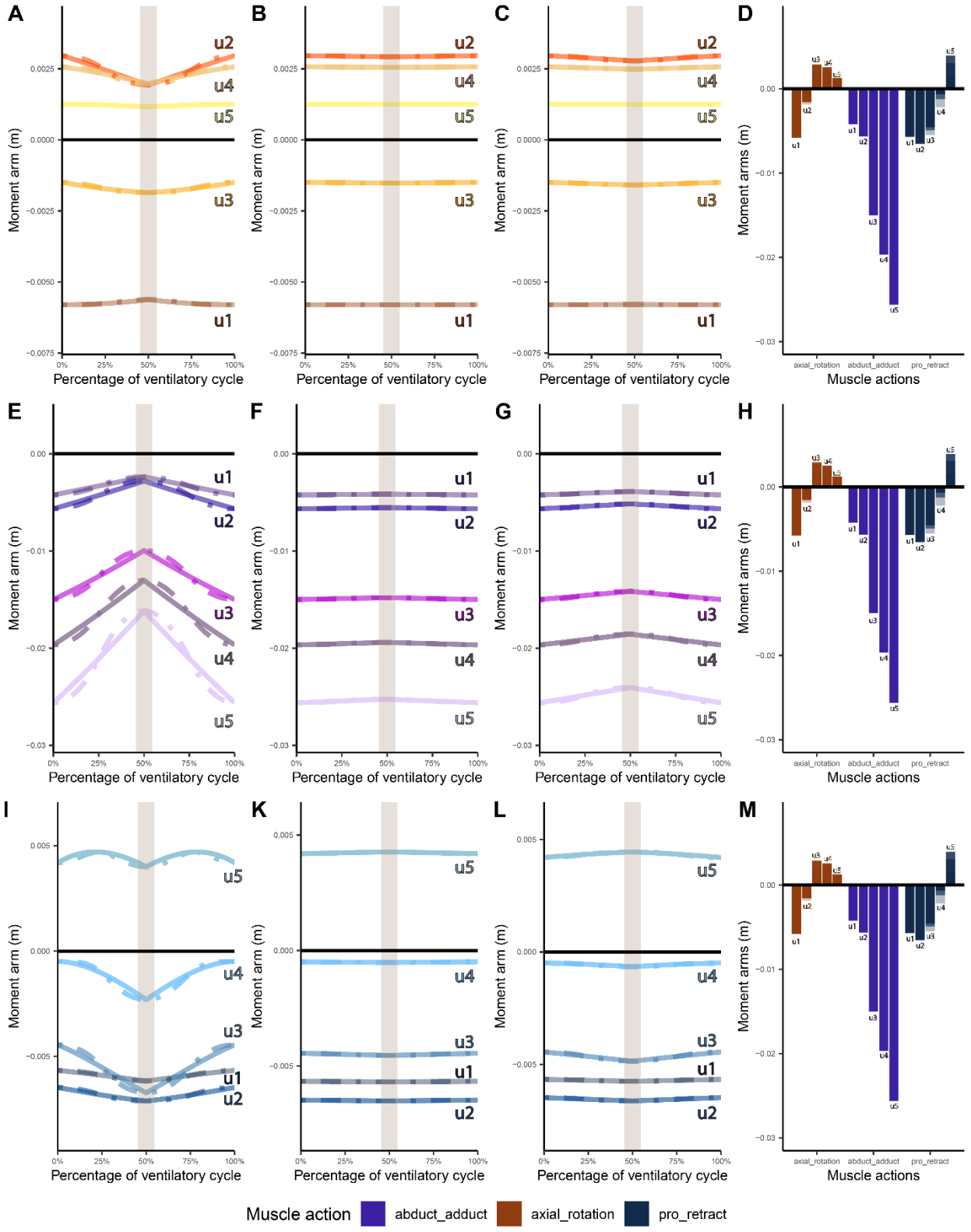
A
B
C
D
E
F
G
H
I
K
L
M
Moment arm (m)
Moment arms (m)
Percentage of ventilatory cycle
Muscle actions
axial_rotation
abduct_adduct
pro_retract
u1
u2
u3
u4
u5
Muscle action
abduct_adduct
axial_rotation
pro_retract

8.5 Literature Cited

Baier, D.B. and Gatesy, S.M. 2013. Three-dimensional skeletal kinematics of the shoulder girdle and forelimb in walking *Alligator*. *Journal of Anatomy* 223(5), pp. 462–473. doi: 10.1111/joa.12102.

Baumel, J.J., King, A.S., Breazile, J.E., Evans, H.E. and Vanden Berge, J.C. 1993. *Handbook of avian anatomy: Nomina anatomica avium*. second edition. Cambridge: Nuttall Ornithological Club.

Baumel, J.J., Wilson, J.A. and Bergren, D.R. 1990. The ventilatory movements of the avian pelvis and tail: function of the muscles of the tail region of the pigeon (*Columba livia*). *Journal of Experimental Biology* 151, pp. 263–277.

Benton, M.J. 2014. *Vertebrate Palaeontology*. John Wiley & Sons.

Berger, M., Roy, O.Z. and Hart, J.S. 1970. The co-ordination between respiration and wing beats in birds. *Zeitschrift für vergleichende Physiologie* 66(2), pp. 190–200. doi: 10.1007/BF00297778.

Boggs, D.F. 1997. Coordinated control of respiratory pattern during locomotion in birds. *American Zoologist* 37(1), pp. 41–53. doi: 10.1093/icb/37.1.41.

Boggs, D.F., Jenkins, F.A. and Dial, K.P. 1997a. The effects of the wingbeat cycle on respiration in black-billed magpies (pica pica). *The Journal of Experimental Biology* 200, pp. 1403–1412.

Boggs, D.F., Seveyka, J.J., Kilgore, D.L. and Dial, K.P. 1997b. Coordination of Respiratory Cycles with Wingbeat Cycles in the Black-Billed Magpie (*Pica pica*). *The Journal of Experimental Biology* 200, pp. 1413–1420.

Brackenbury, J.H., Gleeson, M. and Avery, P. 1982. Respiration in exercising fowl. III. ventilation. *Journal of Experimental Biology* 96(1), pp. 315–324. doi: 10.1242/jeb.96.1.315.

Brainerd, E.L., Baier, D.B., Gatesy, S.M., Hedrick, T.L., Metzger, K.A., Gilbert, S.L. and Crisco, J.J. 2010. X-ray reconstruction of moving morphology (XROMM): precision, accuracy and applications in comparative biomechanics research. *Journal of Experimental Zoology Part A: Ecological Genetics and Physiology* 9999A, p. n/a-n/a. doi: 10.1002/jez.589.

Brochu, C.A. 2003. Osteology of *Tyrannosaurus Rex*: Insights from a nearly complete skeleton and high-resolution computed tomographic analysis of the skull. *Journal of Vertebrate Paleontology* 22(sup 4), pp. 1–138. doi: 10.1080/02724634.2003.10010947.

Brocklehurst, R.J., Moritz, S., Codd, J., Sellers, W.I. and Brainerd, E.L. 2017. Rib kinematics during lung ventilation in the American alligator (*Alligator mississippiensis*): an XROMM analysis. *Journal of Experimental Biology* 220(17), pp. 3181–3190. doi: 10.1242/jeb.156166.

Brocklehurst, R.J., Moritz, S., Codd, J., Sellers, W.I. and Brainerd, E.L. 2019. XROMM kinematics of ventilation in wild turkeys (*Meleagris gallopavo*). *Journal of Experimental Biology* 222(23), p. jeb209783. doi: 10.1242/jeb.209783.

Brocklehurst, R.J., Schachner, E.R. and Sellers, W.I. 2018. Vertebral morphometrics and lung structure in non-avian dinosaurs. *Royal Society Open Science* 5(10), p. 180983. doi: 10.1098/rsos.180983.

Brusatte, S.L., Benton, M.J., Desojo, J.B. and Langer, M.C. 2010. The higher-level phylogeny of Archosauria (Tetrapoda: Diapsida). *Journal of Systematic Palaeontology* 8(1), pp. 3–47. doi: 10.1080/14772010903537732.

Butler, P.J. 1981. Respiration during flight. In: *Respiration*. Elsevier, pp. 155–164. Available at: https://linkinghub.elsevier.com/retrieve/pii/B9780080268231500247 [Accessed: 11 January 2023].

Carrier, D.R. 1996. Function of the intercostal muscles in trotting dogs: Ventilation or locomotion? *The Journal of Experimental Biology* 199, pp. 1455–1465.

Carrier, D.R. and Farmer, C.G. 2000a. The evolution of pelvic aspiration in archosaurs. *Paleobiology* 26(2), pp. 271–293. doi: 10.1666/0094-8373(2000)026<0271:TEOPAI>2.0.CO;2.

Carrier, D.R. and Farmer, C.G. 2000b. The integration of ventilation and locomotion in archosaurs. *American Zoologist* 40, pp. 87–100.

Claessens, K.P. 2015. Anatomical transformations and respiratory innovations of the archosaur trunk. In: *Great Transformations in Vertebrate Evolution*. University of Chicago Press. doi: 10.7208/chicago/9780226268392.001.0001.

Claessens, L.P.A.M. 2009a. A cineradiographic study of lung ventilation in *Alligator mississippiensis*. *Journal of Experimental Zoology Part A: Ecological Genetics and Physiology* 311A(8), pp. 563–585. doi: 10.1002/jez.530.

Claessens, L.P.A.M. 2009b. The skeletal kinematics of lung ventilation in three basal bird taxa (emu, tinamou, and guinea fowl). *Journal of Experimental Zoology Part A: Ecological Genetics and Physiology* 311A(8), pp. 586–599. doi: 10.1002/jez.501.

Claessens, L.P.A.M. and Vickaryous, M.K. 2012. The evolution, development and skeletal identity of the crocodylian pelvis: Revisiting a forgotten scientific debate. *Journal of Morphology* 273(10), pp. 1185–1198. doi: 10.1002/jmor.20059.

Codd, J.R. 2010. Uncinate processes in birds: Morphology, physiology and function. *Comparative biochemistry and physiology part a: molecular & integrative physiology* 156(3), pp. 303–308. doi: 10.1016/j.cbpa.2009.12.005.

Codd, J.R., Boggs, D.F., Perry, S.F. and Carrier, D.R. 2005. Activity of three muscles associated with the uncinate processes of the giant Canada goose *Branta canadensis maximus*. *Journal of Experimental Biology* 208(5), pp. 849–857. doi: 10.1242/jeb.01489.

Codd, J.R., Manning, P.L., Norell, M.A. and Perry, S.F. 2008. Avian-Like Breathing Mechanics in Maniraptoran Dinosaurs. *Proceedings: Biological Sciences* 275(1631), pp. 157–161.

Codd, J.R., Rose, K.A.R., Tickle, P.G., Sellers, W.I., Brocklehurst, R.J., Elsey, R.M. and Crossley, D.A. 2019. A novel accessory respiratory muscle in the American alligator (*Alligator mississippiensis*). *Biology Letters* 15(7), p. 20190354. doi: 10.1098/rsbl.2019.0354.

Cohn, J.E. and Shannon, R. 1968. Respiration in unanathesitized geese. *Respiration Physiology* 5, pp. 259–268.

Cong, L.Y., Hou, L.H. and Wu, X.C. 1988. *The Gross anatomy of Alligator sinensis Fauvel: Integument, Osteology, and Myology (In Chinese with English summary)*. Beijing, China: China Science Publishing & Media Ltd.

Currie, P.J., Holmes, R.B., Ryan, M.J. and Coy, C. 2016. A juvenile chasmosaurine ceratopsid (Dinosauria, Ornithischia) from the Dinosaur Park Formation, Alberta, Canada. *Journal of Vertebrate Paleontology* 36(2), p. e1048348. doi: 10.1080/02724634.2015.1048348.

dewet, P.D., Fedde, M.R. and Kitchell, R.L. 1967. Innervation of the respiratory muscles of *Gallus domesticus*. *Journal of Morphology* 123(1), pp. 17–34. doi: 10.1002/jmor.1051230103.

Drysdale, E.T., Therrien, F., Zelenitsky, D.K., Weishampel, D.B. and Evans, D.C. 2018. Description of juvenile specimens of *Prosaurolophus maximus* (Hadrosauridae: Saurolophinae) from the Upper Cretaceous Bearpaw Formation of southern Alberta, Canada, reveals ontogenetic changes in crest morphology. *Journal of Vertebrate Paleontology* 38(6), p. e1547310. doi: 10.1080/02724634.2018.1547310.

Duncker, H.-R. 1972. Structure of avian lungs. *Respiration Physiology* 14(1), pp. 44–63. doi: 10.1016/0034-5687(72)90016-3.

Farmer, C.G. and Carrier, D.R. 2000a. Pelvic aspiration in alligators. *The Journal of Experimental Biology* 203, pp. 1679–1687.

Farmer, C.G. and Carrier, D.R. 2000b. Respiration and gas exchange during recovery from exercise in the American alligator. *Respiration Physiology* 120(1), pp. 81–87. doi: 10.1016/S0034-5687(00)00098-0.

Farmer, C.G. and Sanders, K. 2010. Unidirectional airflow in the lungs of alligators. *Science* 327(5963), pp. 338–340. doi: 10.1126/science.1180219.

Fedde, M.R., Burger, R.E. and Kitchell, R.L. 1964. Anatomic and electromyographic studies of the costo-pulmonary muscles in the cock. *Poultry Science* 43(5), pp. 1177–1184. doi: 10.3382/ps.0431177.

Frey, T. von E. 1988. Anatomie des Körperstammes von *Alligator mississippiensis* Daudin. *Stuttgarter Beitraege zur Naturkunde, Serie A* 424, pp. 1–106.

Funk, G.D., Sholomenko, G.N., Valenzuela, I.J., Steeves, J.D. and Milsom, W.K. 1993. Coordination of wing beat and respiration in Canada geese during free flight. *Journal of Experimental Biology* 175, pp. 317–323.

Gans, C. and Clark 1976. Studies on ventilation of *Caiman crocodilus* (Crocodylia: Reptilia). *Respiration Physiology* 26, p. 1.

Gatesy, S.M., Baier, D.B., Jenkins, F.A. and Dial, K.P. 2010. Scientific rotoscoping: a morphology-based method of 3-D motion analysis and visualization. *Journal of Experimental Zoology Part A: Ecological Genetics and Physiology* 9999A, p. n/a-n/a. doi: 10.1002/jez.588.

Ghetie, V. 1976. *Atlas de anatomie a păsărilor domestice*. Academiei Republicii Socialiste România.

Hildebrand, M. 1982. *Analysis of vertebrate structure*. New York: Wiley Blackwell.

Janis, C.M. and Keller, J.C. 2001. Modes of ventilation in early tetrapods: Costal aspiration as a key feature of amniotes. *Acta Palaeontologica Polonica* 46(2), pp. 137–170.

Kadono, H., Okada, T. and Ono, K. 1963. Electromyographic studies on the respiratory muscles of the chicken. *Poultry Science* 42(1), pp. 121–128. doi: 10.3382/ps.0420121.

Kiley, J.P., Kuhlmann, W.D. and Fedde, M.R. 1982. Ventilatory and blood gas adjustments in exercising isothermic ducks. *Journal of comparative physiology* 147(1), pp. 107–112. doi: 10.1007/BF00689298.

Lord, R.D., Bellrose, F.C. and Cochran, W.W. 1962. Radiotelemetry of the Respiration of a Flying Duck. *Science* 137(3523), pp. 39–40. doi: 10.1126/science.137.3523.39.

Maina, J.N. 2002. *Functional Morphology of the Vertebrate Respiratory Systems*. Science Publishers.

Maina, J.N., Singh, P. and Moss, E.A. 2009. Inspiratory aerodynamic valving occurs in the ostrich, Struthio camelus lung: A computational fluid dynamics study under resting unsteady state inhalation. *Respiratory Physiology & Neurobiology* 169(3), pp. 262–270. doi: 10.1016/j.resp.2009.09.011.

Munns, S.L., Owerkowicz, T., Andrewartha, S.J. and Frappell, P.B. 2012. The accessory role of the diaphragmaticus muscle in lung ventilation in the estuarine crocodile *Crocodylus porosus*. *Journal of Experimental Biology* 215(5), pp. 845–852. doi: 10.1242/jeb.061952.

Nesbitt, S.J. 2011. The early evolution of archosaurs: relationships and the origin of major clades. *Bulletin of the American Museum of Natural History* 352, pp. 1–292. doi: 10.1206/352.1.

O'Connor, P.M. 2006. Postcranial pneumaticity: An evaluation of soft-tissue influences on the postcranial skeleton and the reconstruction of pulmonary anatomy in archosaurs. *Journal of Morphology* 267(10), pp. 1199–1226. doi: 10.1002/jmor.10470.

Perry, S.F. 1988. Functional morphology of the lungs of the nile crocodile, *Crocodylus niloticus:* non-respiratory parameters. *Journal of Experimental Biology* 134(1), pp. 99–117. doi: 10.1242/jeb.134.1.99.

Perry, S.F., Lambertz, M. and Schmitz, A. 2019. Respiratory faculties of amphibious and terrestrial craniotes. In: *Respiratory Biology of Animals: evolutionary and functional morphology*. Oxford University Press, pp. 139–163.

Powell, F.L. 2015. Respiration. In: *Sturkie's Avian Physiology*. Elsevier, pp. 301–336. doi: 10.1016/B978-0-12-407160-5.00013-0.

RStudio Team 2020. RStudio: Integrated Development for R.

Schachner, E.R., Farmer, C.G., McDonald, A.T. and Dodson, P. 2011. Evolution of the dinosauriform respiratory apparatus: New evidence from the postcranial axial skeleton. *The Anatomical Record: Advances in Integrative Anatomy and Evolutionary Biology* 294(9), pp. 1532–1547. doi: 10.1002/ar.21439.

Schachner, E.R., Lyson, T.R. and Dodson, P. 2009. Evolution of the respiratory system in nonavian theropods: evidence from rib and vertebral morphology. *The Anatomical Record: Advances in Integrative Anatomy and Evolutionary Biology* 292(9), pp. 1501–1513. doi: 10.1002/ar.20989.

Schmidt-Nielsen, K., Kanwisher, J., Lasiewski, R.C., Cohn, J.E. and Bretz, W.L. 1969. Temperature regulation and respiration in the ostrich. *The Condor* 71(4), pp. 341–352. doi: 10.2307/1365733.

Schneider, C.A., Rasband, W.S. and Eliceiri, K.W. 2012. NIH Image to ImageJ: 25 years of image analysis. *Nature Methods* 9(7), pp. 671–675. doi: 10.1038/nmeth.2089.

Shufeldt, R.W. 1988. *The myology of the raven (Corvus corax sinuatus): A guide to the study of the muscular system in birds*. Macmillan and Company.

Tickle, P.G., Ennos, A.R., Lennox, L.E., Perry, S.F. and Codd, J.R. 2007. Functional significance of the uncinate processes in birds. *Journal of Experimental Biology* 210(22), pp. 3955–3961. doi: 10.1242/jeb.008953.

Turner, A.H. 2006. Osteology and phylogeny of a new species of *Araripesuchus* (Crocodyliformes: Mesoeucrocodylia) from the Late Cretaceous of Madagascar. *Historical Biology* 18(3), pp. 255–369. doi: 10.1080/08912960500516112.

Walker, W.F. and Liem, K.F. 2001. *Functional Anatomy of the Vertebrates: An Evolutionary Perspective*. New York: Fort Worth : Harcourt College Publishers.

Wedel, M.J. 2009. Evidence for bird-like air sacs in saurischian dinosaurs. *Journal of Experimental Zoology Part A: Ecological Genetics and Physiology* 311A(8), pp. 611–628. doi: 10.1002/jez.513.

Welty, J.C. and Baptista, L. 1972. *The life of birds*. London: W. B. Saunders and Co.

Wickham, H. 2009. *ggplot2*. New York, NY: Springer New York. Available at: http://link.springer.com/10.1007/978-0-387-98141-3 [Accessed: 12 January 2023].

Xu, X. et al. 2015. The taxonomic status of the Late Cretaceous dromaeosaurid *Linheraptor exquisitus* and its implications for dromaeosaurid systematics. *Vertebrata PalAsiatica* 53, pp. 29–62.

York, J.M. et al. 2017. Respiratory mechanics of eleven avian species resident at high and low altitude. *Journal of Experimental Biology* 220(6), pp. 1079–1089. doi: 10.1242/jeb.151191.

Zimmer, K. 1935. Beiträge zur Mechanik der Atmung bei den Vögeln in Stand-und Flug. *Zoologica* 33, pp. 1–69.

8.6 Supplementary Information

8.6.1 Detailed description of the procedure used to construct kinetic models and infer ventilatory functions in this study.

In this section, individual presacral and presacral ribs is referred by the sequential number of the respective regions (i.e. P#, C#, D#, PR#, IR#, SR#) where necessary.

Sampling for digitalisation — For the palaeognath model, 20 elements were sampled from *Struthio camelus* (UAMZ 7159), including seven vertebrae from P19 to P25, left PR19 to PR25, five left SR21 to SR25, and the sternum. For both crocodylian with m. diaphragmaticus (crocodylian W) and crocodylian without m. diaphragmaticus (crocodylian WOD), 33 elements were sampled from *Caiman crocodilus* (UAMZ unnumbered), including 12 vertebrae from P8 to P19, left PR9 to PR18, left IR10 to IR16, and left SR10 to SR15.

Meshing — the sampled elements were scanned over several sessions using a light reflected scanner (Polyga Carbon series) controlled by the program FlexScan 3D housed in the Sullivan Lab at the University of Alberta. Scanner was calibrated using 10mm calibration board, and the spatial coverage of each scanning sessions was at least 85%. For clean up in FlexScan 3D, erosion of the edges of holes were performed once or twice followed by one to two iterations of smoothing for each scanned bone.

Some areas of the sampled bones were not completely captured by the scanner: (1) internal surfaces of the neural canals of all sampled vertebrae, as they are underexposed and filtered out by the scanner; (2) anterior and posterior rugose surface of the neural spines near their proximal ends in *Su. camelus* (UAMZ 7159), as the rugose textures created many noisy polygons when captured by the scanner; (3) distal articular facet of PR13 and PR18, articular facet of capitulum of PR15, and articular facet of tuberculum of PR14 in *Cai. crocodilus* (UAMZ unnumbered), as remnants of soft tissues were present at the time of scanning; (4) proximal end of IR11 as it was damaged during dissection performed in Chapter 6.

Meshes of ribcages were exported from FlexScan 3D as .obj files, and were refined in ZBrush 2018. For each mesh, the .obj file was imported in ZBrush as tool, Dyna mesh was

performed once to fill holes with blur set to zero, resolution of mesh set to 1024. The mesh was decimated using decimation master in ZBrush, the levels of decimation were set differently for individual mesh, such that the key morphological features such as outline of the articular facets were preserved. Masking key area before decimation can limit the amount of anatomical features lost in the process of decimation. However, the unmasked portion would lose more anatomical features, and masking was therefore not used in this study. With target polygon count set to 100, ZRemesher was then used to change the mesh from being composed of triangular geometry to evenly distributed quadrangulate geometry. Of the sampled meshes, Dyna mesh and ZRemesher were used twice for PR10 of *Cai. crocodilus* (UAMZ unnumbered), to fill all holes. Then, meshes were exported as .obj files.

As left SR16, the cartilaginous uncinate processes and the sternum in *Cai. crocodilus* (UAMZ unnumbered) were not preserved, a simple rod was created using geometric primitive in Maya to represent SR16; five compressed cubes were created from using primitive geometric in Maya to represent the cartilaginous uncinate processes; a low poly mesh was created using reference images of crocodylian sternum from the literature to represent the cartilaginous sternum (Cong et al. 1988; Baier and Gatesy 2013). The scales of these interpreted meshes were adjusted such that they approximate the approximate size of the sternum in *Cai. crocodilus* (UAMZ unnumberd).

Three scenes were created in Autodesk Maya 2022 with working unit set to metre for palaeognath, crocodylian W, crocodylian WOD kinematic models, and ribcage meshes were imported as bone meshes (Bmesh) for digital articulation.

Digital articulation — For all kinematic models, Bmesh of the last cervical vertebra (P19 and P8) was positioning such that the cranial side of the vertebra was aligned with the Z-axis of the world, and the dorsal side of the vertebra was aligned with the Y-axis of the world. The remaining vertebra, rib segments, and sternum were positioned such that the ribcage represent maximal expiration. Using operations such as centre pivots and freeze transformation may facilitate the process of digital articulation. A maximal gap of 1 cm was allowed between articular facets of Bmesh, which were estimated using the distance tool in Maya (Bonus tool add-

on in Maya can perform similar functions). Variations are likely present between trials of using distance tool, as placement of the locators could not guaranteed to be the same. All Bmeshes of the left side were mirrored to the right side. After all Bmeshes were digitally articulated, free transformation was performed to set the translation and rotation values at zero. History of each mesh was deleted to avoid complications in Bmesh attribute.

Creating thoracic volume and m. diaphragmaticus — A incline plane was created from geometric primitive in Maya to represent m. diaphragmaticus (Dmesh), which was then scaled and placed at the position representing maximal expiration according to anatomical landmarks from the literature (Claessens 2009a).

Landmarks were placed on the ventral aspects of the vertebrae, medial aspects of the left rib segments, and dorsal aspects of the sternum. A low poly mesh was then created based on the landmarks using create polygon tool. Vertices of the low poly mesh were moved manually to limit the amount of overlapping with Bmeshes of the ribcage. The low poly mesh was then mirrored into a closed mesh, which was then duplicated and scaled to 95% to 96% of its size called lung mesh (Lmesh). Lmesh was then remeshed and retopoligised in Maya, such that deformations of the Lmesh appear natural. The exact threshold for remesh and retopology are subjected to hardware of computers, and a clear threshold at which optimal results may be obtained was not found in this study. If edge flows of the remesh and retopoligised Lmesh appear unnatural, the subsequent deformation used for estimating plausible oROM may be affected. If needed, tools such as live retopology can be used to create a new Lmesh.

A deformer was setup to drive the deformation of Lmesh. The low poly mesh created from landmarks in this step was used as a hulk to drive deformation of the slightly smaller Lmesh. A wrap deformer in Maya was used, such that motions of vertices of the hulk would deform Lmesh.

To have vertices of the hulk follow ventilatory motions of Bmeshes, Vertices of the hulk were assigned to cluster deformers that were parent constrained to the nearest Bmeshes. For vertices positioned between two Bmeshes (e.g. vertices positioned within an intercostal space), clusters

of the vertices were parent constrained by both adjacent Bmeshes. The resulting deformation should expand smoothly, and reassigning vertices to clusters may be required to achieve desirable effects.

For crocodylian W model, the Lmesh was created also using landmarks from the Dmesh. As Lmesh does not reach the posterior aspects of the ribcage, additional edge loops were created near the posterior end of Lmesh, such that ventilatory motions of the posterior ribcage can drive deformations of Lmesh. Setup of deformer could be done after oROM is estimated.

Joint coordinate systems (JCS) —JCS were created using Maya joints (Mjoints) to describe anatomical rotations of Bmeshes around three axes using Euler angles following the AB setup in Chapter 7. Mjoints were placed at the anterior aspect of the centrum near the centres of the centrum. To place an intervertebral joint, a landmark was placed at the left lateral most aspect of the centrum, and a mirror landmark was created across Z-axis of the world using mirror tool in Maya. The intervertebral joint was placed in the midpoint between two landmarks. For sternum, Mjoints was placed at near its centroid. Orientations of intervertebral joints and sternum are setup as follow:

Ventilatory motions for intervertebral joints and sternum are described as rotations around x-axis as flexion/extensions. Translations were allowed only for sternum.

Taking the long axis of Bmeshes as morphological features in considerations, AB setup describes ventilatory motions around x-axis as axial rotations, around y-axis as abduction/adductions, and around z-axis as protractions/retractions.

For costal joints, Mjoints were placed at the midpoint between capitulum and tuberculum. To place a costal joint, landmarks were placed near the centres on the articular facets of capitulum and tuberculum. The costal joint was then positioned to the midpoint of two landmarks by point constraint of the costal joints. Constraint was removed after the placement of costal joint was completed.

For intracostal joints, Mjoints were placed at the midpoints on the proximal articular facets of rib segments. To place an intracostal joint, two landmarks were placed at the ends of the long axis on the articular facet (e.g. long axis of the surface at the proximal end of the articulated sternal rib). The intracostal joint was then placed in the midpoint of two landmarks. Constraints, if used, were removed after the intracostal joint was placed.

To orient a costal/intracostal joint in AB manner, a child joint was created and placed near the centre of the articular facet at the distal end of the rib segment. The child joint was parented under the costal/intracostal joint. The costal/intracostal joint was then oriented using Orient Joint Option in Maya with X-axis as the primary axis, Y-axis as the secondary axis, and positive Z-axis as the secondary axis world orientation.

Rigging and setting up connections — controllers were setup using AJ setup described in Chapter 7. AJ setup only account for the positions of articular facets of rib segmetns, AJ setup describes ventilatory motions around x-axis as axial rotations, around y-axis as abduction/adductions, and around z-axis as protractions/retractions.

Placements of costal and intracostal joints were the same as CBP setup. To orient a costal joint in palaeognath model, a child joint was created at the midpoint between capitulum and tuberculum. The costal joint was then oriented using Orient Joint Option in Maya with X-axis as the primary axis, Y-axis as the secondary axis, and positive Z-axis as the secondary axis world orientation. To orient an intracostal joint in palaeognath model, a child joint was created at the midpoint on the articular facet of the sternal rib. The intracostal joint was then oriented using Orient Joint Option in Maya with X-axis as the primary axis, Z-axis as the secondary axis, and positive Y-axis as the secondary axis world orientation. To orient a costal joint in crocodylian W and crocodylian WOD, the procedure was the same as orienting a costal joint in palaeognath model. To orient a dorsal intracoastal joint, a child joint was created at the midpoint on the articular facet along the long axis of intermediate rib, and the child joint was parented under the costal joint. The dorsal intracostal joint was then oriented using Orient Joint Option in Maya with X-axis as the primary axis, Y-axis as the secondary axis, and positive Z-axis as the secondary axis world orientation. To orient a ventral intracostal joint, a child joint was created at the

midpoint on the articular facet along the long axis of sternal rib, and the child joint was parented under the ventral intraocostal joint. The ventral intracostal joint was then oriented using Orient Joint Option in Maya with X-axis as the primary axis, Y-axis as the secondary axis, and positive Y-axis as the secondary axis world orientation.

To connect Mjoints between AB, and AJ setups, joint locators (JLocators) were then placed and oriented in the same way as the Mjoints with AJ setup. All Mjoints with AB, and AJ setups were parent constrained under the JLocators.

Duplicates of joints from AJ setup were created to drive motions of the ribcage in Maya. NURB curves were created as controller to record oROM as animation key frames. Pivot points and orientations of Bmeshes and NURB controllers were matched to those of the Mjoints duplicated from AJ setup. Maya tools such as Match Transformation may facilitate this process. Then, freeze transformation were applied to Bmeshes. To have clean channel boxes for the NURB controllers, we could create groups that house the NURB controllers, and Match Transformation of the group to Mjoints.

Bmehes were then parent constrained to Mjoints, which were parent constrained to NURB controllers. Accordingly, we can use NURB controller to drive movement of individual Bmesh. Bmeshes of vertebrae would need to drive motions of rib segments, so that translations were not required for rib segments. To achieve this effect, NURB controllers of the ventral rib segments (e.g. sternal ribs) were hierarchically parent constrained to the dorsal rib segments (e.g. vertebral rib), and then parent constrained to the NURB controller of the corresponding vertebral Bmeshes. NURB controller of the posterior vertebral Bmeshes were then hierarchically parent constrained to those of the anterior vertebral Bmeshes. To have clean connections, empty groups can be created as parent objects to house NURB controllers, and parent constrains can be placed on the group. Note that NURB controller of the ventral Bmeshes (e.g. sternal ribs) under this setup would inherit transformations driven by the those of the dorsal Bmeshes (e.g. vertebrae), which is why JLocators were used to record pure rotations of the ventral Bmeshes.

Rotation orders of all objects in the scene were set to xyz with Script 8.1 (see digital supplementary information).

Estimate plausible oROM — NURB controller were manually rotate such that the ribcage was expanded to a state representing maximal inspiration, and the manual rotations were recorded as animation keyframes representing oROM. Bmeshes were allowed to approached other Bmeshes without direct contact. Xray view in Maya may facilitate the estimations. For crocodylian W model, Dmesh was manually translated to a position representing maximal inspiration by referencing the literature (Claessens 2009a).

To estimate plausible oROM, oROM of all Bmeshes were scaled until changes of the thoracic volume approximated the tidal volumes taken from the literature (Schmidt-Nielsen et al. 1969; Perry 1988; Maina et al. 2009) (Table 7.1 in Chapter 7). Noted that tidal volume used for crocodylian W and crocodylian WOD models were computed from V_{Lr} and V_{Lm} reported by Perry (1988). Volumes of Lmesh were estimated using the MEL command *ComputePolysetVolume*. Multiple trial and error may be needed to approximate the tidal volume, and we did not recover the exact value of tidal volumes documented in the literature.

Three versions of ventilatory motions were created: (1) vertebra-rib-sternum (VRS) version represents ventilation with vertebrae, rib segments, and sternum; (2) rib-sternum (RS) represents ventilation with rib segments and sternum; and (3) rib (R) represents ventilation with only rib segments. For AB and AJ setups of each version of ventilation, both oROM and plausible oROM were recorded as animation keyframes and were saved in .atom format. JLocators were also keyframed with the same values as NURB controller, so that pure rotations of the Mjoints of AB and AJ can be recorded and exported.

To describe oROM and plausible oROM from maximal expiration to maximal inspiration in a ventilatory cycle, the ratio of duration of inspiration to expiration as expressed by animation keyframes in Maya was set to 1:2 for paleognath and 1:1 for crocodylian, which are based on respiratory studies in neognath and crocodylians (Table S8.1). To test the potential impacts of different kinematic assumptions, rotations were prescribed both as linear angular motions and

motions with a constant angular acceleration estimated from oROM and duration of ventilation. Linear angular motions were prescribed as equal steps each of the size determined by the following formula:

$$S_s = (ROM)/(t)$$

S_s: the increments of angular rotation between successive keyframes.

ROM: oROM or plausible oROM.

t: duration of inspiration and/or expiration as expressed by animation keyframes.

Motions with a constant angular acceleration was prescribed using kinematic equations as follow:

$$S_s = (\omega_{(f+1)}^2 - \omega_f^2) / (2 * \alpha)$$

$$\omega_f = \alpha * f$$

$$\alpha = (ROM)/t^2$$

S_s: the increments of angular rotation between successive keyframes.

ω_f: angular velocity at a given point in time during ventilation.

α = angular acceleration.

ROM: oROM or plausible oROM.

All computed oROM and plausible oROM were written manually transferred to SIMM motion file. Only a header would need to be added for each motion file, and the computed values

could be copied directed from Excel, or other software packages such as R. Noted that names of motion files (.mot) should be the same as the names mentioned in joint file (.jnt) of SIMM.

Transferring kinematic models from Maya to SIMM — Bmeshes in Maya were translated to the world origin of the scene, which were then exported as individual .obj file. As SIMM does not have a built-in working unit, all Bmeshes retained the millimetre scale from the initial capture using the light reflected scanner. Bmeshes exported from Maya were scaled to metre scale using Autodesk Meshmixer. As all morphological information were captured in Maya, Bmeshes were decimated to 5000 polygons, before being placed in SIMM.

To obtain the joint orientation using AB setup, Script 8.2 were used to extract axial rotations from MMatrix in maya, which were then written in the joint file for SIMM model.

Representing trunk muscles — Trunk muscles were represented as vectors connecting bony elements of the ribcage. As many hypaxial muscles (e.g. mm. intercostales externi) have broad insertions on the ribs, and cannot be accurately represented as single vectors. Instead, muscles were represented by vectors of multiple muscle units evenly spaced throughout the area of osteological correlates (see Chapter 6 for osteological correlates), with each muscle unit representing a bundle of similarly oriented fibres.

To represent a muscle, maya scenes were created with all Bmeshes located at the world origin, as SIMM takes pivot points of Bmehes as origin for muscles attached to them. Then, landmarks were placed on the osteological correlates. Vertex snapping or geometric constraints may facilitate this process. For muscles attached to an area along the rib segments (e.g. mm. intercostales externi), Four to five landmarks were created according to the number of units needed. Point constraints without maintaining offset and geometric constraints were used to positioned landmarks such that they were evenly distributed along the osteological correlate.

A total of 136 and 300 muscle units were created for the kinetic Palaeognath and Crocodylian models using Script 8.3. All muscle coordinates were then manually transferred to a muscle file in SIMM. Noted that the name of muscle file (.msl) should be consistent with the name mentioned in the joint file (.jnt) for SIMM model. As this study focused on hypaxial trunk

muscles, only 67 and 84 muscle units were sampled as representatives for functional interpretations. Where appropriate, wrap objects were added in SIMM to prevent vectors of muscle units from passing through bony elements. To evaluate the functional significance of uncinate processes from the perspective of moment arms, pseudo-muscle units were created for ventral part of m. iliocostalis and m. appendicocostalis, which were attached directly to the vertebral ribs, neglecting the presence of uncinate processes. Accordingly, the pseudo-muscle unites represent hypothetical muscle without mechanical leverages that may be provided by the uncinate processes.

Analysing moment arm plots — For a given ventilatory cycle, changes in moment arms of sampled muscle units were plotted in SIMM. To generate a moment arm plot, x variable was set to respective motion file, and y variable was set to moment arm (numeric). Moement arm instead of moment arm (numeric) can also be used for similar results, though moment arm (numeric) took in account for the moment arm values from adjacent frames by estimating the derivatives. The moment arm plots were then exported as .plt file for AutoCAD. Unfortunately SIMM does not seem to have other options for exporting moment arm plots. Moment arm plots in .plt format were then opened in Excel such that moment arm data was organised and named in a consistent format for subsequent analyses.

Moment arm data were imported and analysed in RStudio 4.1(RStudio Team 2020) using Script 8.4 and Script 8.5, such that magnitudes of moment arms and changes of moment arms throughout a ventilatory cycle can be compared between three kinematic motions and among anatomical joints. As signs of moment arms are indicative of the directions at which the muscles would drive the skeletal elements to rotate, ventilatory functions of each muscle unit were inferred by comparing the signs of moment arms to those of the kinematic motions. Muscle units with moment arms of the same and opposite signs as those of kinematic motions were inferred to have inspiratory and expiratory functions, respectively. Muscle units with moment arms that change signs during a ventilatory cycle were inferred to have mixed ventilatory functions. Only the VRS version of plausible oROM from Palaeognath and Crocodylian W kinematic models were used to infer ventilatory function.

As many vertebral ribs carry attachment sites cranially and caudally for ventral part of m. iliocostalis, mm. intercostales externi, and mm. intercostales interni (see Chapter 6), the simultaneous contractions of muscle units cranial and caudal to a given vertebral ribs may result in inspiratory or expiratory function. Combinations of muscle moment arms were computed, and the signs of combined moment arms were used to inferred whether the combinations of cranial and caudal units of ventral part of m. iliocostalis, mm. intercostales externi, and mm. intercostales interni would rotate vertebral ribs for inspiration or expiration. The third and fourth costal joints were sampled as representative in Palaeognath and Crocodylian models, respectively. Results were visualised using the R package GGplot2 (Wickham 2009).

Table S8. 1. Duration of inspiration and expiration estimated from the literature.

Taxa	Active level	Condition	Inspiration (s)	Expiration (s)	I:E ratio
Domestic goose (Cohn and Shannon 1968)	resting	unanathetized	2.44	2.41	1.01
			2.52	2.54	0.99
Canada geese (Funk et al. 1993)	in flight	unanathetized	1.99	4.86	0.41
			1.85	4.92	0.38
			1.67	5.13	0.33
			1.79	4.72	0.38
Mallard duck * (Lord et al. 1962)	resting	unanathetized	1.5	3	0.50
	in flight	unanathetized	0.4	0.4	1.00
Chicken (Kadono et al. 1963)	resting	unanathetized	0.96	1.1	0.87
			1.1	0.89	1.24
			0.95	1.22	0.78
			1.11	1.2	0.93
			0.91	0.96	0.95
			0.5	0.92	0.54
			0.99	0.85	1.16
			0.95	0.97	0.98
			1.09	0.87	1.25
			1.26	1.27	0.99
			1.05	1.13	0.93
			0.96	1.12	0.86
			0.9	1.22	0.74
			1.09	1.23	0.89
			1.02	1.24	0.82
			0.99	1.21	0.82
			1.29	1.16	1.11
			1.27	1.19	1.07
			1.28	0.98	1.31
			1.1	1.28	0.86
			1.38	1.14	1.21
			1.02	1.13	0.90
			0.9	1.19	0.76
			0.48	0.55	0.87
			0.44	0.42	1.05
			0.38	0.48	0.79
			0.39	0.43	0.91
			0.46	0.48	0.96
			0.4	0.45	0.89

			0.4	0.46	0.87
			0.39	0.44	0.89
			0.39	0.42	0.93
			0.38	0.5	0.76
			0.36	0.43	0.84
			0.89	0.71	1.25
			0.83	0.76	1.09
			0.66	1.24	0.53
			0.58	1.29	0.45
			0.46	0.5	0.92
			0.44	0.47	0.94
			0.4	0.5	0.80
			0.48	0.54	0.89
			0.81	0.91	0.89
			0.81	1.02	0.79
			0.73	0.72	1.01
			0.75	0.85	0.88
			0.29	0.37	0.78
			0.24	0.41	0.59
			0.3	0.41	0.73
			0.29	0.46	0.63
			0.27	0.5	0.54
			0.27	0.49	0.55
			0.48	0.48	1.00
			0.49	0.45	1.09
			0.47	0.43	1.09
			0.46	0.45	1.02
			0.44	0.41	1.07
			0.45	0.5	0.90
			0.46	0.51	0.90
			0.44	0.59	0.75
Black duck (Berger et al. 1970)	in flight	unanathetized	0.21	0.75	0.28
			0.22	0.84	0.26
			0.22	0.95	0.23
			0.13	0.89	0.15
			0.22	0.87	0.25
			0.35	1.39	0.25
			0.41	1.38	0.30
			0.42	1.28	0.33
			0.43	0.78	0.55
			0.46	0.74	0.62
			0.49	0.69	0.71
			0.46	0.88	0.52

			0.36	0.66	0.55
Evening grosbeak (Berger et al. 1970)	in flight	unanathetized	0.06	0.14	0.43
			0.07	0.14	0.50
			0.06	0.09	0.67
			0.06	0.09	0.67
			0.07	0.14	0.50
Magpie (Boggs 1997)	in flight	unanathetized	0.19	0.24	0.79
			0.24	0.26	0.92
			0.19	0.23	0.83
Magpie (Boggs et al. 1997a)	in flight	unanathetized	0.19	0.21	0.90
			0.23	0.34	0.68
			0.15	0.18	0.83
Magpie (Boggs et al. 1997b)	in flight	unanathetized	0.24	0.26	0.92
			0.12	0.25	0.48
American alligator (Carrier and Farmer 2000b)	in walk	unanathetized	2.19	1.62	1.35
			1.74	1.95	0.89
			1.69	2.17	0.78
American alligator (Farmer and Carrier 2000a)	recovering	unanathetized	2.74	8.46	0.32
			3.27	10.39	0.31
			3.85	9.11	0.42
			3.97	7.98	0.50
American alligator (Farmer and Carrier 2000a)	in walk	unanathetized	2.22	1.76	1.26
			1.76	1.94	0.91
			1.63	2.26	0.72
American alligator (Farmer and Carrier 2000a)	in walk	unanathetized	1.98	2.14	0.93
			0.9	1.28	0.70
			1.46	1.74	0.84
			1.86	1.35	1.38

* indicates taxon where durations of inspiration and expiration were described. Durations of inspiration and expiration in other taxa were measured from figures using ImageJ (Schneider et al. 2012).

8.7 Digital supplementary information

Digital supplementary data is stored and managed by the author, the documents of which are listed as follow:

(1) two SIMM models to recreate moment arm plots and estimate other ventilatory functions.

(2) two Maya scenes to show landmarks on the osteological correlates of trunk muscles

(3) raw data exported from SIMM in .plt format

(4) Script 8.1 used to adjust rotation order in Maya

Latest version of this script may be found at:

https://github.com/Wani2Y/3D-modelling/blob/main/Maya/change_rotation_order.py

(5) Script 8.2 used to get joint orientation values from MMatrix in Maya for SIMM joint file

Latest version of this script may be found at:

https://github.com/Wani2Y/3D-modelling/blob/main/Maya/get_joint_info_for_SIMM.py

(6) Script 8.3 used to export muscle coordinates in Maya for muscle file in SIMM

Latest version of this script may be found at:

https://github.com/Wani2Y/3D-modelling/blob/main/Maya/export_channel_box_info.py

(7) raw data and Script 8.4 and Script 8.5 to recreated analyses and functional inferences in R

Latest version of this script may be found at:

https://github.com/Wani2Y/Bioinformatics/tree/main/EDA%20of%20moment%20arms%20from%20SIMM

CHAPTER 9
Conclusions and future directions

9.1 General conclusions

The primary aims of this thesis have been to provide updated anatomical information on the archosaur trunk, to use biomechanical principles to analyse the ventilatory process, and to gain insights into the evolutionary transitions that have occurred over deep time with respect to archosaur ventilation.

Before the twenty-first century, ventilatory studies of archosaurs focused on understanding three key points: (1) pulmonary morphology (Brackenbury 1972; Powell and Wagner 1982), (2) the amount of air that passed into and out of the respiratory organs during ventilation (Lord et al. 1962; Kadono et al. 1963; Cohn and Shannon 1968; Schmidt-Nielsen et al. 1969; Berger et al. 1970; Perry 1988; Funk et al. 1993; Boggs et al. 1997), and (3) the ventilatory roles of various muscles, as inferred from their activity patterns (Lord et al. 1962; Berger et al. 1970; Duncker 1972; Butler 1982; Perry 1988; Boggs et al. 1997; Boggs et al. 1997). Only Zimmer (1935) attempted to analyse ventilation using mechanical principles. Since then, these lines of investigation have continued to expand, and have yielded key insights into how the trunk musculature and lungs behave during ventilation in archosaurs (Codd et al. 2005; Tickle et al. 2007; Farmer and Sanders 2010; Munns et al. 2012; Codd et al. 2019). With the advent of and subsequent improvements in non-invasive techniques, ventilatory motions have also been documented in several extant archosaurs to further scientific understanding of mechanical aspects of their ventilation (Claessens 2009a; Claessens 2009b; Brocklehurst et al. 2017; Brocklehurst et al. 2019).

In addition to research on extant archosaurs, a growing body of work has accumulated on transformations that have affected respiration, including ventilation, over the course of archosaur evolution (Carrier and Farmer 2000a; Carrier and Farmer 2000b; Claessens 2004; O'Connor and Claessens 2005; Codd et al. 2008; Schachner et al. 2009; Schachner et al. 2011; Claessens and

Vickaryous 2012; Brocklehurst et al. 2018). In this thesis, we continued the path set by scholars that came before us, to gain insights into the mechanics and evolution of archosaur ventilation.

In Chapter 2 and Chapter 3, we proposed qualitative criteria, and developed supervised statistical models, intended to regionalise the presacral vertebrae accurately and consistently. The goal was to use vertebral morphological features to identify the first presacral vertebra that would have been connected to the sternum via rib segments, traditionally defined as the first dorsal (Romer 1956). Although the morphological criteria proposed in Chapter 2 could not pinpoint the cervicodorsal transition, as traditionally defined, they were capable of delineating a transitional region that would likely contain the first sternal connection in extant and fossil archosaurs. By comparison, the supervised statistical models proposed in Chapter 3 could pinpoint the first sternal connection with relatively high accuracy, but only in extant archosaurs. Therefore, the best currently available basis for identifying the cervicodorsal transition in extinct archosaurs, and by extension for assessing regional variation in features of the presacral vertebrae that are relevant to pulmonary morphology and ventilation (Schachner et al. 2009; Brocklehurst et al. 2018), may be the transitional criteria proposed in Chapter 2.

In Chapter 4, we established an osteological correlate of uncinate process attachment, called uncinate scars, as indirect evidence that can be used to infer the presence of uncinate processes when the processes themselves are not preserved. From the distribution of uncinate processes in Archosauria, as determined both from preserved examples and based on uncinate scars, we proposed that uncinate processes and their ventilatory function (Codd et al. 2005; Tickle et al. 2007; Codd et al. 2019) may have first appeared in early dinosaurs, or even in early archosaurs, and been widely inherited as a homologous feature.

In Chapter 5, we further examined the attachment sites of the uncinate processes in extant and fossil dinosaurs. We proposed that uncinate processes are anchored to vertebral ribs by coarse collagen fibres passing through the periosteum, and that very little movement, if any, would be expected to occur between uncinate processes and vertebral ribs. In addition, features within the cortical bone of vertebral ribs at the attachment sites of uncinate processes in taxa we

sampled suggests that the attachment sites have been modified presumably by natural selection on the evolutionary path to extant birds.

In Chapter 6, we presented an updated comparative study on trunk and pelvic muscles in extant archosaurs. We proposed osteological correlates for both trunk and pelvic muscles, and identified correlates for three of the trunk muscles in at least 33 fossil dinosaurs. We also found that m. appendicocostalis, a trunk muscle that normally attaches to the uncinate processes and the shafts of vertebral ribs in birds, exists in the emu *Dromaius novaehollandiae* (UAMZ unnumbered) even though uncinate processes are absent. This would suggest that the absence of uncinate processes in the emu, and likely also in anhimid and megapodid birds (Baumel et al. 1993), is most likely secondary, strengthening the idea proposed in Chapter 4 that uncinate processes likely represent a homologous feature shared by most archosaurs.

In Chapter 7, we documented a workflow for estimating the plausible osteological range of motion (oROM) of the ribcage, which in turn provided a basis for estimating tidal volume in three kinematic models using *ex vivo* skeletal remains. The oROM estimates scaled by tidal volume in our study were similar to results from *in vivo* studies (Claessens 2009a; Claessens 2009b; Brocklehurst et al. 2017; Brocklehurst et al. 2019). Additionally, moving the ribcage through the oROM using an assumed angular acceleration resulted in a kinematic profile comparable to those recorded in *in vivo* studies (Brocklehurst et al. 2017; Brocklehurst et al. 2019). Furthermore, the workflow proposed in Chapter 7 links different conventions for establishing joint coordinates, so that the different joint coordinate systems can be interconverted semi-automatically. Accordingly, the oROM associated with ventilation can be reasonably estimated using skeletal remains, which opens the possibility of generating and comparing oROM estimates in fossil archosaurs.

In Chapter 8, we documented a workflow for constructing kinetic models to estimate moment arms of trunk muscles, which in turn were used to infer the ability of various muscles to contribute to ventilation in three-dimensional fashion. Overall, trunk muscles would protract and retract segments of the ribcage to help drive inspiration and expiration, respectively. Although we agreed with Zimmer (1935) and Tickle et al. (2007) that uncinate processes enhance

archosaurs' ability to inspire air, we have observed additional details on how the uncinate processes can improve muscles' inspiratory function. In our Palaeognath model, uncinate processes enhance the bird's ability to protract the vertebral ribs while constraining abduction of the vertebral ribs. In our Crocodylian models, however, uncinate processes enhance the crocodylian's ability to both protract and abduct the vertebral and intermediate ribs. Therefore, the configuration and morphology of the ribcage (e.g. relative anatomical positions of rib segments, orientations of muscle fibres) may have a substantial impact on the extent to which uncinate processes can improve inspiratory functions of associated trunk muscles.

9.2 Plausible future directions

In this thesis, we focused on establishing baseline information from extant archosaurs regarding the anatomy of archosaur trunks and the biomechanical significance of some of their anatomical features. Conclusions proposed by this thesis can be expanded upon in five major directions, as follows.

(1) Cervicodorsal transition. The criteria proposed in Chapter 2 are mostly based on observations from extant birds, extant crocodylians, and fossil dinosaurs. Other fossil archosaurs, especially those positioned near the root of Archosauria, could be sampled in the future, to provide a stronger basis for evolutionary inferences regarding how the presacral region of the vertebral column may have been altered in the evolutionary history of archosaurs.

Although the supervised statistical models proposed in Chapter 3 could only regionalise presacral vertebrae with high accuracy in extant archosaurs, collecting additional data from fossil archosaurs with articulated skeletons (Xu et al. 2015; Currie et al. 2016) would allow the supervised statistical models to be trained using a combined data set from both extant and fossil archosaurs. This may increase the accuracy of the models in regionalising presacral vertebrae in fossil archosaurs. Both the qualitative criteria proposed in Chapter 2 and the statistical models in Chapter 3 may be compiled together as an R package, such that presacral vertebrae could be regionalised consistently, and model accuracy could be improved continuously with new training data.

(2) In Chapter 4, we proposed that uncinate processes might be a homologous feature across Dinosauria and even Archosauria. However, we only sampled four pseudosuchian archosaurs, so the "crocodylian-line" archosaurs are relatively poorly represented in our analysis. Examining vertebral ribs in more fossil pseudosuchians and other basal archosaurs could further test our hypothesis of homology.

We found uncinate scars in an indeterminate member of Phytosauria which we placed within Archosauria following Nesbitt et al. (2017). However, Phytosauria is sometimes recovered outside Archosauria (Ezcurra 2016; Marsh et al. 2020), which suggests a potential pre-archosaurian advent of uncinate processes. This presents an additional reason to search more widely for uncinate scars in basal archosaurs, and even in archosauriforms that fall outside Archosauria.

(3) In Chapter 5, we found histological evidence suggesting that the uncinate processes are anchored to vertebral ribs via coarse collagen fibres. In the tyrannosaurids we sampled, we also found evidence for an increase in vasculature near the attachment sites of uncinate processes, resembling the condition observed in the sampled turkey *Meleagris gallopavo* (UAMZ unnumbered). Sampling histological evidence associated with uncinate scars in theropod dinosaurs on the line to birds would make it possible to test whether increased vascularisation at uncinate process attachments is a feature that originated in fossil theropods and was inherited by extant birds, as the tyrannosaurid evidence suggests.

(4) In Chapter 7, we proposed a workflow for generating plausible estimates of oROM using tidal volume. This opens up the possibility of estimating plausible oROM using tidal volume for a wider range of activity levels, as tidal volumes change during locomotion, recovery, and resting (Lord et al. 1962; Kadono et al. 1963; Cohn and Shannon 1968; Schmidt-Nielsen et al. 1969; Berger et al. 1970; Perry 1988; Funk et al. 1993; Boggs et al. 1997; Carrier and Farmer 2000b; Farmer and Carrier 2000; Claessens 2009a). The plausible oROM estimates could then be linked to anatomical aspects of ribcage morphology and physiological aspects of gas exchange through estimated tidal volumes, which would in turn provide a more comprehensive understanding of respiration in archosaurs.

As well-preserved articulated or associated ribcages have been documented in the fossil record (Norell and Makovicky 1999; Maidment et al. 2015; Xu et al. 2015; Currie et al. 2016), the workflow proposed in Chapter 7 may be modified to generate plausible estimates of oROM and tidal volume for fossil archosaurs using such specimens. It would then be possible to search for an evolutionary link between tidal volume and changing ambient oxygen levels through deep time (Belcher and McElwain 2008; Farmer 2015).

(5) In Chapter 8, we created two kinetic models to infer ventilatory functions of trunk muscles during tidal ventilation, but neither the full plausible oROM nor the entire set of trunk muscles was considered in the analysis of the models. The ventilatory functionalities of the trunk muscles in specific situations, such as in a sitting bird (Claessens 2009b), may warrant examination of a different plausible oROM. In addition, electromyographic studies have suggested that some of the epaxial muscles may be involved in ventilation (Fedde et al. 1964; deWet et al. 1967; Baumel et al. 1990), and inferring their potential ventilatory utility using moment arms may be warranted. Functional inferences using moment arms are relevant only under the assumption that the muscles are activated in the course of the activity being modelled (i.e. inspiration and expiration), but the assumption was not tested. Combining the kinetic modeling introduced in Chapter 8 with muscle activity data from electromyographic studies to create a predictive simulation of trunk musculoskeletal activity and skeletal motions may lead to improved interpretations of trunk muscle function.

Inferences presented in Chapter 8 about muscle function, based on moment arms, hint that ribcage morphology would impact the ventilatory function of the trunk muscles. Therefore, creating kinetic models of archosaurs that vary widely in ribcage structure (Xu et al. 2015; Currie et al. 2016; Drysdale et al. 2018) may provide insights into evolutionary transitions in the ventilatory role of the trunk musculature since the dawn of Archosauria.

9.3 Literature Cited

Baumel, J.J., King, A.S., Breazile, J.E., Evans, H.E. and Vanden Berge, J.C. 1993. *Handbook of avian anatomy: Nomina anatomica avium*. second edition. Cambridge: Nuttall Ornithological Club.

Baumel, J.J., Wilson, J.A. and Bergren, D.R. 1990. The ventilatory movements of the avian pelvis and tail: function of the muscles of the tail region of the pigeon (*Columba livia*). *Journal of Experimental Biology* 151, pp. 263–277.

Belcher, C.M. and McElwain, J.C. 2008. Limits for combustion in low O2 redefine paleoatmospheric predictions for the Mesozoic. *Science* 321(5893), pp. 1197–1200.

Berger, M., Roy, O.Z. and Hart, J.S. 1970. The co-ordination between respiration and wing beats in birds. *Zeitschrift für vergleichende Physiologie* 66(2), pp. 190–200. doi: 10.1007/BF00297778.

Boggs, D.F., Jenkins, F.A. and Dial, K.P. 1997. The effects of the wingbeat cycle on respiration in black-billed magpies (pica pica). *The Journal of Experimental Biology* 200, pp. 1403–1412.

Brackenbury, J.H. 1972. Physical determinants of air flow pattern within the avian lung. *Respiration Physiology* 15(3), pp. 384–397. doi: 10.1016/0034-5687(72)90078-3.

Brocklehurst, R.J., Moritz, S., Codd, J., Sellers, W.I. and Brainerd, E.L. 2017. Rib kinematics during lung ventilation in the American alligator (*Alligator mississippiensis*): an XROMM analysis. *Journal of Experimental Biology* 220(17), pp. 3181–3190. doi: 10.1242/jeb.156166.

Brocklehurst, R.J., Moritz, S., Codd, J., Sellers, W.I. and Brainerd, E.L. 2019. XROMM kinematics of ventilation in wild turkeys (*Meleagris gallopavo*). *Journal of Experimental Biology* 222(23), p. jeb209783. doi: 10.1242/jeb.209783.

Brocklehurst, R.J., Schachner, E.R. and Sellers, W.I. 2018. Vertebral morphometrics and lung structure in non-avian dinosaurs. *Royal Society Open Science* 5(10), p. 180983. doi: 10.1098/rsos.180983.

Butler, P.J. 1982. Respiration during Flight and Diving in Birds. In: *Invited Lectures*. Elsevier, pp. 103–114. Available at: https://linkinghub.elsevier.com/retrieve/pii/B9780080279862500153 [Accessed: 11 January 2023].

Carrier, D.R. and Farmer, C.G. 2000a. The evolution of pelvic aspiration in archosaurs. *Paleobiology* 26(2), pp. 271–293. doi: 10.1666/0094-8373(2000)026<0271:TEOPAI>2.0.CO;2.

Carrier, D.R. and Farmer, C.G. 2000b. The integration of ventilation and locomotion in archosaurs. *American Zoologist* 40, pp. 87–100.

Claessens, L.P.A.M. 2004. Archosaurian respiration and the pelvic girdle aspiration breathing of crocodyliforms. *Proceedings of the Royal Society of London. Series B: Biological Sciences* 271(1547), pp. 1461–1465. doi: 10.1098/rspb.2004.2743.

Claessens, L.P.A.M. 2009a. A cineradiographic study of lung ventilation in *Alligator mississippiensis*. *Journal of Experimental Zoology Part A: Ecological Genetics and Physiology* 311A(8), pp. 563–585. doi: 10.1002/jez.530.

Claessens, L.P.A.M. 2009b. The skeletal kinematics of lung ventilation in three basal bird taxa (emu, tinamou, and guinea fowl). *Journal of Experimental Zoology Part A: Ecological Genetics and Physiology* 311A(8), pp. 586–599. doi: 10.1002/jez.501.

Claessens, L.P.A.M. and Vickaryous, M.K. 2012. The evolution, development and skeletal identity of the crocodylian pelvis: Revisiting a forgotten scientific debate. *Journal of Morphology* 273(10), pp. 1185–1198. doi: 10.1002/jmor.20059.

Codd, J.R., Boggs, D.F., Perry, S.F. and Carrier, D.R. 2005. Activity of three muscles associated with the uncinate processes of the giant Canada goose *Branta canadensis maximus*. *Journal of Experimental Biology* 208(5), pp. 849–857. doi: 10.1242/jeb.01489.

Codd, J.R., Manning, P.L., Norell, M.A. and Perry, S.F. 2008. Avian-like breathing mechanics in maniraptoran dinosaurs. *Proceedings of the Royal Society B: Biological Sciences* 275(1631), pp. 157–161. doi: 10.1098/rspb.2007.1233.

Codd, J.R., Rose, K.A.R., Tickle, P.G., Sellers, W.I., Brocklehurst, R.J., Elsey, R.M. and Crossley, D.A. 2019. A novel accessory respiratory muscle in the American alligator (*Alligator mississippiensis*). *Biology Letters* 15(7), p. 20190354. doi: 10.1098/rsbl.2019.0354.

Cohn, J.E. and Shannon, R. 1968. Respiration in unanathesitized geese. *Respiration Physiology* 5, pp. 259–268.

Currie, P.J., Holmes, R.B., Ryan, M.J. and Coy, C. 2016. A juvenile chasmosaurine ceratopsid (Dinosauria, Ornithischia) from the Dinosaur Park Formation, Alberta, Canada. *Journal of Vertebrate Paleontology* 36(2), p. e1048348. doi: 10.1080/02724634.2015.1048348.

deWet, P.D., Fedde, M.R. and Kitchell, R.L. 1967. Innervation of the respiratory muscles of *Gallus domesticus*. *Journal of Morphology* 123(1), pp. 17–34. doi: 10.1002/jmor.1051230103.

Drysdale, E.T., Therrien, F., Zelenitsky, D.K., Weishampel, D.B. and Evans, D.C. 2018. Description of juvenile specimens of *Prosaurolophus maximus* (Hadrosauridae: Saurolophinae) from the Upper Cretaceous Bearpaw Formation of southern Alberta, Canada, reveals ontogenetic changes in crest morphology. *Journal of Vertebrate Paleontology* 38(6), p. e1547310. doi: 10.1080/02724634.2018.1547310.

Duncker, H.-R. 1972. Structure of avian lungs. *Respiration Physiology* 14(1), pp. 44–63. doi: 10.1016/0034-5687(72)90016-3.

Ezcurra, M.D. 2016. The phylogenetic relationships of basal archosauromorphs, with an emphasis on the systematics of proterosuchian archosauriforms. *PeerJ* 4, p. e1778. doi: 10.7717/peerj.1778.

Farmer, C.G. 2015. The evolution of unidirectional pulmonary airflow. *Physiology* 30(4), pp. 260–272.

Farmer, C.G. and Carrier, D.R. 2000. Respiration and gas exchange during recovery from exercise in the American alligator. *Respiration Physiology* 120(1), pp. 81–87. doi: 10.1016/S0034-5687(00)00098-0.

Farmer, C.G. and Sanders, K. 2010. Unidirectional airflow in the lungs of alligators. *Science* 327(5963), pp. 338–340. doi: 10.1126/science.1180219.

Fedde, M.R., Burger, R.E. and Kitchell, R.L. 1964. Anatomic and electromyographic studies of the costo-pulmonary muscles in the cock. *Poultry Science* 43(5), pp. 1177–1184. doi: 10.3382/ps.0431177.

Funk, G.D., Sholomenko, G.N., Valenzuela, I.J., Steeves, J.D. and Milsom, W.K. 1993. Coordination of wing beat and respiration in Canada geese during free flight. *Journal of Experimental Biology* 175, pp. 317–323.

Kadono, H., Okada, T. and Ono, K. 1963. Electromyographic studies on the respiratory muscles of the chicken. *Poultry Science* 42(1), pp. 121–128. doi: 10.3382/ps.0420121.

Lord, R.D., Bellrose, F.C. and Cochran, W.W. 1962. Radiotelemetry of the Respiration of a Flying Duck. *Science* 137(3523), pp. 39–40. doi: 10.1126/science.137.3523.39.

Maidment, S.C.R., Brassey, C. and Barrett, P.M. 2015. The postcranial skeleton of an exceptionally complete individual of the plated dinosaur *Stegosaurus stenops* (Dinosauria: Thyreophora) from the Upper Jurassic Morrison Formation of Wyoming, U.S.A. *PLOS ONE* 10(10), p. e0138352. doi: 10.1371/journal.pone.0138352.

Marsh, A.D., Smith, M.E., Parker, W.G., Irmis, R.B. and Kligman, B.T. 2020. Skeletal anatomy of *Acaenasuchus geoffreyi* Long and Murry, 1995 (Archosauria: Pseudosuchia) and its implications for the origin of the aetosaurian carapace. *Journal of Vertebrate Paleontology* 40(4), p. e1794885.

Munns, S.L., Owerkowicz, T., Andrewartha, S.J. and Frappell, P.B. 2012. The accessory role of the diaphragmaticus muscle in lung ventilation in the estuarine crocodile *Crocodylus porosus*. *Journal of Experimental Biology* 215(5), pp. 845–852. doi: 10.1242/jeb.061952.

Nesbitt, S.J. et al. 2017. The earliest bird-line archosaurs and the assembly of the dinosaur body plan. *Nature* 544(7651), pp. 484–487. doi: 10.1038/nature22037.

Norell, M.A. and Makovicky, P.J. 1999. Important features of the dromaeosaurid skeleton II: Information from newly collected specimens of *Velociraptor mongoliensis*. *American Museum Novitates* (3282), pp. 1–48.

O'Connor, P.M. and Claessens, L.P.A.M. 2005. Basic avian pulmonary design and flow-through ventilation in non-avian theropod dinosaurs. *Nature* 436(7048), pp. 253–256. doi: 10.1038/nature03716.

Perry, S.F. 1988. Functional morphology of the lungs of the nile crocodile, *Crocodylus niloticus:* non-respiratory parameters. *Journal of Experimental Biology* 134(1), pp. 99–117. doi: 10.1242/jeb.134.1.99.

Powell, F.L. and Wagner, P.D. 1982. Ventilation-perfusion inequality in avian lungs. *Respiration Physiology* 48(2), pp. 233–241. doi: 10.1016/0034-5687(82)90083-4.

Romer, A.S. 1956. The axial skeleton. In: *The osteology of reptiles*. Illinois: University of Chicago Press, pp. 275–279.

Schachner, E.R., Farmer, C.G., McDonald, A.T. and Dodson, P. 2011. Evolution of the dinosauriform respiratory apparatus: New evidence from the postcranial axial skeleton. *The*

Anatomical Record: Advances in Integrative Anatomy and Evolutionary Biology 294(9), pp. 1532–1547. doi: 10.1002/ar.21439.

Schachner, E.R., Lyson, T.R. and Dodson, P. 2009. Evolution of the respiratory system in nonavian theropods: evidence from rib and vertebral morphology. *The Anatomical Record: Advances in Integrative Anatomy and Evolutionary Biology* 292(9), pp. 1501–1513. doi: 10.1002/ar.20989.

Schmidt-Nielsen, K., Kanwisher, J., Lasiewski, R.C., Cohn, J.E. and Bretz, W.L. 1969. Temperature regulation and respiration in the ostrich. *The Condor* 71(4), pp. 341–352. doi: 10.2307/1365733.

Tickle, P.G., Ennos, A.R., Lennox, L.E., Perry, S.F. and Codd, J.R. 2007. Functional significance of the uncinate processes in birds. *Journal of Experimental Biology* 210(22), pp. 3955–3961. doi: 10.1242/jeb.008953.

Xu, X. et al. 2015. The taxonomic status of the Late Cretaceous dromaeosaurid *Linheraptor exquisitus* and its implications for dromaeosaurid systematics. *Vertebrata PalAsiatica* 53, pp. 29–62.

Zimmer, K. 1935. Beiträge zur Mechanik der Atmung bei den Vögeln in Stand-und Flug. *Zoologica* 33, pp. 1–69.

Comprehensive Bibliography

Abourachid, A. et al. 2011. Bird terrestrial locomotion as revealed by 3D kinematics. *Zoology* 114(6), pp. 360–368. doi: 10.1016/j.zool.2011.07.002.

Ajiboye, A.R., Abdullah-Arshah, R., Qin, H. and Isah-Kebbe, H. 2015. Evaluating the effect of dataset size on predictive model using supervised learning technique. *International Journal of Computer Systems & Software Engineering* 1(1), pp. 75–84. doi: 10.15282/ijsecs.1.2015.6.0006.

Allen, V., Molnar, J., Parker, W., Pollard, A., Nolan, G. and Hutchinson, J.R. 2015. Comparative architectural properties of limb muscles in Crocodylidae and Alligatoridae and their relevance to divergent use of asymmetrical gaits in extant Crocodylia. *Journal of Anatomy* 225(6), pp. 569–582. doi: 10.1111/joa.12245.

Allen, V.R., Kilbourne, B.M. and Hutchinson, J.R. 2021. The evolution of pelvic limb muscle moment arms in bird-line archosaurs. *Science Advances* 7(12), p. eabe2778.

An, Y.H. and Martin, K.L. eds. 2003. *Handbook of Histology Methods for Bone and Cartilage*. Totowa, NJ: Humana Press. doi: 10.1007/978-1-59259-417-7.

Anten-Houston, M.V., Ruta, M. and Deeming, D.C. 2017. Effects of phylogeny and locomotor style on the allometry of body mass and pelvic dimensions in birds. *Journal of Anatomy* 231(3), pp. 342–358. doi: 10.1111/joa.12647.

Aoyama, H., Mizutani-Koseki, S. and Koseki, H. 2005. Three developmental compartments involved in rib formation. *The International Journal of Developmental Biology* 49(2–3), pp. 325–333. doi: 10.1387/ijdb.041932ha.

Arbour, V.M. and Currie, P.J. 2016. Systematics, phylogeny and palaeobiogeography of the ankylosaurid dinosaurs. *Journal of Systematic Palaeontology* 14(5), pp. 385–444. doi: 10.1080/14772019.2015.1059985.

Arbour, V.M. and Evans, D.C. 2017. A new ankylosaurine dinosaur from the Judith River Formation of Montana, USA, based on an exceptional skeleton with soft tissue preservation. *Royal Society Open Science* 4(5), p. 161086. doi: 10.1098/rsos.161086.

Art, T., Desmecht, D., Amory, H. and Lekeux, P. 1990. Synchronization of Locomotion and Respiration in Trotting Ponies. *Journal of Veterinary Medicine Series A* 37(1–10), pp. 95–103. doi: 10.1111/j.1439-0442.1990.tb00880.x.

Baier, D.B. and Gatesy, S.M. 2013. Three-dimensional skeletal kinematics of the shoulder girdle and forelimb in walking *Alligator*. *Journal of Anatomy* 223(5), pp. 462–473. doi: 10.1111/joa.12102.

Bakker, R.T. 1971. Dinosaur physiology and the origin of mammals. *Evolution* 25(4), pp. 636–658.

Barrowclough, G.F., Cracraft, J., Klicka, J. and Zink, R.M. 2016. How Many Kinds of Birds Are There and Why Does It Matter? *PLOS ONE* 11(11), p. e0166307. doi: 10.1371/journal.pone.0166307.

Baumel, J.J., King, A.S., Breazile, J.E., Evans, H.E. and Vanden Berge, J.C. 1993. *Handbook of avian anatomy: Nomina anatomica avium*. second edition. Cambridge: Nuttall Ornithological Club.

Baumel, J.J., Wilson, J.A. and Bergren, D.R. 1990. The ventilatory movements of the avian pelvis and tail: function of the muscles of the tail region of the pigeon (*Columba livia*). *Journal of Experimental Biology* 151, pp. 263–277.

Beddard, F.E. 1898. *The structure and classification of birds*. Longmans, Green, and Company.

Belcher, C.M. and McElwain, J.C. 2008. Limits for combustion in low O2 redefine paleoatmospheric predictions for the Mesozoic. *Science* 321(5893), pp. 1197–1200.

Benson, R.B., Butler, R.J., Carrano, M.T. and O'Connor, P.M. 2012. Air-filled postcranial bones in theropod dinosaurs: physiological implications and the 'reptile'–bird transition. *Biological Reviews* 87(1), pp. 168–193.

Benton, M.J. 2014. *Vertebrate Palaeontology*. John Wiley & Sons.

Berger, M., Hart, J.S. and Roy, O.Z. 1970a. Respiration, oxygen consumption and heart rate in some birds during rest and flight. *Zeitschrift für vergleichende Physiologie* 66(2), pp. 201–214. doi: 10.1007/BF00297779.

Berger, M., Roy, O.Z. and Hart, J.S. 1970b. The co-ordination between respiration and wing beats in birds. *Zeitschrift für vergleichende Physiologie* 66(2), pp. 190–200. doi: 10.1007/BF00297778.

Bishop, P.J. et al. 2018. Cancellous bone and theropod dinosaur locomotion. Part I—an examination of cancellous bone architecture in the hindlimb bones of theropods. *PeerJ* 6, p. e5778. doi: 10.7717/peerj.5778.

Bishop, P.J., Brocklehurst, R.J. and Pierce, S.E. 2023. Intelligent sampling of high-dimensional joint mobility space for analysis of articular function. *Methods in Ecology and Evolution* 14(2), pp. 569–582. doi: 10.1111/2041-210X.14016.

Bishop, P.J., Falisse, A., De Groote, F. and Hutchinson, J.R. 2021. Predictive simulations of running gait reveal a critical dynamic role for the tail in bipedal dinosaur locomotion. *Science Advances* 7(39), p. eabi7348.

Bivand, R., Ono, H., Dunlap, R. and Stigler, M. 2013. ClassInt: Choose univariate class intervals. *URL http://CRAN. R-project. org/package= classInt. R package version 0.1–21*.

Blitz, E. et al. 2009. Bone ridge patterning during musculoskeletal assembly is mediated through SCX regulation of Bmp4 at the tendon-skeleton junction. *Developmental Cell* 17(6), pp. 861–873. doi: 10.1016/j.devcel.2009.10.010.

Boggs, D.F. 1997. Coordinated control of respiratory pattern during locomotion in birds. *American Zoologist* 37(1), pp. 41–53. doi: 10.1093/icb/37.1.41.

Boggs, D.F., Jenkins, F.A. and Dial, K.P. 1997a. The effects of the wingbeat cycle on respiration in black-billed magpies (pica pica). *The Journal of Experimental Biology* 200, pp. 1403–1412.

Boggs, D.F., Seveyka, J.J., Kilgore, D.L. and Dial, K.P. 1997b. Coordination of Respiratory Cycles with Wingbeat Cycles in the Black-Billed Magpie (*Pica pica*). *The Journal of Experimental Biology* 200, pp. 1413–1420.

Böhmer, C., Plateau, O., Cornette, R. and Abourachid, A. 2019. Correlated evolution of neck length and leg length in birds. *Royal Society Open Science* 6(5), p. 181588. doi: 10.1098/rsos.181588.

Böhmer, C., Rauhut, O.W.M. and Wörheide, G. 2015. Correlation between Hox code and vertebral morphology in archosaurs. *Proceedings of the Royal Society B: Biological Sciences* 282(1810), p. 20150077. doi: 10.1098/rspb.2015.0077.

Bona, P. and Barrios, F. 2015. The alligatoroidea of Argentina: an update of its fossil record. *Publicación Electrónica de la Asociación Paleontológica Argentina* 15(1), pp. 143–158. doi: 10.5710/PEAPA.15.06.2015.103.

Borinder, N. 2015. *Postcranial anatomy of* Tanius sinensis *Wiman, 1929 (Dinosauria; Hadrosauroidea)*. PhD Dissertation, Uppsala University.

Bourdon, E. and Lindow, B. 2015. A redescription of *Lithornis vulturinus* (Aves, Palaeognathae) from the Early Eocene Fur Formation of Denmark. *Zootaxa* 4032(5), pp. 493–514.

Boyd, C.A. 2015. The systematic relationships and biogeographic history of ornithischian dinosaurs. *PeerJ* 3, p. e1523. doi: 10.7717/peerj.1523.

Boyd, C.A., Brown, C.M., Scheetz, R.D. and Clarke, J.A. 2009. Taxonomic revison of the basal neornithischian taxa *Thescelosaurus* and *Bugenasaura*. *Journal of Vertebrate Paleontology* 29(3), pp. 758–770. doi: 10.1671/039.029.0328.

Boyd, C.A., Cleland, T.P. and Novas, F. 2011. Osteogenesis, homology, and function of the intercostal plates in ornithischian dinosaurs (Tetrapoda, Sauropsida). *Zoomorphology* 130(4), pp. 305–313. doi: 10.1007/s00435-011-0136-x.

Brackenbury, J.H. 1972. Physical determinants of air flow pattern within the avian lung. *Respiration Physiology* 15(3), pp. 384–397. doi: 10.1016/0034-5687(72)90078-3.

Brackenbury, J.H., Gleeson, M. and Avery, P. 1982. Respiration in exercising fowl. III. ventilation. *Journal of Experimental Biology* 96(1), pp. 315–324. doi: 10.1242/jeb.96.1.315.

Brainerd, E.L., Baier, D.B., Gatesy, S.M., Hedrick, T.L., Metzger, K.A., Gilbert, S.L. and Crisco, J.J. 2010. X-ray reconstruction of moving morphology (XROMM): precision, accuracy and applications in comparative biomechanics research. *Journal of Experimental Zoology Part A: Ecological Genetics and Physiology* 9999A, p. n/a-n/a. doi: 10.1002/jez.589.

Brainerd, E.L., Moritz, S. and Ritter, D.A. 2015. XROMM analysis of rib kinematics during lung ventilation in the green iguana, *Iguana iguana*. *Journal of Experimental Biology* 219, p. jeb.127928. doi: 10.1242/jeb.127928.

Brainerd, E.L. and Owerkowicz, T. 2006. Functional morphology and evolution of aspiration breathing in tetrapods. *Respiratory Physiology & Neurobiology* 154(1–2), pp. 73–88. doi: 10.1016/j.resp.2006.06.003.

Bramwell, C.D., Whitfield, G.R. and Parrington, F.R. 1997. Biomechanics of *Pteranodon*. *Philosophical Transactions of the Royal Society of London. B, Biological Sciences* 267(890), pp. 503–581. doi: 10.1098/rstb.1974.0007.

Brink, K.S. et al. 2015. Developmental and evolutionary novelty in the serrated teeth of theropod dinosaurs. *Scientific Reports* 5(1), p. 12338. doi: 10.1038/srep12338.

Brochu, C. 2011. Phylogenetic relationships of *Necrosuchus ionensis* Simpson, 1937 and the early history of caimanines. *Zoological Journal of the Linnean Society* 163(sup 1), pp. S228–S256. doi: 10.1111/j.1096-3642.2011.00716.x.

Brochu, C.A. 2003. Osteology of *Tyrannosaurus Rex*: Insights from a nearly complete skeleton and high-resolution computed tomographic analysis of the skull. *Journal of Vertebrate Paleontology* 22(sup 4), pp. 1–138. doi: 10.1080/02724634.2003.10010947.

Brocklehurst, R.J., Moritz, S., Codd, J., Sellers, W.I. and Brainerd, E.L. 2017. Rib kinematics during lung ventilation in the American alligator (*Alligator mississippiensis*): an XROMM analysis. *Journal of Experimental Biology* 220(17), pp. 3181–3190. doi: 10.1242/jeb.156166.

Brocklehurst, R.J., Moritz, S., Codd, J., Sellers, W.I. and Brainerd, E.L. 2019. XROMM kinematics of ventilation in wild turkeys (*Meleagris gallopavo*). *Journal of Experimental Biology* 222(23), p. jeb209783. doi: 10.1242/jeb.209783.

Brocklehurst, R.J., Schachner, E.R., Codd, J.R. and Sellers, W.I. 2020. Respiratory evolution in archosaurs. *Philosophical Transactions of the Royal Society B: Biological Sciences* 375(1793), p. 20190140. doi: 10.1098/rstb.2019.0140.

Brocklehurst, R.J., Schachner, E.R. and Sellers, W.I. 2018. Vertebral morphometrics and lung structure in non-avian dinosaurs. *Royal Society Open Science* 5(10), p. 180983. doi: 10.1098/rsos.180983.

Brown, B. and Schlaikjer, E.M. 1942. The skeleton of *Leptoceratops* with the description of a new species. *American Museum Novitates* 1169, pp. 1–15.

Brown, C.M., Boyd, C.A. and Russell, A.P. 2011. A new basal ornithopod dinosaur (Frenchman Formation, Saskatchewan, Canada), and implications for late Maastrichtian ornithischian diversity in North America. *Zoological Journal of the Linnean Society* 163(4), pp. 1157–1198.

Brusatte, S.L., Benton, M.J., Desojo, J.B. and Langer, M.C. 2010a. The higher-level phylogeny of Archosauria (Tetrapoda: Diapsida). *Journal of Systematic Palaeontology* 8(1), pp. 3–47. doi: 10.1080/14772010903537732.

Brusatte, S.L., Nesbitt, S.J., Irmis, R.B., Butler, R.J., Benton, M.J. and Norell, M.A. 2010b. The origin and early radiation of dinosaurs. *Earth-Science Reviews* 101(1–2), pp. 68–100. doi: 10.1016/j.earscirev.2010.04.001.

Bryant, H.N. and Seymour, K.L. 1990. Observations and comments on the reliability of muscle reconstruction in fossil vertebrates. *Journal of Morphology* 206(1), pp. 109–117.

Bui, H.-N.N. and Larsson, H.C.E. 2021. Development and evolution of regionalization within the avian axial column. *Zoological Journal of the Linnean Society* 191(1), pp. 302–321. doi: 10.1093/zoolinnean/zlaa038.

Burness, G.P., Diamond, J. and Flannery, T. 2001. Dinosaurs, dragons, and dwarfs: The evolution of maximal body size. *Proceedings of the National Academy of Sciences* 98(25), pp. 14518–14523. doi: 10.1073/pnas.251548698.

Buscalioni, Á.D., Alcalá, L., Espílez, E. and Mampel, L. 2020. European Goniopholididae from the Early Albian Escucha Formation in Ariño (Teruel, Aragón, Spain). *Spanish Journal of Palaeontology* 28(1), pp. 103–122.

Buscalioni, A.D., Piras, P., Vullo, R., Signore, M. and Barbera, C. 2011. Early eusuchia crocodylomorpha from the vertebrate-rich Plattenkalk of Pietraroia (Lower Albian, southern Apennines, Italy). *Zoological Journal of the Linnean Society* 163, pp. S199–S227. doi: 10.1111/j.1096-3642.2011.00718.x.

Butler, P.J. 1981. Respiration during flight. In: *Respiration*. Elsevier, pp. 155–164. Available at: https://linkinghub.elsevier.com/retrieve/pii/B9780080268231500247 [Accessed: 11 January 2023].

Butler, P.J. 1982. Respiration during Flight and Diving in Birds. In: *Invited Lectures*. Elsevier, pp. 103–114. Available at: https://linkinghub.elsevier.com/retrieve/pii/B9780080279862500153 [Accessed: 11 January 2023].

Butler, R.J., Brusatte, S.L., Reich, M., Nesbitt, S.J. and Schoch, R.R. 2011. The sail-backed reptile *Ctenosauriscus* from the latest Early Triassic of Germany and the timing and biogeography of the early archosaur radiation.

Butler, R.J. and Galton, P.M. 2008. The 'dermal armour' of the ornithopod dinosaur *Hypsilophodon* from the Wealden (Early Cretaceous: Barremian) of the Isle of Wight: a reappraisal. *Cretaceous Research* 29(4), pp. 636–642. doi: 10.1016/j.cretres.2008.02.002.

Butler, R.J., Jones, A.S., Buffetaut, E., Mandl, G.W., Scheyer, T.M. and Schultz, O. 2019. Description and phylogenetic placement of a new marine species of phytosaur (Archosauriformes: Phytosauria) from the Late Triassic of Austria. *Zoological Journal of the Linnean Society* 187(1), pp. 198–228. doi: 10.1093/zoolinnean/zlz014.

Campione, N.E. 2014. Postcranial anatomy of *Edmontosaurus regalis* (Hadrosauridae) from the Horseshoe Canyon Formation, Alberta, Canada. In: *Hadrosaurs*. Indiana University Press, pp. 208–244.

Canalis, R.F. and Burstein, F.D. 1985. Osteogenesis in vascularized periosteum: interactions with underlying bone. *Archives of Otolaryngology - Head and Neck Surgery* 111(8), pp. 511–516. doi: 10.1001/archotol.1985.00800100059007.

Capano, J.G., Moritz, S., Cieri, R.L., Reveret, L. and Brainerd, E.L. 2019. Rib motions don't completely hinge on joint design: costal joint anatomy and ventilatory kinematics in a teiid

lizard, *Salvator merianae*. *Integrative Organismal Biology* 1(1), p. oby004. doi: 10.1093/iob/oby004.

Carboneras, C. 1992. Anseriformes. In: *Handbook of birds of the world*. Barcelona: Lynx Edicions, pp. 528–628.

Carpenter, K. 2004. Redescription of *Ankylosaurus magniventris* Brown 1908 (Ankylosauridae) from the Upper Cretaceous of the Western Interior of North America. *Canadian Journal of Earth Sciences* 41(8), pp. 961–986. doi: 10.1139/e04-043.

Carrano, M.T. 1999. What, if anything, is a cursor? Categories versus continua for determining locomotor habit in mammals and dinosaurs. *Journal of Zoology* 247(1), pp. 29–42. doi: 10.1111/j.1469-7998.1999.tb00190.x.

Carrano, M.T., Benson, R.B.J. and Sampson, S.D. 2012. The phylogeny of Tetanurae (Dinosauria: Theropoda). *Journal of Systematic Palaeontology* 10(2), pp. 211–300. doi: 10.1080/14772019.2011.630927.

Carrano, M.T. and Hutchinson, J.R. 2002. Pelvic and hindlimb musculature of *Tyrannosaurus rex* (Dinosauria: Theropoda). *Journal of Morphology* 253(3), pp. 207–228.

Carrier, D.R. 1987. The evolution of locomotor stamina in tetrapods: Circumventing a mechanical constraint. *Paleobiology* 13(3), pp. 326–341.

Carrier, D.R. 1996. Function of the intercostal muscles in trotting dogs: Ventilation or locomotion? *The Journal of Experimental Biology* 199, pp. 1455–1465.

Carrier, D.R. and Farmer, C.G. 2000a. The evolution of pelvic aspiration in archosaurs. *Paleobiology* 26(2), pp. 271–293. doi: 10.1666/0094-8373(2000)026<0271:TEOPAI>2.0.CO;2.

Carrier, D.R. and Farmer, C.G. 2000b. The evolution of pelvic aspiration in archosaurs. *Paleobiology* 26(2), pp. 271–293. doi: 10.1666/0094-8373(2000)026<0271:TEOPAI>2.0.CO;2.

Carrier, D.R. and Farmer, C.G. 2000c. The integration of ventilation and locomotion in archosaurs. *American Zoologist* 40, pp. 87–100.

Chatterjee, S. 1985. *Postosuchus*, a new thecodontian reptile from the Triassic of Texas and the origin of tyrannosaurs. *Philosophical Transactions of the Royal Society of London. B, Biological Sciences* 309, pp. 395–460.

Cieri, R.L., Hatch, S.T., Capano, J.G. and Brainerd, E.L. 2020. Locomotor rib kinematics in two species of lizards and a new hypothesis for the evolution of aspiration breathing in amniotes. *Scientific Reports* 10(1), p. 7739. doi: 10.1038/s41598-020-64140-y.

Claessens, K.P. 2015. Anatomical transformations and respiratory innovations of the archosaur trunk. In: *Great Transformations in Vertebrate Evolution*. University of Chicago Press. doi: 10.7208/chicago/9780226268392.001.0001.

Claessens, L.P.A.M. 2004. Archosaurian respiration and the pelvic girdle aspiration breathing of crocodyliforms. *Proceedings of the Royal Society of London. Series B: Biological Sciences* 271(1547), pp. 1461–1465. doi: 10.1098/rspb.2004.2743.

Claessens, L.P.A.M. 2009a. A cineradiographic study of lung ventilation in *Alligator mississippiensis*. *Journal of Experimental Zoology Part A: Ecological Genetics and Physiology* 311A(8), pp. 563–585. doi: 10.1002/jez.530.

Claessens, L.P.A.M. 2009b. The skeletal kinematics of lung ventilation in three basal bird taxa (emu, tinamou, and guinea fowl). *Journal of Experimental Zoology Part A: Ecological Genetics and Physiology* 311A(8), pp. 586–599. doi: 10.1002/jez.501.

Claessens, L.P.A.M., O'Connor, P.M. and Unwin, D.M. 2009. Respiratory Evolution Facilitated the Origin of Pterosaur Flight and Aerial Gigantism. Sereno, P. ed. *PLoS ONE* 4(2), p. e4497. doi: 10.1371/journal.pone.0004497.

Claessens, L.P.A.M. and Vickaryous, M.K. 2012. The evolution, development and skeletal identity of the crocodylian pelvis: Revisiting a forgotten scientific debate. *Journal of Morphology* 273(10), pp. 1185–1198. doi: 10.1002/jmor.20059.

Clark, J.M., Xu, X., Forster, C.A. and Wang, Y. 2004. A Middle Jurassic 'sphenosuchian' from China and the origin of the crocodylian skull. *Nature* 430(7003), pp. 1021–1024. doi: 10.1038/nature02802.

Codd, J.R. 2010. Uncinate processes in birds: Morphology, physiology and function. *Comparative biochemistry and physiology part a: molecular & integrative physiology* 156(3), pp. 303–308. doi: 10.1016/j.cbpa.2009.12.005.

Codd, J.R., Boggs, D.F., Perry, S.F. and Carrier, D.R. 2005. Activity of three muscles associated with the uncinate processes of the giant Canada goose *Branta canadensis maximus*. *Journal of Experimental Biology* 208(5), pp. 849–857. doi: 10.1242/jeb.01489.

Codd, J.R., Manning, P.L., Norell, M.A. and Perry, S.F. 2008a. Avian-like breathing mechanics in maniraptoran dinosaurs. *Proceedings of the Royal Society B: Biological Sciences* 275(1631), pp. 157–161. doi: 10.1098/rspb.2007.1233.

Codd, J.R., Manning, P.L., Norell, M.A. and Perry, S.F. 2008b. Avian-Like Breathing Mechanics in Maniraptoran Dinosaurs. *Proceedings: Biological Sciences* 275(1631), pp. 157–161.

Codd, J.R., Rose, K.A.R., Tickle, P.G., Sellers, W.I., Brocklehurst, R.J., Elsey, R.M. and Crossley, D.A. 2019. A novel accessory respiratory muscle in the American alligator (*Alligator mississippiensis*). *Biology Letters* 15(7), p. 20190354. doi: 10.1098/rsbl.2019.0354.

Cohn, J.E. and Shannon, R. 1968. Respiration in unanathesitized geese. *Respiration Physiology* 5, pp. 259–268.

Cong, L.Y., Hou, L.H. and Wu, X.C. 1988. *The Gross anatomy of Alligator sinensis Fauvel: Integument, Osteology, and Myology (In Chinese with English summary)*. Beijing, China: China Science Publishing & Media Ltd.

Cuesta, E., Vidal, D., Ortega, F., Shibata, M. and Sanz, J.L. 2022. *Pelecanimimus* (Theropoda: Ornithomimosauria) postcranial anatomy and the evolution of the specialized manus in Ornithomimosaurs and sternum in maniraptoriforms. *Zoological Journal of the Linnean Society* 194(2), pp. 553–591. doi: 10.1093/zoolinnean/zlab013.

Cullen, T.M., Evans, D.C., Ryan, M.J., Currie, P.J. and Kobayashi, Y. 2014. Osteohistological variation in growth marks and osteocyte lacunar density in a theropod dinosaur (Coelurosauria: Ornithomimidae).

Currey, J.D. 2003. The many adaptations of bone. *Journal of Biomechanics* 36(10), pp. 1487–1495. doi: 10.1016/S0021-9290(03)00124-6.

Currie, P.J. 2003. Cranial anatomy of tyrannosaurid dinosaurs from the Late Cretaceous of Alberta,Canada. *Acta Palaeontologica Polonica* 48(2), pp. 191–226.

Currie, P.J. and Evans, D.C. 2019. Cranial Anatomy of New Specimens of *Saurornitholestes langstoni* (Dinosauria, Theropoda, Dromaeosauridae) from the Dinosaur Park Formation (Campanian) of Alberta. *The Anatomical Record* 303(4), pp. 691–715. doi: 10.1002/ar.24241.

Currie, P.J., Holmes, R.B., Ryan, M.J. and Coy, C. 2016. A juvenile chasmosaurine ceratopsid (Dinosauria, Ornithischia) from the Dinosaur Park Formation, Alberta, Canada. *Journal of Vertebrate Paleontology* 36(2), p. e1048348. doi: 10.1080/02724634.2015.1048348.

Currie, P.J., Koppelhus, E.B., Shugar, M.A. and Wright, J.L. 2004. *Feathered Dragons: Studies on the Transition from Dinosaurs to Birds*. Indiana University Press.

Currie, P.J. and Zhao, X.-J. 1993. A new carnosaur (Dinosauria, Theropoda) from the Jurassic of Xinjiang, People's Republic of China. *Canadian Journal of Earth Sciences* 30(10), pp. 2037–2081. doi: 10.1139/e93-179.

Dai, J. and Rabie, A.B.M. 2007. VEGF: an essential mediator of both angiogenesis and endochondral ossification. *Journal of Dental Research* 86(10), pp. 937–950. doi: 10.1177/154405910708601006.

Dalla Vecchia, F.M. 2009. *Tethyshadros insularis* , a new hadrosauroid dinosaur (Ornithischia) from the Upper Cretaceous of Italy. *Journal of Vertebrate Paleontology* 29(4), pp. 1100–1116. doi: 10.1671/039.029.0428.

Dececchi, T.A., Mloszewska, A.M., Holtz, T.R., Habib, M.B. and Larsson, H.C.E. 2019. The fast and the frugal: Divergent locomotory strategies drive limb lengthening in theropod dinosaurs. doi: 10.1101/785238.

Demuth, O.E., Rayfield, E.J. and Hutchinson, J.R. 2020. 3D hindlimb joint mobility of the stem-archosaur Euparkeria capensis with implications for postural evolution within Archosauria. *Scientific Reports* 10(1), p. 15357. doi: 10.1038/s41598-020-70175-y.

deWet, P.D., Fedde, M.R. and Kitchell, R.L. 1967. Innervation of the respiratory muscles of *Gallus domesticus*. *Journal of Morphology* 123(1), pp. 17–34. doi: 10.1002/jmor.1051230103.

Dial, K.P. 2003. Evolution of avian locomotion: Correlates of flight style, locomotor modules, nesting biology, body size, development, and the origin of flapping flight. *The Auk* 120(4), pp. 941–952. doi: 10.1093/auk/120.4.941.

Dilkes, D. and Sues, H.-D. 2009. Redescription and phylogenetic relationships of *Doswellia kaltenbachi* (Diapsida: Archosauriformes) from the Upper Triassic of Virginia. *Journal of Vertebrate Paleontology* 29, pp. 58–79.

Dollman, K.N., Clark, J.M., Viglietti, P.A., Browning, C. and Choiniere, J.N. 2021. Revised anatomy, taxonomy and biostratigraphy of Notochampsa istedana Broom, 1904, a Lower Jurassic crocodyliform from the Clarens Formation (Stormberg Group), and its implications for early crocodyliform phylogeny. *Journal of Systematic Palaeontology* 19(9), pp. 651–675.

Dollman, K.N., Viglietti, P.A. and Choiniere, J.N. 2019. A new specimen of *Orthosuchus stormbergi* (Nash 1968) and a review of the distribution of Southern African Lower Jurassic crocodylomorphs. *Historical Biology* 31(5), pp. 653–664. doi: 10.1080/08912963.2017.1387110.

Dong, Z.M., Zhou, S.W. and Zhang, X. 1983. Dinosaurs from the Jurassic of Sichuan. *Palaeontologia Sinica* 162, pp. 1–151.

Drysdale, E.T., Therrien, F., Zelenitsky, D.K., Weishampel, D.B. and Evans, D.C. 2018. Description of juvenile specimens of *Prosaurolophus maximus* (Hadrosauridae: Saurolophinae) from the Upper Cretaceous Bearpaw Formation of southern Alberta, Canada, reveals ontogenetic changes in crest morphology. *Journal of Vertebrate Paleontology* 38(6), p. e1547310. doi: 10.1080/02724634.2018.1547310.

Dumbravă, M., Codrea, V., Solomon, A. and Andrei, R. 2013. Hind leg myology of the Maastrichtian (latest Cretaceous) euornithischian dinosaur *Zalmoxes shquiperorum* from the HaDeg Basin, Romania: preliminary data. *Oltenia. Studii Di comunicări. DtiinDele Naturii* 29(2), pp. 7–18.

Duncker, H.-R. 1972a. Structure of avian lungs. *Respiration Physiology* 14(1), pp. 44–63. doi: 10.1016/0034-5687(72)90016-3.

Duncker, H.-R. 1972b. Structure of avian lungs. *Respiration Physiology* 14(1), pp. 44–63. doi: 10.1016/0034-5687(72)90016-3.

Dunning Jr, J.B. 2007. *CRC handbook of avian body masses*. CRC press.

Eberth, D.A. and Evans, D.C. 2014. *Hadrosaurs*. Indiana University Press.

Efimov, M.B. 1975. Late Cretaceous crocodiles of Soviet Central Asia and Kazakhstan. *Paleontologicheskii Zhurnal* 9, pp. 417–420.

Evans, D.C., Brown, C.M., You, H. and Campione, N.E. 2021. Description and revised diagnosis of Asia's first recorded pachycephalosaurid, *Sinocephale bexelli* gen. nov., from the Upper Cretaceous of Inner Mongolia, China. *Canadian Journal of Earth Sciences* 58(10), pp. 981–992.

Evans, H.E. and Miller, M.E. 2013. *Miller's anatomy of the dog*. Fourth edition. St. Louis, Missouri: Elsevier.

Ezcurra, M.D. 2016. The phylogenetic relationships of basal archosauromorphs, with an emphasis on the systematics of proterosuchian archosauriforms. *PeerJ* 4, p. e1778. doi: 10.7717/peerj.1778.

Farke, A.A. 2011. Anatomy and taxonomic status of the chasmosaurine ceratopsid *Nedoceratops hatcheri* from the Upper Cretaceous Lance Formation of Wyoming, U.S.A. *PLOS ONE* 6(1), p. e16196. doi: 10.1371/journal.pone.0016196.

Farmer, C.G. 2015a. The evolution of unidirectional pulmonary airflow. *Physiology* 30(4), pp. 260–272.

Farmer, C.G. 2015b. Unidirectional flow in lizard lungs: a paradigm shift in our understanding of lung evolution in Diapsida. *Zoology* 118(5), pp. 299–301. doi: 10.1016/j.zool.2015.06.001.

Farmer, C.G. 2017. Pulmonary Transformations of Vertebrates. In: *The Biology of the Avian Respiratory System*. Cham: Springer International Publishing, pp. 99–112. doi: 10.1007/978-3-319-44153-5_3.

Farmer, C.G. and Carrier, D.R. 2000a. Pelvic aspiration in alligators. *The Journal of Experimental Biology* 203, pp. 1679–1687.

Farmer, C.G. and Carrier, D.R. 2000b. Respiration and gas exchange during recovery from exercise in the American alligator. *Respiration Physiology* 120(1), pp. 81–87. doi: 10.1016/S0034-5687(00)00098-0.

Farmer, C.G. and Sanders, K. 2010. Unidirectional airflow in the lungs of alligators. *Science* 327(5963), pp. 338–340. doi: 10.1126/science.1180219.

Fedde, M.R., Burger, R.E. and Kitchell, R.L. 1964. Anatomic and electromyographic studies of the costo-pulmonary muscles in the cock. *Poultry Science* 43(5), pp. 1177–1184. doi: 10.3382/ps.0431177.

Filipowska, J., Tomaszewski, K.A., Niedźwiedzki, Ł., Walocha, J.A. and Niedźwiedzki, T. 2017. The role of vasculature in bone development, regeneration and proper systemic functioning. *Angiogenesis* 20(3), pp. 291–302. doi: 10.1007/s10456-017-9541-1.

Fisher, P.E., Russell, D.A., Stoskopf, M.K., Barrick, R.E., Hammer, M. and Kuzmitz, A.A. 2000. Cardiovascular evidence for an intermediate or higher metabolic rate in an ornithischian dinosaur. *Science* 288(5465), pp. 503–505. doi: 10.1126/science.288.5465.503.

Forster, C. 1990. The postcranial skeleton of the ornithopod dinosaur *Tenontosaurus tilletti*. *Journal of Vertebrate Paleontology* 10(3), pp. 273–294. doi: 10.1080/02724634.1990.10011815.

Foth, C. and Rauhut, O.W.M. eds. 2020. *The Evolution of Feathers: From Their Origin to the Present*. Cham: Springer International Publishing. Available at: http://link.springer.com/10.1007/978-3-030-27223-4 [Accessed: 12 January 2023].

Francillon-Vieillot, H. et al. 1990. Microstructure and mineralization of vertebrate skeletal tissues. In: *Skeletal Biomineralization: Patterns, Processes and Evolutionary Trends*. New York: Van Nostrand Reinhold, pp. 471–530.

Francisco Botelho, J., Smith-Paredes, D., Soto-Acuña, S., Mpodozis, J., Palma, V. and Vargas, A.O. 2015. Skeletal plasticity in response to embryonic muscular activity underlies the

development and evolution of the perching digit of birds. *Scientific Reports* 5(1), p. 9840. doi: 10.1038/srep09840.

Frey, T. von E. 1988. Anatomie des Körperstammes von *Alligator mississippiensis* Daudin. *Stuttgarter Beitraege zur Naturkunde, Serie A* 424, pp. 1–106.

Fujiwara, S., Kuwazuru, O., Inuzuka, N. and Yoshikawa, N. 2009. Relationship between scapular position and structural strength of rib cage in quadruped animals. *Journal of Morphology* 270(9), pp. 1084–1094. doi: 10.1002/jmor.10744.

Funk, G.D., Sholomenko, G.N., Valenzuela, I.J., Steeves, J.D. and Milsom, W.K. 1993. Coordination of wing beat and respiration in Canada geese during free flight. *Journal of Experimental Biology* 175, pp. 317–323.

Funston, G.F. and Currie, P.J. 2016. A new caenagnathid (Dinosauria: Oviraptorosauria) from the Horseshoe Canyon Formation of Alberta, Canada, and a reevaluation of the relationships of Caenagnathidae. *Journal of Vertebrate Paleontology* 36(4), p. e1160910.

Galton, P.M. 2009. Notes on Neocomian (Lower Cretaceous) ornithopod dinosaurs from England–*Hypsilophodon*, *Valdosaurus*, "*Camptosaurus*", "*Iguanodon*" – and referred specimens from Romania and elsewhere. *Revue de Paléobiologie* 28(1), pp. 211–73.

Gangl, D., Weissengruber, G.E., Egerbacher, M. and Forstenpointner, G. 2004. Anatomical description of the muscles of the pelvic limb in the ostrich (*Struthio camelus*). *Anatomia, Histologia, Embryologia* 33(2), pp. 100–114.

Gans, C. and Clark. 1976. Studies on ventilation of *Caiman crocodilus* (Crocodylia: Reptilia). *Respiration Physiology* 26, p. 1.

Gatesy, S.M. 1991. Hind limb movements of the American alligator (*Alligator mississippiensis*) and postural grades. *Journal of Zoology* 224(4), pp. 577–588.

Gatesy, S.M. 1997. An electromyographic analysis of hindlimb function in *Alligator* during terrestrial locomotion. *Journal of Morphology* 234(2), pp. 197–212. doi: 10.1002/(SICI)1097-4687(199711)234:2<197::AID-JMOR6>3.0.CO;2-9.

Gatesy, S.M., Baier, D.B., Jenkins, F.A. and Dial, K.P. 2010. Scientific rotoscoping: a morphology-based method of 3-D motion analysis and visualization. *Journal of Experimental Zoology Part A: Ecological Genetics and Physiology* 9999A, p. n/a-n/a. doi: 10.1002/jez.588.

Gatesy, S.M., Bäker, M. and Hutchinson, J.R. 2009. Constraint-based exclusion of limb poses for reconstructing theropod dinosaur locomotion. *Journal of Vertebrate Paleontology* 29(2), pp. 535–544. doi: 10.1671/039.029.0213.

Gatesy, S.M. and Biewener, A.A. 1991. Bipedal locomotion: effects of speed, size and limb posture in birds and humans. *Journal of Zoology* 224(1), pp. 127–147. doi: 10.1111/j.1469-7998.1991.tb04794.x.

Gatesy, S.M. and Middleton, K.M. 1997. Bipedalism, flight, and the evolution of theropod locomotor diversity. *Journal of Vertebrate Paleontology* 17(2), pp. 308–329.

Gauthier, J., Padian, K., Hecht, M.K., Ostrom, J.H., Viohl, G. and Wellnhofer, P. 1985. Phylogenetic, functional, and aerodynamic analyses of the origin of birds and their flight. *The beginning of birds*, pp. 185–197.

Gauthier, J.A. 1984. *A cladistic analysis of the higher systematic categories of the Diapsida*. PhD Dissertation, University of California, Berkeley.

George, J.C. and Berger, A.J. 1966. *Avian myology*. New York and London: Academic Press.

Georgi, J.A. and Krause, D.W. 2010. Postcranial axial skeleton of *Simosuchus clarki* (Crocodyliformes: Notosuchia) from the Late Cretaceous of Madagascar. *Journal of Vertebrate Paleontology* 30(sup1), pp. 99–121. doi: 10.1080/02724634.2010.519172.

Ghetie, V. 1976. *Atlas de anatomie a păsărilor domestice*. Academiei Republicii Socialiste România.

Gilmore, C.W. 1920. Osteology of the carnivorous Dinosauria in the United States National Museum: with special reference to the Genera *Antrodemus* (*Allosaurus*) and *Ceratosaurus*. *Bulletin of the United States National Museum* 110, pp. 1–154.

Gorscak, E. and O'Connor, P.M. 2019. A new African titanosaurian sauropod dinosaur from the Middle Cretaceous Galula Formation (Mtuka member), Rukwa Rift Basin, Southwestern Tanzania. *PLOS ONE* 14(2), p. e0211412. doi: 10.1371/journal.pone.0211412.

Griffin, B., Martin-Silverstone, E., Demuth, O., Pêgas, R., Palmer, C. and Rayfield, E. 2022. Constraining pterosaur launch: range of motion in the pectoral and pelvic girdles of a medium-sized ornithocheiraean pterosaur. *Biological Journal of the Linnean Society* 137(2), pp. 250–266. doi: 10.1093/biolinnean/blac063.

Griffin, C.T., Stefanic, C.M., Parker, W.G., Hungerbühler, A. and Stocker, M.R. 2017. Sacral anatomy of the phytosaur *Smilosuchus adamanensis*, with implications for pelvic girdle evolution among archosauriformes. *Journal of Anatomy* 231(6), pp. 886–905. doi: 10.1111/joa.12681.

Grigg, G. 2015. *Biology and Evolution of Crocodylians*. Csiro Publishing.

Hall, B.K. 2005. *Bones and cartilage: developmental and evolutionary skeletal biology*. Elsevier Academic Press.

Halliday, T. 2013. A re-evaluation of goniopholidid crocodylomorph material from Central Asia: Biogeographic and phylogenetic implications. *Acta Palaeontologica Polonica* 60(2). doi: 10.4202/app.2013.0018.

Halvorson, D.B. 1972. Differences in naming muscles of the pelvic limb of chicken. *Poultry Science* 51(3), pp. 727–738. doi: 10.3382/ps.0510727.

Han, F., Forster, C.A., Xu, X. and Clark, J.M. 2018. Postcranial anatomy of *Yinlong downsi* (Dinosauria: Ceratopsia) from the Upper Jurassic Shishugou Formation of China and the phylogeny of basal ornithischians. *Journal of Systematic Palaeontology* 16(14), pp. 1159–1187. doi: 10.1080/14772019.2017.1369185.

Harris, J.D. 2004. Confusing dinosaurs with mammals: tetrapod phylogenetics and anatomical terminology in the world of homology. *The Anatomical Record Part A: Discoveries in Molecular, Cellular, and Evolutionary Biology: An Official Publication of the American Association of Anatomists* 281(2), pp. 1240–1246.

Hastings, A.K., Bloch, J.I. and Jaramillo, C.A. 2015. A new blunt-snouted dyrosaurid, *Anthracosuchus balrogus* gen. et **sp. nov.** (Crocodylomorpha, Mesoeucrocodylia), from the Palaeocene of Colombia. *Historical Biology* 27(8), pp. 998–1020. doi: 10.1080/08912963.2014.918968.

Haughton, S. 1867. The muscular anatomy of the emu (*Dromaius novaehollandiae*). *Proceedings of the Royal Irish Academy* 9, pp. 487–497.

Heckert, A.B. and Lucas, S.G. 2003. Stratigraphy and paleontology of the Lower Chinle Group (Adamanian: latest Carnian) in the vicinity of St. Johns, Arizona. *New Mexico Geological Society Guidebook* 54, pp. 281–288.

Heckert, A.B., Lucas, S.G., Hunt, A.P. and Harris, J.D. 2001. A giant phytosaur (Reptilia: Archosauria) skull from the Redonda Formation (Upper Triassic: Apachean) of East-Central New Mexico. *New Mexico Geological Society Guidebook* 52, pp. 171–178.

Hendrickx, C., Araújo, R. and Mateus, O. 2015. The non-avian theropod quadrate I: standardized terminology with an overview of the anatomy and function. *PeerJ* 3, p. e1245. doi: 10.7717/peerj.1245.

Hennig, W. 1971. *Insect Phylogeny*. New York: Wiley.

Herbst, E.C., Eberhard, E.A., Richards, C.T. and Hutchinson, J.R. 2022. *In vivo* and *ex vivo* range of motion in the fire salamander *Salamandra salamandra*. *Journal of Anatomy* 241(4), pp. 1066–1082. doi: 10.1111/joa.13738.

Heritage, S. 2021. MBASR: Workflow-simplified ancestral state reconstruction of discrete traits with MrBayes in the R environment. *BioRxiv*, pp. 2021–01.

Hildebrand, M. 1982. *Analysis of vertebrate structure*. New York: Wiley Blackwell.

Hoffman, D.K., Heckert, A.B. and Zanno, L.E. 2018. Under the armor: X-ray computed tomographic reconstruction of the internal skeleton of *Coahomasuchus chathamensis* (Archosauria: Aetosauria) from the Upper Triassic of North Carolina, USA, and a phylogenetic analysis of Aetosauria. *PeerJ* 6, p. e4368. doi: 10.7717/peerj.4368.

Holliday, C.M. 2009. New Insights Into Dinosaur Jaw Muscle Anatomy. *The anatomical record: advances in integrative anatomy and evolutionary biology* 292(9), pp. 1246–1265. doi: 10.1002/ar.20982.

Holliday, C.M. and Witmer, L.M. 2007. Archosaur adductor chamber evolution: Integration of musculoskeletal and topological criteria in jaw muscle homology. *Journal of Morphology* 268(6), pp. 457–484. doi: 10.1002/jmor.10524.

Hone, D.W.E. and Rauhut, O.W.M. 2009. Feeding behaviour and bone utilization by theropod dinosaurs: Theropod feeding behaviour. *Lethaia* 43(2), pp. 232–244. doi: 10.1111/j.1502-3931.2009.00187.x.

Hudson, G.E. 1937. Studies on the muscles of the pelvic appendage in birds. *The American Midland Naturalist* 18, pp. 1–108.

Hudson, G.E., Lanzillotti, P.J. and Edwards, G.D. 1959. Muscles of the pelvic limb in galliform birds. *The American Midland Naturalist* 61(1), pp. 1–67. doi: 10.2307/2422340.

Hudson, L.N., Isaac, N.J.B. and Reuman, D.C. 2013. The relationship between body mass and field metabolic rate among individual birds and mammals. *Journal of Animal Ecology* 82(5), pp. 1009–1020. doi: 10.1111/1365-2656.12086.

Hunt, A.P., Lucas, S.G. and Bircheff, P. 1993. *Biochronological Significance of the Co-occurrence of the Phytosaurs (Reptilia: Archosauria) Angistorhinus and Rutiodon in the Los Esteros Member of the Santa Rosa Formation, Santa Fe County, New Mexico, USA*. New Mexico Museum of Natural History Bulletins.

Hunt, A.P., Lucas, S.G. and Spielmann, J.A. 2006. Sexual dimorphism in a large brachyrostral phytosaur (Archosauria: Crurotarsi) from the Late Triassic of western North America. *New Mexico Museum of Natural History and Science Bulletin* 37, pp. 563–567.

Hutchinson, J.R. 2001a. The evolution of femoral osteology and soft tissues on the line to extant birds (Neornithes). *Zoological Journal of the Linnean Society* 131(2), pp. 169–197. doi: 10.1111/j.1096-3642.2001.tb01314.x.

Hutchinson, J.R. 2001b. The evolution of pelvic osteology and soft tissues on the line to extant birds (Neornithes). *Zoological Journal of the Linnean Society* 131(2), pp. 123–168. doi: 10.1111/j.1096-3642.2001.tb01313.x.

Hutchinson, J.R. 2002. The evolution of hindlimb tendons and muscles on the line to crown-group birds. *Comparative Biochemistry and Physiology Part A: Molecular & Integrative Physiology* 133(4), pp. 1051–1086. doi: 10.1016/S1095-6433(02)00158-7.

Hutchinson, J.R. and Gatesy, S.M. 2000. Adductors, abductors, and the evolution of archosaur locomotion. *Paleobiology* 26(4), pp. 734–751. doi: 10.1666/0094-8373(2000)026<0734:AAATEO>2.0.CO;2.

Hutchinson, J.R., Rankin, J.W., Rubenson, J., Rosenbluth, K.H., Siston, R.A. and Delp, S.L. 2015. Musculoskeletal modelling of an ostrich (*Struthio camelus*) pelvic limb: influence of limb orientation on muscular capacity during locomotion. *PeerJ* 3, p. e1001. doi: 10.7717/peerj.1001.

Hutson, J.D. and Hutson, K.N. 2012. Using the American alligator and a repeated-measures design to place constraints on *in vivo* shoulder joint range of motion in dinosaurs and other fossil archosaurs. *Journal of Experimental Biology*, p. jeb.074229. doi: 10.1242/jeb.074229.

Huxley, T.H. 1877. *The crocodilian remains found in the elgin sandstones: With remarks on the ichnites of Cummingstone*. HM Stationery Office.

Iijima, M. and Kubo, T. 2019. Comparative morphology of presacral vertebrae in extant crocodylians: taxonomic, functional and ecological implications. *Zoological Journal of the Linnean Society*. doi: 10.1093/zoolinnean/zly096.

Janis, C.M. and Keller, J.C. 2001. Modes of ventilation in early tetrapods: Costal aspiration as a key feature of amniotes. *Acta Palaeontologica Polonica* 46(2), pp. 137–170.

Jones, A.S. and Butler, R.J. 2018. A new phylogenetic analysis of Phytosauria (Archosauria: Pseudosuchia) with the application of continuous and geometric morphometric character coding. *PeerJ* 6, p. e5901. doi: 10.7717/peerj.5901.

Jones, K.E., Brocklehurst, R.J. and Pierce, S.E. 2021. AutoBend: an automated approach for estimating intervertebral joint function from bone-only digital models. *Integrative Organismal Biology* 3(1), p. obab026. doi: 10.1093/iob/obab026.

Junchang, L., Xingsheng, J., Yiming, S., Yihong, L., Guoping, W. and Azuma, Y. 2007. New nodosaurid dinosaur from the Late Cretaceous of Lishui, Zhejiang Province, China. *Acta Geologica Sinica - English Edition* 81(3), pp. 344–350. doi: 10.1111/j.1755-6724.2007.tb00958.x.

Kadono, H., Okada, T. and Ono, K. 1963. Electromyographic studies on the respiratory muscles of the chicken. *Poultry Science* 42(1), pp. 121–128. doi: 10.3382/ps.0420121.

Kambic, R.E., Biewener, A.A. and Pierce, S.E. 2017. Experimental determination of three-dimensional cervical joint mobility in the avian neck. *Frontiers in Zoology* 14(1), p. 37. doi: 10.1186/s12983-017-0223-z.

Kambic, R.E., Roberts, T.J. and Gatesy, S.M. 2014. Long-axis rotation: a missing degree of freedom in avian bipedal locomotion. *Journal of Experimental Biology*, p. jeb.101428. doi: 10.1242/jeb.101428.

Kardong, K.V. 2015. *Vertebrates: comparative anatomy, function, evolution*. Seventh edition. New York, NY: McGraw-Hill Education.

Kellner, A.W.A. 2003. Pterosaur phylogeny and comments on the evolutionary history of the group. *Geological Society, London, Special Publications* 217(1), pp. 105–137. doi: 10.1144/GSL.SP.2003.217.01.10.

Kiley, J.P., Kuhlmann, W.D. and Fedde, M.R. 1982. Ventilatory and blood gas adjustments in exercising isothermic ducks. *Journal of comparative physiology* 147(1), pp. 107–112. doi: 10.1007/BF00689298.

Kim, J.H. 2019. Multicollinearity and misleading statistical results. *Korean Journal of Anesthesiology* 72(6), pp. 558–569. doi: 10.4097/kja.19087.

Klein, W. and Owerkowicz, T. 2006. Function of intracoelomic septa in lung ventilation of amniotes: lessons from lizards. *Physiological and Biochemical Zoology* 79(6), pp. 1019–1032. doi: 10.1086/507656.

Klinkhamer, A.J., Wilhite, D.R., White, M.A. and Wroe, S. 2017. Digital dissection and three-dimensional interactive models of limb musculature in the Australian estuarine crocodile (*Crocodylus porosus*). *PLOS ONE* 12, p. e0175079.

Kuhn, M. 2008. Building predictive models in R using the *Caret* package. *Journal of Statistical Software* 28, pp. 1–26. doi: 10.18637/jss.v028.i05.

Kursa, M.B. and Rudnicki, W.R. 2010. Feature Selection with the *Boruta* Package. *Journal of Statistical Software* 36(11). doi: 10.18637/jss.v036.i11.

Kurzanov, S.M. 1976. Braincase structure in the carnosaur <i>Itemirus<i/> n. gen. and some aspects of the cranial anatomy of dinosaurs. *Paleontological Journal* 10(36), pp. 1–369.

Lamas, L.P., Main, R.P. and Hutchinson, J.R. 2014. Ontogenetic scaling patterns and functional anatomy of the pelvic limb musculature in emus (*Dromaius novaehollandiae*). *PeerJ* 2, p. e716. doi: 10.7717/peerj.716.

Lambertz, M. 2016. Recent advances on the functional and evolutionary morphology of the amniote respiratory apparatus: Morphology of the amniote respiratory apparatus. *Annals of the New York Academy of Sciences* 1365(1), pp. 100–113. doi: 10.1111/nyas.13022.

Leardi, J.M., Pol, D. and Clark, J.M. 2017. Detailed anatomy of the braincase of *Macelognathus vagans* Marsh, 1884 (Archosauria, Crocodylomorpha) using high resolution tomography and new insights on basal crocodylomorph phylogeny. *PeerJ* 5, p. e2801. doi: 10.7717/peerj.2801.

Leardi, J.M., Pol, D., Novas, F.E. and Suárez Riglos, M. 2015. The postcranial anatomy of *Yacarerani boliviensis* and the phylogenetic significance of the notosuchian postcranial skeleton. *Journal of Vertebrate Paleontology* 35(6), p. e995187. doi: 10.1080/02724634.2014.995187.

Levin, S., de Solórzano, S.L. and Scarr, G. 2017. The significance of closed kinematic chains to biological movement and dynamic stability. *Journal of Bodywork and Movement Therapies* 21(3), pp. 664–672. doi: 10.1016/j.jbmt.2017.03.012.

Levin, S.M. 2013. Closed kinematic chain mechanisms comprise the fundamental mechanics of biologic movement and stability. doi:https://www.researchgate.net/publication/256196463_Closed_kinematic_chain_mechanisms_comprise_the_fundamental_mechanics_of_biologic_movement_and_stability.

Li, J. and Downs, T.B.W. 1985. A revision of *Edentosuchus tienshanensis* Young from the Tugulu Group of Xinjiang Autonomous Region. *Vertebrata PalAsiatica* 23, pp. 196–206.

Liaw, A. and Wiener, M. 2002. Classification and regression by randomForest. *R News* 2, pp. 18–22.

Lio, G., Agnolin, F.L., Martinelli, A.G., Ezcurra, M.D. and Novas, F.E. 2018. New specimen of the enigmatic, Late Cretaceous crocodyliform *Neuquensuchus universitas* sheds light on the anatomy of the species. *Cretaceous Research* 83, pp. 62–74. doi: 10.1016/j.cretres.2017.09.014.

Liparini, A. and Schultz, C.L. 2013. A reconstruction of the thigh musculature of the extinct pseudosuchian *Prestosuchus chiniquensis* from the *Dinodontosaurus* Assemblage Zone (Middle Triassic Epoch), Santa Maria 1 Sequence, southern Brazil. *Geological Society, London, Special Publications* 379(1), pp. 441–468. doi: 10.1144/SP379.20.

Longrich, N.R. 2010. *Mojoceratops perifania*, a new chasmosaurine ceratopsid from the Late Campanian of Western Canada. *Journal of Paleontology* 84(4), pp. 681–694. doi: 10.1666/09-114.1.

Lord, R.D., Bellrose, F.C. and Cochran, W.W. 1962. Radiotelemetry of the Respiration of a Flying Duck. *Science* 137(3523), pp. 39–40. doi: 10.1126/science.137.3523.39.

Madzia, D., Boyd, C.A. and Mazuch, M. 2018. A basal ornithopod dinosaur from the Cenomanian of the Czech Republic. *Journal of Systematic Palaeontology* 16(11), pp. 967–979.

Madzia, D., Jagt, J.W.M. and Mulder, E.W.A. 2020. Osteology, phylogenetic affinities and taxonomic status of the enigmatic Late Maastrichtian ornithopod taxon *Orthomerus dolloi* (Dinosauria, Ornithischia). *Cretaceous Research* 108, p. 104334. doi: 10.1016/j.cretres.2019.104334.

Mai, Q. 2013. A review of discriminant analysis in high dimensions: Discriminant analysis in high dimensions. *Wiley Interdisciplinary Reviews: Computational Statistics* 5(3), pp. 190–197. doi: 10.1002/wics.1257.

Maidment, S.C. and Barrett, P.M. 2011a. The locomotor musculature of basal ornithischian dinosaurs. *Journal of Vertebrate Paleontology* 31(6), pp. 1265–1291.

Maidment, S.C.R. and Barrett, P.M. 2011b. A new specimen of *Chasmosaurus belli* (Ornithischia: Ceratopsidae), a revision of the genus, and the utility of postcrania in the taxonomy and systematics of ceratopsid dinosaurs. *Zootaxa* 2963(1), p. 1. doi: 10.11646/zootaxa.2963.1.1.

Maidment, S.C.R., Brassey, C. and Barrett, P.M. 2015. The postcranial skeleton of an exceptionally complete individual of the plated dinosaur *Stegosaurus stenops* (Dinosauria: Thyreophora) from the Upper Jurassic Morrison Formation of Wyoming, U.S.A. *PLOS ONE* 10(10), p. e0138352. doi: 10.1371/journal.pone.0138352.

Maina, J.N. 2002. *Functional Morphology of the Vertebrate Respiratory Systems*. Science Publishers.

Maina, J.N. 2007. Spectacularly robust! Tensegrity principle explains the mechanical strength of the avian lung. *Respiratory Physiology & Neurobiology* 155(1), pp. 1–10. doi: 10.1016/j.resp.2006.05.005.

Maina, J.N., Singh, P. and Moss, E.A. 2009. Inspiratory aerodynamic valving occurs in the ostrich, Struthio camelus lung: A computational fluid dynamics study under resting unsteady state inhalation. *Respiratory Physiology & Neurobiology* 169(3), pp. 262–270. doi: 10.1016/j.resp.2009.09.011.

Majka, M. 2019. Naivebayes: High performance implementation of the Naive Nayes algorithm in R.

Mammoto, T. and Ingber, D.E. 2010. Mechanical control of tissue and organ development. *Development* 137(9), pp. 1407–1420.

Manafzadeh, A.R. 2020. A practical guide to measuring ex vivo joint mobility using XROMM. *Integrative Organismal Biology* 2(1), p. obaa041. doi: 10.1093/iob/obaa041.

Manafzadeh, A.R. and Padian, K. 2018. ROM mapping of ligamentous constraints on avian hip mobility: Implications for extinct ornithodirans. *Proceedings of the Royal Society B: Biological Sciences* 285(1879), p. 20180727. doi: 10.1098/rspb.2018.0727.

Mannion, P.D. 2009. A rebbachisaurid sauropod from the Lower Cretaceous of the Isle of Wight, England. *Cretaceous Research* 30(3), pp. 521–526. doi: 10.1016/j.cretres.2008.09.005.

Mannion, P.D., Upchurch, P., Schwarz, D. and Wings, O. 2019. Taxonomic affinities of the putative titanosaurs from the Late Jurassic Tendaguru Formation of Tanzania: phylogenetic and biogeographic implications for eusauropod dinosaur evolution. *Zoological Journal of the Linnean Society* 185(3), pp. 784–909. doi: 10.1093/zoolinnean/zly068.

Mansfield, J.H. and Abzhanov, A. 2010. Hox expression in the American alligator and evolution of archosaurian axial patterning. *Journal of Experimental Zoology Part B: Molecular and Developmental Evolution* 314B(8), pp. 629–644. doi: 10.1002/jez.b.21364.

Marschner, I. 2011. glm2: Fitting generalized linear models with convergence problems. *The R Journal* 3, pp. 12–15.

Marsh, A.D., Smith, M.E., Parker, W.G., Irmis, R.B. and Kligman, B.T. 2020. Skeletal anatomy of *Acaenasuchus geoffreyi* Long and Murry, 1995 (Archosauria: Pseudosuchia) and its implications for the origin of the aetosaurian carapace. *Journal of Vertebrate Paleontology* 40(4), p. e1794885.

Marsh, O.C. 1871. Notice of some fossil mammals from the Tertiary Formation. *American Journal of Science* 2, pp. 35–44.

Maryañska, T. 1977. Ankylosauridae (Dinosauria) from Mongolia. *Acta Palaeontologica Polonica* 37, pp. 85–151.

Mateus, O., Maidment, S.C.R. and Christiansen, N.A. 2009. A new long-necked "sauropod-mimic" stegosaur and the evolution of the plated dinosaurs. *Proceedings: Biological Sciences* 276(1663), pp. 1815–1821.

Maxwell, E.E. 2008. Comparative embryonic development of the skeleton of the domestic turkey (*Meleagris gallopavo*) and other galliform birds. *Zoology* 111(3), pp. 242–257. doi: 10.1016/j.zool.2007.08.004.

Maxwell, E.E. and Larsson, H.C.E. 2009. Comparative ossification sequence and skeletal development of the postcranium of palaeognathous birds (Aves: Palaeognathae). *Zoological Journal of the Linnean Society* 157(1), pp. 169–196. doi: 10.1111/j.1096-3642.2009.00533.x.

McDonald, A.T., Maidment, S.C.R., Barrett, P.M., You, H. and Dodson, P. 2014. Osteology of the basal hadrosauroid *Equijubus normani* (Dinosauria, Ornithopoda) from the Early Cretaceous of China. In: *Hadrosaurs*. Bloomington and Indianapolis: Indiana University Press.

McDonald, A.T., Wolfe, D.G., Fowler, E.A.F. and Gates, T.A. 2021. A new brachylophosaurin (Dinosauria: Hadrosauridae) from the Upper Cretaceous Menefee Formation of New Mexico. *PeerJ* 9, p. e11084. doi: 10.7717/peerj.11084.

McKitrick, M.C. 1991. Phylogenetic analysis of avian hindlimb musculature.

Mehl, M.G. 1928. The Phytosauria of the Wyoming. *Journal of the Denison University Laboratories, Denison University* 28, pp. 141–172.

Meilak, E.A., Gostling, N.J., Palmer, C. and Heller, M.O. 2021. On the 3D nature of the magpie (aves: *pica pica*) functional hindlimb anatomy during the take-off jump. *Frontiers in Bioengineering and Biotechnology* 9.

Mellett, F.D. 1994. The pelvic limb of the ostrich (*Struthio camelus*). *Journal of the South African Veterinary Association* 65(1), pp. 5–9.

Melstrom, K.M. and Irmis, R.B. 2019. Repeated evolution of herbivorous crocodyliforms during the age of dinosaurs. *Current Biology* 29(14), pp. 2389-2395.e3. doi: 10.1016/j.cub.2019.05.076.

Mescher, A.L. and Junqueira, L.C.U. 2016. *Junqueira's basic histology: text and atlas*. Fourteenth edition. New York: Mcgraw-Hill Education.

Mivart, St.G. 1877. On the axial skeleton of the Struthionidce. *The Transactions of the Zoological Society of London* 10(1), pp. 1–52. doi: 10.1111/j.1096-3642.1877.tb00282.x.

Molnar, J.L., Pierce, S.E., Bhullar, B.-A.S., Turner, A.H. and Hutchinson, J.R. 2015. Morphological and functional changes in the vertebral column with increasing aquatic adaptation in crocodylomorphs. *Royal Society Open Science* 2(11), p. 150439. doi: 10.1098/rsos.150439.

Molnar, J.L., Pierce, S.E. and Hutchinson, J.R. 2014. An experimental and morphometric test of the relationship between vertebral morphology and joint stiffness in Nile crocodiles (*Crocodylus niloticus*). *Journal of Experimental Biology* 217(5), pp. 758–768. doi: 10.1242/jeb.089904.

Müller, L. 1927. Ergebnisse der Forschungsreisen Prof. E. Stromers in den Wüsten Ägypteus. In: Abhandlungen der Bayerischen Akademie der Wissenschaften. Mathematisch-Naturwissenschaftliche Abteilung. Oldenbourg Wissenschaftsverlag, pp. 1–97.

Müller, R.T., Langer, M.C., Bronzati, M., Pacheco, C.P., Cabreira, S.F. and Dias-Da-Silva, S. 2018a. Early evolution of sauropodomorphs: anatomy and phylogenetic relationships of a remarkably well-preserved dinosaur from the Upper Triassic of southern Brazil. *Zoological Journal of the Linnean Society* 184(4), pp. 1187–1248.

Müller, R.T., Langer, M.C. and Dias-da-Silva, S. 2018b. An exceptionally preserved association of complete dinosaur skeletons reveals the oldest long-necked sauropodomorphs. *Biology Letters* 14(11), p. 20180633. doi: 10.1098/rsbl.2018.0633.

Munns, S.L., Owerkowicz, T., Andrewartha, S.J. and Frappell, P.B. 2012. The accessory role of the diaphragmaticus muscle in lung ventilation in the estuarine crocodile *Crocodylus porosus*. *Journal of Experimental Biology* 215(5), pp. 845–852. doi: 10.1242/jeb.061952.

Murakami, G., Keniichi, A. and Tatsuo, S. 1991. Arrangement and innervation of the iliocostalis and longissimus muscles of the brown caiman (*Caiman crocodilus* fuscus: Alligatoridae, Crocodilia). *The American Journal of Anatomy* 192, pp. 241–256.

Naifeh, K.H., Huggins, S.E., Hoff, H.E., Hugg, T.W. and Norton, R.E. 1970. Respiratory patterns in crocodilian reptiles. *Respiration Physiology* 9(1), pp. 21–42. doi: 10.1016/0034-5687(70)90003-4.

Nascimento, P.M. and Zaher, H. 2010. A new species of *Baurusuchus* (Crocodyliformes, Mesoeucrocodylia) from the Upper Cretaceous of Brazil, with the first complete postcranial skeleton described for the Family Baurusuchidae. *Papéis Avulsos de Zoologia (São Paulo)*. doi: 10.1590/S0031-10492010002100001.

Nesbitt, S.J. 2011. The early evolution of archosaurs: relationships and the origin of major clades. *Bulletin of the American Museum of Natural History* 352, pp. 1–292. doi: 10.1206/352.1.

Nesbitt, S.J. et al. 2017. The earliest bird-line archosaurs and the assembly of the dinosaur body plan. *Nature* 544(7651), pp. 484–487. doi: 10.1038/nature22037.

Nesbitt, S.J., Desojo, J.B. and Irmis, R.B. 2013. Anatomy, phylogeny and palaeobiology of early archosaurs and their kin. *Geological Society, London, Special Publications* 379(1), pp. 1–7. doi: 10.1144/SP379.21.

Neumann, D.A. 2017. *Kinesiology of the musculoskeletal system-e-book: foundations for rehabilitation*. third. Elsevier Health Sciences.

Nobre, P.H. and Carvalho, I. de S. 2013. Postcranial skeleton of *Mariliasuchus amarali* Carvalho and Bertini, 1999 (Mesoeucrocodylia) from the Bauru Basin, Upper Cretaceous of Brazil. *Ameghiniana* 50(1), pp. 98–113. doi: 10.5710/AMGH.15.8.2012.500.

Norell, M.A. and Makovicky, P.J. 1999. Important features of the dromaeosaurid skeleton II: Information from newly collected specimens of *Velociraptor mongoliensis*. *American Museum Novitates* (3282), pp. 1–48.

Norman, D.B. 1980. On the ornithischian dinosaur *Iguanodon bernissartensis* from the Lower Cretaceous of Bernissart (Belgium). *Institut royal des Sciences naturelles de Belgique*, pp. 1–106.

Novas, F.E. et al. 2015. An enigmatic plant-eating theropod from the Late Jurassic period of Chile. *Nature* 522(7556), pp. 331–334. doi: 10.1038/nature14307.

Novas, F.E., Cambiaso, A.V. and Ambrosio, A. 2004. A new basal iguanodontian (Dinosauria, Ornithischia) from the Upper Cretaceous of Patagonia.

O'Connor, P.M. 2006a. Postcranial pneumaticity: An evaluation of soft-tissue influences on the postcranial skeleton and the reconstruction of pulmonary anatomy in archosaurs. *Journal of Morphology* 267(10), pp. 1199–1226. doi: 10.1002/jmor.10470.

O'Connor, P.M. 2006b. Postcranial pneumaticity: An evaluation of soft-tissue influences on the postcranial skeleton and the reconstruction of pulmonary anatomy in archosaurs. *Journal of Morphology* 267(10), pp. 1199–1226. doi: 10.1002/jmor.10470.

O'Connor, P.M. 2007. The postcranial axial skeleton of *Majungasaurus crenatissimus* (Theropoda: Abelisauridae) from the Late Cretaceous of Madagascar. *Journal of Vertebrate Paleontology* 27(sup2), pp. 127–163. doi: 10.1671/0272-4634(2007)27[127:TPASOM]2.0.CO;2.

O'Connor, P.M. and Claessens, L.P.A.M. 2005. Basic avian pulmonary design and flow-through ventilation in non-avian theropod dinosaurs. *Nature* 436(7048), pp. 253–256. doi: 10.1038/nature03716.

Organ, C.L. 2006. Thoracic epaxial muscles in living archosaurs and ornithopod dinosaurs. *The Anatomical Record Part A: Discoveries in Molecular, Cellular, and Evolutionary Biology* 288A(7), pp. 782–793. doi: 10.1002/ar.a.20341.

Ortega, F., Gasparini, Z., Buscalioni, A.D. and Calvo, J.O. 2000. A new species of *Araripesuchus* (Crocodylomorpha, Mesoeucrocodylia) from the lower Cretaceous of Patagonia (Argentina). *Journal of Vertebrate Paleontology* 20(1), pp. 57–76. doi: 10.1671/0272-4634(2000)020[0057:ANSOAC]2.0.CO;2.

Ostrom, J.H. 1969. Osteology of *Deinonychus antirrhopus*, an unusual theropod from the Lower Cretaceous of Montana. *Bulletin of the Peabody Museum of Natural History* 30, pp. 1–165.

Ostrom, J.H. 1978. The osteology of *Compsognathus longipes* WAGNER. *Zitteliana* 4, pp. 73–118.

Otero, A. and Pol, D. 2013. Postcranial anatomy and phylogenetic relationships of *Mussaurus patagonicus* (Dinosauria, Sauropodomorpha). *Journal of Vertebrate Paleontology* 33(5), pp. 1138–1168. doi: 10.1080/02724634.2013.769444.

Paradis, E., Claude, J. and Strimmer, K. 2004. APE: analyses of phylogenetics and evolution in R language. *Bioinformatics* 20(2), pp. 289–290. doi: 10.1093/bioinformatics/btg412.

Park, J.-Y. et al. 2021. A new ankylosaurid skeleton from the Upper Cretaceous Baruungoyot Formation of Mongolia: its implications for ankylosaurid postcranial evolution. *Scientific Reports* 11(1), p. 4101. doi: 10.1038/s41598-021-83568-4.

Patak, A.E. and Baldwin, J. 1998. Pelvic limb musculature in the emu *Dromaius novaehollandiae* (Aves: Struthioniformes: Dromaiidae): Adaptations to high-speed running. *Journal of Morphology* 238(1), pp. 23–37.

Paxton, H., Anthony, N.B., Corr, S.A. and Hutchinson, J.R. 2010. The effects of selective breeding on the architectural properties of the pelvic limb in broiler chickens: A comparative study across modern and ancestral populations. *Journal of Anatomy* 217(2), pp. 153–166.

Perry, S.F. 1988. Functional morphology of the lungs of the nile crocodile, *Crocodylus niloticus:* non-respiratory parameters. *Journal of Experimental Biology* 134(1), pp. 99–117. doi: 10.1242/jeb.134.1.99.

Perry, S.F. and Duncker, H.-R. 1980. Interrelationship of static mechanical factors and anatomical structure in lung evolution. *Journal of Comparative Physiology B* 138(4), pp. 321–334. doi: 10.1007/BF00691567.

Perry, S.F., Lambertz, M. and Schmitz, A. 2019a. *Respiratory Biology of Animals: evolutionary and functional morphology*. Oxford University Press.

Perry, S.F., Lambertz, M. and Schmitz, A. 2019b. Respiratory faculties of amphibious and terrestrial craniotes. In: *Respiratory Biology of Animals: evolutionary and functional morphology*. Oxford University Press, pp. 139–163.

Persons IV, W.S. and Currie, P.J. 2011. The tail of *Tyrannosaurus*: Reassessing the size and locomotive importance of the M. caudofemoralis in non-avian theropods. *The Anatomical Record: Advances in Integrative Anatomy and Evolutionary Biology* 294(1), pp. 119–131.

Peters, S.E. and McClennen, M. 2015. The Paleobiology Database application programming interface. *Paleobiology* 42(1), pp. 1–7. doi: 10.1017/pab.2015.39.

Pittman, M., O'Connor, J., Field, D.J., Turner, A.H., Waisum, M. and Xu, X. 2020. Pennaraptora systematics. *Bulletin of the American Museum of Natural History* 440, pp. 7–36.

Pol, D. and Goloboff, P.A. 2020. The impact of unstable taxa in coelurosaurian phylogeny and resampling support measures for parsimony analyses.

Pol, D. and Leardi, J.M. 2015. Diversity patterns of Notosuchia (Crocodyliformes, Mesoeucrocodylia) during the Cretaceous of Gondwana. *Publicación Electrónica de la Asociación Paleontológica Argentina*. doi: 10.5710/PEAPA.10.06.2015.108.

Pol, D., Leardi, J.M., Lecuona, A. and Krause, M. 2012. Postcranial anatomy of *Sebecus icaeorhinus* (Crocodyliformes, Sebecidae) from the Eocene of Patagonia. *Journal of Vertebrate Paleontology* 32(2), pp. 328–354. doi: 10.1080/02724634.2012.646833.

Pol, D. and Powell, J.E. 2011. A new sebecid mesoeucrocodylian from the Rio Loro Formation (Palaeocene) of north-western Argentina. *Zoological Journal of the Linnean Society* 163(suppl_1), pp. S7–S36.

Powell, F.L. 2015. Respiration. In: *Sturkie's Avian Physiology*. Elsevier, pp. 301–336. doi: 10.1016/B978-0-12-407160-5.00013-0.

Powell, F.L. and Wagner, P.D. 1982. Ventilation-perfusion inequality in avian lungs. *Respiration Physiology* 48(2), pp. 233–241. doi: 10.1016/0034-5687(82)90083-4.

Prondvai, E., Stein, K.H.W., de Ricqlès, A. and Cubo, J. 2014. Development-based revision of bone tissue classification: the importance of semantics for science: Development-based bone tissue classification. *Biological Journal of the Linnean Society* 112(4), pp. 799–816. doi: 10.1111/bij.12323.

Puértolas Pascual, E., Rabal Garcés, R. and Canudo, J. 2015. Exceptional crocodylomorph biodiversity of "La Cantalera" site (lower Barremian; Lower Cretaceous) in Teruel, Spain. *Palaeontologia Electronica*. doi: 10.26879/514.

Qiao, Z., Zhou, L. and Huang, J.Z. 2008. Effective linear discriminant analysis for high dimensional, low sample size data. *Proceedings of the World Congress on Engineering* 2.

R Core Team. 2021. R: A language and environment for statistical computing. R Foundation for Statistical Computing.

Rauhut, O.W.M., Remes, K., Fechner, R., Cladera, G. and Puerta, P. 2005. Discovery of a short-necked sauropod dinosaur from the Late Jurassic period of Patagonia. *Nature* 435(7042), pp. 670–672. doi: 10.1038/nature03623.

Raven, T.J. and Maidment, S.C.R. 2017. A new phylogeny of Stegosauria (Dinosauria, Ornithischia). *Palaeontology* 60(3), pp. 401–408. doi: 10.1111/pala.12291.

Renous, S., Gasc, J. -P., Bels, V.L. and Wicker, R. 2002. Asymmetrical gaits of juvenile *Crocodylus johnstoni*, galloping Australian crocodiles. *Journal of Zoology* 256(3), pp. 311–325. doi: 10.1017/S0952836902000353.

Revelle, W. 2022. Psych: Procedures for psychological, psychometric, and personality research.

Rhodes, M.M., Funston, G.F. and Currie, P.J. 2020. New material reveals the pelvic morphology of Caenagnathidae (Theropoda, Oviraptorosauria). *Cretaceous Research* 114, p. 104521. doi: 10.1016/j.cretres.2020.104521.

Rhodes, M.M., Henderson, D.M. and Currie, P.J. 2021. Maniraptoran pelvic musculature highlights evolutionary patterns in theropod locomotion on the line to birds. *PeerJ* 9, p. e10855. doi: 10.7717/peerj.10855.

Rio, J.P. and Mannion, P.D. 2021. Phylogenetic analysis of a new morphological dataset elucidates the evolutionary history of Crocodylia and resolves the long-standing gharial problem. *PeerJ* 9, p. e12094. doi: 10.7717/peerj.12094.

Ristevski, J., Young, M.T., de Andrade, M.B. and Hastings, A.K. 2018. A new species of *Anteophthalmosuchus* (Crocodylomorpha, Goniopholididae) from the Lower Cretaceous of the Isle of Wight, United Kingdom, and a review of the genus. *Cretaceous Research* 84, pp. 340–383. doi: 10.1016/j.cretres.2017.11.008.

Rivera Sylva, H.E. 2012. Bite marks of a large theropod on an hadrosaur limb bone from Coahuila, Mexico. *Boletín de la Sociedad Geológica Mexicana* 64(1), pp. 155–159. doi: 10.18268/BSGM2012v64n1a11.

Roberto-Da-Silva, L., Müller, R.T., França, M.A.G. de, Cabreira, S.F. and Dias-Da-Silva, S. 2020. An impressive skeleton of the giant top predator *Prestosuchus chiniquensis* (Pseudosuchia: Loricata) from the Triassic of Southern Brazil, with phylogenetic remarks. *Historical Biology* 32(7), pp. 976–995. doi: 10.1080/08912963.2018.1559841.

Romer, A.S. 1923. Crocodilian pelvic muscles and their avian and reptilian homologues. *Bulletin of the American Museum of Natural History* 48, pp. 533–552.

Romer, A.S. 1956. The axial skeleton. In: *The osteology of reptiles*. Illinois: University of Chicago Press, pp. 275–279.

Romer, A.S. 1966. *Vertebrate paleontology*. 3rd ed. Chicago: University of Chicago Press.

Rose, K.A., Tickle, P.G., Elsey, R.M., Sellers, W.I., Crossley, D.A. and Codd, J.R. 2021. Scaling of axial muscle architecture in juvenile *Alligator mississippiensis* reveals an enhanced performance capacity of accessory breathing mechanisms. *Journal of Anatomy* 239(6), pp. 1273–1286.

Rowe, T. 1986. Homology and evolution of the deep dorsal thigh musculature in birds and other Reptilia. *Journal of Morphology* 189(3), pp. 327–346.

RStudio Team. 2020. RStudio: Integrated Development for R.

Rummy, P. et al. 2022. A new paralligatorid (Crocodyliformes, Neosuchia) from the mid-Cretaceous of Jilin Province, northeastern China. *Cretaceous Research* 129, p. 105018. doi: 10.1016/j.cretres.2021.105018.

Ryan, M.J., Chinnery-Allgeier, B.J. and Eberth, D.A. 2010. *New Perspectives on Horned Dinosaurs: The Royal Tyrrell Museum Ceratopsian Symposium*. Indiana University Press.

Ryan, M.J., Evans, D.C., Currie, P.J. and Loewen, M.A. 2014. A new chasmosaurine from northern Laramidia expands frill disparity in ceratopsid dinosaurs. *Naturwissenschaften* 101(6), pp. 505–512. doi: 10.1007/s00114-014-1183-1.

Salgado, L. and Gasparini, Z. 2006. Reappraisal of an ankylosaurian dinosaur from the Upper Cretaceous of James Ross Island (Antarctica). *Geodiversitas* 28(1), pp. 119–135.

Salisbury, S.W., Molnar, R.E., Frey, E. and Willis, P.M.A. 2006. The origin of modern crocodyliforms: new evidence from the Cretaceous of Australia. *Proceedings of the Royal Society B: Biological Sciences* 273(1600), pp. 2439–2448. doi: 10.1098/rspb.2006.3613.

Scaal, M. 2021. Development of the amniote ventrolateral body wall. *Developmental Dynamics* 250(1), pp. 39–59. doi: 10.1002/dvdy.193.

Schachner, E.R., Farmer, C.G., McDonald, A.T. and Dodson, P. 2011. Evolution of the dinosauriform respiratory apparatus: New evidence from the postcranial axial skeleton. *The Anatomical Record: Advances in Integrative Anatomy and Evolutionary Biology* 294(9), pp. 1532–1547. doi: 10.1002/ar.21439.

Schachner, E.R., Hutchinson, J.R. and Farmer, C. 2013. Pulmonary anatomy in the Nile crocodile and the evolution of unidirectional airflow in Archosauria. *PeerJ* 1, p. e60. doi: 10.7717/peerj.60.

Schachner, E.R., Lyson, T.R. and Dodson, P. 2009. Evolution of the respiratory system in nonavian theropods: evidence from rib and vertebral morphology. *The Anatomical Record: Advances in Integrative Anatomy and Evolutionary Biology* 292(9), pp. 1501–1513. doi: 10.1002/ar.20989.

Scheid, P. 1979. Mechanisms of gas exchange in bird lungs. In: *Reviews of Physiology, Biochemistry and Pharmacology, Volume 86*. Reviews of Physiology, Biochemistry and Pharmacology. Berlin, Heidelberg: Springer Berlin Heidelberg, pp. 137–186. Available at: http://link.springer.com/10.1007/BFb0031533 [Accessed: 11 January 2023].

Scheid, P. and Piiper, J. 1969. Volume, ventilation and compliance of the respiratory system in the domestic fowl. *Respiration Physiology* 6(3), pp. 298–308. doi: 10.1016/0034-5687(69)90029-2.

Schliep, K.P. 2011. Phangorn: phylogenetic analysis in R. *Bioinformatics* 27(4), pp. 592–593.

Schmidt-Nielsen, K., Kanwisher, J., Lasiewski, R.C., Cohn, J.E. and Bretz, W.L. 1969. Temperature regulation and respiration in the ostrich. *The Condor* 71(4), pp. 341–352. doi: 10.2307/1365733.

Schneider, C.A., Rasband, W.S. and Eliceiri, K.W. 2012. NIH Image to ImageJ: 25 years of image analysis. *Nature Methods* 9(7), pp. 671–675. doi: 10.1038/nmeth.2089.

Schott, R.K. and Evans, D.C. 2016. Cranial variation and systematics of *Foraminacephale brevis* gen. nov. and the diversity of pachycephalosaurid dinosaurs (Ornithischia: Cerapoda) in the Belly River Group of Alberta, Canada. *Zoological Journal of the Linnean Society*. doi: 10.1111/zoj.12465.

Schwarz-Wings, D. 2009. Reconstruction of the thoracic epaxial musculature of diplodocid and dicraeosaurid sauropods. *Journal of Vertebrate Paleontology* 29(2), pp. 517–534. doi: 10.1671/039.029.0229.

Seeley, H.G. 1883. On the dinosaurs from the Maastricht beds. *Quarterly Journal of the Geological Society* 39(1–4), pp. 246–253.

Sellés, A.G. et al. 2020. A small Cretaceous crocodyliform in a dinosaur nesting ground and the origin of sebecids. *Scientific Reports* 10(1), p. 15293. doi: 10.1038/s41598-020-71975-y.

Senter, P. and Robins, J.H. 2005. Range of motion in the forelimb of the theropod dinosaur Acrocanthosaurus atokensis, and implications for predatory behaviour. *Journal of Zoology* 266(3), pp. 307–318. doi: 10.1017/S0952836905006989.

Sereno, P. and Larsson, H. 2009. Cretaceous crocodyliforms from the Sahara. *ZooKeys* 28, pp. 1–143. doi: 10.3897/zookeys.28.325.

Sereno, P.C. 1991. Basal Archosaurs: Phylogenetic Relationships and Functional Implications. *Journal of Vertebrate Paleontology* 11(sup004), pp. 1–53. doi: 10.1080/02724634.1991.10011426.

Sereno, P.C. 2005. The logical basis of phylogenetic taxonomy. *Systematic Biology* 54(4), pp. 595–619.

Shan, H., Wu, X., Cheng, Y. and Sato, T. 2009. A new tomistomine (Crocodylia) from the Miocene of Taiwan. Sues, H.-D. ed. *Canadian Journal of Earth Sciences* 46(7), pp. 529–555. doi: 10.1139/E09-036.

Shapiro, F. and Wu, J. 2019. Woven bone overview: Structural classification based on its integral role in developmental, repair and pathological bone formation throughout vertebrate groups. *European Cells and Materials* 38, pp. 137–167. doi: 10.22203/eCM.v038a11.

Shufeldt, R.W. 1988. *The myology of the raven (Corvus corax sinuatus): A guide to the study of the muscular system in birds*. Macmillan and Company.

Shuvalov, V.F. 2003. The Cretaceous stratigraphy and palaeobiology of Mongolia. In: *The Age of Dinosaurs in Russia and Mongolia*. Cambridge University Press, pp. 256–278.

Shwartz, Y., Blitz, E. and Zelzer, E. 2013. One load to rule them all: Mechanical control of the musculoskeletal system in development and aging. *Differentiation* 86(3), pp. 104–111. doi: 10.1016/j.diff.2013.07.003.

Simmons, D.J., Menton, D.N., Miller, S. and Lozano, R. 1993. Periosteal attachment fibers in the rat calvarium. *Calcified Tissue International* 53(6), pp. 424–427. doi: 10.1007/BF03549786.

Sire, J.-Y. and Meunier, F.J. 1994. The canaliculi of Williamson in holostean bone (osteichthyes, actinopterygii): a structural and ultrastructural study. *Acta Zoologica* 75(3), pp. 235–247. doi: 10.1111/j.1463-6395.1994.tb01211.x.

Sivaraj, K.K. and Adams, R.H. 2016. Blood vessel formation and function in bone. *Development* 143(15), pp. 2706–2715. doi: 10.1242/dev.136861.

Smith, N.C., Wilson, A.M., Jespers, K.J. and Payne, R.C. 2006. Muscle architecture and functional anatomy of the pelvic limb of the ostrich (*Struthio camelus*). *Journal of Anatomy* 209(6), pp. 765–779.

Sober, E. 1988. *Reconstructing the past: Parsimony, evolution, and inference*. Cambridge, Mass: MIT press.

Souza, R.G. de, Hörmanseder, B.M., Figueiredo, R.G. and Campos, D. de A. 2020. Description of new dyrosaurid specimens from the Late Cretaceous–Early Paleogene of New Jersey, United States, and comments on Hyposaurus systematics. *Historical Biology* 32(10), pp. 1377–1393.

Stefanic, C.M. and Nesbitt, S.J. 2018. The axial skeleton of *Poposaurus langstoni* (Pseudosuchia: Poposauroidea) and its implications for accessory intervertebral articulation evolution in pseudosuchian archosaurs. *PeerJ* 6, p. e4235. doi: 10.7717/peerj.4235.

Stickford, A.S.L. and Stickford, J.L. 2014. Ventilation and locomotion in humans: Mechanisms, implications, and perturbations to the coupling of these two rhythms. *Springer Science Reviews* 2(1–2), pp. 95–118. doi: 10.1007/s40362-014-0020-4.

Stocker, M.R. 2012. A new taxonomic arrangement for *Paleorhinus scurriensis*. *Earth and Environmental Science Transactions of The Royal Society of Edinburgh* 103(3–4), pp. 251–263. doi: 10.1017/S1755691013000340.

Stocker, M.R., Zhao, L.-J., Nesbitt, S.J., Wu, X.-C. and Li, C. 2017. A short-snouted, Middle Triassic phytosaur and its implications for the morphological evolution and biogeography of Phytosauria. *Scientific Reports* 7(1), pp. 1–9.

Sullivan, C. 2007. *Function and evolution of the hind limb in Triassic archosaurian reptiles*. PhD Dissertation, Harvard University.

Tanke, D. and Currie, P.J. 1998. Head-biting behavior in theropod dinosaurs: paleopathological evidence.

Terray, L., Plateau, O., Abourachid, A., Böhmer, C., Delapré, A., de la Bernardie, X. and Cornette, R. 2020. Modularity of the neck in birds (Aves). *Evolutionary Biology* 47(2), pp. 97–110. doi: 10.1007/s11692-020-09495-w.

Tickle, P., Nudds, R. and Codd, J. 2009. Uncinate process length in birds scales with resting metabolic rate. Lucia, A. ed. *PLoS ONE* 4(5), p. e5667. doi: 10.1371/journal.pone.0005667.

Tickle, P.G. and Codd, J.R. 2009. Ontogenetic development of the uncinate processes in the domestic turkey (*Meleagris gallopavo*). *Poultry Science* 88(1), pp. 179–184. doi: 10.3382/ps.2008-00349.

Tickle, P.G., Ennos, A.R., Lennox, L.E., Perry, S.F. and Codd, J.R. 2007. Functional significance of the uncinate processes in birds. *Journal of Experimental Biology* 210(22), pp. 3955–3961. doi: 10.1242/jeb.008953.

Townson, R. 1799. *Tracts and observations in natural history and physiology*. London: Printed for the author by J. White.

Tsai, H.P., Turner, M.L., Manafzadeh, A.R. and Gatesy, S.M. 2020. Contrast-enhanced XROMM reveals in vivo soft tissue interactions in the hip of Alligator mississippiensis. *Journal of Anatomy* 236(2), pp. 288–304. doi: 10.1111/joa.13101.

Tsuihiji, T. 2007. Homologies of the longissimus, iliocostalis, and hypaxial muscles in the anterior presacral region of extant Diapsida. *Journal of Morphology* 268(11), pp. 986–1020.

Tucker, V.A. 1972. Respiration during flight in birds. *Respiration Physiology* 14, pp. 75–82.

Turner, A.H. 2006. Osteology and phylogeny of a new species of *Araripesuchus* (Crocodyliformes: Mesoeucrocodylia) from the Late Cretaceous of Madagascar. *Historical Biology* 18(3), pp. 255–369. doi: 10.1080/08912960500516112.

Turner, A.H. and Calvo, J.O. 2005. A new sebecosuchian crocodyliform from the Late Cretaceous of Patagonia. *Journal of Vertebrate Paleontology* 25(1), pp. 87–98.

Turner, A.H., Makovicky, P.J. and Norell, M.A. 2012. A review of dromaeosaurid systematics and paravian phylogeny. *Bulletin of the American Museum of Natural History* 371, pp. 1–206. doi: 10.1206/748.1.

Uriona, T.J. and Farmer, C.G. 2008. Recruitment of the diaphragmaticus, ischiopubis and other respiratory muscles to control pitch and roll in the American alligator (*Alligator mississippiensis*). *Journal of Experimental Biology* 211(7), pp. 1141–1147. doi: 10.1242/jeb.015339.

Vabalas, A., Gowen, E., Poliakoff, E. and Casson, A.J. 2019. Machine learning algorithm validation with a limited sample size. *PLOS ONE* 14(11), p. e0224365. doi: 10.1371/journal.pone.0224365.

Vatcheva, K.P., Lee, M., McCormick, J.B. and Rahbar, M.H. 2016. Multicollinearity in regression analyses conducted in epidemiologic studies. *Epidemiology (Sunnyvale, Calif.)* 6(2), p. 227. doi: 10.4172/2161-1165.1000227.

Venables, W.N. and Ripley, B.D. 2013. *Modern applied statistics with S-Plus*. Springer Science & Business Media.

Verstappen, M., Aerts, P. and Van Damme, R. 1998. Terrestrial locomotion in the black-billed magpie: kinematic analysis of walking, running and out-of-phase hopping. *Journal of Experimental Biology* 203(14), pp. 2159–2170.

Walker, A.D. 1990. A revision of *Sphenosuchus acutus* Haughton, a crocodylomorph reptile from the Elliot Formation (Late Triassic or Early Jurassic) of South Africa. *Philosophical Transactions: Biological Sciences* 330(1256), pp. 1–120.

Walker, W.F. and Liem, K.F. 2001. *Functional Anatomy of the Vertebrates: An Evolutionary Perspective*. New York: Fort Worth : Harcourt College Publishers.

Wang, M. and Zhou, Z. 2017. The evolution of birds with implications from new fossil evidences. *The biology of the avian respiratory system: evolution, development, structure and function*, pp. 1–26.

Wang, X. et al. 2018. Archaeorhynchus preserving significant soft tissue including probable fossilized lungs. *Proceedings of the National Academy of Sciences* 115(45), pp. 11555–11560. doi: 10.1073/pnas.1805803115.

Wang, X., Kellner, A.W.A., Zhou, Z. and Campos, D. de A. 2005. Pterosaur diversity and faunal turnover in Cretaceous terrestrial ecosystems in China. *Nature* 437(7060), pp. 875–879. doi: 10.1038/nature03982.

Wedel, M.J. 2006. Origin of postcranial skeletal pneumaticity in dinosaurs. *Integrative Zoology* 1(2), pp. 80–85. doi: 10.1111/j.1749-4877.2006.00019.x.

Wedel, M.J. 2009a. Evidence for bird-like air sacs in saurischian dinosaurs. *Journal of Experimental Zoology Part A: Ecological Genetics and Physiology* 311A(8), pp. 611–628. doi: 10.1002/jez.513.

Wedel, M.J. 2009b. Evidence for bird-like air sacs in saurischian dinosaurs. *Journal of Experimental Zoology Part A: Ecological Genetics and Physiology* 311A(8), pp. 611–628. doi: 10.1002/jez.513.

Weinbaum, J.C. 2013. Postcranial skeleton of *Postosuchus kirkpatricki* (Archosauria: Paracrocodylomorpha), from the Upper Triassic of the United States. *Geological Society, London, Special Publications* 379(1), pp. 525–553. doi: 10.1144/SP379.7.

Weiner, S. and Wagner, H.D. 1998. The material bone: Structure-mechanical function relations. *Annual Review of Materials Science* 28(1), pp. 271–298. doi: 10.1146/annurev.matsci.28.1.271.

Weishampel, D.B., Dodson, P. and Osmólska, H. 2007. *The Dinosauria*. Univ of California Press.

Welty, J.C. and Baptista, L. 1972. *The life of birds*. London: W. B. Saunders and Co.

Wickham, H. 2009. *ggplot2*. New York, NY: Springer New York. Available at: http://link.springer.com/10.1007/978-0-387-98141-3 [Accessed: 12 January 2023].

Wilson, J.A. 2006. Anatomical nomenclature of fossil vertebrates: standardized terms or 'lingua franca'? *Journal of Vertebrate Paleontology* 26(3), pp. 511–518.

Wilson, J.A., D'Emic, M.D., Ikejiri, T., Moacdieh, E.M. and Whitlock, J.A. 2011. A Nomenclature for Vertebral Fossae in Sauropods and Other Saurischian Dinosaurs. Farke, A. ed. *PLoS ONE* 6(2), p. e17114. doi: 10.1371/journal.pone.0017114.

Witmer, L.M. 1995. The extant phylogenetic bracket and the importance of reconstructing soft tissues in fossils. *Functional morphology in vertebrate paleontology* 1, pp. 19–33.

Wu, X.C. 1981. The discovery of a new thecodont from north east Shanxi. *Vertebrata PalAsiatica* 19, pp. 122–132.

Wu, X.-C. and Chatterjee, S. 1993. *Dibothrosuchus elaphros*, a crocodylomorph from the Lower Jurassic of China and the phylogeny of the Sphenosuchia. *Journal of Vertebrate Paleontology* 13(1), pp. 58–89. doi: 10.1080/02724634.1993.10011488.

Xu, X. et al. 2015. The taxonomic status of the Late Cretaceous dromaeosaurid *Linheraptor exquisitus* and its implications for dromaeosaurid systematics. *Vertebrata PalAsiatica* 53, pp. 29–62.

Xu, X., Zhou, Z. and Wang, X. 2000. The smallest known non-avian theropod dinosaur. *Nature* 408(6813), pp. 705–708. doi: 10.1038/35047056.

Yates, A.M., Wedel, M.J. and Bonnan, M.F. 2012. The Early Evolution of Postcranial Skeletal Pneumaticity in Sauropodomorph Dinosaurs. *Acta Palaeontologica Polonica* 57(1), pp. 85–100. doi: 10.4202/app.2010.0075.

York, J.M. et al. 2017. Respiratory mechanics of eleven avian species resident at high and low altitude. *Journal of Experimental Biology* 220(6), pp. 1079–1089. doi: 10.1242/jeb.151191.

Yu, C., Prieto-Marquez, A., Chinzorig, T., Badamkhatan, Z. and Norell, M. 2020. A neoceratopsian dinosaur from the early Cretaceous of Mongolia and the early evolution of ceratopsia. *Communications Biology* 3(1), pp. 1–8. doi: 10.1038/s42003-020-01222-7.

Yu, G., Smith, D.K., Zhu, H., Guan, Y. and Lam, T.T.-Y. 2017. GGtree: an R package for visualization and annotation of phylogenetic trees with their covariates and other associated data. *Methods in Ecology and Evolution* 8(1), pp. 28–36. doi: 10.1111/2041-210X.12628.

Zhou, S.W. 1983. A nearly complete skeleton of a stegosaur from the Middle Jurassic of Dashanpu, Zigong, Sichuan. *Journal of Chengdu University of Geology* 1, pp. 15–26.

Zhou, Z.H., Wang, X.L., Zhang, F.C. and Xu, X. 2000. Important features of *Caudipteryx* - evidence from two nearly complete new specimens. *Vertebrata PalAsiatica* 38(4), pp. 241–254.

Zimmer, K. 1935. Beiträge zur Mechanik der Atmung bei den Vögeln in Stand-und Flug. *Zoologica* 33, pp. 1–69.

Zinoviev, A.V. 2006. Notes on the hind limb myology of the ostrich (*Struthio camelus*). *Ornithologia* 33, pp. 53–62.

Zusi, R.L. and Bentz, G.D. 1984. Myology of the purple-throated Carib (*Eulampis jugularis*) and other hummingbirds (Aves: Trochilidae). *Smithsonian Contributions to Zoology* (385), pp. 1–70. doi: 10.5479/si.00810282.385.